

Institut für Geologische Wissenschaften  
**Planetologie und Fernerkundung**  
Freie Universität Berlin

HABILITATIONSSCHRIFT

# The Morphology of Volatile-rich Regoliths on Asteroids and Comets



verfasst von  
*Dr. Katharina A. Otto*  
aus Geseke, Germany

Berlin, April 2023





*To my family - Jon and Tristan*



# Abstract

Recent space missions to asteroids and comets, have revealed diverse morphologic features on multiple scales that can be linked to the presence of volatiles in the regolith of small bodies. The research presented in this thesis investigates the physics of these volatile-related morphologies addressing (1) the relationship between surface morphologies and the presence of volatiles, (2) the regolith's volatile content linked to morphologic features, (3) the difference of asteroidal and cometary outgassing, and (4) the role of volatiles in the evolution of the surfaces and interiors of small bodies. For a comprehensive understanding a combination of three analysis techniques was applied including the geologic interpretation of remote sensing and in situ space mission data, the investigation of sublimation processes on the morphology of volatile-rich analogue materials in the laboratory, and discrete element method modelling assessing the physical and mechanical properties of cometary regolith through the simulation of dynamic surface processes.

While morphologic features of many small bodies are considered in this thesis, a focus lies on those observed by the Dawn, Rosetta and Hayabusa2 missions. They include concentric crater fractures on Ceres and their relation to a volatile-rich subsurface layer, pitted impact deposits in volatile-rich ejecta on Vesta, mass-wasting features in volatile-poor/rich regoliths on Vesta and Ceres, aeolian-like features created by volatile-driven particle redistribution on comet 67P/Churyumov-Gerasimenko, and pond-like features generated through volatile fluidisation of Vesta's regolith. In situ analyses of Ryugu and 67P/Churyumov-Gerasimenko revealed a link between volatile sublimation and surface roughness and the similarity of Ryugu's regolith and that of aqueously altered carbonaceous chondrites. In the laboratory, analogue materials and the effect of volatile content, particle shape, insolation and organic material on the morphologic evolution of cliffs were established. Discrete element method modelling extracted the mechanical and physical regolith properties by simulating boulder drops and cliff collapses on 67P/Churyumov-Gerasimenko and helped constraining the formation process of aeolian-like features.

The work shows that morphologic features give access to the composition, geology and evolution of small solar system bodies and paves the way for future research involving other planetary objects and new data sets.



# Zusammenfassung

Weltraummissionen zu Asteroiden und Kometen zeigen vielseitige Morphologien auf verschiedenen Größenordnungen, die mit dem Vorhandensein volatiler Materialien im Regolith von Kleinkörpern in Verbindung gebracht werden können. Die hier vorgestellte Habilitationsschrift befasst sich mit der Physik dieser Morphologien und erläutert (1) die Verbindung zwischen Oberflächenmorphologien und dem Vorhandensein von volatilen Materialien, (2) den Gehalt an volatilen Materialien im Regolith in Verbindung mit diesen Morphologien, (3) den Unterschied zwischen Asteroiden- und Kometenaktivität (4) die Rolle von volatilen Materialien bei der Entwicklung kleiner Körper. Dazu wurde eine Kombination von drei Analysetechniken angewandt: die geologische Interpretation von Fernerkundungs- und In-situ-daten, die Untersuchung von Sublimationsprozessen im Labor und die diskrete Elemente Modellierung dynamischer Prozesse.

Während viele Kleinkörpermorphologien in dieser Arbeit berücksichtigt werden, stehen die von den Missionen Dawn, Rosetta und Hayabusa2 im Vordergrund. Sie umfassen durch eine volatilreiche unterirdische Schicht erzeugte konzentrische Rissstrukturen um Krater auf Ceres, Sublimationssenken in volatilreichem Auswurfmaterial auf Vesta, Massenbewegungen in volatilarmem/-reichem Regolith auf Vesta und Ceres, ausgasungsinduzierte äolisch-ähnliche Strukturen auf 67P/Churyumov-Gerasimenko und flache, durch Fluidisierung erzeugte, Ablagerungen auf Vesta. In-situ-analysen zeigen auch den Zusammenhang zwischen Sublimation und Oberflächenrauigkeit sowie die Ähnlichkeit der Regolithtextur von Ryugu und wässrig veränderten kohligen Chondriten. Darüber hinaus wurden im Labor kometare Analogmaterialien hergestellt und die Auswirkungen des Gehalts an Eis, der Partikelform, der Energieeinstrahlung und des organischen Materials auf die morphologische Entwicklung von Klippen untersucht. Diskrete Elemente Modellierungen leiteten mechanische und physikalische Regolitheigenschaften durch die Simulation von Gesteins- und Klippenstürzen auf Kometen her. Sie tragen auch dazu bei den Entstehungsprozess von äolisch-ähnlichen Strukturen zu erklären.

Die Arbeit zeigt, dass Morphologien Aufschluss über die Zusammensetzung, die Geologie und die Entwicklung kleiner Körper im Sonnensystem geben und ebnet den Weg für künftige Forschungen an weiteren planetaren Objekten und neuen Datensätzen.



# Contents

<b>List of Abbreviations</b>	<b>xi</b>
<b>Preface</b>	<b>xiii</b>
<b>1 Introduction</b>	<b>1</b>
1.1 Volatiles on Asteroids and Comets . . . . .	1
1.2 Small Body Regolith . . . . .	4
1.3 Space Missions to Asteroids and Comets . . . . .	5
1.4 Research Questions . . . . .	7
1.5 Methods . . . . .	8
1.5.1 Space Mission Image Analysis . . . . .	8
1.5.2 Laboratory Experiments . . . . .	9
1.5.3 Discrete Element Method Modeling . . . . .	10
<b>2 Synergy of Conducted Research</b>	<b>11</b>
2.1 Volatile Morphologies Examined Using Image Data . . . . .	11
2.1.1 Otto et al. (2021a) . . . . .	15
2.1.2 Otto et al. (2021b) . . . . .	32
2.1.3 Otto et al. (2019) . . . . .	55
2.1.4 Michalik et al. (2021) . . . . .	72
2.1.5 Parekh et al. (2021a) . . . . .	99
2.1.6 Parekh et al. (2021b) . . . . .	119
2.2 Volatile Morphologies Examined Using Laboratory Experiments . . . . .	137
2.2.1 Haack et al. (2020) . . . . .	139
2.2.2 Haack et al. (2021a) . . . . .	150
2.2.3 Haack et al. (2021b) . . . . .	165
2.3 Volatile Morphologies Examined Using Discrete Element Method Modelling	177
2.3.1 Kappel et al. (2020) . . . . .	179
2.3.2 Sachse et al. (2022) . . . . .	202



*Contents*

<b>3 Summary and Conclusion</b>	<b>219</b>
<b>4 Outlook</b>	<b>225</b>
4.1 Multi-scale and Multi-instrument Analyses . . . . .	226
4.1.1 Otto et al. (2023) . . . . .	228
<b>5 References</b>	<b>245</b>
<b>6 Acknowledgments</b>	<b>259</b>

# List of Abbreviations

**67P** 67P/Churyumov-Gerasimenko

**CAI** Calcium-aluminium-rich inclusions

**CK4** Karoonda type carbonaceous chondrite of petrologic type 4

**CM2** Mighei type carbonaceous chondrite of petrologic type 2

**CO3** Ornans type carbonaceous chondrite of petrologic type 3

**CoPhyLab** Comet Physics Laboratory

**CV3** Vigarano type carbonaceous chondrite of petrologic type 3

**DEM** Discrete element method

**Destiny<sup>+</sup>** Demonstration and Experiment of Space Technology for INterplanetary voYage  
with Phaethon fLyby and dUst Science

**DLR** Deutsches Zentrum für Luft- und Raumfahrt

**ESA** European Space Agency

**JAXA** Japan Aerospace Exploration Agency

**LED** Light emitting diode

**MasCam** MASCOT Camera

**MASCOT** Mobile Asteroid Surface Scout

**MfN** Museum für Naturkunde

**MMX** Martian Moons eXploration

**NASA** National Aeronautics and Space Administration

**NEAR** Near Earth Asteroid Rendezvous

*List of Abbreviations*

**ONC** Optical Navigation Camera

**OSIRIS-REx** Origins Spectral Interpretation Resource Identification Security – Regolith Explorer

**PID** Pitted impact deposit

**ROLIS** Rosetta Lander Imaging System

**SBMT** Small Body Mapping Tool

**TIR** Thermal Infrared Imager

**VIR** Visible and Infrared Mapping Spectrometer

# Preface

The main theme of this habilitation thesis falls in the discipline "Planetary Science" and concerns the volatile-related processes that shape the surfaces of small planetary bodies (e.g. asteroids and comets). A variety of morphologic features on small bodies, such as mass wasting, smooth pond-like and pitted impact deposits, fractures, boulders, cliffs, aeolian-like features and surface roughness, are investigated to determine their relation to the volatile content of the hosting body and its regolith. The research is based on data returned by space missions to small bodies and focuses on the interpretation of the surface morphology through multi-spectral remote sensing and in situ images spanning a wide range of spatial scales from sub-millimeters to kilometres. Additionally, it includes laboratory experiments and numerical modelling of surface processes caused by volatile sublimation. The research also comprises comparative studies with meteorites as regolith analogues.

The habilitation thesis summarises the work of the junior research group "The Physics of Volatile-related Morphologies of Asteroids and Comets", which implemented the research from March 2017 to August 2021 at the Institute of Planetary Research of the German Aerospace Center (DLR) in Berlin. Next to the group leader (myself, K. A. Otto), three doctoral students (D. Haack, T. Michalik, R. Parekh) and two post-doctoral researchers (D. Kappel, M. Sachse) worked in the group. The PhD students successfully defended their theses at the end of the project. The group was also occasionally supported by interns and university students.

Chapter 1 gives an introduction to small planetary bodies and space missions to them along with an overview of the applied research methods. This is followed by Chapter 2, a compilation of the conducted research comprising eleven articles that were published by members of the research group. Each article is preceded by a description setting out the context and the contribution of the authors, in particular the contribution of myself as submitter of this habilitation thesis. The papers are then attached in their original format. Chapter 3 summarises and concludes the presented work. Finally, Chapter 4 gives an outlook to future research and presents an article furthering the original research idea.

## *List of Abbreviations*

I am the first author of four of the included articles. One of these articles is incorporated as an outlook on how to pursue the initiated research (Chapter 4). Six articles were published by the junior research group's PhD students, who I provided guidance for as their main supervisor. Two further articles were published by the post-doctoral researchers under my supervision. I am the corresponding author of one of their articles and second or last author of all included articles that I did not lead as first author.

The articles included in this thesis have been sketched in my proposal to form a junior research group. Thus, I not only provided guidance to the students and post-doctoral researchers while working on the articles, but I also had a significant scientific input from providing the original idea of the articles to writing specific sections and contributing interpretations. For some articles I also provided preparatory material (Sections 2.1.5 and 2.3.2). More details on my specific contributions can be found in conjunction with the articles attached in this thesis.

# 1 Introduction

## 1.1 Volatiles on Asteroids and Comets

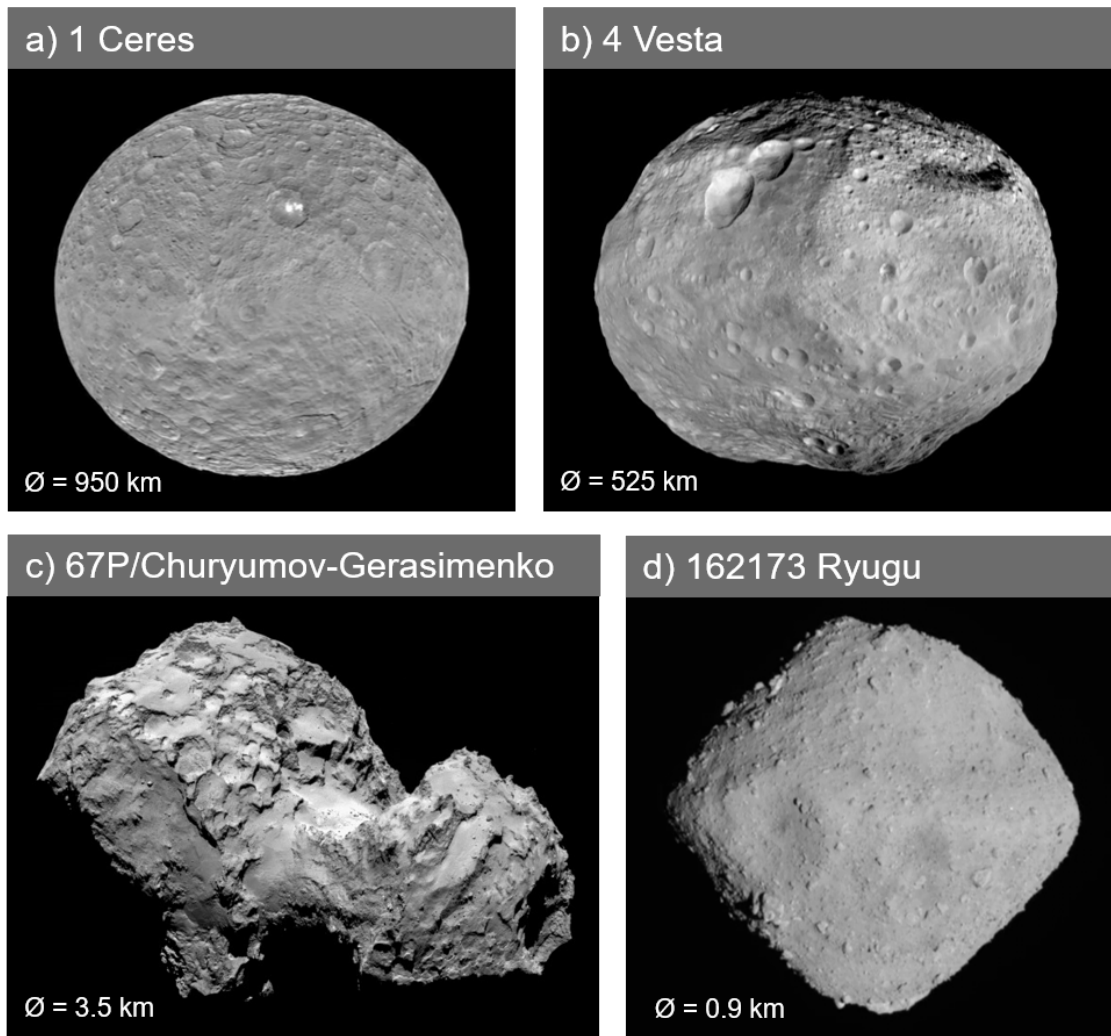
Asteroids and comets play a significant role in planetary research, because they bear the potential to have preserved information from the early epoch of our Solar System. Although they may have undergone some alteration, they are small remnants of an epoch when the planets of our Solar System formed and enable the investigation of this process (Figure 1.1). But due to their small mass, asteroids and comets can also easily be diverted from their orbits by more massive objects into potentially collisional orbits with other planetary bodies. This makes them deliverers of materials which includes volatiles such as water, the main ingredient of a habitable environment.

A large collection of asteroids can be found between 2.1 and 3.3 AU from the Sun in the Main Asteroid Belt. The members orbit the Sun on relatively stable and predictable orbits. Many asteroids are fragments or rubble piles (Figure 1.1d) resulting from the disruption of planetesimals in the early epoch of our Solar System (e.g. DeMeo et al., 2015), but some larger objects, such as Ceres (Figure 1.1a) and Vesta (Figure 1.1b), can be described as protoplanets that evolved through the early stages of planetary formation and had already begun the process of differentiation (Russell et al., 2004).

Some asteroids have been scattered into orbits accompanying planets, such as the Trojan and Greek asteroids located in Jupiter's Lagrange points (Emery et al., 2015), or approaching planetary orbits. Earth possesses such a near-Earth asteroid population and although some of these asteroids are a potential impact hazard (Perna et al., 2015), they are also relatively easy to reach by spacecraft.

Three major compositional classes of asteroids can be distinguished (Tholen, 1989; Bus et al., 2002; DeMeo et al., 2009): M-type asteroids are metal-rich, such as Psyche; S-type asteroids are stony, such as Itokawa and Eros; and C-type asteroids are carbonaceous, such as Ryugu and Bennu. C-type asteroids represent the majority of the known asteroids (DeMeo et al., 2022) and are rich in volatiles. In the past, C-type asteroids accommodated conditions allowing liquid water to exist and initiate aqueous alteration of the asteroidal material. This has also been the case for dwarf-planet Ceres whose com-

## 1 Introduction



**Figure 1.1: Examples of small planetary bodies orbited by spacecraft.** a) Ceres and b) Vesta are the two most massive bodies in the Main Asteroid Belt (Dawn Mission). c) 67P/Churyumov-Gerasimenko is a Jupiter family comet (Rosetta Mission) and d) Ryugu is a near-Earth C-type rubble pile asteroid (Hayabusa2 Mission). *Image credit: Ceres: NASA/JPL-Caltech/UCLA/MPS/DLR/IDA/PSI, Vesta: NASA/JPL-Caltech/UCLA/MPS/DLR/IDA, 67P: ESA/Rosetta/MPS for OSIRIS Team MPS/UPD/LAM/IAA/SSO/INTA/UPM/DASP/IDA, Ryugu: JAXA.*

position matches that of C-type asteroids (Feierberg et al., 1981). The pyroxene-rich Vesta, on the other hand, is accompanied by its own family called the V-type asteroids (Bus et al., 2002).

Despite the presence of volatiles in some asteroids, their surfaces are generally depleted in such (e.g. Rivkin et al., 2010), because without a protective atmosphere or dust cover

volatiles sublimate under the thermal conditions present in the Main Asteroid Belt and closer to the Sun. Nevertheless, volatile outgassing has been observed on Ceres (Küppers et al., 2014) and may be an explanation for particle ejections on Bennu (Lauretta et al., 2019b).

Comets, on the other hand, originate from the region beyond the giant planets and are often on highly eccentric orbits (Levison, 1996). Their volatile-rich composition indicates formation in the cooler outer region of the Solar System where volatile ices condensed (e.g. Bockelée-Morvan et al., 2004). They are best known for their striking tails made of gas and dust ejected into space when approaching the Sun.

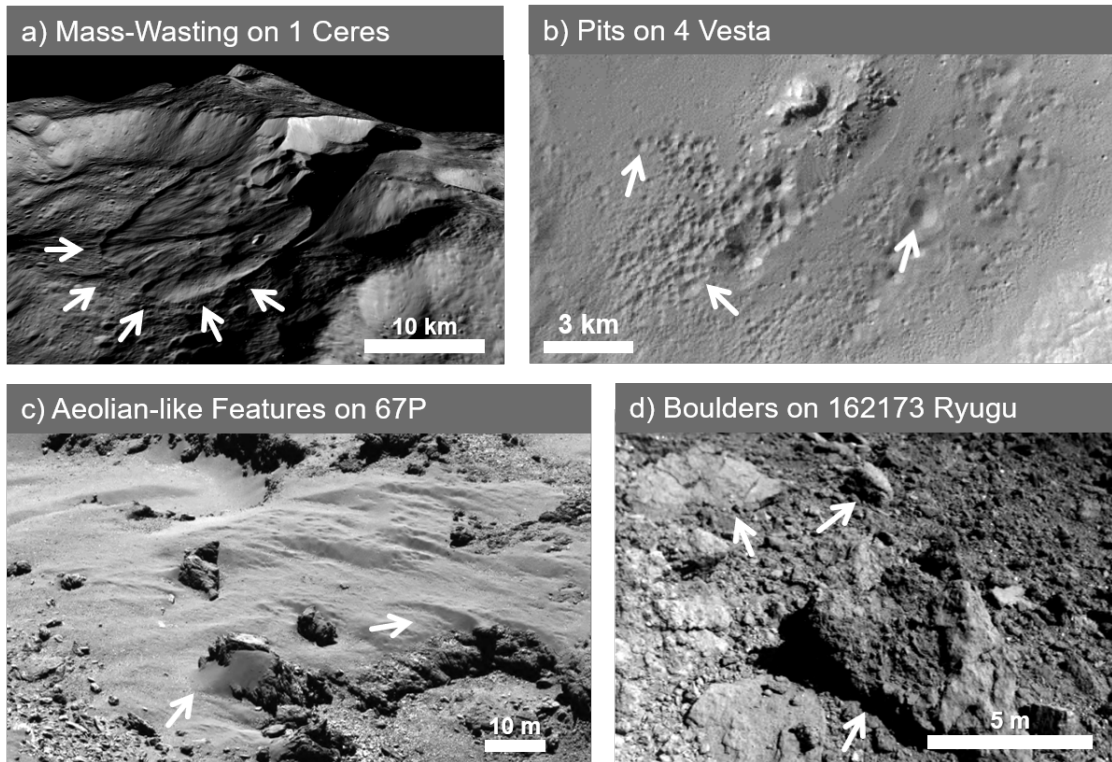
Although some comets have parabolic or hyperbolic orbits, two major types of comets can be distinguished: long-period ( $>200$  yrs) originating from the Oort cloud and short-period comets ( $<200$  yrs) originating from the Kuiper Belt (Levison, 1996). The Rosetta mission recently visited comet 67P/Churyumov-Gerasimenko (hereafter 67P, (Figure 1.1c)), a short-period Jupiter family comet with an orbit remaining within Jupiter's orbit and a period of 6.55 yrs (Lamy et al., 2007).

If the thermal conditions are favourable, volatiles encountering the vacuum will sublimate and form distinct morphologic features not only by the sublimation process itself, but also by induced processes such as the redeposition of particles lifted by outgassing forming aeolian-like features (Thomas et al., 2015; Keller et al., 2017) (Figure 1.2,c). Asteroids in near-Earth orbits and most asteroids in the main belt accommodate such thermal environments. Comets on highly eccentric orbits may meet sublimation conditions temporarily. Morphologic differences between asteroid and comet surfaces are evident (compare Figure 1.1c and d), but the cause of these differences is still in discussion.

The presence of subsurface water or ice reservoirs, which can exist on larger asteroids such as Vesta and Ceres (Scully et al., 2015; Castillo-Rogez et al., 2020), may form surface features such glacier-like thick mass-wasting features (Schmidt et al., 2017) (Figure 1.2,a) or pits in smooth crater deposits created through volatile sublimation (Denevi et al., 2012) (Figure 1.2,b). Some large scale volatile-related features, such as the impact crater Occator (Scully et al., 2019) and the mount Ahuna Mons on Ceres (Ruesch et al., 2016), indicate that volatiles contribute to interior processes, including differentiation and tectonic deformation (Sizemore et al., 2019). These processes are directly related to the evolution of the host body and its surface. On small scales, volatile-rich boulders, such as those on asteroid Ryugu (Figure 1.2d), exhibits distinct surface textures (Jauermann et al., 2019). However, more research is needed to refine the role of volatiles in the formation of surface morphologies on multiple spatial scales. Moreover, it is desirable to



## 1 Introduction



**Figure 1.2: Examples of small volatile-related surface features.** Shown are a) a mass-wasting feature exhibiting thick lobate tongues indicative of volatile content in the regolith on dwarf-planet Ceres, b) the pitted floor of Marcia crater on asteroid Vesta generated through volatile loss, c) aeolian-like features on comet 67P created through the volatile-driven redistribution of regolith and d) boulders composing the carbonaceous volatile-containing regolith of asteroid Ryugu. The white arrows point at the features of interest. *Image credit: a) NASA/JPL-Caltech/UCLA/MPS/DLR/IDA/PSI, b) NASA/JPL-Caltech/UCLA/MPS/DLR/IDA/JHUAPL, c) MPS/UPD/LAM/IAA/SSO/INTA/UPM/DASP/IDA, d) MASCOT/DLR/JAXA.*

constrain the volatile content from such surface morphologies.

## 1.2 Small Body Regolith

The surfaces of asteroids and comets are covered with a soil-like and often boulder-rich layer that weathers and evolves under space conditions (Clark et al., 2002). This layer, called regolith (Greek: *reghos* (blanket) + *lithos* (stone)), is the building material for the geology and morphology visible in remote sensing and in situ space mission data.

Regolith is exposed to the complex physical environment present on asteroids and

### 1.3 Space Missions to Asteroids and Comets

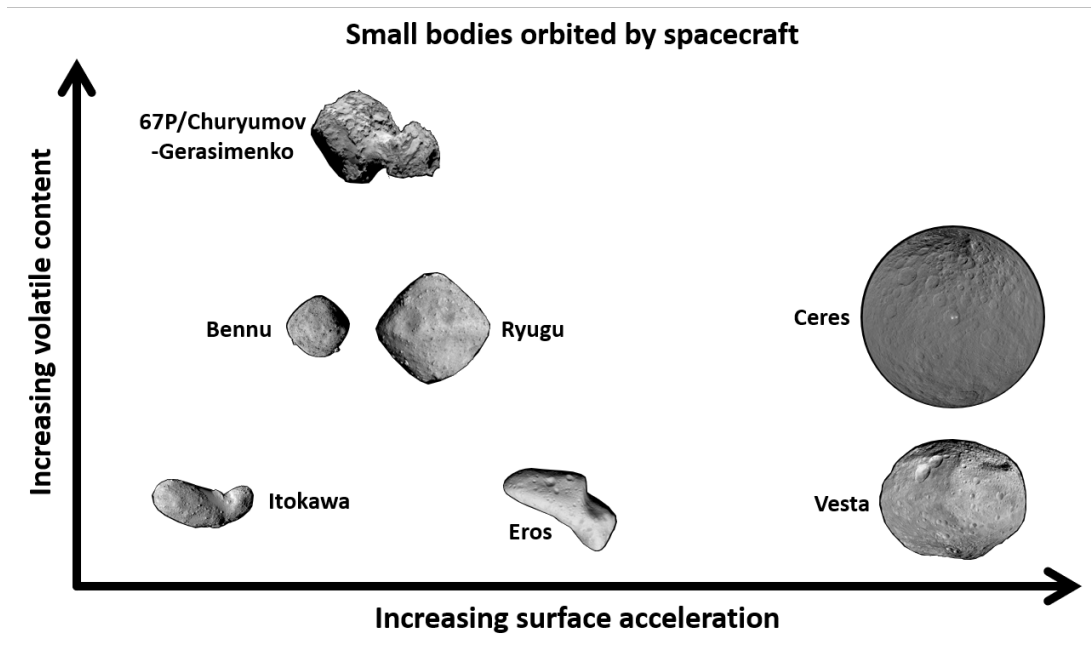
comets and weathers accordingly (Hapke, 2001; Clark et al., 2002; Pieters and Noble, 2016). Not only are these bodies airless and thus their surfaces are directly exposed to the impingement of energetic solar wind particles, solar radiation, galactic cosmic rays and the vacuum of space, but their surface gravitational acceleration is significantly smaller than that known from Earth while surface temperatures and their gradients can be extreme. The morphology of the regolith not only reflects these extreme conditions, but it can also be indicative of the physical and mechanical properties of the regolith. For example, the angle of repose of a mass-wasting deposit hints at the inter-particle friction of the mass-wasting constituents and may be influenced by the ambient gravity (Kleinhans et al., 2011; Nakashima et al., 2011).

Meteorites are considered samples of regolith ejected from the surface of asteroids and delivered to Earth. As such, meteorites can be related to the different asteroid classes based on their composition (DeMeo et al., 2022). An example is the suggested connection between carbonaceous chondrites and C-type asteroids (Jaumann et al., 2019, Lauretta et al., 2019a; DeMeo et al., 2022). Chondrites are named after the fact that they are meteorites containing chondrules, small millimetre-sized spheres formed from molten droplets in space before aggregating into a larger asteroid. Other refractory objects in chondrites include calcium-aluminum-rich inclusions (CAIs) and amoeboid olivine aggregates (Greshake and Fritz, 2018). However, carbonaceous chondrites are fragile meteorites and their relative abundance compared to the stony and metallic meteorites is below the relative abundance of C-type asteroids compared to S- and M-type asteroids. This indicates that the entry through Earth's atmosphere and the subsequent terrestrial weathering introduces a bias in the meteorite selection with the more fragile meteorites being less common (Grott et al., 2019).

### 1.3 Space Missions to Asteroids and Comets

The originally Earth-bound telescopic research into asteroids and comets was significantly complemented, when comet 1P/Halley and asteroid (951) Gaspra were the first objects of their kind photographed by the Giotto Mission in 1986 and the Galileo Mission in 1991, respectively (Keller et al., 1988; Belton et al., 1992).

The data from space missions has tremendously increased in quantity and quality in recent years (e.g. Figure 1.1). Figure 1.3 illustrates small bodies that were orbited by space missions organized by their surface acceleration and volatile content. The first small body to be orbited by a spacecraft was near-Earth S-type asteroid Eros which was visited by NASA's NEAR-Shoemaker mission for one year arriving in February



**Figure 1.3:** Sketch illustrating the surface acceleration and volatile content of small bodies orbited by spacecraft. While the S-type asteroids are low in volatile content, comets possess abundant volatiles. The surface acceleration depends on the bodies' size and density. Small bodies that have been flown past by spacecraft are not included. With the exception of asteroid Benu\*, all shown small bodies have been considered in this habilitation thesis. The sketch is for illustrative purposes only and is not to scale.

2000 (Veverka et al., 2000). NEAR-Shoemaker was equipped with six instruments allowing to investigate Eros' geology, topography, gravity, magnetization, structure and composition. NEAR-Shoemaker's mission was followed by JAXA's Hayabusa sample return mission arriving at S-type asteroid Itokawa in September 2005. Next to its sampling devices, Hayabusa was equipped with five instruments focussing on the geology, topography and composition of Itokawa (Fujiwara et al., 2006). NASA's Dawn mission was the first mission to orbit two objects in the Main Asteroids Belt. With three instruments on board, a framing camera, a spectrometer and a gamma ray and neutron detector, Dawn orbited Vesta for almost 14 months in 2011/12 before setting out to Ceres where it arrived in 2016 and operated 28 months before the depletion of its hydrazine (Rayman, 2020). ESA's Rosetta mission accompanied Jupiter family comet 67P/Churyumov-Gerasimenko from early 2014 until 2016. Rosetta carried a lander, Phi-

\*OSIRIS-REx started exploring Benu in October 2018 and thus data had not yet been available for most of the time in which the research group was active.

lae, which was deployed onto 67P's surface in 2014. Rosetta and Philae were equipped with eleven and ten instruments, respectively, and focused on the characterisation of the comet nucleus' physical properties, chemistry, mineralogy and isotopic composition, as well as the study of cometary activity (Boehnhardt et al., 2017; Taylor et al., 2017). In 2018, near-Earth C-type asteroids Bennu and Ryugu have been reached by the OSIRIS-REx and Hayabusa2 missions, respectively (Lauretta et al., 2019a; Watanabe et al., 2019). Both missions are sample return missions but also investigated the composition, geology, topography and thermal properties of their target asteroids with five orbiter instruments. They operate cameras, a near-infrared spectrometer, a thermal imager and a laser altimeter. OSIRIS-REx additionally carries a x-ray spectrometer and Hayabusa2 is equipped with a small carry-on impactor that was shot onto Ryugu to expose fresh sampling (Arakawa et al., 2020). Hayabusa2 also deployed two rovers and the MASCOT lander onto Ryugu's surface performing in situ regolith science (Lange et al., 2020; Ho et al., 2021). Hayabusa2 collected regolith samples in two touch down maneuvers and delivered a total of 5.4 g to Earth in 2020 (Yada et al., 2022). Samples of Bennu are expected to arrive on Earth in 2023. Both missions have been extended: OSIRIS-REx will rendezvous with the potentially hazardous asteroid Apophis in 2029 (DellaGiustina et al., 2022) and Hayabusa2 will fly by a rare L-type near-Earth asteroid in 2026 and rendezvous with a fast rotator in 2031 (Mimasu et al., 2022).

These space missions delivered a wealth of data from remote sensing and in situ observations complemented by returned sample material. Analyses of these data sets are still ongoing and will be enhanced by future space mission, equipped with landers and sample return devices, to small bodies such as JAXA's MMX and Destiny<sup>+</sup> missions to Mars moon Phobos and active asteroid Phaethon (Kuramoto et al., 2022; Ozaki et al., 2022), respectively, ESA's Hera mission to the binary asteroid system of Didymos and Dimorphos (Michel et al., 2022), and NASA's Psyche and Lucy missions to metal-rich asteroid Psyche and Jupiter's Trojans, respectively.

## 1.4 Research Questions

The significance of asteroids and comets lies in their role as remnants of the epoch of planetary formation, but it has also been suggested that they are carriers and deliverers of the ingredients necessary for life. As described above, volatiles, of which water is the most abundant species in our Solar System, may reveal their presence through morphologic features on small body surfaces. Although the known diversity of these features has recently enhanced by a number of space missions to asteroids and comets, the relation-

## 1 Introduction

ship between surface morphologies and the presence of volatiles as well as the amount of volatiles related to them is often unknown. A variation in surface morphology on asteroids and the more active comets has been observed, however, it is unclear to which extent this variation is introduced by volatile outgassing and how volatiles contribute to the evolution of a small body's surface and interior. Thus, this thesis addresses the following key questions:

- What is the relationship between surface morphologies and the presence of volatiles on small bodies?
- Can we constrain the volatile content and abundance from surface morphologies observed in small body environments?
- How are asteroidal and cometary outgassing features related?
- What is the role of volatiles in the evolution of small body surfaces and their interiors?

## 1.5 Methods

Various methods have been applied to interpret space mission data comprehensively. This section briefly introduces the three techniques applied in this thesis including geologic and morphologic space mission image analysis, laboratory experiments of sublimating analogue materials and discrete element method (DEM) modelling of regolith dynamics. A more detailed description of the methods can be found in the presented publications.

### 1.5.1 Space Mission Image Analysis

Cameras are standard instruments on space missions that not only provide a view of the object, but that are also necessary for navigation. After the initial calibration and correction of the images (e.g. Schröder et al., 2013b; 2021; Tubiana et al., 2015; Tatsumi et al., 2019), they can be processed knowing the instrument pointing to generate a variety of products including mosaics of combined individual images, digital terrain models, photometrically corrected images and shape models (e.g. Gaskell et al., 2008; Gwinner et al., 2009; Raymond et al., 2011; Roatsch et al., 2012; 2013; Schröder et al., 2013a; 2017b; Preusker et al., 2015; 2017; 2019; Scholten et al., 2019). Body referenced data products allow the measurement of length and bearing and are indispensable for geologic interpretations.

Often, space mission image detectors are monochrome, but with the help of colour filters or local illumination with coloured LEDs, colour composite images can be produced that also provide spectral information in the visible wavelength range (e.g. Reddy et al., 2012; Fornasier et al., 2015; Schröder et al., 2017a; 2017b; Jaumann et al., 2019; Sugita et al., 2019). For example, the ROLIS and MasCam in situ cameras with four coloured LED arrays were operated on Rosetta’s Philae and Hayabusa2’s MASCOT lander, respectively (Mottola et al., 2007; Jaumann et al., 2017).

Maps of bodies that are close to spherical (e.g. Ceres, Vesta) can be evaluated using standard geoinformation systems (van Gasselt and Nass, 2011). However, the more the shape of a small body differs from a sphere, the more the analysis increases in complexity and distortion effects can become severe (Stooke, 1998). A prominent example of such a non-spherical object is comet 67P whose bi-lobed shape does not allow to assign a unique latitude and longitude value to each point on its surface (Preusker et al., 2015). In such cases, images or map products have to be projected onto the body’s shape model for spatial measurements and a proper geologic interpretation. For this purpose and for searching, retrieving and projecting data of small bodies a variety of tools is available, e.g. the Small Bodies Data Ferret<sup>†</sup> or the Small Body Mapping Tool (SBMT) (Ernst et al., 2018) are commonly used tools for NASA missions.

### 1.5.2 Laboratory Experiments

A number of comet simulation chambers (Grün et al., 1991; Pommerol et al., 2015; Kaufmann and Hagermann, 2018; Kreuzig et al., 2021) has been used to explore volatile outgassing as the main driver for cometary activity in the laboratory. Such chambers are usually composed of a liquid nitrogen cooled vacuum chamber, a solar simulator and various sensors to monitor the chamber’s environmental condition. They can accommodate up to decimeters sized samples. Analysis instruments vary depending on the focus of the experiments and include among others cameras, spectrometers, optical coherence tomographs, and radiometers (Pommerol et al., 2015; Kreuzig et al., 2021).

One of the major challenges is represented by spatially and gravitationally scaling earthbound experiments to small body environments. The difference in feature size and gravitational acceleration may be counterbalanced by reducing the particle size in the laboratory, so that the ratio between cohesive and gravitational forces of grains can be adapted to match the ratio on a small body. The ratio between the cohesive and gas drag forces from sublimating ice-rich surfaces can be tweaked by increasing the energy

---

<sup>†</sup><http://sbn.psi.edu/ferret/>

input in the laboratory (Bischoff et al., 2019; Haack et al., 2021a).

### 1.5.3 Discrete Element Method Modeling

DEM modelling reproduces the dynamics and behaviour of granular, discontinuous materials that consist of separate, discrete particles (N-body simulation). Typically, these particles are polydisperse spheres presenting a high degree of symmetry minimizing the computational resources needed for a simulation. As regolith is composed of individual particles, fragments, and loosely consolidated material, DEM modelling is a powerful tool to investigate the motion, interplay and mixing of regolith. It is capable of simulating the dynamics of assemblies of particles in the complex environments present on asteroids and comets. Particularly, the low gravity as well as the large size of some solar system objects (e.g. rubble pile asteroids) is not easily accessible in laboratories but manageable with DEM simulations (Tancredi et al., 2012). In small planetary body research, DEM modelling has been used, for example, to simulate impact cratering processes (Wada et al., 2006), the Brazil nut effect (Tancredi et al., 2012), material ejection via strong centrifugal forces (Hirabayashi et al., 2015), lander-regolith interactions (e.g. Maurel et al., 2018; Murdoch et al., 2021; Sunday et al., 2021; 2022; Thuillet et al., 2021) and spacecraft sample collection mechanisms (Thuillet et al., 2020). Applying parameter studies to the simulation of morphologic features and dynamic processes, such as overhangs, boulder drops or cliff collapses, also allows constraining the physical and mechanical properties of the involved regolith (Kappel et al., 2020).

However, in reality regolith particles are usually non-spherical and the amount of particles involved in a dynamic process can be extremely large. To handle such scenarios, particle angularity is usually represented by rolling friction, but codes including angular particles have also been established (Ferrari and Tanga, 2020). Additionally, connecting individual particles with bonds enables creating complexly shaped particles in a simulation. Larger scenarios (e.g. mass-wasting processes) can easily exceed the computational capabilities, in which case scaling methods, such as coarse graining, have to be applied. This technique describes particles collectively in computational parcels whose physical properties are scaled such that the macroscopic simulation results become statistically similar to those obtained without coarse graining (Bierwisch et al., 2009).

## 2 Synergy of Conducted Research

### 2.1 Volatile Morphologies Examined Using Image Data

The following six articles concern the investigation of various surface morphologies on small bodies and their relation to volatiles in the regolith. The investigations span a wide range of small bodies from small near-Earth asteroid Ryugu and comet 67P to some of the largest objects in the Main Asteroid Belt, Vesta and Ceres. They utilise in situ as well as remote sensing image data and thus allow a multi-scale interpretation of regolith morphology from local sub-millimetre-sized to global metre-sized pixel resolutions. Comparisons with carbonaceous chondrites as regolith analogue for C-type asteroids are also included.

The articles Otto et al. (2021a) and Otto et al. (2021b) focus on small-scale and in situ observations of asteroid and comet regolith and carbonaceous chondrites as terrestrial analogue materials. They evaluate data collected by the lander cameras ROLIS on 67P and MasCam on Ryugu. Otto et al. (2021a) compares the roughness of asteroid and comet regolith on sub-millimetre scales using in situ image data from both lander cameras. This study determines a set of roughness parameters including the fractal dimension, Hurst exponent, joint roughness coefficient, root-mean-square slope, hemispherical crater density, small-scale roughness parameter, and Hapke mean slope angle using an automated image analysis technique for in situ image data developed for this research. It reveals that on sub-millimetre scales comet 67P's surface is about 6% rougher than that of Ryugu. A possible contribution to this variation in roughness could be the different regolith volatile contents and their sublimation on C-type asteroid Ryugu and active comet 67P.

Otto et al. (2021b) links the texture on sub-millimetre scales of asteroid regolith and aqueously altered carbonaceous chondrites. A total of 14 carbonaceous chondrites have been imaged in four different colours using the MasCam qualification model. Similar to the analysis of inclusions on asteroid Ryugu (Jaumann et al., 2019; Schröder et al., 2021), bright spots were mapped and analysed in terms of their brightness relative to the matrix in the red light, the relative spectral slope, the size frequency distribution and



## 2 Synergy of Conducted Research

the matrix volume abundance. The study finds that the inclusions seen in in situ images on Ryugu fit well in the parameter space spanned by carbonaceous chondrite inclusions supporting findings that Ryugu's regolith is similar to carbonaceous chondrites that once has been in contact with liquid water.

The articles Otto et al. (2021a) and Otto et al. (2021b) can be cited using:

- Otto, K. A., Matz, K.-D., Schröder, S. E., Parekh, R., Krohn, K., Honda, R., Kameda, S., Jaumann, R., Schmitz, N., ... Yoshioka, K. (2021a). Surface Roughness of Asteroid (162173) Ryugu and Comet 67P/Churyumov-Gerasimenko Inferred from in Situ Observations. *Monthly Notices of the Royal Astronomical Society*, 500(3), 3178–3193. <https://doi.org/10.1093/mnras/staa3314>.
- Otto, K. A., Schröder, S. E., Scharf, H. D., Greshake, A., Schmitz, N., Trauthan, F., Pieth, S., Stephan, K., Ho, T.-M., ... Yabuta, H. (2021b). Spectral and Petrographic Properties of Inclusions in Carbonaceous Chondrites and Comparison with In Situ Images from Asteroid Ryugu. *The Planetary Science Journal*, 2(5), 188. <https://doi.org/10.3847/PSJ/ac034b>.

The following four articles employ remote sensing data predominantly from the Dawn Mission to asteroid Vesta and dwarf-planet Ceres.

Otto et al. (2019) and Michalik et al. (2021) each focus on a specific morphologic feature observed on Ceres and Vesta, e.g. concentric fractures around some craters on Ceres and pitted impact deposits (PIDs) associated with the crater Marcia on Vesta, respectively. The article by Otto et al. (2019) investigates the link between a volatile-rich layer in the subsurface of Ceres and the presence of concentric fracturing observed around some medium-sized craters (~50 km in diameter) employing a finite element relaxation model. The investigation shows that over a few million years a crater cavity in a regolith with a shallow (<10 km) low-viscosity subsurface layer generates stresses that can lead to the observed concentric fracturing. The best match is found for a 2 km thick layer buried underneath 1 km of regolith. A correlation between craters with concentric fractures and other volatile related features, such as pitted impact deposits, suggest that the shallow low-viscosity subsurface layer is enriched in ice.

Michalik et al. (2021) use clear filter and colour images as well as spectral data to discuss the morphology and compositional variation of outgassing-related PIDs and the origin of the volatiles involved in their formation. They investigate features inside the crater and in the ejecta blanket of the young Marcia crater on Vesta and find that the PIDs in the ejecta blanket occur in topographically induced ejecta accumulations and the accompanying increase of deposit thickness. They exhibit higher reflectance

## 2.1 Volatile Morphologies Examined Using Image Data

and pyroxene band strength than their immediate surroundings. Their unique spectral characteristics suggest a unique formation involving the loss of volatiles delivered by exogenic sources (e.g. through meteorite impacts). However, high volatile contents are not necessary to generate PIDs and  $\sim 1$  wt% may be enough to induce the formation of PIDs.

The articles by Parekh et al. (2021a) and Parekh et al. (2021b) apply an inter-planetary body comparison focussing on mass-wasting and pond-like features. The research described in Parekh et al. (2021a) concerns the effect of volatiles on mass-wasting behaviour on Vesta and Ceres. Both bodies are similar in their physical environment (e.g. heliocentric distance, surface acceleration) but possess regoliths with different volatile contents. While Vesta is comparatively dry, Ceres' regolith includes volatiles. The study finds that mass-wasting deposits on Vesta have shorter run-out lengths compared to Ceres. But the volatile content in the regolith does not significantly influence the effective coefficient of friction of the regolith which is represented by the ratio of fall height and run-out length of a landslide. This indicates that volatile content is not the only parameter that plays a role in the morphology of mass-wasting features.

The work shown in Parekh et al. (2021b) focuses on the contribution of volatiles in the formation of pond-like features on Vesta and smaller planetary bodies including asteroids Eros and Itokawa. Pond-like features are flat deposits on the crater floor and were first detected on Eros. The article introduces a classification of pond-like features on Vesta, namely ejecta ponds and dust ponds. While dust ponds possess an undulating surface with an abrupt change in slope towards the crater wall, ejecta ponds occur in the vicinity of large craters and form as a result of melt pooling creating a smooth crater floor. The morphology of the dust ponds indicates that a combination of seismic shaking and volatile-induced fluidisation of the regolith is likely responsible for the formation of pond-like features on Vesta.

The above mentioned articles can be cited using:

- Otto, K. A., Marchi, S., Trowbridge, A., Melosh, H. J., & Sizemore, H. G. (2019). Ceres Crater Degradation Inferred from Concentric Fracturing. *Journal of Geophysical Research: Planets*, *124*(0), 1–16. <https://doi.org/10.1029/2018JE005660>.
- Michalik, T., Matz, K.-D., Schröder, S., Jaumann, R., Stephan, K., Krohn, K., Preusker, F., Raymond, C., Russell, C., & Otto, K. A. (2021). The Unique Spectral and Geomorphological Characteristics of Pitted Impact Deposits Associated with Marcia Crater on Vesta. *Icarus*, *369*, 114633. <https://doi.org/10.1016/j.icarus.2021.114633>.

## 2 Synergy of Conducted Research

- Parekh, R., Otto, K. A., Jaumann, R., Matz, K. D., Roatsch, T., Kersten, E., Elgner, S., & Raymond, C. A. (2021a). Influence of Volatiles on Mass Wasting Processes on Vesta and Ceres. *Journal of Geophysical Research: Planets*, 126(3), e2020JE006573. <https://doi.org/https://doi.org/10.1029/2020JE006573>.
- Parekh, R., Otto, K. A., Matz, K. D., Jaumann, R., Krohn, K., Roatsch, T., Kersten, E., Elgner, S., Russell, C. T., & Raymond, C. A. (2021b). Formation of Ejecta and Dust Pond Deposits on Asteroid Vesta. *Journal of Geophysical Research: Planets*, 126(11), e2021JE006873. <https://doi.org/10.1029/2021JE006873>.

**2.1.1 Otto et al. (2021a)**

Otto, K. A., Matz, K.-D., Schröder, S. E., Parekh, R., Krohn, K., Honda, R., Kameda, S., Jaumann, R., Schmitz, N., . . . Yoshioka, K. (2021a). Surface Roughness of Asteroid (162173) Ryugu and Comet 67P/Churyumov-Gerasimenko Inferred from in Situ Observations. *Monthly Notices of the Royal Astronomical Society*, 500(3), 3178–3193. <https://doi.org/10.1093/mnras/staa3314>.

As first author of this article, I conducted the presented research including the computer-based image analysis and the data generation and interpretation. K.-D. Matz provided support in preparing the data for analysis. S. E. Schröder, R. Parekh, K. Krohn and R. Jaumann contributed preparatory analyses and helped with the interpretation of the subsequently derived roughness parameters. The remaining authors were involved in processing image data and building, calibrating and operating the ONC and MASCOT instruments.

# Surface roughness of asteroid (162173) Ryugu and comet 67P/Churyumov–Gerasimenko inferred from *in situ* observations

K. A. Otto<sup>1</sup>,<sup>\*</sup> K.-D. Matz,<sup>1</sup> S. E. Schröder,<sup>1</sup> R. Parekh,<sup>1</sup> K. Krohn,<sup>1</sup> R. Honda, S. Kameda,<sup>2</sup> R. Jaumann,<sup>1,3</sup> N. Schmitz,<sup>1</sup> K. Stephan,<sup>1</sup> S. Sugita,<sup>4,5</sup> E. Tatsumi,<sup>4,6</sup> T.-M. Ho,<sup>7</sup> A. Koncz,<sup>1</sup> F. Trauthan,<sup>1</sup> Y. Cho,<sup>4</sup> M. Hayakawa,<sup>8</sup> C. Honda,<sup>9</sup> T. Kouyama,<sup>10</sup> M. Matsuoka,<sup>8</sup> T. Morota,<sup>4</sup> S. Mottola,<sup>1</sup> K. Ogawa,<sup>8</sup> F. Preusker,<sup>1</sup> N. Sakatani,<sup>2</sup> H. Sawada,<sup>8</sup> F. Scholten,<sup>1</sup> H. Suzuki,<sup>11</sup> M. Yamada,<sup>5</sup> Y. Yokota<sup>7</sup> and K. Yoshioka<sup>12</sup>

<sup>1</sup>German Aerospace Center, Institute of Planetary Research, Rutherfordstraße 2, D-12489 Berlin, Germany

<sup>2</sup>Department of Physics, Rikkyo University, 3-34-1 Nishi-Ikebukuro, Toshima, Tokyo, Japan

<sup>3</sup>Institute of Geosciences, Free University of Berlin, Malteserstraße 74-100, D-12249 Berlin, Germany

<sup>4</sup>Department of Earth and Planetary Science, University of Tokyo, 7-3-1 Hongo, Bunkyo, Tokyo, Japan

<sup>5</sup>Planetary Exploration Research Center, Chiba Institute of Technology, 2-17-1 Tsudanuma, Narashino, Chiba, Japan

<sup>6</sup>Instituto de Astrofísica de Canarias, University of La Laguna, Calle Vía Láctea, s/n, E-38205 San Cristóbal de La Laguna, Santa Cruz de Tenerife, Spain

<sup>7</sup>German Aerospace Center, Institute of Space Systems, Robert-Hooke-Str 7, D-28359 Bremen, Germany

<sup>8</sup>Japan Aerospace Exploration Agency, Institute of Space and Astronautical Science, 3-3-1 Yoshinodai, Chuo, Sagami-hara, Kanagawa, Japan

<sup>9</sup>Aizu Research Center for Space Informatics, University of Aizu, Aizu-Wakamatsu, 965-8580, Fukushima, Japan

<sup>10</sup>National Institute of Advanced Industrial Science and Technology, 2-3-26 Aomi, Koto, Tokyo, Japan

<sup>11</sup>Department of Physics, Meiji University, 1-1-1 Higashimita, Tama, Kawasaki, Kanagawa, Japan

<sup>12</sup>Department of Complexity Science and Engineering, University of Tokyo, 5-1-5 Kashiwanoha, Kashiwa, Chiba, Japan

Accepted 2020 October 16. Received 2020 October 6

## ABSTRACT

Alteration processes on asteroid and comet surfaces, such as thermal fracturing, (micrometeorite) impacts or volatile outgassing, are complex mechanisms that form diverse surface morphologies and roughness on various scales. These mechanisms and their interaction may differ on the surfaces of different bodies. Asteroid Ryugu and comet 67P/Churyumov–Gerasimenko, both, have been visited by landers that imaged the surfaces in high spatial resolution. We investigate the surface morphology and roughness of Ryugu and 67P/Churyumov–Gerasimenko based on high-resolution *in situ* images of 0.2 and 0.8 mm pixel resolution over an approximately 25 and 80 cm wide scene, respectively. To maintain comparability and reproducibility, we introduce a method to extract surface roughness descriptors (fractal dimension, Hurst exponent, joint roughness coefficient, root-mean-square slope, hemispherical crater density, small-scale roughness parameter, and Hapke mean slope angle) from *in situ* planetary images illuminated by LEDs. We validate our method and choose adequate parameters for an analysis of the roughness of the surfaces. We also derive the roughness descriptors from 3D shape models of Ryugu and orbiter camera images and show that the higher spatially resolved images result in a higher roughness. We find that 67P/Churyumov–Gerasimenko is up to 6 per cent rougher than Ryugu depending on the descriptor used and attribute this difference to the different intrinsic properties of the materials imaged and the erosive processes altering them. On 67P/Churyumov–Gerasimenko sublimation appears to be the main cause for roughness, while on Ryugu micrometeoroid bombardment as well as thermal fatigue and solar weathering may play a significant role in shaping the surface.

**Key words:** Comets: individual: 67P/Churyumov-Gerasimenko – Minor planets, asteroids: individual: (162173) Ryugu – Planets and satellites: fundamental parameters – Planets and satellites: surfaces – Techniques: image processing..

## 1 INTRODUCTION

The roughness of airless planetary surfaces is an influential parameter for remote sensing observations of celestial bodies. It has important impact on the photometric behaviour of a surface and therefore influ-

ences measurements of reflectance spectroscopy including imagery (Hapke 1984) and thermal emission (Davidsson et al. 2015).

Methods to derive the surface roughness from a planetary body have been developed for various scales. On large scales, roughness is an important parameter for the geologic interpretation of planetary terrains (Helfenstein 1988; Steinbrügge et al. 2020). It also causes effects such as self-heating when light is reflected and radiated to another point on a planetary surface due to the local tilt of the

\* E-mail: [katharina.otto@dlr.de](mailto:katharina.otto@dlr.de)

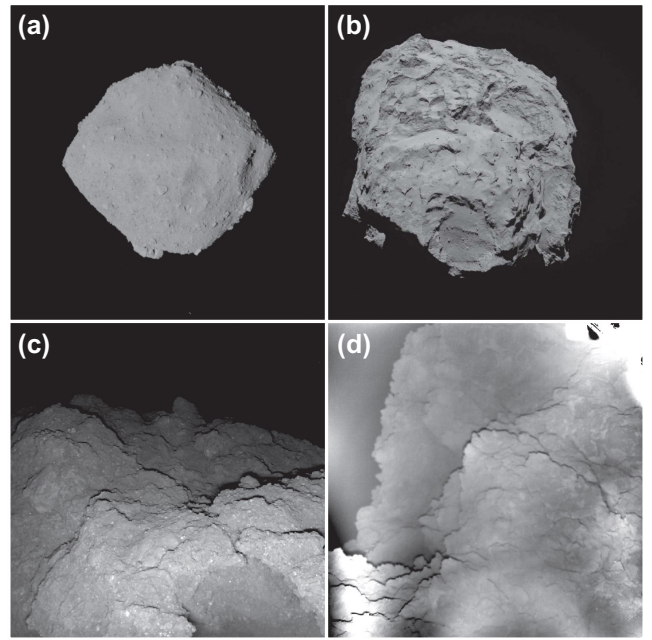
terrain. This can increase local erosion or activity on comets and the Yarkovsky and YORP-effects on asteroids (Keller et al. 2015; Rozitis & Green 2013, 2012). These effects are usually accounted for with a sufficiently high-resolution shape models that have been derived for many planetary missions from image data (Preusker et al. 2019, 2015) or laser altimetry (Barnouin-Jha et al. 2008). The latter allows the derivation of surface roughness from the pulse width of the reflected laser beam (Steinbrügge et al. 2018).

On smaller scales, surface roughness influences the spectral rock signature at wavelengths from the visible to thermal spectrum (Hapke 1981; Davidsson & Rickman 2014). Generally, it is assumed that planetary surfaces are covered with a particulate medium that depending on the particle size and shape influences the reflectance spectra of the observed surface (Hiroi & Peters 1991). However, with increasing spatial resolution of the spectral data the porosity and roughness of the surface material can influence the spectral contrast, spectral shape, and the absolute reflectance/emission due to additional volume scattering and cavity effects (Rost et al. 2018) and should be taken into account in order to avoid a misinterpretation. In addition, the roughness on scales that cause shadowing effects or small-scale self-heating have to be considered when interpreting near-infrared and thermal measurements (Davidsson, Gutiérrez & Rickman 2009). However, only topographic features larger than the thermal skin depth, usually in the centimetre scale, affect these measurements (Davidsson et al. 2015). For example, the thermal skin depth of asteroid Ryugu is approximately 1.5–3 cm (Hamm 2019) and 0.6 cm for comet Churyumov–Gerasimenko (Davidsson et al. 2016).

The Hayabusa2 sample collection procedure revealed that boulders on C-type asteroid Ryugu are covered with a layer of fine-grained particles (<1 mm) that were removed from the boulder surfaces during the collection process (Morota et al. 2020). *In situ* observations of Ryugu as well as comet Churyumov–Gerasimenko reveal that their surfaces are depleted in fine-grained materials and that the majority of surface features are bare rocks or centimetre- to decimetre-sized particle assemblies (Yano et al. 2006; Mottola et al. 2015; Schröder et al. 2017a; Jaumann et al. 2019). The rock surface roughness has implications for the shear strength and friction angles of the regolith with higher surface roughness introducing higher friction between the constituents (Reeves 1985; Xu & Sun 2005; Jiang, Li & Tanabashi 2006).

In applied geological sciences, the roughness is often estimated by visually comparing a rock profile with a standard roughness scale (Barton & Choubey 1977). More objective methods involve determining the fractal dimension or the root mean square of the slope distribution (RMS-slope) of rock profiles (Tse & Cruden 1979; Lee, Lee & Park 1997). The RMS-slope is also commonly used as roughness parameter in thermal modelling (Rozitis & Green 2013; Davidsson et al. 2015). Another roughness parameter taking into account more complex surface structures, including overhangs and caves, is the small-scale roughness parameter, which is the geometric measure of the surface area in relation to its flat projected area (Lagerros 1997; Davidsson & Rickman 2014)

In this work, we will extract roughness parameters from the only two surfaces of small bodies imaged *in situ*: asteroid Ryugu and comet Churyumov–Gerasimenko. This allows us to derive the millimetre scale roughness measured over a horizontal scale of a few tens of centimetres of the two volatile-rich bodies, compare them quantitatively and discuss the different alteration processes' influence on the surface structure. To gain insight of the dependence of roughness on the spatial scale, we also apply our method to two global images from Ryugu and Churyumov–Gerasimenko. By doing



**Figure 1.** Asteroid Ryugu and comet 67P/Churyumov–Gerasimenko imaged from orbit (upper row) and *in situ* (lower row). (a) Ryugu is approximately 900 m in diameter. (b) Churyumov–Gerasimenko from a frontal view with the small lobe in front of the big lobe (~2.5 km across). (c) *In situ* image of Ryugu illuminated with MasCam's red LED. The scene is approximately 25 cm across. The darker appearing area in the lower right corner is a cave (~7 cm wide). (d) *In situ* image at Philae's second landing site on Churyumov–Gerasimenko illuminated with ROLIS' red LED. The scene is approximately 80 cm across. Stray light is clearly visible as alternating light and dark circular areas originating from the lower edge of the image. The overexposed feature in the top right is caused by Philae's leg.

so, we avoid any influence that the method of derivation may have on the result.

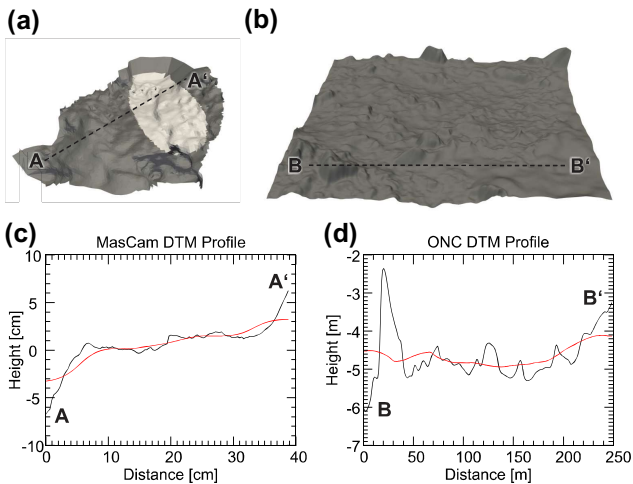
In the following sections, we first summarize the space mission operation at Ryugu and 67P and their main observations (Section 2), followed by a detailed description of the data used in this work (Section 3). In Section 4, we introduce the roughness parameters and methods developed to extract them. Section 5 includes an analysis of the model parameters and summarizes the roughness parameters of Ryugu and 67P. Section 6 discusses the influence of the model parameters and possible formation mechanisms of surface roughness. Finally, a discussion of the wider context of the results and its conclusion is given in Sections 7 and 8, respectively.

## 2 IN SITU OBSERVATIONS

Before deriving roughness parameters for Ryugu and Churyumov–Gerasimenko, we first introduce the general scene of the landing sites.

### 2.1 Scene of the MASCOT landing site

In 2018 June, JAXA's Hayabusa2 mission rendezvoused with Cb-type near-Earth asteroid Ryugu (Watanabe et al. 2017, 2019). Ryugu is a top-shaped asteroid of approximately 950 m diameter (Fig. 1a). Its relatively low density of  $1.19 \text{ g cm}^{-3}$  suggests a high bulk porosity (>50 per cent) and rubble pile structure (Watanabe et al. 2019). Ryugu is relatively dark with a geometric albedo of 4.0 per cent at  $0.55 \mu\text{m}$  (Sugita et al. 2019; Tatsumi et al. 2020) and has been



**Figure 2.** The 3D shape models used in this work and representative profiles. (a) The MasCam shape model from the *in situ* observation of Ryugu. The scene is approximately 25 cm across and a facet is about 3 mm wide. The light-shaded area is the MARA footprint. (b) ONC DTM of the area around Mascot’s landing site (50 m × 50 m at 20 cm spatial resolution). (c and d) Profiles through MasCam and ONC DTM (the black lines) as indicated in (a) and (b), respectively. The red line is the reference surface.

linked to CI or CM meteorites (Jaumann et al. 2019; Kitazato et al. 2019; Sugita et al. 2019). The surface and regolith appear rough, covered with rocks and boulders of various sizes and shapes (Sugita et al. 2019), while smaller particles in the sub-centimetre size range and dust are missing (Jaumann et al. 2019). Four morphologic types of boulders have been identified (Sugita et al. 2019): the unique bluish boulder Otohime Saxum near the south pole, bright and mottled, bright and smooth, and dark and rugged boulders. The last two types have also been observed by the Mobile Asteroid Surface Scout (MASCOT) during its descent and the rugged boulder type has additionally been observed *in situ* in high image resolution on Ryugu’s surface (Fig. 1c).

MASCOT was detached from the Hayabusa2 spacecraft on 2018 October 3 and after the initial descent phase and relocation on the surface, MASCOT landed near a crumbly and rough boulder that it observed *in situ* with four on-board instruments [Jaumann et al. 2019; camera, radiometer, magnetometer, and spectrometer (unable to return expected data; Ho et al. 2017)] including a high-resolution camera (MasCam; Jaumann et al. 2017). Due to a slight tilt towards the surface (22° with respect to the surface plane), a field of view of 55° and the Scheimpflug optics of MasCam, resolutions down to 0.15 mm could be achieved in the lower part of the images while at the same time maintaining image sharpness for larger distances. Additionally, MasCam was equipped with an LED array composed of four individual colours (blue, green, red, NIR) for illumination during night time. A mini-move by MASCOT allowed observing of the scene from two different directions, which was used to derive a 3D shape model of the observed rough boulder on a spatial scale down to ~3 mm (Fig. 2a; Scholten et al. 2019).

MasCam showed a scene, approximately 25 cm across, highlighting a bare boulder with bright inclusions in the millimetre scale, but visible absence of sand and pebble-sized particles (Jaumann et al. 2019). This in combination with the radiometric measurements led to the conclusion that the boulder is highly porous (28–55 per cent) and that the tensile strength is relative low (200–280 kPa; Grott et al. 2019). In fact, small pores larger than 1 mm could not be observed while smaller pores may be present but not resolvable within the

MasCam image (Grott et al. 2019). The 3D scene shows a prominent hollow in the foreground with a size of approximately 7 cm with multiple smaller indentations (~2 cm) and a roughly 2 cm extended overhang at the right-hand corner of the scene (Fig. 1c). The hollow and indentations have a convex shape. Cauliflower-like undulations on the scale of ~1 cm form the surface texture of the boulder. They are covered with further, smaller undulations of approximately 2–3 mm, which suggest a fractal nature of the surface. Although there are exceptions, the feature size of 1 cm and 2–3 mm appears to be a characteristic for this scene.

The images of MasCam show a cauliflower-like rock surface texture, which can also be observed for cohesive fine-grained materials. This is particularly evident in the images acquired during night when the LEDs were used to illuminate the surface. This structural appearance resembles pristine cometary material observed *in situ* by the Philae lander comet Churyumov–Gerasimenko (Bibring et al. 2015; Schröder et al. 2017a) and is also similar to fracture surfaces of aqueously altered carbonaceous chondrites (Fuchs, Olsen & Jensen 1973; Gounelle & Zolensky 2014). We will discuss the similarities and differences between Ryugu’s and Churyumov–Gerasimenko’s surface texture in more detail in this work.

## 2.2 Scene of the ROLIS landing site

On November 12, the Philae lander on board the Rosetta mission was detached and landed on comet Churyumov–Gerasimenko (Ulamec et al. 2016). After the initial touchdown and bounce, Philae got to rest at the Abydos site, a relatively rough terrain on the comet. Churyumov–Gerasimenko is a bi-lobate Jupiter family comet with dimensions 4.3 km × 2.6 km × 2.1 km (Jorda et al. 2016). With an estimated bulk porosity of 70–75 per cent (Jorda et al. 2016), Churyumov–Gerasimenko is more porous than asteroid Ryugu. Churyumov–Gerasimenko is relatively dark with a geometric albedo of 6.2 per cent at 0.55 μm (Ciarniello et al. 2016). Geomorphologically, Churyumov–Gerasimenko possesses a north–south dichotomy exhibiting a rough consolidated terrain in the south and a smooth airfall-covered terrain in the north. This is probably caused by the increased erosion of the Southern hemisphere during the perihelion passage (Keller et al. 2015). The rough terrain of the Southern hemisphere, where Philae came to its final rest, is composed of consolidated material of 10–50 cm thickness (Knappmeyer et al. 2018). This layer probably formed by sintering and cementing of volatiles and dust in the near surface layers (Spohn et al. 2015). Two camera systems on-board Philae, CIVA, and ROLIS, showed this consolidated rough terrain in detail (Poulet et al. 2016; Schröder et al. 2017a). Similar to MasCam on Ryugu (Jaumann et al. 2019), CIVA reports on two types of textures within the field of view – a smooth fine-grained and a rough granular texture (Poulet et al. 2016). ROLIS describes a consolidated jagged surface with cracked plates. Schröder et al. (2017a) also note the fractal nature of Churyumov–Gerasimenko’s surface by describing similar surface morphologies on various scales.

The ROLIS camera on-board Philae operated in a similar manner to MasCam on Ryugu. Both cameras possess a 1024 m × 1024 sensor and a four colour LED array [465–812 nm (MasCam), 470–870 nm (ROLIS)] for illuminating the near surface (Mottola et al. 2007; Jaumann et al. 2017). ROLIS was mounted underneath the Philae lander and was focusing on a surface 30 cm away from the lens. At this distance, the field of view of 58° has a pixel resolution of 0.33 mm (Mottola et al. 2007). However, as Philae landed on its side and thus ROLIS partly pointed to the horizon ROLIS’ infinity lens, aimed to be employed for long distances during descent, yielded



the best image of the scene on Churyumov–Gerasimenko (Schröder et al. 2017a).

ROLIS showed an approximately 80 cm × 80 cm scene at Philae’s second landing site on comet Churyumov–Gerasimenko (Fig. 1d). Similar to Ryugu, no individual grains or pebbles were detected on the surface, but some ejected particles were visible moving along the horizon (Schröder et al. 2017a). A bimodal brightness distribution with dark smooth patches and bright areas running along rough edges are visible. The albedo variation has been suggested to be the result of different degrees of consolidation of the same material with the light areas being less consolidated compared to the dark areas. The surface also appears to have no visible inclusions or pores above ~1 mm in size (Schröder et al. 2017a). The surface morphology of Churyumov–Gerasimenko appears similar to Ryugu with cauliflower-like patterns and undulations, but of slightly larger extent of ~5 cm. The cometary structure seems somewhat more ragged, illustrated by small ~1 cm slots and pointy ridges.

### 3 DATA

#### 3.1 MASCOT on Ryugu

We used *in situ* images acquired by MasCam at the second landing site at 22°S and 317°E (Jaumann et al. 2019). At this location, the main science cycle was conducted and day and night time images were taken. For the evaluation of roughness, we chose the image acquired during night time illuminated with the red LED (image tag: F1087378791\_701\_29464\_r2, exposure time: 3 ms, image depth: 14 bit) as the stray light in this image appears the least prominent (Schröder et al. 2020) and the contrast highest compared to the other illumination colours (Fig. 1c). This image is 1024 × 1024 pixels large and has a pixel resolution of approximately 0.2 mm across the foreground of the image which is the focus of our analysis. A geometric correction of the image was not applied as the effects are negligible.

A shape model of the scene observed by MASCOT and a 50 m × 50 m large shape model with a spatial resolution of 20 cm and 124000 facets derived from Hayabusa2’s optical navigation cameras (ONC) images of MASCOT’s landing site (Preusker et al. 2019; Scholten et al. 2019) were used to independently derive the RMS-slope and small scale roughness parameter for comparison with our method (Fig. 2).

#### 3.2 Philae on 67P/Churyumov–Gerasimenko

We analyse the roughness of a cometary rock using images taken on Churyumov–Gerasimenko by the ROLIS camera on-board the Philae lander on Rosetta (Mottola et al. 2007). However, the ROLIS images are highly affected by stray light introduced by the lens system and an overexposed part of the lander foot in one corner of the image. Thus, we used the enhanced and processed red image published by Schröder et al. (2017a) for our analysis (Fig. 1d). The image is slightly out of focus, however, as we will see below (Section 4.2) this will not affect our conclusions. The pixel resolution of this image is approximately 0.8 mm in the foreground with a total of 1024 × 1024 pixels.

#### 3.3 Global analysis

Finally, we used two global images acquired with the red filters of the orbiter cameras on-board Hayabusa2 (ONC-T; Kameda et al.

2017) and Rosetta (OSIRIS; Keller et al. 2007) to extract large-scale roughness values with our method (Fig. 1a and b). The image of Ryugu (image tag: hyb2\_onc\_20180925\_091520\_twf\_12d) has an image depth of 10 bit and a size of 1024 × 1024 pixels. For validating the quality of our method, we also used the blue version of this image that was taken a minute after the red image and is visually almost identical to the red image (image tag: hyb2\_onc\_20180925\_091624\_tbf\_12d). The image of Churyumov–Gerasimenko (image tag: NAC\_2014-08-06T01.20.01.282Z\_ID30\_1397549600.F28) has an image depth of 14 bit and is with 2028 × 2048 pixels twice as large as the other images used in this work. Both images have a spatial resolution of approximately 2 m. Here, we chose an image showing a frontal view of Churyumov–Gerasimenko to avoid the bi-lobate shape of the comet to influence our results. Both global images are geometrically corrected to minimize large-scale distortion effects on the analysis.

## 4 METHOD

In this work, we report on the topographic surface roughness on asteroid Ryugu and comet Churyumov–Gerasimenko from space mission images. We introduce a new objective and reproducible method to extract eight commonly used roughness parameters including the RMS-slope, hemispherical crater density, fractal dimension, Hurst exponent, JRC, small-scale roughness parameter, and Hapke mean slope angle from such images. Before describing the method (Sections 4.2 and 4.3), we first introduce the roughness parameters in detail (Section 4.1).

### 4.1 Description of roughness parameters

#### 4.1.1 RMS-slope

The RMS-slope distribution of a planetary surface can be derived when the topography of a body is known. Given a local or global shape model composed of  $N$  connected facets, the RMS-slope  $s$  is defined as the root of the square of each facet’s slope  $\theta_i$  weighted by the projection of the facet area  $a_i$  on to the local reference plane (Spencer 1990; Rozitis & Green 2011; Davidsson et al. 2015):

$$s = \sqrt{\frac{\sum_{i=1}^N \theta_i^2 a_i \cos \theta_i}{\sum_{i=1}^N a_i \cos \theta_i}}. \quad (1)$$

In order to assess spatially unresolved roughness of remote sensing data from space missions, specifically those of thermal infrared emission observations, various roughness models have been established (Davidsson et al. 2015). A commonly used model assumes that the unresolved roughness can be represented by a flat surface speckled with spherical-section craters (Buhl, Welch & Rea 1968; Spencer 1990). The parameters defining the roughness are the crater density  $f$  and the ratio between crater depth and crater curvature diameter  $\delta = \frac{1}{2}(1 - \cos \gamma)$ , where  $\gamma$  is the largest slope angle of the crater. The RMS-slope is then defined as (Lagerros 1996; Davidsson et al. 2015):

$$s = \sqrt{\frac{f}{2} \left( \gamma^2 - \frac{(\gamma \cos \gamma - \sin \gamma)^2}{\sin \gamma^2} \right)}. \quad (2)$$

The RMS-slope in this model depends on two parameters  $f$  and  $\gamma$ , however, in many cases of modelling roughness on airless bodies, hemispherical craters are assumed ( $\gamma = 90^\circ$ ,  $\delta = 0.5$ ) so that the



RMS-slope simplifies:

$$s_{\delta=0.5} = \sqrt{\frac{f}{2} \left( \frac{\pi}{4} - 1 \right)}. \quad (3)$$

A saturation of hemispherical craters results in an RMS-slope of  $49^\circ$ . This model has also been applied by Grott et al. (2019) when calculating the thermal conductivity of the boulder observed on Ryugu from thermal infrared measurements. A hemispherical crater density of  $f = 0.34$  represents a good agreement with their measurement. On Churyumov–Gerasimenko, the hemispherical crater density is highly dependent on the geologic setting and varies between 0.1 and 0.8 (Marshall et al. 2018). For comparability, we will also use the hemispherical crater density in this work.

#### 4.1.2 Small-scale roughness parameter

The small-scale roughness parameter  $\xi$  describes the ratio between the area of a rough surface  $a_r$  and its projection on to a reference surface  $a_p$  (Davidsson et al. 2009; Davidsson & Rickman 2014):

$$\xi = 1 - \frac{a_p}{a_r}. \quad (4)$$

The advantage of this parameter is that it considers the contribution of cavities and overhangs of a rough surface that cannot be represented by the RMS-slope. It approaches 1 for very rough surfaces. For some thermal roughness models, including the crater roughness model described above, the small-scale roughness parameter is identical to the small-scale self-heating parameter when scattering is neglected (Davidsson & Rickman 2014; Lagerros 1998, 1997). Using a thermophysical model reproducing temperatures extracted from the near-infrared spectrum of comet 9P/Tempel 1, Davidsson et al. (2009) found that small-scale self-heating parameter values between 0.6 and 0.75 are common for the comet and values as low as 0.2 were also found in smoother areas.

#### 4.1.3 Hapke mean slope angle

Another popular roughness parameter, commonly used in spectral investigations of remote sensing data, is the Hapke mean slope angle  $\bar{\theta}$  of a rough surface. Hapke (1984) assumes that the roughness is introduced by flat facets with normally distributed orientations and defines the Hapke mean slope angle of these facets as

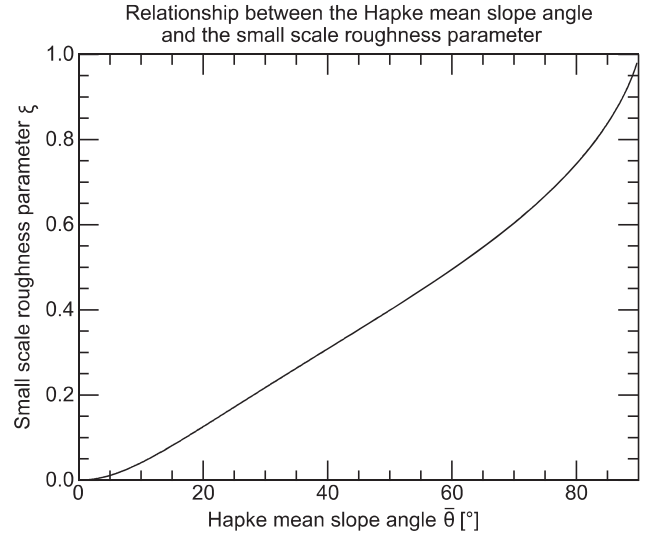
$$\tan \bar{\theta} = \frac{2}{\pi} \int_0^{\pi/2} \tan \theta a(\theta) d\theta, \quad (5)$$

where  $a$  is a normalized Gaussian distribution of not too large slope angles  $\theta$ . Following Lagerros (1997), the relationship between Hapke's mean slope angle and the small-scale roughness parameter  $\xi$  (equation 4) can be expressed as

$$\xi = 1 - \frac{E_1(\cot^2 \bar{\theta} / \pi)}{\pi \tan \bar{\theta} \operatorname{erfc}(\cot \bar{\theta} / \sqrt{\pi})}, \quad (6)$$

if the slopes follow a Gaussian distribution. Here,  $E_1(x) = \int_1^\infty \exp(-xt)/t dt$ . In the roughness regime of most planetary surfaces ( $\bar{\theta} \approx 20^\circ$ – $40^\circ$ ), the relationship between  $\xi$  and  $\bar{\theta}$  is nearly linear with a slope of 0.009 [ $1/^\circ$ ] (Fig. 3).

As we will see later, the criterion that the slope distribution is normally distributed is a consequence of the method we will apply and this assumption is therefore valid. However, the constraint to small angles will pose some difficulties as we will discuss in Section 7.



**Figure 3.** Relationship between the Hapke mean slope angle and small scale roughness parameter (equation 6). The relationship is approximately linear in the regime of most planetary surfaces with  $\xi \approx 0.009[1/^\circ] \cdot \bar{\theta}$ .

#### 4.1.4 Fractal dimension, Hurst exponent, and joint roughness coefficient

The fractal dimension is a measure of the surface roughness of self-affine structures (Zahouani, Vargiolu & Loubet 1998). Fractal surfaces possess the characteristic that with decreasing measuring unit  $r$  the total length of the measured surface  $L$  increases monotonically (Mandelbrot 1967; Huang, Oelfke & Speck 1992):

$$L(r) = r^{D-1}, \quad (7)$$

where  $D$  is the fractal dimension, which varies between 1 for smooth and 2 for rough 2D surfaces. Fractal descriptions have been found to be useful in various geologic applications including the description of coastlines and the joint surfaces of rocks (Mandelbrot 1967; Odling 1994).

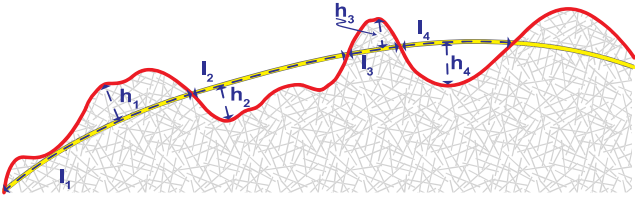
The fractal dimension is dependent on the dimension of the space, e.g. 2D or 3D, it has been determined for. The Hurst exponent  $H$  is linearly related to the fractal dimension, independent of the dimension of space and varies between 0 and 1 for smooth and rough contours/surfaces, respectively (Shepard & Campbell 1998):

$$H = 2 - D \quad (\text{for 2D profiles}), \quad (8a)$$

$$H = 3 - D \quad (\text{for 3D surfaces}). \quad (8b)$$

A way to construct such a fractal surface is the Koch curve. Starting with a straight line segment, a triangle with base length  $l$  and height  $h$  is placed in the centre of the line forming the first-order Koch curve. The repetition of this procedure on each of the first-order line segments generates the second order and so on, creating a fractal structure. In geoscientific applications, natural rock joints are often assumed to follow a construction similar to the Koch curve (Xie & Pariseau 1994). The advantage is that the fractal dimension can be estimated from a single length-scale of a 2D contour using the equation

$$D = \frac{\log 4}{\log (2 (1 + \cos (\tan^{-1} (2h/l))))}, \quad (9)$$



**Figure 4.** Illustration of the derivation of the fractal dimension of a 2D profile. Shown is the measurement (the blue-dashed lines) of base length and asperity height of a natural contour (the red line). The reference contour is sketched as the yellow line.

where  $h$  and  $l$  are the average height and the base length of high-order asperities of a rock joint (Xie & Pariseau 1994; Li & Huang 2015; Fig. 4). The fractal dimension of the equilateral Koch curve with  $h = \sqrt{3}/2l$  yields  $D = \log 4/\log 3 = 1.26$ .

The fractal dimension can be correlated to the joint roughness coefficient (JRC), a measure of the roughness of rock joints used to estimate the peak shear strength of a material. The JRC has been empirically related to the fractal dimension by the formula (Li & Huang 2015)

$$\text{JRC} = 118.89(D - 1)^{0.4343}. \quad (10)$$

The peak shear strength  $\tau$  of a joint rock surface is given by

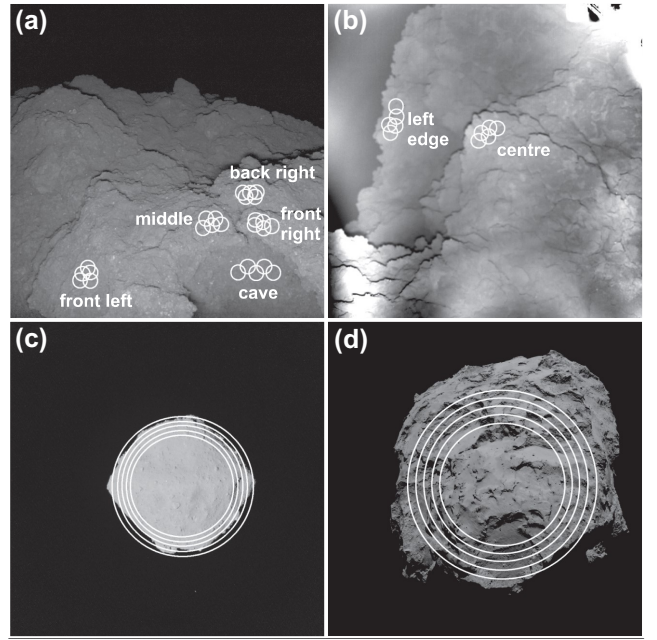
$$\tau = \sigma_n \tan \left( \text{JRC} \log \left( \frac{\text{JCS}}{\sigma_n} \right) + \Phi_b \right), \quad (11)$$

where  $\sigma_n$  is the effective normal stress, JCS is the joint wall compressive strength, and  $\Phi_b$  is the basic friction angle (Barton 1976). Note that both,  $\tau$  and  $\sigma_n$ , have the unit of a pressure.

## 4.2 Roughness from 2D images

To extract the surface roughness from images acquired *in situ* on asteroid Ryugu and comet Churyumov–Gerasimenko with the highest available spatial resolution, we derive the RMS-slope, hemispherical crater density, small-scale roughness parameter, Hapke mean slope angle, fractal dimension, Hurst exponent, and JRC from the outline of imaged rocks applying an objective and reproducible method suitable for images acquired with LED illumination. Due to its high quality and resolution, we tested our method and its dependence on the input parameters using the MasCam image (Section 5.1).

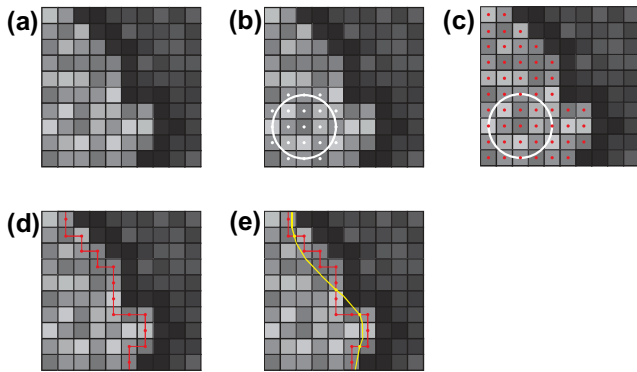
Our method is based on the observation that the texture and material imaged is relatively homogeneous over an area smaller than the rock but large enough to be statistically relevant ( $>1000$  pixels). Within the illuminated images, it can be assumed that parts of the rock with the same distance to the LED have a similar radiance and that with increasing distance the radiance decreases ( $\propto r^2$ ). This makes areas with the same distance from the camera similarly bright in the image. Thus, we aim at determining the 2D surface at a specific distance, represented by pixels of similar radiance. It can be imagined as a cut through the rock perpendicular to the camera at a specific distance. The texture caused by bright or dark inclusions and varying surface tilts at this specific distance is considered by computing the histogram of pixel brightness values at the given distance and by assuming a Gaussian distribution of these pixel values. The mean and variance of this distribution allow constraining pixels belonging to a specific distance by their brightness values.



**Figure 5.** The four images used in this work. Each region to be analysed (labelled in upper row) was investigated using five slightly varying starting regions (the white circles). Note that the number of regions investigated in each image varies and that a different starting region selection procedure was applied for the global images. Here, the size of the starting regions varies with the smaller starting regions being a subset of the larger ones, whereas the *in situ* images have overlapping starting regions of the same size. (a) The red MasCam image of Ryugu ( $\sim 0.2$  mm spatial resolution). (b) The red ROLIS image of Churyumov–Gerasimenko ( $\sim 0.8$  mm spatial resolution). Note the stray light emerging from the lower image boundary as quasi-circular alternating light and dark regions. The starting regions were chosen in areas that are less dominated by stray light. (c) ONC image of Ryugu at  $\sim 2$  m spatial resolution. (d) OSIRIS image of Churyumov–Gerasimenko at  $\sim 2$  m spatial resolution.

More precisely, looking at the *in situ* images (Fig. 5a and b), for each image investigated we identified structures [labelled front left, middle, cave, front right, and back right on Ryugu and left edge and centre on Churyumov–Gerasimenko (Fig. 5a and b)] of which to measure the surface roughness. Where available, we also used a shape model to make sure that the structures had a more or less constant distance to the camera. Within these structures, we defined five circular starting regions that covered a representative texture and colour of the structure to investigate (Fig. 5). The regions comprised  $\sim 1835$  pixels within the *in situ* images. Within the MasCam image this corresponds to a roughly 1 cm in diameter circle on the rock surface. For each structure, we derived the roughness parameters by growing all of the five circular starting regions using a standard growing algorithm (see below for details) and averaged the results to generate a representative value.

We also used two global images of Ryugu and Churyumov–Gerasimenko to derive the roughness parameters on a larger scale. For these, we used a slightly different approach taking advantage of the fact that the background of the images is black space and therefore easily distinguishable. The five circular starting regions covered the majority of the imaged object (Fig. 5c and d). Comprising dark pixels showing space in the circular starting regions, results in a pixel value histogram with two peaks, one at the average asteroid/comet pixel value and one at the average space pixel value, which would allow a precise determination of the object’s limb. However, we used circular



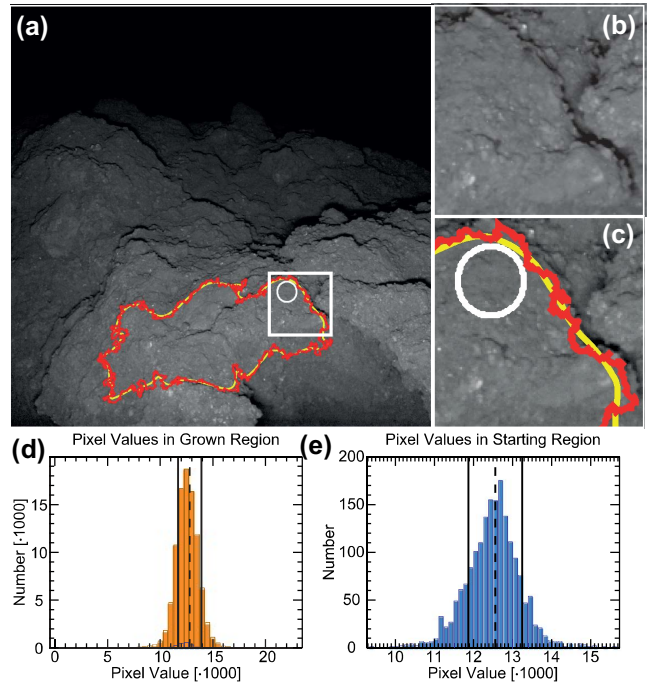
**Figure 6.** Sketch illustrating the method used in this work. (a) Image composed of pixels with lighter area to the left separated from a darker area to the right by a dark shadow. (b) Starting region in the light area. The large white circle illustrates the starting region. Pixels with the white dots belong to the starting region. (c) The grown region marked by the red dots. (d) Boundary pixels (the red dots) and their connection (the red lines). (e) Boundary contour (red) and reference contour (yellow). The yellow dots illustrate the boundary between adjacent sections as needed for deriving the fractal dimension (compare with Fig. 4b).

starting regions that predominantly cover the object to be consistent with the approach used for structures in the *in situ* images. The five circular starting regions had varying sizes ranging from  $0.5\text{--}1.2 \times 10^6$  pixels for Churyumov–Gerasimenko and  $0.8\text{--}1.4 \times 10^5$  for Ryugu. Each smaller circular starting region was a subset of the larger ones.

We then grew each of these regions using a region growing algorithm. Figs 6 and 7 illustrate our method. We determined the mean and standard deviation of the pixels’ values within each circular starting region (7e) and added all connected neighbouring pixels (each pixel has eight neighbours) that had radiance values falling within the mean plus/minus a multiple of the standard deviation to the region (Figs 6c and 7e). Pixels not fulfilling this criteria but being surrounded by pixels fulfilling it were also considered part of the grown region. In general, we constrained the values using one standard deviation around the mean, but also investigated the effect when changing this range (Section 5.1). The boundary of this grown region was then used as the structure’s boundary profile. The boundary pixels are connected in a closed loop (the red line in 7a) with each boundary pixel having exactly one preceding and one following neighbour within the eight surrounding pixels (6d).

Although in some cases, specifically the MasCam observations, the image quality appears relatively good the roughness on the pixel scale is not solely introduced by the topography of the rock surface. Instead effects such as image noise, point spreading of particularly bright features, and rock texture introduce a roughness to the rock surface that needs to be neglected when deriving the topographic roughness. In order to remove such factors, we applied a morphologic operator to the grown region. By mathematically closing the grown region with a circular structural element (dilation followed by erosion), we filled indentations of the size of the structural element along the contour boundary (e.g. Gonzalez & Woods 2018). This process also counteracts any biases arising from blurry image boundaries.

Inclusions are the most prominent disturbance along the boundary within the rocks on Ryugu. Their size ranges from 0.1 to 2 mm with a characteristic size of 3 pixels in the area investigated. We therefore chose the size of the structural element for the closing operation to be



**Figure 7.** Illustration of the growing region algorithm in the middle of the MasCam image. (a–c) The MasCam image with circular starting region (white), rough detected outline (red), and smoothed reference contour (yellow). (b) and (c) are subsets of (a) as indicated by the white box. Note that the rough outline follows the shadow detected closest to the starting region rather than the most prominent one. (d) Histogram of all pixel values within the grown region. The blue histogram represents the histogram of the starting region as shown in (e). The dashed and dash-dotted lines indicate the mean and the 1 standard deviation, respectively.

3 pixels across, but also investigated the influence of different sizes of the structural element.

To derive the above described roughness parameters from the boundary, a reference contour is needed. This reference contour represents the assumed local rock topography without any roughness. Although all roughness parameters depend on this reference contour, it is often chosen arbitrarily in the literature. Here, we derived the reference contour by applying a running mean along the rough boundary contour. For each point along the boundary, we derived the mean  $x$ – $y$  position including the preceding 50 and following 50 pixels along the boundary. Within the MasCam images, 100 pixels correspond to roughly 2 cm length, which is an appropriate length-scale given the size of indentations and overhangs described in Section 2.1. This smoothed boundary was used as the reference contour (Figs 6e, and 7a and c). We also experimented with changing the length of the running mean. Note that the constraint formulated by Hapke (1984), that the slope angles follow a Gaussian distribution (Section 4.1.3), is automatically fulfilled when applying a running mean to define the reference contour.

Given the reference contour and the rough boundary contour of a specific structure identified in the high-resolution images, we derived the RMS-slope of the rough contour by determining the angle between the line connecting two adjacent pixels along the rough boundary contour and the line connecting the corresponding pixels on the reference contour. Following equation (1), we derived the RMS-slope from this angle and the length of the section between the two adjacent pixels on the rough contour. Because the derivation of the RMS-slope requires a 3D surface boundary rather than a 2D surface



contour, we assumed that the depth of the pixel along the direction of the boresight vector is the same as the pixel dimension in the image, e.g. 1. This allowed us to simply use the distance between two pixels as the facet area required in equation (1). Using the angle between the reference and rough boundary contour as described above and again assuming that the extent of the pixels along the boresight vector is 1, we derived the small-scale roughness parameter by projecting the rough boundary segment on to the reference contour and applying equation (4).

Finally, we derived the fractal dimension of the rough boundary contour with respect to the reference contour by finding the intersections of the rough boundary contour and the reference contour. For each section bounded by two adjacent intersections (Fig. 6e) we derived the base length by calculating the distance between the two adjacent intersections along the reference contour and the local height by calculating the maximum distance of any rough boundary pixel located in this section to the reference contour (Fig. 4b). We then derived the fractal dimension applying equation (9) by repeating these calculations for each section bounded by two adjacent intersections and determining the average base length and height from all sections. We then applied equation (10) to estimate the JRC.

### 4.3 Roughness from 3D shape models

Additionally, we derived the roughness parameters from two local shape models. For a comparison with the roughness estimated by fitting thermal measurements (Grott et al. 2019), we considered the roughness of the MARA footprint in the MasCam DTM separately. As reference surface we used an arbitrary sphere. Note that the radius of this sphere is not necessary to determine because the angle between a facet's and the sphere's local normal vectors is independent of the radius of the sphere.

Furthermore, we determined the fractal dimension and corresponding Hurst exponent and JRC for these differently resolved shape models near the MASCOT landing site. These parameters are derived from 2D contours. Thus, we extracted 10 arbitrary profiles each and calculated the reference contour for the 20 cm resolution ONC DTM by smoothing the profiles consisting of 250 data points (50 m) with a running mean of 100, which corresponds to approximately 20 m, maintaining the same ratio between the DTM spatial resolution and smoothing resolution (0.01) as applied in the image-based method described above. Due to the small length of the profiles of the 3 mm resolution MasCam DTM (53–121 data points, 16–39 cm), the smoothing factor was chosen to be 34 (10 cm), which is on average the same ratio between profile length and smoothing factor as chosen for the ONC DTM, and thus maintains comparability. Profiles crossing through the cave in the front of the MasCam DTM were not considered due to restrictions of our 2.5D profile extraction tool. To derive a representative fractal dimension, Hurst exponent and JRC we averaged the results from the individual profiles. The so-derived 2D fractal dimension is comparable to the 3D value (Tatone & Grasselli 2009; Cai et al. 2018)

## 5 APPLICATION AND RESULTS

### 5.1 Effect of input parameters on roughness

In order to access the reliability of our results and its sensitivity to the chosen parameters, we used the basic parameter set as described in Section 4.2 for the middle region in the MasCam image (smoothing factor of reference contour = 100, standard deviation multiplier =

1, size of structural element = 3, image pixel resolution = 1) and varied one parameter at a time. The result is summarized in Table 1.

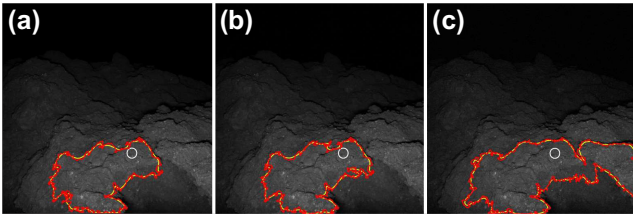
To explore the robustness of our method against image noise, we added a Gaussian random noise to the MasCam image with a scale factor of 10 per cent and 50 per cent of the mean pixel value of the image. As shown in Fig. 8, the area detected by the grow region algorithm varies slightly in the 10 per cent noise image (Fig. 8b) and expands to the right-hand side in the 50 per cent noise image (Fig. 8c) compared to the original image (Fig. 8a). This can be explained by noisy pixels bridging shadows and allowing the algorithm to grow into areas that are separated by a shadow in the image without or little noise. We then extracted the roughness values and found that the RMS-slope and corresponding hemispherical crater density slightly decrease (for 10 per cent noise level) and increase (for 50 per cent noise level) when introducing noise, but they agree within their errors. The fractal dimension and derived values (Hurst exponent and JRC) show the opposite effect of a very small increase in roughness for a 10 per cent noise level and a decrease for 50 per cent noise level. This decrease can be explained by the growing region reaching the image border to the right and therefore artificially detecting a flat boundary. The small-scale roughness parameters and Hapke mean slope angles are constant within their errors. This inconsistency in roughness variation and the low variation within the derived roughness values with additive noise shows that the image noise does not have a systematic effect on the roughness derived. This is achieved by the mathematical closing of the detected boundary, which effectively erases any noise along the boundary on the scale of the structural element.

The filters and camera settings also have an effect on the point spread function on the detector and therefore on the quality of an image. The point spread function is dependent on the incident angle, camera temperature, and wavelength. We investigated whether the wavelength influences the result of our method by repeating the global analysis of Ryugu with a blue Ryugu image taken a minute after the red image shown in Fig. 5(c). Both, the red and blue image, are visually nearly identical and so we used the exact same starting region locations. The roughness derived from the blue and red images are either identical or agree within  $1\sigma$  standard deviation. We thus conclude that the wavelength the image was taken at and the according point spread function does not have a significant effect on the roughness derived from an image.

The smoothing factor to generate a reference contour was chosen to be 100, e.g. a running mean of 100 points was applied to the boundary surface. Increasing this number results in a smoother and decreasing in a rougher, more similar to the boundary surface, reference contour. The RMS-slope and corresponding hemispherical crater density increase steadily with increasing smoothing factor. This behaviour is expected because the reference contour's similarity to the boundary contour decreases with increasing smoothing factor and therefore results in a higher roughness. A similar trend is observed for the small-scale roughness parameter and Hapke mean slope angle with an exception for the highest smoothing factor of 300, which is the lowest value. However, the error on this value is comparatively large and points at an outlier within the individual starting regions' results. The fractal dimension and derived parameters (Hurst exponent and JRC) show no obvious trend with increasing smoothing factor. The more similar the reference contour is to the boundary contour (e.g. the smaller the smoothing factor), the more intersections of the reference and boundary contour exist and the more values for the average section length and height can be taken into consideration generating a larger statistic, but not necessarily different values. Thus, a smoothing factor of 100 is reasonable for the scene observed.

**Table 1.** Parameters describing the roughness of the rock on Ryugu derived directly from the *in situ* image for the representative region in the middle of the image. The effect of different input parameters on the derived roughness parameters is shown. The errors are the  $1\sigma$  standard deviation derived from five locally varying starting regions and, where deduced from other values, derived via standard error propagation.

Input Standard deviation multiplier	Size of structural element	Image resolution	Smoothing factor reference contour	Result					Small scale roughness parameter	Hapke mean slope angle (°)
				Hemispherical crater density	Fractal dimension	Hurst exponent	JRC	RMS slope (°)		
1	3	1	100	0.56 ± 0.01	1.18 ± 0.01	0.82 ± 0.01	55.9 ± 1.0	36.8 ± 0.4	0.331 ± 0.006	42.6 ± 0.8
↔	↔	↔	↔ 10% noise	0.56 ± 0.03	1.18 ± 0.01	0.82 ± 0.01	56.5 ± 1.8	36.6 ± 0.9	0.330 ± 0.006	42.4 ± 0.8
↔	↔	↔	↔ 50% noise	0.59 ± 0.01	1.15 ± 0.01	0.85 ± 0.01	52.4 ± 1.3	37.6 ± 0.4	0.330 ± 0.004	42.4 ± 0.5
1	3	1	50	0.55 ± 0.01	1.16 ± 0.003	0.84 ± 0.003	53.6 ± 0.5	36.3 ± 0.3	0.322 ± 0.004	41.6 ± 0.5
1	3	1	200	0.60 ± 0.02	1.19 ± 0.01	0.81 ± 0.01	58.0 ± 1.2	38.1 ± 0.3	0.333 ± 0.003	42.8 ± 0.4
1	3	1	300	0.63 ± 0.01	1.18 ± 0.01	0.82 ± 0.01	56.4 ± 1.6	38.9 ± 0.3	0.329 ± 0.008	42.3 ± 1.0
1.5	3	1	100	0.54 ± 0.01	1.14 ± 0.02	0.86 ± 0.02	51.2 ± 2.6	36.2 ± 0.2	0.314 ± 0.003	40.1 ± 0.4
2	3	1	100	0.54 ± 0.01	1.14 ± 0.01	0.86 ± 0.01	50.5 ± 1.8	36.0 ± 0.2	0.304 ± 0.003	39.5 ± 0.4
3	3	1	100	0.50 ± 0.01	1.12 ± 0.02	0.88 ± 0.02	46.7 ± 3.2	34.6 ± 0.6	0.287 ± 0.010	37.6 ± 1.3
1	1 (no erosion)	1	100	0.60 ± 0.003	1.28 ± 0.04	0.72 ± 0.04	68.4 ± 4.2	37.9 ± 0.1	0.343 ± 0.003	43.8 ± 0.4
1	5	1	100	0.56 ± 0.01	1.14 ± 0.01	0.86 ± 0.01	51.0 ± 1.1	36.8 ± 0.2	0.310 ± 0.005	40.2 ± 0.6
1	3	2	100/2 → 50	0.57 ± 0.02	1.20 ± 0.02	0.80 ± 0.02	59.5 ± 2.0	37.0 ± 0.8	0.333 ± 0.015	42.8 ± 1.9
1	3	2	100	0.58 ± 0.02	1.21 ± 0.04	0.79 ± 0.04	59.6 ± 4.5	37.3 ± 0.6	0.328 ± 0.011	42.2 ± 1.4
1	3	4	100/4 → 25	0.56 ± 0.02	1.22 ± 0.01	0.78 ± 0.01	61.1 ± 1.2	36.6 ± 0.7	0.328 ± 0.013	42.2 ± 1.7
1	3	4	100	0.58 ± 0.02	1.29 ± 0.04	0.71 ± 0.04	69.0 ± 4.7	37.4 ± 0.6	0.340 ± 0.008	43.6 ± 1.0
1	3	8	100/8 → 12.5	0.52 ± 0.05	1.18 ± 0.06	0.82 ± 0.06	55.3 ± 8.7	35.4 ± 1.7	0.292 ± 0.034	38.2 ± 4.4
1	3	16	100/16 → 6.25	0.43 ± 0.09	1.12 ± 0.04	0.88 ± 0.04	46.8 ± 8.3	32.0 ± 3.3	0.239 ± 0.025	32.4 ± 3.4



**Figure 8.** The effect of noise on growing a region in the middle of the image. The white, red, and yellow outlines represent the starting region from which the growing algorithm started (compare with Fig. 5a), rough contour and reference contour. (a) Original image, (b) additive noise of 10 per cent of the mean pixel value, (c) additive noise of 50 per cent of the mean pixel value. Note that the grown region approaches the image boundary on the right in (c) that causes a smaller fractal dimension.

The standard deviation multiplier is used to define the cut-off value for the growing region. All pixels with values lying within the mean plus/minus the standard deviation times its multiplier of the starting region are considered for growing the region. Changing the standard deviation multiplier results in different cut-off values with larger regions for larger multipliers. All roughness values show a decrease in roughness with increasing standard deviation multiplier. The larger the standard deviation multiplier, the larger are the grown regions and the distances to the camera they cover. Particularly at a large distance from the camera, the brightness gradient is smaller and borders of the grown region are smoother, which is represented in the lower roughness values. Also, boundaries that align with the image frame and that were not taken out of consideration, further smooth the roughness values. It is therefore advisable to use a small standard deviation multiplier and constrain the grown region to a small area.

Before determining the roughness of the grown region, a mathematical closing operation was applied to the boundary to remove any roughness introduced by inclusions, local surface tilts or image noise. The standard size of the structural element was 3 pixels. A smaller (1 pixel) and larger (5 pixels) structural element resulted in a higher and lower roughness, respectively, for all roughness values. This trend is expected because the size of the structural element removes any roughness on the scale of the structural element or smaller. Consequently, the larger the structural element, the smoother is the boundary and the lower the roughness. A structural element of 3 pixels, which is the approximate size of the inclusions and also removes blurriness and noise on the one pixel scale, is therefore the best choice for the size of the structural element.

Finally, we investigated the effect of the image scale by artificially decreasing the pixel resolution. For this, we reduced the image pixel resolution by averaging the pixel values within cells of  $2 \times 2$ ,  $4 \times 4$ ,  $8 \times 8$ , and  $16 \times 16$  original pixels. We also explored the effect of decreasing the smoothing factor of the reference contour with the according image pixel resolution factor that maintains the spatial scale of the smoothing at about 2 cm. Dividing the smoothing factor by the image pixel resolution factor generally results in smaller roughness values because the smoothed reference contour approaches the shape of the rough boundary contour which naturally decreases the roughness relative to the reference contour. The only exception can be observed at a small-scale roughness parameter and deduced Hapke mean slope angle at an image pixel resolution factor of 2. Here, the roughness of the adjusted smoothing factor (divided by the image pixel resolution factor of 2) is larger. Nevertheless, since the values agree within their  $1\sigma$  standard deviation, these values can be considered outliers.

For large image pixel resolution factors (8 and 16), all roughness values decrease with decreasing image resolution (e.g. increasing image resolution factors). At these low image resolutions, the grown regions only exist of a few pixels and the boundary contour is comparatively smooth accordingly. However, when considering the adjusted smoothing of the reference contour (e.g. maintaining the spatial scale of the smoothing for the reference contour by dividing the smoothing factor of the reference contour by the image pixel resolution factor), the roughness values do not peak at the highest pixel resolutions, but at an image pixel resolution factor of 2 for the RMS-slope, hemispherical crater density, small-scale roughness parameter, and Hapke mean slope angle and at an image pixel resolution of 4 for the fractal dimension, Hurst exponent, and JRC. This observation is probably caused by a few very bright boundary pixels (e.g. bright inclusions). Given the method of artificially reducing the image resolution by averaging the values in a given cell (e.g.  $2 \times 2$  and  $4 \times 4$ ), such pixels affect the boundary roughness on a larger scale when the image resolution is decreased. However, this roughness will not be removed by the subsequent erosion procedure as it is the case for the original image because its structural element is on the scale of or smaller than the image resolution. Thus, the effect of an increased roughness for a slightly reduced image resolution is probably an effect of the methods applied rather than a natural observation.

Following the analysis above, we conclude that the following parameters are most suitable for our subsequent analysis of Ryugu's (Section 5.2) and Churyumov–Gerasimenko's (Section 5.3) small-scale roughness derived from *in situ* images: smoothing factor of reference contour = 100, standard deviation multiplier = 1, size of structural element = 3, and image pixel resolution = 1.

## 5.2 Ryugu roughness

Fig. 5(a) shows the location of the five circular starting regions from which the growing algorithm was started in five different locations (structures) on Ryugu. According to their location, they are labelled back right, cave, front right, left-hand side, and middle. Table 2 lists the roughness parameters for the five regions in the MasCam image of Ryugu. For all structures, the approximate pixel resolution in horizontal and vertical direction is 0.2 mm, but depending on the local topography it varies slightly (Table 3).

In addition to the roughness values derived from the MasCam image using our new method, we also extracted the roughness values using shape models from MasCam and ONC. The region on Ryugu's rock which was observed by MARA was additionally evaluated for comparison with thermally derived roughness parameters (Table 2).

The values for the RMS-slope of the five regions imaged by MasCam on Ryugu determined with the above described method is larger than the RMS-slope of the global image derived with the same method. The values derived from the MasCam shape model is in between these two values. At the location of MARA's footprint on the Ryugu rock the RMS-slope is smallest, possibly caused by the comparatively flat local topography. The approximate roughness derived by fitting thermal measurements to the MARA night time data yields a similar value to the geometrically derived RMS-slope of this region. The shape model's RMS-slopes are generally smoother than the RMS-slope derived with our new method as they have a lower spatial resolutions compared to the image they are derived from and particularly steep slopes are averaged out. Consequently, the ONC shape model with a resolution of 20 cm has the lowest RMS-slope. The hemispherical crater density is proportional to the squared RMS-slope (equation 3) and thus shows the same trend.

**Table 2.** Parameters describing the roughness of Ryugu derived from different data sets.

Data set	Method	RMS slope (°)	Hemispherical crater density	Fractal dimension	Hurst exponent	JRC	Small scale roughness parameter	Hapke mean slope angle (°)
ONC shape model of 50 m × 50 m around MASCO landing site, spatial resolution of ~20 cm (124000 facets)	Spencer (1990), from profiles	26.7	0.3	1.008 ± 0.003	0.992 ± 0.003	14.1 ± 2.7	0.128	20.3
MasCam shape model, spatial resolution of ~3 mm (14111 facets)	Spencer (1990), from profiles	34.9	0.51	1.011 ± 0.006	0.989 ± 0.006	16.4 ± 3.8	0.321	41.4
MasCam shape model of MARA's footprint with spatial resolution of ~3 mm (4711 facets)	Spencer (1990)	26.2	0.28				0.141	21.7
MARA 8–12 μm filter daytime measurement	Thermal fitting	28.6	0.34					
MasCam image back right	This work <sup>a</sup>	35.4 ± 0.3	0.52 ± 0.01	1.11 ± 0.01	0.89 ± 0.01	46.3 ± 2.2	0.279 ± 0.003	36.8 ± 0.4
MasCam image cave	This work <sup>a</sup>	38.1 ± 0.9	0.60 ± 0.03	1.19 ± 0.02	0.81 ± 0.02	57.4 ± 2.7	0.342 ± 0.010	43.7 ± 1.3
MasCam image front right	This work <sup>a</sup>	34.9 ± 1.4	0.51 ± 0.04	1.11 ± 0.01	0.89 ± 0.01	45.6 ± 1.8	0.293 ± 0.015	38.3 ± 2.0
MasCam image front left	This work <sup>a</sup>	37.6 ± 0.3	0.59 ± 0.01	1.20 ± 0.04	0.80 ± 0.04	58.7 ± 4.4	0.330 ± 0.007	42.4 ± 0.9
MasCam image middle	This work <sup>a</sup>	36.8 ± 0.4	0.56 ± 0.01	1.18 ± 0.01	0.82 ± 0.01	55.9 ± 1.0	0.331 ± 0.006	42.6 ± 0.8
MasCam image mean	This work <sup>a</sup>	36.6 ± 1.4	0.56 ± 0.04	1.16 ± 0.04	0.84 ± 0.04	52.8 ± 6.3	0.315 ± 0.027	40.8 ± 3.5
ONC global image (red)	This work <sup>a</sup>	32.9 ± 2.2	0.45 ± 0.06	1.08 ± 0.02	0.92 ± 0.02	38.8 ± 4.0	0.263 ± 0.038	35.0 ± 5.1
ONC global image (blue)	This work <sup>a</sup>	32.0 ± 1.5	0.43 ± 0.04	1.08 ± 0.03	0.92 ± 0.03	39.4 ± 6.1	0.251 ± 0.022	33.7 ± 3.0

*Notes.* <sup>a</sup>The average contour was derived by smoothing with a running mean of 100, the standard deviation multiplier for the region growing method was set to 1 and all neighbours were considered. Outline indentations in the order of the bright inclusion size (3 pixels across) were removed from the high-resolution images. The errors are the 1σ standard deviation derived from five locally varying starting regions and, where deduced from other values, were derived via standard error propagation. The outlines of the global images were not smoothed.

**Table 3.** Approximate distance of the structures on Ryugu from the camera and the according approximate pixel resolutions in horizontal and vertical direction with reference to the image frame.

Region	Approximate distance from camera (cm)	Pixel resolution horizontal (mm)	Pixel resolution vertical (mm)
Back right	27.9	0.25	0.25
Cave	26.5	0.23	0.21
Front right	24.7	0.21	0.20
Front left	22.5	0.19	0.17
Middle	24.9	0.23	0.211

The fractal dimension, Hurst exponent, and JRC also show an increased roughness with decreasing spatial resolution of the data set. The only exception to this trend is found for the small-scale roughness parameter and the deduced Hapke mean slope angle. Here, the mean roughness of the five regions imaged by MasCam at a spatial resolution of 0.2 mm is slightly smaller than the roughness derived from the MasCam shape model at a spatial resolution of  $\sim 3$  mm. Nevertheless, the deviation is smaller than the error of the roughness values and is thus not significant.

With the exception of the location in the front right of the MasCam image, all roughness values derived with our method have a relatively small standard deviation (Table 2). The front right part of the image is close to the bottom right corner of the image that constrained the growing region. Because the image boundary is a straight line, the roughness of a grown region reaching the image boundary is underestimated and causes the comparatively small roughness values and large errors. The fractal dimension and deduced parameters are not affected as significantly by this because the straight image boundary introduces only a small number of smooth sections that have a negligible effect on the derivation of the fractal dimension (equation 9). Nevertheless, it should be avoided to extract roughness values too close to the image boundary.

### 5.3 67P/Churyumov–Gerasimenko roughness

We derived the roughness parameters from the ROLIS image of Churyumov–Gerasimenko in two locations, in the centre and at the left edge of the image (Fig. 5b, Table 4). As mentioned above, the image is slightly out of focus, which results in a systematic underestimation of the roughness as small-scale topography will not be resolved. Thus, the roughness reported on here is only a lower limit. In both locations, most roughness values are similar and agree within their errors. Only the small-scale roughness parameters and Hapke mean slope angles for both locations vary more significantly (Table 4). As seen by comparing the roughness parameters derived from the ONC and MasCam images, the roughness parameters derived from the global OSIRIS image of Churyumov–Gerasimenko are also generally smaller compared to the values derived from the high resolution images. It is also noticeable that due to the large image size ( $2048 \times 2048$  instead of  $1024 \times 1024$  pixels) the errors of the roughness values derived from the OSIRIS image are comparatively small.

## 6 SMALL-SCALE SURFACE ROUGHNESS

### 6.1 Influence of spatial resolution, data sets, and method

Our method is sensitive to the decision made on the input parameters including the standard deviation multiplier of the circular region,

the size of the structural element of the boundary contour, and the smoothing factor for the reference contour. Testing the influence of these input parameters, we conclude that the best set of parameters in order to achieve comparability between different images is a standard deviation multiplier of 1, a structural element size of 3, and a reference contour smoothing factor of 100. Using these values as a base, we can achieve comparability and reproducibility for this and future data sets. However, the parameters may have to be adjusted for possible future images depending on the data set and its quality. Varying point spread functions for different camera filters do not affect the results of the roughness values derived using our method. Image noise may influence the results on roughness with an increased noise level introducing larger roughness; however, the effect is not dramatic even for high noise levels, so that our method is capable of generating comparable results for a variety of images at similar spatial resolutions.

The roughness values of Ryugu derived from the MasCam and ONC shape models and images using the newly introduced method described in Section 4 shows that the roughness is dependent on the data set and its spatial resolution with higher spatial resolutions presenting lower roughness values. The same applies when comparing the roughness derived from the ROLIS and OSIRIS images at different spatial resolutions using our method. The spatially higher resolved images result in higher roughness. Because fractal surfaces have the characteristic that with decreased spatial resolution the total contour length decreases, it is expected that small-scale roughness remains unresolved at lower resolution.

When using the same data format and looking at the same planetary body, the roughness is spatially variable. For example, using the MasCam shape model, the roughness of the entire scene is much larger than the roughness of the MARA footprint area which is a subset of the entire scene (RMS-slope:  $34.9^\circ$  versus  $26.2^\circ$ , small-scale roughness parameter: 0.321 versus 0.141). The MasCam shape model shows that the MARA footprint is indeed on a relatively flat plateau surrounded by steeper slopes (Fig. 2a). Even though the five regions in the MasCam image have similar distances and orientations to the camera, our image-based method results in noticeably different roughness values in the five regions. The surface roughness has a significant influence on many remote sensing observations, but assuming a constant roughness value for an observation may not be advisable.

Nevertheless, considering the data sets from Ryugu and Churyumov–Gerasimenko used in this work, the roughness is higher for higher spatial resolution when considering the DTM-based and our image-based method separately. Generally, our image-based method derives higher roughness values compared to the DTM-based method that can be explained by the higher spatial resolution and the shape models' tendency to underestimate the roughness when meshing the topography. Extracting profiles from the DTMs to estimate the traditionally 2D roughness parameters, the fractal dimension, Hurst exponent, and JRC, results in even lower roughness values (Tatone & Grasselli 2010). Following this observation, it is not advisable to use 3D shape models for extracting these roughness parameters as they are significantly underestimated.

### 6.2 Roughness of Ryugu and 67P/Churyumov–Gerasimenko

Although the surface texture of undulating cauliflower-like features appears similar on asteroid Ryugu and comet Churyumov–Gerasimenko, the surface of Churyumov–Gerasimenko is slightly rougher compared to Ryugu on both the *in situ* sub-millimetre scale and the global scale. The fact that the spatial resolution of the Ryugu



**Table 4.** Parameters describing the roughness of comet 67P/Churyumov–Gerasimenko derived from a high-resolution ROLIS image and a global OSIRIS image. The reference contour was derived by smoothing with a running mean of 100, standard deviation multiplier for region growing method set to 1 and all neighbours considered. For comparability with the Ryugu analysis, outline indentations with a size of 3 pixels across were removed from the high resolution images. The outline of the global image was not smoothed.

Location	RMS slope (°)	Hemispherical crater density	Fractal dimension	Hurst exponent	JRC	Small scale roughness parameter	Hapke mean slope angle (°)
ROLIS image centre	$38.3 \pm 0.6$	$0.61 \pm 0.02$	$1.18 \pm 0.03$	$0.82 \pm 0.03$	$56.4 \pm 3.4$	$0.346 \pm 0.015$	$44.2 \pm 1.9$
ROLIS image left edge	$38.1 \pm 0.7$	$0.60 \pm 0.02$	$1.17 \pm 0.02$	$0.83 \pm 0.02$	$55.1 \pm 2.2$	$0.323 \pm 0.006$	$41.7 \pm 0.3$
OSIRIS global image	$34.1 \pm 0.2$	$0.48 \pm 0.01$	$1.11 \pm 0.003$	$0.89 \pm 0.003$	$45.7 \pm 0.5$	$0.277 \pm 0.004$	$36.5 \pm 0.5$

MasCam image is higher (0.2 mm versus  $\sim 0.8$  mm) and that the Churyumov–Gerasimenko ROLIS image is slightly out of focus implies that comet Churyumov–Gerasimenko is indeed rougher than asteroid Ryugu because a higher spatial resolution and sharper image would result in higher resolved roughness. For example, the RMS-slope of Ryugu at a 0.8 mm spatial resolution (image pixel resolution factor of 4 in Table 1) is  $36.6^\circ \pm 0.7^\circ$ , 4.6 per cent less than the RMS-slope of  $38.3^\circ \pm 0.6^\circ$  for the same scale on Churyumov–Gerasimenko (in the image centre). The same observation can be made for the Hapke mean slope angle which is 4.7 per cent less.

The spatial resolution of the Ryugu and Churyumov–Gerasimenko global images is similar, but all roughness parameters at this scale also indicate that Churyumov–Gerasimenko is rougher than Ryugu. The RMS-slope and Hapke mean slope angle of Ryugu at the 2 m resolution global scale are  $32.9^\circ \pm 2.2^\circ$  and  $35.0^\circ \pm 5.1^\circ$ , respectively, 3.6 per cent and 4.3 per cent less than that of Churyumov–Gerasimenko (RMS-slope:  $34.1^\circ \pm 0.2^\circ$ , Hapke mean slope angle:  $36.5^\circ \pm 0.5^\circ$ ). With the exception of the fractal dimension at the *in situ* scale, which is probably slightly distorted by the applied method as argued in Section 5.1, all roughness parameters show the same trend with Churyumov–Gerasimenko being between 2.8 per cent and 5.5 per cent rougher compared to Ryugu. However, given the comparatively large errors at this scale for Ryugu, the conclusion is less reliable than at smaller scales.

### 6.3 Roughness caused by sublimation of volatiles

Given that Ryugu is a rubble pile Cb-type asteroid (Sugita et al. 2019; Kitazato et al. 2019) and Churyumov–Gerasimenko is an active comet, differences in roughness can be expected. Laboratory experiments have shown that volatile outgassing under cometary conditions increases the near surface porosity and generates fluffy particles or aggregates from the sublimation residues that are ejected from the surface (Grün et al. 1993; Kossacki et al. 1997). The Rosetta mission at Churyumov–Gerasimenko confirmed the existence of fluffy aggregates in the size range of a 10–500  $\mu\text{m}$  (Langevin et al. 2016) and 0.2–2.5 mm (Fulle et al. 2015), a scale comparable to the image resolution used in this work. It is probable that their fluffy nature is also preserved in Churyumov–Gerasimenko’s near surface (Poch et al. 2016) and contribute to the observed rough texture of the comet. On the other hand, Ryugu has been reported to be neither pristine nor active and its surface materials, which were potentially compressed within the parent body and subsequently during a catastrophic impact event (Okada et al. 2020; Sugita et al. 2019), are likely more compacted and thus may show a lower roughness compared to Churyumov–Gerasimenko.

### 6.4 Roughness caused by micrometeoroid impacts

Surface roughness on the centimetre and millimetre scale may also be caused by micrometeoroid impacts, as was argued for the Moon (Bastin 1966) and observed on near-Earth asteroids Itokawa and Bennu (Miyamoto et al. 2007; Ballouz et al. 2020). As described in Section 2.1, the surface of Ryugu is characterized by cauliflower-like undulations of  $\sim 1$  cm that are covered with smaller undulations of approximately 2–3 mm. The smaller undulation size is also confirmed by our measurements of the fractal dimension, in which the contour is divided into sections by the intersection of the rough and reference contour. These intersections are approximately 2.5 mm long. Furthermore, impact experiments on to carbonaceous chondrite analogue materials simulating micrometeoroid bombardment show resemblance to the observed surface morphology of Ryugu and result in a mean surface slope ( $32^\circ$ ) similar to the one derived for Ryugu (Avdellidou et al. 2020).

To test if the cauliflower-like structures may be a result of spallation and compaction of micrometeoroid bombardment into a highly porous and low strength rock, we assume that a hypervelocity impact into a highly porous material can be assumed to be 10 times larger than the impactor (Tedeschi et al. 1995), thus a 250  $\mu\text{m}$  particle would cause a 2.5 mm impact feature. Based on the Interplanetary Meteoroid Environment Model 2 by Soja et al. (2019), the mean impact speed of a 250  $\mu\text{m}$  dust particle in a near Earth orbit is approximately  $16 \text{ km s}^{-1}$  and has a flux of  $\sim 8 \times 10^{-9} \text{ m}^{-2} \text{ s}^{-1}$ . Assuming that the rock imaged by MasCam has been exposed at the surface since Ryugu’s formation [approximately  $10^7$  yr ago (Arakawa et al. 2020)], this flux results in about  $1.6 \times 10^5$  accumulated impacts in the imaged 25 cm  $\times$  25 cm scene or 250 impacts per  $\text{cm}^2$ . This implies that the total area affected by an impact of this size is approximately 10 times larger than the area of the scene meaning that the surface should show traces of such impact crater features and that micrometeoroid bombardment plays a role in the formation of Ryugu’s surface roughness. However, impactors of various sizes hit the surface and specifically smaller particle impacts occur much more frequently (e.g.  $\sim 5 \times 10^{-7} \text{ m}^{-2} \text{ s}^{-1}$  for 50  $\mu\text{m}$  particles). They should erode larger crater features with time. For example, in the considered timeframe the total crater feature area of 50  $\mu\text{m}$  impactors is about 30 times larger than the target area.

Further processes eroding the surface of airless bodies include solar weathering and thermal fatigue. It is possible that Ryugu’s cauliflower-like texture represents an intrinsic property of the rock when exposed to multiple surface processes, including solar space weathering and thermal fatigue in addition to micrometeoroid bombardment. Given the different strength of regolith on differently classified objects and the expectation that thermal erosion of carbonaceous chondritic material is more efficient than thermal erosion of ordinary chondritic material (Delbo et al. 2014), the small-

scale surface morphology and roughness may vary between different bodies. These processes are most effective on asperities and round rock surfaces (Delbo et al. 2014; Gault, H<sup>o</sup>rz & Hartung 1972). Given that Ryugu is a product of a catastrophic impact and has been bombarded by meteoroids since its rocks should exhibit impact-induced intrinsic fracture patterns on various scales (Tomeoka, Yamahana & Sekine 1999) encouraging thermally induced foliation along them and possibly supporting the cauliflower-like texture. In contrast, the surface of Churyumov–Gerasimenko is renewed approximately every 6.5 yr when the comet passes its perihelion and ejects large amounts of its surface material. Micrometeoroid bombardment should therefore not play a significant role in the formation of surface roughness on Churyumov–Gerasimenko.

A combination of the above-mentioned processes and the differences in bulk material composition and texture is likely the cause for the observation that Churyumov–Gerasimenko is rougher than Ryugu.

## 7 DISCUSSION

It is challenging to relate the roughness of Ryugu and Churyumov–Gerasimenko to previously derived values on other planetary bodies and materials on the Earth because of the variations in applied methods, scales, and data sets. Nevertheless, to achieve a sense for their roughness, we will discuss a few values of other materials and planetary bodies.

The fractal dimension and derived JRC are acknowledged parameters used in geological sciences for the estimation of the peak shear strength of a material. Common values for the fractal dimension for typical rocks (quartz, granite, sandstone, limestone, shale) range between 1.05 and 1.19 (Pal et al. 2017). The best match for Ryugu ( $D = 1.16 \pm 0.04$ ) as well as Churyumov–Gerasimenko ( $D = 1.18 \pm 0.03$ ) appears to be the comparatively rough limestone investigated in their survey. On larger scales, the fractal dimension has been investigated for geologic features such as lava flows on the Earth ( $D = 1.06–1.19$ ) as well as the Moon ( $D = 1.20$ ; Bruno et al. 1992). Note that all comparative values have been derived with the box counting method. The application of different methods may have an influence on the derived values (Klinkenberg 1994), but the method used in this work yields the most reliable correlation with the JRC (Li & Huang 2015).

The JRC relates the shear peak strength and normal stress following equation (11). Although the assumption that Ryugu’s rock is jointed due to its impact history seems reasonable, the JRC may not be an adequate parameter on Ryugu and Churyumov–Gerasimenko given the small gravitational field in which the rocks exist. The values presented in this work are guidance but do not claim that they represent the actual behaviour of rock on the small bodies.

The Hurst exponent has been derived for Eros and Itokawa, two small S-type asteroids previously visited by spacecraft, from laser ranging data. Over a range of 3 m–1 km the global Hurst exponent of Eros was found to range between 0.81 and 0.97 (Cheng et al. 2002; Susorney & Barnouin 2018) and from scales between 8 and 32 m the global Hurst exponent of Itokawa is  $0.51 \pm 0.07$  (Susorney et al. 2019). The differences in roughness have been attributed to different geologic processes and internal structures of the two bodies, with Eros possessing a stronger intact interior with surface impact craters and Itokawa being a rubble pile asteroid with large variations in the geopotential and induced regolith migration as main surface process (Susorney et al. 2019). At a scale of 2 m, we derived a similar global Hurst exponent of Ryugu of  $0.92 \pm 0.02$  [and Churyumov–Gerasimenko ( $0.89 \pm 0.003$ )] to the one derived for Eros. Although

Ryugu as a rubble pile asteroid should geologically resemble Itokawa more than Eros, it is possible that the discrepancy is caused by Ryugu’s comparatively symmetric shape and the different boulder size distributions at this scale. Smaller boulders seem to be buried in the regolith on Ryugu and the different composition of Ryugu and Itokawa probably results in different sized impact fragments because S-type asteroid materials (ordinary chondrites) are stronger than C-type asteroid materials (carbonaceous chondrites; Popova et al. 2011; Michikami et al. 2019).

The RMS-slope has been retrieved from many data sets of planetary missions applying different methods and scales. Generally, the values range between  $20^\circ$  and  $40^\circ$  for airless bodies, but variations are common with scale and location. Thermal modelling is able to retrieve roughness estimates on the scale of the thermal skin depth (centimetre scale). The best-fitting RMS-slope of Ryugu at the Mascot landing deduced by a thermal model site is  $28.6^\circ$ . Similar investigations of Ceres and the Moon result in higher RMS-slopes of  $40^\circ$  (Davidsson et al. 2015; Müller et al. 1999; Spencer 1990) and  $30^\circ–39^\circ$  (Rozitis & Green 2011; Shkuratov et al. 2000; Spencer 1990), respectively. Radar observations of slightly higher wavelength (decimetre scale) confirm these values (Mitchell et al. 1996). The comparatively high roughness has been attributed to a fine-grained regolith covered surface that, in contrast to Ryugu (Jaumann et al. 2019), is able to form on these objects with larger gravitational pull. The roughness from thermal measurements on Churyumov–Gerasimenko has been shown to be locally highly variable and covers the range from  $16^\circ$  to  $44^\circ$  (Marshall et al. 2018). Given the high variation in published values, our estimates of the RMS-slope of Ryugu ( $36.6^\circ \pm 1.4^\circ$ ) and Churyumov–Gerasimenko ( $38.3^\circ \pm 0.6^\circ$ ) agrees with these estimates.

The RMS deviation (difference in height between points separated by a constant distance/measuring length) of planetary bodies has also been derived from shape models and laser altimeters at different resolutions (Barnouin-Jha et al. 2008; Ermakov et al. 2019). The RMS deviation directly relates to the Hurst exponent and the RMS slope can be deduced from the RMS deviation at a given measuring length (Shepard et al. 2001). Unfortunately, on the spatial scales of the data sets investigated in this work (0.2 mm–2 m), there are no comparable data sets from any other planetary bodies to date.

Based on the stereophotogrammetric analysis of Apollo Lunar Surface Closeup Camera images, Helfenstein & Shepard (1999) were able to derive the RMS slope and Hapke roughness parameter for lunar soil on sub-millimetre scales. They found values of  $16^\circ–25^\circ$  for the RMS-slope and  $24^\circ–27^\circ$  for Hapke’s mean slope angle of different regolith types (lunar mare, Fra Mauro regolith). Comparing these values with the stereophotogrammetrically derived shape model of Ryugu at slightly larger scales (3 mm), we find larger values of  $34.9^\circ$  and  $26.2^\circ$  (RMS-slope) for the entire rock and MARA footprint area, respectively. The Hapke mean slope angle of Ryugu for these two areas is  $21.7^\circ$  and  $41.4^\circ$ , slightly smaller and larger compared to the values derived from the Moon. Because the Moon’s surface regolith is a fine-grained soil covering bare rock surfaces, which is not present on Ryugu, differences in roughness values are expected. This example illustrated how significantly these values can vary locally when using 3D shape models at small scales.

The Hapke mean slope angle is generally derived from photometric models and gives the roughness on a microscopic scale at which shadows influence photometric observations (Hapke 1984). In our work, the Hapke mean slope angle was derived from the small-scale roughness parameter (equation 6). Our values for the Hapke mean slope angle are generally high (Ryugu:  $40.8^\circ \pm 3.5^\circ$ , Churyumov–Gerasimenko:  $44.2^\circ \pm 1.9^\circ$ ) compared with values derived from pho-

tomeric analyses of Churyumov–Gerasimenko ( $19^\circ \pm 9^\circ$ , Ciarniello et al. 2015) and comet Tempel 1 ( $16^\circ$ – $32^\circ$ , Li et al. 2007). The same trend is observed for values from asteroids Eros ( $24^\circ$ – $28^\circ$ , Clark et al. 2002; Li, A’Hearn & McFadden 2004), Itokawa ( $26^\circ$ – $38^\circ$ , Kitazato et al. 2008; Tatsumi et al. 2018) and Ceres ( $18^\circ$ – $29^\circ$ , Ciarniello et al. 2017; Li et al. 2019; Schröder et al. 2017b). The Hapke mean slope angle of Ryugu derived from photometric fitting was found to be  $28^\circ \pm 6^\circ$  (Tatsumi et al. 2020). The discrepancy between geometrically and photometrically derived mean slope angles has previously been explained for the Moon by Helfenstein & Shepard (1999). They suggest that below spatial resolutions of approximately 0.1 mm roughness may not be photometrically detectable. As we approach such scales in our investigation, this limitation may be applicable. Furthermore, by comparing geometrically and photometrically derived roughness values from an artificially generated terrain, Labarre, Ferrari & Jacquemoud (2017) showed that the Hapke mean slope angle systematically underestimates the surface roughness. They attribute this behaviour to the often unsuitable assumption of a Gaussian distribution of not too large slope angles and a moderately bright material. All the latter two assumptions are not valid for the scene observed on Ryugu and Churyumov–Gerasimenko and may thus explain the significantly higher value for the Hapke mean slope angle that we derive geometrically in this work.

## 8 CONCLUSIONS

Based on a newly developed image analysis technique suitable to extract surface roughness, we derived a set of roughness descriptors for asteroid Ryugu and comet Churyumov–Gerasimenko based on high-resolution images with  $0.2 \text{ mm pixel}^{-1}$  and  $\sim 0.8 \text{ mm pixel}^{-1}$  covering a scene of approximately 25 and 80 cm horizontal extent, respectively and two global images with 2 m spatial resolution. We complemented our survey with two local shape models of Ryugu at 3 mm and 20 cm spatial resolution. The roughness descriptors include the fractal dimension and the deduced Hurst exponent and JRC, the RMS-slope and derived hemispherical crater density, and the small-scale self-heating parameter and deduced Hapke mean slope angle. As a Cb-type asteroid and an active comet, Ryugu’s and Churyumov–Gerasimenko’s composition is expected to be different. However, the general cauliflower-like texture of both bodies visible in the high resolution *in situ* images appears similar. The structure on Ryugu is most likely linked to erosion via micrometeoroid bombardment, solar weathering, and thermal fatigue of a compacted impact rock fragment, whereas on Churyumov–Gerasimenko sublimation-driven erosion of a volatile-rich regolith is potentially the most dominant process for forming surface roughness. We suggest that these different processes and compositions combined are represented by the slightly rougher descriptors (2.8–5.5 per cent) for Churyumov–Gerasimenko than for Ryugu on the investigated scales.

## ACKNOWLEDGEMENTS

We thank the Hayabusa2 and MASCOT as well as the Rosetta and Philae teams for making this work possible. KO and RP gratefully acknowledge the financial support and endorsement from the German Aerospace Center (DLR) Management Board Young Research Group Leader Program and the Executive Board Member for Space Research and Technology. This study was supported by Japanese Society for the Promotion of Science (JSPS) International Planetary Network. We thank an anonymous reviewer for the helpful and productive comments.

## DATA AVAILABILITY

All data derived in this work are incorporated in the article. Images from the Hayabusa2 mission will be published in the Data Archives and Transmission System at [https://www.darts.isas.jaxa.jp/pub/hayabusa2/onc\\_bundle/](https://www.darts.isas.jaxa.jp/pub/hayabusa2/onc_bundle/). The image from the Rosetta mission is available at ESA’s Planetary Science Archive at <https://archives.esac.esa.int/psa/> and can be accessed by searching for ‘OSIRIS [instrument]’ (Product identifier: N20140806T012001282ID30F28). The original ROLIS image is available at <ftp://psa.esac.esa.int/pub/mirror/INTERNATIONAL-ROSETTA-MISSION/ROLIS/RL-C-ROLIS-2-FSS-V1.0/DATA/> (Product identifier: ROL\_FS2\_141113001408\_336\_04) and was processed using the method described in Schröder et al. (2017a) and the polynomial coefficients provided as supplementary material to this publication. The MasCam image is available at <http://europlanet.dlr.de/Hayabusa2/MASCAM/index.html> (Product identifier: F1087378791\_701\_29464\_r1). The digital terrain models shown in Fig. 2 are available at <http://europlanet.dlr.de/Hayabusa2/MASCOT/index.html> under the according publication.

## REFERENCES

- Arakawa M. et al., 2020, *Science*, 368, 67  
 Avdellidou C. et al., 2020, *Icarus*, 341, 113648  
 Ballouz R.-L. et al., 2019, in *Asteroid Science 2019*. Lunar and Planetary Institute, p. 2123  
 Barnouin-Jha O. S. et al., 2008, *Icarus*, 198, 108  
 Barton N., 1976, *Int. J. Rock Mech. Mining Sci. Geomech. Abstr.*, 13, 255  
 Barton N., Choubey V., 1977, *Rock Mech. Felsmechanik Méc. Roches*, 10, 1  
 Bastin J. A., 1966, *Nature*, 212, 171  
 Bibring J.-P. et al., 2015, *Science*, 349, aab0671  
 Bruno B. C., Taylor G. J., Rowland S. K., Lucey P. G., Self S., 1992, *Geophys. Res. Lett.*, 19, 305  
 Buhl D., Welch W. J., Rea D. G., 1968, *J. Geophys. Res.*, 73, 5281  
 Cai Y., Tang H.-m., Wang D.-j., Wen T., 2018, *Math. Probl. Eng.*, 2018, 1  
 Cheng A. F. et al., 2002, *Icarus*, 155, 51  
 Ciarniello M. et al., 2015, *A&A*, 583, 1  
 Ciarniello M. et al., 2016, *MNRAS*, 462, S443–S458  
 Ciarniello M. et al., 2017, *A&A*, 598, 1  
 Clark B. E. et al., 2002, *Icarus*, 155, 189  
 Davidsson B. J. R., Rickman H., 2014, *Icarus*, 243, 58  
 Davidsson B. J. R., Gutiérrez P. J., Rickman H., 2009, *Icarus*, 201, 335  
 Davidsson B. J. R. et al., 2015, *Icarus*, 252, 1  
 Davidsson B. J. R. et al., 2016, *A&A*, 592, 1  
 Delbo M. et al., 2014, *Nature*, 508, 233  
 Ermakov A. I., Kreslavsky M. A., Scully J. E. C., Hughson K. H. G., Park R. S., 2019, *J. Geophys. Res.*, 124, 14  
 Fuchs L. H., Olsen E., Jensen K. J., 1973, *Smithsonian Contrib. Earth Sci.*, 10, 1  
 Fulle M. et al., 2015, *ApJ*, 802, L12  
 Gault D. E., H’orz F., Hartung J. B., 1972, in *Proceedings of the 3rd Lunar and Planetary Science Conference*. The MIT Press, p. 2713  
 Gonzalez R. C., Woods R. E., 2018, *Morphological Image Processing*, 4th edn. Pearson, p. 694  
 Gounelle M., Zolensky M. E., 2014, *Meteorit. Planet. Sci.*, 49, 1769  
 Grott M. et al., 2019, *Nat. Astron.*, 3, 971  
 Grün E. et al., 1993, *J. Geophys. Res.*, 98, 15091  
 Hamm M., 2019, PhD thesis, Freie Univ. Berlin  
 Hapke B., 1981, *J. Geophys. Res.*, 86, 3039  
 Hapke B., 1984, *Icarus*, 59, 41  
 Helfenstein P., 1988, *Icarus*, 73, 462  
 Helfenstein P., Shepard M. K., 1999, *Icarus*, 141, 107  
 Hiroi T., Peters C. M., 1991, in *Proceedings of Lunar and Planetary Science*. Lunar and Planetary Institute, p. 313



- Ho T.-M. et al., 2017, *Space Sci. Rev.*, 208, 339
- Huang S. L., Oelfke S. M., Speck R. C., 1992, *Int. J. Rock Mech. Min. Sci. Geomech. Abstr.*, 29, 89
- Jaumann R. et al., 2017, *Space Sci. Rev.*, 208, 375
- Jaumann R. et al., 2019, *Science*, 365, 817
- Jiang Y., Li B., Tanabashi Y., 2006, *Int. J. Rock Mech. Min. Sci.*, 43, 837
- Jorda L. et al., 2016, *Icarus*, 277, 257
- Kameda S. et al., 2017, *Space Sci. Rev.*, 208, 17
- Keller H. U. et al., 2007, *Space Sci. Rev.*, 128, 433
- Keller H. U. et al., 2015, *A&A*, 583, 1
- Kitazato K. et al., 2008, *Icarus*, 194, 137
- Kitazato K. et al., 2019, *Science*, 364, 272
- Klinkenberg B., 1994, *Math. Geol.*, 26, 23
- Knapmeyer M., Fischer H.-H., Knollenberg J., Seidensticker K. J., Thiel K., Arnold W., Faber C., M<sup>o</sup>hlmann D., 2018, *Icarus*, 310, 165
- Kossacki K. J., K<sup>o</sup>mlle N. I., Leliwa-Kopystynski J., Kargl G., 1997, *Icarus*, 128, 127
- Labarre S., Ferrari C., Jacquemoud S., 2017, *Icarus*, 290, 63
- Lagerros J. S. V., 1996, *A&A*, 310, 1011
- Lagerros J. S. V., 1997, *A&A*, 325, 1226
- Lagerros J. S. V., 1998, *A&A*, 332, 1123
- Langevin Y. et al., 2016, *Icarus*, 271, 76
- Lee S. D., Lee C. I., Park Y., 1997, *Int. J. Rock Mech. Min. Sci.*, 34, 174
- Li Y., Huang R., 2015, *Int. J. Rock Mech. Min. Sci.*, 75, 15
- Li J., A'Hearn M. F., McFadden L. A., 2004, *Icarus*, 172, 415
- Li J.-Y. et al., 2007, *Icarus*, 187, 41
- Li J.-Y. et al., 2019, *Icarus*, 322, 144
- Mandelbrot B., 1967, *Science*, 156, 636
- Marshall D. et al., 2018, *A&A*, 616, 1
- Michikami T. et al., 2019, *Icarus*, 331, 179
- Mitchell D. L. et al., 1996, *Icarus*, 124, 113
- Miyamoto H. et al., 2007, *Science*, 316, 1011
- Morota T. et al., 2020, *Science*, 368, 654
- Mottola S., Arnold G., Grothues H.-G., Jaumann R., Michaelis H., Neukum G., Bibring J.-P., 2007, *Space Sci. Rev.*, 128, 241
- Mottola S. et al., 2015, *Science*, 349, aab0232.1–4
- Müller T. G., Lagerros J. S. V., Burgdorf M., Lim T., Morris P. W., Salama A., Schulz B., Vandenbussche B., 1999, in Cox P., Kessler M., Danesy D., eds, *ESA Special Publication, Vol. 427, The Universe as Seen by ISO*. ESA Special Publication, p. 141
- Odling N. E., 1994, *Rock Mech. Rock Eng.*, 27, 135
- Okada T. et al., 2020, *Nature*, 579, 518
- Pal S. K., Rao K. U. M., Kumar P. S., Rajasekar R., 2017, *Arch. Metall. Mater.*, 62, 1787
- Poch O., Pommerol A., Jost B., Carrasco N., Szopa C., Thomas N., 2016, *Icarus*, 267, 154
- Popova O., Borovicka J., Hartmann W. K., Spurný P., Gnos E., Nemtchinov I., Trigo-Rodríguez J. M., 2011, *Meteorit. Planet. Sci.*, 46, 1525
- Poulet F. et al., 2016, *MNRAS*, 462, S23
- Preusker F. et al., 2015, *A&A*, 583, A33
- Preusker F. et al., 2019, *A&A*, 632, 1
- Reeves M. J., 1985, *Int. J. Rock Mech. Min. Sci. Geomech. Abstr.*, 22, 429
- Rost E., Hecker C., Schodlok M. C., Van der Meer F. D., 2018, *Minerals*, 8, 1
- Rozitis B., Green S. F., 2011, *MNRAS*, 415, 2042
- Rozitis B., Green S. F., 2012, *MNRAS*, 423, 367
- Rozitis B., Green S. F., 2013, *MNRAS*, 433, 603
- Scholten F. et al., 2019, *A&A*, 632, 1
- Schröder S. E. et al., 2017a, *Icarus*, 285, 263
- Schröder S. E. et al., 2017b, *Icarus*, 288, 201
- Schröder S. E. et al., 2020, *Planet. Sci. J.*, Submitted
- Shepard M. K., Campbell B. A., 1998, *Icarus*, 134, 279
- Shepard M. K., Campbell B. A., Bulmer M. H., Farr T. G., Gaddis L. R., Plaut J. J., 2001, *J. Geophys. Res.*, 106, 32777
- Shkuratov Y., Stankevich D., Sitko M. L., Sprague L. A., 2000, in Sitko M. L., Sprague A. L., Lynch D. K., eds, *ASP Conf. Ser., Vol. 196, Thermal Emission Spectroscopy and Analysis of Dust, Disks, and Regoliths*. Astron. Soc. Pac., San Francisco, p. 211
- Soja R. H. et al., 2019, *A&A*, 628, 1
- Spencer J. R., 1990, *Icarus*, 83, 27
- Spohn T. et al., 2015, *Science*, 349, aab0464.1–4
- Steinbrügge G., Stark A., Hussmann H., Wickhusen K., Oberst J., 2018, *Planet. Space Sci.*, 159, 84
- Steinbrügge G. et al., 2020, *Icarus*, 343, 113669
- Sugita S. et al., 2019, *Science*, 364, 1
- Susorney H. C. M., Barnouin O. S., 2018, *Icarus*, 314, 299
- Susorney H. C. M., Johnson C. L., Barnouin O. S., Daly M. G., Seabrook J. A., Bierhaus E. B., Lauretta D. S., 2019, *Icarus*, 325, 141
- Tatone B. S. A., Grasselli G., 2009, *Rev. Sci. Instrum.*, 80, 125110.1–10
- Tatone B. S. A., Grasselli G., 2010, *Int. J. Rock Mech. Min. Sci.*, 47, 1391
- Tatsumi E. et al., 2018, *Icarus*, 311, 175
- Tatsumi E. et al., 2020, *A&A*, 639, 1
- Tedeschi W. J., Remo J. L., Schulze J. F., Young R. P., 1995, *Int. J. Impact Eng.*, 17, 837
- Tomeoka K., Yamahana Y., Sekine T., 1999, *Geochim. Cosmochim. Acta*, 63, 3683
- Tse R., Cruden D. M., 1979, *Int. J. Rock Mech. Min. Sci. Geomech. Abstr.*, 16, 303
- Ulamec S. et al., 2016, *Acta Astron.*, 125, 80
- Watanabe S. et al., 2019, *Science*, 364, 268
- Watanabe S.-i., Tsuda Y., Yoshikawa M., Tanaka S., Saiki T., Nakazawa S., 2017, *Space Sci. Rev.*, 208, 3
- Xie H.-P., Pariseau W. G., 1994, *Sci. China B*, 37, 1516
- Xu Y. F., Sun D. A., 2005, *Géotechnique*, 55, 691
- Yano H. et al., 2006, *Science*, 312, 1350
- Zahouani H., Vargiolu R., Loubet J. L., 1998, *Math. Comput. Modelling*, 28, 517

This paper has been typeset from a  $\text{\TeX}/\text{\LaTeX}$  file prepared by the author.

**2.1.2 Otto et al. (2021b)**

Otto, K. A., Schröder, S. E., Scharf, H. D., Greshake, A., Schmitz, N., Trauthan, F., Pieth, S., Stephan, K., Ho, T.-M., . . . Yabuta, H. (2021b). Spectral and Petrographic Properties of Inclusions in Carbonaceous Chondrites and Comparison with In Situ Images from Asteroid Ryugu. *The Planetary Science Journal*, 2(5), 188. <https://doi.org/10.3847/PSJ/ac034b>.

This article was published in tandem with Schröder et al. (2021) and is one of two articles evaluating image data of carbonaceous chondrites taken with MasCam's qualification model at the Natural History Museum in Berlin (MfN). S. E. Schröder, A. Greshake, N. Schmitz, F. Trauthan, K. Stephan and I prepared the experimental setup and conducted the measurements at the MfN. After an initial image processing by S. E. Schröder, H. D. Scharf, a student assistant, conducted the mapping. I wrote the code to statically evaluate the mapped inclusions' size, colour, brightness and abundance. I illustrated, compared and discussed the results with each other, previous publications and findings from the surface of Ryugu. S. Pieth formatted the photos of the meteorites and compiled the supplementary material. T.-M. Ho, R. Jaumann, A. Koncz and N. Schmitz were involved in managing and building MasCam and its qualification model. All authors contributed to discussions on the results and refining the manuscript.

The supplementary material of this publication is attached after the article.



# Spectral and Petrographic Properties of Inclusions in Carbonaceous Chondrites and Comparison with In Situ Images from Asteroid Ryugu

K. A. Otto<sup>1</sup>, S. E. Schröder<sup>1</sup>, H. D. Scharf<sup>1,2</sup>, A. Greshake<sup>3</sup>, N. Schmitz<sup>1</sup>, F. Trauthan<sup>1</sup>, S. Pieth<sup>1</sup>, K. Stephan<sup>1</sup>, T.-M. Ho<sup>4</sup>, R. Jaumann<sup>5</sup>, A. Koncz<sup>1</sup>, T. Michalik<sup>1</sup>, and H. Yabuta<sup>6</sup>

<sup>1</sup> German Aerospace Center, Institute of Planetary Research, Rutherfordstraße 2, D-12489 Berlin, Germany; [katharina.otto@dlr.de](mailto:katharina.otto@dlr.de)

<sup>2</sup> Technical University Freiberg, D-09599 Freiberg, Germany

<sup>3</sup> Natural History Museum Berlin, D-10115 Berlin, Germany

<sup>4</sup> German Aerospace Center, Institute of Space Systems, D-28359 Bremen, Germany

<sup>5</sup> Free University Berlin, Institute of Geological Sciences, D-12249 Berlin, Germany

<sup>6</sup> Hiroshima University, Department of Earth and Planetary Systems Science, 739-8526 Hiroshima, Japan

Received 2020 December 23; revised 2021 May 5; accepted 2021 May 17; published 2021 September 9

## Abstract

We imaged a set of carbonaceous chondrites from the CM2, CO3, CV3, and CK4 groups using the qualification model of MasCam, the camera on board the asteroid lander MASCOT, which touched down on asteroid Ryugu in 2018 October. A CII meteorite was also imaged but excluded from the analysis due to prominent terrestrial weathering. Following the methods used to image the rock on Ryugu, we placed a total of 14 meteorites approximately 20 cm in front of the camera to achieve a spatial resolution of about 0.2 mm per pixel and illuminated the samples with onboard light-emitting diodes of four different colors in the visible wavelength range. We mapped bright and dark inclusions within the meteorites and derived the inclusion brightness relative to the matrix in the red light, the relative spectral slope of each inclusion, the inclusion size frequency distribution and the matrix volume abundance. We find that the meteorite groups overlap within these parameters, but individual samples, as well as individual inclusions, can have deviating values. Terrestrial weathering appears to have no systematic influence on these parameters. Relating our analysis to the inclusions found in the rock on Ryugu, we find that the spectral parameters of Ryugu's inclusions fit well in the parameter space of the carbonaceous chondrites. Compared with the most common types of carbonaceous chondrites, Ryugu's rock has larger inclusions (mean diameter:  $0.63 \pm 0.91$  mm) and a higher upper limit to the matrix abundance (92.4 vol%).

*Unified Astronomy Thesaurus concepts:* Meteorites (1038); Carbonaceous chondrites (200); Asteroids (72); Asteroid surfaces (2209); Spectroscopy (1558); Planetary science (1255); Landers (901)

*Supporting material:* figure set

## 1. Introduction

Chondrite meteorites are the oldest and most primitive rocks of the solar system and predominantly consist of chondrules, refractory objects (calcium-aluminum-rich inclusions (CAIs) and amoeboid olivine aggregates), FeNi metal, and fine-grained matrix. Refractory inclusions, chondrules, and FeNi metal formed very early in the solar nebula by high-temperature processes including condensation and evaporation. In contrast, fine-grained matrix consisting of silicates, oxides, sulfides, and carbon-rich material formed at much lower temperatures. Mixing and accretion of high- and low-temperature fractions finally lead to the formation of chondritic rocks. The carbonaceous chondrite meteorites are the most volatile-rich and least thermally processed of the chondrites and are the closest to matching the bulk composition of the Sun (Greshake & Frits 2018). As such, they are of greatest interest also for comparison with C- and K-type asteroidal material (Clark et al. 2009; Greenwood et al. 2020).

JAXA's Hayabusa2 sample-return mission arrived at the near-Earth asteroid (162173) Ryugu in 2018 June (Watanabe et al. 2019). Ryugu is a top-shaped rubble pile asteroid (950 m in maximum diameter) comprising fragments that

re-accumulated after a catastrophic disruption of its parent body (Watanabe et al. 2019). Compositionally, Ryugu is classified as a Cb-type asteroid (Sugita et al. 2019) and is suggested to be linked to carbonaceous chondrites (Wada et al. 2018; Jaumann et al. 2019; Sugita et al. 2019), and its comparatively low albedo (4.5% at  $0.55 \mu\text{m}$ ) best matches thermally or shock-metamorphosed carbonaceous chondrites (Kitazato et al. 2019; Sugita et al. 2019). A detailed compositional analysis will be possible upon the return of the samples collected in two touchdown maneuvers in 2019 February and July. The samples were returned to Earth on 2020 December 6 (Tsuda et al. 2020).

In preparation for the sample collection and for obtaining ground truth for the collected samples, Hayabusa2 deployed two MINERVA-II1 rovers (Yoshimitsu et al. 2017) and its Mobile Asteroid Surface Scout (MASCOT) onto the surface of Ryugu in 2018 September and October (Jaumann et al. 2019; Tsuda et al. 2020). MASCOT observed Ryugu's surface with four scientific instruments (Ho et al. 2017): a camera, MasCam (Jaumann et al. 2017); a radiometer, MARA (Grott et al. 2017); a magnetometer, MasMag (Herčík et al. 2017); and a near-infrared spectrometer, MicrOmega (Bibring et al. 2017). After being deployed onto Ryugu's surface from a height of 41 m, MASCOT landed on a bare, dust-free rock where it operated for two Ryugu days (17 hr) before the battery was empty (Jaumann et al. 2019). MasCam, equipped with an LED array allowing the illumination of the surface during the night,



Original content from this work may be used under the terms of the [Creative Commons Attribution 4.0 licence](https://creativecommons.org/licenses/by/4.0/). Any further distribution of this work must maintain attribution to the author(s) and the title of the work, journal citation and DOI.

imaged the landing site rock in detail with spatial resolutions up to  $0.2 \text{ mm pixel}^{-1}$ . The LED illumination enabled the identification of millimeter-sized bright inclusions with red, neutral, and blue spectral slopes within the Ryugu rock (Schröder et al. 2021). These inclusions were suggested to be a mixture of chondrules and refractory inclusions, leading to the conclusion that Ryugu's rock is linked to carbonaceous chondrites (Jaumann et al. 2019). The accompanying MASCOT instruments including the radiometer MARA and the Magnetometer MasMag revealed a high porosity and missing magnetic field in agreement with expectations for carbonaceous material (Grott et al. 2019; Hercik et al. 2020). The spectrometer MicrOmega was not able to take any measurement.

In our previous work, we analyzed the size distribution and spectrophotometric characteristics of inclusions identified in the Ryugu rock imaged by MasCam and found that Ryugu's rock does not easily fit into the carbonaceous chondrite categories (Schröder et al. 2021). The inclusions in Ryugu's rock are large compared to those in the most common carbonaceous chondrites but are closest in size to those in CR2 and CV3 carbonaceous chondrites. In contrast, matrix abundance in Ryugu's rock is most similar to that in CM2s. However, the data on matrix abundance and inclusion size distributions in the millimeter size range for meteorites that were published are relatively limited compared to what is published on petrographic analyses that are nowadays possible in the laboratory. A comparatively old data set on inclusion size distributions in carbonaceous chondrites in the millimeter range from King & King (1978) proves difficult to relate to in situ measurements from Ryugu, which will be addressed in this work. We note that it has been suggested that material from a Ryugu-like body may not survive the entry into Earth atmosphere given its high porosity (Grott et al. 2019) and that a corresponding meteorite analog may not be present in our collection on Earth.

In this work, we aim to bridge the gap of information in the size range accessible to in situ observations by imaging a set of well-characterized carbonaceous chondrites. We obtained these meteorites from the meteorite collection of the Natural History Museum in Berlin and used the MasCam qualification model (QM) to image them under similar conditions to MasCam on Ryugu. We investigate the visual comparability of in situ images of Ryugu and images of carbonaceous chondrites obtained in the laboratory and discuss whether such comparisons can be used as guidance for the upcoming returned sample analysis and for future missions with in situ experiments, such as the MMX mission.

## 2. Data

### 2.1. MasCam Specifications

MasCam and its QM possess a  $1024 \times 1024$  CMOS detector behind a Scheimpflug optical layout (Scheimpflug angle:  $7.395^\circ$ ). This allows an image to be in focus at varying distances from the camera. The optical axis is tilted  $22^\circ$  downward in relation to the camera mounting so that the entire scene along the camera's depth of field, from 15 cm to the local horizon, is in focus. At a distance of 15 cm, the pixel resolution reaches a minimum of 0.15 mm (Jaumann et al. 2017). MasCam is equipped with a four-color LED array (36 LEDs per color) with wavelength centered at 471 nm (blue), 532 nm (green), 630 nm (red), and 809 nm (near-infrared) (Table 1, Figure 1). The LED

**Table 1**  
Wavelength of the Four Color LEDs on MasCam's LED Array

Color	Abbreviation	Wavelength (nm)
Blue	B	$471_{-16}^{+6}$
Green	G	$532_{-24}^{+12}$
Red	R	$630_{-7}^{+10}$
Near-infrared	IR	$809_{-17}^{+18}$

**Note.** The errors on the wavelength are the FWHM. From Schröder et al. (2021).

array is located 2 cm below the aperture. It allows the illumination at night to derive spectral information in the visible to near-infrared wavelength based on the four colors of the LEDs (Jaumann et al. 2017). The image depth of MasCam is 14 bits.

### 2.2. Description of the Studied Carbonaceous Chondrites

The carbonaceous chondrites selected for the present study cover the range of major carbonaceous chondrite groups. CI and CM chondrites are the most carbon-rich carbonaceous chondrites and have experienced severe aqueous alteration on their parent body/bodies. In CI chondrites nearly all anhydrous silicates have been altered to phyllosilicates, while in CM chondrites many very small chondrules and CAIs have been preserved. Neither of these meteorite types has experienced thermal metamorphism. In contrast, CO and CV chondrites are at most only weakly altered but have experienced thermal metamorphism to different degrees. Both types contain abundant chondrules and CAIs, with COs being much more fine-grained. CK carbonaceous chondrites are thermally altered at even higher temperatures compared to CVs and COs and have a high abundance of matrix. They contain large up to 1 mm size chondrules, rare CAIs, and do not contain any FeNi metal.

None of the samples used has been subject to any kind of destructive research work, and the investigated surfaces are free of artificial marks. Most meteorite surfaces were rough and fractured, in analogy to the rocks on Ryugu, but some of them were cut or possessed a fusion crust from the entry into Earth's atmosphere. The latter surfaces were not considered in this work, but we also investigated the influence of the surface structure (cut or fractured) on the identification of inclusions (Section 4.1).

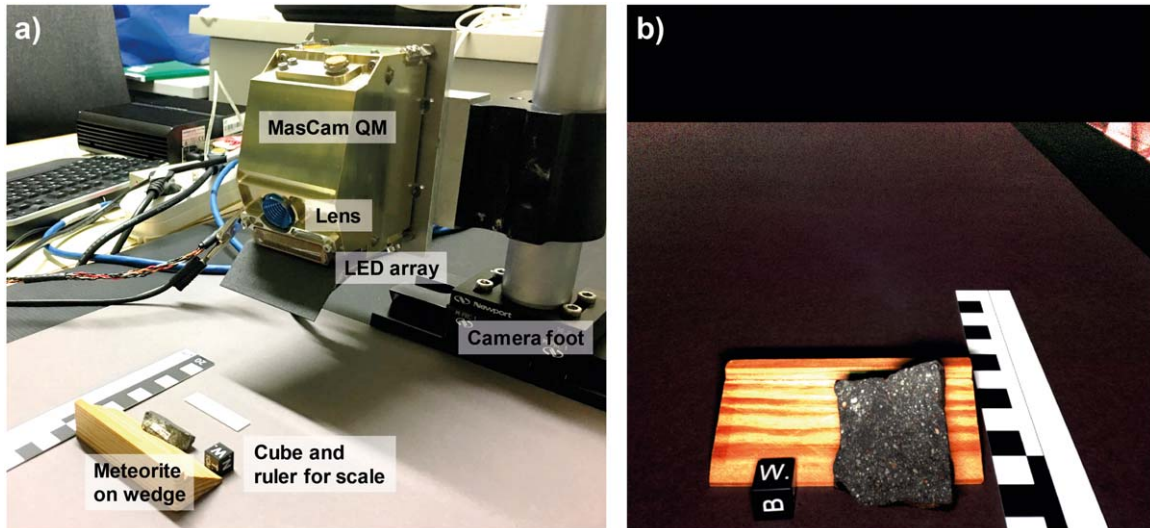
## 3. Method

### 3.1. Experimental Setup

In order to achieve comparability with the measurements taken on the surface of Ryugu, we mounted the MasCam QM on a stand approximately 10 cm above the surface of our experiment table. The table was covered with uniformly gray paper on which we placed the meteorite samples about 20 cm in front of the camera. We arranged the meteorite surface to be imaged approximately perpendicular to the boresight vector of the camera lens by using small wooden wedges when necessary. For scale we also imaged a 1 cm cube and millimeter labeled measuring stick (Figure 1).

We then darkened the room completely and imaged each of the 14 meteorites listed in Table 2 using only the illumination in each of the four LED colors. Where possible, we imaged multiple sides of the meteorites and also included flat cut and





**Figure 1.** Experimental setup (a) and color composite image of Murchison taken by the QM. The black bar on the top of (b) is manually removed background.

**Table 2**

List of Carbonaceous Chondrites Imaged with the MasCam Qualification Model at the Natural History Museum in Berlin

Meteorite Name	Petrographic Type	Collection	Year
Allende	CV3	Fall	1969
Colony	CO3	Find	1975
El-Quss	CM2	Find	1999
Karoonda	CK4	Fall	1930
Lancé	CO3	Fall	1872
Mighei	CM2	Fall	1889
Murchison	CM2	Fall	1969
Murray	CM2	Fall	1950
Ningqiang	C3-ungrouped	Fall	1983
Nogoya	CM2	Fall	1879
NWA 11118	CM2	Find	2016
Orgueil	CI1	Fall	1864
Ornans	CO3	Fall	1868
Warrenton	CO3	Fall	1877

**Note.** Note that we imaged Orgueil (CI1) but excluded it from the analysis due to surficial terrestrial weathering (Figure 6).

rough fractured surfaces to analyze the effect of the surface structure on the identification of inclusions. This summed up to a total of 23 image setups (Table 3). For some meteorites, multiple pieces were available, allowing us to evaluate the variability of inclusion distributions within different samples of the same meteorite. Furthermore, we imaged the same surface at different perspectives of the largest piece from the Murchison meteorite to analyze the effect of the sample orientation on the inclusion identification. For every image, we adjusted the exposure time according to the reflectivity at a given wavelength to make maximum use of the camera's full dynamic range of 14 bits while ensuring that there were no under- or overexposed pixels. In exceptional cases we allowed a few overexposed pixels that were presumably due to specular reflection on crystal facets. We defined overexposure as the signal exceeding 10,500 DN, the threshold for which the nonlinearity correction is invalid (Jaumann et al. 2017). Table 3 summarizes the setup parameters for each meteorite imaged.

The camera's distance to the meteorites plays a crucial role in the determination of the inclusion sizes. As shown in

Figure 1(a), the camera was attached at about 10 cm above the surface at which the meteorites were positioned. Therefore, we had to calculate the distance between the camera and the meteorites from measurements of the camera height and the horizontal distance between the camera stand and the meteorite. We validated this estimate by calculating the apparent size of a 1 cm-size cube, which we imaged next to the meteorite.

### 3.2. Image Calibration

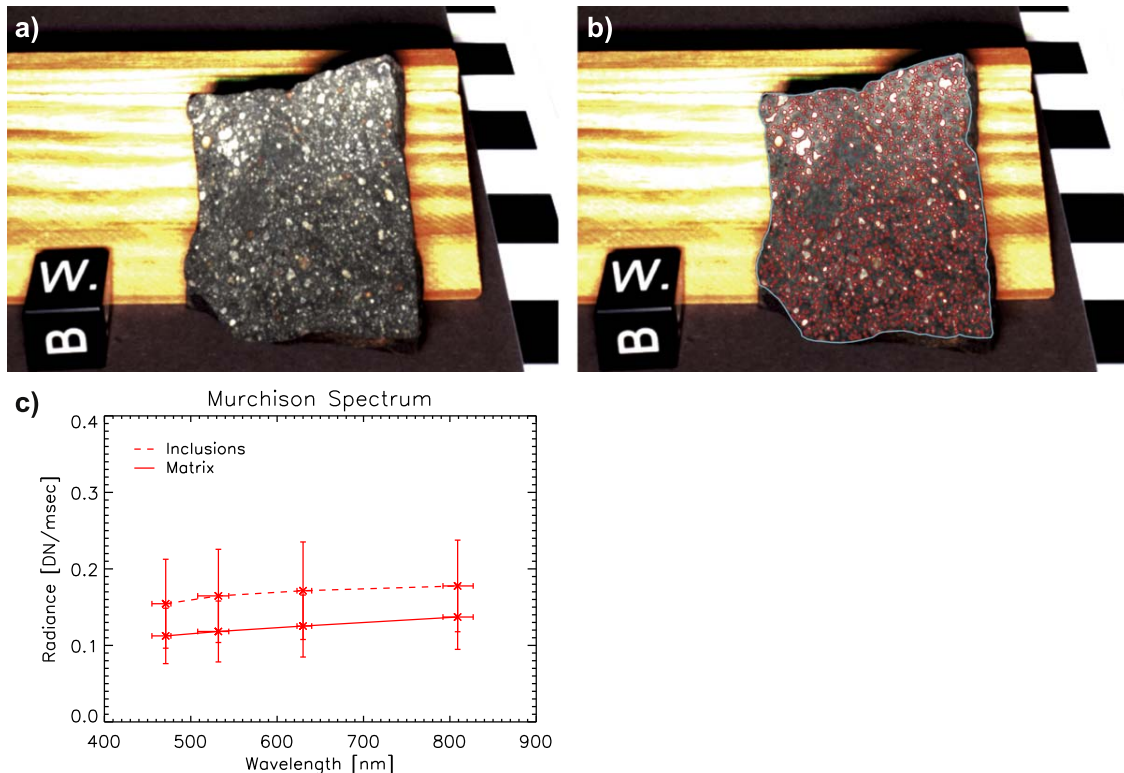
All image acquisitions were performed in a darkened room except for reference images, for which we temporarily switched on the room lights generating a diffuse illumination condition. The meteorite imaging campaign was performed over the course of several days. We started every day by acquiring nine bias images. A bias image is an image taken with a minimum exposure time of 0.2138 ms. We constructed a bias frame as the median over these images. For each meteorite we acquired the following set of images: five reference images in room light followed by a sequence of 10 images for each LED color (40 in total). Each set of 10 images comprised five LED-illuminated images and five dark (nonilluminated) images, with each LED-illuminated image immediately followed by a dark image with the same exposure time. Each image was corrected for bias using the bias frame for that day, and the result was corrected for nonlinearity. For each of the five image pairs, the corrected dark image was subtracted from the preceding, corrected illuminated image. The calibrated image (with units of DN/ms) was constructed as the median of the five dark-subtracted images, divided by the exposure time and a color flat field. A flat field for each color had been created at the start of the experiment by imaging a BaSO<sub>4</sub> plate parallel to the bottom of the camera, which was at a height of 7.5 cm (five image pairs per color, alternating illuminated and dark). Division by these color flat fields corrected, to first order, differences in illumination over the field of view. However, we note that the correction does not consider the three-dimensionality of the meteorites imaged, which introduces different illumination patterns for each color. For larger meteorites, such as the big piece of Allende, the correction may be less adequate than for smaller meteorites.



**Table 3**  
Sample Characteristics and Experimental Parameters Used to Image Carbonaceous Chondrites

Meteorite Name	Meteorite Mass (g)	Analysis Area (cm <sup>2</sup> )	Surface Structure	Camera Meteorite Distance (cm)	Camera Height (cm)	Exposure Time Red (ms)	Exposure Time Green (ms)	Exposure Time Blue (ms)	Exposure Time IR (ms)
Allende big	219.2	22.3	cut	15.9	10.1	700	800	1100	1500
Allende small	79.2	1.3	fractured	16.2	9.6	500	500	700	900
Colony	3.1	1.7	cut	15.2	8.5	700	900	1500	1500
El-Quss	4.5	3.2	cut	13.4	7.5	700	700	1100	1600
Karoonda side 1	15.5	7.9	fractured	15.6	9.4	550	550	800	1000
Karoonda side 2	15.5	6.0	fractured	16.7	9.4	800	800	1200	1600
Lancé side 1	62.2	10.3	fractured	15.1	9.6	500	500	700	1100
Lancé side 2	62.2	6.4	fractured	15.1	9.6	550	550	800	1200
Mighei side 1	18.5	6.5	fractured	14.6	8.9	300	300	400	600
Mighei side 2	18.5	4.7	cut	14.7	8.9	800	800	1000	1400
Murchison big tilt 1	118.0	9.8	fractured	15.8	9.6	400	300	450	900
Murchison big tilt 2	118.0	7.6	fractured	15.8	9.6	700	700	1000	1300
Murchison slap	35.4	17.6	cut	16.1	9.6	700	700	1200	1500
Murchison small	11.2	6.2	fractured	14.6	8.0	600	600	900	1200
Murray	6.7	1.4	fractured	14.3	7.5	600	600	800	1200
Ningqiang side 1	9.0	3.2	fractured	15.0	8.5	500	450	600	800
Ningqiang side 2	9.0	3.2	fractured	15.0	8.5	600	550	800	1100
Nogoya	1.3	1.1	fractured	14.3	7.5	800	800	1200	1400
NWA 11118 side 1	1.8	2.0	fractured	14.1	7.8	700	700	1000	1400
NWA 11118 side 2	1.8	1.3	fractured	14.1	7.8	1300	1500	2300	2500
Orgueil	114.3	...	fractured	17.4	10.7	700	700	1100	1700
Ornans	8.0	5.0	fractured	17.7	8.5	700	700	1100	1500
Warrenton	5.7	2.6	fractured	18.0	8.5	700	700	1000	1300

**Note.** The first column states the names of the meteorites. If multiple pieces of the same meteorite were imaged, we added a descriptive word (e.g., big, small, side, tilt, slap) to identify the different pieces or imaging conditions. The camera meteorite distance was calculated from the camera height and the mean horizontal distance between the meteorite and camera foot considering the expansion of the imaged meteorite and the location of the aperture in the camera (Figure 1). Note that we imaged Orgueil (CI1) but excluded it from the analysis due to surficial terrestrial weathering (Figure 6).



**Figure 2.** Example of the QM image of Murchison (big tilt 1) (a), the identified inclusions in red and the mapping area in blue (b), and the spectrum of inclusions (dashed red line) and matrix (solid red line) (c). The errors on the wavelength are the FWHM according to Table 1. The spectral slope of the inclusions  $((R - B)/B)$  is  $0.12 \pm 0.11$  and the relative brightness between inclusions and matrix at the red wavelength (relative R brightness) is  $1.37 \pm 0.51$ . The matrix volume abundance is 71.1%.

### 3.3. Inclusion Mapping

Using a red, green, and blue radiance color composite image, we mapped inclusions within meteorites imaged by the QM using ArcGIS's mapping tools. We define an inclusion as a distinctly bright or dark region within the surrounding matrix and include all features regardless of their shapes. Mapped inclusions therefore comprise chondrules as well as refractory inclusions. This definition of inclusions also implies that the derived matrix abundance represents an upper limit, because inclusions smaller than the image resolution cannot be resolved and are thus considered as matrix. Without assigning a spatial reference, we outlined inclusions as polygons and converted these polygons into a raster data set of the same size as the QM images ( $1024 \times 1024$  pixels). Within this data set, all pixels belonging to the same inclusion/polygon have a distinct number, allowing a straightforward subsequent analysis of the color and size of each individual inclusion. Note that due to the Scheimpflug principle, the pixel resolution increases toward the bottom of the image.

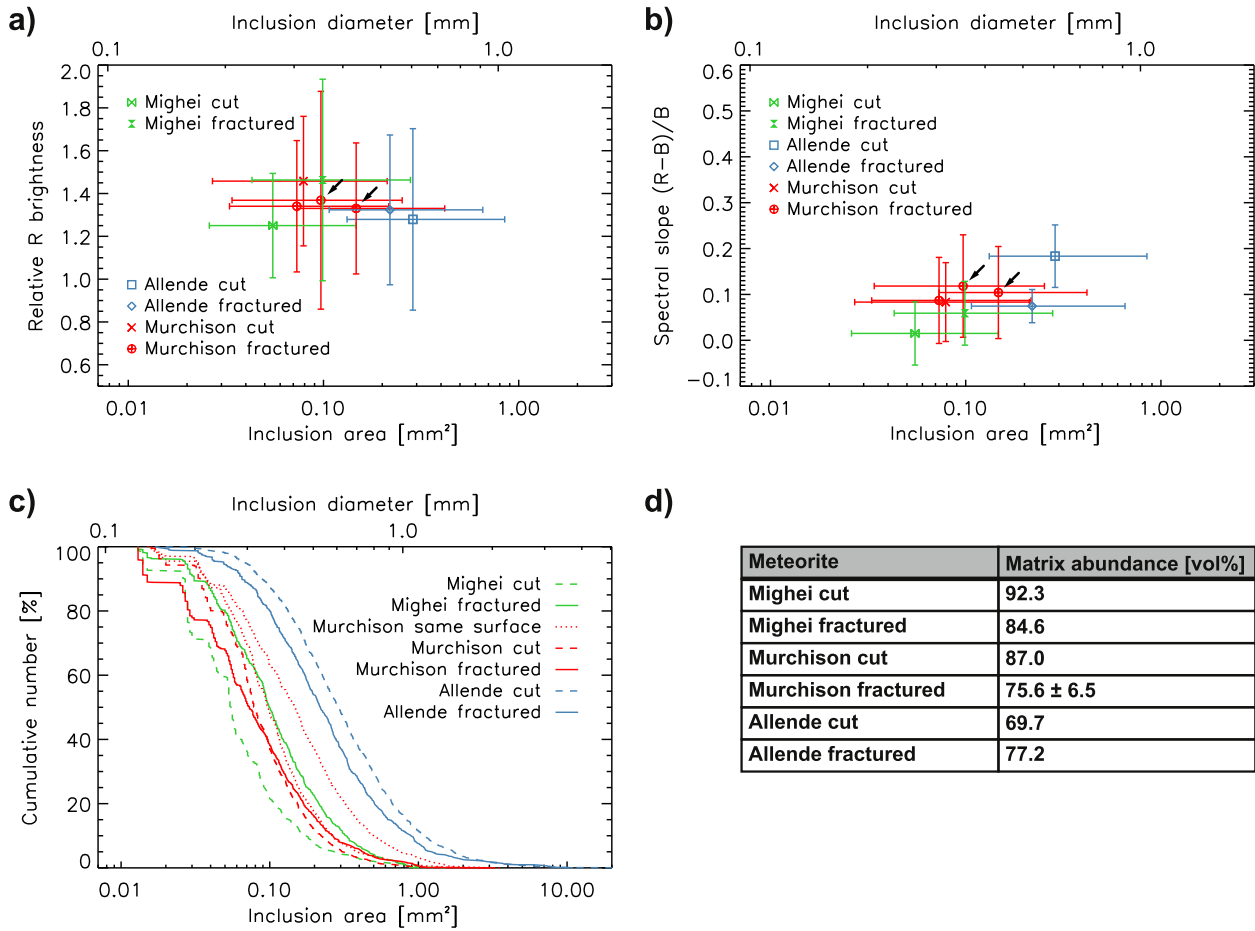
Before identifying inclusions in the images, we first determined the outline of an area of interest on the meteorite. For each meteorite we enclosed an area of similar distance and orientation to the camera by locating a region of similar texture and brightness in the image. In general, this region was a fractured or cut surface of the meteorite. Features such as labels or fusion crusts on the outside of the meteorite were not considered in this area of interest. We then mapped the most prominent inclusions first. The subsequently mapped inclusions were identified with an increasingly smaller field of view so that each location was looked at multiple times at different

spatial resolutions. When an inclusion had similar brightness values to the matrix, we compared the inclusion in question to other inclusions of similar brightness and morphology in the context of the entire area of interest. In nondefinite cases the features were not mapped. The minimum size of mapped inclusions was one pixel ( $\sim 0.2$  mm). The area of the region of interest that was not mapped as an inclusion is considered to be matrix.

To determine the area of the matrix and inclusions, we assumed that each image pixel showing the meteorite surface had the same distance to the camera, which we tried to achieve by placing the meteorite surface to be analyzed perpendicular to the boresight vector of the camera aperture. We derived the distance of the meteorite from the camera (Table 3) to calculate the pixel resolution and additionally verified the pixel resolution from the distance and the size of the 1 cm cube using its location inside the image. Each inclusion area was then calculated from the number of pixels and their resolutions.

## 4. Results and Interpretation

We investigated 23 images of 14 different carbonaceous chondrites. An example showing the QM image of Murchison (big tilt 1), the inclusion mapping, and the average inclusion and matrix radiance at each LED wavelength is given in Figure 2. To gain insight into the meteorites' spectral and inclusion properties, we generated three plots (Figures 3, 4, 7, and 9). In the first plot, we show the ratio between the brightness of the inclusions and the brightness of the matrix in the red LED image (relative R brightness) as a function of the inclusion size. Here we include all pixels that were mapped as inclusions and average their



**Figure 3.** Relative brightness (a), spectral slope (b), and cumulative size distribution (c) of fractured and cut surfaces in comparison. The median inclusion size and the 25th and 75th percentile are shown in (a) and (b). The two black arrows indicate the same fractured surface of Murchison that was imaged from two different orientations. In (c), these two surfaces are indicated by the dotted lines. (d) lists the matrix volume abundance. In the case of Murchison, for which multiple surfaces were imaged, the mean and standard deviation is shown.

values. We note that this approach only allows us to distinguish between a meteorite with all neutrally colored inclusions and a meteorite with equal numbers of blue- and red-colored inclusions by looking at a range of values and the standard deviation on the average value, which should be larger in the second case compared to the first. The size is given in square millimeters as well as the diameter of a circle with the same area as the mapped inclusion. The second plot shows the relative spectral slope,  $(R - B)/B$ , where  $R$  and  $B$  are the red and blue radiance, respectively. A positive spectral slope means a reddish color and a negative spectral slope denotes a bluish color. In both plots, the spectral values for all inclusions have been averaged and are presented as a data point with error bars according to the standard deviation. The inclusion size is presented by the median size and the 25th and 75th percentile as errors bars. We used this representation instead of the mean and standard deviation, because the large variation in inclusion sizes occasionally results in errors that are larger than mean value, giving the unphysical impression that inclusions could have negative sizes. A third plot shows the cumulative inclusion size distribution of the mapped inclusions. Combined cumulative inclusion size distributions of more than one meteorite are derived by simply combining the lists on mapped inclusion sizes into one data set. Plots of individual images in combination with an inclusion and matrix spectrum and a color composite image

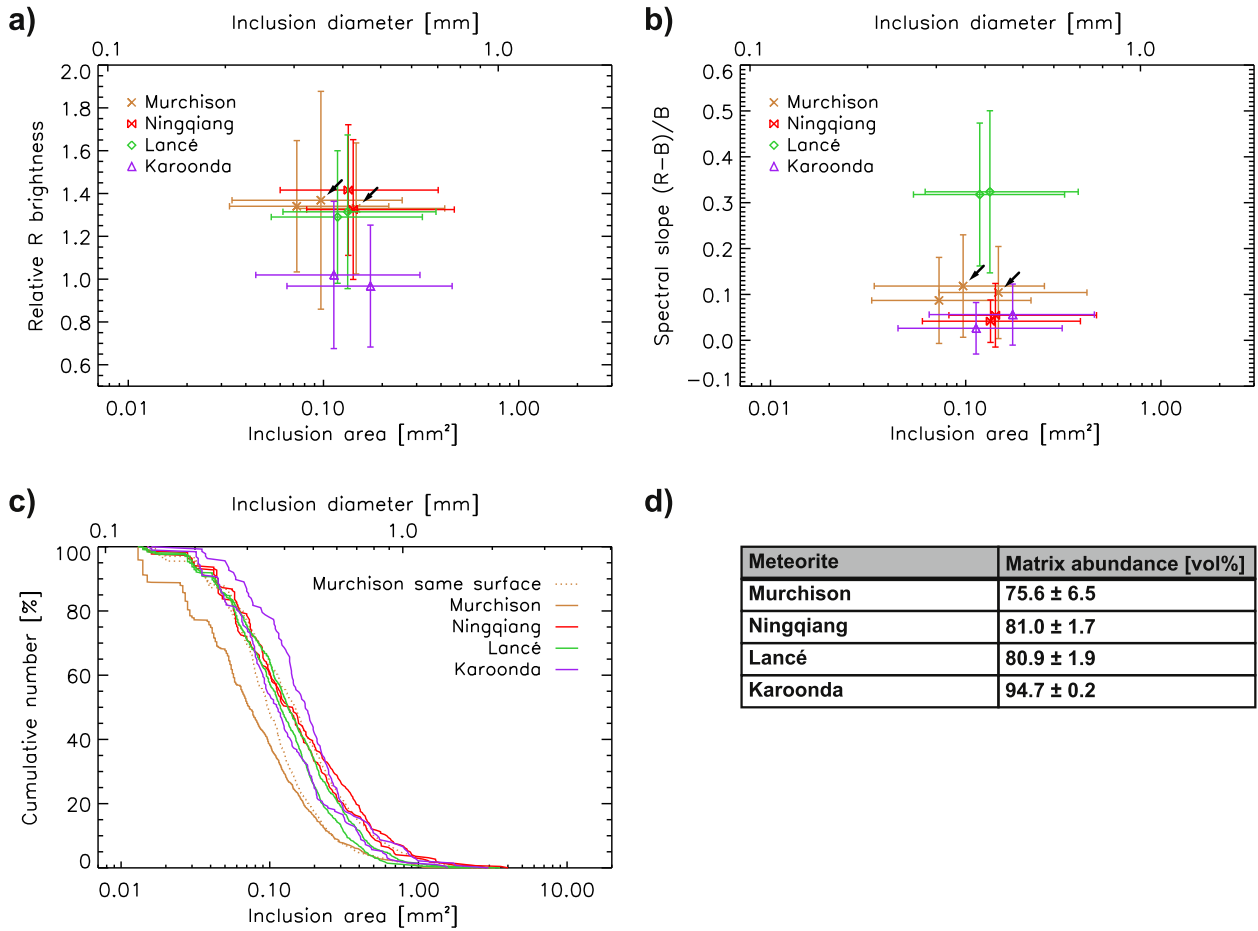
of the meteorite with its mapped inclusions are available in the figure set in the [Appendix](#).

We also estimated the areal inclusion density by simply dividing the total inclusion area by the mapping area. The areal density can be assumed to be equal to the volumetric density following the Delesse Principle (Royet 1991).

In the following, we will first investigate the influence of the measuring setup and sample preparation on the spectral and petrographic parameters (Section 4.1). We will then focus on the variations observed within one meteorite (Section 4.2), within the different carbonaceous chondrite groups (Section 4.4) and the effect that terrestrial weathering might have on the spectral parameters (Section 4.4). Finally, we will put our results into context with previous investigations (Section 5.1) and the asteroid Ryugu (Section 5.2).

#### 4.1. Influences of the Meteorite Surface Structure and Orientation

To investigate the influence of surface structure on the identification of inclusions in the meteorites, we imaged, next to fractured surfaces, three cut surfaces of meteorite falls including Allende (CV3) and Mighei and Murchison (CM2) and mapped the inclusions using the same procedure as for the images of the fractured surfaces. Figure 3 shows the relative brightness, spectral slope, and inclusion size distribution in



**Figure 4.** Relative brightness (a), spectral slope (b), and cumulative size distribution (c) of different fractured surfaces of the same meteorite in comparison. Only fractured surfaces of meteorite falls are included. The median inclusion size and the 25th and 75th percentile are shown in (a) and (b). The two black arrows indicate the same surface of Murchison that was imaged in two different orientations. In (c), these two surfaces are indicated by the dotted lines. (d) lists the matrix volume abundance.

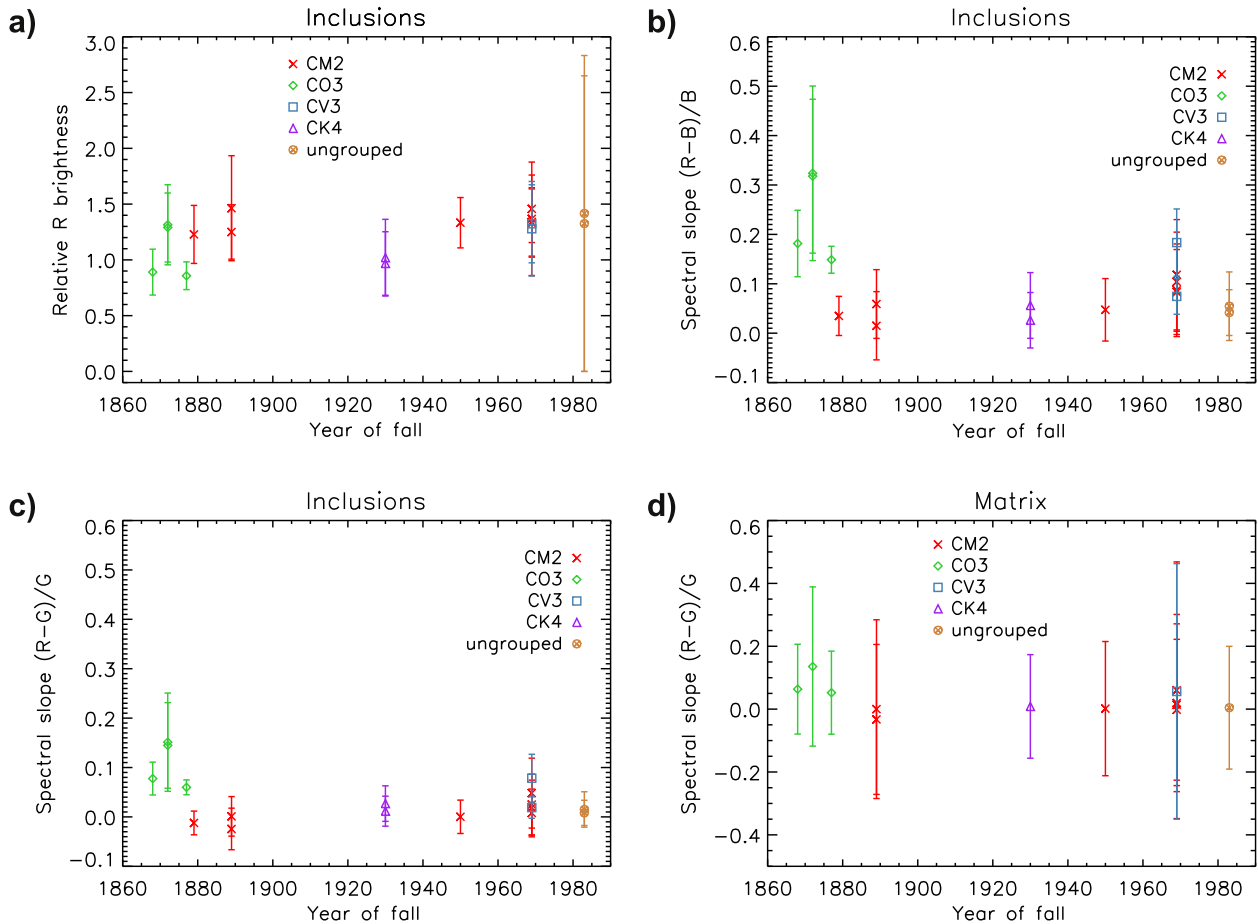
comparison with the fractured surfaces. The variations in relative brightness and spectral slope of individual inclusions are too large to allow a clear distinction between the different surface textures. The cumulative inclusion size distribution appears to be shifted toward both larger and smaller values for the cut pieces compared to the fractured ones. The same can be observed for the matrix volume abundance, which is also larger and smaller for the cut surfaces (Figure 3(d)). It is therefore not possible to state if a cut meteorite surface leads to a systematic error in evaluating the inclusion size distribution. Moreover, the slope of the cumulative size distribution in the near-linear region (around 50%) is similar for all samples, which implies that the rate of decrease in inclusion number with increasing size is similar for all meteorites. Thus, there is no systematic effect on the relative R brightness, spectral slope, inclusion size distribution, and matrix volume abundance caused by the texture of the meteorite surface.

Using Murchison, we imaged the same meteorite surface at two different orientations to investigate the influence of the imaging setup on the inclusion identification (Murchison big tilt 1 and 2). Compared to the first meteorite orientation in front of the QM, the second orientation was upside down. The variations in the relative brightness and spectral slope are minimal; however, the size distribution varies significantly. The two distributions (red dotted lines in Figure 3(c)) deviate at larger

inclusion sizes, so that the median inclusion size is  $0.10^{+0.06}_{-0.04}$  mm and  $0.15^{+0.12}_{-0.08}$  mm for the two distributions. This also influences the apparent matrix abundance, which is given by 78.9 vol% and 85.0 vol% for the two measurements. The large variation between the two distributions is related to distortion effects that occur for different surface orientations and distances to the QM. We assumed in our analysis that the meteorite surface had the same distance to the camera at all locations, and this example shows that a deviation from this assumption can have a significant influence on the inclusion size distribution. This is particularly prominent for meteorites that cover a larger area within the image and the Murchison used in this example was one of our largest meteorites. It is therefore necessary to point out the high degree of measurement uncertainty that can derive from the orientation and position of larger meteorites. It also emphasizes the necessity to know the exact topography when analyzing in situ images of Ryugu (Section 5.2). The structure of the meteorite surface (cut or fractured) influences the parameters derived to a similar degree.

#### 4.2. Variations within One Meteorite

We imaged different fractured surfaces of the same meteorite piece to analyze the variation within one meteorite (Figure 4). This was done for Murchison, Ningqiang and NWA 11118



**Figure 5.** Relative brightness of the inclusions compared to the matrix brightness using the green LED (a) and the relative spectral slope (b) plotted against the year of meteorite fall. (c) and (d) show the relative slope from green (532 nm) to red (630 nm), which may be indicative of weathering-related iron oxidation, for the inclusions and matrix, respectively. The data are grouped into the different carbonaceous chondrite groups and include cut as well as fractured surfaces. A correlation is not evident.

(CM2), Lancé (CO3), and Karoonda (CK4). For Murchison we also included the same side that was imaged from two different directions as mentioned in Section 4.1. We exclude NWA 11118 from the following analysis as it is a find, and thus, the weathering history is unknown.

We find a slight variation in relative brightness, spectral slope, and inclusion size distribution within one meteorite, but all values of one meteorite agree within their errors. The most significant variation is observed for the inclusion size distribution. As explained above, the determination of the inclusion size is highly dependent on the exact knowledge of the distance between the meteorite and the QM, which is one of the major uncertainties in our work. The error on the matrix volume abundance is less than 5% for all samples, with the smallest value of 0.2% found for Karoonda. The variation of the parameters between the different surfaces of the same meteorite is less than the variation that is introduced by cutting the surface (Section 4.1). We will therefore exclude the cut meteorite surfaces from the following analysis.

#### 4.3. Effect of Terrestrial Weathering

Meteorites react with the environment and atmosphere on Earth, which influences the compositional and therefore spectral properties of the meteorite matrix and inclusions (Bland et al. 2006; Salisbury & Hunt 1974). Depending on the

duration, humidity, and temperature a meteorite is stored at, weathering such as element mobilization, oxidation of metal and mafic silicates, or veining may occur on various timescales (Gounelle & Zolensky 2001; Sephton et al. 2004; Bland et al. 2006). A variation in inclusion color may be most detectable from the oxidation of iron oxyhydroxides, which can introduce an absorption feature near 900 nm, an absorption edge between 500 nm and 600 nm and a steep drop in reflectance toward shorter colors (Salisbury & Hunt 1974; Cloutis et al. 2011, 2012b). However, a variation in the size distribution of inclusions is not expected.

Figure 5 illustrates the average relative brightness of inclusions compared to the matrix using the red LED image (relative R brightness), the average spectral slope between red and blue ( $(R - B)/B$ ), and the average spectral slope between red and green ( $(R - G)/G$ , 532 nm and 630 nm), which would be most diagnostic of the absorption edge between 500 nm and 600 nm of the inclusions in dependence of the year of fall onto Earth. We also show the matrix's  $(R - G)/G$  slope for comparison. For each meteorite image, one data point was derived. Both the relative R brightness and the spectral slopes of the inclusions as well as the matrix seem to be independent of the time these meteorites spent on Earth as well as of the carbonaceous chondrite group they belong to. Fluctuations of these parameters are large, even within the same group and do





**Figure 6.** C11 Orgueil as imaged by the QM (color composite). The bright patches are not inclusions but terrestrial weathering features. This example illustrates the challenges in identifying inclusions in weathered meteorites.

not allow us to constrain the terrestrial alteration stage of the meteorites. A general reddening in spectral slope of the meteorites related to weathering (Rubin & Huber 2005) cannot be observed. The only exception may be made for the relatively old CO3 group in our work which appears to have increased spectral slopes for both, the inclusions and the matrix. The fact that CO3s are more susceptible to terrestrial weathering in comparison to the other meteorite groups investigated in this work has also been reported previously (Cloutis et al. 2011, 2012a, 2012b, 2012c).

Furthermore, terrestrial weathering may create surface features that appear similar to meteorite inclusions. To illustrate this, we imaged a piece of the C11 Orgueil, which fell onto Earth more than 150 years ago (Figure 6). This piece does not have any inclusions and inclusion statistics are thus not shown here. However, terrestrial weathering is common in CI meteorites and introduces brightness variations in the surficial appearance via, e.g., the formation of sulphate veins or crystals (Dufresne & Anders 1962; Cloutis et al. 2011; Gounelle & Zolensky 2001). These may appear similar to inclusions in the other meteorite images. This demonstrates that the effect of terrestrial weathering influences the inclusion identification process and needs to be considered as a main source of error. Using our QM imaging technique, this phenomenon introduces an overestimation of inclusion abundances and/or sizes when bright weathering features are falsely identified as inclusions or merge individual smaller inclusions into a single larger one. With our method it is not possible to distinguish between inclusion-like weathering features and real inclusions, however, given the protected storage capabilities at the Natural History Museum, and after a thorough visual inspection of the samples before imaging them, we chose meteorites with minimal terrestrial weathering features.

#### 4.4. The Carbonaceous Chondrite Groups

Figure 7 shows the relative brightness, spectral slope and cumulative size distribution of the carbonaceous chondrite groups CM2, CV3, CO3, and CK4 as well the ungrouped Ningqiang in comparison. Here, we only show the values of meteorite falls with a fractured surface as labeled in Table 3.

The relative inclusion brightness and the spectral slope as a function of the median inclusion size cluster for each carbonaceous chondrite group with the exception of the CO3 group (Lancé Ormans and Warrenton) in which Lancé is distinguished from the

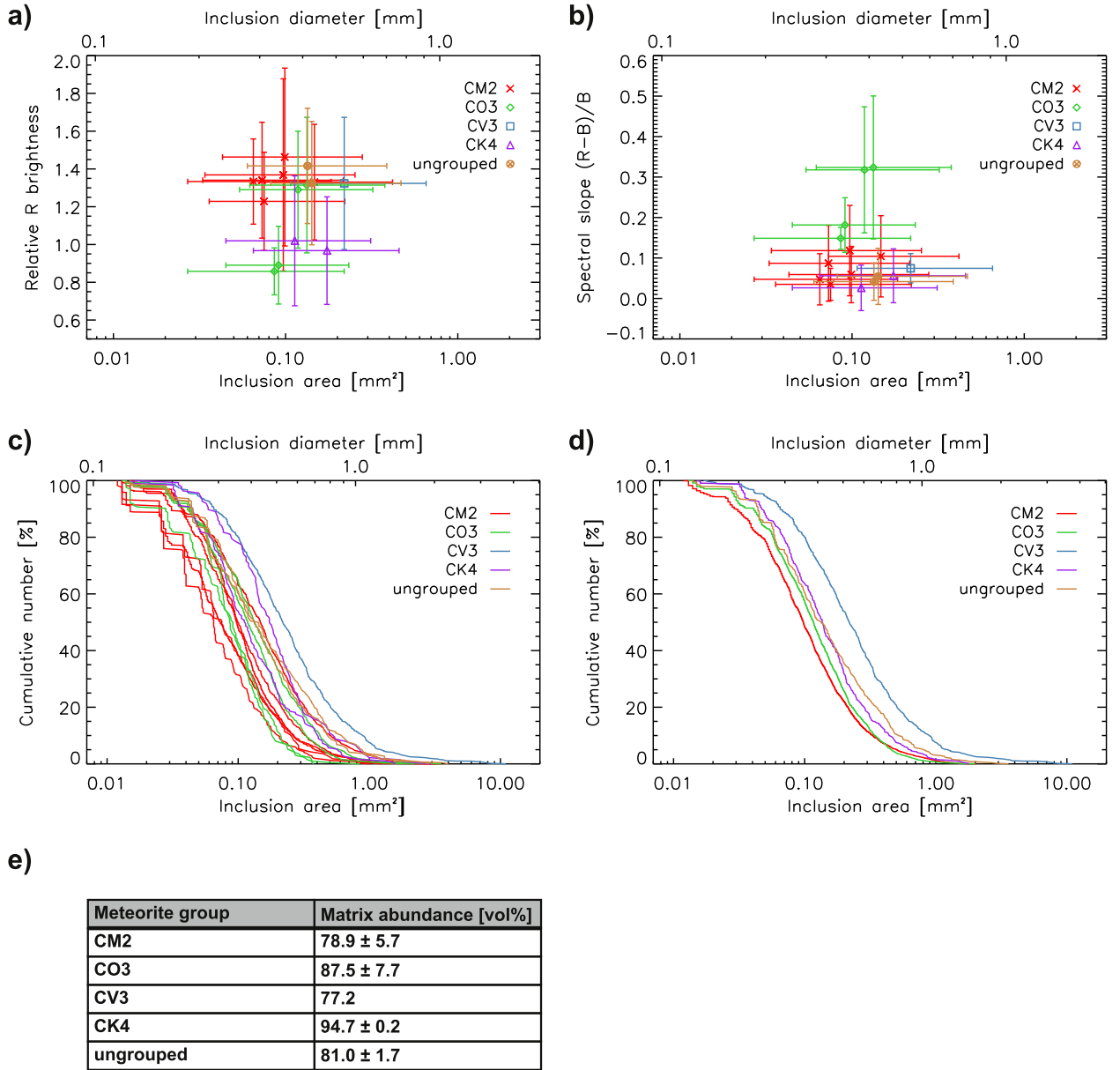
other two meteorites by its comparatively large relative brightness and spectral slope. Lancé has previously been found to differ from other CO3s by having an overall high 600/500 [nm] ratio, which may be attributed to more abundant hydrous phases and ferrihydrite-like materials (Keller & Buseck 1990; Cloutis et al. 2012a). However, the large error bars on our measurements indicate that individual inclusions can have values that significantly deviate from the clusters.

The average spectral slope of the inclusions of all carbonaceous chondrite groups is positive (i.e., red, Figure 4(b)). The CO3 inclusions generally have the largest (reddest) spectral slope with mean values ranging from 0.15 to 0.32 distinguishing them from the other groups. Concerning the relative brightness, Lancé fits well in the cluster of the CM2s and CV3s, but the other two CO3 meteorites imaged (Ormans and Warrenton) as well as the CK4 meteorite Karoonda have lower relative inclusion brightness values, which are even below 1 (Figure 4(a)). This means that in the red LED light the matrix is brighter than the average inclusion. This distinguishes Ormans, Warrenton, and Karoonda from the other meteorites, which all have relative R brightness values above 1.2.

The CV3 Allende (the only meteorite of this group in our experiment) most prominently distinguishes from the other meteorite groups in terms of the sizes of its inclusions. Although the slope of the cumulative size distribution of all carbonaceous chondrite groups is similar, the CV3 distribution is shifted toward larger inclusion sizes. In Section 5.1 we will show that this observation has been confirmed previously which validates our method.

Matrix volume abundances vary between 73.5% (CV3) and  $94.7\% \pm 0.2\%$  (CK4) and do not correlate with the median inclusion size (also see Figure 8(d)). For example, the matrix volume abundances of the CV3s and the CM2s are similar (84.4% and  $85.9\% \pm 3.8\%$ , respectively), but the CV3s and CM2s have the largest and smallest median inclusion sizes ( $0.22^{+0.22}_{-0.11}$  and  $0.10^{+0.08}_{-0.04}$ ), respectively.

We also had a C11 sample available, Orgueil. Within our sample collection, Orgueil, which fell in 1864, is the meteorite with the longest retention time on Earth. Thus, this sample was unfortunately weathered to a degree that bright spots (possibly surficial sulphate deposits) covered the surface and were easily confused as bright inclusions. Because such inclusions are actually not found in C11 carbonaceous chondrites (Cloutis et al. 2011), we excluded Orgueil from our analysis.



**Figure 7.** Relative brightness (a), spectral slope (b), and cumulative size distribution (c) of individual measurements of the different carbonaceous chondrite groups in comparison. The median inclusion size and the 25th and 75th percentile are shown in (a) and (b). (d) shows the inclusion size distributions of each carbonaceous chondrite group derived by considering all inclusions identified within this group. (e) lists the average matrix volume abundance of the different groups. Measurements of fractured surfaces of meteorite falls are included.

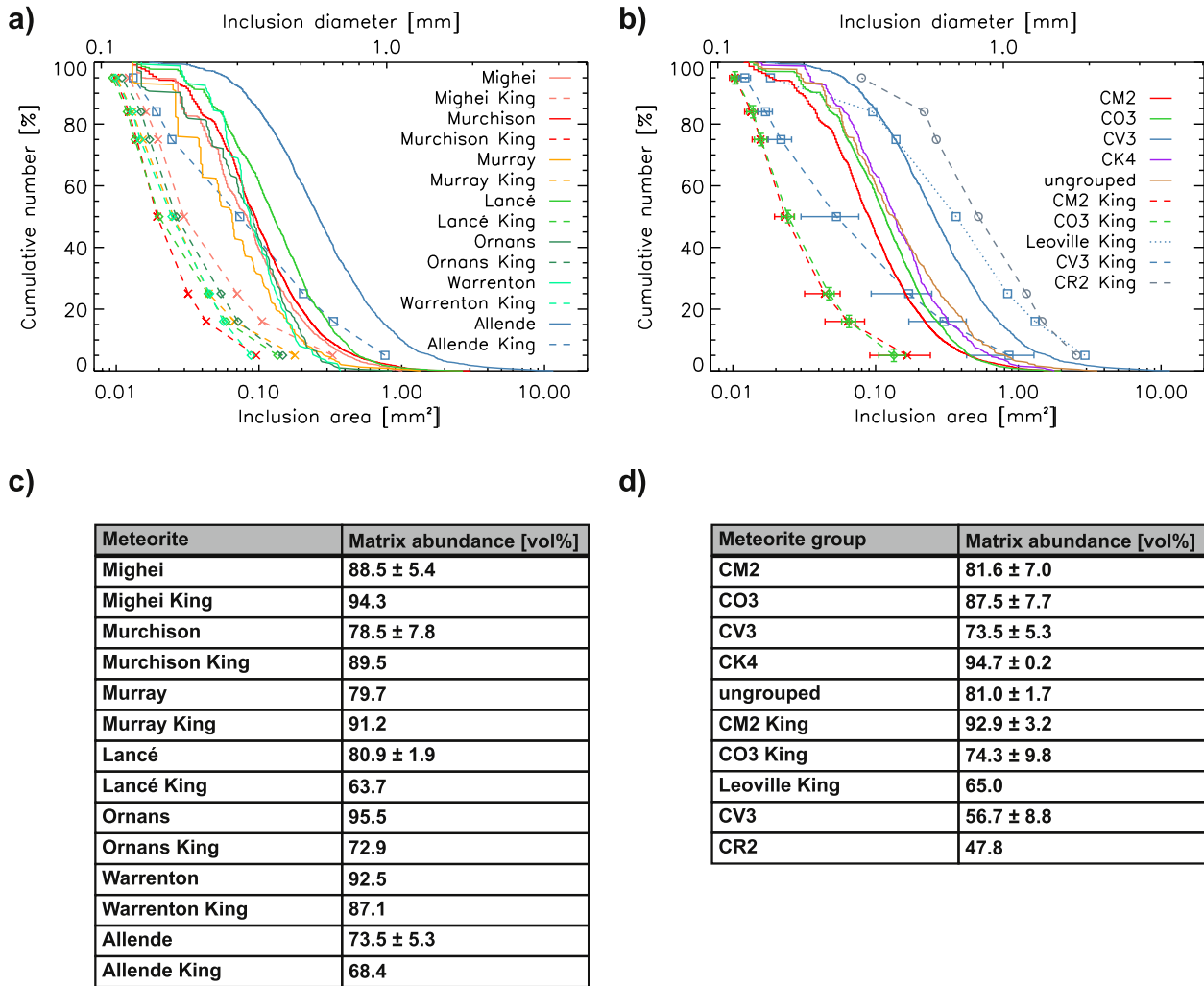
## 5. Scientific Context and Discussion

### 5.1. Previous Investigations of Meteorite Inclusions

Given the availability of high spatial resolution instruments (e.g., optical or electron microscopes) in Earth-based laboratories, many analyses on meteoritic inclusions focus on size scales below the pixel resolution of the QM ( $\sim 0.2$  mm; e.g., Rubin & Wasson 1986; Ebel et al. 2016; Simon et al. 2018). King & King (1978), however, measured the inclusion size distribution of inclusions larger than 0.1 mm in CM2, CO3, CV3, and CR2 carbonaceous chondrites using polished thin sections and a microscope. Their sample analysis areas were between  $13 \text{ mm}^2$  and  $210 \text{ mm}^2$  in size, whereas our sample areas were generally larger, varying between  $111 \text{ mm}^2$  and  $2234 \text{ mm}^2$  (Table 3). One has to take into consideration that the

different inclusion identification techniques, as well as the sample preparation (e.g., thin sections, fractured surface), will affect the identification of inclusions; however, their analysis best matches our work in terms of spatial resolution. Figure 8 shows their findings in comparison with our measurements.

Generally, our method results in larger inclusion sizes compared to the data derived by King & King (1978), and with the exception of the CM2s, we derive about 10% lower matrix volume abundances. This is also represented by the individual meteorites in each carbonaceous chondrite group. The coarser appearance in our measurements is probably related to the larger sample sizes used in our work, which allows us to identify more larger inclusions and our minimum inclusion size of one pixel ( $\sim 0.2$  mm), which increases the relative abundance of larger inclusions compared to King & King (1978), who measured



**Figure 8.** Cumulative size distribution of the meteorites imaged in this work in comparison with previously published results by King & King (1978). (a) shows the comparison between individual meteorites. For a more general overview, we combined the inclusions of all meteorites of a specific carbonaceous chondrite group of our measurements and calculated the mean and standard deviation of a specific group using the measurements of King & King (1978) in (b). Please note that Leoville and the CR2 do not have error bars because they comprise only one measurement. The CV3 Leoville is shown individually as it separates significantly from the other CV3 meteorites. Measurements of fractured and cut surfaces of meteorite falls are included. Tables (c) and (d) list the matrix volume abundance of the samples shown in (a) and (b), respectively. Where multiple samples were combined, the mean and standard deviation of the matrix volume abundance is given.

inclusions down to a size of 0.1 mm. Nevertheless, the King & King (1978) cumulative size distribution flattens less significantly toward larger inclusion sizes. This implies that compared to the King & King (1978) method, our analysis identified fewer large inclusions in relation to the total number of inclusions. This discrepancy is most likely introduced by the more thorough visual inspection that was conducted by King & King (1978), including the usage of reflected as well as transmitted light, which cannot be accomplished by our method. This may have allowed them to identify faint large inclusions that we may have interpreted as matrix. The discrepancy is particularly evident for the CV3 meteorites (blue lines in Figure 8) whose inclusion size distribution shows the shallowest slope.

King & King (1978) note that the inclusion size distributions of the CM2 and CO3 meteorites are virtually identical. We observe the same behavior for the CM2s and CO3s, and the CK4 Karoonda and the ungrouped Ningqiang also have very similar inclusion size distributions. The largest deviation from this group of inclusion size distributions is presented by the CV3 Allende, which has much larger inclusions. These coarser

inclusions are evident in our as well as the King & King (1978) work.

King & King (1978) also investigated the inclusion size distribution of the CR2 Renazzo and the CV3 Leoville, which deviate from their other carbonaceous chondrite measurements due to comparatively large inclusion sizes. Unfortunately, we did not have these samples available for our measurements, but we show them here (Figure 8) to illustrate the possible variations within the carbonaceous chondrite groups.

Brearely & Jones (1998) and Scott & Krot (2014) summarize the petrographic characteristics of carbonaceous chondrites (Table 4). Comparing their summary to our results, we find that we derive significantly higher matrix and lower chondrule and refractory volume abundances for all carbonaceous chondrite groups. King & King (1978) also derive higher matrix and lower chondrule and refractory inclusion volume abundances with the exception of the CM2 group. This discrepancy may be attributed to a different definition of matrix material or different derivation methods on which Scott & Krot (2014) and Brearely & Jones (1998) are not very specific. Additionally, analytical



**Table 4**  
Summary of the Petrographic Characteristics of the Carbonaceous Chondrites Investigated in This and Other Works

Carbonaceous Chondrite Group	Chondrule + Refractory Inclusions Abundance (vol%)			Matrix Abundance (vol%)			Chondrule Mean Dia- meter (mm)		Chondrule + Inclusions Median Diameter (mm)	
	S&K	K&K	This Work	S&K	K&K	This Work	This Work: Chon- drules + Inclusions		K&K	This Work
							S&K	K&K		
CI	<0.001	...	...	95	...	...	...	...	...	...
CM	25	4.7 ± 2.1	12.3 ± 4.7	70	92.9 ± 3.2	83.1 ± 7.1	0.3	0.48 ± 0.20	0.023 ± 0.003	0.09 <sup>+0.07</sup> <sub>-0.04</sub>
CR	51–61	34.8	...	30–50	47.8	...	0.7	...	0.525	...
CO	43	17.1 ± 6.6	9.4 ± 4.0	30	74.3 ± 9.8	86.3 ± 7.2	0.15	0.41 ± 0.19	0.024 ± 0.003	0.12 <sup>+0.09</sup> <sub>-0.05</sub>
CV	55	28.9 ± 5.9	17.7 ± 3.5	40	56.7 ± 8.8	73.5 ± 5.3	1.0	0.68 ± 0.46	0.053 ± 0.023	0.26 <sup>+0.26</sup> <sub>-0.12</sub>
CK	19	...	3.5 ± 0.2	75	...	94.7 ± 0.2	0.7	0.47 ± 0.24	...	0.14 <sup>+0.10</sup> <sub>-0.06</sub>
Ryugu	7.6			92.4			0.63 ± 0.91		0.37 <sup>+0.36</sup> <sub>-0.19</sub>	

**Note.** The values have been extracted from Scott & Krot (2014, abbreviated as S&K) and King & King (1978, abbreviated as K&K). Three dots indicate that no data has been collected for the according position. We also show the results from Ryugu derived by Schröder et al. (2021) with the same method. Mean and median inclusion sizes of Ryugu are directly derived from their data set, but only considering inclusions less than 25.5 cm away from the camera to avoid distortion effects introduced by the shape model, which becomes less reliable at larger distances (Scholten et al. 2019). Please note that we did not distinguish between refractory inclusions and chondrules in our work. Our values are averages of all cut and fractured surfaces of a specific carbonaceous chondrite group including finds and falls. The matrix abundance is directly calculated from the chondrule and refractory abundance (100% – inclusion abundance). The values from Scott & Krot (2014) may not sum up to 100% due to excluded sulfide and metal components.

instruments became more precise over the time span of these works. On the other hand, our definition of matrix as the material that is not an inclusion is likely oversimplified compared to other definitions, and our resolution limit of 0.2 mm may have led to the exclusion of small inclusions further contributing to an overestimation of the matrix volume abundance.

Brearley & Jones (1998) describe the size frequency distribution of chondrules as log-normal distributions with well-defined mean diameters. Although we are not able to distinguish between chondrules and inclusions, we also observe a distribution of combined chondrules and inclusions with a log-normal shape. However, a well-defined mean value is not obvious. Instead our derived inclusion sizes span over a wide range of sizes, whose mean and median size cover the values from Scott & Krot (2014) within their errors. The only exception is given by the CO3 group with smaller mean chondrule sizes compared to our measurements. However, May et al. (1999) report larger average inclusion sizes varying between 0.19–0.30 mm for this group, which is in agreement with our values. Scott & Krot (2014) also report a significantly larger chondrule and refractory inclusion abundance as well as lower matrix volume abundances for the CO3 group not only compared to our work, but also compared to the work by King & King (1978). This illustrates the difficulties in comparing these parameters when different methods or samples of the same group are used. Nevertheless, in agreement with Scott & Krot (2014) and King & King (1978), we find the largest inclusion and chondrule sizes for the CV3 group, while the sizes for the other groups are similar.

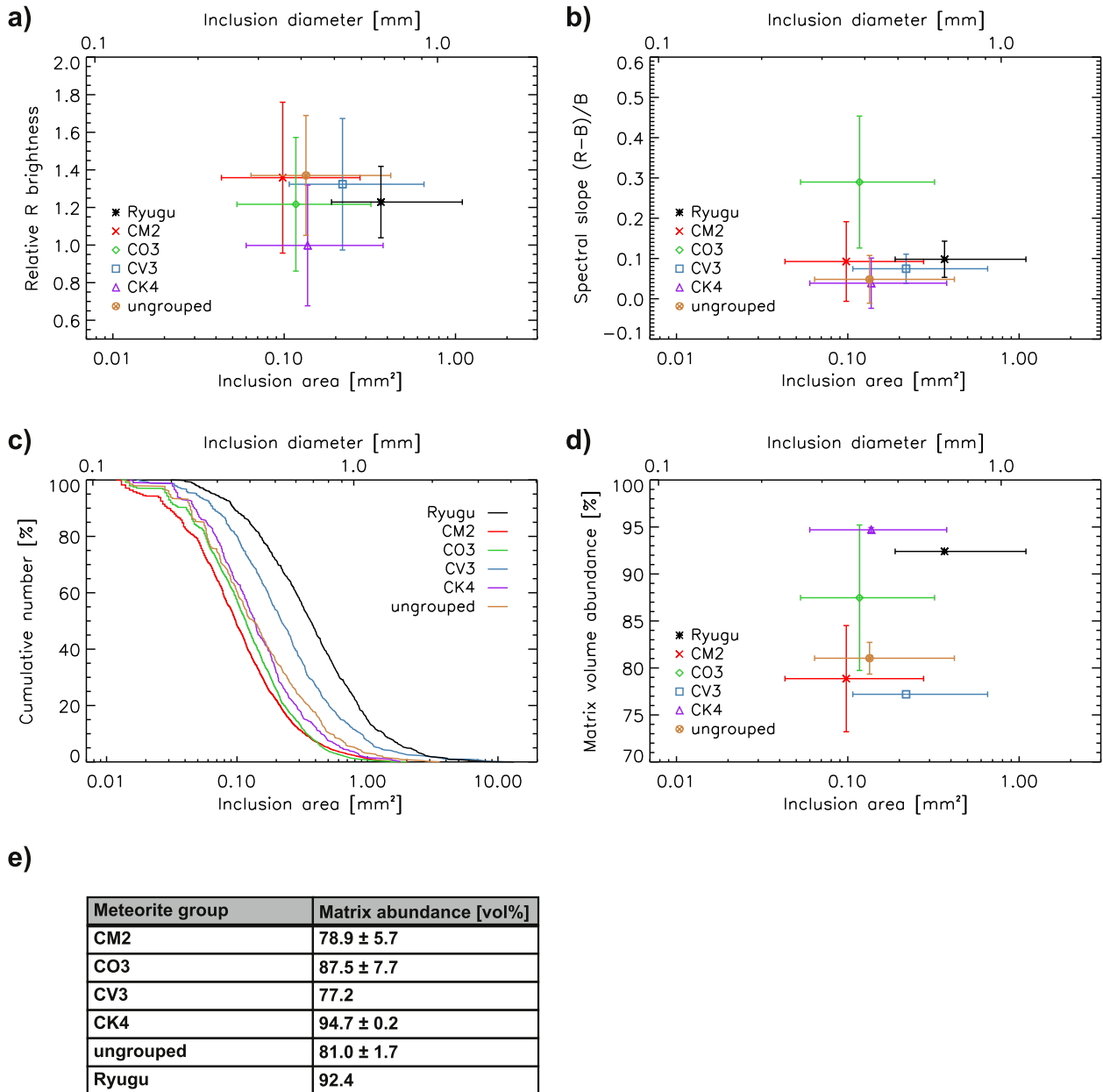
To illustrate the dependence of measuring technique on the derived chondrule and inclusion sizes, we consider the example of the Allende meteorite (CV3), which has been investigated in numerous studies (Friedrich et al. 2015) including those of Simon et al. (2018), who evaluated SEM images with a 3 μm pixel resolution, and Teitler et al. (2010), who picked chondrules from fines. Simon et al. (2018) report relatively small average particle sizes of 0.34 mm ± 0.48 mm, whereas Teitler et al. (2010) derive mean sizes of 0.92 mm ± 0.74 mm. This underlines the necessity of deriving meteorite inclusions with

MasCam’s QM for an adequate comparison with the inclusions found in the Ryugu rock.

Although absorption features of phyllosilicates, iron-rich oxides, and spinel are present in the wavelength covered by the QM and should be present in the carbonaceous chondrites imaged (e.g., Cloutis et al. 2011), the limited spectral range and resolution provided by our experiment unfortunately does not allow us to observe such features. Comparing the spectral slope and the relative brightness of the inclusions with previous investigations also proves difficult due to the lack of publications focusing on the spectral behavior of inclusions in carbonaceous chondrites in the visible range. Therefore, we cannot validate our observed relative brightness and overall red slope of the inclusions. However, the reflectance spectra of carbonaceous chondrite slabs including matrix as well as inclusions also generally possess a red slope in the visible due to the presence of iron oxyhydroxides (Trigo-Rodríguez et al. 2014).

## 5.2. Relation to Inclusions in Ryugu’s Rock

Meteorites are believed to be fragments that were ejected from asteroids via impacts or catastrophic disruptions. Ryugu is a rubble pile asteroid and formed as a result of a catastrophic disruption (Watanabe et al. 2019). So, rocks on Ryugu are probably similar in texture and composition to meteorites found on Earth. The surface of Ryugu appears free of dust (Jaumann et al. 2019), which allowed the imaging of bare rock textures comparable to those of meteorites on Earth. Thus, it is reasonable to analyze the inclusion size distribution as well as the color of inclusions of meteorites in the same manner as done by Schröder et al. (2021), who analyzed the rock and its inclusions imaged by MasCam on asteroid Ryugu (Figure 10). Figure 9 and the last row in Table 3 show their findings in comparison with the meteorites evaluated here. Note that the mapping of inclusions on Ryugu and the mapping of the meteorites was conducted by the same co-author (H.S.). Thus, systematic differences between Ryugu and the meteorites should be minimal. Our analysis of meteorite inclusions confirms the link between the rubble pile asteroid Ryugu’s

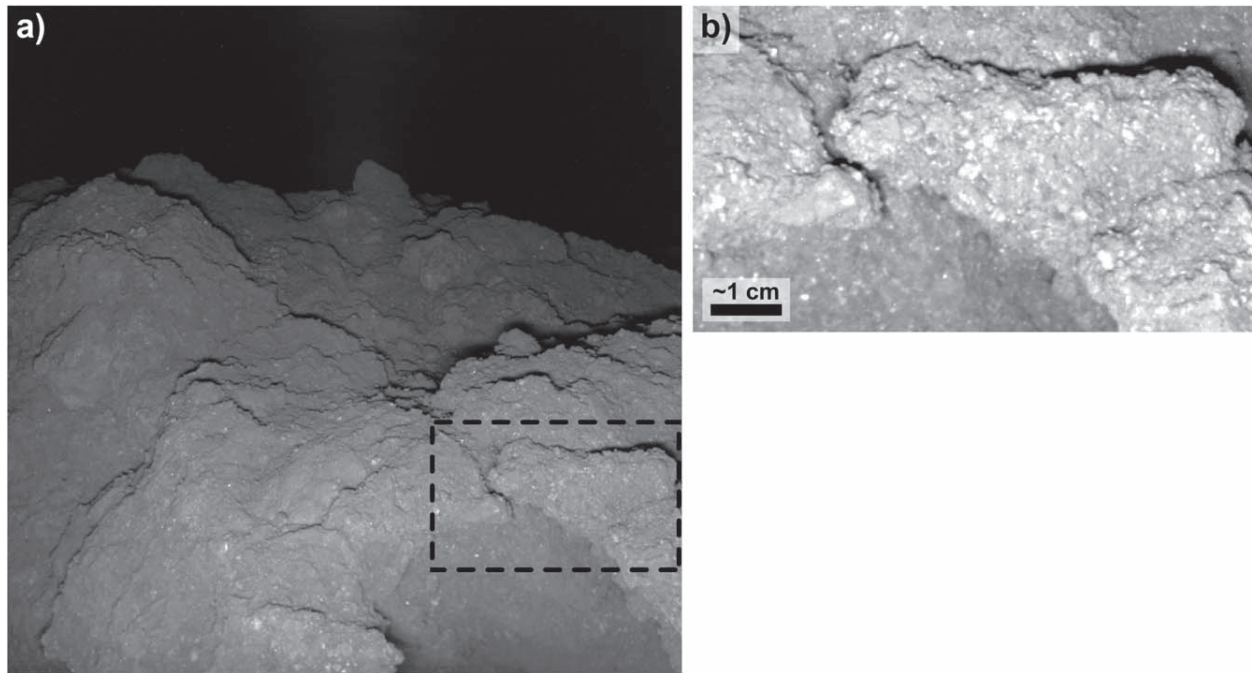


**Figure 9.** Relative brightness (a), spectral slope (b), and cumulative size distribution (c) of measurements combined in different carbonaceous chondrite groups in comparison with Ryugu. The median inclusion size and the 25th and 75th percentile are shown in (a), (b), and (c). (d) shows the dependence of the matrix volume abundance on the median inclusion size. Note that the values shown here are upper limits of the matrix volume abundance introduced by the spatial resolution limit of our method. (e) lists the values of (d). Measurements of fractured surfaces of meteorite falls are included.

rock and meteorites by finding generally comparable inclusion colors and size distributions.

Schröder et al. (2021) conclude that based on the inclusion size distribution, Ryugu appears similar to CV3 and CR2 groups as analyzed by King & King (1978). Based on the upper limit to the matrix abundance, the CM2s may be most representative for Ryugu. In agreement with Schröder et al. (2021), who could only base their analysis on a comparison with the data provided by King & King (1978), we also conclude that Ryugu’s rock’s inclusion size distribution best fits with the CV3 group, but the Ryugu rock is coarser than that of CV3s. The matrix volume abundances of the CK4 group and Ryugu are almost identical ( $94.7\% \pm 0.2\%$  and  $92.4\%$ , respectively). In contrast the matrix volume abundance of the CM2 group is comparatively small ( $78.9\% \pm 5.7\%$ ).

Generally, the relative brightness, as well as the spectral slope of the inclusions in the meteorites and the inclusions found on Ryugu, is similar, despite the terrestrial weathering, which may have reddened the inclusions (Rubin & Huber 2005). On the other hand, the inclusions found in the rock on Ryugu are likely to have experienced some degree of space weathering, including micrometeoroid bombardment, solar radiation, and thermal stresses (Jaumann et al. 2019; Otto et al. 2020). It is unlikely that meteorites possess any material that has been exposed to space weathering because their entry into Earth’s atmosphere would have removed or fused the outer layer of the meteorites that would have been exposed to space before the fall. Although space weathering also tends to darken and redden the spectra of the matrix and inclusions (Noble et al. 2001; Fiege et al. 2019),



**Figure 10.** The rock on Ryugu imaged by MasCam while illuminated with the red LED at night (a). The scene is approximately 25 cm across. (b) shows a contrast stretched zoom of the rock and its inclusions. The location of (b) is indicated by the box in (a).

the reddening due to terrestrial weathering appears to occur to a similar degree.

Sugita et al. (2019) and Kitazato et al. (2019) compared spectra of Ryugu in the visible wavelengths with meteorites partly overlapping with the meteorites considered in this work (e.g., Murchison, Allende, Orgueil). The spectra of Ryugu are taken from orbit and the meteorite spectra used in their work are taken from powders and thus do not allow inclusions and matrix to be distinguished as done in this work. However, they show that Ryugu's spectrum is generally darker and flatter than that of carbonaceous chondrites. The spectra of both inclusions and matrix of the meteorites we imaged follow the expected spectral behavior of carbonaceous chondrites in the visible wavelengths and possess a slightly reddish slope (see Figure 11 in the Appendix).

Considering the four parameters derived in this work (relative brightness, spectral slope, inclusion size distribution, and matrix volume abundance), Ryugu is most similar to a different group for every parameter, e.g., the mean brightness of the CO3s, the mean spectral slope of the CM2s, the median grain size of the CV3s, and the matrix abundance of the CK4s is most similar to Ryugu's values of these parameters. The most prominent difference between the inclusions in the rock on Ryugu and those in the meteorites are the presence of comparatively large inclusions on Ryugu (Table 4).

The spectral parameters of the inclusions of Ryugu's rock (relative brightness, spectral slope), as well as the matrix volume abundance, fit well within the total parameter space of the carbonaceous chondrites imaged in this work (Figure 9), with the exception that Ryugu's rock appears to have larger inclusions. For the inclusion size analysis on Ryugu, a three-dimensional shape model was used (Scholten et al. 2019). In Sections 4.1 and 4.2, we showed that not knowing the exact distance of our samples to the camera and their three-dimensional shape can introduce errors in the size frequency distribution, which could be minimized for the

Ryugu analysis for which a shape model was available. Thus, our analysis of individual meteorites is more prone to errors and may increase or reduce the similarity to Ryugu's inclusion size distribution. The averaged inclusion size distributions of the meteorite groups (Figure 9(c)) should balance these distortion effects, but it is still not possible to attribute Ryugu's rock to one of the meteorite groups based on the presented parameters alone given that the groups themselves overlap significantly within the parameter space. A more sophisticated chemical analysis, which will be possible upon the collected sample return by Hayabusa2, will be necessary to find the best match. It is also possible that the Ryugu rock is not represented in the meteorite collections, because it would have not survived the entry through Earth's atmosphere due to its low intrinsic tensile strength (Grott et al. 2019).

## 6. Summary and Conclusions

In order to interpret and relate in situ images of a rock showing bright inclusions on asteroid Ryugu, we imaged a set of carbonaceous chondrites from the CM2, CO3, CV3, and CK4 groups using the QM of MasCam, the camera on board MASCOT. We also imaged a C11 (Orgueil) but excluded it from our analysis due to terrestrial weathering giving false impressions of inclusions. Using the same method used for images taken on Ryugu, we imaged the meteorite samples illuminated by colored camera LEDs (blue, green, red, and infrared) and mapped bright inclusions in a color composite image of the blue, green, and red images. We then evaluated the inclusion size distribution, the relative brightness of the inclusions against the matrix in the red image, the inclusion spectral slope  $((R - B)/B)$ , and the matrix volume abundance.

First, we investigated the influence of the laboratory conditions on the parameters of interest by imaging cut as well as fractured surfaces and different sides of the same meteorite. We found that the variations between the two types of surfaces are on the same order as the fluctuations between

different sides of the same meteorite. The derived inclusion size distribution is the most sensitive parameter and can vary significantly, indicating that the distortion introduced by the camera needs to be compensated by knowledge of the exact shape of the samples imaged. This was not available for the meteorites but has been derived for the MASCOT's landing site on Ryugu (Scholten et al. 2019).

The influence of terrestrial weathering on the spectral properties of the inclusions is not evident as a systematic variation with age.

Considering only fractured surfaces, we find that all meteorite groups overlap within their relative inclusion brightness, spectral slope, inclusion sizes, and matrix volume abundance. The most significant deviations from the average spectral slope can be observed for the CO3 group including Lancé with the largest spectral slope. The relative inclusion brightness of the CK4 group and two CO3s (Ormans and Warrenton) is lower than the average. The CV3 group, represented by Allende in our work, shows the largest inclusion sizes and largest matrix abundance.

Our analysis results in consistently larger inclusion sizes compared to previous investigations. With the exception of the CM2 group, our analysis also shows a higher matrix volume abundance, which is likely caused by our simple definition of matrix as the parts of the meteorite that are not an inclusion.

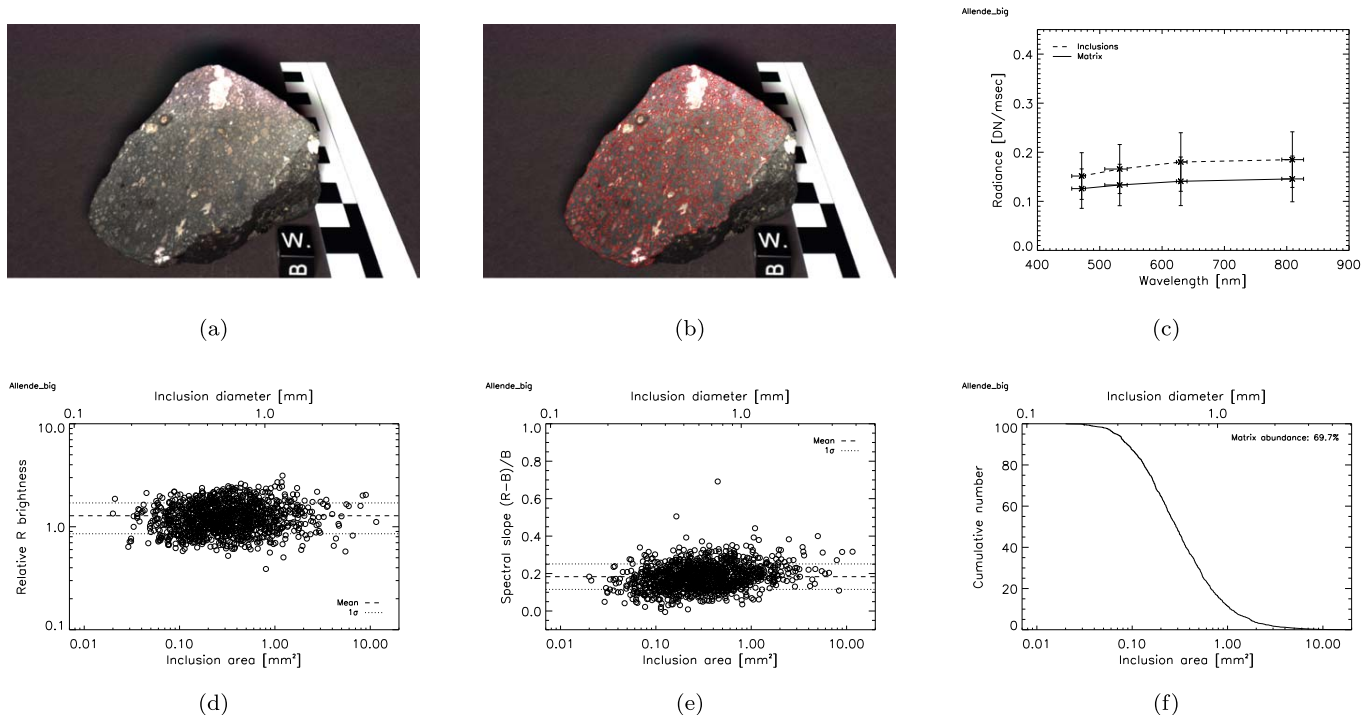
In conclusion, the parameters derived in this work, which are limited by the spectral resolution of the LEDs on MasCam and its QM, cannot be used alone to distinguish between different

meteorite groups. But it is possible to identify individual meteorites with prominent parameters. Comparing our results to the rock on Ryugu imaged by MasCam thus allows us to predict that the inclusions in Ryugu's rock are probably larger compared to those known from the carbonaceous chondrites imaged in this work. The rock's matrix abundance, relative inclusion brightness, and spectral slope fit well within the parameter space of the carbonaceous chondrites.

We thank the Hayabusa2 and MASCOT teams and the Natural History Museum Berlin for making this work possible. We also thank D. Takir and the anonymous reviewer for their insightful comments and suggestions. K.A.O. and T.M. gratefully acknowledge the financial support and endorsement from the German Aerospace Center (DLR) Management Board Young Research Group Leader Program and the Executive Board Member for Space Research and Technology.

## Appendix

This appendix contains a figure set for all 22 meteorites imaged in this work (Figure 11). Each figure in the set has six panels that show the plain and mapped images, the average matrix and inclusion spectrum, the relative R brightness of individual inclusions, the relative spectral slope of individual inclusions, and the cumulative size distribution of the inclusions.






**Figure 11.** Supplemental figure images of the Allende (big) meteorite. The panels show a plain QM image (a) and a QM image with mapped inclusions (b), the average matrix and inclusion spectrum (c), the relative R brightness of individual inclusions (d), the relative spectral slope of individual inclusions (e), and the cumulative inclusion size distribution (f). Dashed and dotted lines in (d) and (e) indicate the mean and  $1\sigma$  standard deviation.

(The complete figure set (22 images) is available.)



## ORCID iDs

K. A. Otto  <https://orcid.org/0000-0002-0675-1177>  
 S. E. Schröder  <https://orcid.org/0000-0003-0323-8324>  
 A. Greshake  <https://orcid.org/0000-0001-6475-9751>  
 N. Schmitz  <https://orcid.org/0000-0001-6481-6189>  
 F. Trauthan  <https://orcid.org/0000-0001-6563-4758>  
 K. Stephan  <https://orcid.org/0000-0003-1009-0145>  
 T.-M. Ho  <https://orcid.org/0000-0003-3378-3227>  
 R. Jaumann  <https://orcid.org/0000-0002-9759-6597>  
 A. Koncz  <https://orcid.org/0000-0001-8231-1109>  
 T. Michalik  <https://orcid.org/0000-0002-9556-1737>  
 H. Yabuta  <https://orcid.org/0000-0002-4625-5362>

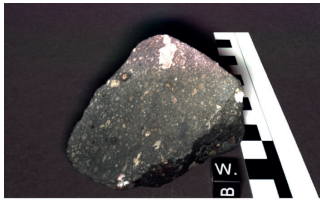
## References

- Bibring, J.-P., Hamm, V., Langevin, Y., et al. 2017, *SSRv*, **208**, 401  
 Bland, P. A., Zolensky, M. E., Benedix, G. K., & Sephton, M. A. 2006, in *Meteorites and the Early Solar System II*, ed. D. S. Lauretta & H. Y. McSween (2nd ed.; Tucson, AZ: Univ. of Arizona Press), 853  
 Brearley, A. J., & Jones, H. J. 1998, in *Planetary Materials*, ed. J. J. Papike (36th ed.; Washington, D C: Mineralogical Society of America), 3  
 Clark, B. E., Ockert-Bell, M. E., Cloutis, E. A., et al. 2009, *Icar*, **202**, 119  
 Cloutis, E. A., Hiroi, T., Gaffey, M. J., Alexander, C. M. O., & Mann, P. 2011, *Icar*, **212**, 180  
 Cloutis, E. A., Hudon, P., & Gaffey, M. J. 2012, *Icar*, **221**, 911  
 Cloutis, E. A., Hudon, P., Hiroi, T., et al. 2012b, *Icar*, **221**, 328  
 Cloutis, E. A., Hudon, P., Hiroi, T., Gaffey, M. J., & Mann, P. 2012a, *Icar*, **220**, 466  
 Cloutis, E. M., Hudon, P., Hiroi, T., Gaffey, M. J., & Mann, P. 2011, *Icar*, **216**, 309  
 Dufresne, E. R., & Anders, E. 1962, *GeCoA*, **26**, 1085  
 Ebel, D. S., Brunner, C., Konrad, K., et al. 2016, *GeCoA*, **172**, 322  
 Fiege, K., Guglielmino, M., Altobelli, N., et al. 2019, *JGRE*, **124**, 1084  
 Friedrich, J. M., Weisberg, M. K., Ebel, D. S., et al. 2015, *ChEG*, **75**, 419  
 Gounelle, M., & Zolensky, M. E. 2001, *M&PS*, **36**, 1321  
 Greenwood, R. C., Burbine, T. H., & Franchi, I. A. 2020, *GeCoA*, **277**, 377  
 Greshake, A., & Fritz, J. 2018, in *Planetary Geology*, ed. A. P. Rossi & S. van Gasselt (Cham: Springer), 103  
 Grott, M., Knollenberg, J., Borgs, B., et al. 2017, *SSRv*, **208**, 413  
 Grott, M., Knollenberg, J., Hamm, M., et al. 2019, *NatAs*, **3**, 971  
 Herčík, D., Auster, H.-U., Blum, J., et al. 2017, *SSRv*, **208**, 433  
 Hercik, D., Auster, H.-U., Constantinescu, D., et al. 2020, *JGRE*, **125**, e06035  
 Ho, T.-M., Baturkin, V., Grimm, C., et al. 2017, *SSRv*, **208**, 339  
 Jaumann, R., Schmitz, N., Ho, T.-M., et al. 2019, *Sci*, **365**, 817  
 Jaumann, R., Schmitz, N., Koncz, A., et al. 2017, *SSRv*, **208**, 375  
 Keller, L. P., & Buseck, P. R. 1990, *GeCoA*, **54**, 1155  
 King, T. V. V., & King, E. A. 1978, *Metic*, **13**, 47  
 Kitazato, K., Milliken, R. E., Iwata, T., et al. 2019, *Sci*, **364**, 272  
 May, C., Russell, S. S., & Grady, M. M. 1999, *LPSC*, **30**, 1688  
 Noble, S. K., Pieters, C. M., Taylor, L. A., et al. 2001, *M&PS*, **36**, 31  
 Otto, K. A., Matz, K.-D., Schröder, S. E., et al. 2020, *MNRAS*, **500**, 3178  
 Royet, J.-P. 1991, *Progress in Neurobiology*, **37**, 433  
 Rubin, A. E., & Huber, H. 2005, *M&PS*, **40**, 1123  
 Rubin, A. E., & Wasson, J. T. 1986, *GeCoA*, **50**, 307  
 Salisbury, J. W., & Hunt, G. R. 1974, *JGR*, **79**, 4439  
 Scholten, F., Preusker, F., Elgner, S., et al. 2019, *A&A*, **632**, L1  
 Schröder, S., Otto, K., Scharf, H., et al. 2021, *PSJ*, **2**, 58  
 Scott, E. R. D., & Krot, A. N. 2014, *Treatise on Geochemistry* (Amsterdam: Elsevier), 65  
 Sephton, M. A., Bland, P. A., Pillinger, C. T., & Gilmour, I. 2004, *M&PS*, **39**, 747  
 Simon, J. I., Cuzzi, J. N., McCain, K. A., et al. 2018, *E&PSL*, **494**, 69  
 Sugita, S., Honda, R., Morota, T., et al. 2019, *Sci*, **364**, eaaw0422  
 Teitler, S. A., Paque, J. M., Cuzzi, J. N., & Hogan, R. C. 2010, *M&PS*, **45**, 1124  
 Trigo-Rodríguez, J. M., Moyano-Camero, C. E., Llorca, J., et al. 2014, *MNRAS*, **437**, 227  
 Tsuda, Y., Saiki, T., Terui, F., et al. 2020, *AcAau*, **171**, 42  
 Wada, K., Grott, M., Michel, P., et al. 2018, *PEPS*, **5**, 82  
 Watanabe, S., Hirabayashi, M., Hirata, N., et al. 2019, *Sci*, **364**, 268  
 Yoshimitsu, T., Kubota, T., Tomiki, A., Otsuki, M., & Yoshikawa, K. 2017, *Readiness of Proximity Operation on Minerva-II Rovers Onboard Hayabusa2 Asteroid Explorer*. IEICE Technical Report 117. 321, [https://robotics.estec.esa.int/i-SAIRAS/isairas2018/Papers/Session%202b/1\\_paper\\_submit-6-27-Yoshimitsu-Tetsuo.pdf](https://robotics.estec.esa.int/i-SAIRAS/isairas2018/Papers/Session%202b/1_paper_submit-6-27-Yoshimitsu-Tetsuo.pdf)

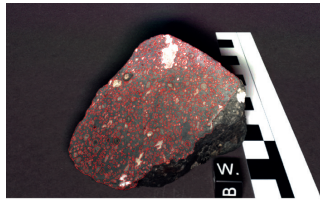
Meteorite name	Petrographic type	Meteorite mass [g]	Analysis area [cm <sup>2</sup> ]	Surface structure	Camera meteorite distance [cm]	Camera height [cm]	Exposure time red [ms]	Exposure time green [ms]	Exposure time blue [ms]	Exposure time IR [ms]
Allende big	CV3	219.2	22.3	cut	15.9	10.1	700	800	1100	1500
Allende small	CV3	79.2	1.3	fractured	16.2	9.6	500	500	700	900
Colony	CO3	3.1	1.7	cut	15.2	8.5	700	900	1500	1500
El-Quss	CM2	4.5	3.2	cut	13.4	7.5	700	700	1100	1600
Karoonda side 1	CK4	15.5	7.9	fractured	15.6	9.4	550	550	800	1000
Karoonda side 2	CK4	15.5	6.0	fractured	16.7	9.4	800	800	1200	1600
Lancé side 1	CO3	62.2	10.3	fractured	15.1	9.6	500	500	700	1100
Lancé side 2	CO3	62.2	6.4	fractured	15.1	9.6	550	550	800	1200
Mighei side 1	CM2	18.5	6.5	fractured	14.6	8.9	300	300	400	600
Mighei side 2	CM2	18.5	4.7	cut	14.7	8.9	800	800	1000	1400
Murchison big tilt 1	CM2	118.0	9.8	fractured	15.8	9.6	400	300	450	900
Murchison big tilt 2	CM2	118.0	7.6	fractured	15.8	9.6	700	700	1000	1300
Murchison slap	CM2	35.4	17.6	cut	16.1	9.6	700	700	1200	1500
Murchison small	CM2	11.2	6.2	fractured	14.1	8.0	600	600	900	1200
Murray	CM2	6.7	1.4	fractured	14.3	7.5	600	600	800	1200
Ningqiang side 1	C3-ungrouped	9.0	3.2	fractured	15.0	8.5	500	450	600	800
Ningqiang side 2	C3-ungrouped	9.0	3.2	fractured	15.0	8.5	600	550	800	1100
Nogoya	CM2	1.3	1.1	fractured	14.3	7.5	800	800	1200	1400
NWA 11118 side 1	CM2	1.8	2.0	fractured	14.1	7.8	700	700	1000	1400
NWA 11118 side 2	CM2	1.8	1.3	fractured	14.1	7.8	1300	1500	2300	2500
Ornans	CO3	8.0	5.0	fractured	17.7	8.5	700	700	1100	1500
Warrenton	CO3	5.7	2.6	fractured	18.0	8.5	700	700	1000	1300

### Allende big

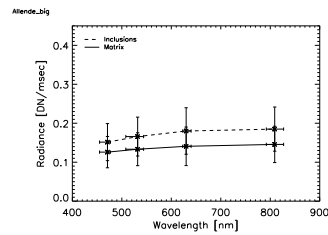
QM Image



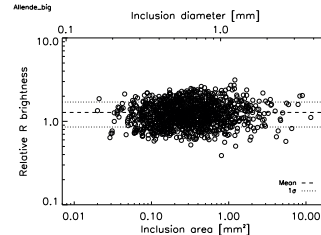
QM Image with Mapped Inclusions



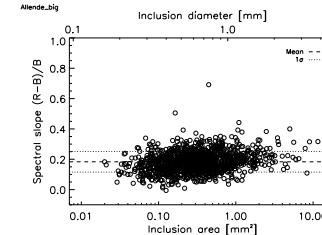
Matrix and Inclusion Spectrum



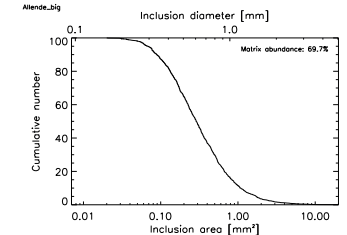
Relative R Brightness



Relative Spectral Slope (R-B)/B

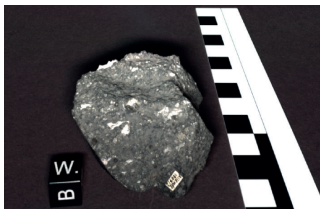


Cumulative Size Distribution

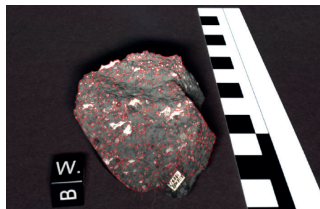


### Allende small

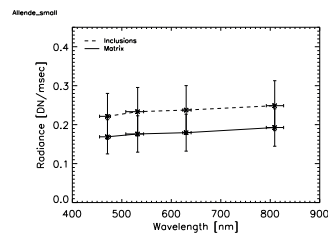
QM Image



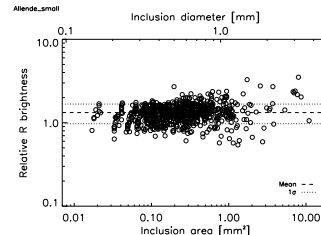
QM Image with Mapped Inclusions



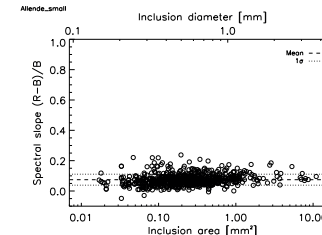
Matrix and Inclusion Spectrum



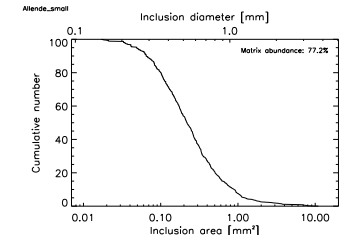
Relative R Brightness



Relative Spectral Slope (R-B)/B

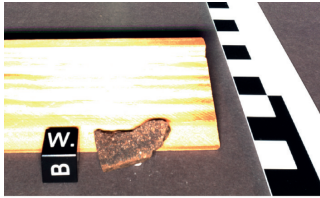


Cumulative Size Distribution

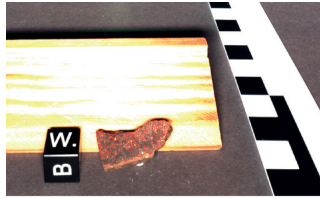


## Colony

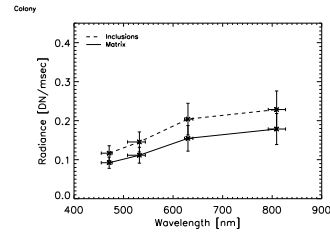
QM Image



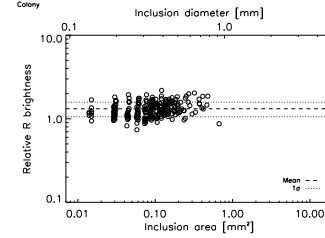
QM Image with Mapped Inclusions



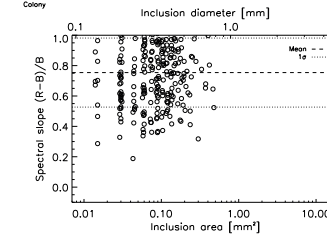
Matrix and Inclusion Spectrum



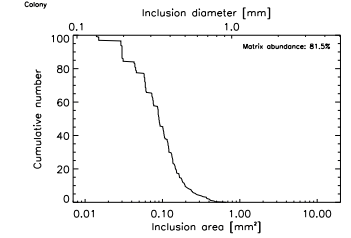
Relative R Brightness



Relative Spectral Slope (R-B)/B

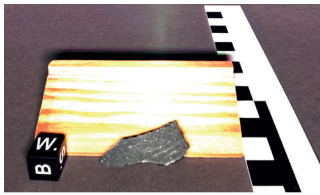


Cumulative Size Distribution

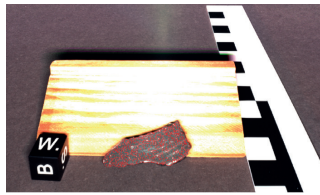


## EI-Quss

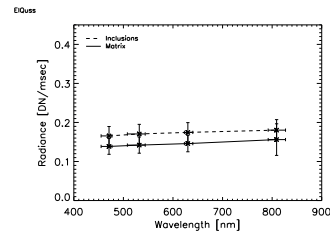
QM Image



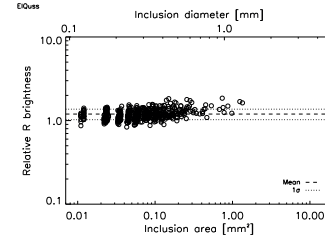
QM Image with Mapped Inclusions



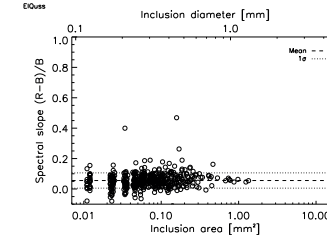
Matrix and Inclusion Spectrum



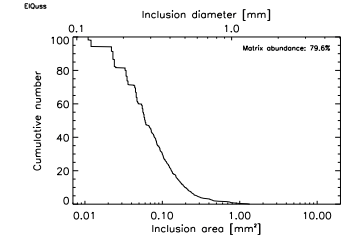
Relative R Brightness



Relative Spectral Slope (R-B)/B

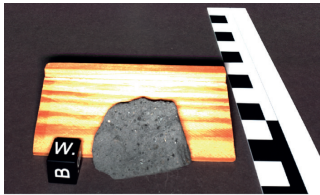


Cumulative Size Distribution

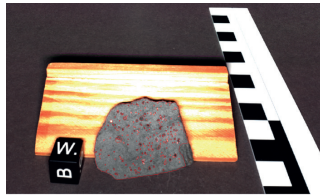


## Karoonda side 1

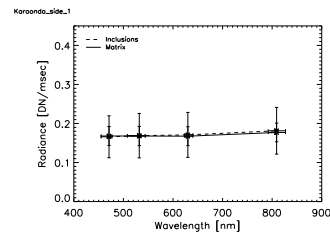
QM Image



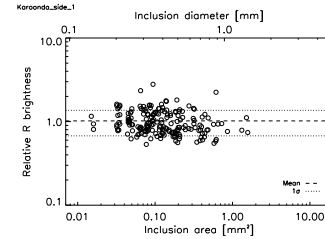
QM Image with Mapped Inclusions



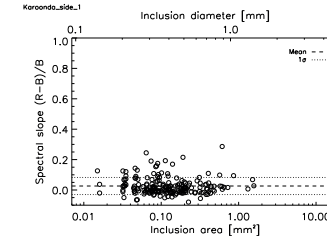
Matrix and Inclusion Spectrum



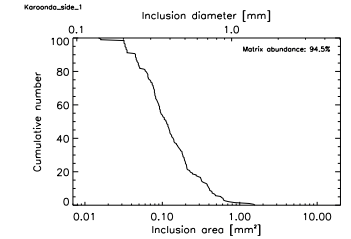
Relative R Brightness



Relative Spectral Slope (R-B)/B

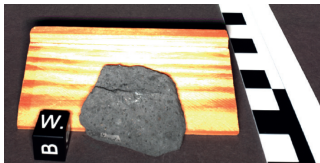


Cumulative Size Distribution

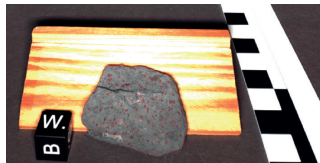


## Karoonda side 2

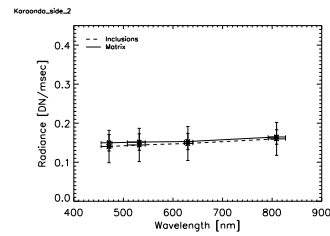
QM Image



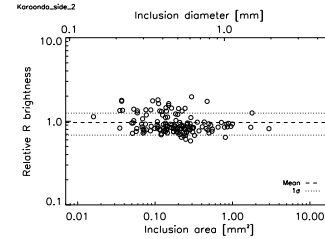
QM Image with Mapped Inclusions



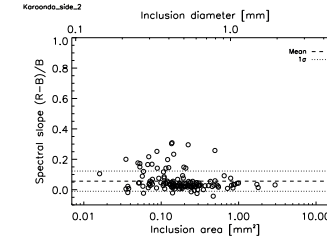
Matrix and Inclusion Spectrum



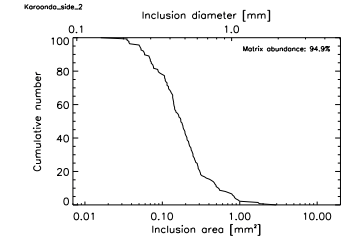
Relative R Brightness



Relative Spectral Slope (R-B)/B

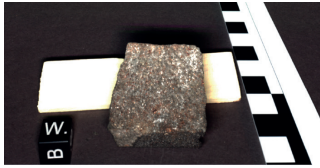


Cumulative Size Distribution

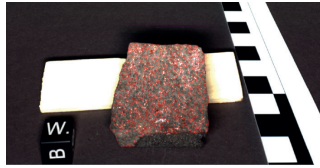


### Lancé side 1

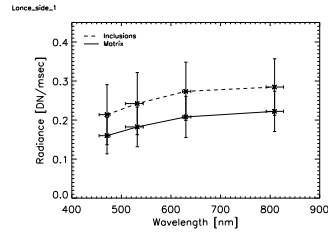
QM Image



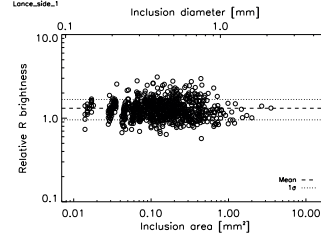
QM Image with Mapped Inclusions



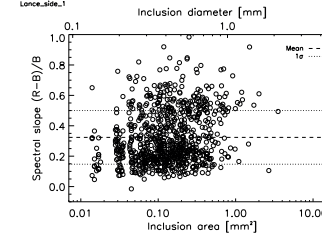
Matrix and Inclusion Spectrum



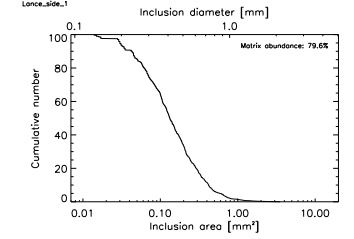
Relative R Brightness



Relative Spectral Slope (R-B)/B

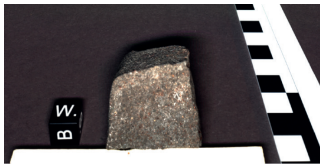


Cumulative Size Distribution

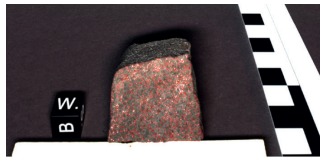


### Lancé side 2

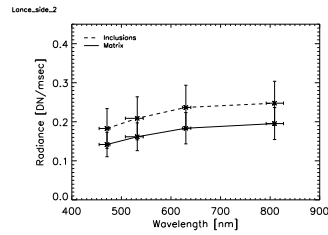
QM Image



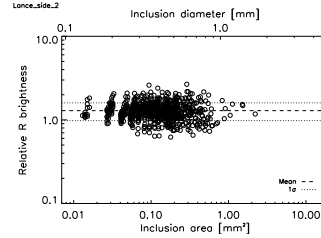
QM Image with Mapped Inclusions



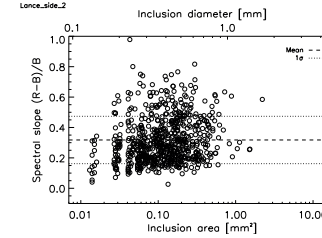
Matrix and Inclusion Spectrum



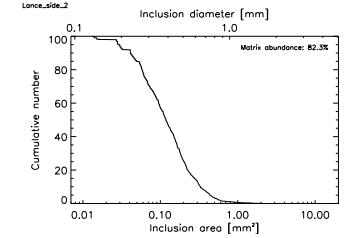
Relative R Brightness



Relative Spectral Slope (R-B)/B

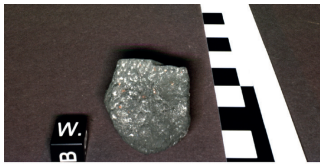


Cumulative Size Distribution

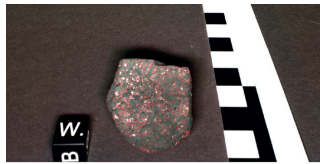


### Mighei side 1

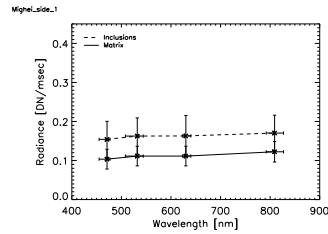
QM Image



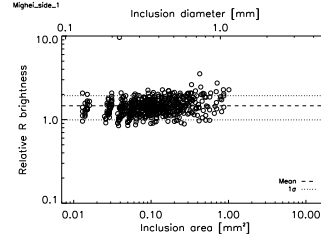
QM Image with Mapped Inclusions



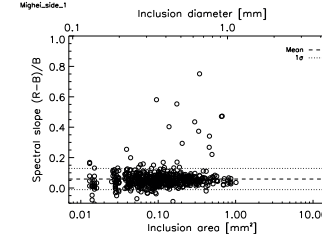
Matrix and Inclusion Spectrum



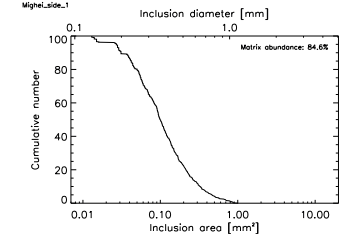
Relative R Brightness



Relative Spectral Slope (R-B)/B

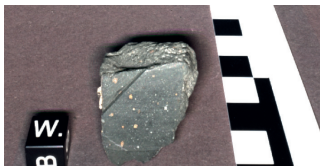


Cumulative Size Distribution

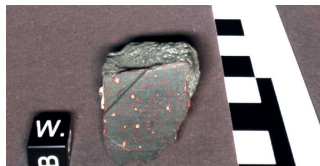


### Mighei side 2

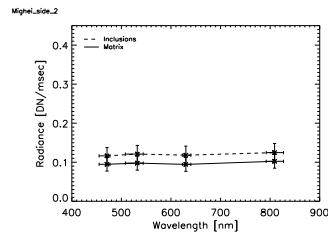
QM Image



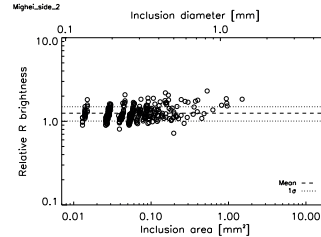
QM Image with Mapped Inclusions



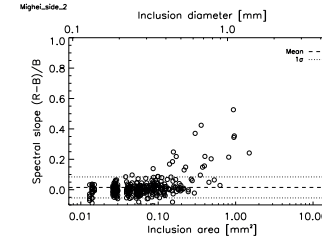
Matrix and Inclusion Spectrum



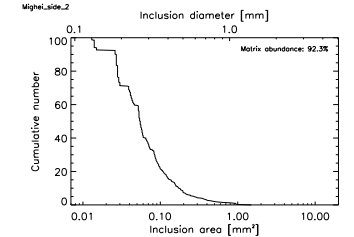
Relative R Brightness



Relative Spectral Slope (R-B)/B



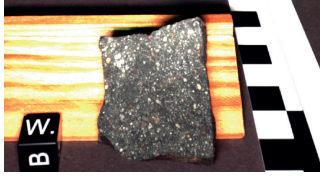
Cumulative Size Distribution



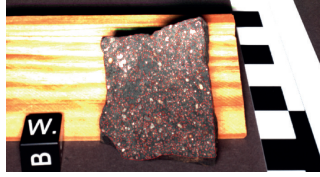


## Murchison big tilt 1

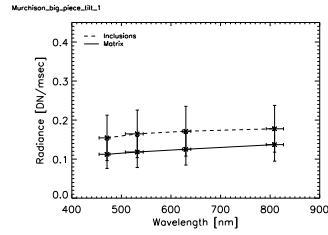
QM Image



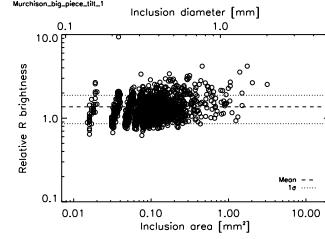
QM Image with Mapped Inclusions



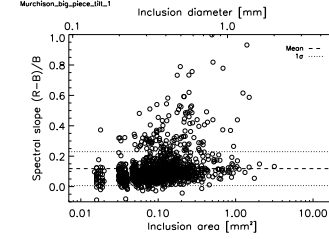
Matrix and Inclusion Spectrum



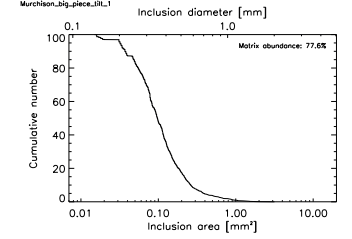
Relative R Brightness



Relative Spectral Slope (R-B)/B

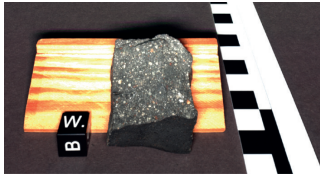


Cumulative Size Distribution

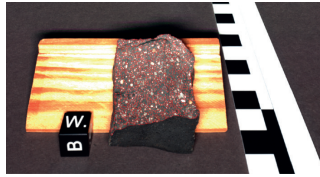


## Murchison big tilt 2

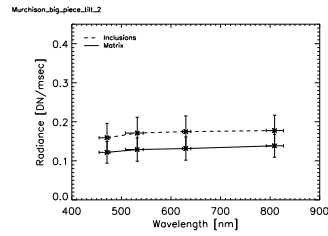
QM Image



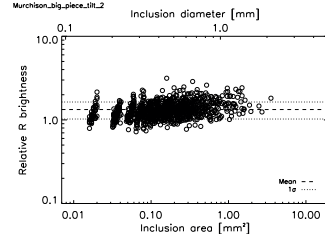
QM Image with Mapped Inclusions



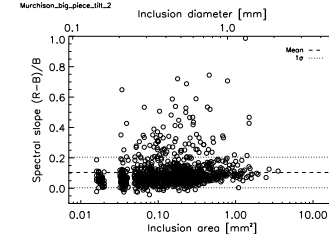
Matrix and Inclusion Spectrum



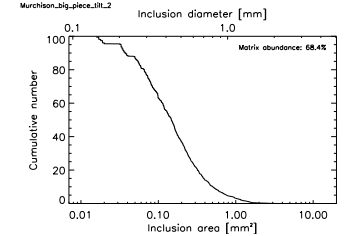
Relative R Brightness



Relative Spectral Slope (R-B)/B

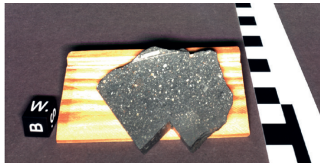


Cumulative Size Distribution

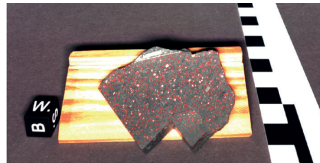


## Murchison slap

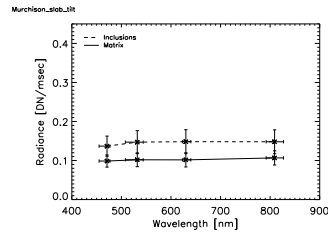
QM Image



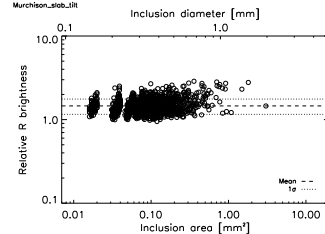
QM Image with Mapped Inclusions



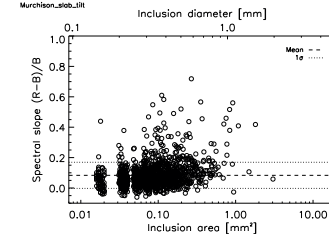
Matrix and Inclusion Spectrum



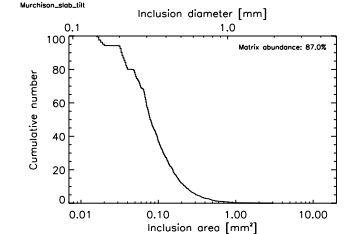
Relative R Brightness



Relative Spectral Slope (R-B)/B

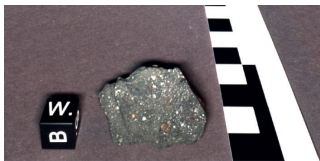


Cumulative Size Distribution

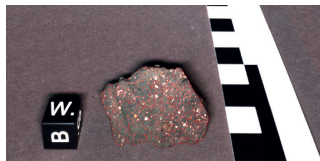


## Murchison small

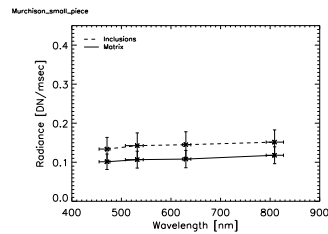
QM Image



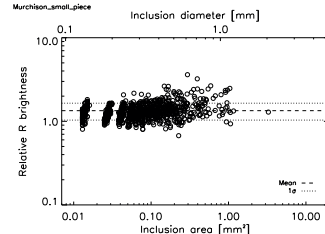
QM Image with Mapped Inclusions



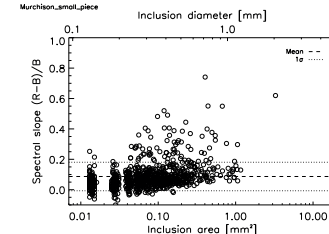
Matrix and Inclusion Spectrum



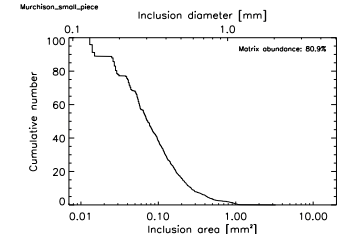
Relative R Brightness



Relative Spectral Slope (R-B)/B

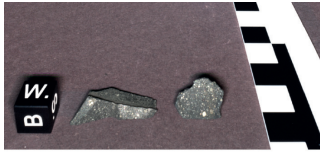


Cumulative Size Distribution

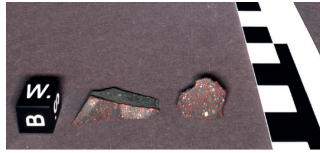


## Murray

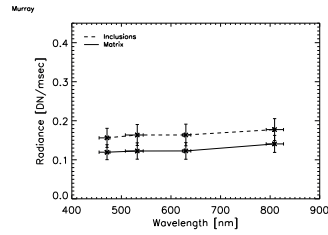
QM Image



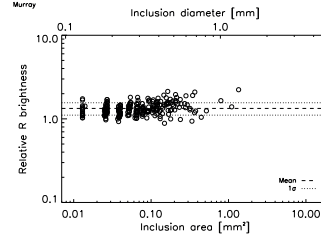
QM Image with Mapped Inclusions



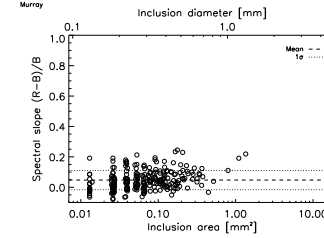
Matrix and Inclusion Spectrum



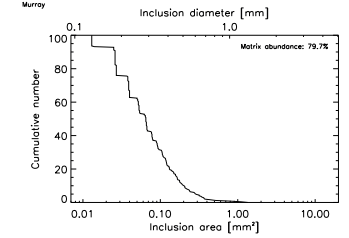
Relative R Brightness



Relative Spectral Slope (R-B)/B

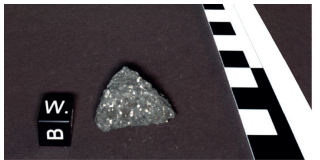


Cumulative Size Distribution

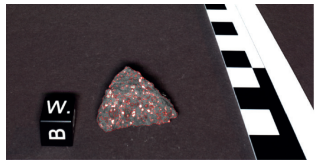


## Ningqiang side 1

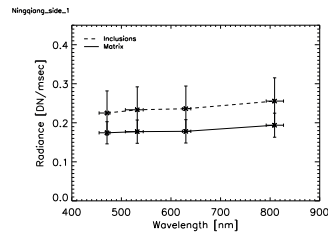
QM Image



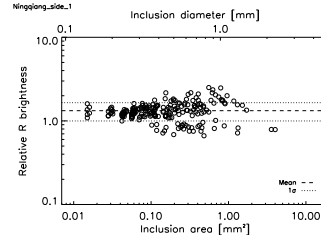
QM Image with Mapped Inclusions



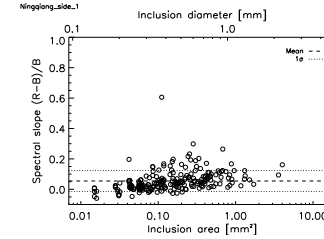
Matrix and Inclusion Spectrum



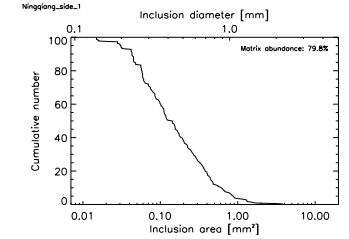
Relative R Brightness



Relative Spectral Slope (R-B)/B

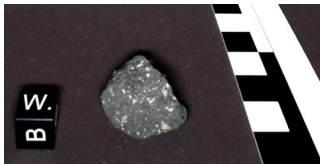


Cumulative Size Distribution

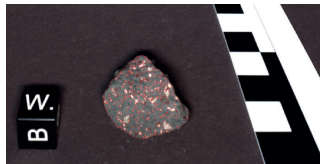


## Ningqiang side 2

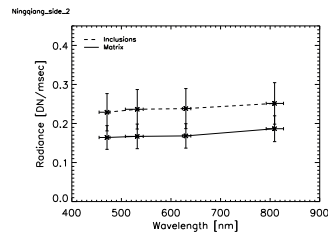
QM Image



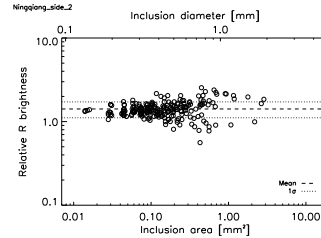
QM Image with Mapped Inclusions



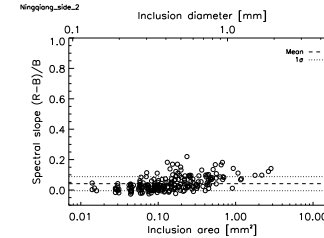
Matrix and Inclusion Spectrum



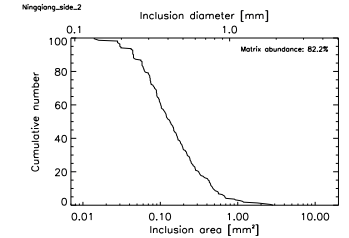
Relative R Brightness



Relative Spectral Slope (R-B)/B

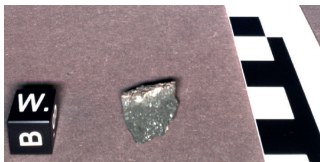


Cumulative Size Distribution

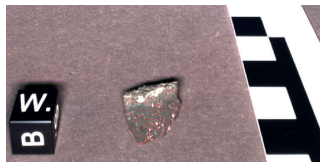


## Nogoya

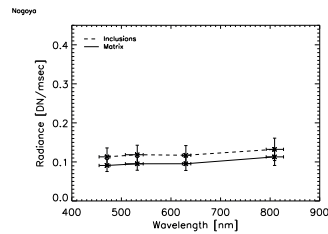
QM Image



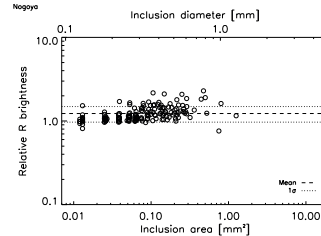
QM Image with Mapped Inclusions



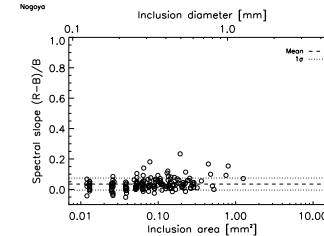
Matrix and Inclusion Spectrum



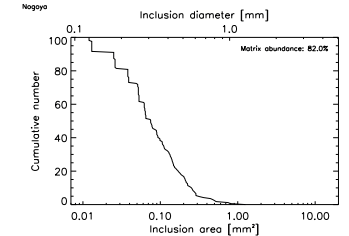
Relative R Brightness



Relative Spectral Slope (R-B)/B

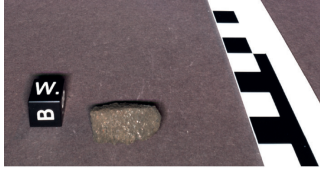


Cumulative Size Distribution

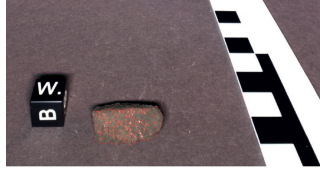


## NWA 11118 side 1

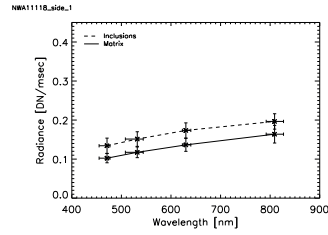
QM Image



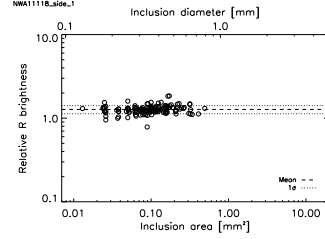
QM Image with Mapped Inclusions



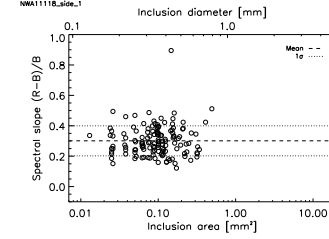
Matrix and Inclusion Spectrum



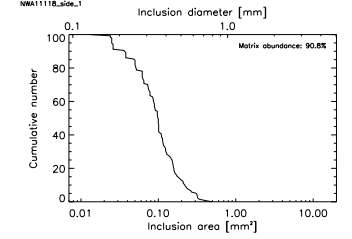
Relative R Brightness



Relative Spectral Slope (R-B)/B

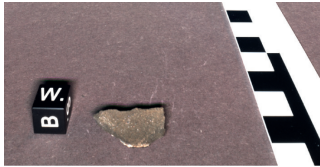


Cumulative Size Distribution

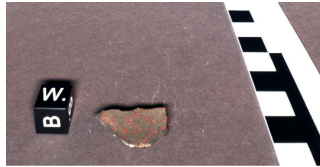


## NWA 11118 side 2

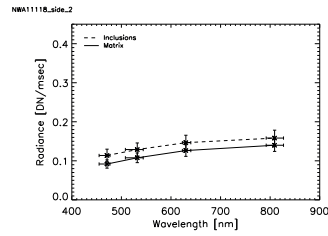
QM Image



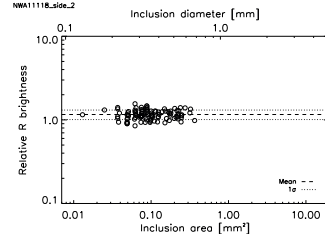
QM Image with Mapped Inclusions



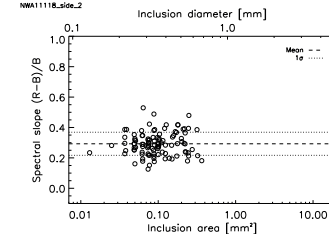
Matrix and Inclusion Spectrum



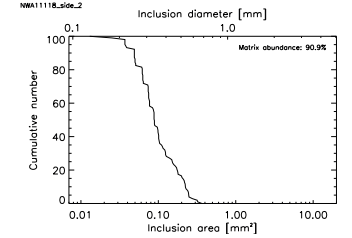
Relative R Brightness



Relative Spectral Slope (R-B)/B

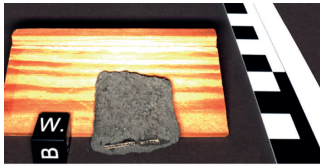


Cumulative Size Distribution

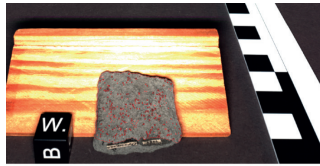


## Ornans

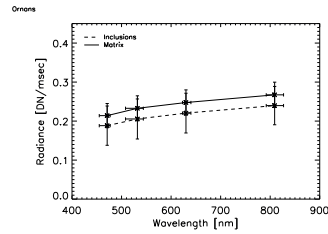
QM Image



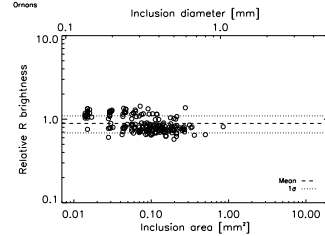
QM Image with Mapped Inclusions



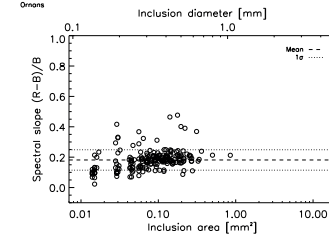
Matrix and Inclusion Spectrum



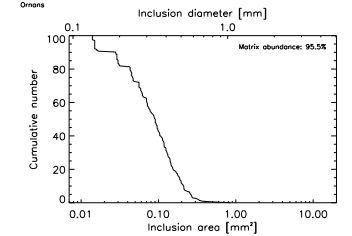
Relative R Brightness



Relative Spectral Slope (R-B)/B

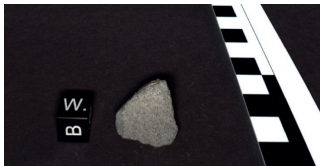


Cumulative Size Distribution

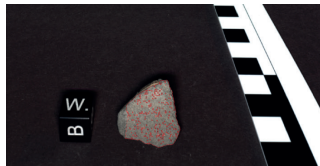


## Warrenton

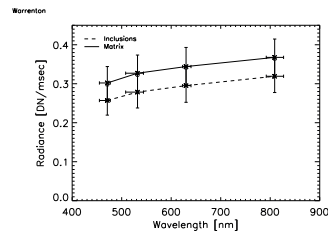
QM Image



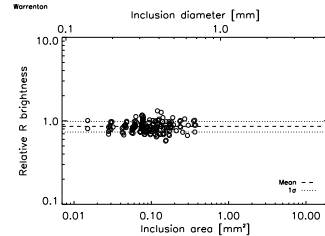
QM Image with Mapped Inclusions



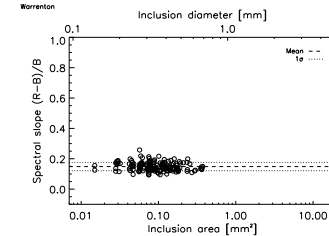
Matrix and Inclusion Spectrum



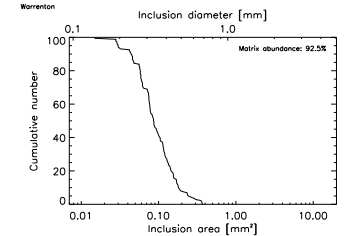
Relative R Brightness



Relative Spectral Slope (R-B)/B



Cumulative Size Distribution



### 2.1.3 Otto et al. (2019)

Otto, K. A., Marchi, S., Trowbridge, A., Melosh, H. J., & Sizemore, H. G. (2019). Ceres Crater Degradation Inferred from Concentric Fracturing. *Journal of Geophysical Research: Planets*, *124*(0), 1–16. <https://doi.org/10.1029/2018JE005660>.

I lead the research summarised in this article and wrote the manuscript. I conducted the geologic analysis by identifying, mapping and measuring concentric fractures around some craters on Ceres. I derived the morphologic measurables (e.g. fracture distance from the crater rim, fracture length and width, crater depth and diameter) used to compare with numerical modeling performed by A. Trowbridge using finite element modeling. I evaluated the combined modelling and mapping results. H. J. Melosh helped with the interpretation of the modelled stresses shown in Figure 9. All authors contributed to the discussion of the results.

## Key Points:

- We analyzed craters on Ceres with concentric fracturing
- We model the relaxation of a low-viscosity subsurface layer to explain the observed fracturing
- The degradation of craters on Ceres may locally be influenced by low-viscosity material in the subsurface

## Supporting Information:

- Supporting Information S1
- Data Set S1
- Data Set S2
- Data Set S3
- Data Set S4
- Data Set S5

## Correspondence to:

K. A. Otto,  
katharina.otto@dlr.de

## Citation:

Otto, K. A., Marchi, S., Trowbridge, A., Melosh, H. J., & Sizemore, H. G. (2019). Ceres Crater degradation inferred from concentric fracturing. *Journal of Geophysical Research: Planets*, 124, 1188–1203. <https://doi.org/10.1029/2018JE005660>

Received 26 APR 2018

Accepted 18 MAR 2019

Accepted article online 26 MAR 2019

Published online 6 MAY 2019

©2019. The Authors.

This is an open access article under the terms of the Creative Commons Attribution-NonCommercial-NoDerivs License, which permits use and distribution in any medium, provided the original work is properly cited, the use is non-commercial and no modifications or adaptations are made.

## Ceres Crater Degradation Inferred From Concentric Fracturing

K. A. Otto<sup>1</sup>, S. Marchi<sup>2</sup>, A. Trowbridge<sup>3</sup>, H. J. Melosh<sup>3</sup>, and H. G. Sizemore<sup>4</sup>

<sup>1</sup>Institute of Planetary Research, German Aerospace Center, Berlin, Germany, <sup>2</sup>Southwest Research Institute, Boulder, CO, USA, <sup>3</sup>Department of Earth, Atmospheric and Planetary Science, Purdue University, Lafayette, IN, USA, <sup>4</sup>Planetary Science Institute, Tucson, Arizona, USA

**Abstract** The dwarf planet Ceres exhibits a collection of craters that possess concentric fractures beyond the crater rim. These fractures typically range from a few hundred meters to a few kilometers in length and are less than 300 m wide. They occur preferentially on elevated regions around the crater and are located less than a crater radius beyond the rim. In total there are 17 craters exhibiting concentric fracturing beyond the rim. They are located in the midlatitudes. The craters' diameters range between 20 and 270 km. We investigate the concentric fractures of three craters (Azacca, Ikapati, and Occator) in detail and suggest that the formation of such concentric fractures can be explained by a shallow (<10-km) low-viscosity ( $\sim 10^{20}$ -Pa·s) subsurface layer extending underneath the crater and its surroundings. Finite element modeling of such a scenario applied to a typical concentrically fractured crater of 50-km diameter implies that the depth of the low-viscosity layer is comparable to the crater depth and the layer does not extend to the surface. Given that not every crater of comparable size on Ceres exhibits concentric fractures, it is also suggested that these conditions are only met locally and may be related to the surface temperature. Correlations of concentrically fractured craters with other volatile related features, such as pitted terrains and floor fracturing, suggest that the low-viscosity subsurface layer may be enriched in ice.

**Plain Language Summary** The dwarf planet Ceres has recently been visited by the Dawn spacecraft, which was able to take high-resolution images of Ceres' surface ( $\sim 35$  m/pixel). These images show that small concentric fractures surround some craters, at distances of up to one crater radius external to the craters' rims. Such fractured craters seem to be unique to Ceres. We investigate the appearance of these fractures and how they may have formed. Previous investigations of Ceres' composition have found that Ceres may possess water ice or salt in its upper layers. We suggest that a deformable, possibly ice-rich or salt-rich, layer under the concentrically fractured craters may have formed the fractures. The weight of the material overlying such a layer over long timescales (60 Myr) may deform it, producing near-surface stresses that cause fracturing. We find that certain conditions (e.g., a layer less than 10 km below the surface, with a thickness of a few kilometers) are more likely to form fractures, and the presence of concentric fracturing therefore hints at the distribution of ice or salt in Ceres' subsurface.

### 1. Introduction

The dwarf planet Ceres, orbited by the Dawn spacecraft since 2015, shows a variety of different impact craters of various ages, sizes, and morphology (Buczowski et al., 2016; Hiesinger et al., 2016). Despite previous assumptions about an upper ice-rich mantle (Castillo-Rogez & McCord, 2010), Dawn showed that many of Ceres' craters are not viscously relaxed (Bland et al., 2016). Their morphology and evolution are directly influenced by the properties of Ceres' upper layers, which seem to be composed of relatively mechanically strong constituents (Russell et al., 2016), such as a silicate-rich rock-ice mixture containing salt and clathrate hydrates, carbonates (Bland et al., 2016; De Sanctis et al., 2015, 2016; Fu et al., 2017), and ammoniated phyllosilicates (De Sanctis et al., 2015, Ammannito et al., 2016). However, there are a number of features suggesting the presence of water ice in Ceres' upper layers (Sizemore et al., 2018), such as lobate landslides (Schmidt et al., 2017), domical features (Ruesch et al., 2016), pitted terrains (Sizemore et al., 2017), and smooth long-wavelength topography (Fu et al., 2017). The shallow subsurface may contain a maximum of 30–40% water ice by volume on average, although there is evidence of regional heterogeneity (Bland et al., 2016; Fu et al., 2017).



Another indicator of Ceres' shallow composition is prominent fracturing of the surface, which is mostly associated with the southern craters Yalode and Uvara (Buczkowski et al., 2016; Crown et al., 2017). North of these craters, linear structures are evident as pit crater chains, grooves, or troughs, which extend in a quasi-radial pattern northwest of Uvara crater and reach lengths of up to 143 km (Crown et al., 2017). They are suggested to have formed as a result of extensional stresses possibly introduced by upwelling of salt or another low-density material mobilized by convection or diapirism (Buczkowski et al., 2016; Scully et al., 2017).

Extensive fracturing within craters as well as floor-fractured craters are abundant on Ceres (Buczkowski et al., 2016; Hiesinger et al., 2016). The fractures occur either in a concentric pattern near the crater rim or central dome or as linear fractures crossing the floor (Buczkowski et al., 2016). Inner crater fracturing may be related to endogenic activity (Nathues et al., 2017), cryomagmatic uplift under the crater floor (Buczkowski et al., 2017), or stresses introduced by the instability of the subsurface (Krohn et al., 2017; Scully et al., 2019). Moreover, the crater Occator has been connected with recent activity generated by volatile reservoirs in the subsurface (Ruesch et al., 2018) and subsequent cryovolcanic activity (Krohn et al., 2016), possibly triggered by the impacts (Bowling et al., 2019).

Investigation of Ceres' crater size frequency distribution shows that craters larger than 100–150 km in diameter are missing on Ceres' surface when compared to predicted impact rates or the cratering record on asteroid Vesta (Marchi et al., 2016). Different mechanisms for crater removal have been discussed including resurfacing by widespread cryovolcanism and viscous relaxation (Bland et al., 2016; Marchi et al., 2016).

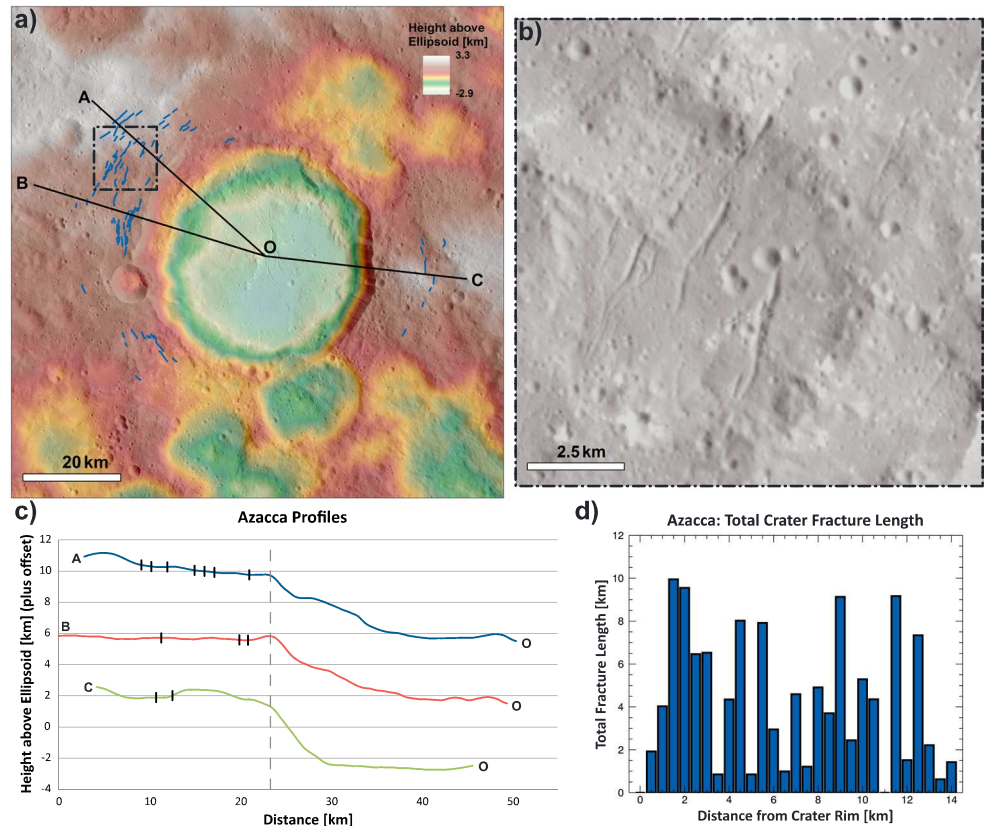
Cryovolcanism seems a viable scenario, particularly early in Ceres' history; however, no clear flow fronts have been detected at the highest spatial scale available (~30 m/pixel). Viscous relaxation results from gravitationally introduced stresses imposed on the ductile material surrounding a crater cavity. The relaxation of a crater includes the uplift of the crater floor and subsidence of material beyond the crater rim (Parmentier & Head, 1981). Viscous material flowing into a crater cavity may also generate concentric or spirally aligned strike-slip faulting beyond the crater rim (Allemand & Thomas, 1999).

Assuming viscous relaxation as the cause of crater removal on Ceres (Bland et al., 2016), crater rims should be topographically evident over geologic time scales due to their comparatively small spatial wavelength. For the same target conditions, the relaxation process is dependent on the size of the relaxing feature and most efficient on larger length scales (Parmentier & Head, 1981). Thus, narrower features, such as crater rims, are preserved compared to the broader crater cavity. However, rims of large craters could not be properly identified on Ceres' surface. This also seems at odds with the inferred rheologically stiff top layer of Ceres (Fu et al., 2017). It is possible that a combination of the above factors, in addition to erosion of the craters, facilitated by the weaker materials found on Ceres (compared to more rocky asteroids, such as Vesta) can explain the lack of large craters (Marchi et al., 2016).

In this regard, in addition to the fracturing processes and features described above, which have also been identified on other planetary objects including Mars (Bamberg et al., 2014) and the Moon (Schultz, 1976), Ceres exhibits another interesting fracture pattern: concentric fractures and pit crater chains beyond the rims of some craters (Buczkowski et al., 2017). Similar features have not been observed for craters on other planetary bodies including bodies with ice-rich surface material, such as Mars or the icy satellites of Saturn and Jupiter. The lower high-resolution surface coverage at the icy satellites, however, may not have allowed detection. In this work, we investigate the nature of these concentric fractures around impact craters on Ceres including their morphology, distribution, and relation to topography. We will present a model for their formation and will discuss the implications these may have on the observed cratering record on Ceres.

## 2. Data

We used the LAMO (Low Altitude Mapping Orbit) mosaic (35 m/pixel) by Roatsch et al. (2017) and the HAMO (High Altitude Mapping Orbit) Digital Terrain Model (DTM, 140 m/pixel, 10 m vertical accuracy) referenced to a 482 km × 446 km biaxial ellipsoid to morphologically and geologically map and characterize concentric fractures around craters on Ceres. Additionally, for the crater Occator, we used a DTM at LAMO spatial resolution with a vertical accuracy of ~1.5 m (Jaumann et al., 2017). At the time of our analysis, LAMO resolution DTMs were not available for the other regions of interest.



**Figure 1.** (a) Crater Azacca with locations of profile lines and close-up frame. The concentric fractures beyond the crater rim are marked as blue lines. (b) A close-up view of concentric fractures in the northwest of Azacca. (a) and (b) are extracted from an equidistant map with north pointing to the top. (c) Profiles through the concentric fractures and the crater floor. For illustrative reasons, profiles A and B are vertically shifted by 8 and 4 km, respectively. The profiles are aligned at the crater rim (dashed line). The black vertical lines indicate individual fracture locations. Profiles A and B show a step-like profile of terraced walls, while profile C shows the relatively steep slope and flat floor associated with less simple mass wasting. (d) The distribution of concentric fractures beyond the crater rim of Azacca. For each range of distance - the bin size is 0.5 km - the combined concentric fracture length at the given distance from the crater rim is shown.

### 3. Observations

#### 3.1. Examples

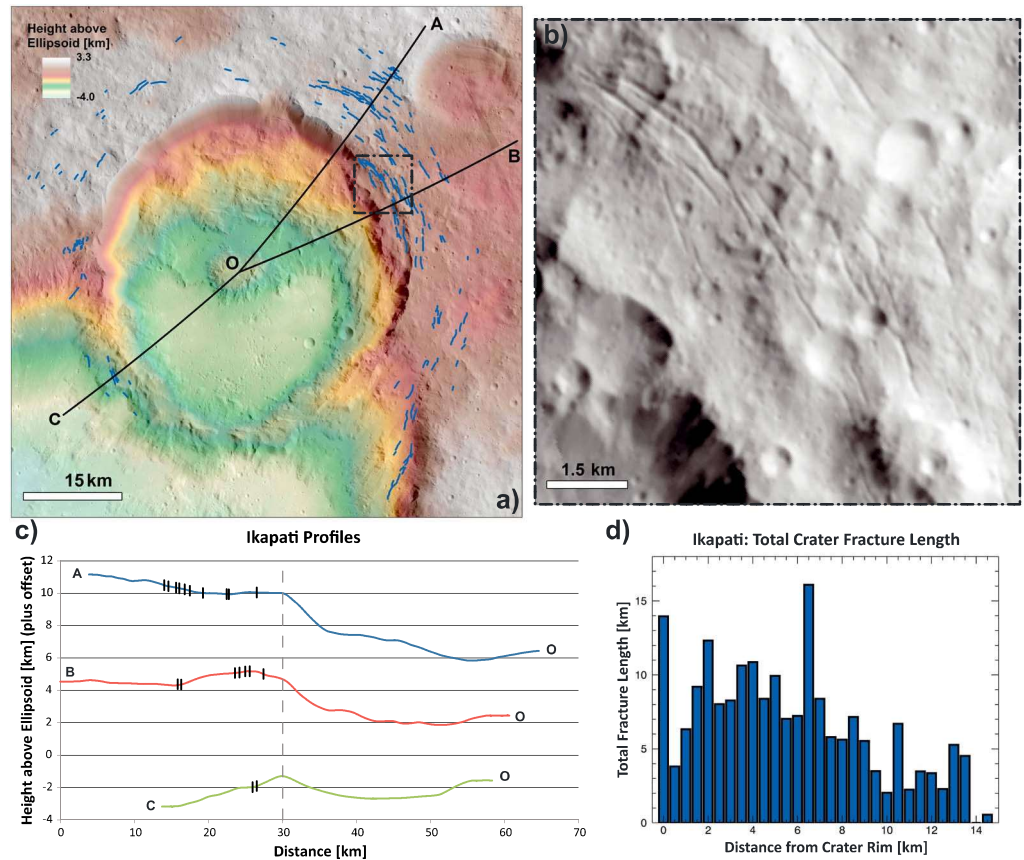
In the following sections we will focus on three characteristic craters on Ceres with concentric fracturing to illustrate the nature of these craters and fractures. In order to investigate the influence of environmental conditions, such as local topography and potential recent geologic activity, on the formation of concentric fractures, we investigate three craters: The first example is Azacca, a 50-km-diameter crater, as an average-sized concentrically fractured crater. Azacca's morphology is relatively simple and thus provides a good basis for analysis. Ikapati is a similarly sized crater, but, in contrast to Azacca, it is positioned on a prominent slope and possesses concentric fractures cross-cutting its rim. Finally, we will focus on Occator as an example of a larger crater (92-km diameter) with concentric fractures. Occator is also of specific interest due to its possible connection to recent activity and cryovolcanism (Krohn et al., 2017).

##### 3.1.1. Azacca

Azacca is a 50-km-diameter large crater located at 6.7°S and 218.4°E (Figure 1). Azacca exhibits prominent linear fractures crossing the crater floor in a rough north-south direction and inner circumferential fractures where the crater wall meets the crater floor. A terraced rim and central ridge are also present (Buczkowski et al., 2017). Azacca's flat floor also accommodates some degraded pitted terrains (Sizemore et al., 2017).

The concentric fractures beyond the crater rim are mostly clustered in the northwest of the crater, but some concentric fractures are also evident in the east and southwest (Figure 1a). These areas are also associated with slightly higher elevation compared to other parts of the crater vicinity. The northwest part of the





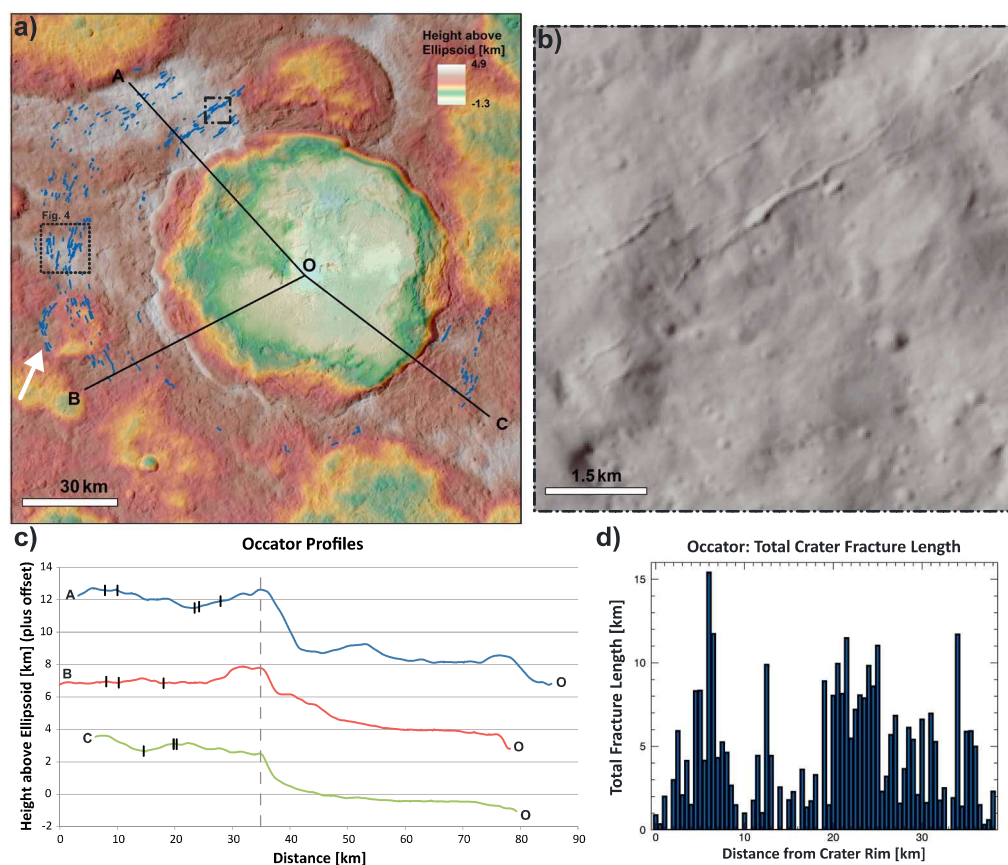
**Figure 2.** (a) Ikapati crater with concentric fracturing beyond the crater rim (blue lines). Profile and close-up locations are marked. (b) Close-up view of concentric fractures beyond and directly on Ikapati’s rim. (a) and (b) are extracted from an equidistant map with north pointing to the top. Ikapati’s fractures on the crater rim are unique within craters with concentric fracturing. (c) Topographic profiles through outer cracks in Ikapati as indicated in (a). The locations of concentric fractures are marked as vertical black lines. Profiles A and B are vertically shifted by 8 and 4 km, respectively. The profiles are aligned at the crater rim (dashed line). Profiles A and B cut through the terraced wall at the higher elevation region of Ikapati, while profile C cuts through the flat floor and preexisting depression. (d) The distribution of concentric fractures beyond Ikapati’s rim and the combined concentric fracture length at the given distance from the crater rim. The bin size is 0.5 km.

crater also shows extensive terrace formation inside Azacca. The crater floor in this region is at higher elevation, which may be explained by the collapse of material into the crater. The concentric fractures extend to 14 km beyond the crater rim, roughly half a crater radius.

### 3.1.2. Ikapati

Ikapati is also a 50-km-diameter complex crater located at 33.8°N and 45.6°E (Figure 2) with noticeable pitted terrain possibly related to volatile outgassing and floor cracking (Pasckert et al., 2017; Sizemore et al., 2017). Floor fractures appear as cracks and pit crater chains with predominantly parallel alignment to the crater terraces and walls. Ikapati is situated at the northeastern edge of a depression, which was probably formed by one or several coalesced impact craters. Thus, Ikapati’s southwestern rim is approximately 5 km lower than the northeastern rim. The terraced crater rim occurs in the higher elevated northern part of the crater, while the floor of Ikapati and the depression to its southwest are filled with smooth material which is most likely impact melt (Pasckert et al., 2017).

Ikapati exhibits most of its outer concentric fractures in the northeast where a transition from the highest (~2.5 km) to the medium elevated region (~0.5 km) occurs (Figure 2a). Some of these concentric fractures are located directly on the crater rim, where a large block of material slumped into the crater (Figure 2b). The crater rim here is lower and broadened (Figure 2c, profile B) compared to other rim regions around Ikapati. The concentric fractures located on the crater rim of Ikapati are unique on Ceres. Further

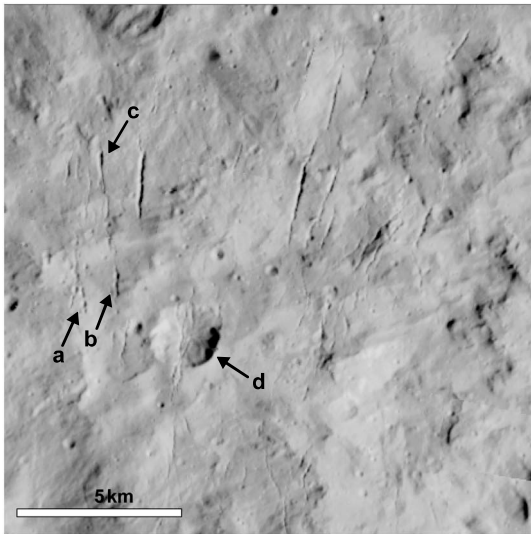


**Figure 3.** (a) Occator crater with profile lines and close-up frames for Figure 4 (left box) and Figure 3b) (box near center). The blue lines sketch the location of concentric fractures beyond Occator's rim. The white arrow points to a buried crater with quasi-concentric fractures aligning with its inner crater wall. (b) Close-up of concentric fractures in the northwest of Occator. (a) and (b) are extracted from an equidistant map with north pointing to the top. (c) Profiles through Occator and concentric fractures beyond the rim as shown in (a). The black vertical lines indicate the locations of individual concentric fractures. Profiles A and B are shifted vertically by 8 and 4 km, respectively. The profiles are shifted horizontally to align at the crater rim (dashed line). Profiles A and B cut through the terraced crater wall, and profile C cuts through a relatively steep crater wall with little slumping. (d) The distribution of Occator's concentric fractures beyond the crater rim and the combined concentric fracture length at the given distance from the crater rim. The bin size is 0.5 km.

concentric fractures are located on the elevated region to Ikapati's northwest and on the steep slopes where Ikapati cuts into the preexisting depression. A small number of concentric fractures are located beyond the crater rim in the southwest inside the preexisting depression. The concentric fractures appear within 14 km beyond the rim of Ikapati, which is approximately half a crater radius.

### 3.1.3. Occator

Occator is a 92-km-diameter crater located at 19.8°N and 239.3°E (Figure 3), which shows evidence for recent activity (Buczowski et al., 2017; Nathues et al., 2017; Ruesch et al., 2017). Its central 9-km-wide depression with a 2-km-wide domical bright feature and a collection of fractured bright spots on the floor suggest the ascent and crystallization of a sodium carbonate-rich brine, possibly triggered by an impact event (Bowling et al., 2019; De Sanctis et al., 2016; Nathues et al., 2017). Occator has extensive terraced walls but also some steep slopes with little evidence for slumping, particularly in the southeast (Figure 3c, profile C). The floor of Occator is extensively fractured, exhibiting linear radial fractures emanating from the crater center, crosscutting fractures near the southwest crater wall, and circumferential fractures along and on the terraced crater wall and surrounding the central pit (Buczowski et al., 2017, 2019). Occator's floor is partly covered by lobate flows (Krohn et al., 2016) but also exhibits hummocky terrain at the slightly elevated northwestern part of the crater. Degraded pitted terrains have also been identified (Sizemore et al., 2017).



**Figure 4.** Concentric fractures and pit crater chains around Occator crater (92-km diameter). The location of this scene is sketched in Figure 3a. An example pit crater chain (a), coalesced pit crater chain (b), and elongated fracture with variable width (c) are labeled. The concentric fractures run relatively parallel (e.g., cracks (a) and (b)) with variable spacing, width, and length. Some concentric fractures are partially disconnected; for example, coalesced pit crater chain (b) integrates into fracture (c). An approximately 2-km-diameter crater with crossing concentric fractures (d) indicates that the concentric fractures formed, or were reactivated, after the formation of craters on the ejecta blanket of Occator crater.

Concentric outer fractures are predominantly present in the relatively high region west and northwest of Occator with some concentric fractures on a higher plateau in the southeast and in the south (Figure 3a). There are no concentric fractures in the north, where a preexisting crater is located and in the northeast where an uneven depression is evident. Most fractures are concentric to Occator's wall, but a set of quasi-concentric fractures follow the shape of a preexisting smaller crater (20-km diameter) in the west. The distribution of the concentric fractures extends up to 40 km from the crater rim, which is slightly less than the crater radius. There is a reduced amount of fracturing between roughly 10- and 20-km distance.

### 3.2. Characteristics of Concentric Crater Fractures

Concentric fractures observed beyond crater rims on Ceres appear as pit crater chains with either individual or coalesced pits or as elongated cracks (Figure 4). The concentric fractures occur on the crater rim (e.g., Ikapati; section 3.1.2), close to the crater rim and may extend up to one crater radius beyond the crater rim.

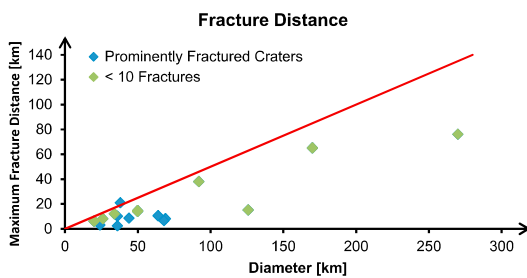
The widths of the observed concentric pit crater chains and concentric fractures range between a lower limit given by the image resolution of 35 m/pixel and a maximum of 300 m. Individual pits of a concentric fracture are separated by 150 to 300 m, while the typical distance between two parallel concentric fractures is on the order 500 m to 2 km. The typical concentric fracture length is on the order of 1 km, and the maximum individual concentric fracture length is about 6 km. Elongated patterns of individual smaller concentric fractures strung together often resemble the appearance of a common large concentric fracture. Some of the con-

centric fractures show a bulbous elongated shape with variable width, while others have a relatively homogenous width. The depth of most concentric fractures is too small to be visible in the DTM; however, in a few cases it was possible to measure their depths in the Occator crater region. A depth of approximately 20–50 m could be derived from the LAMO DTM, but the accuracy in this elevation range has to be considered with caution. The strong contrast between illuminated and shadowed flanks of the concentric fractures suggests relatively steep slope angles and potentially deeper cracks. Assuming a slope angle of 35°, which is comparable to the slope of Occator's wall, the depth of the concentric fractures can be estimated to be 100 m for the widest concentric fractures.

The concentric fractures generally occur in clusters around an impact crater. The radial distance of the concentric fractures from the crater rim is less than a crater radius, and most concentric fractures are located within 15 km of the crater rims (Figure 5). Generally, the maximum distance of concentric fractures from the crater rim increases with crater radius; however, the variation is large for individual craters. These variations may be introduced by variations in the geologic setting, for example, the topography or subsurface layout, or the observational conditions that may be different for different craters.

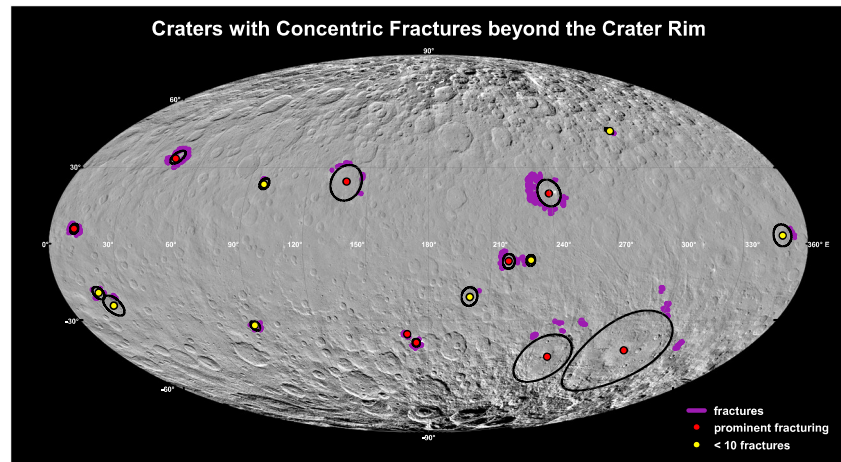
Although these clusters appear on various elevations and slopes, they are in general not present in lower regions. Most commonly the concentric fractures are evident on higher areas or steep slopes and exhibit radial extension. On the smaller scale, individual concentric fractures occur in depressions and on hills. Neighboring concentric fractures are generally aligned in parallel. Topographic irregularities may locally diverge the concentric fracture alignment. Nevertheless, cross-cutting concentric fractures have not been observed.

The concentric fractures occur on topographically smooth as well as hummocky regions of the ejecta blanket. An interesting observation is that in some cases the concentric fractures crosscut smaller impact



**Figure 5.** The maximum distance of concentric fractures from the crater rim versus the crater size. The different colors represent craters with prominent concentric fracturing and less than 10 concentric fractures (see Table 1). The area below the red line indicates locations within one crater radius beyond the crater rim.





**Figure 6.** Global distribution of craters on Ceres with concentric fracturing beyond the crater rim. Seventeen craters have been identified; most of them are found in the midlatitudes. There are nine craters with prominent concentric fracturing (>10 fractures, red) and eight craters with fewer, less evident concentric fractures (<10, yellow). The distribution of concentric fractures (purple lines) and the outline of the relevant craters (black polygons) are marked.

craters on top of the ejecta blanket (Figure 4). This indicates that the concentric fractures formed after the formation of the small impact craters, which themselves must have formed after the emplacement of the impact ejecta. Additionally, the concentric fractures sometimes align with preexisting topography, such as the rim of an impact crater that has been covered by emplaced ejecta.

### 3.3. Distribution of Craters With Concentric Fracturing Beyond the Crater Rim

We found a total of 17 craters with concentric fractures on Ceres (Figure 6). We distinguish between craters with prominent concentric fracturing and less obvious concentric fracturing. There are nine prominently concentrically fractured craters, in which the concentric fractures are abundant (> 10) and well developed as pit crater chains or fissures (Figures 1–4). These concentric fractures also appear relatively fresh. Less obvious concentrically fractured craters have fewer (<10) concentric fractures. The lower number of identifiable concentric fractures may be a result of erosion. We identified eight craters with <10 concentric fractures.

The distribution of craters with concentric fractures beyond the crater rim does not seem to be correlated with the global distribution of fractures on Ceres, which are abundant between 210°E and 300°E, between 40°N and 60°S, and between the craters Occator and Dantu (0–45°N and 90–260°E; Scully et al., 2017). Craters with concentric fractures beyond the rim also occur in areas depleted in linear fractures suggesting that the causes for forming Ceres' global linear features, such as extensional stresses introduced by upwelling material (Scully et al., 2017), are different from the ones generating concentric fractures.

The craters occur predominantly in the midlatitude range between 46°S (Urvara) and 34°N (Ikapati). The polar region, where colder temperatures are expected, is depleted in craters with concentric fracturing beyond the crater rim. Although low incident angles may accentuate morphological features in these regions, concentric fractures have not been identified above 40°S and 45°N. Toward the poles, this observation may be influenced by the low incidence angles introducing larger shadowed regions. The shadows cast by large scale topographic features, such as crater rims, may obscure possible small scale concentric fractures. Thus, a reliable investigation is only possible up to 60°N/S.

The craters have diameters between 20 km (Juling) and 270 km (Yalode) with an average diameter of approximately 70 km (Table 1).

Most of the craters with concentric fractures appear to be relatively young. With the exception of the basin Yalode, none of the craters with concentric fractures exhibit features of viscous relaxation, such as the shallowing of long wavelength topography. However, other fresh craters in a similar geographic region and with similar diameters may not have concentric fracturing beyond their rims. Examples of such craters are Ezinu (116-km diameter, 43°N) and Oxo (10-km diameter, 42°N).

**Table 1**  
*List of All Craters With Concentric Fractures Beyond the Crater Rim*

Crater name	Diameter (km)	Prominent concentric fracturing	Floor fractures	Pitted terrain	Depth-to-diameter ratio ( $10^{-2}$ )	Maximum concentric fracture distance (km)
Aristareus	36	×	×	×	7.6	2.3
Azacca	50	✓	✓	✓	6.0	14
Consus	64	×	×	×	5.9	10.5
Cozobi	24	×	×	×	10.4	3
Dantu	126	✓	✓	✓	4.0	15
Haulani	34	✓	✓	✓	8.9	12
Ikapati	50	✓	✓	✓	8.0	14.5
Jarimba	69	×	×	×	5.8	8
Juling	20	✓	✓	×	13.8	6
Kondos	44	×	✓	×	6.8	8.5
Kupalo	26	✓	✓	✓	9.6	8
Lociyó	38	×	✓	×	7.2	21
Occator	92	✓	✓	✓	3.8	38
Rongo	68	×	✓	×	5.9	6.5
Tupo	36	×	✓	×	6.9	10
Urvara	170	✓	✓	✓	3.5	65
Yalode	260	✓	✓	×	2.5	76

*Note.* The name, size, and prominence of concentric fracturing are listed. Additionally, the presence of floor fractures and pitted terrain and the craters' depth-to-diameter ratio are noted.

Floor fractured craters are abundant on Ceres and may have formed by the floor uplift of cryomagmatic intrusions (Buczkowski et al., 2016, 2017). They are characterized by a smaller depth-to-diameter ratio compared to other craters on Ceres (Buczkowski et al., 2017). The floor fractures include central and off-central sets of linear parallel and radial cracks crossing the crater floor. Ten of the craters with concentric fractures also exhibit floor fracturing in the crater interior and inner crater concentric fractures close to the crater wall. The depth-to-diameter ratio of the craters with concentric fracturing is slightly lower compared to the general ratio shown by Hiesinger et al. (2016) with two exceptions (Figure 7); however, these outliers are the craters Ikapati and Urvara. As described above, Ikapati is located at the edge of a depression introducing uncertainties in the depth measurements. A similar argument is valid for Urvara which is located in an area of relatively high topography in the rougher southern region.

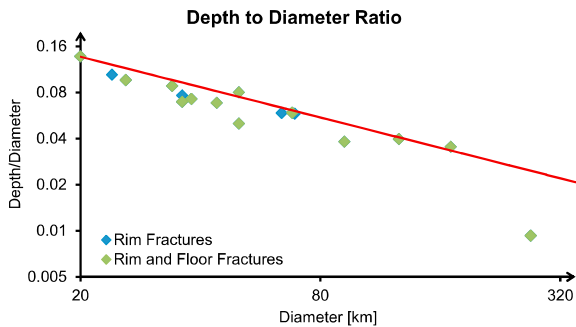
Craters with concentric fractures on Ceres are complex, exhibiting a central peak or ridge. Urvara and Occator craters also have a central depression possibly caused by subsidence related to cryomagmatic intrusions or generated during the impact formation (Buczkowski et al., 2016). Another indication of some of the craters' connection to volatiles is that all craters with pitted terrain (total of 7; Sizemore et al., 2017) are also craters with concentric fractures.

## 4. Formation Scenarios for Rim Fractures

### 4.1. Volumetric Compaction of a Volatile-Rich Ejecta Blanket

Buczkowski et al. (2017) suggest that the concentric fractures around Occator crater are caused by the volumetric compaction of a volatile-rich ejecta blanket. The vertical as well as horizontal compaction of such a deposit due to volatile outgassing and desiccation cause tension in the material. In areas of buried preexisting topography, such as crater rims and slopes, this tension may generate concentric fracturing along the buried topography (Buczkowski & Cooke, 2004; Cooke et al., 2011).

This model is supported by the observation that most concentric fractures around craters on Ceres are relatively close to the crater rim (less than a crater radius), where most tension is expected due to the relatively steep slopes near the crater rim. Assuming that the higher elevated regions are related to a thicker ejecta deposit, these regions will possess more absolute compaction. If compaction is the reason for the



**Figure 7.** The depth-to-diameter ratio of craters with concentric fracturing beyond the crater rim. Green diamonds represent craters with concentric and floor fractures, and blue diamonds mark craters that only have concentric fractures beyond the rim but no floor fractures. The red line indicates the global crater depth-to-diameter ratio on Ceres extracted from Hiesinger et al. (2016). Note the double logarithmic scale.

concentric fracturing, this may explain the observation that the concentric fractures mostly occur on elevated regions.

Specifically, around the crater Occator there is a ~20-km diameter crater buried by Occator ejecta with quasi-concentric fractures aligning with the inside of the buried crater's wall (Figure 3a, white arrow). The occurrence of these fractures on the steep flanks of an ejecta-buried crater is supportive of the volumetric compaction model; however, concentric fractures are not generally related to specific topographic features such as mounds, troughs, or slopes (Figures 1c, 2c, and 3c).

Most craters with concentric fracturing are also classified as floor fractured craters. Specifically the fractures within Occator are suggested to have formed by water or salt-rich magmatic injection (Buczkowski et al., 2017). If so, it is expected that Occator's ejecta blanket was volatile-rich, which is necessary for volumetric compaction.

The craters with concentric fracturing occur within the warmer midlatitudes of Ceres. Due to the illumination difference and the small rotation

axis' tilt (~4°), compaction due to outgassing and desiccation may be slower in the colder pole regions and they may even allow the existence of water ice in permanently shadowed regions (Schorghofer et al., 2016). This lack of desiccation may explain why craters with concentric fracturing are not observed in the polar regions, if volumetric compaction by volatile degassing and desiccation is the cause for the outer concentric fractures.

Thermal contraction cracking and differential sublimation of volatile-rich materials typically results in polygonally shaped fracture patterns (Lachenbruch, 1962; Levy et al., 2009). Although these are observed at some locations on Ceres, for instance, on the crater floors of Occator and Dantu (Buczkowski et al., 2019; Williams et al., 2018), the concentric fractures beyond the crater rim do not intersect each other or form polygons. However, we cannot rule out the presence of intersecting fractures on a smaller scale below spatial resolution of the images used in this study. This observation is not consistent with the theory of volatile loss of the surface layer, which is expected to result in polygon formation (Goehring, 2013).

Following the model of Buczkowski and Cooke (2004), the concentric fracture spacing may be an indication of the deposit thickness and both are roughly of the same order. The typical concentric fracture spacing is 500 m to 2 km. In the case of the buried impact crater west of Occator (white arrow in Figure 3a), the spacing is approximately 500–900 m. This would imply that the covering deposit/ejecta is similarly thick. Although this estimate seems applicable for Occator, it may not be feasible in other locations where the concentric fracture spacing is larger and consequently unreasonably large deposit thicknesses would be derived. Here other mechanisms, such as the relaxation of a low-viscosity subsurface layer, may play a more dominant role.

#### 4.2. Relaxation of a Low-Viscosity Subsurface Layer

Allemand and Thomas (1999) experimentally investigated the development of faulting by relaxation of a cavity cut into a layered target with a ductile lower and a brittle upper layer. They showed that the relaxation may generate concentric normal faulting beyond the crater rim if the ratio of the thickness of the upper brittle and the lower ductile layer is high, for example, the brittle layer has the same as or a higher thickness than the ductile layer.

Walsh and Schultz-Ela (2003) proposed the flow of a viscoelastic subsurface salt layer as cause for the formation of graben in Canyonlands National Park, Utah, USA (McGill & Stromquist, 1979; Walsh & Schultz-Ela, 2003). Gravity spreading generated by the overburden expelled the viscous layer at the base of the canyon. This deformation process creates stresses in the overlying brittle rock formation which results in graben formation parallel to the canyon. Despite the differences in shape, the process of expelling a viscous subsurface layer by overburden pressure may be similarly applicable to craters.

The concentric fractures around craters on Ceres may be caused by the drainage of material into opening faults and fissures caused by the relaxation and deformation of a viscous subsurface layer. The drainage of

material is evident for many concentric fractures because they are often composed of pit crater chains and coalesced pits (Figure 4), which form by material wasting into subsurface hollows. Following drainage experiments with unconsolidated, noncohesive materials (Horstman & Melosh, 1989), the pit spacing can be used to estimate the regolith thickness. The theory suggests that the spacing of the pits and the regolith thickness are of similar size, which allows estimating the thickness of the regolith covering the concentric fractures around craters on Ceres to be equal to the pit spacing of 150 to 300 m. Alternatively, considering a crater rim height of  $\sim 300$  m (compare with crater Azacca, Figure 1c, profile B) and assuming that the regolith near the crater rims is mostly ejecta of the crater itself, the regolith thickness can be estimated to a maximum of approximately 20% of the total crater rim height (Sharpton, 2014; Sturm et al., 2016). This yields a minimum regolith thickness of 60 m. In reality the regolith cover is likely to be thicker due to the accumulation of regolith from subsequent impacts. The estimated 150- to 300-m regolith thickness based on the pit spacing is therefore a reasonable estimate.

The upper brittle layer, required by Allemand and Thomas' and Walsh and Schultz-Ela's model, may be provided by the impact gardened upper regolith of Ceres, and the lower viscoelastic layer may be provided by an ice-rich subsurface. Fu et al. (2017) applied a geodynamical finite element simulation to reproduce Ceres' topography and were able to derive a depth-dependent viscosity of Ceres' crust with a surface viscosity of  $\sim 10^{25}$  Pa-s and a rapid decay of a factor of 10 per 10- to 15-km depth for the uppermost 40 km.

The volatile connection between concentrically fractured craters and volatiles is shown by the fact that all craters with pitted terrains are also concentrically fractured. Additionally, most concentrically fractured craters are floor-fractured, which may be related to cryomagmatic intrusions (Buczkowski et al., 2017). Thus, the viscosity of the subsurface layer is likely related to its water ice content. The preferential occurrence of concentrically fractured craters in the midlatitudes may imply that the warmer temperatures are able to reduce the subsurface viscosity so that concentric fracturing is possible.

Ermakov et al. (2017) report a reduction in topography in Ceres' equatorial region, which is consistent with a temperature dependent relaxation of an ice-rich crust due to insolation. The number of craters with concentric fractures is also increased in the midlatitudes. It is possible that the temperature conditions and coupled material properties in this area provide the necessary conditions for concentric fracturing around craters on Ceres, whereas the colder polar regions are less prone to viscous relaxation (Bland, 2013). Viscous crater relaxation as a condition for the concentric fracturing process is also supported by the fact that most concentrically fractured craters have a relatively low depth-to-diameter ratio (Figure 7) which is expected for viscously relaxed craters (Parmentier & Head, 1981).

Concentric fractures predominantly develop on elevated regions around craters on Ceres (Figures 1a, 2a, and 3a). A higher elevation also implies a larger overload and pressure on the putative subsurface viscoelastic layer. The elevation difference may be as high as 1 km (Figures 1a, 2a, and 3a), while the average concentrically fractured crater depth is about 3.5 km, so that the additional overload may enhance the forces supporting the generation of concentric normal faulting.

Alternatively, the lower viscoelastic layer may be formed by the heat generated by the impact process itself. Bowling et al. (2019) simulated the Occator impact using the iSALE2D shock physics code and were able to infer that the close vicinity of the impact site has an increased temperature compared to the impact site before the impact. Liquid water or warm ice in the subsurface of a fresh impact crater could temporarily create a less viscous subsurface (Bland, 2013).

Given that concentrically fractured craters are sparsely distributed on the surface of Ceres (total of 17 craters), the criteria for concentric crater fracturing seems often not fulfilled. A heterogeneous subsurface with low-viscosity, probably ice-rich or salt-rich patches may be able to explain the occurrence of the craters with concentric fractures beyond the rim. This may also explain the variable maximum distance of concentric fractures beyond the crater rim (Figure 5), and the layer thickness may have an effect on location of the development of concentric fractures (section 4.2.2). Such a composition and distribution is in agreement with investigations on crater relaxation on Ceres (Bland et al., 2016).

Relaxation is a length-scale-dependent process, which is most efficient for large scales (Bland, 2013; Parmentier & Head, 1981). Craters smaller than 20 km in diameter may be too small to undergo a relaxation process that is able to generate concentric fracturing.



#### 4.2.1. Modeling Crater Relaxation on Ceres

In order to test whether it is possible to form concentric fractures around craters on Ceres similar to the process observed at Canyonlands National Park, we use the finite element modeling software package Abaqus (Dassault Systèmes) to simulate several subsurface layering scenarios and explore their influence on crater relaxation.

As a characteristic medium sized impact crater with prominent concentric fracturing, we simulate an Azacca-like crater (Figure 1) with 50-km diameter, 3-km depth, and a parabolic interior (section 3.1.1). A rim height of  $\sim 750$  m and an ejecta thickness decreasing with  $r^{-3}$  (where  $r$  is the radius of the crater; Dombard & McKinnon, 2006) was applied (Figure 8). Based on the results from Fu et al. (2017), we place this Azacca-like crater into a 40-km-thick and  $1,287\text{-kg/m}^3$ -dense crust overlying a mantle with a density of  $2,432\text{ kg/m}^3$ . In this model, we keep the crust at a uniform viscosity of  $10^{25}$  Pa·s, corresponding to the maximum observed viscosity (Fu et al., 2017). To estimate the effects and constrain the thickness of a potential subsurface ice-rich layer, we place a layer with a viscosity of  $10^{20}$  Pa·s (representative of a rock-ice mixture) of varying thickness and depth into the crust (Figure 8, left column). For all materials, we used a Young's modulus of 17 GPa and a Poisson ratio of 0.32 as measured for silica ices with 34% silica by volume (Yasui et al., 2017). Following the investigations by Bland et al. (2016), this is a reasonable amount of ice within Ceres subsurface.

The model parameters, including the layer thickness and burial depth, are summarized in Table 2 and illustrated in Figure 8. In addition to four cases with varying layer depth and thickness, we also simulated a scenario without any low-viscosity layer (run 1). This was done to investigate whether a low-viscosity subsurface layer is mandatory for concentric fracture formation and the effects of the crust and mantle parameters on the formation of stresses and relaxation. In order to investigate the effect of decreasing viscosity of the crust with depth as suggested by Fu et al. (2017), we repeated run 1 with the viscosity decreasing by an order of magnitude every 10 km starting from  $10^{25}$  Pa·s at the surface. This setup, however, did not yield any substantial differences in stresses and thus we used the simpler setup with a constant viscosity of the crust of  $10^{25}$  Pa·s for all runs.

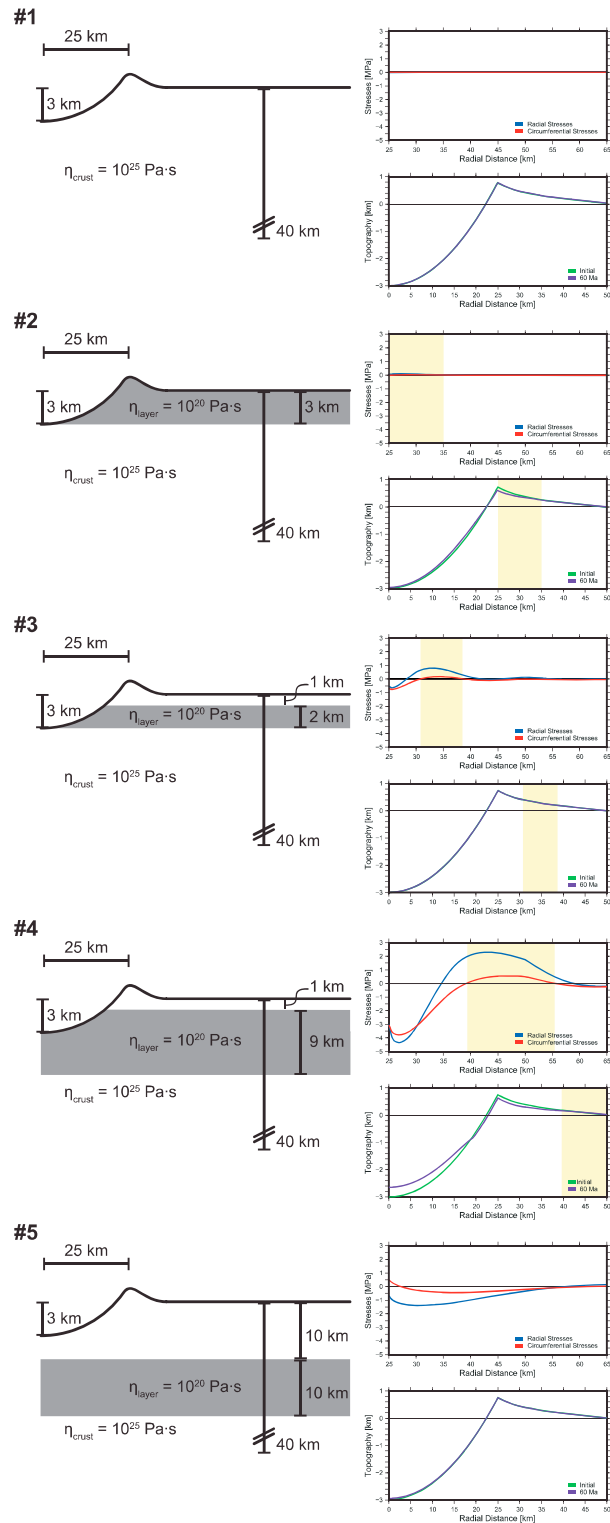
The Abaqus mesh is predominately composed of square elements with some triangular elements to conform to observed crater geometry and to reduce element distortion in geometrically complex regions. The mesh is composed of a high-resolution zone with cells 200 m by 200 m extending to a depth of 50 km. Below 50-km depth the cells gradually increase in size to 1 km by 1 km. Resolution tests showed that a more detailed mesh did not substantially influence the model results. The model dimensions (1,000 km by 250 km) greatly exceed the dimensions of the crater to avoid the influence of boundary conditions. The axial symmetry of the crater allowed the simulation to consider a 2-D slice extending radially from the center of the crater.

The modeling consists of two steps. The first modeling step calculates the overburden pressure within each element to generate a lithostatic prestress as an initial condition for the subsequent viscoelastic calculations. Without this prestress, the application of gravity would cause the mesh to self-compress. After implementing these initial conditions, we run the viscoelastic step. The boundary conditions at the bottom and the far side away from the crater of the simulation box are constrained in the radial, vertical, and circumferential directions.

The simulations are stopped after 60 Myr. At this point, the stresses at the surface change less than 1% over a time span of several million years for all runs and depending on the chronology system, this time is roughly the age of Azacca, which is 40 or 80 Ma (Schmedemann et al., 2016). We output the nodal radial and circumferential stresses at the free surface and show the change in topography of the crater after 60 Myr (Figure 8, right column).

#### 4.2.2. Modeling Results

Figure 8 shows the models, the radial and circumferential stresses at the free surface as a function of the distance from the crater rim, and the topography at the beginning and 60 Myr into the simulation. According to the Anderson theory of faulting (Anderson, 1951), open tension (Mode I) fractures develop perpendicular to the axis of maximum tensile stress. When the mean stress is compressional, tensile fractures are not expected: Instead, normal faults develop perpendicular to the most extensional principal stress. In this case the intermediate principal stress axis lies in the fracture plane, while the maximum principal stress is vertical. For our model, this means that at the surface (where the vertical stress is 0), crater-



**Figure 8.** Models and results. The left-hand side illustrates each of the five modeling runs. The dimensions of the sketches are not to scale. The upper plots to the right of each model show the free horizontal surface stresses after 60 Myr with the radial stress in blue and the circumferential stress in red. The lower plots to the right of each model illustrate the initial topography (green) and the topography after 60 Myr (purple). Note that the radial distances of the two plots are not identical. The plot showing the stresses extends from just outside the crater rim (25 km) to 65 km beyond the crater rim, whereas the topography is shown from the crater center to 50 km beyond the crater rim. At distances where the radial stress is more tensile than the circumferential stress (yellow shaded areas), concentric tensile fracturing may develop.

**Table 2**  
Model Scenarios Used to Investigate the Formation of Concentric Fractures

Run	Low-viscosity layer thickness (km)	Low-viscosity layer depth (km)
1	No layer	No layer
2	3	0
3	2	1
4	9	1
5	10	10

*Note.* For all cases a crust thickness of 40 km and a crust density of 1,287 kg/m<sup>3</sup> are assumed. The density of the underlying mantle is 2,432 kg/m<sup>3</sup>. The viscosity of the target material is 10<sup>25</sup> Pa·s, and the low-viscosity layer viscosity is 10<sup>20</sup> Pa·s. A uniform Young's modulus of 17 GPa and Poisson ratio of 0.32 is used.

concentric open fissures are expected to form when both the radial and circumferential stress are tensional, while at greater depths (as compressive overburden pressures suppress actual tension) the fissures transition into steeply dipping normal faults that may evolve into graben.

As an example of the variation of the stresses with depth, Figure 9 illustrates the depth-dependent stresses for run 3 at 60 Myr after the onset of the simulation and 33 km from the crater center (8 km beyond the crater rim). The above described condition for concentric tensile fracturing is met up to a depth of approximately 500 m which corresponds to a negative elevation of 150 m given the overlain topography of the crater rim. Below this depth the mean stress is compressive and normal faults may develop. The criterion for concentric tensile fracturing is initially reached after 30 Myr inside the yellow shaded region marked on the right-hand side in Figure 8. This region grows with time and covers an area from 6 to 13 km beyond the crater rim after 60 Ma.

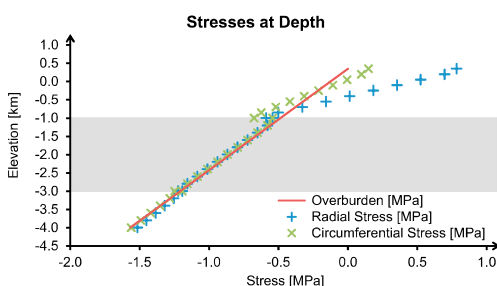
The yellow bands in Figure 8 indicate the radii at which both horizontal stresses are extensional. Adjacent to these bands are narrow annuli where the radial stress is extensional, while the circumferential stress is compressive. By Anderson's criterion these zones may initiate strike-slip faults. We do not, however, indicate these regions in a special manner as they are generally quite narrow and the sense of the strain is exactly the same as in the doubly tensile regions. Furthermore, similar stress conditions near mascon loads fail to exhibit actual strike-slip faults for reasons explored by Freed et al. (2001). The precise tectonic expression of the computed stresses is a sensitive function of the (unknown) strength of the underlying material. For example, if the surface layers are composed of cohesionless regolith, graben should form right at the surface because actual tension cannot be supported by the regolith. On the other hand, if the surface rocks are relatively strong (i.e., having nonzero cohesion and thus some tensile strength), then open fissures underlain by steeply dipping normal faults are expected. However, in all the cases we investigated, we expect concentric extensional structures that are consistent with the observed concentric fractures outside the crater rims on Ceres. Our models in this paper do not include plastic flow, for which we would need more detailed strength information than we possess, but the overall proportionality between stress and strain nevertheless gives an accurate indication of both the existence and general trends of concentric fractures due to the underlying viscous flow.

Three of our runs (runs 2 to 4) fulfill the failure conditions at specific locations beyond the crater rim. We observe an increase in stress magnitudes with increasing thickness of the low-viscosity layer at a given depth (runs 3 and 4) and a decrease in stress magnitude with an increasing depth of the low-viscosity layer at a similar layer thickness (runs 4 and 5). However, the run without a low-viscosity layer (run 1) and the run with the deeply buried low-viscosity layer (run 5) do not fulfill the criteria for concentric fracturing at any location beyond the crater rim.

Runs 2 to 4 show that the location of the zone of concentric fracturing migrates to larger distances with increasing layer thickness when a high-viscosity subsurface layer is present (runs 3 and 4). We also observe an increase in stress magnitudes with increasing thickness of the low-viscosity layer at a given depth (runs 3 and 4) and a decrease in stress magnitude with an increasing depth of the low-viscosity layer at a similar layer thickness (runs 4 and 5).

Runs 2 and 4 show relaxation of the crater shape, while a significant floor uplift (7% of the original depth) is only observed in the run with a thick and shallow low-viscosity subsurface (run 4). Floor uplift agrees well with the observed low depth-to-diameter ratio of craters with concentric fractures (Figure 7).

The viscosity of Ceres' material is dependent on the temperature which decreases with latitude and slightly increases depth (Bland, 2013). In



**Figure 9.** The development of circumferential, radial and overburden stresses with depth. The values are extracted from run 3 after 60 Myr at 33 km from the crater center. The gray shaded area indicates the location of the low-viscosity layer, which introduces a discontinuous change in stresses at the boundary. The condition for concentric tensile fracturing is met up to a depth of approximately -150 m elevation where the mean stress becomes compressional and normal faults may develop.

order to investigate the sensitivity of our modeling on the viscosity, we repeated run 3 with lower crustal viscosities (down to  $10^{23}$  Pa·s) and a higher low-viscosity layer viscosities (up to  $10^{23}$  Pa·s), with the same results for concentric tensile fracture development. Lower crustal and higher low-viscosity layer viscosities do not fulfill the criteria for concentric tensile fracturing.

#### 4.2.3. Interpretation

The observation that only models with a shallow low-viscosity subsurface/surface layer (runs 2 to 4) generate radial stresses that are more tensional than the circumferential stresses after 60 Myr suggests that a low-viscosity layer is necessary in the shallow subsurface (within the uppermost 10 km) of Ceres in order to produce the observed concentric fracturing. However, in the case of the low-viscosity layer extending to the surface (run 2) the stresses generated are relatively low ( $<0.1$  MPa). The tensile strength of crack-free ice of 1-mm sized grains is in the order of 1.5 MPa (Schulson, 2010); thus, a low-viscosity surface layer is probably not able to generate the observed concentric fractures.

Because the zone of concentric fracturing migrates to larger distances with increasing layer thickness and the observed concentric fractures around craters on Ceres develop close to the crater rim (maximum distance of 14 km, Figure 1d), the subsurface layer thickness should be relatively small (in the order of the crater depth,  $\sim 3$  km). The observed variations of the maximum concentric fracture distance from the crater rim may be introduced by different layer thicknesses. Additionally, the variation in concentric fracture development and location with the layer burial depth suggests that an uneven topography may affect the formation of concentric fractures. Specifically a very small overburden (run 2) does not support the formation of concentric fractures. This is in agreement with the observation that concentric fractures around Craters on Ceres are predominantly found on elevated terrain.

All things considered, it is likely that a low-viscosity subsurface layer at an impact site can generate concentric fracturing at the observed locations beyond the rim of an Azacca-like crater on Ceres. A scenario similar to our run 3 (a 2-km-thick low-viscosity subsurface layer with a burial depth of 1 km) best reproduces the observed concentric fractures near the crater rim (Figure 1d). Although this scenario does not show any floor uplift after 60 Ma, other processes such as cryomagmatic uplift (Buczkowski et al., 2017), may be responsible for the floor uplift.

## 5. Conclusion: Implications for Crater Degradation on Ceres

Our investigation of craters with concentric fractures beyond the crater rim on Ceres suggest that Ceres' near-subsurface is composed of a patchy, low-viscosity, possibly ice-rich or salt-rich layer. The presence of such a layer may have an effect on the degradation of craters on Ceres that is not applicable to other similar planetary objects, such as Vesta or the icy satellites.

Given the fact that concentric fracturing is not a general observation for craters on Ceres, the low-viscosity layer can only locally meet the geologic conditions for concentric fracturing or may not be globally present.

It is possible that the process of rim collapse due to concentric normal faulting and tensile fracturing beyond the crater rim is an effective mechanism to erode and remove crater rims. A crater with concentric fractures possesses lines of weakness at which failure should preferentially occur. For example, nearby impacts and subsequent seismic shaking may trigger the collapse of crater walls along preexisting concentric fractures. Thus, the crater rims of concentrically fractured craters should erode more efficiently compared to craters with no preexisting fractures. An example is the crater rim of Ikapati, where concentric fracturing on the crater rim is associated with a broader, flatter, and partly collapsed crater rim (Figure 2c, profile B).

Marchi et al. (2016) reported on the missing large craters on Ceres of diameters  $\geq 100$  km. No evidence of their rims remains on the surface of Ceres today, although degradation due to viscous relaxation should have preserved small-scale topographic features, such as crater rims, on geological timescales. It is possible that a process such as the mechanism of a deforming subsurface layer described above may be responsible for the erosion and removal of crater rims in the past. The craters with concentric fractures investigated here have an average diameter of  $\sim 70$  km, which is less than the size of the missing large crater population. Nevertheless, three of the investigated craters have diameters  $>100$  km (Dantu with 126-km, Urvara with 170-km, and Yalode with 270-km diameter) suggesting that a similar mechanism may be also applicable

to larger craters. In particular, the largest concentrically fractured crater, Yalode, possesses a poorly defined and mostly destroyed/collapsed crater rim (Crown et al., 2017).

## 6. Summary

We investigated craters on Ceres with concentric fracturing beyond the crater rim. The concentric fractures and pit crater chains are from a few hundred meters to a few kilometers long, with a characteristic length of 1 km. They develop beyond the crater rim, preferentially on higher regions and extend less than one crater radius beyond the rim. In total we found 17 concentrically fractured craters with an average size of ~70-km diameter.

We suggest that the concentric fracturing occurs as a result of creep of a low-viscosity subsurface layer superimposed by a brittle regolith layer. The low-viscosity layer appears to be disrupted so that the conditions to generate concentric fractures are met only locally. The frequent coincidence of craters with concentric fractures and craters with floor fractures and pitted terrains implies that this low-viscosity subsurface layer may be enriched in ice or other volatiles. Finite element modeling further suggests that an Azacca-like crater of 50-km diameter may form concentric surface fractures after 60 Myr in the observed location when a low-viscosity layer of 2-km thickness is buried 1 km below the surface. Locally, the desiccation of a volatile-rich ejecta blanket deposited on top of a preexisting topography may also generate quasi-concentric fracturing in alignment with preexisting topographic features.

Ceres' complexly structured crust may be able to erode crater rims more effectively than homogenous viscous relaxation and explain the missing crater rims of large craters on Ceres.

## Acknowledgments

Dawn data are archived with the NASA Planetary Data System (<http://sbn.pds.nasa.gov/>), and our modeling results are provided in the supporting information. The authors would like to thank the editors and reviewers for their constructive comments. K. A. O. would like to gratefully acknowledge the financial support and endorsement from the DLR Management Board Young Research Group Leader Program and the Executive Board Member for Space Research and Technology.

## References

- Allemand, P., & Thomas, P. (1999). Small-scale models of multiring basins. *Journal of Geophysical Research*, *104*(E7), 16,501–16,514. <https://doi.org/10.1029/1999JE900008>
- Ammannito, E., DeSanctis, M. C., Ciarniello, M., Frigeri, A., Carrozzo, F. G., Combe, J.-P., et al. (2016). Distribution of phyllosilicates on the surface of Ceres. *Science*, *353*(6303), aaf4279. <https://doi.org/10.1126/science.aaf4279>
- Anderson, E. M. (1951). *The dynamics of faulting and dyke formation with applications to Britain* (2nd ed., p. 206). Edinburg: Oliver and Boyd.
- Bamberg, M., Jaumann, R., Asche, H., Kneissl, T., & Michael, G. G. (2014). Floor-fractured craters on Mars—Observations and origin. *Planetary and Space Science, Planetary evolution and life*, *98*, 146–162. <https://doi.org/10.1016/j.pss.2013.09.017>
- Bland, M. T. (2013). Predicted crater morphologies on Ceres: Probing internal structure and evolution. *Icarus*, *226*(1), 510–521. <https://doi.org/10.1016/j.icarus.2013.05.037>
- Bland, M. T., Raymond, C. A., Schenk, P. M., Fu, R. R., Kneissl, T., Pasckert, J. H., et al. (2016). Composition and structure of the shallow subsurface of Ceres revealed by crater morphology. *Nature Geoscience*, *9*(7), 538–542. <https://doi.org/10.1038/ngeo2743>
- Bowling, T. J., Ciesla, F. J., Davison, T. M., Scully, J. E. C., Castillo-Rogez, J. C., Marchi, S., & Johnson, B. C. (2019). Post-impact thermal structure and cooling timescales of Occator crater on asteroid 1 Ceres. *Icarus*, *320*, 110–118. <https://doi.org/10.1016/j.icarus.2018.08.028>
- Buczkowski, D. L., & Cooke, M. L. (2004). Formation of double-ring circular grabens due to volumetric compaction over buried impact craters: Implications for thickness and nature of cover material in Utopia Planitia, Mars. *Journal of Geophysical Research*, *109*, E02006. <https://doi.org/10.1029/2003JE002144>
- Buczkowski, D. L., Schmidt, B. E., Williams, D. A., Mest, S. C., Scully, J. E. C., Ermakov, A. I., et al. (2016). The geomorphology of Ceres. *Science*, *353*(6303), aaf4332. <https://doi.org/10.1126/science.aaf4332>
- Buczkowski, D. L., Scully, J. E. C., Quick, L., Castillo-Rogez, J., Schenk, P. M., Park, R. S., et al. (2019). Tectonic analysis of fracturing associated with Occator crater. *Icarus*, *320*, 49–59. <https://doi.org/10.1016/j.icarus.2018.05.012>
- Buczkowski, D. L., Williams, D. A., Scully, J. E. C., Mest, S. C., Crown, D. A., Schenk, P. M., et al. (2017). The geology of the Occator quadrangle of dwarf planet Ceres: Floor-fractured craters and other geomorphic evidence of cryomagmatism. *Icarus*, *316*, 128–139. <https://doi.org/10.1016/j.icarus.2017.05.025>
- Castillo-Rogez, J. C., & McCord, T. B. (2010). Ceres' evolution and present state constrained by shape data. *Icarus*, *205*(2), 443–459. <https://doi.org/10.1016/j.icarus.2009.04.008>
- Cooke, M., Islam, F., & McGill, G. (2011). Basement controls on the scale of giant polygons in Utopia Planitia, Mars. *Journal of Geophysical Research*, *116*(E9). <https://doi.org/10.1029/2011JE003812>
- Crown, D. A., Sizemore, H. G., Yingst, R. A., Mest, S. C., Platz, T., Berman, D. C., et al. (2017). Geologic mapping of the Urvara and Yalode quadrangles of Ceres. *Icarus*, *316*, 167–190. <https://doi.org/10.1016/j.icarus.2017.08.004>
- De Sanctis, M. C., Ammannito, E., Raponi, A., Marchi, S., McCord, T. B., McSween, H. Y., et al. (2015). Ammoniated phyllosilicates with a likely outer solar system origin on (1) Ceres. *Nature*, *528*(7581), 241–244. <https://doi.org/10.1038/nature16172>
- De Sanctis, M. C., Raponi, A., Ammannito, E., Ciarniello, M., Toplis, M. J., McSween, H. Y., et al. (2016). Bright carbonate deposits as evidence of aqueous alteration on (1) Ceres. *Nature*, *536*(7614), 54–57. <https://doi.org/10.1038/nature18290>
- Dombard, A. J., & McKinnon, W. B. (2006). Elastoviscoplastic relaxation of impact crater topography with application to Ganymede and Callisto. *Journal of Geophysical Research*, *111*, E01001. <https://doi.org/10.1029/2005JE002445>
- Ermakov, A. I., Fu, R. R., Castillo-Rogez, J. C., Raymond, C. A., Park, R. S., Preusker, F., et al. (2017). Constraints on Ceres' internal structure and evolution from its shape and gravity measured by the Dawn spacecraft. *Journal of Geophysical Research: Planets*, *122*, 2267–2293. <https://doi.org/10.1002/2017JE005302>



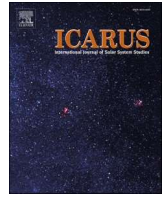
- Freed, A. M., Melosh, H. J., & Solomon, S. C. (2001). Tectonics of mascon loading: Resolution of the strike-slip faulting paradox. *Journal of Geophysical Research*, 106(E9), 20,603–20,620. <https://doi.org/10.1029/2000JE001347>
- Fu, R. R., Ermakov, A. I., Marchi, S., Castillo-Rogez, J. C., Raymond, C. A., Hager, B. H., et al. (2017). The interior structure of Ceres as revealed by surface topography. *Earth and Planetary Science Letters*, 476, 153–164. <https://doi.org/10.1016/j.epsl.2017.07.053>
- Goehring, L. (2013). Evolving fracture patterns: Columnar joints, mud cracks and polygonal terrain. *Philosophical Transactions of the Royal Society A: Mathematical, Physical and Engineering Sciences*, 371(2004), 1–18. <https://doi.org/10.1098/rsta.2012.0353>
- Hiesinger, H., Marchi, S., Schmedemann, N., Schenk, P., Pasckert, J. H., Neesemann, A., et al. (2016). Cratering on Ceres: Implications for its crust and evolution. *Science*, 353(6303), aaf4759. <https://doi.org/10.1126/science.aaf4759>
- Horstman, K. C., & Melosh, H. J. (1989). Drainage pits in cohesionless materials: Implications for the surface of Phobos. *Journal of Geophysical Research*, 94(B9), 12,433–12,441. <https://doi.org/10.1029/JB094iB09p12433>
- Jaumann, R., Preusker, F., Krohn, K., von der Gathen, I., Stephan, K., Matz, K. D., et al. (2017). Topography and geomorphology of the interior of Occator Crater on Ceres. *European Planetary Science Congress 2017*, Riga Latvia, id. EPSC2017–507.
- Krohn, K., Jaumann, R., Otto, K. A., Schulzeck, F., Neesemann, A., Nass, A., et al. (2017). The unique geomorphology and structural geology of the Haulani crater of dwarf planet Ceres as revealed by geological mapping of equatorial quadrangle Ac-6 Haulani. *Icarus*, 316, 84–98. <https://doi.org/10.1016/j.icarus.2017.09.014>
- Krohn, K., Jaumann, R., Stephan, K., Otto, K. A., Schmedemann, N., Wagner, R. J., et al. (2016). Cryogenic flow features on Ceres: Implications for crater-related cryovolcanism. *Geophysical Research Letters*, 43, 11,994–12,003. <https://doi.org/10.1002/2016GL070370>
- Lachenbruch, A. H. (1962). *Mechanics of thermal contraction cracks and ice-wedge polygons in permafrost*. in: *Geological Society of America Special Papers* (pp. 1–66). New York: Geological Society of America. <https://doi.org/10.1130/SPE70-p1>
- Levy, J., Head, J., & Marchant, D. (2009). Thermal contraction crack polygons on Mars: Classification, distribution, and climate implications from HRISE observations. *Journal of Geophysical Research*, 114, E01007. <https://doi.org/10.1029/2008JE003273>
- Marchi, S., Ermakov, A. I., Raymond, C. A., Fu, R. R., O'Brien, D. P., Bland, M. T., et al. (2016). The missing large impact craters on Ceres. *Nature Communications*, 7(1), 1–9. <https://doi.org/10.1038/ncomms12257>
- McGill, G. E., & Stromquist, A. W. (1979). The grabens of Canyonlands National Park, Utah: Geometry, mechanics, and kinematics. *Journal of Geophysical Research*, 84(B9), 4547–4563. <https://doi.org/10.1029/JB084iB09p04547>
- Nathues, A., Platz, T., Thangjam, G., Hoffmann, M., Mengel, K., Cloutis, E. A., et al. (2017). Evolution of Occator crater on (1) Ceres. *The Astronomical Journal*, 153(3), 1–12. <https://doi.org/10.3847/1538-3881/153/3/112>
- Parmentier, E. M., & Head, J. W. (1981). Viscous relaxation of impact craters on icy planetary surfaces: Determination of viscosity variation with depth. *Icarus*, 47(1), 100–111. [https://doi.org/10.1016/0019-1035\(81\)90095-6](https://doi.org/10.1016/0019-1035(81)90095-6)
- Pasckert, J. H., Hiesinger, H., Ruesch, O., Williams, D. A., Naß, A., Kneissl, T., et al. (2017). Geologic mapping of the Ac-2 Coniraya quadrangle of Ceres from NASA's Dawn mission: Implications for a heterogeneously composed crust. *Icarus*, 316, 28–45. <https://doi.org/10.1016/j.icarus.2017.06.015>
- Roatsch, T., Kersten, E., Matz, K.-D., Preusker, F., Scholten, F., Jaumann, R., Raymond, C. A., & Russell, C. T. (2017). High-resolution Ceres Low Altitude Mapping Orbit Atlas derived from Dawn Framing Camera images. *Planetary and Space Science*, 140, 74–79. <https://doi.org/10.1016/j.pss.2017.04.008>
- Ruesch, O., Platz, T., Schenk, P., McFadden, L. A., Castillo-Rogez, J. C., Quick, L. C., et al. (2016). Cryovolcanism on Ceres. *Science*, 353(6303), aaf4286. <https://doi.org/10.1126/science.aaf4286>
- Ruesch, O., Quick, L. C., Landis, M. E., Sori, M. M., Cadek, O., Brož, P., et al. (2018). Bright carbonate surfaces on Ceres as remnants of salt-rich water fountains. *Icarus*, 320, 39–48. <https://doi.org/10.1016/j.icarus.2018.01.022>
- Russell, C. T., Raymond, C. A., Ammannito, E., Buczkowski, D. L., Sanctis, M. C. D., Hiesinger, H., et al. (2016). Dawn arrives at Ceres: Exploration of a small, volatile-rich world. *Science*, 353(6303), 1008–1010. <https://doi.org/10.1126/science.aaf4219>
- Schmedemann, N., Kneissl, T., Neesemann, A., Stephan, K., Jaumann, R., Krohn, K., et al. (2016). Timing of optical maturation of recently exposed material on Ceres. *Geophysical Research Letters*, 43, 11,987–11,993. <https://doi.org/10.1002/2016GL071143>
- Schmidt, B. E., Hughson, K. H. G., Chilton, H. T., Scully, J. E. C., Platz, T., Nathues, A., et al. (2017). Geomorphological evidence for ground ice on dwarf planet Ceres. *Nature Geoscience*, 10(5), 338–343. <https://doi.org/10.1038/ngeo2936>
- Schorghofer, N., Mazarico, E., Platz, T., Preusker, F., Schröder, S. E., Raymond, C. A., & Russell, C. T. (2016). The permanently shadowed regions of dwarf planet Ceres. *Geophysical Research Letters*, 43, 6783–6789. <https://doi.org/10.1002/2016GL069368>
- Schulson, E. M. (2010). The fracture of water ice Ih: A short overview. *Meteoritics & Planetary Science*, 41(10), 1497–1508. <https://doi.org/10.1111/j.1945-5100.2006.tb00432.x>
- Schultz, P. H. (1976). Floor-fractured lunar craters. *The Moon*, 15(3-4), 241–273. <https://doi.org/10.1007/BF00562240>
- Scully, J. E. C., Bowling, T., Bu, C., Buczkowski, D. L., Longobardo, A., Nathues, A., et al. (2019). Synthesis of the special issue: The formation and evolution of Ceres' Occator crater. *Icarus, Occator Crater on Ceres*, 320, 213–225. <https://doi.org/10.1016/j.icarus.2018.08.029>
- Scully, J. E. C., Buczkowski, D. L., Schmedemann, N., Raymond, C. A., Castillo-Rogez, J. C., King, S. D., et al. (2017). Evidence for the interior evolution of Ceres from geologic analysis of fractures. *Geophysical Research Letters*, 44, 9564–9572. <https://doi.org/10.1002/2017GL075086>
- Sharpton, V. L. (2014). Outcrops on lunar crater rims: Implications for rim construction mechanisms, ejecta volumes and excavation depths. *Journal of Geophysical Research: Planets*, 119, 154–168. <https://doi.org/10.1002/2013JE004523>
- Sizemore, H. G., Platz, T., Schorghofer, N., Prettyman, T. H., de Sanctis, M. C., Crown, D. A., et al. (2017). Pitted terrains on (1) Ceres and implications for shallow subsurface volatile distribution. *Geophysical Research Letters*, 44, 6570–6578. <https://doi.org/10.1002/2017GL073970>
- Sizemore, H. G., Schmidt, B. T., Buczkowski, D. L., Sori, M., Castillo-Rogez, J., Berman, D., et al. (2018). A global inventory of ice-related morphological features on dwarf planet Ceres: Implications for the evolution and current state of the cryosphere. *Journal of Geophysical Research: Planets*, 123. <https://doi.org/10.1029/2018JE005699>
- Sturm, S., Kenkmann, T., & Hergarten, S. (2016). Ejecta thickness and structural rim uplift measurements of Martian impact craters: Implications for the rim formation of complex impact craters. *Journal of Geophysical Research: Planets*, 121, 1026–1053. <https://doi.org/10.1002/2015JE004959>
- Walsh, P., & Schultz-Ela, D. D. (2003). Mechanics of graben evolution in Canyonlands National Park, Utah. *Geological Society of America Bulletin*, 115, 259–270. [https://doi.org/10.1130/0016-7606\(2003\)115<0259:MOGEIC>2.0.CO;2](https://doi.org/10.1130/0016-7606(2003)115<0259:MOGEIC>2.0.CO;2)
- Williams, D. A., Kneissl, T., Neesemann, A., Mest, S. C., Palomba, E., Platz, T., et al. (2018). The geology of the Kerwan quadrangle of dwarf planet Ceres: Investigating Ceres' oldest, largest impact basin. *Icarus*, 316, 99–113. <https://doi.org/10.1016/j.icarus.2017.08.015>
- Yasui, M., Schulson, E. M., & Renshaw, C. E. (2017). Experimental studies on mechanical properties and ductile-to-brittle transition of ice-silica mixtures: Young's modulus, compressive strength, and fracture toughness. *Journal of Geophysical Research: Solid Earth*, 122, 6014–6030. <https://doi.org/10.1002/2017JB014029>

**2.1.4 Michalik et al. (2021)**

Michalik, T., Matz, K.-D., Schröder, S., Jaumann, R., Stephan, K., Krohn, K., Preusker, F., Raymond, C., Russell, C., & Otto, K. A. (2021). The Unique Spectral and Geomorphological Characteristics of Pitted Impact Deposits Associated with Marcia Crater on Vesta. *Icarus*, 369, 114633. <https://doi.org/10.1016/j.icarus.2021.114633>.

The research leading to this article was conducted by T. Michalik. I provided support on the data illustration, interpretation and establishing the formation mechanism for pitted impact deposits, as well as the manuscript writing. K.-D. Matz and F. Preusker generated the data products needed for this research. S. E. Schröder and K. Stephan assisted in the spectral analyses and R. Jaumann, K. Krohn and I helped with the geologic interpretation. R. Jaumann, C. A. Raymond and C. T. Russell led the instrument and mission management. All authors assisted with refining the manuscript.





## The unique spectral and geomorphological characteristics of pitted impact deposits associated with Marcia crater on Vesta

T. Michalik<sup>a,\*</sup>, K.-D. Matz<sup>a</sup>, S.E. Schröder<sup>a</sup>, R. Jaumann<sup>b</sup>, K. Stephan<sup>a</sup>, K. Krohn<sup>a</sup>, F. Preusker<sup>a</sup>, C.A. Raymond<sup>c</sup>, C.T. Russell<sup>d</sup>, K.A. Otto<sup>a</sup>

<sup>a</sup> German Aerospace Center (DLR e.V.), Rutherfordstr. 2, 12489 Berlin, Germany

<sup>b</sup> Institute of Geological Sciences, Freie Universität Berlin, Malteserstr. 74-100, 12249 Berlin, Germany

<sup>c</sup> Jet Propulsion Laboratory, California Institute of Technology, Pasadena, CA, USA

<sup>d</sup> Department of Earth, Planetary, and Space Sciences, University of California Los Angeles, Los Angeles, California, USA

### ARTICLE INFO

#### Keywords:

Asteroid Vesta  
Asteroids  
Surfaces  
Spectroscopy  
Geological processes

### ABSTRACT

The occurrence of pitted impact deposits (PIDs) and widespread OH-bearing minerals on the differentiated asteroid Vesta shows that volatiles delivered by exogenic sources play an important role for surface appearance and processes on airless bodies. The young, large crater Marcia features widely spread PIDs in its crater-fill and ejecta deposits. In order to derive more details on their formation, we studied the spectral and geomorphological properties of PIDs associated with Marcia. Our observations imply that the formation of PIDs is linked to topography-controlled accumulation of ejecta and the accompanying increase of deposit thickness as well as internal heat. This is best illustrated where PIDs are located within pre-existing craters (i.e., pre-Marcia), enabling the estimation of pre-impact topography and deposit thickness.

Previous studies reported a lower than average reflectance at visible wavelengths for the crater-fill PIDs, which we confirm. However, several PIDs outside the crater exhibit higher reflectance and pyroxene band strength than the average Vesta and the majority of PIDs exhibit higher reflectance and pyroxene band strength with respect to their immediate surroundings (which belong to the same impact deposit). Furthermore, at least six PIDs (many are ambiguous) show resolvable, diminished absorption bands at 2.8  $\mu\text{m}$ , corresponding to a depletion in OH. These spectral observations are most consistent with less contamination by exogenic carbonaceous chondrite materials, i.e., a loss of hydroxyl groups as well as dark components. Our observations are inconsistent with differences in grain size, pyroxene composition, glass content or age-related differences. Regarding reflectance at 750 nm and pyroxene band depth (750/917 [nm]), we present a unique spectral trend for PIDs with respect to 'typical Vestan' materials, suggesting a likewise unique formation process occurring on this asteroid. The crater-fill PIDs display ambiguous spectral characteristics that we attribute to post-impact inflow of dark material from the crater rim. PIDs are ubiquitous in the Marcia region (>100 individual clusters). Yet volatiles lost at these sites might only represent a minor fraction (<2%) of volatiles still present in the host ejecta. An average PID only lost ~1 wt% of volatiles upon devolatilization, implying that exceptionally high volatile contents are not critical for PID formation on Vesta.

## 1. Introduction

### 1.1. Crater-related pitted material

Crater-related pitted materials/terrains are relatively newly recognized geomorphologic features associated with the best-preserved craters on Mars as well as on Vesta and Ceres and are linked to the loss of volatiles (Tornabene et al., 2007; Tornabene et al., 2012; Boyce et al.,

2012; Denevi et al., 2012; Sizemore et al., 2017). These pitted materials/terrains consist of polygonal to circular depressions and generally occur in dense clusters within crater-fill, terrace and exterior impact deposits as well as channelized flows. Individual pits lack evidence of ejecta deposits and only show subtle raised rims or a complete lack thereof. The size of individual pits ranges from tens of meters to a few kilometers (Tornabene et al., 2012; Denevi et al., 2012; Sizemore et al., 2017) and parent crater diameters vary between ~1 and 150 km (Tornabene et al.,

\* Corresponding author.

E-mail address: [tanja.michalik@dlr.de](mailto:tanja.michalik@dlr.de) (T. Michalik).

<https://doi.org/10.1016/j.icarus.2021.114633>

Received 7 September 2020; Received in revised form 22 June 2021; Accepted 23 July 2021

Available online 27 July 2021

0019-1035/© 2021 Elsevier Inc. All rights reserved.

2012; Denevi et al., 2012; Sizemore et al., 2017). The term ‘parent crater’ is used here to distinguish between (genetically unrelated, pre-existing) craters that merely host a pitted terrain vs. the crater whose formation led to the creation of these geomorphological features.

Pitted materials on Mars have been recognized as primary impact deposits earlier by Tornabene et al. (2007). Yet it was the extensive survey of more than 200 craters on Mars by Tornabene et al. (2012) that confirmed the primary impact-related nature of these geomorphologic features with the pits representing volatiles escaping from a non-ambient and possibly melt-rich deposit. This and the study by Boyce et al. (2012) revealed more insights in the formation mechanism, the relationship to the host deposit and parent crater, age, as well as global distribution and abundance. They found that pitted materials occur preferentially in mid-latitudes suggesting a dependence on the water/ice-silicate ratio as volatile content increases with latitude on Mars. Furthermore, pit size as well as cluster extent positively correlate with parent crater size as do preservation states of pitted materials and their parent craters. Additionally, similarities to the impact melt-bearing breccia suevite at the Ries impact structure in Germany were concluded as both target materials are/were volatile-rich (e.g., Newsom et al., 1986; Tornabene et al., 2007; Tornabene et al., 2012; Boyce et al., 2012). Tornabene et al. (2012) inferred that the pitted materials on Mars and their host deposits most likely resemble impact melt-bearing breccias. Within the suevite outside of the Ries crater, ‘chimney-like degassing pipes’ were identified (e.g., Engelhardt, 1972; Newsom et al., 1986) which suggests devolatilization after suevite deposition. The pitted materials on Mars could thus result from the formation of similar vents through the host deposit.

Evidence for pitted terrains on asteroid Vesta was firstly presented by Denevi et al. (2012) shortly after NASA’s Dawn mission arrived at this second largest object in the inner asteroid belt. They found striking similarities to the pitted materials observed on Mars and concluded a similar explosive devolatilization process for these Vestan features. Dawn went on to its next target, Ceres, and Sizemore et al. (2017) likewise presented a detailed survey of pitted terrains on the dwarf planet’s surface. They found that Cerean pitted terrains strongly resemble those on Vesta and Mars and accordingly inferred a rapid post-impact formation model. The pitted terrains’ formation models for Vesta and Ceres are based on the extensive analysis from Tornabene et al. (2012) and Boyce et al. (2012) for Mars. However, for the intriguing crater Occator on Ceres (largest well-preserved crater showing ‘bright’ spots), Schenk et al. (2020) found that volatile-related pits are in general less common and distinct from the densely clustered pits observed on Mars. Similar to the lack of pitted materials in high latitudes on Mars (Tornabene et al., 2012), this might result from (too) high volatile contents in the crust (up to ~60% ice and clathrates, Ermakov et al., 2017; Fu et al., 2017). Sizemore et al. (2017) linked Cerean pit formation to available volatiles in the regolith whose source could either be minerals and ice (see also e.g., De Sanctis et al., 2015a; Combe et al., 2016). This is still under debate for Vesta (Denevi et al., 2012; Scully et al., 2015) and will be addressed later on.

The detailed studies of the pitted materials on all three bodies revealed that they clearly represent primary impact-related geomorphologic features and that they are best-preserved where their host craters are also well-preserved. This is why from now on we will refer to the pitted materials/terrains as ‘pitted impact deposits’ (PIDs), which was already mentioned by Tornabene et al. (2012).

## 1.2. Vesta, its surface regolith and pitted impact deposits

Vesta is thought to have fully differentiated (e.g., McCord et al., 1970; Larson and Fink, 1975; Consolmagno and Drake, 1977; Ruzicka et al., 1997; Keil, 2002; Mittlefehldt, 2015; and references therein), losing volatile species in the process. The evidence for the differentiation of Vesta arises from its strong connection to the HED meteorites (howardite, eucrite, diogenite). This suite of meteorites comprises

achondritic igneous rocks that display the upper range of a differentiated body: ultramafic rocks composed of Magnesium-rich orthopyroxenes (diogenites), crustal cumulates and basalts (eucrites) as well as surface regolith (howardites; e.g., Mittlefehldt, 2015 and references therein). The HED-Vesta connection is based on the distinct pyroxene-dominated reflectance spectrum of these objects (McCord et al., 1970) and was confirmed by numerous studies that employed data from NASA’s Dawn mission (e.g., Reddy et al., 2012b; De Sanctis et al., 2012a; De Sanctis et al., 2013; Ammannito et al., 2013a; Prettyman et al., 2012; Thangjam et al., 2013). The discovery of ‘pitted terrains’ (Denevi et al., 2012), transient water flow (Scully et al., 2015), widespread hydrated materials (De Sanctis et al., 2012b) as well as exogenic hydrogen (Prettyman et al., 2012) was therefore surprising.

The Dawn mission moreover revealed that a ‘dark’ surface component mixed within the regolith obscures the Vestan reflectance spectrum at numerous locations (e.g., Jaumann et al., 2014; Stephan et al., 2014) and over a large area extending from an equatorial region to the north pole (roughly 200,000 km<sup>2</sup>, between 70°E to 220°E and 30°N to 30°S; e.g., De Sanctis et al., 2012b; Combe et al., 2015). The reflectance spectra at these sites show decrease of reflectance at visible wavelengths and diminishment of absorption features in contrast to ‘bright’ areas on Vesta (e.g., Zambon et al., 2014). Several studies (e.g., McCord et al., 2012; Reddy et al., 2012a; Cloutis et al., 2013a; Nathues et al., 2014) suggest that this darkening agent most likely originates from the infall of carbonaceous chondrites (possibly CM-type) over geological time scales. This exogenic contamination is important when considering the delivery of water through the solar system. As we have learned from Dawn, even differentiated objects can hold considerable amounts of ‘water’ within their regolith which influences the asteroids’ surface geology.

On Vesta, currently only four parent craters show PIDs (Marcia, Cornelia, Numisia, Licinia; Denevi et al., 2012), of which only two are undoubtedly occurrences (Marcia and Cornelia). Marcia is the only crater featuring PIDs beyond its crater rim (Denevi et al., 2012), though this might be an observational bias due to limited image resolution. The (observable) occurrences associated with Marcia crater account for ~96% of all PIDs on the asteroid (this study). Calpurnia crater adjacent to Marcia could also be the parent crater for some of the PIDs (i.e., PIDs originating from Calpurnia impact deposits), which would add another parent crater to the suite on Vesta. Yet in this study we consider the PIDs in this area as one occurrence, which will be addressed in more detail later on. Calpurnia and Cornelia are well-preserved craters nearby which might have influenced the larger Marcia region studied here (for spatial context see Figs. 2 & 3).

The crater Marcia is situated within the above mentioned spectrally darker extended area (De Sanctis et al., 2012b, 2013; De Sanctis et al., 2015c; Combe et al., 2015) at around 190°E and 10°N (Claudia Coordinate system) and is the best-preserved large crater on Vesta. While the Rheasilvia Basin covering the South Pole is thought to be around 1 or 3.5 Ga old (modelling ages by Marchi et al., 2012 and Schmedemann et al., 2014, respectively), Marcia is the next largest well-preserved crater and considerably younger with a modeled age of ~40 or 390 Ma (Williams et al., 2014b). Marcia has been of high interest to many studies (e.g., Williams et al., 2014a; Williams et al., 2014c; De Sanctis et al., 2015b; De Sanctis et al., 2015c; Denevi et al., 2012; Scully et al., 2015; Keihm et al., 2015) due to its unusual and asymmetric shape, reflectance spectra, thermal properties and geomorphologic features including PIDs as well as gully-like features. Marcia is also the focus of this study due to the remarkable preponderance of PIDs situated in and around this crater.

Marcia is ~58 km wide and 68 km long and possesses a relatively large wall-slump or terrace off the southern rim that also possesses PIDs. Calpurnia and Minucia are two adjacent craters to the NE (Fig. 2a). Marcia and its surroundings exhibit numerous PIDs (we count >100 discrete occurrences). PIDs on Vesta are generally defined as clusters of irregularly shaped, rimless depressions, at times also overlapping with other pits (Denevi et al., 2012) which occur on otherwise smooth

deposits on crater floors, and for Marcia on its southern terrace as well as within its continuous ejecta blanket. Denevi et al. (2012) concluded that the PIDs formed, similarly as on Mars, through explosive volatile outgassing. They suggest that volatile-bearing deposits like those from carbonaceous chondrites have been emplaced in the upper surface of the Vestan crust by pre-Marcia exogenic impactors which subsequently led to the formation of PIDs upon impact of the Marcia impactor. Scully et al. (2015) suggest that icy subsurface deposits could also be responsible for the formation of PIDs, thus the volatile sources for PIDs require further investigation.

The spectral characteristics of PIDs have not been studied in detail yet, except for the PIDs on Marcia's floor. Denevi et al. (2012) and De Sanctis et al. (2015c) both reported that the PIDs on Marcia's floor are darker than the average Vesta and correlated the PIDs with the OH-bearing material prevailing the previously mentioned area that De Sanctis et al. (2012b) described as "OHRT1" (OH-rich terrain). However, not all the PIDs exhibit a generally darker spectrum. Numerous PIDs in Marcia's vicinity exhibit higher reflectance and stronger pyroxene absorptions (i.e. 'purer', with less exogenic contamination) with respect to average Vestan values. Additionally, the 2.8  $\mu\text{m}$  absorption band is weaker at some of the PIDs' sites (consistent with a depletion in OH) with respect to their immediate surroundings.

Our overall objective is to build and expand upon the geomorphological and spectral observations of PIDs on Vesta to: 1) test and place further constraints on the existing hypotheses explaining the origin and emplacement of PIDs, and (2) gain insight into the physical and/or petrological changes that material underwent while rapidly losing volatiles.

We present an extended map of PIDs and analyze the local geomorphological setting of the PIDs in more detail to see if they are consistent with previous observations that support an impact origin for these materials. While Denevi et al. (2012) report that PIDs often occur in topographic lows, a detailed analysis has not yet been undertaken. We also present detailed spectral characteristics of PIDs and their surroundings which have not been reported yet. In this study we use Dawn Framing Camera (FC, Sierks et al., 2011) images, spectral data from the visible and infrared spectrometer (VIR, De Sanctis et al., 2011; Combe et al., 2015) as well as comparisons with meteoritic spectral data.

## 2. Data sets and methods

### 2.1. Dawn's Framing Camera at Vesta

This study's main observations are derived from data collected by the Dawn Framing Camera (FC). The FC has one panchromatic clear filter and seven narrowband color filters in the visible and near infrared ( $\sim 0.43\text{--}0.97\ \mu\text{m}$ , Sierks et al., 2011). The filters of the FC focus on the visible and near infrared wavelength region as Vesta's surface mineralogy is dominated by pyroxenes, showing a distinct iron absorption band at  $\sim 0.9\ \mu\text{m}$  (McCord et al., 1970). All maps shown here are based on the Claudia coordinate system (Russell et al., 2012; Supplementary Text) and presented in equidistant projection orientated with north towards the top. The FC mosaics are photometrically corrected to I/F at  $i = 30^\circ$ ,  $e = 0^\circ$ , and  $p = 30^\circ$  (incidence, emission and phase angle, respectively), using the Akimov function as described in Schröder et al. (2014). We will use the term 'reflectance' for the photometrically corrected I/F throughout this study. Clear filter images for geomorphological observations are depicted at LAMO resolution (Low Altitude Mapping Orbit up to 16 m/px, Roatsch et al., 2013), while the shown RGB composite depicting multispectral information were produced with HAMO resolution (High Altitude Mapping Orbit  $\sim 60$  m/px, Roatsch et al., 2012), which is the highest resolution with complete filter coverage.

In the past, studies using Dawn FC data commonly employed the Clementine-type RGB composite introduced by Pieters et al. (1994) for the lunar data set obtained during the Clementine mission. The

Clementine-type RGB composite include the following ratios for the respective channels:  $R = 750/415$  [nm],  $G = 750/950$  [nm],  $B = 415/750$  [nm], and were used for Vesta in e.g. Reddy et al. (2012b), Denevi et al. (2012), Le Corre et al. (2013) and Williams et al. (2014a). This composite can give valuable information about the surface composition and/or degree of space weathering (especially on the Moon). The red and blue band ratio in the Clementine-type RGB composite is sensitive to soil maturity (spectral 'reddening' positively correlates with maturity) as well as composition, whereas the green band is sensitive to strength and character of the common mafic absorption near 1  $\mu\text{m}$  caused by the presence of  $\text{Fe}^{2+}$ .

In this study, we use another RGB composite to illustrate compositional and/or physical differences. It is tightly connected to our observations of the PIDs and Vesta in general. As low-Ca orthopyroxenes predominate the Vestan spectra, pyroxene absorption band positions of the Vestan surface vary between  $\sim 920$  and  $935$  nm (Ammannito et al., 2013a; De Sanctis et al., 2013), mostly depending on their Fe/Mg contents. Diogenites generally have pyroxene absorption band positions at shorter wavelengths than eucrites due to higher Mg contents of their orthopyroxenes (see Fig. 1 left panel and e.g., Gaffey, 1976; Mittlefehldt, 2015). Therefore, their spectra exhibit higher 965/917 [nm] values than eucrites, while howardites are in between. We therefore use the 965/917 [nm] ratio for the red channel as it is the most significant parameter in order to distinguish between the main Vestan rock types diogenites and eucrites, which was previously described in Le Corre et al. (2011), Reddy et al. (2012b) and Thangjam et al. (2013).

The reflectance of HEDs and Vestan spectra is generally at its highest around 750 nm, before it drops due to the absorption of electromagnetic energy by the iron-bearing pyroxene (see Fig. 1, left panel). As pyroxene absorption band positions on Vesta are closest to the 917 nm filter of the FC, the ratio 750/917 [nm] is best suited to characterize the material's pyroxene absorption strength. The PIDs differ from their immediate surrounding foremost in reflectance at 750 nm and pyroxene absorption band strength. Consequently, we chose the green and blue band of our RGB composite accordingly (750 nm and 750/917 [nm], respectively).

In summary, cyan colors in the applied RGB composite denote higher reflectance and pyroxene absorption band strength. We emphasize that all images of this RGB composite use the same stretch while the standard deviation stretch type with  $n = 1.3$  showed the best results with respect to the perception of the viewer. We also note that artefacts occur in the HAMO RGB composite as a result of the mosaicking process (along single image boundaries) and due to missing or incomplete data, e.g. in shadowed areas.

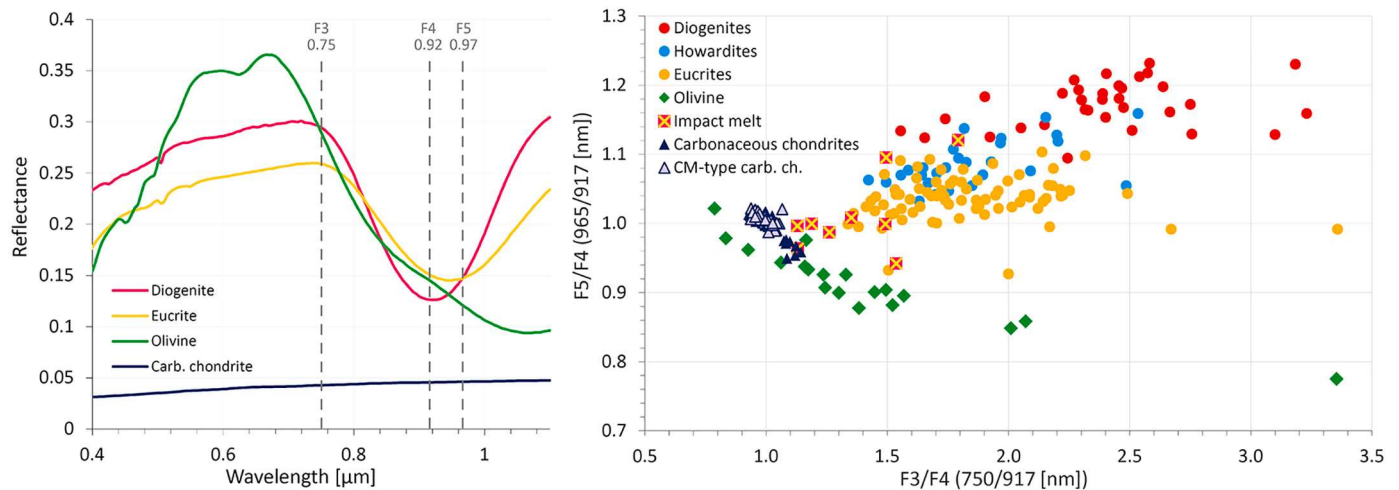
The Digital Terrain Model (DTM) by (Preusker et al., 2014, 2016) was modified by including LAMO images and implementing a triaxial ellipsoid ( $286 \times 279 \times 223$  [km]) in order to reach the most realistic approximation to the actual geophysical altitudes and their relations. With a lateral resolution of  $\sim 70$  m/px and a vertical accuracy of  $\sim 6$  m, the DTM helps to examine the topographic context of the PIDs. No vertical exaggeration was applied. In addition to FC data, we use the VIR-derived 2.8  $\mu\text{m}$  absorption band depth distribution map generated by Combe et al. (2015) in order to evaluate the OH content of relevant locations. In contrast to the RGB composite, we use a dynamic range adjustment in displaying this data which is especially important regarding Fig. 11. This map has an approximate resolution of  $\sim 200$  m/px.

### 2.2. RELAB spectral data

We used HED as well as carbonaceous chondrite and olivine spectral data for comparative observations. These data were obtained from the RELAB database at the Brown University, which is publicly available under:

[http://www.planetary.brown.edu/relabdocs/relab\\_disclaimer.htm](http://www.planetary.brown.edu/relabdocs/relab_disclaimer.htm).

In order to compare the meteorite spectra with space craft camera data, the meteorite spectra were resampled to fit the format of the



**Fig. 1.** Left panel: Wavelengths vs. Reflectance of four different rock types. Dashed vertical lines indicate filter positions of the FC filters used in this study. Diogenite = Elmeett (ID bkr1mp113), eucrite = ALHA81011 (ID bkr1mp122), olivine from Chassigny (ID bkr1dd001) and Carbonaceous chondrite = Mighei (ID bkr1ma062). Right panel: 750/917 [nm] vs. 965/917 [nm] for resampled RELAB meteorite and olivine data.

responsivity functions of the respective filter (Sierks et al., 2011). The resampling of the RELAB meteorite spectra occurred as follows:

$$R_{mfc}(\lambda) = \int R_m r_i(\lambda) d\lambda / \int r_i(\lambda) d\lambda \quad (1)$$

where  $R_{mfc}$  is the reflectance value of the resampled meteorite spectrum for the respective filter,  $R_m$  is the original reflectance of the meteorite spectrum obtained in the laboratory,  $r_i$  is the responsivity function for each filter and  $\lambda$  is the respective FC filter wavelength.

In total, data from 239 RELAB spectra are used in this study, with 142 being from HED meteorites and 82, 33 and 27 spectra from eucrites, diogenites and howardites, respectively. Many meteorites were measured multiple times, e.g. because different grain sizes were measured or powders vs. slabs. We incorporate everything in order to display a great diversity. In total, the following quantities of actual meteorites were measured: 44 eucrites, 16 howardites and 14 diogenites. Only seven samples of our database are official Antarctic pairings of which one is a eucrite, four are howardites and two belong to the impact melt samples. We display all of those as we want to display a great variety of possible lithologies. Yet we acknowledge that unidentified pairing might further decrease the number of actually measured meteorites.

Other spectra used here include the mineral olivine (19, various compositions, see Table S1) as well as carbonaceous chondrites (69 spectra from 44 individual carbonaceous chondrites). Zolensky et al. (1996) analyzed clast contents of HEDs and found a remarkable predominance of CM2 carbonaceous chondrites (~81%). Therefore, we mainly used spectra derived from CM-type chondrites, which are distinguished within the carbonaceous chondrite data points in Fig. 1. We also included spectral data of impact melts (9) originating from howardites, eucrites, ordinary chondrites and an unclassified object. Spectra IDs and corresponding meteorite names are given in the supplementary material (Table S1).

Fig. 1 displays the resampled meteorite data for the two most significant parameters (750/917 [nm] vs. 965/917 [nm], right panel) to distinguish different lithologies on Vesta (i.e., howardites, eucrites, diogenites and olivine-rich regions as well as areas contaminated by 'dark material'). These ratios are especially sensitive to the pyroxene absorption band position and the band strength, which are the main FC-covered spectral variations observed on Vesta (Fig. 1 and e.g., Le Corre et al., 2011; Reddy et al., 2012b; Thangjam et al., 2013). The left panel of Fig. 1 illustrates four representative spectra of a diogenite (red), eucrite (yellow), olivine (green) and carbonaceous chondrite (dark blue)

and the relevant filter positions (grey dashes). This Figure best illustrates the differences of eucrites and diogenites in terms of pyroxene band position and its effect on the ratio 965/917 [nm] as previously described. In Section 3.4, the right panel of Fig. 1 will serve for comparisons with Vestan FC data, which are extracted for different locations from global HAMO mosaics. As there is no uncertainty available for the RELAB measurements, we do not apply any error bars to the data points and as the data are displayed as ratios, possible systematic uncertainties regarding the measurements or the responsivity functions are cancelled out. The instrument error of the RELAB spectrometer is given as 0.25% which is smaller than the data points' symbols in Fig. 1.

We did not use all suitable spectra from the RELAB database. Eucrites with a known oxygen isotopic anomaly (PCA91007, A-881394, Pasamonte, GRA 98098, EET 87542, PCA 82502, NWA 011; Scott et al., 2009; Mittelfeldt et al., 2016) were excluded from the original dataset as they possibly originate from another object (Scott et al., 2009; Mittelfeldt et al., 2016). Furthermore, we excluded samples where distinct "bright" or "dark" spots of the meteorite were measured (mentioned in the comment column of the RELAB sample catalog).

Terrestrial weathering can alter a meteorite significantly, depending on its original mineralogy and the time and place spent on Earth. In particular, the most common changes due to weathering appear as the formation of iron (oxy-) hydroxides and water-bearing phases. The reflectance spectrum of a meteorite can therefore also be affected, which especially applies for meteorites that were found on Earth in contrast to observed falls that have not experienced prolonged terrestrial weathering. Iron oxyhydroxides strongly absorb in the ultraviolet region and water-bearing phases add, among others, an absorption near 3 μm (Salisbury and Hunt, 1974). Thus, they do not affect the wavelength area of the pyroxene absorption, which is studied here.

We still investigated a possible influence of weathering and identified falls and finds among our meteorite samples as well as the weathering grade of finds (where available, source: Meteoritical Bulletin, publicly available under <https://www.lpi.usra.edu/meteor/>). We plotted the different meteorite types according to these data and found no influence of weathering on the used FC-based filter ratios (750/917 [nm] and 965/917 [nm]). Furthermore, we confirmed this observation by using the Salisbury and Hunt (1974) approach. They showed for various meteorites that the 500/600 [nm] slope positively correlates with the formation of a water band at 3 μm, which develops under the oxidizing conditions on Earth. We therefore used the 500/600 [nm] ratio to confirm that the meteorites we used are not significantly affected by terrestrial weathering. The respective plots for each



meteorite type separated into falls and finds can be found in the supplementary material (S2).

Thirteen more meteorite spectra were used to investigate the influence of particle size on the spectral parameters displayed here, which will be discussed in Section 4. These meteorite data were provided by Dr. Edward Cloutis and measured at the University of Winnipeg's Planetary Spectrophotometer Facility (e.g., Cloutis et al., 2013a; Cloutis et al., 2013b). We resampled the spectra according to Eq. (1).

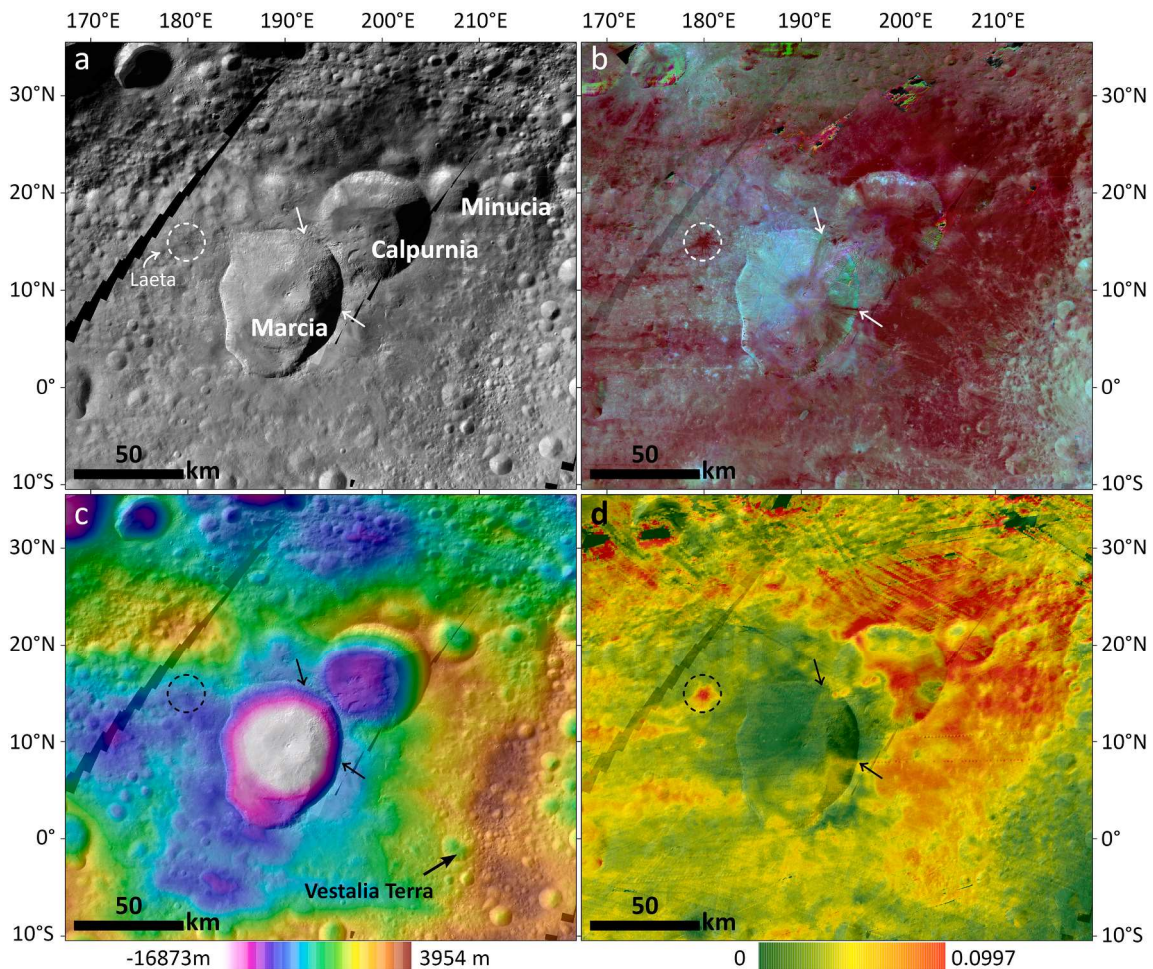
### 3. The PIDs associated with Marcia crater

#### 3.1. Regional overview

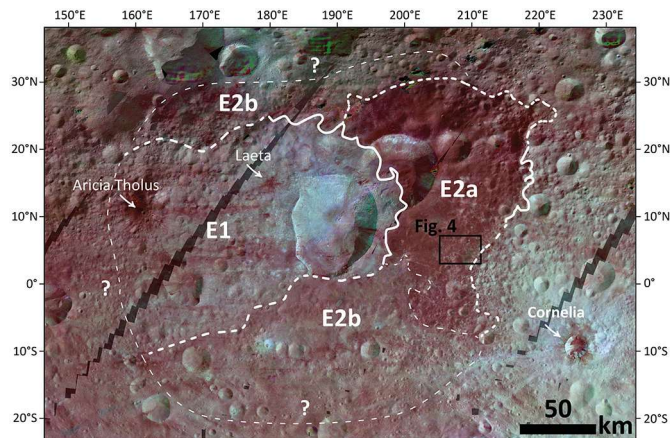
In order to examine the PIDs and identify the process driving the formation of these features, it is necessary to take their surrounding into consideration, especially the spectral and geomorphologic features of Marcia and Calpurnia craters and their ejecta. Fig. 2 displays the broad Marcia region as seen through clear filter LAMO images (a), our HAMO RGB composite (b), DTM data (c) and the 2.8  $\mu\text{m}$  absorption depth (Combe et al., 2015) (d). In Fig. 2b, greenish and cyan colors indicate material with higher reflectance and pyroxene band strength, while red colors indicate regions with lower reflectance and pyroxene band strength values ( $R = 965/917$  [nm],  $G = 750$  nm and  $B = 750/917$  [nm]). In Fig. 2d, dark green colors indicate lower OH content whereas red colors indicate higher OH content.

Fig. 2 illustrates distinct regional differences in spectral and geomorphological properties. In general, regions with higher OH absorptions correlate well with regions of lower reflectance and pyroxene band strength. The NW and center of Marcia crater are strongly depleted in OH with respect to other regions nearby. A few km off the rim in the E and NE, a well-defined boundary between brighter/OH-depleted material and darker/OH-enriched material is visible (Fig. 2b and d). We use this boundary to define two different units of Marcia (and/or Calpurnia) ejecta (Fig. 3): Ejecta unit 1 (E1) is generally higher in reflectance, higher in pyroxene band strength (green/cyan in Fig. 2b) and lower in OH abundance (green in Fig. 2d), while ejecta unit 2 (E2) is lower in reflectance, lower in band strength (reddish in Fig. 2b) and higher in OH abundance (orange/red in Fig. 2d). In E2, pre-existing craters and topography are largely overprinted by Marcia ejecta and hardly recognizable whereas numerous pre-existing craters can be observed in E1, indicating that E1 is thinner than E2.

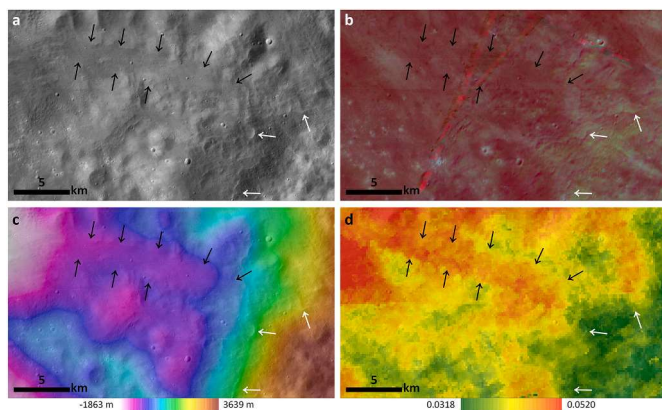
We further subdivided E2 into E2a and E2b, where E2a is strongly influenced by the presence of Vestalia Terra, a mountain range to the east of Marcia (Fig. 2c), and characterized by lobate slope deposits, lobate uphill features as well as lower reflectance/pyroxene band strength and slightly higher OH absorption values than E2b. Fig. 4 illustrates lobate uphill features as well as lobate slope deposits in E2a. E2b does not feature these specifics but is still lower in reflectance and pyroxene band strength than E1 and also shows larger 2.8  $\mu\text{m}$  absorptions band depths than E1. Moreover, the OH-rich spectral signature of



**Fig. 2.** Spatial and spectral context of Marcia crater and its broad surrounding. a) LAMO clear filter data. This is also the base layer for the other panels, b) HAMO RGB composite ( $R = 965/917$  [nm],  $G = 750$  nm and  $B = 750/917$  [nm], 20% transparency), c) DTM (50% transparency), d) VIR 2.8  $\mu\text{m}$  band depth map from Combe et al. (2015) (30% transparency). The arrows just east and northeast of Marcia indicate input of material from the rim into the crater which will be explained later on. Dashed circle NW of Marcia indicates Laeta crater.



**Fig. 3.** Map of the ejecta units E1, E2a and E2b. Clear filter LAMO data overlain by our RGB composite (R = 965/917 [nm], G = 750 nm and B = 750/917 [nm]), 50% transparency). Solid line indicates clear boundary, dashed lines indicate approximate boundaries and faint dashed lines indicate uncertain boundaries. Cornelia crater is displayed in this map on the lower right.



**Fig. 4.** Lobate uphill features (white arrows) and lobate slope deposit (black arrows) in E2a, for spatial context see Fig. 3. a) LAMO clear filter data, b) HAMO RGB composite (R = 965/917 [nm], G = 750 nm and B = 750/917 [nm]), c) DTM (50% transparency) over LAMO clear filter data, d) VIR 2.8  $\mu$ m band depth map from Combe et al. (2015). Straight red lines in b) indicate artefacts from the mosaicking process. (For interpretation of the references to color in this figure legend, the reader is referred to the web version of this article.)

E2a ends quite abruptly near the top of Vestalia Terra and overlaps well with lobate uphill features (Fig. 4d). The high OH abundance is therefore strongly tied to ejecta.

As material of E2a is correlated with thick ejecta, subsequent space weathering processes (Pieters et al., 2012) probably foremost reworked the ejecta and not pre-existing regolith. Therefore, spectral characteristics of this ejecta unit might still be very similar to the characteristics of the original ejecta. Table 1 summarizes the spectral properties of the presented three ejecta units and displays that, in comparison with the whole Vesta, Marcia (and Calpurnia) ejecta are generally darker and richer in OH than the average of Vesta (as observed before by De Sanctis et al., 2012b and Combe et al., 2015). Data for E1 in Table 1 do not include areas obviously contaminated by dark material (e.g. Laeta crater within E1, dashed circle in Fig. 2; Jaumann et al., 2014).

Fig. 3 displays E1, E2a and E2b mapped over clear filter LAMO images and faint overlain HAMO RGB composite. Laeta crater NW of Marcia excavated dark material with the same spectral characteristics as E2a, suggesting that E1 superposes E2a. The spectral signatures of E1 and E2b gradually attenuate to the west, south and north. The boundary

**Table 1**

750 nm reflectance, 750/917 [nm] and 2.8  $\mu$ m band depth values (from Combe et al., 2015) of E1, E2a and E2b. Values are given with one standard deviation.

	Mean 750 nm reflectance	Mean 750/917 [nm]	Mean 2.8 $\mu$ m band depth	n (pixel number)
E1	$0.185 \pm 0.010$	$1.443 \pm 0.042$	$0.031 \pm 0.003$	755,550
E2a	$0.142 \pm 0.012$	$1.291 \pm 0.114$	$0.048 \pm 0.006$	1,675,878
E2b	$0.161 \pm 0.014$	$1.346 \pm 0.041$	$0.038 \pm 0.006$	1,918,785
whole Vesta	$0.194 \pm 0.034$	$1.455 \pm 0.133$	$0.030 \pm 0.009$	$3.56 \times 10^8$

we mapped in these regions is approximate and based on lobate features that we observed and interpret as ejecta flow fronts (similar to the example in Fig. 4a, white arrows). The extent of Marcia and Calpurnia ejecta is larger than what was mapped by Williams et al. (2014a) on the basis of geomorphologic observations at a resolution of 260 m/px (Survey orbit).

It is still under debate whether the OH-rich ejecta unit (E2a) results from the Calpurnia or Marcia impact. The spectrally very different ejecta units E1 and E2a clearly suggest different origins. However, the relationships of E1 and E2a are not easily unraveled. For example, E1 clearly appears to superpose E2a (e.g., as seen at Laeta crater and within Calpurnia), yet just east of Marcia, material from E2a seems to merge into E1 and overprint it. The extent of E2a favors an origin in the older crater Calpurnia, yet the shape of the Vestalia Terra highlands coincide with the shape of the OH-rich and dark margin of E2a, possibly leading to the current shape by coincidence and thus questioning Calpurnia as the origin of E2a. Moreover, there are no PIDs occurring north of Calpurnia. Furthermore, E2b spectrally appears as a mixture between E1 and E2a and its extent is not readily explained by two craters forming at different times. In summary, we are fairly confident that the majority of E1 materials originate from the Marcia-forming impact event, yet we are less confident that all of E2 can be assigned to Marcia and may actually originate from Calpurnia. This would also suggest a possible oblique impact angle for the Marcia projectile, as E1 is distributed asymmetrically around the crater.

While it is likely that at least E2a originates from Calpurnia, we will refer to all PIDs in this area as one large occurrence. As all of the ejecta units appear well-preserved, a large age difference between different PIDs and therefore different preservation states can be excluded. Modeled ages from crater-counting methods could not show definite age differences between these different ejecta units (Williams et al., 2014b, Appendix A), though model age determination shows an increased uncertainty for ‘young’ ejecta blankets (e.g., Williams et al., 2018). It might also be plausible that the Calpurnia and Marcia impactors once built a binary object with different compositions, impacting on Vesta nearly simultaneously with the Calpurnia impactor hitting just before the Marcia impactor. This could also explain the mobility of E2a, slumping into Marcia crater after its final formation as well as the ‘intermediate’ ejecta unit E2b. While the distinction of ejecta units is important for our observations, the determination of the parent crater of PIDs in the broad Marcia region is not a key element in this study and independent from our findings. This is why we will only address this marginally.

Fig. 5 displays our mapped PIDs and indicates craters that existed prior to Marcia and now host PIDs in blue circles. We mapped in total 118 individual PIDs. Some PIDs might be part of a bigger cluster or could be subdivided into smaller units as identification of boundaries is limited due to the given image resolution. 41 of the 118 PIDs mapped are located in E1, 21 in E2a and 39 in E2b. The remaining PIDs are situated within the crater. Additionally, we identified 13 pre-existing craters that host one or more PIDs (excluding the large craters Calpurnia and Minucia). Nine of those craters are situated in E1 and four of these craters in E2b. More details will be discussed and shown in Section 3.2. Fig. 5b, c



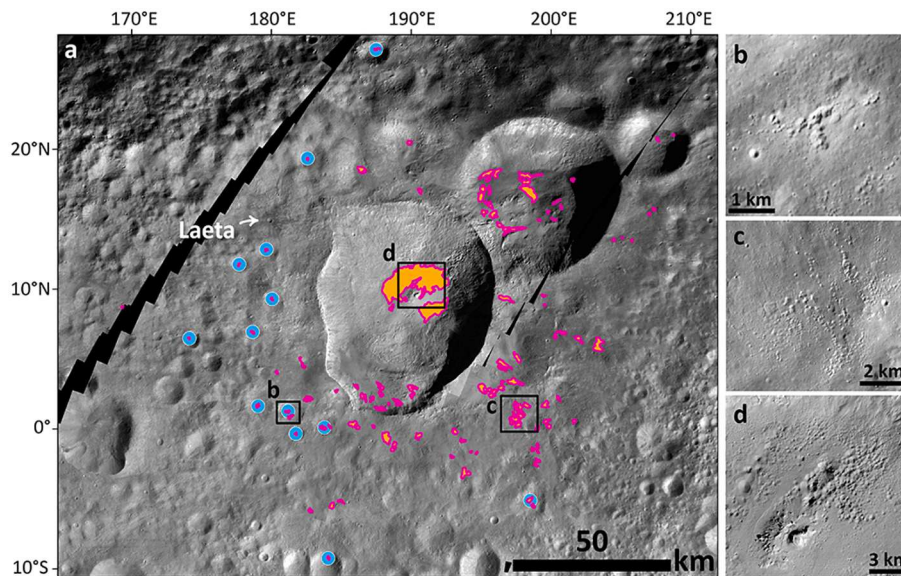


Fig. 5. a) Distribution map of PIDs (in total 118 individual terrains) associated with Marcia ejecta (LAMO clear filter). Blue dots denote small craters housing PIDs which will be described in Section 3.2. b), c) and d) examples of PIDs. b) is situated within E1, c) is situated within E2b and d) is part of the crater-fill PIDs. (For interpretation of the references to color in this figure legend, the reader is referred to the web version of this article.)

and d display high-resolution examples of PIDs whereas 5b is situated in E1, 5c in E2b and 5d is part of the crater-fill PIDs. In this study, we refer the term ‘crater-fill’ only to the PIDs around Marcia’s central peak and not to PIDs on the mentioned southern terrace of Marcia (see Fig. 5 for spatial context) as this material most likely represents material thrown out of the transient cavity during crater formation before the crater wall collapsed. Fig. 6 serves as spatial orientation for close-up images presented in the following sections.

### 3.2. Geomorphological characterization of the PIDs

Identifying a PID on the basis of its visual appearance is not trivial as

a range of possible morphologies indicating volatile loss can be observed within the ejecta blanket of Marcia. PIDs have been defined as clusters of individual, irregular shaped, rimless pits (Tornabene et al., 2012; Denevi et al., 2012). However, already the identification of a cluster of pits is challenging on Vesta. Fig. 7a displays an example of ‘possible’ PIDs. The pits are not densely clustered but rather individually located in each other’s vicinity and could therefore also represent secondary cratering or later impacts. Limited image resolution prevents an analysis of single pit and potential ejecta morphology. A secondary impact origin (i.e., post-Marcia) can therefore not be excluded for these pits although they appear to only occur in smooth deposits as do the PIDs. Moreover, their spectral characteristics are also consistent with PIDs (i.e., cyan colors in

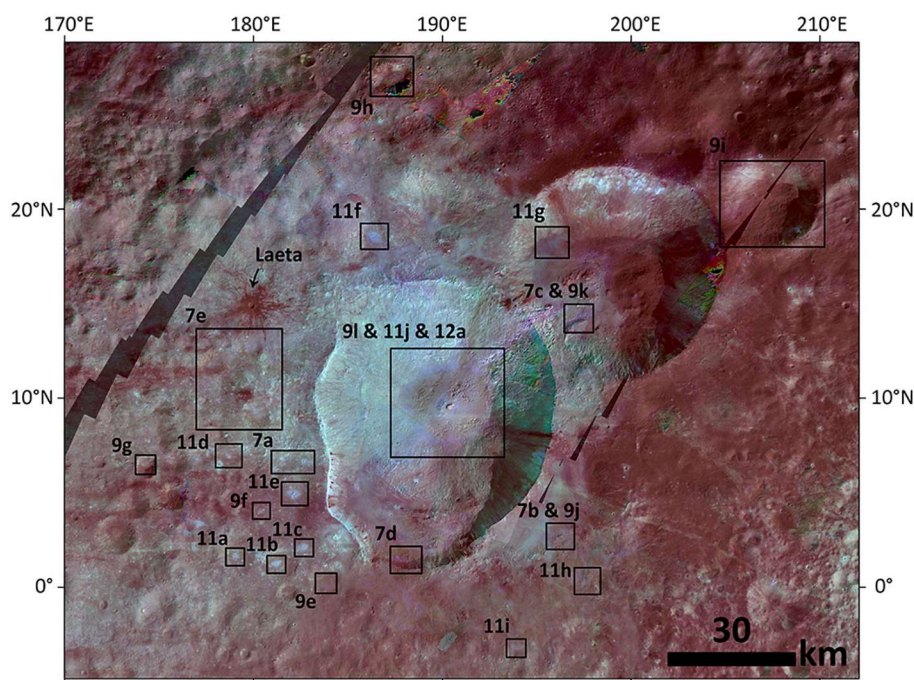
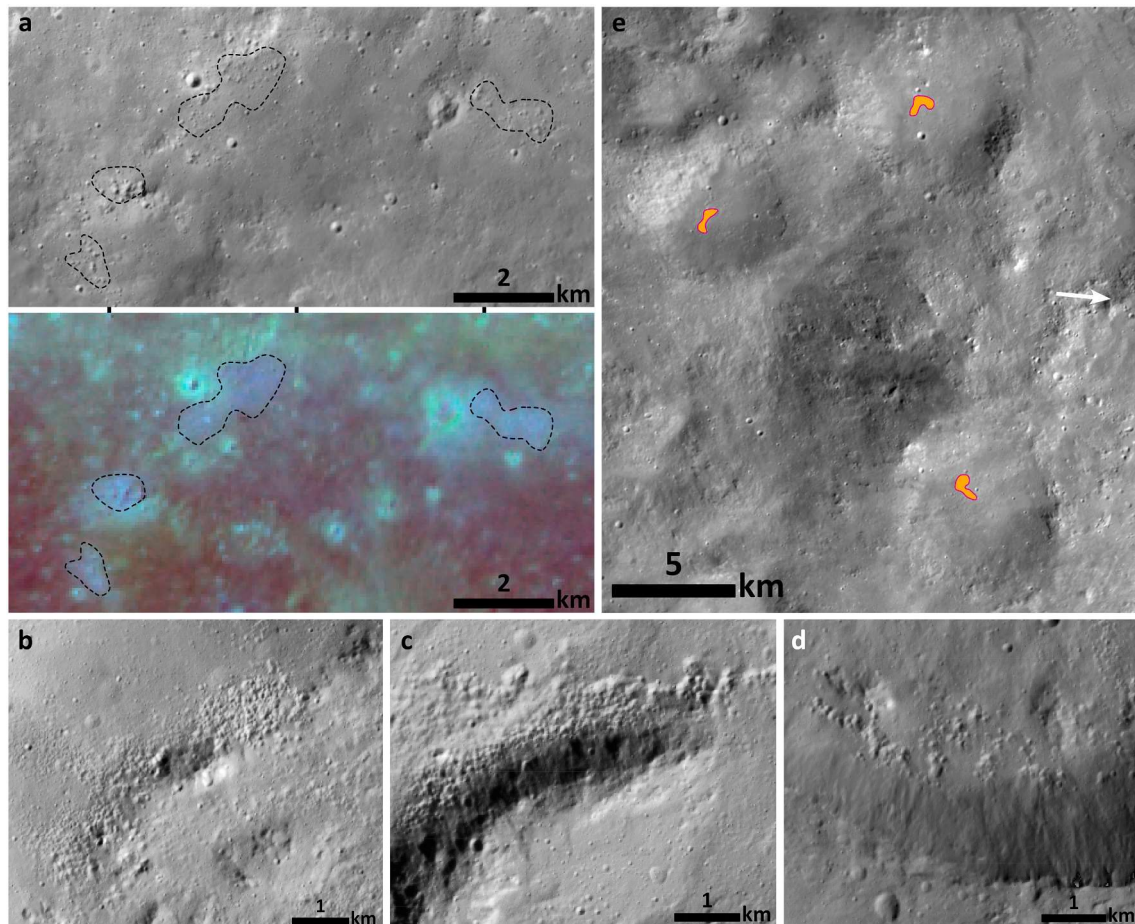


Fig. 6. Spatial context of locations presented throughout this study. Clear filter LAMO data overlain by our HAMO RGB composite (R = 965/917 [nm], G = 750 nm and B = 750/917 [nm], 50% transparency).



**Fig. 7.** a) ‘Possible’ PIDs (dashed lines) with a lack of obvious clustering and distinct pit morphology but showing the characteristic spectral properties of PIDs (upper panel: clear filter LAMO image, lower panel: HAMO RGB composite). b), c) & d): Examples of PIDs that exist adjacent to a topographic high. e) Example of three PIDs west of Marcia which are situated in craters (yet do not exhibit a detectable positive topography); colored polygons indicate PID (as in Fig. 5). For spatial context of a)-e) see Fig. 6.

our RGB composite, Fig. 7a, lower panel; more details on the spectral characteristics in Section 3.3). Those ‘possible’ PIDs can be observed especially within E1 and their presence indicates a more widespread and pervasive devolatilization process than previously suspected. We did not include the particular feature from Fig. 7a into our counts but several others not mapped in Denevi et al. (2012). The identification of a cluster of pits is biased and strongly depends on the individual mapping the feature. Several ‘possible’ PIDs were not included due to identification uncertainty.

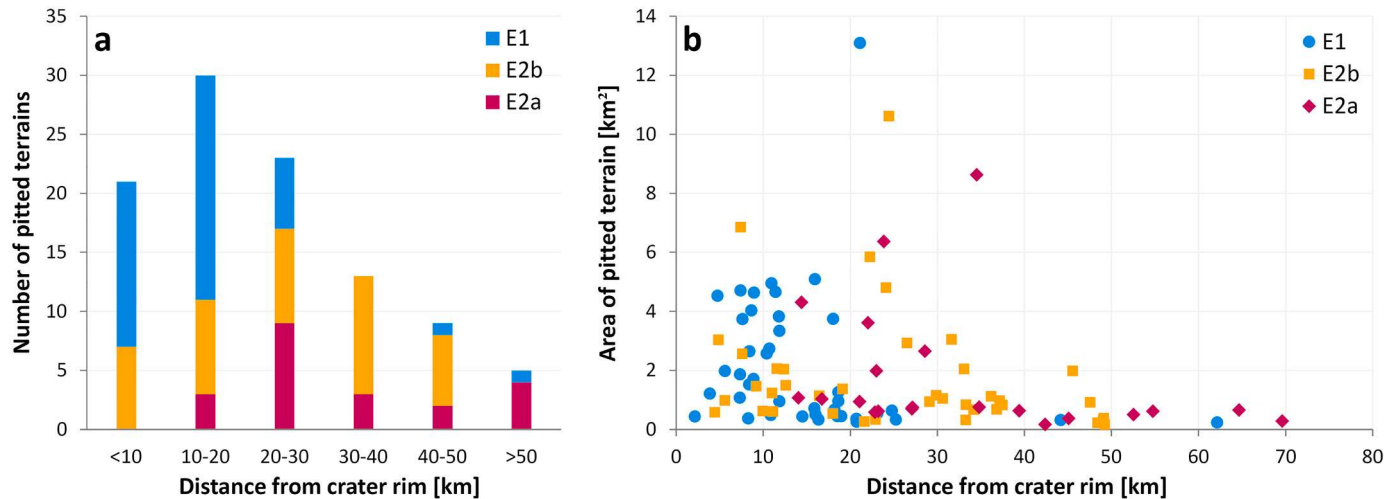
Excluding the crater-fill PIDs around Marcia’s central peak, PIDs have an average areal extent of a few square km ( $1.9 \text{ km}^2$ ) and roughly range from less than 10 to more than 80 individual pits per cluster. As individual pits often reach the resolution limit, we point out that counting of individual pits and measuring pit diameters occurred for representative clusters only. The diameter of individual pits ranges from less than 50 m (resolution limit) to more than 500 m with the largest ones occurring within Marcia’s crater-fill deposits. The average pit size within ejecta PIDs is 120 m while it is 290 m for PIDs within the crater-fill deposit. This is consistent with what has been observed for Martian PIDs (i.e., pits are largest in crater-fill deposits; Tornabene et al., 2012). An increase in pit size of PIDs on Marcia’s southern terrace with respect to those within the ejecta was not observed. Numerous PIDs show many ‘possible’ smaller pits (i.e., dark individual pixels as possible pit wall shadows), which cannot be identified with confidence due to the limited image resolution. A dependence of PID size vs. parent crater diameter seen on Mars (Tornabene et al., 2012) is hardly derivable for Vesta as the number of parent craters is very low, yet we report crater diameter vs.

the largest pit within the crater-fill deposit for the four parent craters reported in Denevi et al. (2012): Marcia, 63 km vs.  $\sim 1300$  m; Cornelia, 15 km vs.  $\sim 280$  m; Licinia, 22 km vs.  $\sim 400$  m (if devolatilization pit exists), Numisia, 30 km vs.  $\sim 590$  m (if devolatilization pit exists).

The depth of the individual pits can also not be resolved by the existing data, yet an assumption of depth by considering shadows and incidence angles gives a rough average depth of 25–50% of the pit diameter, though smaller and higher values are observable as well (e.g., Fig. 8h shows relatively shallow pits). PIDs appear to be flatter in E2a and E2b. These values are higher than what Tornabene et al. (2012) found for Martian PIDs (pit depth  $\sim 0.1$  pit diameters). Boyce et al. (2012) present a rapid formation model for the PIDs where steam release is expended in days to weeks after deposition, strongly depending on the volatile content and energetics of the degassing process. Lower volatile contents within the hot ejecta deposits of the Marcia impact would be exhausted earlier. This could produce steeper pits as the vents on the top progressively widen with time (Boyce et al., 2012). A lower gravitational acceleration can also increase the steam escape rates (Boyce et al., 2012) which could favor the formation of steeper pits. However, Sizemore et al. (2017) applied the Boyce et al. (2012) model for Cerean pits and found that they are broadly comparable on Ceres and Mars.

The shape of individual pits within a PID appears more cone-like and less bowl-shaped as for nearby small craters which is helping the identification (as can be observed in e.g., Fig. 5a & b, Fig. 12). Assuming a conical shape for the pits and a depth of the respective pit radius (upper limit), we calculated volumes (Table 2) of the now lost volatiles of the PIDs shown in Fig. 11, divided into the crater-fill PIDs around the central





**Fig. 8.** a) Distance of PIDs from Marcia crater rim (closest distance) vs. the number of PIDs occurring within the given ranges. b) Distance of PIDs from Marcia crater rim (closest distance) vs. the area spanned by the individual clusters separated into the three different ejecta classes within which they occur (see Section 3.1).

**Table 2**

Estimates of lost volatile volumes due to explosive devolatilization.

	Area [km <sup>2</sup> ]	Volume [m <sup>3</sup> ]	Volume/km <sup>2</sup>
PIDs Fig. 11a-i	~ 29	~ 7*10 <sup>7</sup>	~ 2.3*10 <sup>6</sup>
All PIDs (excl. crater-fill)	~ 212	~ 5*10 <sup>8</sup>	~ 2.3*10 <sup>6</sup>
Crater-fill PIDs	~ 180	~ 9*10 <sup>8</sup>	~ 5.0*10 <sup>6</sup>

peak and all other PIDs (incl. PIDs on the southern terrace of Marcia). The calculations assume that the voids within the pits equal the volume of volatiles released which is a rough simplification. The given volumes are therefore upper limits as other materials might also have been extracted during this process (Boyce et al., 2012) and are part of the volume now lost. We measured only the largest pits within a cluster as smaller pits are close to the resolution limit and do not contribute significant amounts to the total volume. We interpolated the values of the representative PIDs shown in Fig. 11a-i to infer the total amount of volatiles lost for all PIDs (except the crater-fill PIDs).

Table 2 summarizes the calculated volumes and shows that a higher volume of volatiles has been released from the crater-fill material than from the ejecta material. The volume per km<sup>2</sup>-value for the crater-fill PIDs is more than twice the value of the other PIDs which likely results from the difference in pit size and volume of the initial crater-fill impact deposit. If Calpurnia is the source of E2a PIDs, the difference between the volatile volumes of Marcia crater-fill PIDs and external PIDs is even larger. The individual pits measured within the crater-fill material are on average significantly larger than elsewhere (290 m vs. 120 m) and moreover the largest connected crater-fill PID is 145 km<sup>2</sup> while the largest PID elsewhere is around 13 km<sup>2</sup>. This illustrates a significant difference between crater-fill PIDs and elsewhere around (or on the southern terrace of) Marcia crater. In summary, the total volumes of lost volatiles are similar for the PIDs around the central peak and all other PIDs altogether, yet the number of volatiles per km<sup>2</sup> and the connected area of pitted terrain is larger for the crater-fill PIDs.

The PIDs are not distributed uniformly around the crater. Most clusters are found from the SW to the SE and inside Calpurnia (see Fig. 5), but a few also occur in other areas. All of the external PIDs are in proximal distance to the crater rim (i.e., about one crater diameter). Fig. 8 illustrates the dependency of distance vs. number of PIDs as well as distance vs. area of the PIDs for all PIDs external to Marcia. The farthest PID is located 69 km off the crater rim (within Minucia crater) while about 50% of the PIDs are located within 20 km off the crater rim and 73% are located within 30 km (i.e., one crater radius). On average, PIDs within E1 (blue circles in Fig. 8b) are slightly larger than PIDs

elsewhere (2.2 km<sup>2</sup> vs. 1.8 km<sup>2</sup>) and are located closer to Marcia than PIDs within E2a (red diamonds) and E2b (orange squares). This might reflect the thinning of the ejecta with distance from Marcia and therefore the decrease in pit size and abundance. This relationship has been observed for Mars as well (Tornabene et al., 2012).

PIDs are less abundant within 10 km off the rim than at 10–20 km (Fig. 8a). This could have several reasons. The most likely explanation is that post-impact modification processes (slumping, collapsing) prevail in the closest regions to the rim (e.g., Melosh, 1989) and might have overprinted existing PIDs. Furthermore, the considered area increases with distance, i.e. so that the number of PIDs/km<sup>2</sup> is nearly identical for the first two columns (assuming an elliptical shape for Marcia with a = 27 km, b = 34 km) before this value drops significantly for distances >20 km. Lastly, E2a PIDs possibly originate from Calpurnia and therefore do not naturally occur near the rim of Marcia, possibly adding to this slight variation in PID distribution.

Higher numbers of individual pits within a cluster imply a higher local volatile content, assuming that PIDs are related to volatile outgassing (Tornabene et al., 2012; Boyce et al., 2012; Denevi et al., 2012). Individual pits in the clusters do not always overlap and the arrangements of individual pits within the clusters often do not seem to follow any systematics. The clusters exhibit diverse shapes (circular, circular with a lack of pits in the center, oval, polygonal or as directional ‘pit chains’, see Fig. 11), which illustrates a heterogeneous distribution of the degassing conduits within the host material. The ‘soap froth’ pattern of PIDs described in Tornabene et al. (2012) and Boyce et al. (2012) is present at multiple PID locations (best-developed within the crater fill-deposits), yet many PIDs do not feature shared rims and this extensive close packing which can be seen in Figs. 5 and 11. This is likely due to the lower availability of volatiles on Vesta with respect to Mars and the concomitant decreased duration of volatile loss. Intervening smooth regions between pits also occur frequently (best illustrated in Fig. 11 in Section 3.3) which has also been reported for Martian PIDs (Tornabene et al., 2012).

PIDs always occur within ‘smooth material’ (Denevi et al., 2012; Williams et al., 2014a), which could be impact melt or an impact melt-bearing breccia linked to Marcia ejecta. A connection of pitted material with fluid flow features and smooth melt-bearing impact deposits was also observed for Mars and Ceres (Tornabene et al., 2012; Sizemore et al., 2017). This smooth material is characterized by very few and small impact craters and an even surface appearance within the resolution limits. PIDs are mostly located on slight slopes (~2°–15° with respect to the triaxial ellipsoid, see Section 2.1) and with minor exceptions (e.g. in Calpurnia & Minucia craters), these slopes are facing the

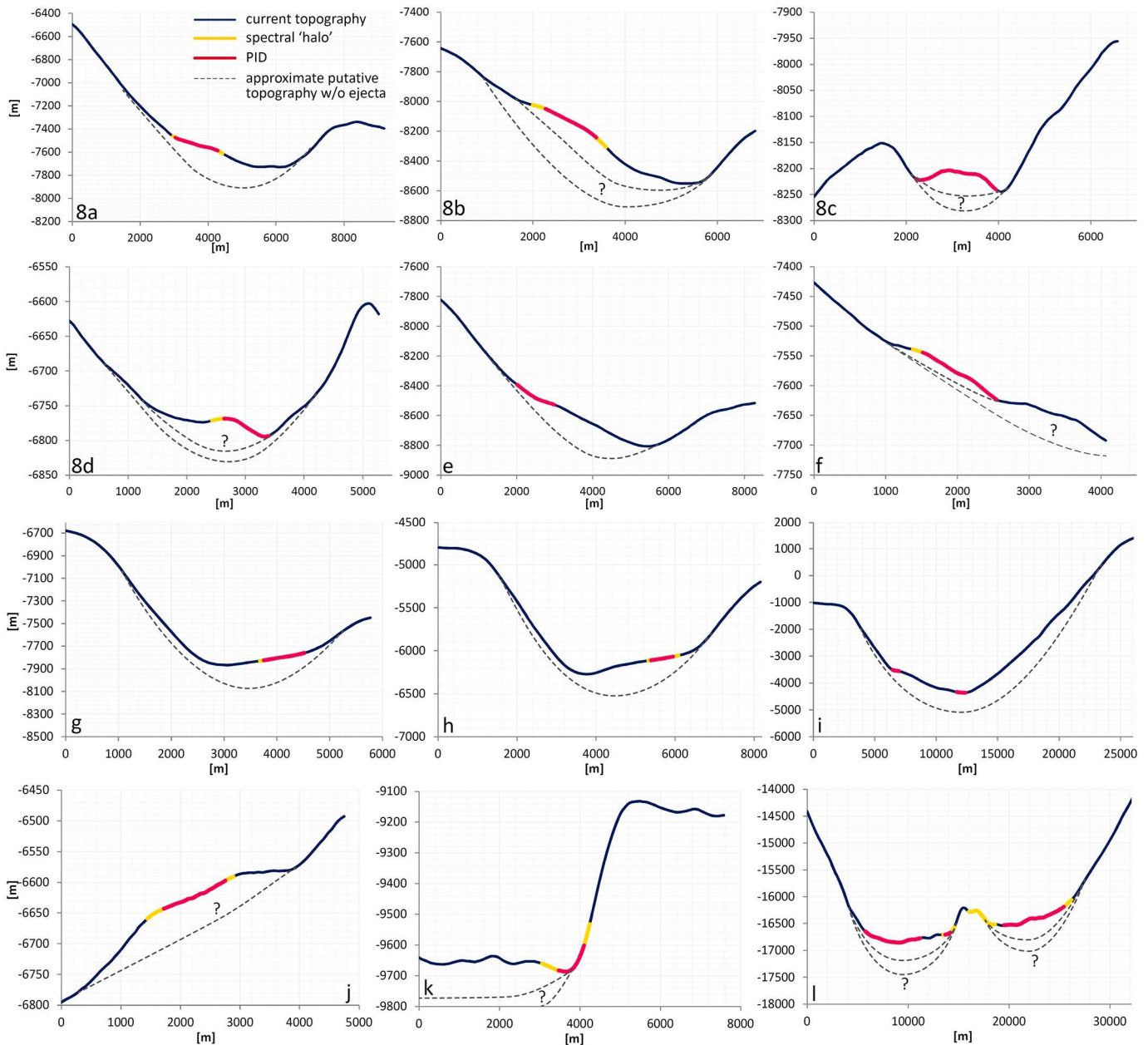
direction from where Marcia ejecta were excavated (e.g., Fig. 7e, white arrow indicates the direction towards the Marcia center). These slopes are consistent with the slope range in which Martian PIDs are present ( $<15^\circ$ , Tornabene et al., 2012), indicating that the critical slope below which pits can form is independent of the body's gravitation. Within Calpurnia and Minucia, PIDs occur near the margins of the crater-fill deposits, at the lowest elevations and at topographic highs (i.e. crater wall, large blocks).

Furthermore, we found 17 PIDs located within 13 relatively small craters (2–9 km, see Fig. 5) that existed prior to the Marcia impact (as seen by smooth rims and ejecta-filled crater interiors, e.g. Figs. 7e and 11d). In this consideration, we exclude the large craters Calpurnia and Minucia due to possibly misleading statistics and interpretations. These small pre-existing craters occur foremost in E1 (compare Figs. 3 and 5) and there are no small pre-existing craters hosting PIDs within E2a.

Some ambiguous 'craters' hosting a PID were found but not included here. Moreover, we identified several locations where the DTM shows a positive local topography (bulge) linked to the PIDs.

Another important observation is that some PIDs occur near or directly at topographic highs, i.e., the pits are aligned and densest where the deposit is in contact with crater walls and ridges/large blocks. This can be observed, for example, a few kilometers SE of Marcia (Fig. 7b), within Calpurnia (Fig. 7c) and at the Marcia southern crater wall (Fig. 7d). PIDs are clearly aligned along these features, indicating a structural control on the formation of PIDs.

Fig. 9 illustrates twelve profiles of PIDs where a PID is connected to positive local topography, is identified within a pre-existing small crater or is aligned along a topographic high (Fig. 9k). The red part of the current topography indicates a pitted surface and the dashed grey line indicates an approximate putative surface profile without overlying



**Fig. 9.** DTM-derived profiles: Dark blue line displays the current topography. Dashed line represents the putative topography prior to the emplacement of Marcia ejecta. Red colored part denotes a PID, yellow color denotes the halo around the respective PID and for the Marcia profile (l), also the halo near the central peak not associated with a pitted surface. Spatial context is given in Fig. 6 while exact profile locations are displayed in the supplements (S3). No vertical exaggeration applied. (For interpretation of the references to color in this figure legend, the reader is referred to the web version of this article.)

ejecta assuming the steepest parts of the slopes/crater walls still display the pre-Marcia-impact topography (simple bowl shape for craters). The ‘halo’ (yellow part of the current topography) within Marcia is a spectrally distinct part of the crater-fill PIDs and will be described in detail in Section 3.3. The halo for all other PIDs represents smooth material exhibiting the distinct spectral characteristics of the adjacent PID, which will also be shown in detail in Section 3.3. A PID host deposit thus differs greatly in both spectral (i.e., ‘dark’ and ‘bright’) and geomorphological (pitted and smooth) characteristics. View Fig. 6 for the spatial context of the profiles and the supplementary material (S3) for the exact location and course of the profiles. S3 also includes an indication of the excavation direction from Marcia; e.g., for profiles a, b, c, e and i Marcia ejecta arrived from the right of the profile and for profiles e, h and j, from the left of the profile.

The occurrence of a PID therefore appears to be linked to accumulation of volatile-bearing ejecta controlled by pre-impact topography. According to our estimated pre-Marcia topography (dashed line), PIDs mainly reside where the host deposit is thickest, yet they can also occur near the margins of the host deposit (e.g., within Minucia, 9i and along topographic highs). We did not observe a correlation of the 13 presented host crater diameters and area or thickness of the PID deposit. Thus, PID size does not appear to be related to the deposit thickness, possibly as a result of heterogeneous compositions within the ejecta.

For the examples in Fig. 9, the thickness of the PIDs’ material ranges from 20 m to roughly 300 m. In the larger craters Marcia (9 l) and Minucia (9i), the thickness of the host deposits might be in the order of ~500 m and are therefore significantly larger than the deposits elsewhere. Furthermore, the profiles clearly illustrate that the PIDs are part of larger impact deposits, whose surfaces are otherwise smooth. This is

best illustrated where host deposits of PIDs reside in pre-Marcia-existing craters (9a, b, d, e, g, h, i).

### 3.3. Spectral characterization of the PIDs

Williams et al. (2014a) report a “distinctive color signature” of pitted terrain in FC false color ratio images, which they describe as “gray-brown” in the Clementine-type ratios (Pieters et al., 1994;  $R = 750/438$  [nm],  $G = 750/917$  nm,  $B = 438/750$  [nm]). This statement applies to the large PIDs on Marcia’s floor, which were described by Denevi et al. (2012) and De Sanctis et al. (2015c) to exhibit a spectrum darker than the average of Vesta. However, some PIDs outside of Marcia exhibit a significantly higher reflectance and pyroxene band strength than the average of Vesta or Marcia’s crater-fill PIDs. Fig. 10 displays FC spectra of nine sample locations and Vesta’s average spectrum. Included is also the spectrum of the crater-fill PID within Cornelia crater, which is slightly darker with a higher visible slope than the crater-fill PIDs of Marcia. Cornelia is a very well-preserved, bright crater SE of Marcia (Fig. 3) located on top of the Vestalia Terra highlands that also contains very dark material in its walls and a single PID on its floor (Fig. 7, upper right panel). The contrast between the PID on the floor and bright material within Cornelia crater is higher than the contrast between Marcia’s crater-fill PIDs and bright material from its rim, possibly due to age differences between the craters. Fig. 10 illustrates that PIDs exhibit stronger absorptions with respect to locations with similar reflectance levels in the visible region. Most notably is the spectrum of the crater (light orange) right next to the PID SW of Marcia (orange) in comparison with the PID itself and also to the halo of the crater-fill deposit. The spectrum of this crater shows a discernibly smaller absorption band

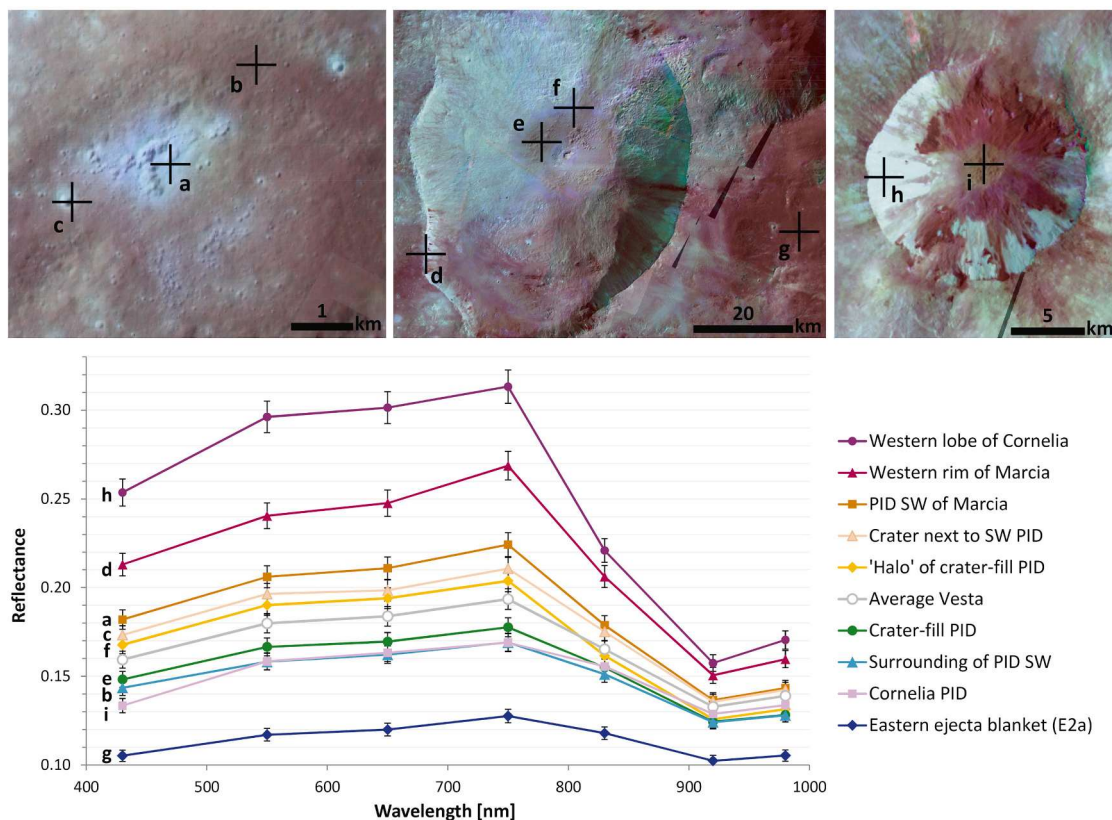


Fig. 10. Upper panel: Spatial context for spectra displayed in lower panel. Lower panel: FC spectra of different regions of interest on Vesta (mostly Marcia-related but for comparison, the Cornelia PID and a bright slope deposit inside Cornelia are shown). Note that reflectance and pyroxene band strength are positively correlated. The vertical error displays 1σ for the Vestan FC data according to the approximate calibration uncertainty after Schröder et al. (2014). Here, an uncertainty of 3% was assumed. The uncertainty is mostly caused by the stray light removal, which varies from image to image and from filter to filter (e.g. Schröder et al., 2014). For spatial context of the upper left two panels, see Fig. 5a & b and for Cornelia crater Fig. 3.



than the halo and the nearby PID while showing very similar patterns from 400 to 750 nm. We do not show normalized spectra in order to emphasize the different absolute reflectance values of the sample locations.

All PIDs mapped during this study exhibit higher reflectance and pyroxene band strengths (i.e., cyan or even bluish in our RGB composite) than their immediate surrounding except the crater-fill PIDs, which generally exhibit lower reflectance and weaker pyroxene absorptions with respect to their immediate surrounding. The surroundings of PIDs comprise smooth materials from the same ejecta host deposit (e.g., Figs. 5b, c & d, 9) which do not exhibit the same spectral characteristics (Fig. 11). The majority of PIDs only exhibit minor differences with respect to their surroundings, but they are still distinguishable (e.g., Fig. 11 g-i). In general, the PIDs exhibit an increase in reflectance of up to ~7% at 750 nm (Fig. 10). The Marcia crater-fill PIDs are the only ones showing a decrease of reflectance and pyroxene band strength with respect to their immediate surrounding, which will be discussed later on.

External to the crater, there are numerous examples of spectrally distinct PIDs located in different topographic settings distributed in all directions (see Fig. 5a). Fig. 11 displays several examples of the most characteristic PIDs (high 750/917 [nm] and 750 nm values and/or distinct geomorphologic appearance) in clear filter LAMO images (1st panel), topographic setting (2nd panel) and FC false color ratio RGB (3rd panel,  $R = 965/917$  [nm],  $G = 750$  nm and  $B = 750/917$  [nm]). Reflectance and pyroxene band strength of the PIDs are positively correlated (see also Fig. 10 and Table 3). The 4th panel in each row of Fig. 11 displays the absorption band depth at 2.8  $\mu\text{m}$  (i.e., the abundance of OH-bearing minerals) created with VIR data by Combe et al. (2015) who derived the absorption depth from the reflectance between a calculated continuum above the 2.8  $\mu\text{m}$  absorption and the band center. These maps show a definite local depletion of OH-bearing minerals for six of the external PIDs with respect to their immediate surrounding, indicating the loss of hydroxyl groups upon PID formation. We note that many PIDs show ambiguous OH depletions, likely due to the limited resolution of the VIR instrument (~200 m/px).

The lowest OH abundances of the Marcia area are observed within the Marcia crater and even for the PIDs within the crater-fill material, which generally exhibit a lower average reflectance and pyroxene band strength values as seen in Figs. 2, 10, 11j and Table 3. The lower than average reflectance was previously described in Denevi et al. (2012) and De Sanctis et al. (2015c). This is a contrary observation to all other PIDs, where lower 2.8  $\mu\text{m}$  band depth values are linked to higher reflectance and stronger pyroxene absorptions (i.e., bright = OH-depleted). External PIDs with similar reflectance and pyroxene band strength values as the crater-fill PIDs (e.g., Fig. 11h) show higher 2.8  $\mu\text{m}$  band depth values as well as darker and more featureless immediate surroundings than the PIDs within the crater-fill material. We therefore emphasize here that the crater-fill PIDs are different to all other PIDs.

However, the PIDs within the crater-fill material are not exclusively 'darker' and appear to have a spectral 'halo' where they meet and embay the crater wall (Fig. 12a, dashed outline and arrows). Especially at the northern and western margins of the crater-fill material areas with higher reflectance and pyroxene band strength are visible (Fig. 12b and Table 3), consistent with those of external PIDs. These areas comprise significantly smaller pits than the rest of the PID (Fig. 12b), and appear smooth where the halo does not show a pitted surface. The northern halo material generally resides on larger slopes (~5° to 15°) than the rest of the crater-fill PIDs towards the central peak (~1° to 6°). The southwestern halo (Fig. 12a, arrows) is located at lower elevations and generally smaller slopes than the northern halo (Fig. 12a, dashed line) and appears smooth with minor pitting. Small pits down to the resolution limit can be observed in the close-up image in Fig. 12b. The crater-fill PIDs are therefore not homogenous in terms of their spectral characteristics which makes them unique among the 118 mapped PIDs in and around Marcia. An important observation is moreover that in some parts the described halo is superposed by material input from the crater

wall which is best illustrated on the right side of Fig. 12b. This is also valid for the spectral characteristics as the superposing slumps show lower reflectance and pyroxene band strength (compare with Fig. 12a).

Moreover, an area with the same spectral characteristics as the 'halo' is found around the central peak (Fig. 12c). The higher reflectance and pyroxene band strength is strongly correlated with a confined area of pitted and smooth terrain showing signs of subsidence along a small topographical scarp (arrows in Fig. 12c). Signs of subsidence were already reported for other regions within the crater-fill deposit (Denevi et al., 2012), but these do not show this distinct spectral signature. In the northwestern part, it cannot be determined if the topographic feature is a scarp or a ridge and the DTM does not resolve this topographical difference. The highest reflectance and pyroxene band strength values in this central peak halo are observed for a smooth appearing area WNW of the central peak and for a pitted area ESE of the central peak.

Table 3 displays the mean reflectance at 750 nm, 750/917 [nm] and 2.8  $\mu\text{m}$  band depth values of Marcia-related regions of interest relevant for this study. Values for 'PIDs' (1st row) include the nine PIDs in Fig. 11 a-i and values of their 'surroundings' (2nd row) include only the surroundings of these nine PIDs. The 3rd row denotes the PIDs surrounding the central peak of Marcia crater, excluding the ones on the southern terrace. 'Halo floor' denotes the outlined area in Fig. 12a.

Table 3 and Fig. 11 demonstrate that the PIDs significantly differ from their immediate surroundings, especially considering the 750/917 [nm] values. In comparison with the PIDs on the crater floor and the whole Vesta, PIDs have a similar mean in reflectance at 750 nm but a higher mean in the 750/917 [nm] values, as does the halo. A more intuitive Figure is displayed in Section 3.5. PIDs have similar mean reflectance values like the average Vesta as they comprise both brighter and darker PIDs which will also be shown in Section 3.5. Additionally, 2.8  $\mu\text{m}$  band depth values show that the PIDs and their surroundings (i.e., ejecta material) are both enriched in OH with respect to materials within the crater (PIDs, halo and NW crater wall).

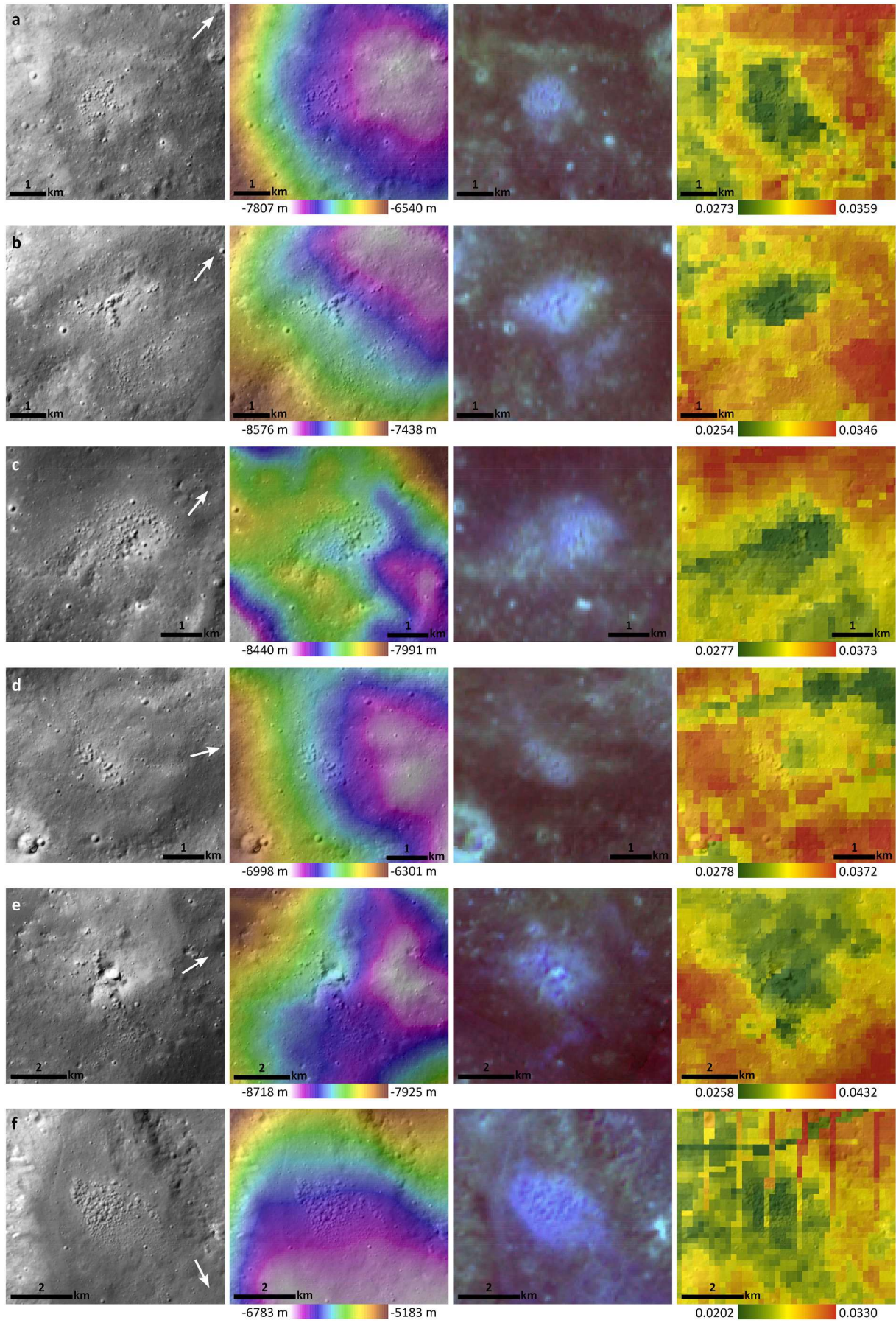
The distinct spectral characteristics of the PIDs are not exclusively confined to the pits themselves. Instead, the spectral signatures reach several tens of meters outward building another sort of halo around the PIDs (see especially Fig. 11b, e & f). Thus, some parts of the smooth surface of the host deposit show the same spectral characteristics as the pitted parts. However, due to the resolution limit, it cannot be excluded that there are smaller pits inside these halos (<50 m). We note that for other (potential) PIDs identified on Vesta by Denevi et al. (2012) we did not observe such apparent spectral variations (i.e., in craters Cornelia, Licinia and Numisia).

### 3.4. Spectral comparison with HEDs

Fig. 13 displays FC data ratios of the most prominent PIDs (i.e., 11a, b, c and f which exhibit the highest 750/917 [nm] values, magenta colored data cloud) in comparison with other locations of interest on Vesta and the meteorite spectra from RELAB (Fig. 1, now black & grey symbols), showing that the data points of these PIDs overlap with the main data cloud of eucrites (light grey circles). The NW crater wall of Marcia shows very similar values like the PIDs, but with slightly lower 750/917 [nm] values. The surroundings of the PIDs (light turquoise), as well as the PIDs on the Marcia crater floor (purple) have relatively equal values and also overlap with eucrite data points but with lower 750/917 [nm] values with respect to the selected PIDs. E2a (light blue) and Aricia Tholus (dark blue) have even lower 750/917 [nm] values. All of these regions of interest together plot on a mixing line between eucrite and carbonaceous chondrite data (indicated by shortly-dashed line). They show a slight difference in 965/917 [nm] values. This observation is consistent with previous studies suggesting carbonaceous chondrites as the source for the observed dark material on Vesta.

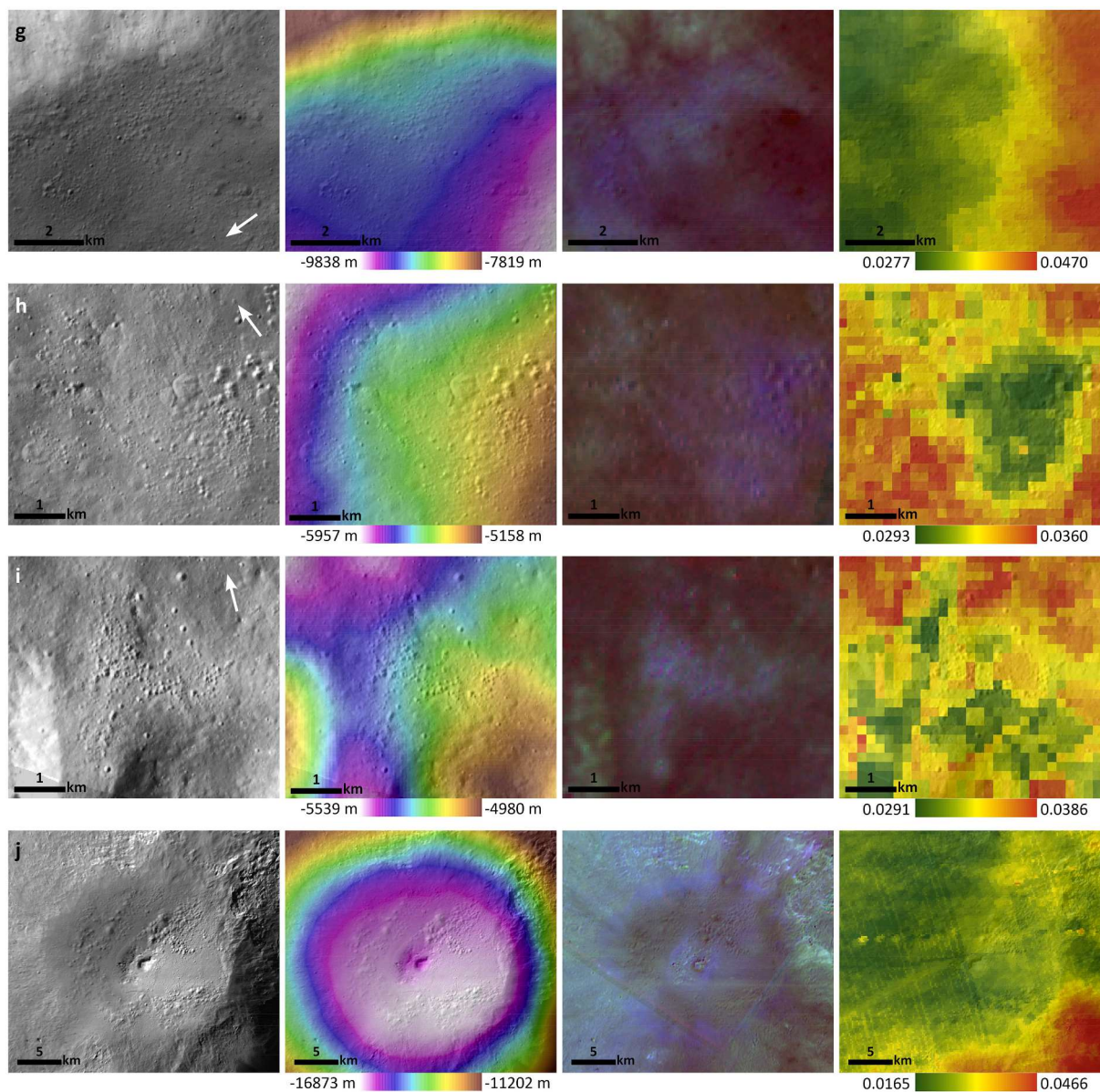
On this 'contamination mixing line', PIDs appear to represent the eucrite-rich endmember. Eucritic regions of interest with even 'purer' (i.e., less contaminated) eucritic compositions (orange) likely representing







**Fig. 11.** Ten examples of PIDs in and around Marcia showing euclite-like spectral features and in six cases definite local depletions of hydroxyl groups (i.e., decrease of absorption at  $2.8 \mu\text{m}$ ). The first panel in each row shows clear filter LAMO data and white arrows indicate the direction to the primary cavity of Marcia. 2nd panel: DTM data (50% transparency over LAMO clear filter data). 3rd panel: HAMO RGB composite ( $R = 965/917 \text{ [nm]}$ ,  $G = 750 \text{ nm}$  and  $B = 750/917 \text{ [nm]}$ , same stretch in every row), greenish/cyan/bluish colors represent higher reflectance and/or pyroxene band strength. 4th panel:  $2.8 \mu\text{m}$  band depth distribution map from Combe et al. (2015). Row j shows the central PIDs of the Marcia crater floor. Spatial context is displayed in Fig. 6. (For interpretation of the references to color in this figure legend, the reader is referred to the web version of this article.)



**Fig. 11.** (continued).

exposed euclitic bedrock, such as at the rim of Marcia crater (Fig. 10, upper middle panel) and the bright slope deposit on Cornelia's western wall (Fig. 10, upper right panel), show even higher  $750/917 \text{ [nm]}$  and significantly higher  $965/917 \text{ [nm]}$  values.

Matronalia Rupes – a scarp at the Rheasilvia Basin rim – was previously reported to be composed of diagenitic rock (e.g., McSween et al., 2013a; Ammannito et al., 2013a; Stephan et al., 2015), which is consistent with our comparison in Fig. 13 (dark orange). Carbonaceous chondrites have values around 1.0 for  $965/917 \text{ [nm]}$  and  $750/917 \text{ [nm]}$ , while Vestan data generally have higher values for both ratios (Fig. S4). This suggests that larger values for  $965/917 \text{ [nm]}$  and  $750/917 \text{ [nm]}$  indicate less contamination with carbonaceous chondrite material (or other reflectance-lowering components). Moreover, seemingly “pure” regions (euclitic and diagenitic characteristics) are

characterized by another dependency than contaminated areas and plot on a different trend line (dashed lines in Fig. 13).

The cause for these two distinct trend lines is 1) the contamination by dark (carbonaceous chondrite) material and 2) that the Marcia region is characterized by a high euclitic abundances with no diagenitic occurrences (Ammannito et al., 2013a; Prettyman et al., 2013). Therefore, the slope of the “contaminated trend line” in Fig. 13 is significantly lower than the HED trendline including diogenites. For the Marcia region, we only observe a very subtle change in the pyroxene band position (indicated by the  $965/917 \text{ [nm]}$  ratio), which can be attributed to the described contamination.

The mineral olivine, which commonly occurs in planetary materials, does not contribute to the spectral characteristics of the PIDs either. Firstly, it has not been detected in the Marcia area (Ammannito et al.,



2013b; Thangjam et al., 2014; Palomba et al., 2015), and secondly, olivine exhibits lower values in both considered ratios (see Figs. 1 and 13), which is contrary to our observations of the PIDs. However, detection of olivine by the Dawn instruments is challenging and might not be possible below 30 vol% (Beck et al., 2013; Le Corre et al., 2013), adding uncertainties in these interpretations.

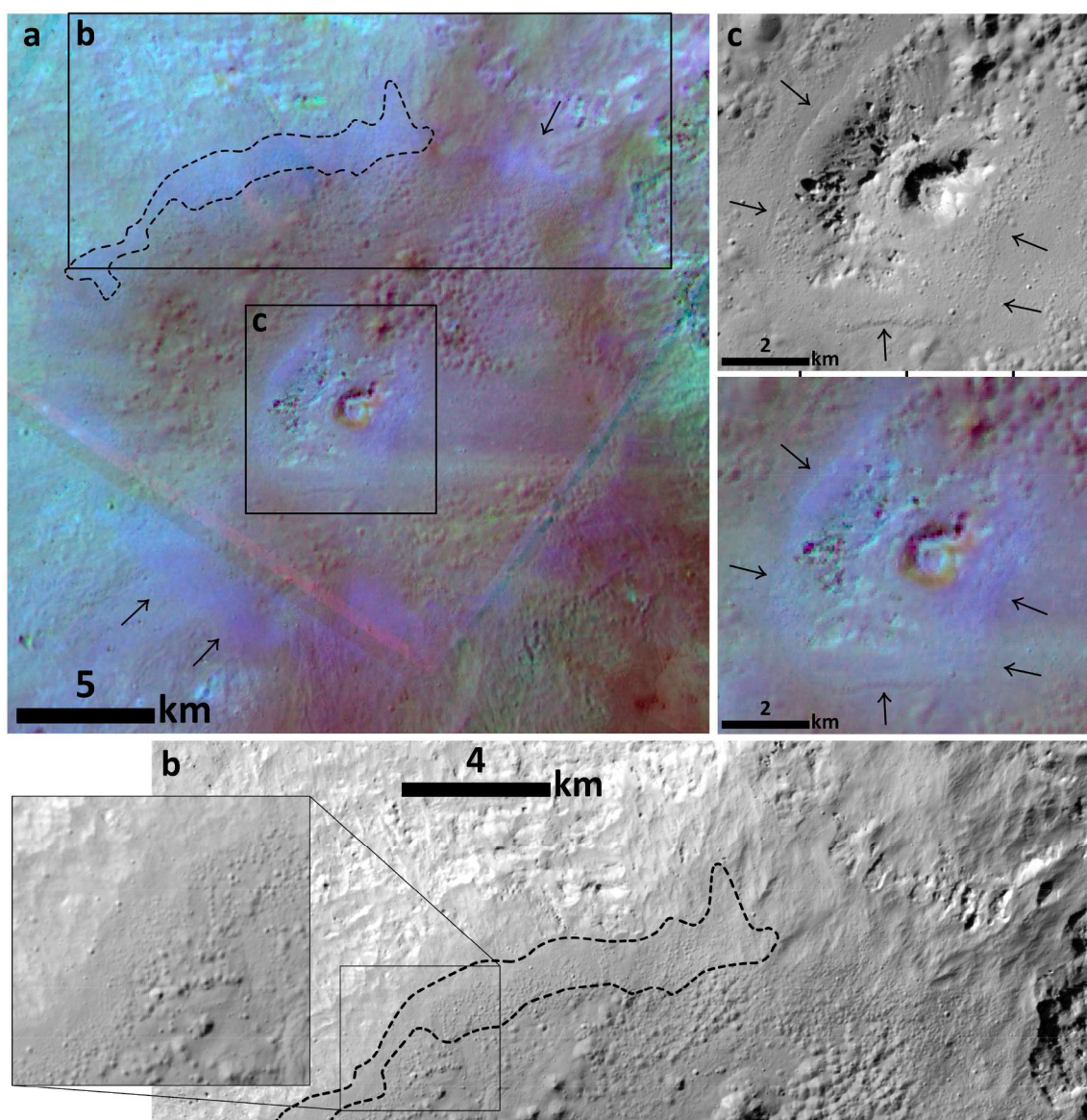
HED data plot on a trend line when the pyroxene band I center is plotted against the pyroxene band II center (e.g., De Sanctis et al., 2012a; De Sanctis et al., 2015c). Most of the Vestan surface is slightly deviating from this trend, which can again be explained by the contamination of impacting carbonaceous chondritic material. The same is observed when plotting FC color ratios against each other (Thangjam et al., 2013 and this study, long dashes in Figs. 13 & S4), which only cover the first pyroxene absorption band. The vast majority of Vestan FC data plot near eucrites/howardites but with a small bulge towards carbonaceous chondrites. This is displayed in the supplementary Fig. S4. The highest density of the Vestan surface plots around 1.44,

1.05 (ratio values), whereas some of the PIDs plot around 1.65 (and more) and 1.04, which furthermore suggests that the main parameter to distinguish the different terrains is the indicator for pyroxene band strength, 750/917 [nm].

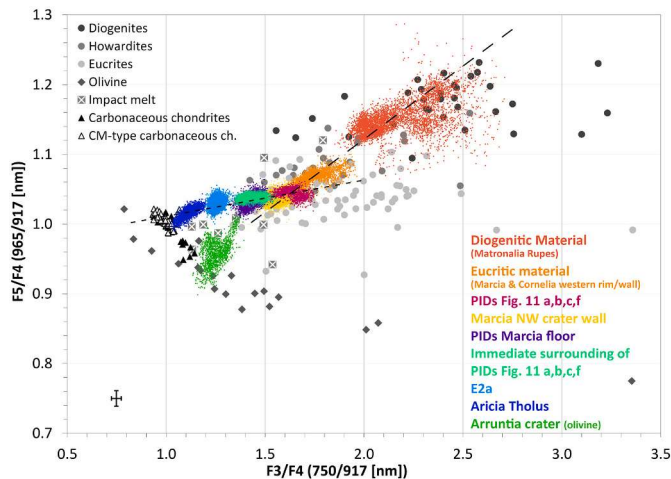
In summary, the major parameter for the distinction between the PIDs and their surrounding is the FC ratio 750/917 [nm] (F3/F4). The data points of selected PIDs outside of Marcia overlap with data points of eucrites, consistent with previous findings that the Marcia region is enriched in eucritic rock types (e.g., Prettyman et al., 2012; De Sanctis et al., 2015b). The spectral comparison with HED meteorites shows that PID-related regions of interest (PIDs, PID surroundings and E2a) are consistent with contamination by carbonaceous chondrites. Changes in pyroxene mineralogy towards diagenetic lithologies is not observed.

### 3.5. Comprehensive analysis of observations

Linking all our observations, we can separate the PIDs external to



**Fig. 12.** a) HAMO RGB composite of the Marcia crater-fill PIDs. The spectral halo of the crater-fill PIDs at the margin towards the crater wall appears cyan/bluish. One part of the halo is indicated by dashed lines, others are indicated by arrows. b) LAMO clear filter image, area of the spectral halo appears to contain both pitted and smooth material while the pits are close to the resolution limit. c) displays the area around the central peak showing signs of subsidence as well as distinct PIDs comprising very small pits (upper panel) and higher reflectance and pyroxene band strength (cyan/bluish in lower panel). Spatial context is given in Fig. 6. (For interpretation of the references to color in this figure legend, the reader is referred to the web version of this article.)



**Fig. 13.** 750/917 [nm] vs. 965/917 [nm] of various locations of interest (colored data) with RELAB meteorite data from Fig. 1 in black, white, and grey colors. The FC ratio values of selected external PIDs overlap with data points of eucrites as well as partly with data for the most eucritic regions on Vesta (orange data points, taken from Marcia western rim and Cornelia western wall). These PIDs can therefore be spectrally separated from their immediate surroundings (light turquoise) and from the PIDs on the Marcia floor (purple). Dashed lines represent spectral trends of contaminated material (flatter line between carbonaceous chondrites and eucrites) and uncontaminated material (long dashes, purely HED). The error indicator on the lower left displays an approximate calibration uncertainty of 3% after Schröder et al. (2014). Note that the diogenitic material (dark orange) overlaps well with the diogenite data points (black circles), indicating an accurate calibration and the feasibility of this comparison. (For interpretation of the references to color in this figure legend, the reader is referred to the web version of this article.)

Marcia (101 PIDs) into two different types according to the ejecta units defined in Section 3.1. PIDs of type 1 comprise PIDs located in E1, where the ejecta blanket generally exhibits higher reflectance and stronger pyroxene absorptions (as does the NW part of Marcia, see Fig. 2b). These PIDs exhibit higher mean reflectance at 750 nm (Table 4), a higher mean value for the 750/917 [nm] ratio and slightly lower 2.8  $\mu\text{m}$  absorption depths compared with average Vestan values. Furthermore, they have larger spatial extents (mean of 2.2  $\text{km}^2$ ) than type 2 PIDs (mean of 1.8  $\text{km}^2$ ). In total, 41 out of 101 external PIDs are of type 1 and ten of them occur within craters that existed prior to the Marcia impact (i.e., ~24% of PIDs in E1 are located in small pre-existing craters).

Type 2 PIDs exhibit lower than average mean reflectance at 750 nm (Table 4) and their 750/917 [nm] ratios resemble the value of the average Vesta. Their 2.8  $\mu\text{m}$  absorption depths are above the average of Vesta. Seven of the 17 identified PIDs in pre-existing craters are of type 2 (i.e., ~12% from type 2 PIDs are located in small pre-existing craters), yet all of these seven occurrences are located within E2b, which corresponds to ~18% of this ejecta unit's PIDs (39 PIDs within E2b and 21 within E2a). Type 2 PIDs are more abundant and are located within E2a and E2b. Considering PIDs/ $\text{km}^2$ , PIDs are more abundant in E1. This indicates that E1 contained more volatiles than E2a and E2b (all have roughly the same spatial extent), which is contrary to the general higher reflectance and pyroxene band strength nature of E1. However, if E2a (and possibly E2b) were to originate from Calpurnia, the Marcia impactor would have hit a relatively young ejecta blanket (i.e., Calpurnia ejecta shows a similar age as Marcia ejecta, Williams et al., 2014b; Appendix A) and overprinted possibly already existing PIDs sourced from Calpurnia. The impact event forming Marcia could have incorporated volatiles from the well-preserved Calpurnia ejecta. Furthermore, as ejecta deposits are more abundant close to the parent crater, E1 might comprise more PIDs/ $\text{km}^2$  as it represents the closest ejecta deposits to Marcia.

Fig. 14 is a key figure in this study and summarizes the values given

in Tables 3 and 4, showing that PIDs show a deviating trend regarding both reflectance at 750 nm and OH content (i.e., 2.8  $\mu\text{m}$  band depth) with respect to 750/917 [nm] values. The surroundings of PIDs, the NW crater wall, the crater next to the SW PID (shown in Fig. 10) and the average Vesta roughly plot on a common trend line (dashed) in both displayed diagrams, indicating a 'typical' dependence of reflectance (and OH content) and pyroxene band strength for Marcia-related regions of interest and the average Vestan values. PIDs clearly deviate from this trend (dotted line). PIDs generally have higher 750/917 [nm] values with respect to 750 nm reflectance and 2.8  $\mu\text{m}$  band depth values of other more typical Marcia-related materials. This furthermore illustrates that the PIDs' materials have undergone a process changing the original spectral nature of Vestan material.

We note that while the crater-fill PIDs show similar reflectance and pyroxene band strength values as for example the average Vesta, their OH contents are significantly lower, putting them in their own category (purple circle in Fig. 14, right panel). As described before, the crater-fill PIDs are not nearly as spectrally homogeneous like all other PIDs (see Section 3.3 and Figs. 11 & 12). Instead, these PIDs show spectral and geomorphological variations (see 'halo' and 'crater-fill' PIDs in Figs. 14 and 12) and furthermore are the only PIDs that exhibit lower reflectance and pyroxene band strength values than their immediate surroundings (Figs. 2, 11j and 12) while also showing the lowest OH abundance of all PIDs. The crater-fill PIDs and their individual pits moreover are significantly larger than all other PIDs (see Section 3.2 and Fig. 5). The crater-fill halo (orange circle in Fig. 14) likewise represents its own category linked to the crater-fill PIDs, yet comprise very small individual pits down to the resolution limit (Fig. 12b) and also smooth material. In the left panel of Fig. 14, the halo plots roughly on the same trend line as the external PIDs (dotted). If we would plot a regression line for the data points of the halo and the crater-fill PID, it would show an even steeper slope in the left panel and a line roughly parallel to the PID regression line in the right panel, indicating similar characteristics.

The presence of two types of PIDs is closely linked to the ejecta units described in Section 3.1. Therefore, we again acknowledge that PIDs of type 2 might originate from the impact that formed Calpurnia crater. It remains challenging to explain the occurrence, extent and spectral characteristics of E2b if Calpurnia is the source. Again, the determination of the PID parent crater is not crucial for this study. The most important observations and interpretations are not tied to this separation. Moreover, if the ejecta units did not form from a single event, it shows that the unique spectral changes the material underwent upon PID formation is not a singularity, but instead can form during other impact events too. Yet we note that Calpurnia and Marcia are adjacent to each other and likely sampled the same target material. Unfortunately, there are no other large and well-preserved craters on Vesta's surface in order to see whether impact events in other areas of Vesta could likewise have generated spectrally distinct PIDs.

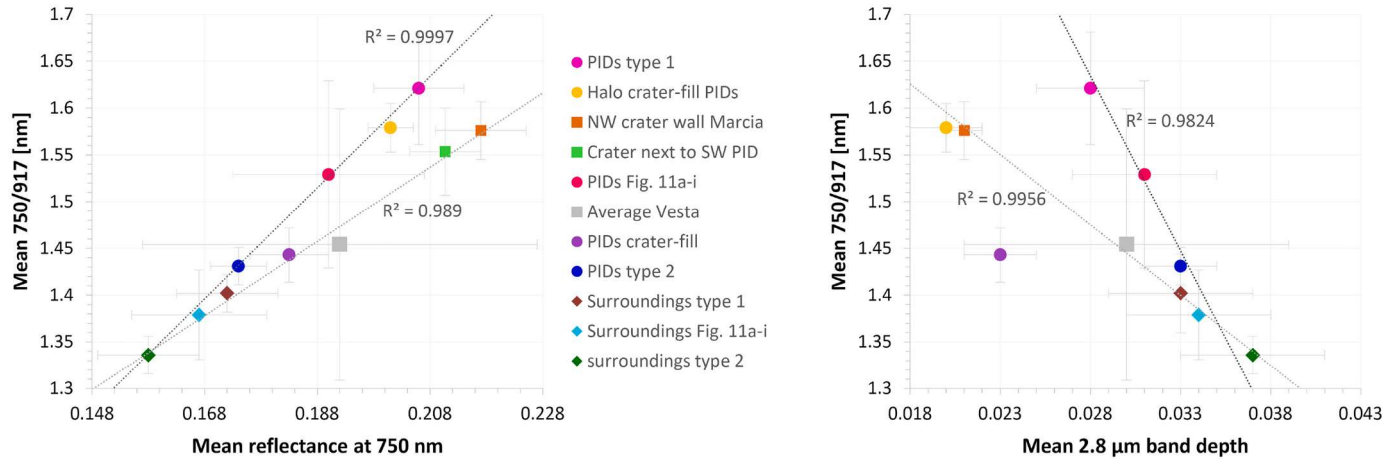
Lastly, we emphasize the unique spectral trend for PIDs by presenting the left panel of Fig. 14 with additional data from known diogenitic sites (i.e., Matronalia Rupes scarp and craters Aelia, Lollia and Antonia) which is displayed in Fig. S5. These diogenitic sites plot parallel to the 'Marcia-related' regression line, strengthening the unique trend for PIDs.

## 4. Implications on the formation of the Marcia-related PIDs

### 4.1. Origin of the PIDs

On Mars, Ceres and Vesta, PIDs occur within smooth impact deposits (Tornabene et al., 2012; Sizemore et al., 2017; Pasckert et al., 2018; Denevi et al., 2012), implying that smooth and pitted surfaces share the same host deposit and originate from the same event. Our analysis adds more occurrences of PIDs to the already existing data on Vesta (Denevi et al., 2012) and further confirms the relationship of the pitted and smooth ejecta deposits. The spectral characteristics of these two deposit surface types are different from each other, yet their analysis also





**Fig. 14.** Left panel: Mean reflectance at 750 nm vs. Mean 750/917 [nm] of regions of interest reported in Tables 3 & 4 and a small crater next to a PID (Fig. 10, left panel). Right panel: Mean 2.8  $\mu\text{m}$  band depth vs. mean 750/917 [nm] reported in Tables 3 & 4. Error bars indicate the given standard deviations, for the ‘crater next to SW PID’, an uncertainty of 3% is displayed, as described for Fig. 10. There is no 2.8  $\mu\text{m}$  band depth available for this crater due to the limited resolution of the VIR instrument. Regression line for PIDs contains the three PID data points. Regression line for the Marcia-related regions of interest contains the NW crater wall, the crater next to the SW PID (only for the left panel, Fig. 10), the average Vesta and the three surroundings of PIDs.

**Table 3**

750 nm reflectance, 750/917 [nm] and 2.8  $\mu\text{m}$  band depth values (from Combe et al., 2015) of locations of interest. Values are given with one standard deviation.

	Mean 750 nm reflectance	Mean (750/917 [nm])	Mean 2.8 $\mu\text{m}$ band depth	n (pixel number)
PIDs (Fig. 7a-i)	$0.190 \pm 0.017$	$1.529 \pm 0.100$	$0.031 \pm 0.004$	3707
Surroundings	$0.167 \pm 0.012$	$1.379 \pm 0.048$	$0.034 \pm 0.004$	22,982
PIDs (floor, Fig. 7j)	$0.183 \pm 0.007$	$1.443 \pm 0.029$	$0.023 \pm 0.002$	26,089
Halo floor	$0.201 \pm 0.004$	$1.579 \pm 0.026$	$0.020 \pm 0.002$	4509
NW crater wall	$0.217 \pm 0.008$	$1.576 \pm 0.031$	$0.021 \pm 0.001$	64,213
Whole Vesta	$0.192 \pm 0.035$	$1.454 \pm 0.145$	$0.030 \pm 0.009$	$3.56 \cdot 10^8$

**Table 4**

750 nm reflectance, 750/917 [nm] and 2.8  $\mu\text{m}$  band depth values (from Combe et al., 2015) of the two PID types. Values are given with one standard deviation.

	Mean 750 nm reflectance	Mean (750/917 [nm])	Mean 2.8 $\mu\text{m}$ band depth	n (pixel number)
PIDs type 1 (Fig. 11a-f)	$0.206 \pm 0.008$	$1.621 \pm 0.060$	$0.028 \pm 0.003$	1667
Surroundings type 1 (Fig. 11a-f)	$0.172 \pm 0.010$	$1.402 \pm 0.042$	$0.033 \pm 0.004$	14,784
PIDs type 2 (Fig. 11g-i)	$0.174 \pm 0.005$	$1.431 \pm 0.020$	$0.033 \pm 0.002$	2040
Surroundings type 2 (Fig. 11g-i)	$0.158 \pm 0.009$	$1.336 \pm 0.020$	$0.037 \pm 0.004$	8198

confirms a relationship of the two: PIDs show higher reflectance and pyroxene band strength with respect to the smooth deposit surroundings and the absolute values of PID reflectance and pyroxene band strength are directly related to those of their surroundings; i.e., where the surrounding host material has less pronounced pyroxene characteristics and lower reflectance (ejecta unit E2), the PIDs’ material likewise exhibits a less pronounced ‘enhancement’ of these properties (PIDs type 2) and vice versa. This confirms a simultaneous emplacement of the

original material before pits formed on some of the deposits surface, as was shown in detail by Tornabene et al. (2012) for Mars. Therefore, it can be excluded that the material of the PIDs was introduced later, e.g. by some sort of extraordinary secondary impact process at a later stage of Marcia’s formation. As a result, differences in age and exposure to the various kinds of space weathering processes (Pieters et al., 2012) are very unlikely causes for the spectral differences.

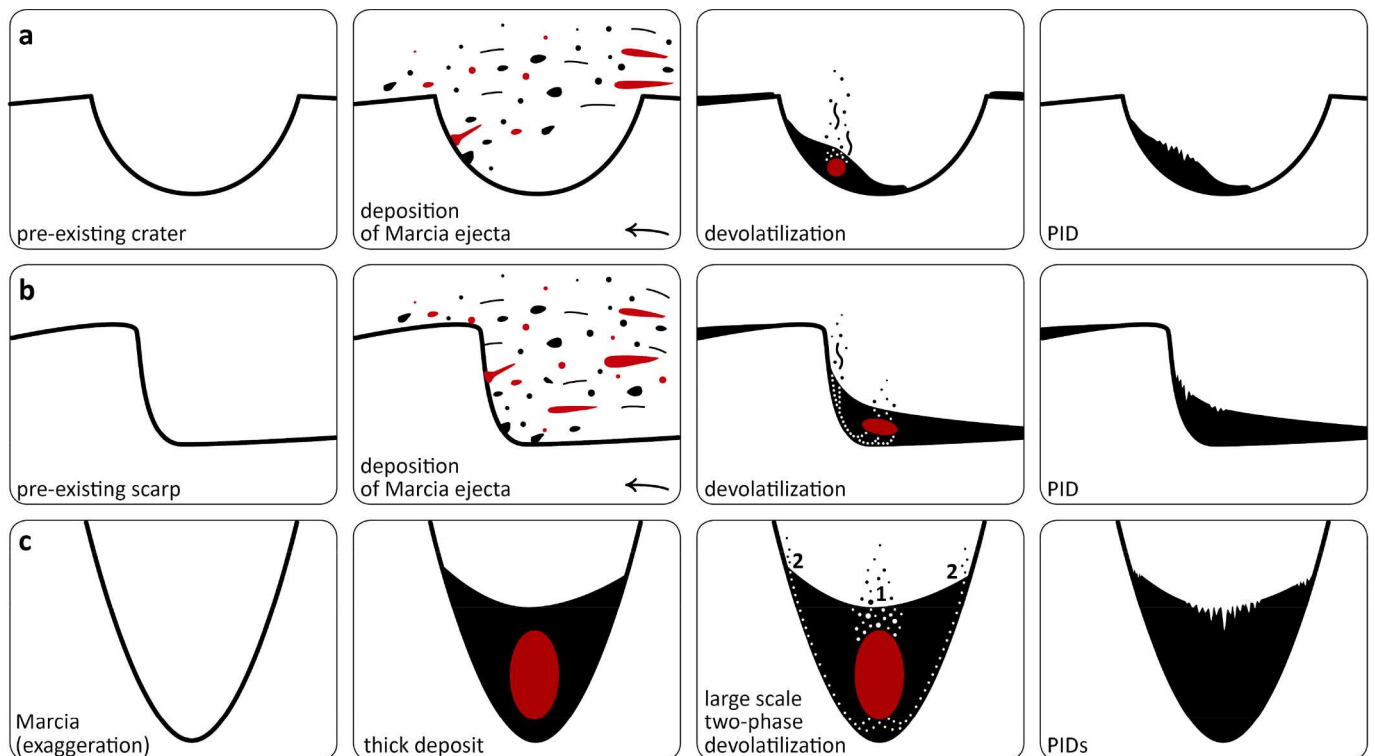
We furthermore observe that the spectral characteristics of PIDs reach several tens of meters outward into the smooth zones of the host deposits, building another sort of halo around the PIDs. This indicates that the formation of the individual pits inside a PID is linked to ejection of material, not e.g. the loss of material through subsurface voids, which was also shown for Mars (Tornabene et al., 2012). Thus, solid material was likely ejected along with volatile phases. This is consistent with the interpretation of Denevi et al. (2012).

We observe several PIDs occurring in pre-existing craters and with positive local topographies, facing Marcia crater. Their origin therefore appears to be linked to the accumulation of ejecta (Fig. 15). Accumulation of material is accompanied by an increase of impact deposit thickness and an increase in the amount of internal heat. The volume of heat-bearing material increases significantly whereas the surface area – where heat can freely radiate into space – remains small. This possibly results in the liberation of hydroxyl groups from their host minerals as well as the buildup of pressure within the pore spaces. The crater-fill PIDs do not feature a positive topography, yet they naturally represent accumulated, possibly partially melted impact material within a large cavity, likewise leading to an increased volume of volatiles per surface area and an increased internal amount of heat.

Furthermore, we identified several locations where PIDs reside along scarps and crater walls (Fig. 15b), likewise indicating a structural control facilitating the liberation of volatiles along contacts between the host deposits and bedrock. Although a relationship to pre-existing topography is only observed for a minor population of the PIDs, it is reasonable to assume that this mechanism also plays a role for other PIDs where pre-existing topography cannot be determined anymore, especially within E2b and E2a, where the pre-existing topography has been largely obscured by overlying ejecta. In summary, we present evidence that the formation of PIDs is controlled by the geomorphological setting into which the impact deposit was placed. This is consistent with what Denevi et al. (2012) already suggested (i.e., ‘topographic lows’) and what Tornabene et al. (2012) found for Martian PIDs.

Stubbs and Wang (2012) suggested the long-term survivability of





**Fig. 15.** Simplified schematic depiction of the mechanism leading to the formation of PIDs according to profiles shown in Fig. 9: a) within pre-existing small craters, b) at topographic highs, c) within Marcia (deposit thickness > 500 m). White circles indicate paths for volatile escape. Red color within a deposit indicates the thickest part which likely retains heat for the longest time spans (highly simplified). (For interpretation of the references to color in this figure legend, the reader is referred to the web version of this article.)

water ice a few meters below the surface of Vesta and therefore Scully et al. (2015) suggested that the heating of heterogeneously distributed subsurface ice deposits could also have caused the formation of PIDs. However, it is unlikely that subsurface ice would coincidentally be present within pre-existing craters, facing the excavation direction of a non-existent crater at that point in time. The redistribution of icy material by the impact and preferred deposition within craters is also questionable. Considering the spectral characteristics this possibility likewise seems implausible as the sublimation of water ice would not result in a spectral change of the rocky material considering a rapid degassing within hours. In conclusion, our observations do not favor a role of (water) ice in the formation process which instead is controlled by accumulation of ejecta and therefore the possibility of the material to liberate volatile species (i.e., increased amount of internal heat) and to build up the necessary pressure and vent pipes.

Our analysis of topographic profiles indicates that PIDs both form where their host deposit is thickest, but also on the margins of a host deposit. In the former case, this indicates an internal volatile source as such that the volatiles directly originate from the impact ejecta, which is likely a melt-bearing breccia (Tornabene et al., 2012; Denevi et al., 2012). In the latter case (formation on the margins of a deposit), pit formation occurs close to the colder target rock, which could indicate a contribution of target rock volatiles. However, an easier explanation consistent with observations by Tornabene et al. (2012) is that the contact provides a zone of weakness or conduit that would provide a path for volatile release and thus concentrate pits along those margins (Fig. 15b and c, white circles). PID formation on margins of a host deposit is especially present within Calpurnia, Minucia and also Marcia, where host deposit thicknesses are considerably larger than in other areas. The heavier overburden could additionally lead to the preferred release of volatiles along pathways adjacent to the colder target rock. Within Marcia, it is astonishing to observe very large PIDs in the center of the host deposit and very small PIDs located on the margins within the

spectrally distinct halo. This might suggest more than one phase of devolatilization where the largest number of volatiles is released very rapidly through the direct pathways within the deposit and residual volatiles from deeper regions within the host deposit ascend along the margins to form smaller PIDs (Fig. 15c). The presence of the spectral halo itself as well as signs of subsidence within the crater-fill deposit (Fig. 12 in this study and Denevi et al., 2012) might support this hypothesis of different devolatilization phases.

The majority of PIDs (~73%) occur within 30 km (i.e., one crater radius) of the Marcia rim. This correlates well with the positive correlation of ejecta deposit thickness and PID occurrence as ejecta thicknesses gradually become lower with distance from the crater (e.g., Melosh, 1989). We observe the largest and thickest PIDs within the parent crater (Marcia) and a decrease of pit occurrences (i.e., dependent on deposit thickness) with distance from the parent crater. However, we did not observe a correlation of deposit thickness and PID size (area) within the 13 identified pre-existing small craters that host PIDs. This could be due to an erroneous estimation of pre-Marcia topography but also to compositional inhomogeneities within the ejecta (especially in terms of volatile content). Tornabene et al. (2012) present evidence for Tooting crater on Mars that shows that volatile contents of the target rock might vary in different portions of the crater, resulting in pit-poor and densely pitted regions within this crater. Given the possibility that Marcia crater was formed by an oblique impact (oval shape), heterogeneities within the ejecta deposits appear likely and could cause various pit size:deposit thickness ratios not dependent on each other.

#### 4.2. Origin of the PIDs' spectral distinctness

PIDs are characterized by an increase in reflectance as well as pyroxene band strength with respect to their immediate smooth surroundings (excluding the crater-fill PIDs), yet to a varying degree (Fig. 11). This spectral change occurred after deposition and could result

from changes in grain size, structure or composition.

Regarding grain size, higher reflectance of a pyroxene-bearing material can be attributed to a smaller grain size (e.g., Clark, 1999) as the larger number of reflective surfaces (crystal faces) increases the probability of light scattering. In contrast, stronger pyroxene absorptions can be attributed to larger grain sizes as absorption of light is more likely with lower numbers of reflective surfaces and larger crystal bodies. Harloff and Arnold (2001) have shown that differences in roughness behave similar to differences in grain size. Therefore, the spectral characteristics of PIDs do not conform to general grain size or roughness effects. We nevertheless evaluate the effect of grain size variations

specifically for HED meteorites in order to evaluate whether grain size might still have an influence on the spectral appearance of the PIDs.

Fig. 16 shows the same spectral parameters as Figs. 1 & 13 but for 16 individual HED meteorites which were ground and separated into different grain size fractions. For 14 of these HEDs the largest grain size fraction exhibits the lowest 965/917 [nm] values which probably results – in contrast to a compositional difference due to different band centers – from the decrease of pyroxene band depth with larger grain sizes (e.g., Clark, 1999; Cloutis et al., 2013a). Absorption band saturation for the first pyroxene band of HEDs commonly starts around grain sizes of 67 μm on average (Cloutis et al., 2013a). The spectra of grain sizes beyond

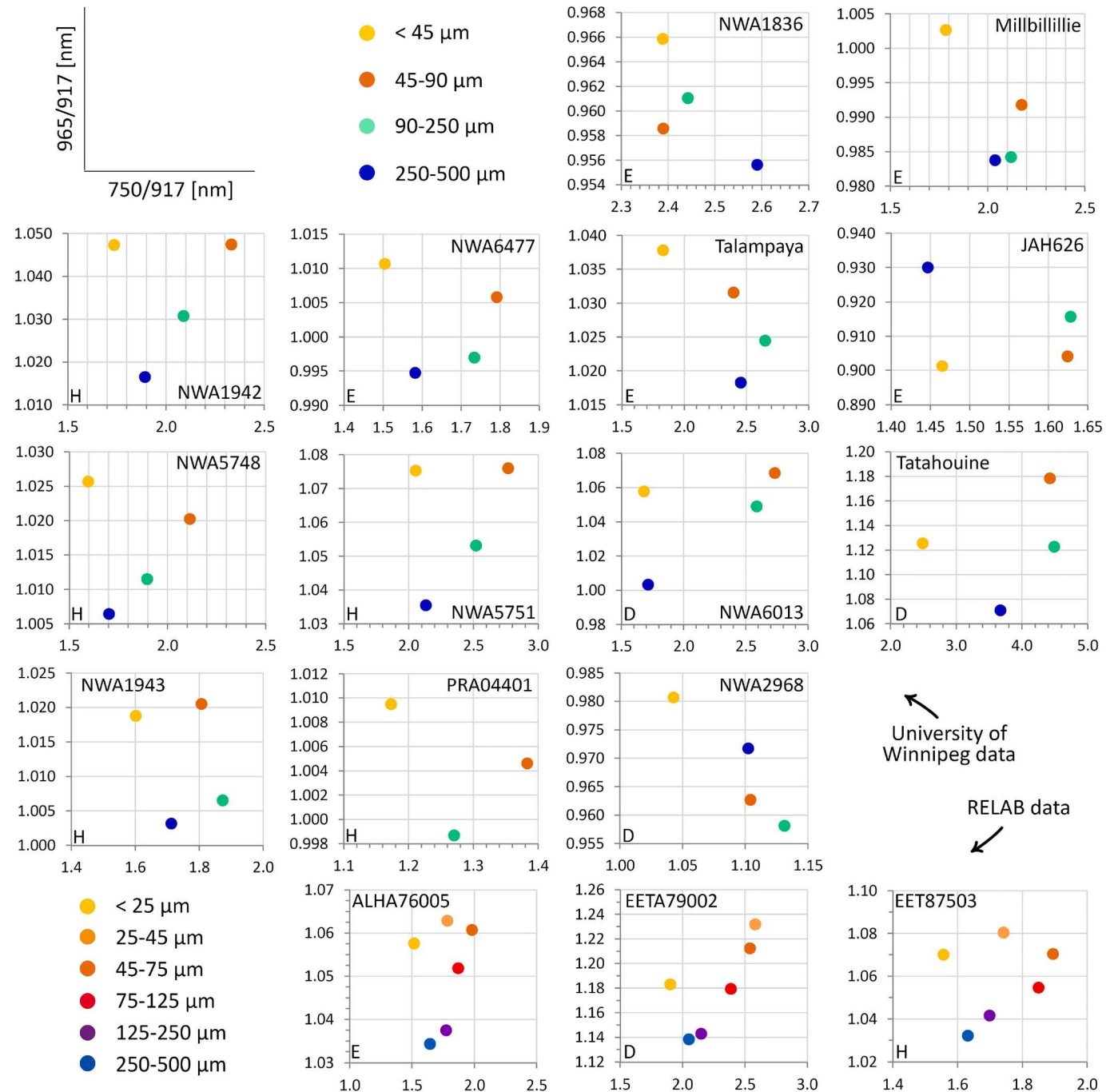


Fig. 16. 750/917 [nm] vs. 965/917 [nm] for 16 different HED's that have been separated in several grain size fractions. Note that for PRA04401, only three size fractions were available and that for the three RELAB HED's, six grain size fractions were available. The small letters in the lower left corners indicate the HED species. The first 13 sample spectra were provided by Dr. Edward Cloutis and measured at the University of Winnipeg's Planetary Spectrophotometer Facility (e.g., Cloutis et al., 2013a; Cloutis et al., 2013b).

that average value show more similar reflectance for 965 and 917 nm which reduces 965/917 [nm] values. Vice versa, the smaller grain sizes show the highest 965/917 [nm] values.

Except for JAH626, the finest fractions of all HED's exhibit the lowest 750/917 [nm] values, yet the largest grain size fractions exhibit the second lowest values for 12 of these meteorites. A possible reason for this is also the saturation of the absorption band. As grain sizes get larger, pyroxene band depth and reflectance become lower. Once a maximum of band depth is reached, reflectance can continue to decrease while the band depth cannot, causing 750/917 [nm] values to decrease again (e.g., Clark, 1999; Harloff and Arnold, 2001). PRA04401 contains carbonaceous chondrite clasts but does not exhibit any distinct spectral properties in terms of grain size. In summary, the presented spectra of different grain size fractions of HED meteorites are consistent with general grain size-related observations which do not conform with those of the PIDs on Vesta.

As we have just described, the difference of the PIDs associated with Marcia with respect to their surroundings is very systematic (higher 750/917 [nm] values, almost no change for 965/917 [nm]), indicating no observable consistency of spectral characteristics related to particle size or roughness. Zambon et al. (2014) also found that the bright material on Vesta does not result from differences in grain size. In their spectral study on HED meteorites mixed with CM2-type chondrites, Cloutis et al. (2013a) also found that contamination with carbonaceous chondrite material is the most plausible explanation for the 'dark material' on Vesta and the diminishment of spectral features. Other studies also investigated the 'dark material' on Vesta (McCord et al., 2012; Reddy et al., 2012a). They likewise concluded that the occurrence of 'dark material' is most likely caused by contamination with carbonaceous chondrite material and did not find consistencies with other possible explanations like shock effects, opaque phases and plagioclase content.

The differences between the PIDs and their surroundings follow the same systematics like the difference between HED properties and 'dark material': a positive correlation between reflectance and pyroxene band strength. In our case, this is furthermore supported by the slight depletion in OH that we observe for the PIDs (Fig. 11) consistent with devolatilization of exogenic, OH-bearing minerals. Therefore, we find the differences between PIDs and their surroundings with respect to reflectance and pyroxene band strength to likely result from a small difference in composition, i.e. due to the loss and/or decomposition of dark, volatile-bearing phases.

Regarding our spectral analysis of HED grain size fractions, it is important to note that terrestrial weathering, especially of Antarctic meteorites, can alter the grinding behavior of meteorites and thus result in unrealistic spectra for different grain sizes with respect to material still residing on an airless body. Most of the presented Antarctic meteorites have weathering grade A or W0/W1 which are the least altered grades, thus we assume – in agreement with our observations regarding basic spectral behavior of absorption bands and reflectance with respect to grain size – that these weathering effects do not or minorly affect the visible and near infrared analysis undertaken here. JAH626 is considered an outlier in the analysis. The meteorite is highly shocked (e.g., Ruesch et al., 2015) with little signs of terrestrial weathering. NWA2968 is a find and not characterized regarding its weathering grade in the Meteoritical Bulletin so far, so it is possible that the largest grain size fraction behaves anomalous with respect to the other grain size fractions of this meteorite due to terrestrial weathering. Additionally, this meteorite is officially regarded as an ungrouped olivine-rich achondrite, so it might not be representative for Vesta.

Tornabene et al. (2012) present evidence of outcropping meter to decameter-sized rock fragments within the walls of the pits with significantly "brighter" albedo which they do not observe for the smooth surroundings. They interpret this finding as evidence for the deposit being an impact melt-bearing breccia. For a suevite outcrop at Ries crater in Germany, Newsom et al. (1986) similarly report on coarse-

grained surfaces of a degassing pipe system, devoid of soil/matrix. Boyce et al. (2012) additionally suggest that the high escape rates can also eject cm-sized clasts into the surrounding of the PIDs which could represent the spectral halo presented in this study. If Vestan PIDs also show outcropping rock fragments – which is not determinable with the given image resolutions – then the spectral differences could originate from this exposure. These spectral signatures might additionally differ from typical Vestan lithologies as Marcia is the largest well-preserved crater and might have excavated deeper materials not seen anywhere else beyond the Rheasilvia basin. Within Marcia's impact melt-bearing breccia, larger clasts and rock fragments would predominantly be of HED lithology due to their higher internal strength with respect to carbonaceous chondrite material and could therefore dominate the reflectance spectrum. However, if this is true, other materials in the vicinity of Marcia like small post-impact craters or 'fresh' crater wall material still subject to modification should experience similar spectral characteristics. Yet as we have presented in our study, PIDs are characterized by stronger pyroxene absorptions (750/917 [nm] values) with respect to other Marcia-related materials with similar reflectance at 750 nm. We have shown that a 'younger' crater (i.e., post-Marcia) that impacted into the smooth part of the host deposit right next to a PID shows similar reflectance values but lower pyroxene band strength. Thus, the younger crater shows less pronounced pyroxene characteristics than the older PID within the same host deposit. This strongly indicates that another process changed the typical spectral nature of the original material at the PIDs' sites which is not related to differences in pyroxene proportions.

A significant shift of the pyroxene band center towards shorter wavelength and therefore to more Mg-rich pyroxene is not observed (Fig. 13), although the 965/917 [nm] ratio is sensitive to this mineralogical difference. Hence, there is no difference in the proportion of diogenitic/eucritic lithologies with respect to PIDs and their surroundings which favors the theory of carbonaceous contamination in addition to a unique process related to accumulation and heat retention. The more endogenic and OH-depleted nature of the PIDs could theoretically also arise from phase transitions of phyllosilicates to olivine and pyroxene due to shock metamorphism and heating to >500 °C and 750 °C, respectively (e.g., Akai, 1992; Nakamura, 2005 and references therein). However, as Sizemore et al. (2017) similarly describe for Ceres, average impact velocities of ~5 km/s in the asteroid belt (Bottke et al., 1994) would generate maximum target temperatures of ~800 K (Marchi et al., 2013; Supplementary Fig. S3) which suggests that for average projectiles impacting on Vesta, no phase transitions of phyllosilicates would occur. Furthermore, even if Marcia was a result of a high velocity impact, no olivine has been detected in the Marcia area (Ammannito et al., 2013b; Thangjam et al., 2014; Palomba et al., 2015). Yet we again note that detection of olivine might not be possible with the given instrumentation below 30 wt% (Beck et al., 2013; Le Corre et al., 2013).

Liberation of hydroxyl groups in phyllosilicates of carbonaceous chondrites starts around 400 °C (Garenne et al., 2014) implicating that the formation of PIDs can result from devolatilization of phyllosilicates at average main belt impact velocities. However, the spectral characteristics of PIDs do not conform to devolatilization studies that investigated the spectral properties of mixtures containing volatile-bearing phases upon heating and sublimation. The different mixtures (cometary analogs with silicate components) used in Poch et al. (2016) exhibited lower reflectance and diminishment of spectral features after sublimation occurred (< -70 °C). Moderate heating of a Ceres analog material (maximum of 300 K, Galiano et al., 2020) likewise resulted in darkening of spectral properties in the VIS-NIR wavelength region as does heating of phyllosilicates (up to 700 °C, e.g., Hiroi and Zolensky, 1999; Alemanno et al., 2020). The water-related band near 3 μm of the CM2 meteorite Murchison vanishes around 500–700 °C (Miyamoto, 1991; Hiroi et al., 1996) which indicates that the PIDs' materials have not seen temperatures above those values (as VIR data show absorption bands there). Below this temperature, Murchison shows a decrease in

reflectance upon heating (Cloutis et al., 2012). Cloutis et al. (2012) also showed that prolonged heating (72 h) of a subbituminous coal at 450 °C results in an increase of reflectance. In this example, organics are lost or aggregated which changes the phyllosilicate-organic ratio and makes the phyllosilicates spectrally more dominant. Hence, the loss of organic compounds might trigger the change in reflectance and pyroxene band strength for the PIDs' material; yet this effect has not been shown on carbonaceous chondrite material unless fully melted and recrystallized (Clark et al., 1993). There are no studies that reflect the situation on Vesta; yet the studies reported here show that most heating/sublimation experiments with different planetary analogs result in the darkening of overall reflectance and diminishment of spectral features, in contrary to what we observe for the PIDs.

Differences in glass content can also affect a material's spectral characteristics. For pyroxene-rich lunar impact-melt-bearing deposits, Neish et al. (2021) found a possible contribution of glass to explain a smooth optical appearance of certain melt deposits while showing high roughness from radar observations. Given the high likelihood that the PID host material is an impact melt-bearing breccia (Tornabene et al., 2012; Denevi et al., 2012), glass content could also play a role during the formation process of PIDs (i.e., the PIDs' surface might be devoid of glass due to the destruction of the surface layer through devolatilization). Tompkins and Pieters (2010) analyzed the effects of glass content in lunar Apollo samples and observed 'redder' spectra for the quenched glass samples vs. their crystalline counterpart as well as an inconsistent dependency of the reflectance at 750 nm. They found that higher glass contents shift the mafic absorption band position near 1 µm towards longer wavelength which decreases the 750/917 [nm] ratio of a glassy-crystalline mixture. Thus, the surrounding material of the PIDs could indeed contain higher glass contents, yet there is no difference regarding pyroxene band positions for PIDs and their surroundings. The observations of Tompkins and Pieters (2010) regarding the spectral properties of glass-crystalline mixtures are not consistent with our observations of PID-related material so differences in glass content do not seem to play a role in the context of the PIDs either.

We conclude that the most likely explanation for the spectral distinctness of the PIDs is the effect of prolonged internal heating due to the accumulation of material and the devolatilization accompanied by the possible loss of organics and decomposition of darkening agents, although heating studies of meteorites have only shown a general loss of spectral features and reflectance upon heating. Other processes might enhance this effect, like the ejection of entrained pyroxene-rich clasts during the rapid release of steam. Experimental work could refine this hypothesis which is beyond the scope of this study. Lastly, we note that the 'hollows' identified on Mercury (Blewett et al., 2011; Blewett et al., 2013) likewise exhibit an increase in reflectance and are linked to a loss of volatiles. While their origin is likely not impact-related (Blewett et al., 2013), the process of volatile release might share similar aspects as the PIDs on Vesta.

#### 4.3. The crater-fill PIDs of Marcia

The crater-fill PIDs of Marcia are slightly lower in reflectance than the average Vesta but exhibit the lowest OH abundance of all observed PIDs including the much brighter ones (see Tables 3 & 4 and Figs. 2, 11 and 14). This is contrary to the general negative correlation between reflectance/pyroxene band strength and OH abundance. Very few exceptions to this observation (e.g., Oppia's ejecta) on Vesta were reported by Combe et al. (2015) and Le Corre et al. (2013). De Sanctis et al. (2015c) report higher OH abundances for the pitted material on the floor (with respect to the western crater wall material) and conclude that this material is linked to volatile-rich exogenic material. However, our observations including the brighter halo of the PIDs and newly calibrated VIR data from Combe et al. (2015) do not confirm their conclusion entirely.

The crater-fill PIDs are depleted in OH with respect to other typical

Vesta materials with the same reflectance and pyroxene band strength values. The 2.8 µm band absorption depth values are even lower than for the bright PIDs west and north of the crater. The presence of the halo (Fig. 12), which comprises very small pits, shows that the crater-fill PIDs of Marcia are not homogeneously darker and that there is compositional diversity among this material. The halo shows the same trend regarding reflectance and pyroxene band strength (Fig. 14) as the external PIDs. We therefore propose that for the central PIDs, their darker appearance in the VNIR range could result from the infall of 'dark material' from the crater rim due to space weathering mechanisms (Pieters et al., 2012) and mass wasting processes (Otto et al., 2013; Krohn et al., 2014) that prevail on Vesta. Especially on the eastern crater wall inflow of dark and partly also OH-rich material is observable (see Figs. 2b & d, 12b and Scully et al., 2015). Thus, we speculate that the OH-depleted pitted floor originally exhibited high reflectance and pyroxene band strength similar to the halo at the margins of the crater-fill PIDs as well as to the area around the central peak. This would also be consistent with the spectral characteristics of the external PIDs. The crater-fill PIDs would then have gradually lost these spectral characteristics due to the input of dark material from the rim. As presented with DTM data (Fig. 9), the halo reaches higher slopes at the NW crater wall and might thus not be affected by the input of darker material. Moreover, the crater wall in the NW is much more pyroxene-dominated than other areas of the crater wall, possibly also leading to less input of dark material and/or more input of pyroxene-rich material from the walls. The large depletion of OH within the crater is consistent with the presence of the largest PIDs, i.e., the crater-fill deposit has been subject to higher temperatures and constitutes the most voluminous impactite deposit associated with craters. They are thereby the most prolonged heat source and continued to lose volatiles long after the smaller external deposits had cooled.

The observations by Tosi et al. (2014) might support this hypothesis. They found a higher thermal inertia for the crater-fill deposits of Marcia indicating a larger component of less porous material (Tosi et al., 2014; De Sanctis et al., 2015c; Scully et al., 2015). Furthermore, there is no indication of a heterogeneous subsurface where the crater-fill PIDs reside. Instead, the surrounding bedrock exposed north and west of the crater-fill PIDs shows a eucritic signature with only a very small spectral indication of contamination (see supplementary Fig. S4) which is likely due to surficial processes (e.g., Pieters et al., 2012). The crater is currently roughly 8–9 km deep (from the current rim) while the excavation depth ranges from 3 to 7 km depending on the estimation method (one third of the transient cavity depth, Melosh, 1989; estimates based on lower ballistic and upper melt-rich ejecta for Haughton crater on Earth, Osinski et al., 2011). Jaumann et al. (2014) reported the regolith layer in that region to be about 1 km thick, therefore it furthermore seems unlikely to find exogenic material at these depths as hypothesized by Scully et al. (2015). Given that typical crustal lithologies are expected beneath the regolith (i.e., eucrites; e.g., Binzel and Xu, 1993; Keil, 2002; McSween et al., 2011; McSween et al., 2013b and references therein) it seems even more intriguing that the Marcia impact mobilized such a large volume of volatiles shaping the surrounding geology while excavation depths might have reached deep below the surface regolith into a differentiated body. However, estimation of regolith thickness around Marcia by Jaumann et al. (2014) is based on visual observations of dark material while Denevi et al. (2016) assume regolith depths greater than 1 km based on blocky crater population. Thus, ejecta could possibly still be regolith-dominated. Modelling the formation of this crater could perhaps greatly enhance the understanding of volatiles involved in such a large low-gravity collision, especially given the observation that Marcia might have been an oblique impact and that oblique impacts favor survivability of impactor materials (e.g., Pierazzo and Melosh, 2000).

Ejecta and crater fill materials can differ greatly due to the provenance of the materials they are comprised of, so the spectral characteristics of the crater-fill PID could also be a result of a different composition due to shed crater wall material, adding higher reflectance



and pyroxene band strength materials (i.e., crustal material), especially to the margins of the crater-fill. The halo of the crater-fill on the margins and the central peak could therefore also represent added slumped and uplifted material with similar spectral characteristics. However, the halo is characterized by lower reflectance and similar 750/917 [nm] ratios with respect to the crater-wall material, indicating that it is not derived from this compositional variation. Instead, the halo plots on the same unique trend presented in Fig. 14, indicating that crater-fill and external PIDs share a common origin, independent of compositional differences.

#### 4.4. Distribution of volatiles

Ejecta units E1 and E2 significantly differ in their overall OH content (Fig. 2d). The VIR and GRaND instruments have detected higher concentrations of eucritic lithologies in and around Marcia (as opposed to diogenitic and howarditic lithologies, Prettyman et al., 2012; Ammannito et al., 2013a, De Sanctis et al., 2015b) indicating that the Marcia impact excavated eucritic crustal material. This generally conforms to the estimated excavation depth (3 to 7 km) and the estimated regolith thickness in this region (1 km, Jaumann et al., 2014). This higher eucritic concentration appears in both E1 and E2 as presented here (mainly east and west of Marcia, best illustrated in Russell et al., 2015) which could suggest that Calpurnia is not the source of ejecta unit E2a. If these eucrite-dominated lithologies were to source from the Calpurnia event, they would broadly occur around Calpurnia crater as well, which cannot be observed (Prettyman et al., 2013; Russell et al., 2015) though the data presented do not have a high spatial resolution. The Marcia region displays both large differences in OH contents but also increased eucritic lithologies, implying complex relationships between the observed materials. We have presented evidence that pitted surfaces do not form as a result of an especially high volatile content or the presence of ice at this location but rather through structural control. Nevertheless, volatiles are naturally required in the formation of PIDs, which is why we discuss the distribution of volatiles (i.e., the distribution of carbonaceous material) in the Marcia region in more detail.

Our estimates of volatiles that were lost through the PIDs range around  $10^8$ – $10^9$  m<sup>3</sup> (Table 2). As E2a is still very OH-rich (Figs. 2 and 4) clearly not all volatiles were lost during the impact, be it Marcia or Calpurnia. Reddy et al. (2012a) suggest that on average 1–6 vol% of CM2 chondrite material is mixed within the regolith of Vesta and that up to 50 vol% are locally possible. They present three equations (Section 5.2) to calculate the CM2 content (vol%) of which the first two were derived by Le Corre et al. (2011) and are based on the reflectance at 750 nm and the parameter for pyroxene band strength (750/917 [nm]). The third equation was developed by Reddy et al. (2012a) and uses the ratio 750/965 [nm]. We calculated the CM2 content for all of our regions of interest and for all three equations. The three equations and all calculated values can be found in the supplements (S6). Eq. (1) which is based on the 750 nm reflectance gives the highest contents and Eq. (2) using the 750/917 [nm] ratio gives the lowest values. The third equation has similar values as Eq. (2) with slightly higher estimates (typically 2 to 4 vol%). Results of Eq. (1) yield similar values like (2) and (3) for low reflectance regions but significantly higher values for higher reflectance regions which seems unrealistic. In the following, we use Eq. (3) as it appears to yield the most realistic results. We note at this point that the calculated values most likely do not represent the ‘true’ values as PIDs do not follow the ‘typical’ Vestan trend regarding their pyroxene band strength values (Fig. 14), which also affects the 750/965 [nm] ratio.

We calculate the difference in CM2 chondrite material between PIDs and their surroundings (based on values in Table 4) to be about 9 to 12 vol% which is slightly higher than Reddy et al. (2012a) suggest for the average abundance of CM2 chondrite material on a global scale. This difference corresponds to a difference of volatile material of roughly 1 wt% (assuming 11% of mass loss during devolatilization, Garenne et al., 2014). The smooth surroundings of PIDs contain about 19 to 26 vol% CM2 material while the PIDs contain about 7 to 17 vol% of CM2

material. The volatile content of the surrounding of PIDs corresponds to about 2–3 wt%. Boyce et al. (2012) show for Tooting crater on Mars that a relatively low volume of volatiles can lead to extensive pitting as well. They estimate ~12 wt% of volatiles for Tooting crater target material but also acknowledge that for the Ries crater in Germany, Engelhardt et al. (1995) and Osinski (2003) observed that roughly half of the target volatiles were still present in impact glasses, reducing the released volume. This corresponds well to our calculations of volatiles lost (i.e., 1 wt% lost with host material volatile abundances of 2–3 wt%) based on the approaches by Reddy et al. (2012a) and Garenne et al. (2014) and is also consistent with the generally dryer nature of Vesta (i.e., no sub-surface ice as opposed to Mars).

Based on an average of 10 vol% of CM2 material loss, we calculated the volume of CM2 material now lost at the PIDs’ sites (excluding the crater-fill) using the total size of PIDs (212 km<sup>2</sup>, Table 2), average thicknesses of the PIDs’ material (50 m, 100 m, 200 m, see Section 3.2) and a porosity of 25% which results in approximate total volumes of  $0.9 \cdot 10^9$  m<sup>3</sup>,  $1.8 \cdot 10^9$  m<sup>3</sup> and  $3.5 \cdot 10^9$  m<sup>3</sup>, respectively. We roughly estimate the regolith porosity (i.e., 25%) from macro porosity estimates for the silicate portion of Vesta (8%) by Ermakov et al. (2014), average howardite and eucrite porosities (11%) given in Macke et al. (2011a) and the decline in porosity near the surface from 55% at the surface to 37% at one meter depth (Palmer et al., 2015).

Garenne et al. (2014) observe a mass loss of around 11% between 200 and 700 °C (attributed to (oxy) hydroxides and the dehydroxylation of phyllosilicates) for their studied CM chondrites on which they performed thermogravimetric analysis combined with infrared spectroscopy in order to quantify the chondrite’s water content. We assume here that the molecular waters lost between 0 and 200 °C are already gone within the whole ejecta (i.e., both PIDs and their smooth surroundings). Assuming the same percentage of volatiles lost during the devolatilization process occurring at the PIDs’ sites, a grain density of 2900 kg/m<sup>3</sup> for the CM2 material (Macke et al., 2011b) and the assumption that the density of lost volatiles roughly equals 1000 kg/m<sup>3</sup> (the density of water vapor, upper limit), resulting volatile volumes are  $2.8 \cdot 10^8$  m<sup>3</sup>,  $5.7 \cdot 10^8$  m<sup>3</sup> and  $1.1 \cdot 10^9$  m<sup>3</sup>, respectively. These values are in very good agreement with the estimated values in Table 2 from pit statistics. For the crater-fill PIDs in Marcia, we assume a material thickness of 500 m and a lower porosity (15%) accounting for more compacted material (Tosi et al., 2014; De Sanctis et al., 2015c; Scully et al., 2015). The volume of lost volatiles is then  $8.5 \cdot 10^9$  m<sup>3</sup> which is one order of magnitude higher than our estimates in Table 2, possibly resulting from underestimated pit depths in Section 3.2, underestimated porosity or overestimated material thickness in this calculation.

With the same equation derived in Reddy et al. (2012a), we furthermore calculate the average CM2 content of E2a to be around 31 vol%. If we assume that this ejecta part formed exclusively from a 1 km thick contaminated regolith layer (Jaumann et al., 2014; neglecting the possibility E2a originates from the Calpurnia impact) and a crater radius of roughly 30 km, a volume of ~2800 km<sup>3</sup> of regolith material was redistributed by the impact. Assuming a symmetric distribution around Marcia with a radius of about 100 km (the farthest PID is 69 km off the crater rim) we calculate the average thickness of contaminated Marcia ejecta to be roughly 100 m, which is consistent with ejecta thicknesses estimated with the approach by McGetchin et al. (1973) for ejecta about 15 km off the Marcia rim. We acknowledge that this is a rough estimate with high variations between regions closer and farther from the rim and it does also not include Calpurnia as the possible origin of E2a. It is difficult to estimate the thickness of E2a as it is located right on the slopes of Vestalia Terra (mountains rising to ~10 km above the Marcia rim). Ejecta accumulated there and obscured much of the underlying topography. If we assume an average of 200 m thickness roughly accounting for this accumulation for an area of about 13,000 km<sup>2</sup> (E2a, Fig. 3), a regolith porosity of roughly 25% and a CM2 content of 31 vol%, roughly  $6 \cdot 10^{11}$  m<sup>3</sup> of CM2 material are still present within E2a which corresponds to  $1.9 \cdot 10^{11}$  m<sup>3</sup> of volatiles. This is a lower limit as there are



possibly more E2-type ejecta below E1 ejecta (as seen at Laeta crater and possibly even at Aricia Tholus, Fig. 3). For E1 and E2b, the average CM2 content is  $\sim 16$  vol% and 24 vol%, respectively. For E1, with an assumed average thickness of 50 m and an extent of 11,000 km<sup>2</sup>, the volume of still-present volatiles is  $\sim 2 \times 10^{10}$  m<sup>3</sup>. For E2b (100 m and 12,000 km<sup>2</sup>), still-present volatiles are in the order of  $7 \times 10^{10}$  m<sup>3</sup>. The estimated value of  $1.9 \times 10^{11}$  m<sup>3</sup> of volatiles still present in E2a is two to three orders of magnitude higher than our estimates of lost volatiles through volatile degassing at the PIDs' sites. Most of the hydroxyl groups bound in minerals/phylosilicates were therefore not liberated during the impact (be it Marcia or Calpurnia) and the volatiles lost by rapid vent-forming devolatilization represent a small fraction (<2%) of volatiles still present in the whole area. This furthermore illustrates that PID formation does not depend on the volatile content at their specific location as volatiles are still ubiquitous in the ejecta blanket. They were lost at the PIDs' sites due to topography-dependent ejecta accumulation and the resulting increase in deposit thickness and internal heat.

Independent of whether Marcia or Calpurnia generated the ejecta unit E2a, the regolith where the Marcia impactor hit held at least 31 vol % of CM2 material which is an unreasonably high amount (Reddy et al., 2012a) for a large regional area like the  $\sim 30$  km radius of pre-Marcia or  $\sim 25$  km radius of pre-Calpurnia regolith, yet the three equations to calculate CM2 content by Le Corre et al., 2011 and Reddy et al., 2012a generate similar values for E2a (see S6) and E2a furthermore shows the highest large-scale abundance of OH (i.e., strongest absorptions at 2.8  $\mu$ m, Combe et al., 2015). The Veneneia impact basin which is thought to have delivered most of the dark material is close to Marcia (e.g., Schenk et al., 2012; Jaumann et al., 2014) which could be the reason for this abnormally high amount of carbonaceous chondrite material within the regolith, yet does not entirely explain the strong dichotomy of the ejecta units which remains an open question.

## 5. Summary and conclusions

This work studies the spectral and geomorphologic properties of pitted impact deposits (PIDs) related to the young, large impact crater Marcia (and Calpurnia) on Vesta. By analyzing FC data, we find that volatile release shaping the characteristic pits within the PIDs is linked to topography-controlled accumulation of ejecta and the accompanied increase of deposit thickness and internal amount of heat, resulting in the prolonged retention of heat within the material and larger volumes of heat-bearing material with respect to the deposit's surface area. Pitted surfaces on impact deposits are often found within pre-existing craters and along scarps and crater-walls, enabling the estimation of pre-existing topography and deposit thickness. PID formation is therefore most likely not linked to exceptionally high, location-specific volatile contents or subsurface ice deposits as suggested by Scully et al. (2015).

The pitted surfaces of PIDs display an 'enhancement' of eucritic characteristics, i.e. higher reflectance at 750 nm and higher pyroxene band strength (750/917 [nm]). This most likely corresponds to less contamination by carbonaceous chondrite material in contrast to grain size, roughness or glass content. Yet we note that the observed changes to the deposit material do not conform entirely with the trend given by carbonaceous contamination. We observe a unique spectral trend for PIDs with respect to their smooth surroundings and/or other typical Vestan materials regarding reflectance, pyroxene band strength and 2.8  $\mu$ m absorptions. The most likely explanation for this spectral enhancement of eucritic characteristics is the loss and decomposition of exogenic volatile-rich material upon prolonged heating. This is consistent with the hypothesis presented by Denevi et al. (2012) (which was based on findings from Tornabene et al., 2012 and Boyce et al., 2012 for Martian PIDs).

Heating studies of meteorites and analog materials generally show a loss of reflectance and spectral features upon heating, which is why it remains difficult to explain this spectral phenomenon, especially the increase of pyroxene band strength with respect to other Marcia-related

materials with similar reflectance values. However, Vesta-related experiments have not yet been undertaken. The unique PID-forming process on Mars includes excavation of entrained particles/clasts/fragments through the devolatilization conduits (Tornabene et al., 2012; Boyce et al., 2012) which might play an additional role on Vesta if these clasts were eucrite-dominated. This might enhance the effect of the loss of CM2 compounds and explain the unique spectral trend. This is also consistent with the observed spectral halo around the pitted surfaces, covering smooth surfaces beyond the pits. Nevertheless, it remains challenging to judge whether the expected spectral effects from such an excavation of eucrite-dominated clasts could really conform to the observed deviation from the typical Vestan spectral trend which is especially related to the higher band strength values of the PIDs. Thus, the petrologic and geochemical details of PID formation remain uncertain.

The spectral characteristics of the crater-fill PIDs, which are by far the largest of all PIDs observed, are heterogeneous. Most of the PIDs' surface show lower reflectance and pyroxene band strength than their surroundings (i.e., the crater walls) but also the lowest 2.8  $\mu$ m band depth values among PIDs. This contradicts the general anti-correlation between OH abundance and reflectance/pyroxene band strength as observed for all other PIDs related to Marcia. We speculate this might result from inflow of dark material from the crater rim by mass wasting processes. The original surface of the crater-fill PIDs likely exhibited higher reflectance and pyroxene band strength similar to the halo observed on the margins of the crater-fill PIDs and close to the central peak. This halo shows the same unique spectral characteristics as the external PIDs regarding reflectance and pyroxene band strength and therefore, the crater-fill PIDs might still have experienced the same unique process. However, the halo moreover comprises much smaller individual pits as does the immediate surrounding of the central peak which additionally shows signs of subsidence. This might indicate a secondary devolatilization process within the crater-fill deposit.

PIDs occur within spectrally distinct ejecta units and accordingly hold different spectral and morphological properties, likely related to the initial abundance of volatiles/chondritic material in each ejecta unit. Based on Eq. (3) in Reddy et al. (2012a) we calculate the difference in CM2 chondrite material between PIDs and their surroundings to be about 8 to 12 vol% which would correspond to a difference of  $\sim 1$  wt% volatiles. We roughly estimated the volume of volatiles that were lost through the explosive devolatilization within the PIDs material as well as the volume of volatiles still present in the ejecta. We find that volatiles lost from PIDs likewise represent only a small fraction of the volatiles still present in the ejecta (<2%). This furthermore illustrates that PID formation is not tied to an exceptionally high availability of volatiles (i.e., carbonaceous chondrite material). The inferred volumes of now lost volatiles from these calculations are in good agreement with volumes calculated from pit statistics.

## Declaration of Competing Interest

The authors declare that they have no known competing financial interests or personal relationships that could have appeared to influence the work reported in this paper.

## Acknowledgements

This work has benefitted greatly from the revision process. We therefore especially thank Dr. L. L. Tornabene for his thorough and detailed remarks which greatly improved this work. We furthermore thank an anonymous reviewer for enhancing the methodology regarding the meteorite comparisons and additional improvements. We are also very grateful to Dr. Edward Cloutis and the University of Winnipeg's Planetary Spectrophotometer Facility for providing some of the spectral data used in this study (Fig. 16) and for discussions and ideas regarding this work. The samples from which the mentioned spectra were obtained

were provided to the University of Winnipeg by Dr. Andreas Nathues of the Max Planck Institute for Solar System Research and Dr. Kurt Mengel of Clausthal University which we gratefully acknowledge as well. This work is part of the research project „The Physics of Volatile-Related Morphologies on Asteroids and Comets“. We would like to gratefully acknowledge the financial support and endorsement from the DLR Management Board Junior Research Group Leader Program and the Executive Board Member for Space Research and Technology.

## Appendix A. Supplementary data

Supplementary data to this article can be found online at <https://doi.org/10.1016/j.icarus.2021.114633>.

## References

- Akai, J., 1992. T-T-T diagram of serpentine and saponite, and estimation of metamorphic heating degree of Antarctic carbonaceous chondrites. *Antarct. Meteor. Res.* 5, 120.
- Alemanno, G., Maturilli, A., Helbert, J., D'Amore, M., 2020. Laboratory studies on the 3  $\mu\text{m}$  spectral features of Mg-rich phyllosilicates with temperature variations in support of the interpretation of small asteroid surface spectra. *Earth Planet. Sci. Lett.* 546, 116424. <https://doi.org/10.1016/j.epsl.2020.116424>.
- Ammannito, E., De Sanctis, M.C., Capaccioni, F., Capria, M.T., Carraro, F., Combe, J.P., Fonte, S., Frigeri, A., Joy, S.P., Longobardo, A., Magni, G., Marchi, S., McCord, T.B., McFadden, L.A., McSween, H.Y., Palomba, E., Pieters, C.M., Polansky, C.A., Raymond, C.A., Sunshine, J.M., Tosi, F., Zambon, F., Russell, C.T., 2013a. Vestan lithologies mapped by the visual and infrared spectrometer on Dawn. *Meteorit. Planet. Sci.* 48 (11), 2185–2198. <https://doi.org/10.1111/maps.12192>.
- Ammannito, E., de Sanctis, M.C., Palomba, E., Longobardo, A., Mittlefehldt, D.W., McSween, H.Y., Marchi, S., Capria, M.T., Capaccioni, F., Frigeri, A., Pieters, C.M., Ruesch, O., Tosi, F., Zambon, F., Carraro, F., Fonte, S., Hiesinger, H., Magni, G., McFadden, L.A., Raymond, C.A., Russell, C.T., Sunshine, J.M., 2013b. Olivine in an unexpected location on Vesta's surface. *Nature* 504, 122.
- Beck, A.W., McCoy, T.J., Sunshine, J.M., Viviano, C.E., Corrigan, C.M., Hiroi, T., Mayne, R.G., 2013. Challenges in detecting olivine on the surface of 4 Vesta. *Meteorit. Planet. Sci.* 48 (11), 2155–2165. <https://doi.org/10.1111/maps.12160>.
- Binzel, R.P., Xu, S., 1993. Chips off of Asteroid 4 Vesta: Evidence for the Parent Body of Basaltic Achondrite Meteorites, 260, p. 186. <https://doi.org/10.1126/science.260.5105.186>.
- Blewett, D.T., Chabot, N.L., Denevi, B.W., Ernst, C.M., Head, J.W., Izenberg, N.R., Murchie, S.L., Solomon, S.C., Nittler, L.R., McCoy, T.J., Xiao, Z., Baker, D.M.H., Fassett, C.I., Braden, S.E., Oberst, J., Scholten, F., Preusker, F., Hurwitz, D.M., 2011. Hollows on mercury: MESSENGER evidence for geologically recent volatile-related activity. *Science* 333, 1856.
- Blewett, D.T., Vaughan, W.M., Xiao, Z., Chabot, N.L., Denevi, B.W., Ernst, C.M., Helbert, J., D'Amore, M., Maturilli, A., Head, J.W., Solomon, S.C., 2013. Mercury's hollows: constraints on formation and composition from analysis of geological setting and spectral reflectance. *J. Geophys. Res. (Planets)* 118, 1013–1032.
- Botke, W.F., Nolan, M.C., Greenberg, R., Kolvoord, R.A., 1994. Velocity distributions among colliding asteroids. *Icarus* 107, 255–268.
- Boyce, J.M., Wilson, L., Mougins-Mark, P.J., Hamilton, C.W., Tornabene, L.L., 2012. Origin of small pits in martian impact craters. *Icarus* 221, 262–275.
- Clark, B.E., Fanale, F.P., Robinson, M.S., 1993. Simulation of possible regolith alteration effects on carbonaceous chondrite meteorites. In: Paper presented at the Lunar and Planetary Science Conference XXIV, pp. 301–302. Abstract.
- Clark, R.N., 1999. Spectroscopy of rocks and minerals, and principles of spectroscopy. In: Rencz, A.N. (Ed.), *Remote Sensing for the Earth Sciences: Manual of Remote Sensing*, 3. John Wiley & Sons, Inc.
- Cloutis, E.A., Hudon, P., Hiroi, T., Gaffey, M.J., 2012. Spectral reflectance properties of carbonaceous chondrites 4: aqueously altered and thermally metamorphosed meteorites. *Icarus* 220, 586. <https://doi.org/10.1016/j.icarus.2012.05.018>.
- Cloutis, E.A., Izawa, M.R.M., Pompilio, L., Reddy, V., Hiesinger, H., Nathues, A., Mann, P., Le Corre, L., Palomba, E., Bell, J.F., 2013a. Spectral reflectance properties of HED meteorites + CM2 carbonaceous chondrites: comparison to HED grain size and compositional variations and implications for the nature of low-albedo features on asteroid 4 Vesta. *Icarus* 223, 850–877.
- Cloutis, E.A., Mann, P., Izawa, M.R.M., Nathues, A., Reddy, V., Hiesinger, H., Le Corre, L., Palomba, E., 2013b. The 2.5–5.1  $\mu\text{m}$  reflectance spectra of HED meteorites and their constituent minerals: implications for Dawn. *Icarus* 225, 581–601.
- Combe, J.-P., Ammannito, E., Tosi, F., De Sanctis, M.C., McCord, T.B., Raymond, C.A., Russell, C.T., 2015. Reflectance properties and hydrated material distribution on Vesta: global investigation of variations and their relationship using improved calibration of Dawn VIR mapping spectrometer. *Icarus* 259, 21–38.
- Combe, J.-P., McCord, T.B., Tosi, F., Ammannito, E., Carrozzo, F.G., De Sanctis, M.C., Raponi, A., Byrne, S., Landis, M.E., Hughson, K.H.G., Raymond, C.A., Russell, C.T., 2016. Detection of Local H<sub>2</sub>O Exposed at the Surface of Ceres, 353, p. aaf3010. <https://doi.org/10.1126/science.aaf3010>.
- Consolmagno, G.J., Drake, M.J., 1977. Composition and Evolution of the Eucrite Parent Body: Evidence from Rare Earth Elements, 41, p. 1271. [https://doi.org/10.1016/0016-7037\(77\)90072-2](https://doi.org/10.1016/0016-7037(77)90072-2).
- De Sanctis, M.C., Coradini, A., Ammannito, E., Filacchione, G., Capria, M.T., Fonte, S., Magni, G., Barbis, A., Bini, A., Dami, M., Ficaï-Veltroni, I., Preti, G., 2011. The VIR spectrometer. *Space Sci. Rev.* 163 (1), 329–369. <https://doi.org/10.1007/s11214-010-9668-5>.
- De Sanctis, M.C., Ammannito, E., Capria, M.T., Tosi, F., Capaccioni, F., Zambon, F., Carraro, F., Fonte, S., Frigeri, A., Jaumann, R., Magni, G., Marchi, S., McCord, T.B., McFadden, L.A., McSween, H.Y., Mittlefehldt, D.W., Nathues, A., Palomba, E., Pieters, C.M., Raymond, C.A., Russell, C.T., Toplis, M.J., Turrini, D., 2012a. Spectroscopic characterization of mineralogy and its diversity across Vesta. *Science* 336 (6082), 697–700. <https://doi.org/10.1126/science.1219270>.
- De Sanctis, M.C., Combe, J.-P., Ammannito, E., Palomba, E., Longobardo, A., McCord, T.B., Marchi, S., Capaccioni, F., Capria, M.T., Mittlefehldt, D.W., Pieters, C.M., Sunshine, J., Tosi, F., Zambon, F., Carraro, F., Fonte, S., Frigeri, A., Magni, G., Raymond, C.A., Russell, C.T., Turrini, D., 2012b. Detection of widespread hydrated materials on Vesta by the VIR imaging spectrometer on board the dawn mission. *Astrophys. J. Lett.* 758.
- De Sanctis, M.C., Ammannito, E., Capria, M.T., Capaccioni, F., Combe, J.-P., Frigeri, A., Longobardo, A., Magni, G., Marchi, S., McCord, T.B., Palomba, E., Tosi, F., Zambon, F., Carraro, F., Fonte, S., Li, Y.J., McFadden, L.A., Mittlefehldt, D.W., Pieters, C.M., Jaumann, R., Stephan, K., Raymond, C.A., Russell, C.T., 2013. Vesta's mineralogical composition as revealed by the visible and infrared spectrometer on dawn. *Meteorit. Planet. Sci.* 48, 2166–2184.
- De Sanctis, M.C., Ammannito, E., Raponi, A., Marchi, S., McCord, T.B., McSween, H.Y., Capaccioni, F., Capria, M.T., Carrozzo, F.G., Ciarniello, M., Longobardo, A., Tosi, F., Fonte, S., Formisano, M., Frigeri, A., Giardino, M., Magni, G., Palomba, E., Turrini, D., Zambon, F., Combe, J.-P., Feldman, W., Jaumann, R., McFadden, L.A., Pieters, C.M., Prettyman, T., Toplis, M., Raymond, C.A., Russell, C.T., 2015a. Ammoniated Phyllosilicates with a Likely Outer Solar System Origin on (1) Ceres, 528, p. 241. <https://doi.org/10.1038/nature16172>.
- De Sanctis, M.C., Combe, J.P., Ammannito, E., Frigeri, A., Longobardo, A., Palomba, E., Tosi, F., Zambon, F., Stephan, K., Raymond, C.A., Russell, C.T., 2015b. Eucritic crust remnants and the effect of in-falling hydrous carbonaceous chondrites characterizing the composition of Vesta's Marcia region. *Icarus* 259, 91–115. <https://doi.org/10.1016/j.icarus.2015.05.014>.
- De Sanctis, M.C., Frigeri, A., Ammannito, E., Tosi, F., Marchi, S., Zambon, F., Raymond, C.A., Russell, C.T., 2015c. Mineralogy of Marcia, the youngest large crater of Vesta: character and distribution of pyroxenes and hydrated material. *Icarus* 248, 392–406.
- Denevi, B.W., Blewett, D.T., Buczkowski, D.L., Capaccioni, F., Capria, M.T., De Sanctis, M.C., Garry, W.B., Gaskell, R.W., Le Corre, L., Li, J.-Y., Marchi, S., McCoy, T.J., Nathues, A., O'Brien, D.P., Petro, N.E., Pieters, C.M., Preusker, F., Raymond, C.A., Reddy, V., Russell, C.T., Schenk, P., Scully, J.E.C., Sunshine, J.M., Tosi, F., Williams, D.A., Wyrick, D., 2012. Pitted terrain on Vesta and Implications for the presence of volatiles. *Science* 338 (6104), 246. <https://doi.org/10.1126/science.1225374>.
- Denevi, B.W., Beck, A.W., Coman, E.I., Thomson, B.J., Ammannito, E., Blewett, D.T., Sunshine, J.M., de Sanctis, M.C., Li, J.-Y., Marchi, S., Mittlefehldt, D.W., Petro, N.E., Raymond, C.A., Russell, C.T., 2016. Global Variations in Regolith Properties on Asteroid Vesta from Dawn's Low-Altitude Mapping Orbit, 51, p. 2366. <https://doi.org/10.1111/maps.12729>.
- Engelhardt, W.V., 1972. Shock Produced Rock Glasses from the Ries Crater, 36, p. 265. <https://doi.org/10.1007/bf00444336>.
- Engelhardt, W.V., Arndt, J., Fecker, B., Pankau, H.G., 1995. Suevite breccia from the Ries crater, Germany: origin, cooling history and devitrification of impact glasses. *Meteoritics* 30, 279. <https://doi.org/10.1111/j.1945-5100.1995.tb01126.x>.
- Ermakov, A.I., Zuber, M.T., Smith, D.E., Raymond, C.A., Balmino, G., Fu, R.R., Ivanov, B.A., 2014. Constraints on Vesta's interior structure using gravity and shape models from the Dawn mission. *Icarus* 240, 146–160. <https://doi.org/10.1016/j.icarus.2014.05.015>.
- Ermakov, A.I., Fu, R.R., Castillo-Rogez, J.C., Raymond, C.A., Park, R.S., Preusker, F., Russell, C.T., Smith, D.E., Zuber, M.T., 2017. Constraints on Ceres' Internal Structure and Evolution from its Shape and Gravity Measured by the Dawn Spacecraft, 122, p. 2267. <https://doi.org/10.1002/2017je005302>.
- Fu, R.R., Ermakov, A.I., Marchi, S., Castillo-Rogez, J.C., Raymond, C.A., Hager, B.H., Zuber, M.T., King, S.D., Bland, M.T., Cristina De Sanctis, M., Preusker, F., Park, R.S., Russell, C.T., 2017. The Interior Structure of Ceres as Revealed by Surface Topography, 476, p. 153. <https://doi.org/10.1016/j.epsl.2017.07.053>.
- Gaffey, M.J., 1976. Spectral reflectance characteristics of the meteorite classes. *J. Geophys. Res.* 81, 905.
- Galiano, A., Dirri, F., Palomba, E., Longobardo, A., Schmitt, B., Beck, P., 2020. Spectral investigation of Ceres analogue mixtures: in-depth analysis of crater central peak material (ccp) on Ceres. *Icarus* 343, 113692.
- Garenne, A., Beck, P., Montes-Hernandez, G., Chiriach, R., Toche, F., Quirico, E., Bonal, L., Schmitt, B., 2014. The abundance and stability of "water" in type 1 and 2 carbonaceous chondrites (Cl, CM and CR). *Geochim. Cosmochim. Acta* 137, 93.
- Harloff, J., Arnold, G., 2001. Near-Infrared Reflectance Spectroscopy of Bulk Analog Materials for Planetary Crust, 49, p. 191. [https://doi.org/10.1016/s0032-0633\(00\)00132-x](https://doi.org/10.1016/s0032-0633(00)00132-x).
- Hiroi, T., Zolensky, M.E., 1999. UV-Vis-NIR Absorption Features of Heated Phyllosilicates as Remote-Sensing Clues of Thermal Histories of Primitive Asteroids. *Antarct. Meteorite Res.* 12, 108.
- Hiroi, T., Zolensky, M.E., Pieters, C.M., Lipschutz, M.E., 1996. Thermal metamorphism of the C, G, B, and F asteroids seen from the 0.7 micron, 3 micron and UV absorption strengths in comparison with carbonaceous chondrites. *Meteorit. Planet. Sci.* 31, 321. <https://doi.org/10.1111/j.1945-5100.1996.tb02068.x>.

- Jaumann, R., Nass, A., Otto, K., Krohn, K., Stephan, K., McCord, T.B., Williams, D.A., Raymond, C.A., Blewett, D.T., Hiesinger, H., Yingst, R.A., De Sanctis, M.C., Palomba, E., Roatsch, T., Matz, K.-D., Preusker, F., Scholten, F., Russell, C.T., 2014. The geological nature of dark material on Vesta and implications for the subsurface structure. *Icarus* 240, 3–19. <https://doi.org/10.1016/j.icarus.2014.04.035>.
- Keilm, S., Tosi, F., Capria, M.T., De Sanctis, M.C., Longobardo, A., Palomba, E., Russell, C.T., Raymond, C.A., 2015. Separation of thermal inertia and roughness effects from Dawn/VIR measurements of Vesta surface temperatures in the vicinity of Marcia crater. *Icarus* 262, 30–43.
- Keil, K., 2002. Geological history of asteroid 4 Vesta: the "Smallest Terrestrial Planet". In: *Asteroids III*, p. 573.
- Krohn, K., Jaumann, R., Otto, K., Hoogenboom, T., Wagner, R., Buczkowski, D.L., Garry, B., Williams, D.A., Yingst, R.A., Scully, J., De Sanctis, M.C., Kneissl, T., Schmedemann, N., Kersten, E., Stephan, K., Matz, K.D., Pieters, C.M., Preusker, F., Roatsch, T., Schenk, P., Russell, C.T., Raymond, C.A., 2014. Mass movement on Vesta at steep scarps and crater rims. *Icarus* 244, 120–132. <https://doi.org/10.1016/j.icarus.2014.03.013>.
- Larson, H.P., Fink, U., 1975. Infrared Spectral Observations of Asteroid 4 Vesta, 26, p. 420. [https://doi.org/10.1016/0019-1035\(75\)90109-8](https://doi.org/10.1016/0019-1035(75)90109-8).
- Le Corre, L., Reddy, V., Nathues, A., Cloutis, E.A., 2011. How to Characterize Terrains on 4 Vesta using Dawn Framing Camera Color Bands?, 216, p. 376. <https://doi.org/10.1016/j.icarus.2011.09.014>.
- Le Corre, L., Reddy, V., Schmedemann, N., Becker, K.J., O'Brien, D.P., Yamashita, N., Peplowski, P.N., Prettyman, T.H., Li, J.-Y., Cloutis, E.A., Denevi, B.W., Kneissl, T., Palmer, E., Gaskell, R.W., Nathues, A., Gaffey, M.J., Mittlefehldt, D.W., Garry, W.B., Sierks, H., Russell, C.T., Raymond, C.A., De Sanctis, M.C., Ammannito, E., 2013. Olivine or impact melt: nature of the "Orange" material on Vesta from Dawn. *Icarus* 226 (2), 1568–1594. <https://doi.org/10.1016/j.icarus.2013.08.013>.
- Macke, R.J., Britt, D.T., Consolmagno, G.J., 2011a. Density, Porosity, and Magnetic Susceptibility of Achondritic Meteorites, 46, p. 311. <https://doi.org/10.1111/j.1945-5100.2010.01155.x>.
- Macke, R.J., Consolmagno, G.J., Britt, D.T., 2011b. Density, Porosity, and Magnetic Susceptibility of Carbonaceous Chondrites, 46, p. 1842. <https://doi.org/10.1111/j.1945-5100.2011.01298.x>.
- Marchi, S., McSween, H.Y., O'Brien, D.P., Schenk, P., De Sanctis, M.C., Gaskell, R., Jaumann, R., Mottola, S., Preusker, F., Raymond, C.A., Roatsch, T., Russell, C.T., 2012. The violent collisional history of asteroid 4 Vesta. *Science* 336 (6082), 690–694. <https://doi.org/10.1126/science.1218757>.
- Marchi, S., Botke, W.F., Cohen, B.A., Wünnemann, K., Kring, D.A., McSween, H.Y., de Sanctis, M.C., O'Brien, D.P., Schenk, P., Raymond, C.A., Russell, C.T., 2013. High-velocity collisions from the lunar cataclysm recorded in asteroidal meteorites. *Nat. Geosci.* 6, 303–307.
- McCord, T.B., Adams, J.B., Johnson, T.V., 1970. Asteroid Vesta: spectral reflectivity and compositional implications. *Science* 168, 1445–1447.
- McCord, T.B., Li, J.-Y., Combe, J.-P., McSween, H.Y., Jaumann, R., Reddy, V., Tosi, F., Williams, D.A., Blewett, D.T., Turrini, D., Palomba, E., Pieters, C.M., de Sanctis, M.C., Ammannito, E., Capria, M.T., Le Corre, L., Longobardo, A., Nathues, A., Mittlefehldt, D.W., Schröder, S.E., Hiesinger, H., Beck, A.W., Capaccioni, F., Carsenty, U., Keller, H.U., Denevi, B.W., Sunshine, J.M., Raymond, C.A., Russell, C.T., 2012. Dark material on Vesta from the infall of carbonaceous volatile-rich material. *Nature* 491 (7422), 83–86. <https://doi.org/10.1038/nature11561>.
- McGetchin, T.R., Settle, M., Head, J.W., 1973. Radial thickness variation in impact crater ejecta: implications for lunar basin deposits. *Earth Planet. Sci. Lett.* 20, 226–236. [https://doi.org/10.1016/0012-821X\(73\)90162-3](https://doi.org/10.1016/0012-821X(73)90162-3).
- McSween, H.Y., Mittlefehldt, D.W., Beck, A.W., Mayne, R.G., McCoy, T.J., 2011. HED meteorites and their relationship to the geology of Vesta and the Dawn Mission. *Space Sci. Rev.* 163, 141–174.
- McSween, H.Y., Ammannito, E., Reddy, V., Prettyman, T.H., Beck, A.W., Cristina de Sanctis, M., Nathues, A., Corre, L.L., O'Brien, D.P., Yamashita, N., McCoy, T.J., Mittlefehldt, D.W., Toplis, M.J., Schenk, P., Palomba, E., Turrini, D., Tosi, F., Zambon, F., Longobardo, A., Capaccioni, F., Raymond, C.A., Russell, C.T., 2013a. Composition of the Rheasilvia basin, a window into Vesta's interior. *J. Geophys. Res. (Planets)* 118 (2), 335–346. <https://doi.org/10.1002/jgre.20057>.
- McSween, H.Y., Binzel, R.P., de Sanctis, M.C., Ammannito, E., Prettyman, T.H., Beck, A.W., Reddy, V., Corre, L., Gaffey, M.J., McCord, T.B., Raymond, C.A., Russell, C.T., 2013b. Dawn: the Vesta-HED connection; and the geologic context for eucrites, diogenites, and howardites. *Meteorit. Planet. Sci.* 48, 2090–2104.
- Melosh, H.J., 1989. Impact Cratering: A Geologic Process.
- Mittlefehldt, D.W., 2015. Asteroid (4) Vesta: I. the howardite-eucrite-diogenite (HED) clan of meteorites. *Chem. Erde/Geochem.* 75 (2), 155–183. <https://doi.org/10.1016/j.chemer.2014.08.002>.
- Mittlefehldt, D.W., Greenwood, R.C., Peng, Z.X., Ross, D.K., Berger, E.L., Barrett, T.J., 2016. Petrologic and oxygen-isotopic investigations of eucritic and anomalous mafic achondrites. In: Paper presented at the 47th Lunar and Planetary Science Conference, p. 1240. Abstract.
- Miyamoto, M., 1991. Thermal Metamorphism of CI and CM Carbonaceous Chondrites: an Internal Heating Model, 26, p. 111. <https://doi.org/10.1111/j.1945-5100.1991.tb01026.x>.
- Nakamura, T., 2005. Post-hydration thermal metamorphism of carbonaceous chondrites. *J. Mineral. Petrol. Sci.* 100, 260–272. <https://doi.org/10.2465/jmps.100.260>.
- Nathues, A., Schäfer, M., Reddy, V., Hoffmann, M., Thangjam, G., Le Corre, L., Sierks, H., Cloutis, E.A., Christensen, U., Mengel, K., Vincent, J.B., Russell, C.T., 2014. Vesta's diverse lithologies from Dawn FC. In: *European Planetary Science Congress 2014*, EPSC Abstracts, Vol. 9, id. EPSC2014-251, 9.
- Neish, C.D., Cannon, K.M., Tornabene, L.L., Flemming, R.L., Zanetti, M., Pilles, E., 2021. Spectral Properties of Lunar Impact Melt Deposits from Moon Mineralogy Mapper (M<sub>3</sub>) Data, 361, p. 114392. <https://doi.org/10.1016/j.icarus.2021.114392>.
- Newsom, H.E., Graup, G., Searwards, T., Keil, K., 1986. Fluidization and Hydrothermal Alteration of the Suevite Deposit at the Ries Crater, West Germany, and Implications for Mars. *J. Geophys. Res.* 91 (B13), E239. <https://doi.org/10.1029/JB091iB13p0E239>.
- Osinski, G.R., 2003. Impact glasses in fallout suevites from the Ries impact structure, Germany: an analytical SEM study. *Meteorit. Planet. Sci.* 38, 1641–1667. <https://doi.org/10.1111/j.1945-5100.2003.tb00006.x>.
- Osinski, G.R., Tornabene, L.L., Grieve, R.A.F., 2011. Impact ejecta emplacement on terrestrial planets. *Earth Planet. Sci. Lett.* 310, 167–181. <https://doi.org/10.1016/j.epsl.2011.08.012>.
- Otto, K.A., Jaumann, R., Krohn, K., Matz, K.-D., Preusker, F., Roatsch, T., Schenk, P., Scholten, F., Stephan, K., Raymond, C.A., Russell, C.T., 2013. Mass-wasting features and processes in Vesta's south polar basin Rheasilvia. *J. Geophys. Res. (Planets)* 118 (11), 2279–2294. <https://doi.org/10.1002/2013JE004333>.
- Palmer, E.M., Heggy, E., Capria, M.T., Tosi, F., 2015. Dielectric Properties of Asteroid Vesta's Surface as Constrained by Dawn VIR Observations, 262, p. 93. <https://doi.org/10.1016/j.icarus.2015.08.031>.
- Palomba, E., Longobardo, A., De Sanctis, M.C., Zinzi, A., Ammannito, E., Marchi, S., Tosi, F., Zambon, F., Capria, M.T., Russell, C.T., Raymond, C.A., Cloutis, E.A., 2015. Detection of new olivine-rich locations on Vesta. *Icarus* 258, 120–134. <https://doi.org/10.1016/j.icarus.2015.06.011>.
- Pasckert, J.H., Hiesinger, H., Ruesch, O., Williams, D.A., Naß, A., Kneissl, T., Mest, S.C., Buczkowski, D.L., Scully, J.E.C., Schmedemann, N., Jaumann, R., Roatsch, T., Preusker, F., Nathues, A., Hoffmann, M., Schäfer, M., De Sanctis, M.C., Raymond, C.A., Russell, C.T., 2018. Geologic mapping of the ac-2 Coniraya quadrangle of Ceres from NASA's Dawn mission: implications for a heterogeneously composed crust. *Icarus* 316, 28–45. <https://doi.org/10.1016/j.icarus.2017.06.015>.
- Pierazzo, E., Melosh, H.J., 2000. Hydrocode modeling of oblique impacts: the fate of the projectile. *Meteorit. Planet. Sci.* 35 (1), 117–130. <https://doi.org/10.1111/j.1945-5100.2000.tb01979.x>.
- Pieters, C.M., Staid, M.I., Fischer, E.M., Tompkins, S., He, G., 1994. A sharper view of impact craters from Clementine data. *Science* 266, 1844–1848.
- Pieters, C.M., Ammannito, E., Blewett, D.T., Denevi, B.W., de Sanctis, M.C., Gaffey, M.J., Le Corre, L., Li, J.-Y., Marchi, S., McCord, T.B., McFadden, L.A., Mittlefehldt, D.W., Nathues, A., Palmer, E., Reddy, V., Raymond, C.A., Russell, C.T., 2012. Distinctive space weathering on Vesta from regolith mixing processes. *Nature* 491 (7422), 79–82. <https://doi.org/10.1038/nature11534>.
- Poch, O., Pommerol, A., Jost, B., Carrasco, N., Szopa, C., Thomas, N., 2016. Sublimation of water ice mixed with silicates and tholins: evolution of surface texture and reflectance spectra, with implications for comets. *Icarus* 267, 154.
- Prettyman, T.H., Mittlefehldt, D.W., Yamashita, N., Lawrence, D.J., Beck, A.W., Feldman, W.C., McCoy, T.J., McSween, H.Y., Toplis, M.J., Titus, T.N., Tricarico, P., Reddy, R.C., Hendricks, J.S., Forni, O., Le Corre, L., Li, J.-Y., Mizzon, H., Reddy, V., Raymond, C.A., Russell, C.T., 2012. Elemental mapping by Dawn reveals exogenic H in Vesta's regolith. *Science* 338, 242.
- Prettyman, T.H., Mittlefehldt, D.W., Yamashita, N., Beck, A.W., Feldman, W.C., Hendricks, J.S., Lawrence, D.J., McCoy, T.J., McSween, H.Y., Peplowski, P.N., Reddy, R.C., Toplis, M.J., Le Corre, L., Mizzon, H., Reddy, V., Titus, T.N., Raymond, C.A., Russell, C.T., 2013. Neutron absorption constraints on the composition of 4 Vesta. *Meteorit. Planet. Sci.* 48 (11), 2211–2236. <https://doi.org/10.1111/maps.12244>.
- Preusker, F., Scholten, F., Matz, K.-D., Roatsch, T., Jaumann, R., Raymond, C.A., Russell, C.T., 2014. Global shape of (4) Vesta from dawn FC stereo images. In: Paper Presented at the Vesta in the Light of Dawn: First Exploration of a Protoplanet in the Asteroid Belt, p. 2027. Abstract.
- Preusker, F., Scholten, F., Matz, K.-D., Roatsch, T., Jaumann, R., Raymond, C.A., Russell, C.T., 2016. Dawn FC2 Derived Vesta DTM SPG V1.0. DAWN-A-FC2-5-VESTADTMSPG-V1.0. NASA Planetary Data System.
- Reddy, V., Le Corre, L., O'Brien, D.P., Nathues, A., Cloutis, E.A., Durda, D.D., Bortke, W. F., Bhatt, M.U., Nesvorný, D., Buczkowski, D., Scully, J.E.C., Palmer, E.M., Sierks, H., Mann, P.J., Becker, K.J., Beck, A.W., Mittlefehldt, D., Li, J.-Y., Gaskell, R., Russell, C.T., Gaffey, M.J., McSween, H.Y., McCord, T.B., Combe, J.-P., Blewett, D., 2012a. Delivery of dark material to Vesta via carbonaceous chondritic impacts. *Icarus* 221, 544–559. <https://doi.org/10.1016/j.icarus.2012.08.011>.
- Reddy, V., Nathues, A., Le Corre, L., Sierks, H., Li, J.-Y., Gaskell, R., McCoy, T.J., Beck, A.W., Schröder, S.E., Pieters, C.M., Becker, K.J., Burattini, B.J., Denevi, B.W., Blewett, D.T., Christensen, U., Gaffey, M.J., Gutierrez-Marques, P., Hicks, M.D., Keller, H.U., Maue, T., Mottola, S., McFadden, L.A., McSween, H.Y., Mittlefehldt, D., O'Brien, D.P., Raymond, C., Russell, C., 2012b. Color and albedo heterogeneity of Vesta from Dawn. *Science* 336 (6082), 700–704. <https://doi.org/10.1126/science.1219088>.
- Roatsch, T., Kersten, E., Matz, K.-D., Preusker, F., Scholten, F., Jaumann, R., Raymond, C.A., Russell, C.T., 2012. High resolution Vesta high altitude mapping orbit (HAMO) atlas derived from Dawn framing camera images. *Plan. Space Sci.* 73, 283–286.
- Roatsch, T., Kersten, E., Matz, K.-D., Preusker, F., Scholten, F., Elgner, S., Jaumann, R., Raymond, C.A., Russell, C.T., 2013. High-resolution Vesta low altitude mapping orbit atlas derived from Dawn framing camera images. *Plan. Space Sci.* 85, 293–298.
- Ruesch, O., Hiesinger, H., Cloutis, E., Le Corre, L., Kallisch, J., Mann, P., Markus, K., Metzler, K., Nathues, A., Reddy, V., 2015. Near Infrared Spectroscopy of HED Meteorites: Effects of Viewing Geometry and Compositional Variations, 258, p. 384. <https://doi.org/10.1016/j.icarus.2015.06.034>.
- Russell, C.T., Raymond, C.A., Coradini, A., McSween, H.Y., Zuber, M.T., Nathues, A., De Sanctis, M.C., Jaumann, R., Konopliv, A.S., Preusker, F., Asmar, S.W., Park, R.S., Gaskell, R., Keller, H.U., Mottola, S., Roatsch, T., Scully, J.E.C., Smith, D.E.,



- Tricarico, P., Toplis, M.J., Christensen, U.R., Feldman, W.C., Lawrence, D.J., McCoy, T.J., Prettyman, T.H., Reedy, R.C., Sykes, M.E., Titus, T.N., 2012. Dawn at Vesta: testing the Protoplanetary paradigm. *Science* 336 (6082), 684–686. <https://doi.org/10.1126/science.1219381>.
- Russell, C.T., McSween, H.Y., Jaumann, R., Raymond, C.A., 2015. The dawn mission to Vesta and Ceres. In: Michel, P. (Ed.), *Asteroids IV*, pp. 419–432.
- Ruzicka, A., Snyder, G.A., Taylor, L.A., 1997. Vesta as the HED parent body: implications for the size of a core and for large-scale differentiation. *Meteorit. Planet. Sci.* 32.
- Salisbury, J.W., Hunt, G.R., 1974. Meteorite Spectra and Weathering, 79, p. 4439. <https://doi.org/10.1029/JB079i029p04439>.
- Schenk, P., O'Brien, D.P., Marchi, S., Gaskell, R., Preusker, F., Roatsch, T., Jaumann, R., Buczkowski, D., McCord, T., McSween, H.Y., Williams, D., Yingst, A., Raymond, C., Russell, C., 2012. The geologically recent Giant impact basins at Vesta's south pole. *Science* 336 (6082), 694–697. <https://doi.org/10.1126/science.1223272>.
- Schenk, P., Scully, J., Buczkowski, D., Sizemore, H., Schmidt, B., Pieters, C., Neesemann, A., O'Brien, D., Marchi, S., Williams, D., Nathues, A., De Sanctis, M., Tosi, F., Russell, C.T., Castillo-Rogez, J., Raymond, C., 2020. Impact Heat Driven Volatile Redistribution at Occator Crater on Ceres as a Comparative Planetary Process, 11, p. 3679. <https://doi.org/10.1038/s41467-020-17184-7>.
- Schmedemann, N., Kneissl, T., Ivanov, B.A., Michael, G.G., Wagner, R.J., Neukum, G., Ruesch, O., Hiesinger, H., Krohn, K., Roatsch, T., Preusker, F., Sierks, H., Jaumann, R., Reddy, V., Nathues, A., Walter, S.H.G., Neesemann, A., Raymond, C.A., Russell, C.T., 2014. The cratering record, chronology and surface ages of (4) Vesta in comparison to smaller asteroids and the ages of HED meteorites. *Plan. Space Sci.* 103, 104–130. <https://doi.org/10.1016/j.pss.2014.04.004>.
- Schröder, S.E., Mottola, S., Matz, K.-D., Roatsch, T., 2014. In-flight calibration of the Dawn framing camera II: flat fields and stray light correction. *Icarus* 234, 99–108. <https://doi.org/10.1016/j.icarus.2014.02.018>.
- Scott, E.R.D., Greenwood, R.C., Franchi, I.A., Sanders, I.S., 2009. Oxygen isotopic constraints on the origin and parent bodies of eucrites, diogenites, and howardites. *Geochim. Cosmochim. Acta* 73, 5835.
- Scully, J.E.C., Russell, C.T., Yin, A., Jaumann, R., Carey, E., Castillo-Rogez, J., McSween, H.Y., Raymond, C.A., Reddy, V., Le Corre, L., 2015. Geomorphological evidence for transient water flow on Vesta. *Earth Planet. Sci. Lett.* 411, 151–163. <https://doi.org/10.1016/j.epsl.2014.12.004>.
- Sierks, H., Keller, H.U., Jaumann, R., Michalik, H., Behnke, T., Bubenhausen, F., Büttner, I., Carsenty, U., Christensen, U., Enge, R., Fiethe, B., Gutiérrez Marqués, P., Hartwig, H., Krüger, H., Kühne, W., Maue, T., Mottola, S., Nathues, A., Reiche, K.-U., Richards, M.L., Roatsch, T., Schröder, S.E., Szemerey, I., Tschentscher, M., 2011. The Dawn framing camera. *Space Sci. Rev.* 163, 263–327. <https://doi.org/10.1007/s11214-011-9745-4>.
- Sizemore, H.G., Platz, T., Schorhofer, N., Prettyman, T.H., De Sanctis, M.C., Crown, D. A., Schmedemann, N., Neesemann, A., Kneissl, T., Marchi, S., Schenk, P.M., Bland, M.T., Schmidt, B.E., Hughson, K.H.G., Tosi, F., Zambon, F., Mest, S.C., Yingst, R.A., Williams, D.A., Russell, C.T., Raymond, C.A., 2017. Pitted terrains on (1) Ceres and implications for shallow subsurface volatile distribution. *Geophys. Res. Lett.* 44, 6570–6578.
- Stephan, K., Jaumann, R., De Sanctis, M.C., Tosi, F., Ammannito, E., Krohn, K., Zambon, F., Marchi, S., Ruesch, O., Matz, K.-D., Preusker, F., Roatsch, T., Raymond, C.A., Russell, C.T., 2014. Small fresh impact craters on asteroid 4 Vesta: a compositional and geological fingerprint. *J. Geophys. Res. (Planets)* 119, 771–797.
- Stephan, K., Jaumann, R., De Sanctis, M.C., Ammannito, E., Krohn, K., Otto, K.A., Tosi, F., Combe, J.-P., Roatsch, T., Matz, K.-D., McFadden, L.A., Preusker, F., Raymond, C.A., Russell, C.T., 2015. The Sextilia-region on asteroid 4 Vesta - stratigraphy and variegation. *Icarus* 259, 162–180. <https://doi.org/10.1016/j.icarus.2015.05.016>.
- Stubbs, T.J., Wang, Y., 2012. Illumination conditions at the asteroid 4 Vesta: implications for the presence of water ice. *Icarus* 217, 272.
- Thangjam, G., Reddy, V., Le Corre, L., Nathues, A., Sierks, H., Hiesinger, H., Li, J.-Y., Sanchez, J.A., Russell, C.T., Gaskell, R., Raymond, C., 2013. Lithologic mapping of HED terrains on Vesta using Dawn framing camera color data. *Meteorit. Planet. Sci.* 48 (11), 2199–2210. <https://doi.org/10.1111/maps.12132>.
- Thangjam, G., Nathues, A., Mengel, K., Hoffmann, M., Schäfer, M., Reddy, V., Cloutis, E. A., Christensen, U., Sierks, H., Corre, L.L., Vincent, J.-B., Russell, C.T., 2014. Olivine-rich exposures at Bellicia and Arruntia craters on (4) Vesta from Dawn FC. *Meteorit. Planet. Sci.* 49, 1831–1850.
- Tompkins, S., Pieters, C.M., 2010. Spectral characteristics of lunar impact melts and inferred mineralogy. *Meteorit. Planet. Sci.* 45, 1152–1169. <https://doi.org/10.1111/j.1945-5100.2010.01074.x>.
- Tornabene, L.L., McEwen, A.S., Osinski, G.R., Mouginiis-Mark, P.J., Boyce, J.M., Williams, R.M.E., Wray, J.J., Grant, J.A., and the HiRISE Team, July 01, 2007. Impact Melting and the Role of Sub-Surface Volatiles: Implications for the Formation of Valley Networks and Phyllosilicate-rich Lithologies on Early Mars. Seventh International Conference on Mars, Pasadena, abstract #3288.
- Tornabene, L.L., Osinski, G.R., McEwen, A.S., Boyce, J.M., Bray, V.J., Caudill, C.M., Grant, J.A., Hamilton, C.W., Mattson, S., Mouginiis-Mark, P.J., 2012. Widespread crater-related pitted materials on Mars: further evidence for the role of target volatiles during the impact process. *Icarus* 220, 348.
- Tosi, F., Capria, M.T., De Sanctis, M.C., Combe, J.-P., Zambon, F., Nathues, A., Schröder, S.E., Li, J.-Y., Palomba, E., Longobardo, A., Blewett, D.T., Denevi, B.W., Palmer, E., Capaccioni, F., Ammannito, E., Titus, T.M., Mittlefehldt, D.W., Sunshine, J.M., Russell, C.T., Raymond, C.A., 2014. Thermal measurements of dark and bright surface features on Vesta as derived from Dawn/VIR. *Icarus* 240, 36–57.
- Williams, D.A., Denevi, B.W., Mittlefehldt, D.W., Mest, S.C., Schenk, P.M., Yingst, R.A., Buczkowski, D.L., Scully, J.E.C., Garry, W.B., McCord, T.B., Combe, J.-P., Jaumann, R., Pieters, C.M., Nathues, A., Le Corre, L., Hoffmann, M., Reddy, V., Schäfer, M., Roatsch, T., Preusker, F., Marchi, S., Kneissl, T., Schmedemann, N., Neukum, G., Hiesinger, H., De Sanctis, M.C., Ammannito, E., Frigeri, A., Prettyman, T.H., Russell, C.T., Raymond, C.A., 2014a. The geology of the Marcia quadrangle of asteroid Vesta: assessing the effects of large, young craters. *Icarus* 244, 74–88. <https://doi.org/10.1016/j.icarus.2014.01.033>.
- Williams, D.A., Jaumann, R., McSween, H.Y., Marchi, S., Schmedemann, N., Raymond, C. A., Russell, C.T., 2014b. The chronostratigraphy of protoplanet Vesta. *Icarus* 244, 158–165. <https://doi.org/10.1016/j.icarus.2014.06.027>.
- Williams, D.A., O'Brien, D.P., Schenk, P.M., Denevi, B.W., Carsenty, U., Marchi, S., Scully, J.E.C., Jaumann, R., De Sanctis, M.C., Palomba, E., Ammannito, E., Longobardo, A., Magni, G., Frigeri, A., Russell, C.T., Raymond, C.A., Davison, T.M., 2014c. Lobate and Flow-Like Features on Asteroid Vesta, 103, p. 24. <https://doi.org/10.1016/j.pss.2013.06.017>.
- Williams, J.-P., Bogert, C.H., Pathare, A.V., Michael, G.G., Kirchoff, M.R., Hiesinger, H., 2018. Dating very young planetary surfaces from crater statistics: a review of issues and challenges. *Meteorit. Planet. Sci.* 53, 554–582. <https://doi.org/10.1111/maps.12924>.
- Zambon, F., De Sanctis, M.C., Schröder, S., Tosi, F., Longobardo, A., Ammannito, E., Blewett, D.T., Mittlefehldt, D.W., Li, J.-Y., Palomba, E., Capaccioni, F., Frigeri, A., Capria, M.T., Fonte, S., Nathues, A., Pieters, C.M., Russell, C.T., Raymond, C.A., 2014. Spectral analysis of the bright materials on the asteroid Vesta. *Icarus* 240, 73–85.
- Zolensky, M.E., Weisberg, M.K., Buchanan, P.C., Mittlefehldt, D.W., 1996. Mineralogy of carbonaceous chondrite clasts in HED achondrites and the moon. *Meteorit. Planet. Sci.* 31, 518–537.

### 2.1.5 Parekh et al. (2021a)

Parekh, R., Otto, K. A., Jaumann, R., Matz, K. D., Roatsch, T., Kersten, E., Elgner, S., & Raymond, C. A. (2021a). Influence of Volatiles on Mass Wasting Processes on Vesta and Ceres. *Journal of Geophysical Research: Planets*, 126(3), e2020JE006573. <https://doi.org/https://doi.org/10.1029/2020JE006573>.

The research idea for this article arose from previous publications by Otto et al. (2013) and Kohnert et al. (2016). R. Parekh compiled this article and implemented the research including the mapping, characterisation and classification of mass-wasting features. She also conducted the measurements of mass wasting run-out lengths and fall heights. I provided feedback on the morphologic characterisation and helped setting up the measuring techniques. I also assisted interpreting and illustrating the data presented in Figures 6-9. K.-D. Matz, T. Roatsch, E. Kersten and S. Elgner generated the data products and tools needed for this research. R. Jaumann and C. A. Raymond led the instrument and mission management. All authors assisted with the data interpretation and with refining the manuscript.



## Influence of Volatiles on Mass Wasting Processes on Vesta and Ceres

R. Parekh<sup>1,2</sup> , K. A. Otto<sup>1</sup> , R. Jaumann<sup>2</sup> , K. D. Matz<sup>1</sup> , T. Roatsch<sup>1</sup> , E. Kersten<sup>1</sup> , S. Elgner<sup>1</sup> , and C. Raymond<sup>3</sup> 

<sup>1</sup>DLR Institute of Planetary Research, Berlin, Germany, <sup>2</sup>Institute of Geological Science Germany, Freie University of Berlin, Berlin, Germany, <sup>3</sup>Jet Propulsion Laboratory, Pasadena, CA, USA

**Key Points:**

- We classified and estimated the  $H/L$  of mass movements to investigate the mechanisms of deposition on Vesta and Ceres
- Vesta has dry, granular-like slides as dominant mass wasting feature, whereas Ceres has abundant features of flow-like mass movements
- The mass wasting deposit mobility is influenced by the material composition and volatile content on Vesta and Ceres

**Supporting Information:**

- Supporting Information S1

**Correspondence to:**

R. Parekh,  
[rtu.parekh@dlr.de](mailto:rtu.parekh@dlr.de)

**Citation:**

Parekh, R., Otto, K. A., Jaumann, R., Matz, K. D., Roatsch, T., Kersten, E., et al. (2021). Influence of volatiles on mass wasting processes on Vesta and Ceres. *Journal of Geophysical Research: Planets*, 126, e2020JE006573. <https://doi.org/10.1029/2020JE006573>

Received 14 JUN 2020  
 Accepted 18 FEB 2021

**Abstract** We have analyzed mass wasting features, their distribution and deposit geometry on the two largest main asteroid belt objects—protoplanet Vesta and dwarf planet Ceres—and compared their geomorphology and mobility. Both asteroids have similar surface accelerations, but different surface compositions. Based on our observations and previous studies, we categorized three distinct morphological mass wasting classes: slumps, slides, and flow-like movements. We conclude that Ceres has abundant features of flow-like mass movements. Further, sliding and flow-like characteristics are identified in craters within mid-latitudes which supports the possibility of the presence of water ice in the near subsurface of Ceres. Vesta predominantly shows characteristics of dry granular-like slide features which are distributed homogeneously across the surface. By plotting the ratio between fall height ( $H$ ) and run-out length ( $L$ ) (effective coefficient of friction,  $H/L$ ) against the run-out length and spreading width ( $W$ ), we demonstrate that deposits on Vesta terminate on shorter distances, whereas on Ceres they travel longer distances. The deposit geometry and the similar surface gravity on both asteroids suggest that the material composition and volatile component have a significant effect on deposit emplacement. However, both bodies' mass movements have similar effective coefficients of friction, even though Vesta's regolith is comparatively dry, whereas Ceres is rich in water ice. This leads to the conclusion that volatile content alone cannot be responsible for low effective coefficients of friction, and that more than one geological process is needed to explain the mass motion behavior and morphology.

**Plain Language Summary** Landslides are one of the most studied geological events on planetary bodies. Many scientists have contributed to a diverse database of knowledge with the aim to better understand these processes. They have been observed for various environmental conditions and are affected by gravity and the physical and chemical composition of the hosting body. However, it is challenging to delineate which specific type or morphology of landslide is sensitive to which parameter. On airless asteroids Vesta and Ceres, landslides have been well preserved, allowing for in-depth analysis using remote sensing data. Interestingly, Vesta and Ceres' substantially different surface compositions have a major effect on landslides, despite their similar gravity. In our study, we have examined and updated the landslide inventory on both bodies, and performed an analysis of deposit mobility which will further enhance our understanding related to the material conditions, their mobility, and surface evolution.

### 1. Introduction

The Dawn mission was designed to understand the conditions and processes that shaped the formation and evolution of two large planetesimals from the initial stages of planetary accretion (Russell & Raymond, 2011), and was the first mission to visit and orbit two planetary bodies located in main asteroid belt. Both Vesta and Ceres are terrestrial protoplanets with Vesta being a dry rocky body and Ceres a volatile-rich body (Russell & Raymond, 2011). They have provided the opportunity to enhance our understanding of planetary formation related to the existence of volatiles (Buczkowski et al., 2016; Chilton et al., 2019; Combe et al., 2016; De Sanctis et al., 2012, 2013; Jaumann et al., 2012; Sizemore et al., 2019a). As a result of the Gamma Ray and Neutron Detector (GRaND) and Visible and Infrared Mapping Spectrometer (VIR) observations, the connection between the HED meteorites and Vesta has been confirmed. Vesta has experienced significant heating and dehydration (Formisano et al., 2013; Toplis et al., 2013), whereas Ceres appears to be

© 2021. The Authors.  
 This is an open access article under the terms of the Creative Commons Attribution License, which permits use, distribution and reproduction in any medium, provided the original work is properly cited.

rich in water ice, which appears to exert control on short-wavelength surface morphology (Otto et al., 2019; Schmidt et al., 2017; Sizemore et al., 2019a, 2019b).

As a result of high-resolution surface images acquired by the Dawn rendezvous mission, Vesta and Ceres have been of particular interest for studies of their surface morphology and geology. The internal and external conditions that shaped the surface of Vesta and Ceres can be studied with the data returned by the mission, including detailed shape models (Preusker et al., 2016) and geological maps (Jaumann et al., 2012; Krohn et al., 2014; Roatsch et al., 2012, 2015, 2016, 2017; Williams, Denevi, et al., 2014). Both Vesta and Ceres have undergone critical erosional processes, including impact cratering, that gradually changed their chemical and physical composition, playing a significant role in their evolution (Russell & Raymond, 2011; Russell et al., 2004, 2012; Toplis et al., 2013). The high-resolution images gathered by the Framing Camera (FC) of the Dawn mission (Sierks et al., 2011) have provided visual evidence of geologic processes including landslides (Otto et al., 2013, 2019; Schmidt et al., 2017; Sizemore et al., 2019a), impact cratering, and huge impact basins (Rheasilvia and Veneneia) on the southern latitudes of Vesta (Marchi et al., 2012; Otto et al., 2013; Schenk et al., 2012). Similarly, the FC data has also improved our understanding related to cryovolcanic processes (Nathues et al., 2020; Ruesch et al., 2016; Sori et al., 2018), large-scale mass wasting features and the existence of subsurface water ice on Ceres (Bland et al., 2016; Buczkowski et al., 2016; Chilton et al., 2019; Duarte et al., 2019; Reddy et al., 2012; Schmidt et al., 2017; Sizemore et al., 2019a). The VIR instrument also found ammoniated phyllosilicates (De Sanctis et al., 2017) on Ceres which are proposed to be linked to geomorphologic features such as flow-like mass wasting features (Chilton et al., 2019; Otto et al., 2013). Overall, landslides are one of the most prominently studied geological features on Vesta and Ceres because of their ability to expose fresh regolith material (Otto et al., 2013; Schmidt et al., 2017). In fact, mass wasting analyses provided clues of granular-like material behavior on Vesta (Krohn et al., 2014; Otto et al., 2013) and the possible existence of subsurface volatiles that may have triggered lubricated mass wasting processes on Ceres (Schmidt et al., 2017).

On Vesta, the classification of mass wasting features was conducted based on morphological characteristics which include intra-crater mass wasting, flow-like and creep-like features, slumps, slides, and curvilinear features within the Rheasilvia basin (Otto et al., 2013). Considering the varying morphological characteristics throughout the southern latitudes on Vesta, it is thought to be the most geologically active region of the asteroid (Schenk et al., 2012). This region is also rich in ejected materials which cover the original surface of the Rheasilvia and Veneneia basins (Otto et al., 2013; Reddy et al., 2012). Another detailed study of a prominent slumping block at the Matronalia Rupes scarp suggests that forces like friction and cohesion affect slump formation (Krohn et al., 2014). Furthermore, gully formation on Vesta suggests a granular-like brittle regolith (Krohn et al., 2014; Scully et al., 2015; Williams, O'Brien, et al., 2014) with characteristics similar to dry gullies on Mars (Crosta, De Blasio, & Frattini, 2018; Crosta, Frattini, et al., 2018). On Vesta, only very few morphologic features, including pitted terrains (Denevi et al., 2012) and interconnected curvilinear gullies (Scully et al., 2015) suggest the presence of volatiles in the regolith, which may have been delivered via impacts.

Previous investigations of landslides on Ceres focused on morphological appearance and spatial distribution (Chilton et al., 2019; Schmidt et al., 2017). Various flow-like mass movement features were identified and were classified in three categories: deposits with thick frontal lobes, dominating latitudes  $\geq 50^\circ$  (type 1), deposits with broad sheet-like spreading, traveling on longer distances (type 2), and platy lobate sheets with cusped toes (type 3) (Schmidt et al., 2017). Most of the landslides were identified proximal to crater rims. The morphology, spatial distribution of mass movements and variation in the geometry of the deposits suggest the presence of subsurface ice on a global scale on Ceres (Schmidt et al., 2017; Sizemore et al., 2017, 2019). In addition, the low effective coefficient of friction, defined as the ratio of the fall height ( $H$ ) and the run-out length ( $L$ ) of a mass wasting feature, point toward low shear strength which is attributed to icy material in the upper subsurface of Ceres (Chilton et al., 2019). Recently, Duarte et al. (2019) provided a more detailed investigation of Cerean flows based on intermediate flow features. The morphological characteristics of these flows agree with the previously described classification by Schmidt et al. (2017). However, type 2 flows are prominently identified in relatively shallow craters near the polar regions (Duarte et al., 2019), which supports the hypothesis of a shallow subsurface ice layer in the polar latitudes on Ceres, a conclusion also reached by analysis of GRaND data (Prettyman et al., 2017; Schorghofer, 2008, 2016). This ice layer is

thought to be stable for millions of years (Chilton et al., 2019) because of low surface temperatures (Hayne & Aharonson, 2015) and sublimation rates. Further, an extended study conducted by Hughson et al. (2019) showed that type 3 flows resemble fluidized ejecta and they suggest the presence of an ice-rich subsurface with a low coefficient of friction within upper surface material. In a nutshell, the morphology on Ceres is consistent with the ice-rich composition.

Landslides are also commonly studied geological features on other planetary bodies, such as the icy satellites of Jupiter and Saturn including Iapetus, Rhea (Singer et al., 2012) and Callisto (Moore et al., 1999), Pluto's largest satellite Charon (Beddingfield et al., 2020), Mars (Crosta, De Blasio, & Frattini, 2018; Quantin et al., 2004) and the Moon (Brunetti et al., 2015). Previous studies conducted on Iapetus, Rhea, and Callisto provided quantitative measurements of the effective coefficient of friction and demonstrated that landslides on these planetary bodies exhibit unusual long run-out length. The reduction in friction supports the theory of shear heating within icy surfaces (Singer et al., 2012). On Charon, mixtures of H<sub>2</sub>O and ammonia hydrates reduce the melting temperature of the ice, decreasing the internal friction without the necessity of large amounts of energy to melt the ice (Beddingfield et al., 2020). Martian landslides have occurred throughout its history and provide a window into its erosional and environmental evolution (Crosta, Frattini, et al., 2018). On the Moon, landslides, including slumping features, appear as fragmented deposits probably triggered by meteorite impacts and the associated impact shock wave propagation (Scaioni et al., 2017; Xiao et al., 2013).

Landslide run-out length, morphological characteristics (such as hummocky surfaces, brittle deposits, wide alcoves, blocky or lobate frontal margins) and deposit spreading depend on the material and environmental conditions during the time of formation, the presence of ice, water or other volatiles and impurities as well as mass wasting triggering factors (e.g., meteorite impacts and shock wave propagation). Depending on the planetary bodies, the influence of these parameters on landslide formation, appearance, and morphology may vary.

On Ceres, previous investigations of mass movements focused on their flow behavior (Chilton et al., 2019; Combe et al., 2019; Duarte et al., 2019; Schmidt et al., 2017), whereas on Vesta the analysis was limited to the mid-latitudes (Marcia, Calpurnia carter and its neighboring regions) and southern regions (Krohn et al., 2014; Otto et al., 2013, 2016; Williams, Denevi, et al., 2014). Using these investigations as a base, we extend existing findings by classifying and comparing three different types of mass wasting processes under similar gravitational conditions but compositionally different environments as present on Vesta and Ceres. Our aim is to classify landslides based on morphology and highlight the similarities and differences. Next, we quantify the mobility of landslide depositions by estimating the effective coefficient of friction and the spreading efficiency on Vesta and Ceres. Our interpretation is based on the analysis of morphological characteristics and geometrical estimations to constrain the effect of volatiles on the morphology of Vesta and Ceres.

## 2. Data

To identify mass movement features on Vesta and Ceres, we used mosaics of the Low Altitude Mapping Orbit (LAMO) and High-Altitude Mapping Orbit (HAMO) (Roatsch et al., 2012, 2016, 2017) of the Dawn mission's framing camera (Sierks et al., 2011). The Dawn HAMO mosaics have a spatial resolution of ~70 m/pixel for Vesta and 140 m/pixel for Ceres and LAMO mosaics have a spatial resolution of ~20 m/pixel for Vesta and ~35 m/pixel for Ceres (Roatsch et al., 2012, 2015, 2016, 2017). For regions largely shadowed in the mosaics (e.g., the northern hemisphere of Vesta and the polar regions on Ceres), we additionally used individual images (where available) for identification of mass wasting features. Unfortunately, the northern regions of Vesta ( $\geq 60^\circ\text{N}$ ) were mainly in shadow because of the northern winter during the LAMO phase of Dawn and thus, we had to exclude this particular region in our analysis. The measurements of drop height ( $H$ ), run-out length ( $L$ ) and spreading width ( $W$ ) of deposits was carried out by taking surface profiles using digital terrain model (DTM) mosaics with ~135 m/pixel resolution (with ~10 m vertical accuracy) on Ceres and 92 m/pixel resolution (with ~5 m vertical accuracy) on Vesta (Preusker et al., 2016), derived from stereo pairs. All data used in this work on Vesta and Ceres can be downloaded from the Planetary Data System (PDS) at <https://sbn.psi.edu/pds/resource/dawn/dwnvfcL1.html> and <https://sbn.psi.edu/pds/resource/dawn/dwncfcL1.html>, respectively.

**Table 1**  
*Key Indicators Are Considered for the Identification and Classification of Mass Movements*

Characteristics	Slump	Slide	Flow
Deformation during wasting process	Very little	Yes	Yes
Exposed scar	Partly exposed	Yes	Covered
Transverse features/striations	Possible, but not observed on Vesta and Ceres	No	Yes
Lobate trunks	No	Possible but rare	Yes
Sheet-like wide fans	No	No	Yes
Boulders and spur/gullies	Rare	Common	Rare
Albedo variations	No	Common	Rare

*Note.* The indicators were adapted from the classification system developed by Dikau et al. (1996).

### 3. Materials and Method

#### 3.1. Global Mass Movement Feature Classification, Identification, and Mapping

Our mass movement classification is based on the system developed by Dikau et al. (1996). This method categorizes six different mass movement processes namely; falls, topples, slides, lateral spreads, flows, and complex mechanisms. Each category reveals various modes of morphological features, material properties and surface conditions. For example, falls are found on surfaces with steep slopes, topples are recognized in rocky materials, slides are commonly found within dry granular-like materials, lateral spread is prominent in fine grain materials with shallow topography and flow-like movements are common within water rich surfaces (Varnes, 1978). On Vesta and Ceres, based on morphological indicators (Table 1), three common morphological types were noted: slides associated with granular-like behavior (Otto et al., 2013); a wide spread of unconsolidated material, slumps (or rotational slides) exhibiting transverse ridges at lateral margins on large cohesive blocks of material; and, flow-like movements correlated with lobate tongue-like spreading and/or thin sheet-like (Schmidt et al., 2017) large fans with rippled deposition. Each category shows distinct morphological signatures (Table 1) and using this as an identification tool, we mapped and updated the list of mass movement features on Vesta and Ceres. To understand the behavior of mass wasting processes comprehensively, previously identified landslides (Chilton et al., 2019; Duarte et al., 2019; Krohn et al., 2014; Otto et al., 2013; Schmidt et al., 2017) were also included and are marked accordingly in our global maps (Figures 4 and 5).

On Vesta, earlier mapping analyses classified mass wasting features based on geological appearance (Krohn et al., 2014; Otto et al., 2013) in the southern latitudes (30°–60°). These studies either focused on certain regions of the bodies that were of particular interest (e.g., the southern impact basins on Vesta) or concentrated on features of particular interest (e.g., lobate and alcove fan-like flows on Ceres). In our study, the characterization was conducted globally based on multiple morphological impressions of the mass wasting features. To be able to compare the observations on both bodies, we chose the three versatile classes mentioned above (slides, slumps and flow-like movements) (Table 1) which were commonly recognized on both bodies. This classification covers all types of mass wasting features identified at global scale.

In our global mapping campaign on Vesta and Ceres, each of the three mass wasting classes is displayed in a separate color and the symbol geometry is designated to the different mapping surveys. Landslides have been identified and marked by using geomorphological indicators, as listed in Table 1. The mapping was conducted at the scale of 1:125,000 and 1:200,000 in ArcGIS 10.3™ on Vesta and Ceres, respectively, and cataloged in a GIS geodatabase. For a consistent mapping, a fishnet of 150 × 150 m for Vesta and 250 × 250 m for Ceres was evaluated systematically and a minimum feature size of 0.02 and 0.03 km<sup>2</sup> was defined on Vesta and Ceres, respectively.

#### 3.2. Landslide Geometry

One of the most rudimentary methods to estimate the efficiency of landslide deposit mobility is to analyze the effective coefficient of friction represented as the ratio of fall height and run-out length of a mass

wasting feature ( $H/L$ ) (McEwen, 1989), also known as Heim's ratio (Heim, 1932). The ratio  $H/L$  reflects the capacity of material to travel in the direction of movement, whereas the spreading width ( $W$ ) denotes the material spreading efficiency perpendicular to the direction of motion. Another technique known as center of mass estimation (Cruden, 1980; De Blasio, 2011) uses the center of the scarp and deposit to estimate the values. However, it shows a high level of inaccuracy because of the irregular topography of Vesta and Ceres (Chilton et al., 2019) and thus, we avoided using this method.

To measure the length and width of a landslide, we first identified the boundaries of deposited materials of all possible mass wasting sites. The horizontal run-out length ( $L$ ) of the deposit was estimated by taking five profiles (evenly distributed within the boundary of the deposit) in the direction of the movement and averaging it. The boundaries at the top of the deposit and the toe of the deposit were considered as starting and end points for these measurements. Similarly, the spread width ( $W$ ) was estimated by taking five evenly distributed profiles perpendicular to the direction of movement and the average value was considered. Next, the drop height ( $H$ ) was measured from the top of the scarp to the tip of the deposit (Figure S1). However, in a few regions, because of erosion, the scarp was not clearly identifiable. In such cases, the height of the crater rim or ridge from which the mass wasting feature originated was considered as the highest dropping point. This is common practice for the estimation of vertical fall height when using topography alone (Singer et al., 2012). For each possible landslide site, five profiles were taken for all parameters ( $H$ ,  $L$ , and  $W$ ).

Out of our marked mass wasting sites, the estimation of all three parameters ( $H$ ,  $L$ , and  $W$ ) was feasible only for 85 sites on Vesta and 34 on Ceres. The limited number of measurements is because of restrictions in image or DTM resolutions, blurred deposit boundaries or inadequate illumination conditions (e.g., shadowed features), on both bodies. Other than our measurements, we also adapted previous measurements of  $H$  and  $L$  from Duarte et al. (2019) and Schmidt et al. (2017) of Ceres landslides. After determining the parameters, we compared the material mobility on Vesta and Ceres.

## 4. Results

The identified mass-wasting features on Vesta and Ceres show significant similarities and differences in terms of geomorphological signatures (Table 2). In this section, we first present details of morphological classes followed by measurements of the deposit geometry.

### 4.1. Morphological Identification of Landslides on Vesta and Ceres

#### 4.1.1. Slumps (Rotational Slides)

Rotational slides are commonly identified on terrains with extensive slopes and cohesive materials (De Blasio, 2011). A chunk of material detaches from its host surface because of the gravitational pull often triggered via a shock wave propagation (e.g., from a nearby impact) (Shingareva & Kuzmin, 2001), creating a spoon-like circular or semicircular surface of failure (De Blasio, 2011). Cohesion within the sliding mass prevents extensive spreading and the mass maintains most of its original shape along the surface of rupture (Otto et al., 2013), causing a step-like topographic profile with one or multiple scarps (Krohn et al., 2014). At the rest position, the detached material partly exposes the steep surface of rupture and is comparatively flat at the frontal margins. In a few cases, the frontal deposit exhibits transverse ridges or cracks as a result of the material deformation.

Octavia crater (Figure 1a) located at  $-15.47, 168.48$  on Vesta is an examples of a single step rotational slump. The crater is  $\sim 60$  km in diameter and  $\sim 9$  km deep. The slump head appears on the crater wall with a fall height of  $\sim 4.5$  km. The slump deposit covers about  $208.9$  km<sup>2</sup> of the crater floor. The slump major and minor scarp and the exposed slope are seen in Figures 1a and 1b. The slump block moved downwards from the crown region and the top surface of the detached material leans backwards toward the crater wall. However, even though Octavia's landslide possesses most attributes defining a rotational slide, it appears to have formed in granular material leaving a relatively small head compared with the scarp. Nevertheless, we defined it as slump as it shares predominantly slump attributes. More unambiguous rotational slumps are evident in the basins at the southern latitudes of Vesta including the one on the eastern side of Matronalia Rupes (Krohn et al., 2014) where a huge slumping mass covers approximate  $600$  km<sup>2</sup> with multiple ridges



**Table 2**  
*Summary of Mass Wasting Related Geomorphological Features Identified on Vesta and Ceres*

Mass-wasting features	Vesta	Ceres
Slump	Rough, transverse ridges, single and/or multiple heads, located inside craters and along large basin rims	Hummocky, single and/or multiple heads, identified inside large craters
Slide	Overlapping deposits, spur and gullies at crest, boulders on crater floor	Overlapping deposits, spur and gullies, boulders at rim and floor
Flow	Small-scale single frontal lobes, gullies or spur at the rim	Multiple lobate tongues with furrows, thin sheet-like wide fan spreading

and minor scarps. Similar features have also been identified on Ceres, for example, in the crater of Toharu (Figure 1c). The crater is ~150 km in diameter and ~3.5 km in depth, located at  $-48.32, 155.95$ . We have identified two slump regions at the western and eastern rim of this crater. The detached slump material slipped along the direction of the slope, exposing a steep scarp. Multiple heads are evident which locally have given rise to subsequent failure, generating multiple steps-like surface features (Figures 1d and 1e). Similar to Vesta, Ceres also has single step slumping features (Figure S2f). Transverse ridges are also evident within some slumping bodies (Figure S2).

Overall, on Vesta and Ceres we noted two types of slump events: (i) slumping areas with multiple deposit blocks and transverse ridges. They are specifically observed within the largest crater on Vesta (e.g., the Rheasilvia crater covering Vesta's southern hemisphere) and within multiple craters on Ceres (Sintana, Toharu, Urvara, Occator, Tupo craters), and (ii) single slumping block features. However, we find handful of candidates which have a single slumping block on both, Vesta (only within Octavia) and Ceres (at the north west rim of Dantu and within an unnamed crater located at  $43.57, 34.94$ ).

#### 4.1.2. Slides

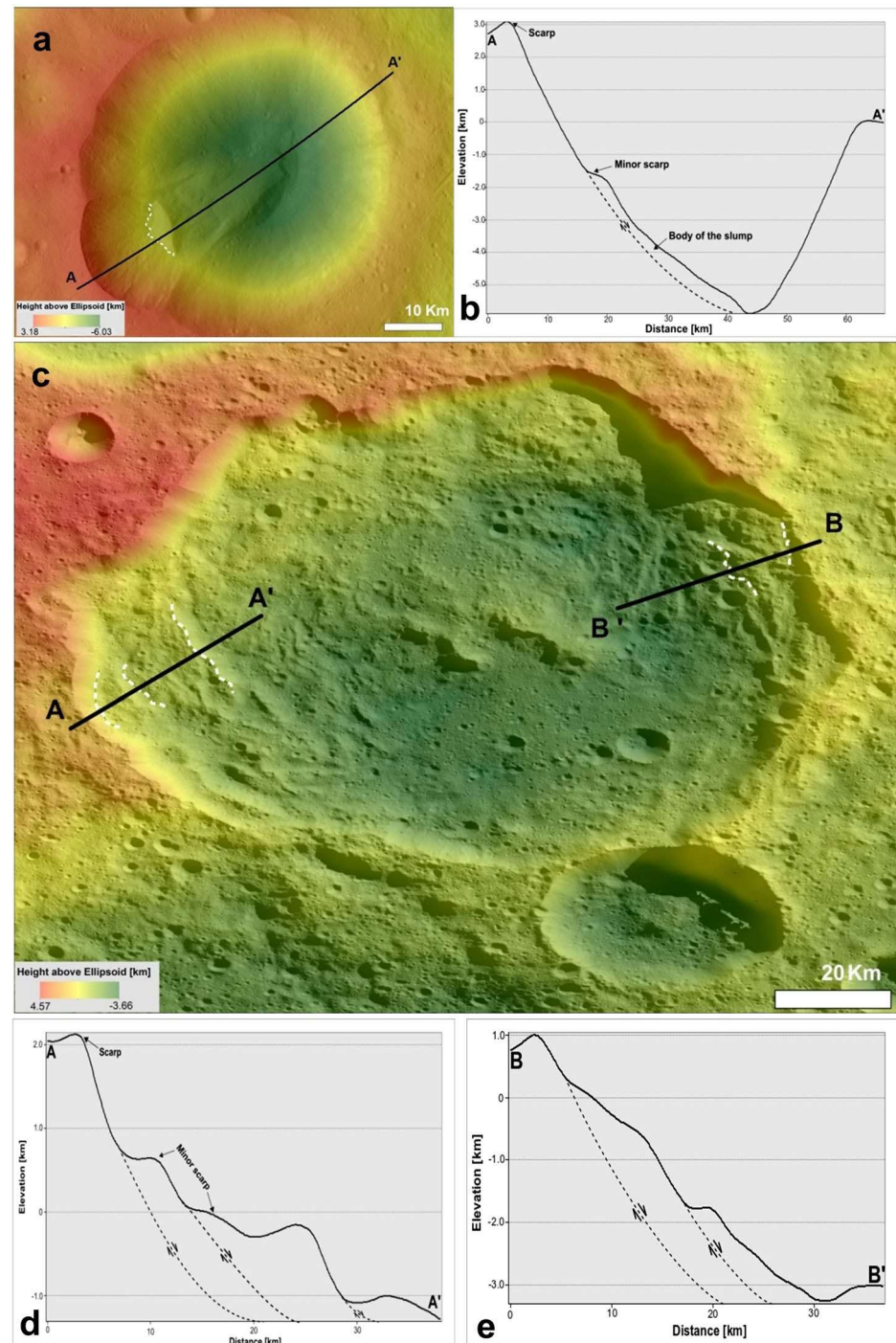
Slides move along a planar shear surface potentially exposing the upper area of the shear surface after coming to a rest (De Blasio, 2011). The foot of the material may undergo disaggregation and the slide material experiences some degree of deformation such as lateral spreading (Otto et al., 2013).

An example of such a slide is seen in Pinaria crater (lat.:  $-29.54$ , long.:  $181.63$ ) on Vesta (Figure 2a). Here, we identify multiple areas of slide material deposition on the crater floor. Slides moved downwards from the crater rim, covering the crater floor and exposing the surface of failure at the northern crater rim. The occurrence and preservation of fragile spur features at the crater rim where the slides originated indicate that Pinaria's slides are relatively young. The slide material traveled on a surface with decreasing slope from  $40^\circ$  to  $20^\circ$ . The process continued until the deposit reached a slope flat enough to hold the material. Similar to Pinaria, an unnamed crater located in the southern part of Ceres (lat.:  $22^\circ\text{S}$ , long:  $80^\circ\text{W}$ ), shows layered piles of slide material on the crater floor (Figure 2b) with spurs and boulders near the crater rim. The boulders' sizes are  $\geq 50$  m and indicate that parts of the wasted material are composed of brittle substances.

In general, on both bodies, slide features involve the disintegration and spreading of the sliding material (Figure S3). Usually within this type of mass wasting feature it is challenging to constrain the deposit boundaries as material originating from various crater wall locations often intermix leaving no particular boundary or spreading margins.

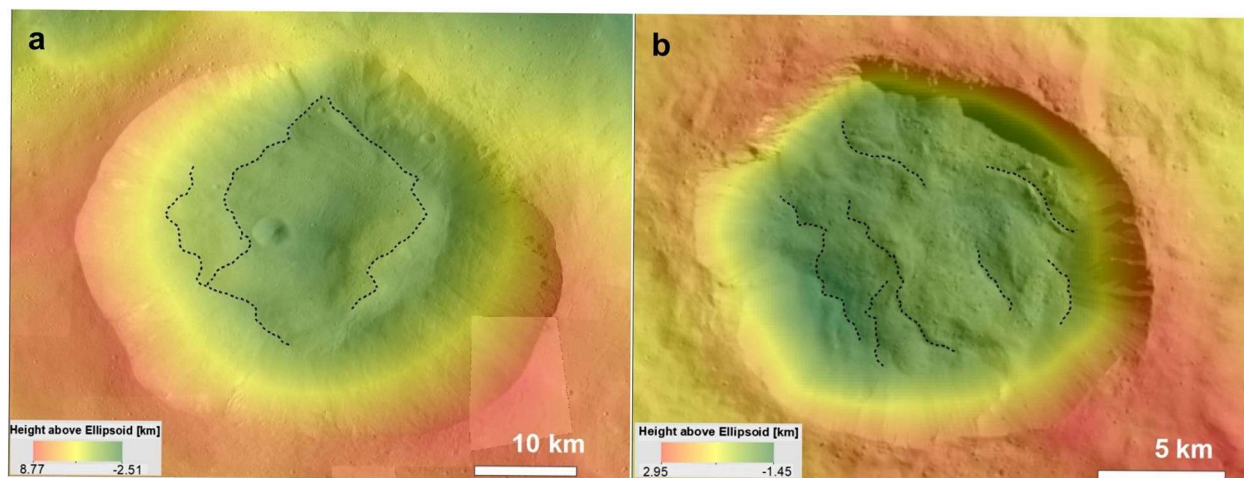
#### 4.1.3. Flow-Like Movements

Large-scale flow-like movements occur when the cohesion between individual wasting particles is limited, the particles travel independently within a moving mass (De Blasio, 2011) and material starts behaving like a fluid. Fluidized behavior can be caused by melting of volatiles within the material (Schmidt et al., 2017), saltation (De Blasio, 2011), acoustic fluidization (De Blasio, 2011; Melosh, 1986), or the presence of trapped air bubbles within the material (Shreve, 1966, 1968). While traveling, the moving fragments (granular material and/or other consolidated particles) within the material collide with each other and because of friction, form multiple striations in the direction of travel on the surface. Upon rest, the deposit morphology appears



**Figure 1.** Examples of rotational slumps on Vesta and Ceres. (a) A slump observed in Octavia crater on Vesta with its topographic profile (b). (c) Multiple slump examples observed along Toharu crater's wall on Ceres. The slumps show a step-like profile (in d and e) with multiple minor scarps (white dotted line in c) and deposits covering an area of  $\sim 1,000$  and  $\sim 800$   $\text{km}^2$ , respectively. There is  $\sim 1.1$  km elevation difference between the western and eastern rim of the crater. Black dotted lines in the topographic profiles (b, d, e) represent the presumed subsurface of rupture joining the scarp outlined in image (a and c).

either in the form of a thin sheet (Schmidt et al., 2017) or multiple lobate tongues at the motion's front depending on the volume of the mass and its spreading efficiency. The striations are the main morphological difference to the slides and slumps described in the sections above.



**Figure 2.** Examples of slides on Vesta and Ceres. Slides emanating from the rim of Pinaria crater on (a) Vesta. (b) Overlapping slide deposits covering an unnamed crater floor on Ceres. Spurs along the crater rim and some larger boulders are evident. The black dotted lines highlight topographic boundaries within the slide material.

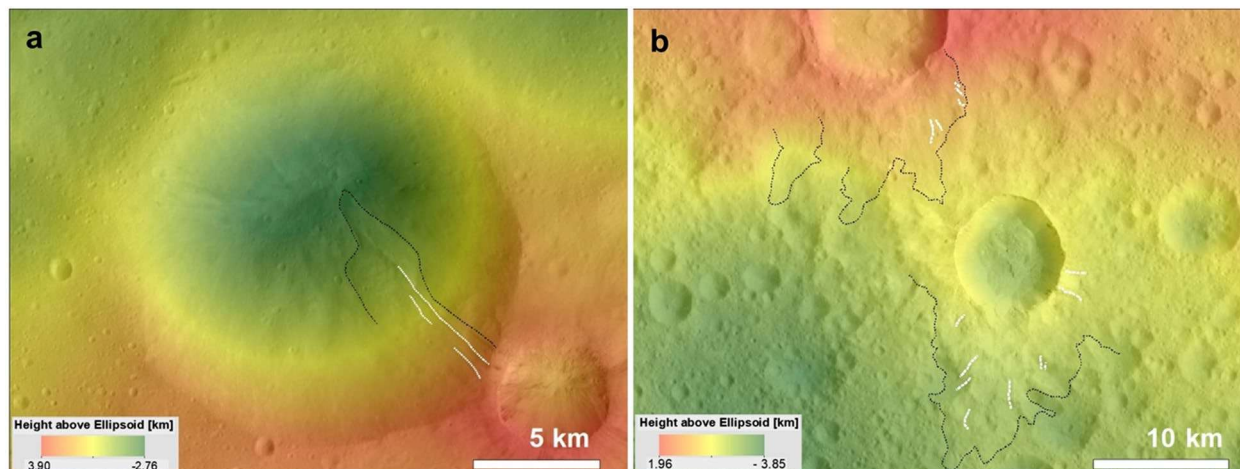
On Vesta, for example, a flow-like movement originates from the south east rim of Ruffilia crater ( $\sim 15$  km in diameter) and travels toward the crater floor at a slope of  $\sim 20^\circ$  generating two frontal lobes (Figure 3a). The flow-like movement was probably generated by the impact of a younger crater, potentially the one in southeast of the flow feature. The well-preserved morphology of the flow-like feature suggests that it is relatively young. On Ceres, similarly well-defined multiple lobate flow units are evident within and outside of the Haulani crater (Krohn et al., 2017). The units include surface characteristics such as high albedo, fine grained material, multiple flow units, and streak-like or swirled patterns (Krohn et al., 2017). Other than Haulani, there are examples in craters such as Juling, Kupalo, and Urvara (Duarte et al., 2019) also displaying similar mass wasting morphologies (Krohn et al., 2017; Schmidt et al., 2017; Scully et al., 2015). In addition to lobate flow-like features, Ceres also shows prominent impressions of sheet like fans around Xevioso (lat.: 0.7, long.: 310.6) and an unnamed crater (lat.: 1.92, long.: 309.68), covering  $\sim 127$  and  $\sim 102$  km<sup>2</sup> area, respectively, masking the surrounding terrain and suggesting it to be related to impact ejecta (Figure 3b). A detailed analysis of morphological characteristics of ejecta related flows can also be found in Hughson et al. (2019). Fluidized impact ejecta does not necessarily follow the topography (Schmidt et al., 2017) but covers the original landscape. Overall on Ceres flow-like features are generally identified in the regions surrounding craters (Chilton et al., 2019; Combe et al., 2019; Duarte et al., 2019; Hughson et al., 2019; Schmidt et al., 2017).

Usually this type of mass movement travels longer distances than the other two described, suggesting a lower internal friction and/or higher momentum involved in the motion. But there are morphological differences in flow-like movements on both targeted bodies. On Vesta the majority of flow-like features appears as small elongated features with lobate shaped fronts (Figures S4a–S4c), whereas on Ceres a large number of sheet-like features expressed as wide fans with multiple lobes at the flow front (Figures S4d and S4e) are present.

#### 4.2. Global Distribution of Mass Wasting Features on Vesta and Ceres

We identified a large number of mass-wasting features within the vicinity of craters, basin walls or on cliffs. In addition, to the previously identified mass wasting features (29 on Vesta by Krohn et al. [2014]; Otto et al. [2013]), we identified 159 further mass-wasting features out of which 74 are slides, 84 flow-like movements, and 1 slump feature (in total 188 mass wasting features) located at mid-latitudes on Vesta. In addition to our inventory, there are a few more slump blocks distributed frequently within Rheasilvia and Veneneia in the southern region of Vesta (Otto et al., 2013) (Figure 4). The strong elevation difference (up to  $\sim 20$  km high basin walls) makes these regions most favorable for slumping processes. Overall, slumping





**Figure 3.** Flow-like movements observed on Vesta and Ceres. (a) A tongue-like flow in Rufillia crater on Vesta and (b) a thin sheet-like flow nearby Xeviosio (center crater in which surroundings are highlighted with black dotted lines) and an unnamed (partially visible in the upper center of b) crater on Ceres. The sheet-like flow appearance is common on Ceres and possibly related to ejecta depositions and regolith volatile content (Hughson et al., 2019; Schmidt et al., 2017). The black dotted lines indicate the extent to which material has traveled. The white dotted lines highlight super imposing furrows.

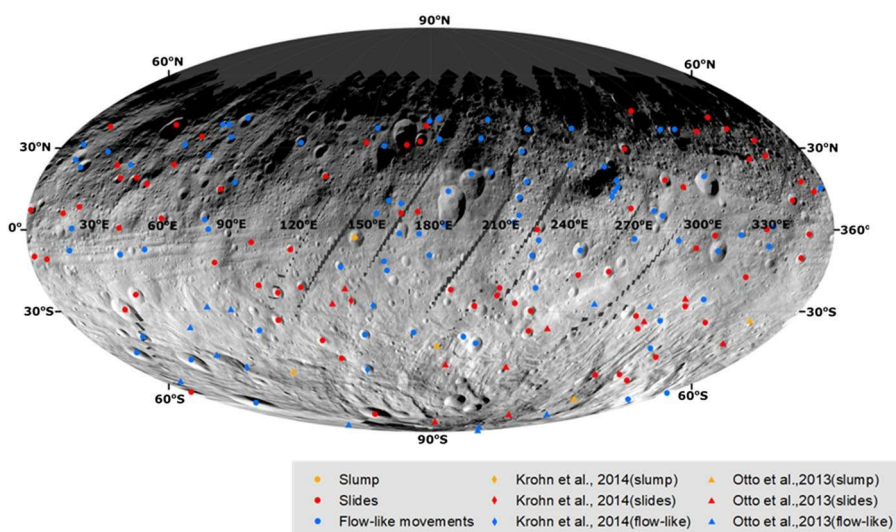
blocks are the largest mass wasting features on Vesta. Nevertheless, the large number of slides on Vesta suggests a prominently dry granular behavior noted at a global scale. Both slides and flow-like movements are correlated with craters of diameters ranging between  $\sim 2.6$  and 53 km (average of 14.88 km).

On Ceres, previous studies reported 150 mass movement features as flow-like movements (Chilton et al., 2019; Duarte et al., 2019; Schmidt et al., 2017). Besides these, we identified an additional 35 flow-like features, 12 slides and 13 rotational slump (in total 210) features (Figure 5). Flow-like movements are the dominant mass wasting process. Overall, the flow-like mass movements are homogeneously distributed on Ceres. However, the other two mass wasting features, slump and sliding features, are not present in Ceres' polar regions and confined within  $0^{\circ}$ – $60^{\circ}$  latitude. Further, slides and flow-like impressions are noted in or around craters which have diameters from  $\sim 5.1$  to  $\sim 77.8$  km (with an average of 26.5 km). Similar to Vesta, slumping blocks are also present on Ceres within large craters (average size  $\sim 61.4$  km). Usually the flow-like morphologies are evident within crater floors and along/around crater rims.

### 4.3. Geomorphologic Measurements

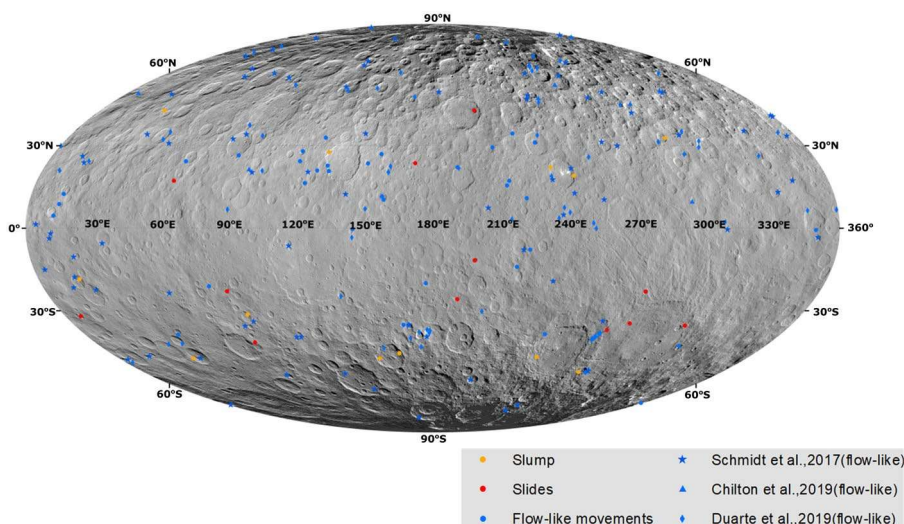
#### 4.3.1. Effective Coefficient of Friction

The friction between the wasting particles has a significant influence on the traveling distance of the material. A common way to describe the friction within a mass movement is to analyze the effective coefficient of friction ( $H/L$ ). We plot the effective coefficient of friction of the different types of mass wasting features identified on Vesta and Ceres against their run-out length ( $L$ ) which can be assumed as a proxy for a mass movement's volume (Figure 6). Here, we compare  $H/L$  and run-out length ( $L$ ) and additionally show the drop-height ( $H$ ), indicated by the size of the data point. In Figure 7, we compare the effective coefficient of friction ( $H/L$ ) with spreading width ( $W$ ) on Vesta and Ceres. From Figures 6 and 7, we observe the following trends: (1) the effective coefficient of friction ( $H/L$ ) of landslides on both Vesta and Ceres follows an approximate linear decrease with run out length ( $L$ ) in a double logarithmic plot; (2) for a given run-out length, there is no strong relation between run-out length and the friction coefficient on Vesta and Ceres (e.g., a range of values is observed for each value of  $L$ ); (3) the drop height ( $H$ ) is lower on Ceres than on Vesta possibly because of the higher topographic relief on Vesta ( $\sim 40$  km elevation difference overall on Vesta compared with 14.5 km on Ceres); and (4) material traveling  $\geq 10$  km is more common on Ceres compared with Vesta with the longest travel distance being  $\sim 66.4$  km on Ceres and  $\sim 60.6$  km on Vesta, despite Ceres' smaller topographic range. On Vesta the southern hemisphere has a prominent difference in elevation because of the large impact basins Veneneia and Rheasilvia which cause high drop heights for wasting materials.



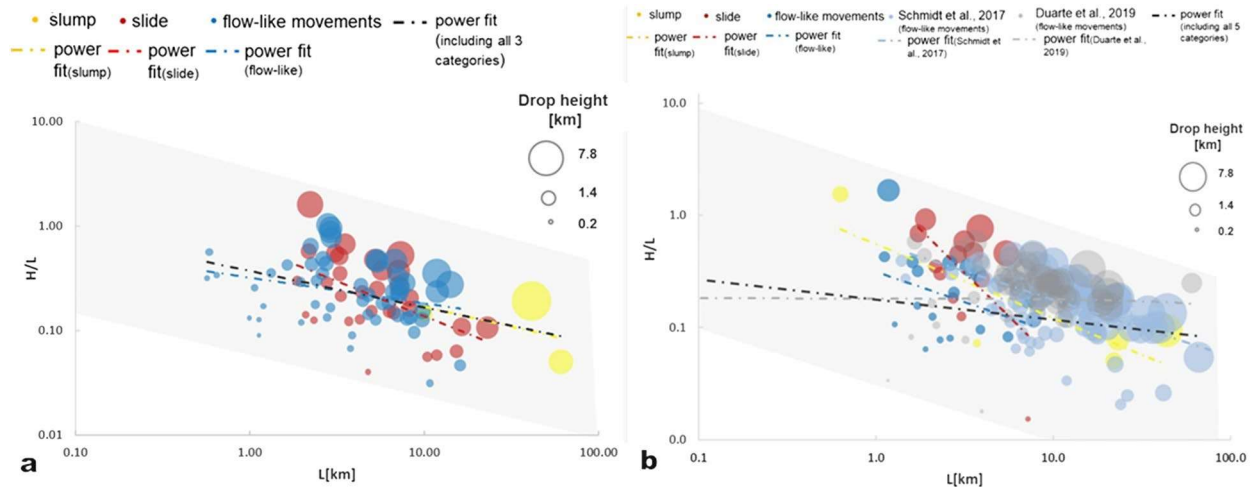
**Figure 4.** Global distribution of classified mass wasting features on Vesta. For a comprehensive analysis, we have also included and categorized mass wasting features identified by Krohn et al. (2014) and Otto et al. (2013) in the southern region. Additional features found and analyzed in this work are marked as dots. The classification map was prepared using a LAMO mosaic in Mollweide projection.

The range of  $H/L$  for each of the three categories on Vesta and Ceres is provided in Table 3. Slides and flow-like movements evenly cover the entire range of measured run-out lengths ( $L$ ) 0.57–23 km on Vesta (Figure 6). Slumps appear to have larger run-out length (10–60 km) possibly because of their comparatively large size. The slope of the least squares fit of a power function to the data (linear in log-log plot) of each morphological class was estimated. To understand the relation between two parameters (here  $H/L$  with  $L$ ) in quantitative manner we derived the slope of least squares fit. The slope in these diagrams shows how strongly the effective coefficient of friction changes when the run-out length increases. A steep slope means that the effective coefficient of friction decreases with run-out length at a higher rate compared with a less steep slope in these diagrams. This rate of decreasing effective coefficient of friction may hint at the different processes which could also be caused by different materials such as volatiles acting within the moving masses. On Vesta the slope is as follows; slump:  $-0.69 \pm 1.15$ , slides:  $-0.40 \pm 0.12$ , and flow-like move-



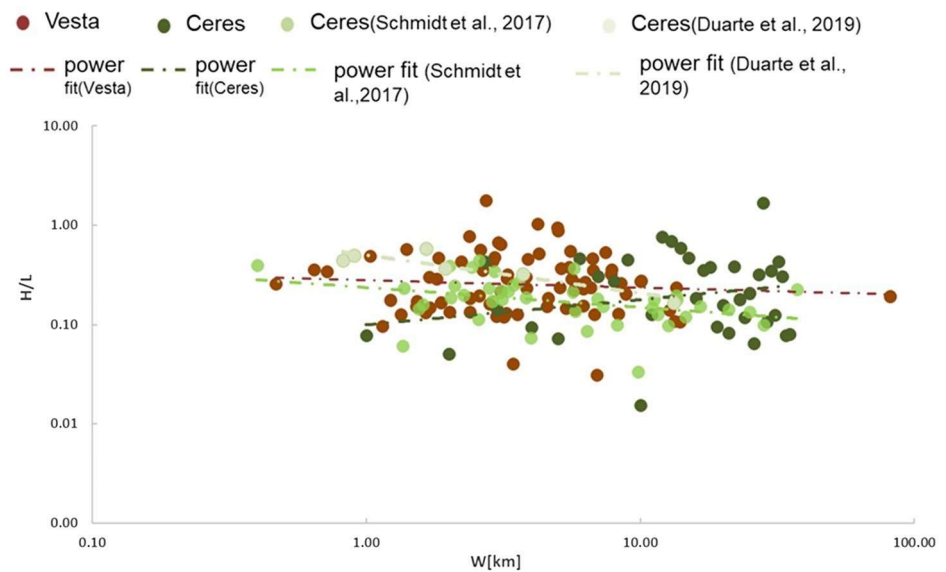
**Figure 5.** Global distribution of classified mass wasting features on Ceres. In earlier studies, mass wasting features were exclusively classified as flows (Chilton et al., 2019; Duarte et al., 2019; Schmidt et al., 2017). The classification map was prepared using a LAMO mosaic in Mollweide projection.





**Figure 6.** Landslide mobility on (a) Vesta and (b) Ceres. Shown is the measurement of the friction coefficient ( $H/L$ ) versus the run-out length ( $L$ ) of the three different types of mass movements. (a) For each category the least squares power law fit between  $H/L$  and  $L$  yields a slope as follows on Vesta: slump:  $-0.69 \pm 1.15$  (yellow dashed-dotted line), slide:  $-0.40 \pm 0.12$  (red dashed-dotted line), flow-like movements:  $-0.33 \pm 0.15$  (blue dashed-dotted line). The combined slope including all types is  $-0.44 \pm 0.11$  (black dashed-dotted line). (b) Similarly, the slopes on Ceres are: slump:  $0.82 \pm 2.80$  (yellow dashed-dotted line), slide:  $-0.22 \pm 0.09$  (red dashed-dotted line), flow-like movements:  $-0.08 \pm 0.06$  (blue dashed-dotted line). In addition to our measurements we also included data from Duarte et al. (2019) and Schmidt et al. (2017). Their slopes are  $0.31 \pm 0.27$  and  $0.0 \pm 0.14$ , respectively. On Ceres the slope of  $H/L$  versus  $L$  for all type of landslides combined is  $-0.03 \pm 0.05$ . The gray shaded area is to highlight the range of  $H/L$  values for a given  $L$  and is for orientation only. The size of the dots corresponds to the drop height.  $x$  and  $y$  axis are in logarithmic scale. Measurements adopted from earlier studies are highlighted in a lighter shade.

ments:  $-0.33 \pm 0.15$  (Table 3, Figure 6a). All three categories are consistent by having a negative slope which means that the effective friction of coefficient ( $H/L$ ) tends to decrease with increasing run-out length ( $L$ ), which can be assumed as a proxy for the mass movement's volume; however, looking at the large error to the fits, the trend is not strong. Likewise, the fitted slope of all types of mass movements on Ceres is as follows; slump:  $0.82 \pm 2.80$ , slides:  $-0.22 \pm 0.09$ , and flow-like moments:  $-0.08 \pm 0.06$  (Table 3, Figure 6b). Similar to Vesta, on Ceres slide and flow-like features have negative correlations between their effective coefficient



**Figure 7.** Deposit width versus landslide mobility. Illustrated is the friction coefficient versus the deposit width. Earlier measurements of the friction coefficient (Duarte et al., 2019; Schmidt et al., 2017) are added. The least squares power fit between  $H/L$  with  $W$  yields slopes as follow: Vesta:  $-0.10 \pm 0.13$ , Ceres:  $0.38 \pm 0.21$ , data from Schmidt et al. (2017):  $-0.68 \pm 0.27$  and Duarte et al. (2019):  $-0.48 \pm 0.14$ . The deposit width was measured from the supporting information provided in the mentioned publications. Note, both axes are in logarithmic scale.

**Table 3**  
Summary of  $H/L$  Range and Their Fitted Slope for All Types of Mass Wasting Movements Identified on Vesta and Ceres

Mass-wasting features	Vesta		Ceres	
	$H/L$ range	Fitted slope	$H/L$ range	Fitted slope
Slump	0.05–0.15 (mean $0.13 \pm 0.06$ )	$0.69 \pm 1.15$	0.05–1.54 (mean $0.31 \pm 0.59$ )	$0.82 \pm 2.80$
Slide	0.04–0.61 (mean $0.30 \pm 0.29$ )	$-0.40 \pm 0.12$	0.02–0.92 (mean $0.43 \pm 0.25$ )	$-0.22 \pm 0.09$
Flow	0.03–1.02 (mean $0.30 \pm 0.22$ )	$-0.33 \pm 0.15$	0.06–1.67 (mean $0.13 \pm 0.17$ )	$-0.08 \pm 0.06$

of friction and run-out length. On both planetary bodies, the slumping fit shows a relatively high value of error which may be influenced by the small number of data points. In the case of Mars and Earth, the  $H/L$  values range from 0.1 to 0.3 for rock avalanches and 0.01 to 0.1 for saturated terrestrial submarine landslides (Quantin et al., 2004). The slides and flow-like movements on Vesta and Ceres appears less confined and cover a wider range of  $H/L$  values. Furthermore, the different gravitational pull and atmospheric condition on the planets and the asteroids makes a direct comparison unreasonable.

There is a prominent distinction between slides and flow-like features in terms of mobility on Ceres; slides terminate at shorter distances (average:  $\sim 3.3 \pm 0.07$  km), whereas flow-like movements have maximum extent up to  $\sim 66.4$  km (average:  $\sim 11.05 \pm 10.2$  km) on Ceres. This is not observed for Vesta (maximum deposits extend  $\sim 16.1$  km with average  $4.98 \pm 3.61$  km). However, the range of  $H/L$  values is similar on Vesta and Ceres (Vesta: 0.03–1.61, Ceres: 0.02–1.67) regardless of their length.

In addition, we have also analyzed the relationship between the deposit width ( $W$ ) and friction coefficient ( $H/L$ ) of mass-wasting features (Figure 7). This provides information about the spreading efficiency of the wasting material perpendicular to the direction of movement. When determining the least squares power fit to the  $H/L$  versus  $W$  plot in double logarithmic scale, it was observed that for Vesta the slope is  $-0.10 \pm 0.13$  and in the case of Ceres the slope is  $0.38 \pm 0.21$ , but the correlation is not strong. By plotting the coefficient of friction ( $H/L$ ) against the width ( $W$ ) of the deposit, we can demonstrate that mass movement features on Vesta generally do not spread as much as on Ceres, where width up to  $\sim 7.5$  km on average is commonly measured. This implies that the deposits on Ceres are more mobile in terms of lateral disintegration compared with Vesta. These conditions may be favorable for generating multiple lobate features or sheet like fluidized spreads which are one of the most prominent features on Ceres.

## 5. Discussion

The global distribution of the identified classes of mass movements illustrates that both Vesta and Ceres have a diverse range of materials at the surface and in their subsurface, resulting in three different mass wasting types. The mass wasting features are present on both bodies but show some similarities (transverse ridges, overlapping slide deposits, boulders and spurs/gullies, brittle material in deposit, lobate tongue-like flow features, single/multiple step like slump, albedo variations) and differences in their morphologies (conglomerate lobate features, hummocky surfaces, sheet-like wide fans). Comparing the global mapping of Vesta and Ceres, slides are the most commonly identified mass wasting type on Vesta, whereas flow-like movements are dominant on Ceres. This is consistent with the fact that Vesta is a dry brittle body (Jaumann et al., 2012) and Ceres is rich in water ice (Prettyman et al., 2017; Schmidt et al., 2017).

### 5.1. Role of Physical and Chemical Conditions of Surface Material

On Vesta most of the slumping blocks are identified within the southern latitudes (Krohn et al., 2014; Otto et al., 2013). The high elevation difference and steep slope ( $\sim 40^\circ$ – $10^\circ$ ) (Jaumann et al., 2012) in this region is thought to be favorable for slump formation on Vesta. Slumping behavior is also common within cohesive materials that have the tendency to collapse when reaching a critical abundance of water or has critical slope (angle of repose) on Earth or Mars (Varnes, 1978). Usually a block of slumping material includes cohesive substances like clay, lithic clasts, igneous rocks, organic minerals and materials enriched in water (Varnes, 1978). In the case of Ceres, VIR observations identified carbonates, phyllosilicates and ammoni-

ated clays with OH and/or H<sub>2</sub>O mixed within the surface materials possibly explaining the occurrence of slumping on Ceres (Ammannito et al., 2016; Chilton et al., 2019; De Sanctis et al., 2017; Rivkin et al., 2006). Various processes can affect the cohesion between particles of the surface material by weakening bonds. On Ceres, a putative process reducing the material's cohesive strength involves the formation of fracture networks generated either by impact shock wave or from the occasional heating cycle during Ceres' history (Chilton et al., 2019). Most slumping blocks on Ceres are in the mid-latitudes where ice rich materials are possibly present at several meters depth (Bland et al., 2016; Chilton et al., 2019; Prettyman et al., 2017; Schmidt et al., 2017). This may influence the cohesion within the wasting material allowing slumps to occur more frequently in this region. Overall, on Vesta the slumping blocks are correlated with terrain conditions (high altitude, steep slope), whereas on Ceres slumping features are best explained by the surface composition (presence of clays, water ice; Ammannito et al., 2016; Chilton et al., 2019).

Slides are a form of mass movements involving brittle and granular-like behavior. Such materials are common on dry Vesta (Otto et al., 2013) and subsequently they are the most abundant mass wasting features on Vesta. The Vestan mineralogy data collected by visible and infrared spectra shows that the majority of the crust consists of dry eucritic basalts and pyroxene (De Sanctis et al., 2012; Prettyman et al., 2013) which has brittle composition. In the case of Ceres, we have identified craters with granular-like slide behavior near the mid-latitudes. The slide behavior is identified inside craters which have depth from ~0.7 to 1.8 km within  $\pm 60^\circ$  latitude. A possible explanation for the high concentration of slides in the mid-latitudes of Ceres is the lower abundance of water ice within the regolith in these regions (Prettyman et al., 2017). GRaND has detected the ice layer within 1 m of the depth at equator and near to surface at poles on Ceres (Prettyman et al., 2017). The lower ice table depth in the lower latitudes may have caused the upper material layer (which is involved in mass wasting processes) to be drier and thus less cohesive, preferentially generating slides rather than flow-like or slumping features. Thus, distribution of fragmented slides within the mid-latitude points to a relatively brittle ice-rock rich regolith on Ceres, assuming that the depth of the ice layer along with presence of brittle material is the main cause for slides on Ceres, whereas global presence of eucrite and pyroxene dry regolith can be the potential cause for slide on Vesta.

Lastly, on both, Vesta and Ceres, the majority of the flow-like features are located within the vicinity of crater ejecta and/or crater rims. When correlated to impact ejecta, the flow-like features are present at a global scale on both asteroids. Usually, flow-like movements follow the downhill direction however; this movement can sometimes be diverted because of the high mobility of materials affected by the impact. Earlier studies of impact related melt production on Vesta (Williams, O'Brien, et al., 2014) suggest that lobate flows are impact-derived and associated with melt displacement of high velocity impacts (8–10 km/s). Another study finds that the presence of highly shocked and fractured material correlates with the presence of flow-like features within the Rheasilvia basin in the southern hemisphere of Vesta (Otto et al., 2013). Moreover, impact flow movements are also present on much smaller and dry asteroids including (433) Eros ( $H/L = \sim 0.03\text{--}0.1$ ) (Cheng et al., 2002; Sullivan et al., 2002) and (21) Lutetia ( $H/L = \sim 0.4$ ) (Elbeshhausen et al., 2012; Massironi et al., 2012). Whereas sheet-like spreading is more commonly identified on Ceres and associated with the presence of water ice in the subsurface (Chilton et al., 2019; Combe et al., 2019; Schmidt et al., 2017). According to GRaND's observations, the presence of shallow subsurface ice (Prettyman et al., 2017) at mid-latitudes and above ( $\sim \geq 50^\circ$ ) correlates with the abundance of flow features (Schmidt et al., 2017). Further, hydrodynamic models suggest low velocity impactors within the asteroid belt (average  $\sim 5$  km/s velocity; Marchi et al., 2013). At this velocity, impact melts on Vesta may achieve temperatures  $>1000$  K (Marchi et al., 2013) and melt the regolith, whereas on Ceres these impactors may only generate  $\sim 300$  K which can melt crystalline ice or liberate OH present within the regolith (Bowling et al., 2019; Marchi et al., 2016). Thus, the contrast in the morphology of flow-like mass wasting movements on Vesta and Ceres may be because of the difference in rheology within these two temperature regime. Flow-like mass wasting behavior can be associated with both impact melt and impact-driven mobility as well as post-impact surface temperature and volatile regolith content on Vesta and Ceres.

Both slides and flow-like movements are identified within craters of diameters ranging from  $\sim 2.6$  to 53 km on Vesta and  $\sim 5.1$ –77.8 km on Ceres. However, considering their average value ( $14.9 \pm 10.6$  km on Vesta and  $26.5 \pm 23.2$  km on Ceres), it is evident that the majority of these features occur within smaller craters which are naturally more abundant (Gou et al., 2018; Hiesinger et al., 2016; Liu et al., 2018) on both asteroid

surfaces. There does not seem to be a correlation between crater size and mass-wasting feature abundance. One thing that is interesting though is that the mass wasting features occur in comparatively larger craters on Ceres than on Vesta. The difference in the size of craters might be because of the fact that (i) large impact craters might have been blanketed by the ejecta of the Rheasilvia and Venetia impact basins (Marchi et al., 2012; Otto et al., 2013; Reddy et al., 2012) and thus are not present on the surface and/or; (ii) because of the lower-resolution LAMO data available for the analysis of Ceres (a factor of  $\sim 3$  less than on Vesta) that may disguise small-scale features.

## 5.2. Landslide Effective Coefficient of Friction

The contrast in the morphology of mass movements on Vesta and Ceres may be quantified statistically by comparing properties of landslide mobility. The effective friction coefficient can be correlated to rheological properties. A previous measurement of friction coefficients (Schmidt et al., 2017) suggests similar behavior of Cerean flows to flows on Saturn's icy moon Iapetus. The large range of friction coefficients at a given run-out length is explained by the presence of slippery ice at the surface of motion on Iapetus (Singer et al., 2012). Our investigation shows that a large range of friction coefficients is present on Vesta as well as Ceres (Figure 6). Given that Vesta's regolith is dry, slippery ice theory cannot be the only explanation for a wide range of friction coefficients. Instead, a complex combination of various geological processes is probably involved in planetary mass wasting processes.

To explore the theory of slippery ice on Ceres, we test whether the amount of energy released during the mass movements would be sufficient to create melt. The required energy to melt a kilogram of ice is calculated using the (Turnbull, 2011) equation,

$$E_m = C_p(T_f - T_a) + \zeta \quad (1)$$

where  $C_p$  = specific heat capacity of ice at constant pressure (2.108 kJ/kg/K),

$T_f$  = freezing temperature of ice (273.15 K),

$T_a$  = surface temperature on Ceres (150 K) (Bland et al., 2016), and

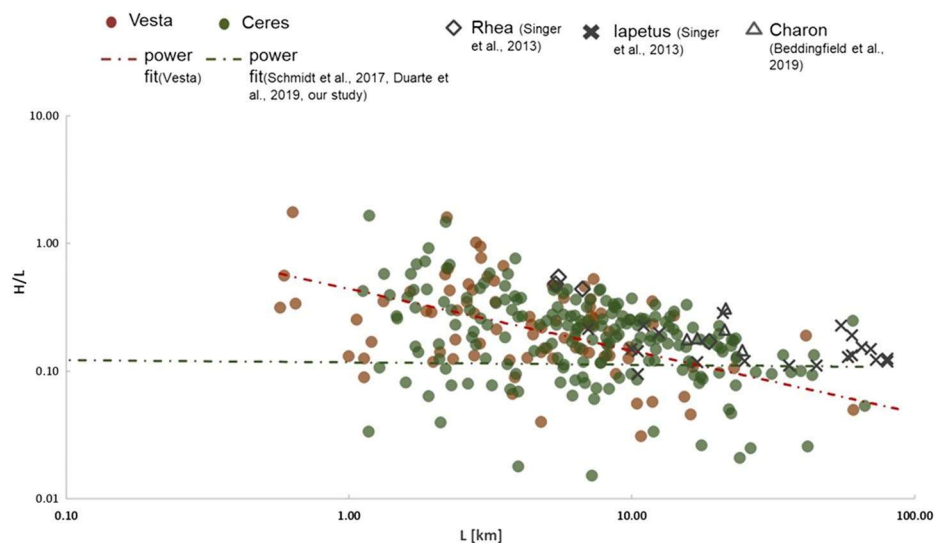
$\zeta$  = latent heat of fusion (334 kJ/kg) (Turnbull, 2011).

We estimate the specific energy released during the mass movements using the drop height ( $H = 0.11$ – $4.60$  km) and the gravitational force on Ceres ( $g = 0.27$  m/s<sup>2</sup>),

$$E_r = gH. \quad (2)$$

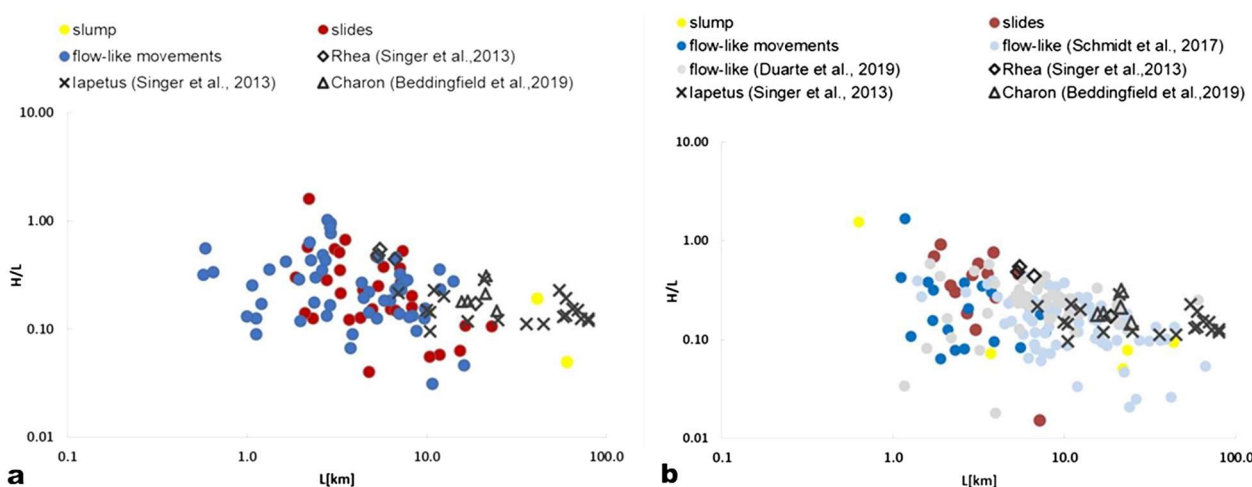
This estimate assumes that the entire energy stored in the gravitational potential will be converted into heat and is thus an upper limit to the real values. Our estimations of  $E_r$  for all movements on Ceres range between 0.03 and 1.24 kJ/kg. The specific energy required for melting pure ice is  $\sim 594$  kJ/kg, which is significantly higher than the estimated energy released during mass wasting processes on Ceres. It is therefore unlikely that substantial amounts of ice melted during mass wasting processes on Ceres, however, it is possible that higher temperatures are reached along the landslide bases (Beddingfield et al., 2020). In addition, the presence of carbonates within the material may also reduce the melting temperature of the mixture (Chilton et al., 2019). Thus, the melting of water ice cannot be excluded as possible cause for fluidized movements, but it is probably a minor effect considering the difference in required and provided energy. Nevertheless, note that the above explained calculation does not include the energy released because of the impact. Similar ideas of ice melting cannot be applied to Vesta's flow-like movements as it lacks substantial amounts of volatile materials in the regolith (Jaumann et al., 2012).

We also compared the friction coefficient of mass wasting features of Vesta and Ceres to other icy planetary bodies (Figures 8 and 9). Previous studies (Schmidt et al., 2017; Singer et al., 2012) have compared the effective coefficient of friction of mass wasting flows with Mars and Earth, however, these bodies have significantly larger gravitational acceleration ( $g$ ). To examine the role of volatiles in the regolith, we compare the  $H/L$  range of Vesta and Ceres mass movements with those of planetary bodies of similar  $g$  including Iapetus (0.22 m/s<sup>2</sup>), Rhea (0.29 m/s<sup>2</sup>), and Charon (0.27 m/s<sup>2</sup>) in Figure 8. To provide a better visual per-



**Figure 8.** Comparison of landslide mobility on planetary bodies with similar surface accelerations. The identified mass wasting features on Vesta and Ceres are compared with lobate blocky landslides on Iapetus, intra-crater slides on Rhea (Singer et al., 2012), and long run-out slides on Charon (Beddingfield et al., 2020). Small Vesta landslides exhibit similar friction coefficients as the rest of the ice rich planetary bodies. Note that different image resolutions lead to differences in the ranges of measured  $H$  and  $L$  values.

spective, we have also plotted the data shown in Figure 8 individually for Vesta and Ceres in Figure 9 highlighting each mass wasting category on Vesta and Ceres individually. The icy bodies are much colder than Vesta and Ceres and consist predominantly of volatiles. Even though Vesta is a comparatively dry asteroid, the effective coefficients of friction fall within a similar range as the other icy bodies which have substantial amounts of volatiles and comparatively lower surface temperatures (Figures 8 and 9). We show that flow-like and sliding movements on Vesta have a similar range in  $H/L$  values, but are shorter in comparison to landslides on Rhea, Iapetus and Charon (Figure 9). Whereas on Ceres, the flow-like mobility is similar to the other planetary bodies, the slides also terminate at shorter distances. It should be noted that the lower limit of  $L$  values of the icy bodies is likely influenced by the generally lower image resolution available for these bodies.



**Figure 9.** Comparison of landslides classes with other planetary bodies. (a) On Vesta, slides and flow-like movements behave similar to the lobate flows of Iapetus and Charon. However, both the movements on Vesta show shorter run-out lengths. (b) On Ceres, flow-like movements behave similar to the rest of the icy bodies however, slides terminate on shorter distances compared with Iapetus, Rhea, and Charon.



We conclude that the presence of volatiles cannot be the single mechanism in the reduction of the effective coefficient of friction, because we did not observe lower values for the icy bodies and Ceres compared with dry Vesta. Instead, mass wasting measurements follow a common trend with degreasing  $H/L$  values for increasing  $L$ . Although the low number of landslides detected on some of the icy bodies may bias this observation, the icy bodies appear to have comparatively high  $H/L$  values (toward the upper end of the range at a given run-out length). This may hint at the temperature having a more significant influence on landslide mobility than previously thought.

## 6. Summary

1. We have mapped, analyzed, and classified landslides on Vesta and Ceres to derive a relationship between landslide morphology, coefficient of friction, and mobility. By choosing two bodies with similar surface accelerations, we were able to focus on the regolith volatile content on affecting these parameters.
2. We have identified three common types of mass wasting features on Vesta and Ceres: slumps, slides and fluidized movements. There are some similarities (overlapping deposit pile, transverse ridges, multiple head slumping features, striations, lobate bulges), and differences (abundance of steps like slump deposits, conglomerate lobes, furrows, alcove-like sheets), which we attribute primarily to a varying degree of volatile content on Vesta and Ceres. Further, we also mapped these features at a global scale on both asteroids. In total, the mapping database includes 188 mass wasting features on Vesta and 210 on Ceres.
3. Various types of mass wasting process carved some of distinct geological impressions which have reshaped the surface of Vesta and Ceres. Huge slumps have distorted the crater rims because of collapse of material, and has significant influence on the surface elevation, contributing toward geologically chaotic terrain. Sliding material has produced spur/gully like fragile features at the crater walls and given rise to an albedo dichotomy which can be easily detectable on Vesta even today. Large-scale alcove fan-like deposition has been wrapped in and around cerean craters, concealing the original topography and average slope of the neighboring regions on Ceres.
4. The identified mass wasting features occur on slopes including in or around craters, basin walls or on cliffs. On Vesta, slide and fluidized features are located nearby smaller craters (average 14.8 km), whereas on Ceres the majority of these characteristics are identified within relatively larger crater (average 26.5 km). Slump characteristics are generally associated with larger craters on both bodies. On Ceres, the pole regions do not show any obvious evidence of slumps and slides but they are evident within mid-latitudes, supporting the speculation of vertical variations of ice in the outer shell. Vesta has predominantly dry granular-like slides, whereas on Ceres fluidized mass wasting behavior is dominant.
5. Based on the comparison of run out length ( $L$ ) and spread width ( $W$ ) on Vesta and Ceres, we show that mass wasting features on Vesta become immobile on shorter distances and spread less, whereas Cerean mass movements are voluminous, extend up to longer distance and cover larger areas. We suggest that the deposit emplacement is influenced by the difference in impact-induced surface temperature achieved because of contrast in material composition and volatile content. Compared with this, terrain conditions seem to have no significant effect on these values.
6. The effective coefficient of friction varies significantly for a given run-out length or width on both bodies. A general decrease in friction coefficient is observed for larger  $L$  values as expected from observations from other planetary mass wasting features. Both bodies have a similar range of friction coefficients (even though Vesta is dry and Ceres is rich in water ice). Thus, the determination of  $H/L$  alone may not be sufficient to identify volatile content in mass wasting material. A combined analysis with geomorphologic characteristics is required.
7. Comparing the friction coefficient of Vesta and Ceres with cold ice-rich planetary bodies of similar gravitational acceleration (Iapetus, Charon, and Rhea), we find similar  $H/L$  values regardless of the volatile content of the regolith involved and deduce that the temperature, which is much lower on the other ice rich planetary bodies compared with main belt asteroids Vesta and Ceres, may have a more significant influence on  $H/L$  on the ice rich planetary bodies than the volatile content.

## Data Availability Statement

Image and topographic data used in this work are available at the Small Bodies Node of the Planetary Data System (for link refer Section 2). Derived data products are available via Figshare: R. Parekh (2020) Data for “Influence of Volatiles on Mass Wasting Processes on Vesta and Ceres”.7z (<https://doi.org/10.6084/m9.figshare.13466642.v1>). Measurement results are listed in the supporting information.

## Acknowledgments

The authors thank two anonymous reviewers for their constructive and helpful comments that greatly improved this work. The authors acknowledge the Dawn team for providing data and support. The authors extend their gratitude to Chloe Beddingfield and Gou Sheng for sharing their data. The authors are also thankful to Stefan Schröder for helpful discussions. This work was part of the research project “The Physics of Volatile Related Morphologies on Asteroids and Comets”. R. Parekh and K. A. Otto gratefully acknowledge the financial support and endorsement from the German Academic Exchange Service (under DLR-DAAD Ph.D. Fellowship) and the DLR Management Board Young Research Group Leader Program by the Executive Board Member for Space Research and Technology. A portion of the work was carried out at the Jet Propulsion Laboratory under contract with NASA.

## References

- Ammannito, E., DeSanctis, M. C., Ciarniello, M., Frigeri, A., Carrozzo, F. G., Combe, J.-P., et al. (2016). Distribution of phyllosilicates on the surface of Ceres. *Science*, *353*, aaf4279.
- Beddingfield, C. B., Beyer, R. A., Singer, K. N., McKinnon, W. B., Runyon, K., Grundy, W., et al. (2020). Landslides on Charon. *Icarus*, *335*, 113383.
- Bland, M. T., Raymond, C. A., Schenk, P. M., Fu, R. R., Kneissl, T., Pasckert, J. H., et al. (2016). Composition and structure of the shallow subsurface of Ceres revealed by crater morphology. *Nature Geoscience*, *9*(7), 538–542.
- Bowling, T. J., Ciesla, F. J., Davison, T. M., Scully, J. E. C., Castillo-Rogez, J. C., Marchi, S., & Johnson, B. C. (2019). Post-impact thermal structure and cooling timescales of Occator crater on asteroid 1 Ceres. *Icarus*, *20*, 110.
- Brunetti, M. T., Xiao, Z., Komatsu, G., Peruccacci, S., & Guzzetti, F. (2015). Large rock slides in impact craters on the Moon and Mercury. *Icarus*, *260*, 289–300.
- Buczowski, D. L., Schmidt, B. E., Williams, D. A., Mest, S. C., Scully, J. E. C., Ermakov, A. I., et al. (2016). The geomorphology of Ceres. *Science*, *353*, aaf4332.
- Cheng, A. F., Barnouin-Jha, O., Prockter, L., Zuber, M. T., Neumann, G., Smith, D. E., et al. (2002). Small-scale topography of 433 Eros from laser altimetry and imaging. *Icarus*, *155*, 51.
- Chilton, H. T., Schmidt, B. E., Duarte, K., Ferrier, K. L., Hughson, K. H. G., Scully, J. E. C., et al. (2019). Landslides on Ceres: Inferences into ice content and layering in the upper crust. *Journal of Geophysical Research: Planets*, *124*, 1512–1524. <https://doi.org/10.1029/2018JE005634>
- Combe, J.-P., McCord, T. B., Tosi, F., Ammannito, E., Carrozzo, F. G., De Sanctis, M. C., et al. (2016). Detection of local H<sub>2</sub>O exposed at the surface of Ceres. *Science*, *353*, aaf3010.
- Combe, J.-P., Raponi, A., Tosi, F., De Sanctis, M. C., Carrozzo, F. G., Zambon, F., et al. (2019). Exposed H<sub>2</sub>O-rich areas detected on Ceres with the dawn visible and infrared mapping spectrometer. *Icarus*, *318*, 22.
- Crosta, G. B., De Blasio, F. V., & Frattini, P. (2018). Introducing a new inventory of large Martian landslides. *Journal of Geophysical Research: Planets*, *5*, 89–119. <https://doi.org/10.1002/2017EA000324>
- Crosta, G. B., Frattini, P., Valbuzzi, E., & De Blasio, F. V. (2018). Global scale analysis of Martian landslide mobility and paleoenvironmental clues. *Journal of Geophysical Research: Planets*, *123*, 872–891. <https://doi.org/10.1002/2017JE005398>
- Cruden, D. M. (1980). The anatomy of landslides. *Canadian Geotechnical Journal*, *17*(2), 295–300.
- De Blasio, F. V. (2011). *Introduction to the physics of landslides: Lecture notes on the dynamics of mass wasting*. Springer Science & Business Media.
- Denevi, B. W., Blewett, D. T., Buczowski, D. L., Capaccioni, F., Capria, M. T., De Sanctis, M. C., et al. (2012). Pitted terrain on Vesta and implications for the presence of volatiles. *Science*, *338*(6104), 246–249.
- De Sanctis, M. C., Ammannito, E., Capria, M. T., Capaccioni, F., Combe, J.-P., Frigeri, A., et al. (2013). Vesta’s mineralogical composition as revealed by the visible and infrared spectrometer on Dawn. *Meteoritics & Planetary Science*, *48*(11), 2166–2184.
- De Sanctis, M. C., Ammannito, E., McSween, H. Y., Raponi, A., Marchi, S., Capaccioni, F., et al. (2017). Localized aliphatic organic material on the surface of Ceres. *Science*, *355*(6326), 719–722.
- De Sanctis, M. C., Combe, J. P., Ammannito, E., Palomba, E., Longobardo, A., McCord, T. B., et al. (2012). Detection of widespread hydrated materials on Vesta by the Vir Imaging Spectrometer on board the Dawn Mission. *The Astrophysical Journal*, *758*(2), L36.
- Dikau, R., Brunsden, D., Schrott, L., & Ibsen, M.-L. (1996). Book review: *Landslide recognition: Identification, movement, and causes* (21). New York, NY: Wiley and Sons.
- Duarte, K. D., Schmidt, B. E., Chilton, H. T., Hughson, K. H. G., Sizemore, H. G., Ferrier, K. L., et al. (2019). Landslides on Ceres: Diversity and geologic context. *Journal of Geophysical Research: Planets*, *124*, 3329–3343. <https://doi.org/10.1029/2018JE005673>
- Elbeshhausen, D., Wünnemann, K., Sierks, H., Vincent, J. B., & Ockay, N. (2012). *Landslides triggered by impacts on asteroid (21) Lutetia?* Paper Presented at the European Planetary Science Congress 2012, September 01, 2012.
- Formisano, M., Federico, C., Turrini, D., Coradini, A., Capaccioni, F., De Sanctis, M. C., & Pauselli, C. (2013). The heating history of Vesta and the onset of differentiation. *Meteoritics & Planetary Science*, *48*, 2316–2332. <https://doi.org/10.1111/maps.12134>
- Gou, S., Yue, Z., Di, K., & Liu, Z. (2018). A global catalogue of Ceres impact craters  $\geq 1$  km and preliminary analysis. *Icarus*, *302*, 296.
- Hayne, P. O., & Aharonson, O. (2015). Thermal stability of ice on Ceres with rough topography. *Journal of Geophysical Research: Planets*, *120*, 1567–1584. <https://doi.org/10.1002/2015JE004887>
- Heim, A. (1932). *Bergsturz und menschenleben*. Fretz & Wasmuth.
- Hiesinger, H., Marchi, S., Schmedemann, N., Schenk, P., Pasckert, J. H., Neesemann, A., et al. (2016). Cratering on Ceres: Implications for its crust and evolution. *Science*, *353*, aaf4758.
- Hughson, K. H. G., Russell, C. T., Schmidt, B. E., Chilton, H. T., Sizemore, H. G., Schenk, P. M., & Raymond, C. A. (2019). Fluidized appearing ejecta on Ceres: Implications for the mechanical properties, frictional properties, and composition of its shallow subsurface. *Journal of Geophysical Research: Planets*, *124*, 1819–1839. <https://doi.org/10.1029/2018JE005666>
- Jaumann, R., Williams, D., Buczowski, D. L., Yingst, R. A., Preusker, F., Hiesinger, H., et al. (2012). Vesta’s shape and morphology. *Science*, *336*(6082), 687–690.
- Krohn, K., Jaumann, R., Otto, K., Hoogenboom, T., Wagner, R., Buczowski, D. L., et al. (2014). Mass movement on Vesta at steep scarps and crater rims. *Icarus*, *244*, 120–132.
- Krohn, K., Jaumann, R., Otto, K. A., Schulzeck, F., Neesemann, A., Nass, A., et al. (2017). The unique geomorphology and structural geology of the Haulani crater of dwarf planet Ceres as revealed by geological mapping of equatorial quadrangle Ac-6 Haulani. *Icarus*, *316*, 84.
- Liu, Z., Yue, Z., Michael, G., Gou, S., Di, K., Sun, S., & Liu, J. (2018). A global database and statistical analyses of (4) Vesta craters. *Icarus*, *311*, 242–257. <https://doi.org/10.1016/j.icarus.2018.04.006>

- Marchi, S., Bottke, W. F., Cohen, B. A., Winnemann, K., Kring, D. A., McSween, H. Y., et al. (2013). High-velocity collisions from the lunar cataclysm recorded in asteroidal meteorites. *Nature Geoscience*, 6, 411.
- Marchi, S., Ermakov, A. I., Raymond, C. A., Fu, R. R., O'Brien, D. P., Bland, M. T., et al. (2016). The missing large impact craters on Ceres. *Nature Communication*, 7, 12257.
- Marchi, S., McSween, H. Y., O'Brien, D. P., Schenk, P., De Sanctis, M. C., Gaskell, R., et al. (2012). The violent collisional history of asteroid 4 Vesta. *Science*, 336, 690.
- Massironi, M., Marchi, S., Pajola, M., Snodgrass, C., Thomas, N., Tubiana, C., et al. (2012). Geological map and stratigraphy of asteroid 21 Lutetia. *Planetary and Space Science*, 66(1), 125–136.
- McEwen, A. S. (1989). Mobility of large rock avalanches: Evidence from Valles Marineris, Mars. *Geology*, 17, 1111.
- Melosh, H. J. (1986). The physics of very large landslides. *Acta Mechanica*, 64(1–2), 89–99.
- Moore, J. M., Asphaug, E., Morrison, D., Spencer, J. R., Chapman, C. R., Bierhaus, B., et al. (1999). Mass movement and landform degradation on the Icy Galilean Satellites: Results of the Galileo nominal mission. *Icarus*, 140, 294.
- Nathues, A., Schmedemann, N., Thangjam, G., Pasckert, J. H., Mengel, K., Castillo-Rogez, J., et al. (2020). Recent cryovolcanic activity at Occator crater on Ceres. *Nature Astronomy*, 4, 794.
- Otto, K., Jaumann, R., Krohn, K., Matz, K.-D., Preusker, F., Roatsch, T., et al. (2013). Mass-wasting features and processes in Vesta's south polar basin Rheasilvia. *Journal of Geophysical Research: Planets*, 118, 2279–2294. <https://doi.org/10.1002/2013JE004333>
- Otto, K., Jaumann, R., Krohn, K., Spahn, F., Raymond, C. A., & Russell, C. T. (2016). The Coriolis effect on mass wasting during the Rheasilvia impact on asteroid Vesta. *Geophysical Research Letters*, 43(24), 12340–12347. <https://doi.org/10.1002/2016GL071539>
- Otto, K., Marchi, S., Trowbridge, A., Melosh, H., & Sizemore, H. (2019). Ceres crater degradation inferred from concentric fracturing. *Journal of Geophysical Research: Planets*, 124, 1188–1203. <https://doi.org/10.1029/2018JE005660>
- Prettyman, T. H., Mittlefehldt, D. W., Yamashita, N., Beck, A. W., Feldman, W. C., Hendricks, J. S., et al. (2013). Neutron absorption constraints on the composition of 4 Vesta. *Meteoritics & Planetary Science*, 48, 2211.
- Prettyman, T. H., Yamashita, N., Toplis, M. J., McSween, H. Y., Schörghofer, N., Marchi, S., et al. (2017). Extensive water ice within Ceres' aqueously altered regolith: Evidence from nuclear spectroscopy. *Science*, 355(6320), 55–59.
- Preusker, F., Scholten, F., Matz, K.-D., Elgner, S., Jaumann, R., Roatsch, T., et al. (2016). Dawn at Ceres – Shape model and rotational state. In Paper Presented at the Lunar and Planetary Science Conference. Retrieved from <https://ui.adsabs.harvard.edu/abs/2016LPL....47.1954P>
- Quantin, C., Allemand, P., & Delacourt, C. (2004). Morphology and geometry of Valles Marineris landslides. *Planetary and Space Science*, 52(11), 1011–1022.
- Reddy, V., Nathues, A., Le Corre, L., Sierks, H., Li, J. Y., Gaskell, R., et al. (2012). Color and albedo heterogeneity of Vesta from Dawn. *Science*, 336(6082), 700–704.
- Rivkin, A. S., Volquardsen, E. L., & Clark, B. E. (2006). The surface composition of Ceres: Discovery of carbonates and iron-rich clays. *Icarus*, 185(2), 563–567.
- Roatsch, T., Kersten, E., Matz, K.-D., Preusker, F., Scholten, F., Elgner, S., et al. (2016). Dawn FC2 derived Ceres HAMO DTM SPG V1.0. NASA Planetary Data System. DAWN-A-FC2-5-CERESHAMODTMSPG-V1.0. Retrieved from <https://ui.adsabs.harvard.edu/abs/2016PDSS..266.....R>
- Roatsch, T., Kersten, E., Matz, K.-D., Preusker, F., Scholten, F., Jaumann, R., et al. (2012). High resolution Vesta High Altitude Mapping Orbit (HAMO) Atlas derived from Dawn framing camera images. *Planetary and Space Science*, 73, 283.
- Roatsch, T., Kersten, E., Matz, K.-D., Preusker, F., Scholten, F., Jaumann, R., et al. (2015). Ceres Survey Atlas derived from Dawn Framing Camera images. *Planetary and Space Science*, 121, 115–120.
- Roatsch, T., Kersten, E., Matz, K.-D., Preusker, F., Scholten, F., Jaumann, R., et al. (2017). High-resolution Ceres low altitude mapping Orbit Atlas derived from dawn framing camera images. *Planetary and Space Science*, 140, 74.
- Ruesch, O., Platz, T., Schenk, P., McFadden, L. A., Castillo-Rogez, J. C., Quick, L. C., et al. (2016). Cryovolcanism on Ceres. *Science*, 353, aaf4286.
- Russell, C. T., Coradini, A., Christensen, U., De Sanctis, M. C., Feldman, W. C., Jaumann, R., et al. (2004). Dawn: A journey in space and time. *Planetary and Space Science*, 52, 465.
- Russell, C. T., & Raymond, C. A. (2011). The Dawn Mission to Vesta and Ceres. *Space Science Reviews*, 163, 3.
- Russell, C. T., Raymond, C. A., Coradini, A., McSween, H. Y., Zuber, M. T., Nathues, A., et al. (2012). Dawn at Vesta: Testing the protoplanetary paradigm. *Science*, 336(6082), 684–686.
- Scaioni, M., Yordanov, V., Brunetti, M. T., Melis, M. T., Zinzi, A., Kang, Z., & Giommi, P. (2017). Recognition of landslides in lunar impact craters. *European Journal of Remote Sensing*, 51(1), 47–61.
- Schenk, P., O'Brien, D. P., Marchi, S., Gaskell, R., Preusker, F., Roatsch, T., et al. (2012). The geologically recent giant impact basins at Vesta's South Pole. *Science*, 336, 694.
- Schmidt, B. E., Hughson, K. H. G., Chilton, H. T., Scully, J. E. C., Platz, T., Nathues, A., et al. (2017). Geomorphological evidence for ground ice on dwarf planet Ceres. *Nature Geoscience*, 10(5), 338–343.
- Schorghofer, N. (2008). The lifetime of ice on main belt asteroids. *The Astrophysical Journal*, 682, 697.
- Schorghofer, N. (2016). Predictions of depth-to-ice on asteroids based on an asynchronous model of temperature, impact stirring, and ice loss. *Icarus*, 276, 88. <https://doi.org/10.1016/j.icarus.2016.04.037>
- Scully, J. E. C., Russell, C. T., Yin, A., Jaumann, R., Carey, E., Castillo-Rogez, J., et al. (2015). Geomorphological evidence for transient water flow on Vesta. *Earth and Planetary Science Letters*, 411, 151–163.
- Shingareva, T. V., & Kuzmin, R. O. (2001). Mass-wasting processes on the surface of phobos. *Solar System Research*, 35, 431.
- Shreve, R. L. (1966). Sherman landslide, Alaska. *Science*, 154(3757), 1639–1643.
- Shreve, R. L. (1968). The Blackhawk Landslide (108). Geological Society of America.
- Sierks, H., Keller, H., Jaumann, R., Michalik, H., Behnke, T., Bubenhausen, F., et al. (2011). The Dawn framing camera. *Space Science Reviews*, 163(1–4), 263–327.
- Singer, K. N., McKinnon, W. B., Schenk, P. M., & Moore, J. M. (2012). Massive ice avalanches on Iapetus mobilized by friction reduction during flash heating. *Nature Geoscience*, 5(8), 574–578.
- Sizemore, H., Platz, T., Schorghofer, N., Prettyman, T. H., De Sanctis, M. C., Crown, D. A., et al. (2017). Pitted terrains on (1) Ceres and implications for shallow subsurface volatile distribution. *Geophysical Research Letters*, 44(13), 6570–6578. <https://doi.org/10.1002/2017GL073970>
- Sizemore, H., Schmidt, B. E., Buczkowski, D. A., Sori, M. M., Castillo-Rogez, J. C., Berman, D. C., et al. (2019a). A global inventory of ice-related morphological features on dwarf planet Ceres: Implications for the evolution and current state of the cryosphere. *Journal of Geophysical Research: Planets*, 124, 1650–1689. <https://doi.org/10.1029/2018JE005699>

- Sizemore, H., Schmidt, B. E., & Castillo-Rogez, J. (2019b). Introduction to the Special Issue: Ice on Ceres. *Journal of Geophysical Research: Planets*, *124*, 1639–1649. <https://doi.org/10.1029/2019JE006012>
- Sori, M. M., Sizemore, H. G., Byrne, S., Bramson, A. M., Bland, M. T., Stein, N. T., & Russell, C. T. (2018). Author Correction: Cryovolcanic rates on Ceres revealed by topography. *Nature Astronomy*, *2*, 995.
- Sullivan, R. J., Thomas, P. C., Murchie, S. L., & Robinson, M. S. (2002). *Asteroid Geology from Galileo and NEAR Shoemaker Data*. In *Asteroids III*, p. 331.
- Toplis, M. J., Mizzon, H., Monnereau, M., Forni, O., McSween, H. Y., Mittlefehldt, D. W., et al. (2013). Chondritic models of 4 Vesta: Implications for geochemical and geophysical properties. *Meteoritics & Planetary Science*, *48*, 2300–2315. <https://doi.org/10.1111/maps.12195>
- Turnbull, B. (2011). Scaling laws for melting ice avalanches. *Physical Review Letters*, *107*, 258001.
- Varnes, D. J. (1978). Slope movement types and processes (176). National Academy of Science.
- Williams, D., Denevi, B. W., Mittlefehldt, D. W., Mest, S. C., Schenk, P. M., Yingst, R. A., et al. (2014). The geology of the Marcia quadrangle of asteroid Vesta: Assessing the effects of large, young craters. *Icarus*, *244*, 74.
- Williams, D., O'Brien, D., Schenk, P., Denevi, B., Carsenty, U., & Marchi, S. (2014). Lobate and flow-like features on asteroid Vesta. *Planetary and Space Science*, *103*, 24–35.
- Xiao, Z., Zeng, Z., Ding, N., & Molaro, J. (2013). Mass wasting features on the Moon – How active is the lunar surface? *Earth and Planetary Science Letters*, *376*, 1–11.

**2.1.6 Parekh et al. (2021b)**

Parekh, R., Otto, K. A., Matz, K. D., Jaumann, R., Krohn, K.,  
Roatsch, T., Kersten, E., Elgner, S., Russell, C. T., &  
Raymond, C. A. (2021b). Formation of Ejecta and Dust Pond  
Deposits on Asteroid Vesta. *Journal of Geophysical Research:  
Planets*, 126(11), e2021JE006873.  
<https://doi.org/10.1029/2021JE006873>.




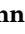
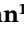





The research leading to this article was conducted and written by R. Parekh. I provided input to the layout and approach of the research and I assisted in generating Table 4. R. Jaumann, K. Krohn and I helped with the geologic interpretation. K.-D. Matz, T. Roatsch, E. Kersten and S. Elgner generated the data products and tools needed for this research. R. Jaumann, C. T. Russell and C. A. Raymond led the instrument and mission management. All authors assisted with refining the manuscript.



## Formation of Ejecta and Dust Pond Deposits on Asteroid Vesta

**Key Points:**

- We identified ejecta and dust pond crater candidates on Vesta within 0°–30°N/S
- Ejecta ponds are smooth deposits and located within the ejecta melt of large craters
- Dust ponds are produced via local-scale seismic shaking and/or volatile fluidization

R. Parekh<sup>1,2</sup> , K. A. Otto<sup>1</sup> , K. D. Matz<sup>1</sup> , R. Jaumann<sup>2</sup> , K. Krohn<sup>1</sup> , T. Roatsch<sup>1</sup> , E. Kersten<sup>1</sup> , S. Elgner<sup>1</sup> , C. T. Russell<sup>3</sup> , and C. A. Raymond<sup>4</sup> 

<sup>1</sup>DLR Institute of Planetary Research, Berlin, Germany, <sup>2</sup>Freie University of Berlin, Institute of Geological Science, Berlin, Germany, <sup>3</sup>University of California, Los Angeles, CA, USA, <sup>4</sup>Jet Propulsion Laboratory, Pasadena, CA, USA

**Correspondence to:**

R. Parekh,  
[rutu.parekh@dlr.de](mailto:rutu.parekh@dlr.de)

**Citation:**

Parekh, R., Otto, K. A., Matz, K. D., Jaumann, R., Krohn, K., Roatsch, T., et al. (2021). Formation of ejecta and dust pond deposits on asteroid Vesta. *Journal of Geophysical Research: Planets*, 126, e2021JE006873. <https://doi.org/10.1029/2021JE006873>

Received 28 FEB 2021  
 Accepted 29 OCT 2021

**Author Contributions:**

**Data curation:** K. D. Matz, T. Roatsch  
**Funding acquisition:** K. A. Otto  
**Resources:** C. A. Raymond  
**Supervision:** K. A. Otto, R. Jaumann  
**Writing – review & editing:** K. A. Otto, R. Jaumann, K. Krohn, E. Kersten, C. T. Russell

**Abstract** Dust and melt ponds have been studied on planetary bodies including Eros, Itokawa, and the Moon. However, depending on the nature of the regolith material properties and the location of the planetary body, the formation mechanism of the ponded features varies. On Eros and Itokawa, ponded features are formed from dry regolith materials whereas on the Moon similar features are thought to be produced by ejecta melt. On the surface of Vesta, we have identified type 1, ejecta ponds, and type 2, dust ponds. On Vesta type 1 ponds are located in the vicinity of ejecta melt of large impact craters. The material is uniformly distributed across the crater floor producing smooth pond surfaces which have a constant slope and shallow depth. The hosting crater of melt-like ponds has a low raised rim and is located on relatively low elevated regions. Whereas, the type 2 ponds on Vesta reveal an undulating surface that is frequently displaced from the crater center or extends toward the crater wall with an abruptly changing slope. We suggested that for the production of the type 2 ponds, localized seismic diffusion and volatile-induced fluidization may be responsible for Vesta. Due to Vesta's large size (in comparison to Eros and Itokawa), the surface may have experienced local-scale rare high-amplitude seismic diffusion which was sufficient to drift fine material. Similarly, short-lived volatile activities were capable to transfer dusty material on to the surface. Segregation and smoothing of transferred material lack further surface activities, hindering the formation of smooth morphology.

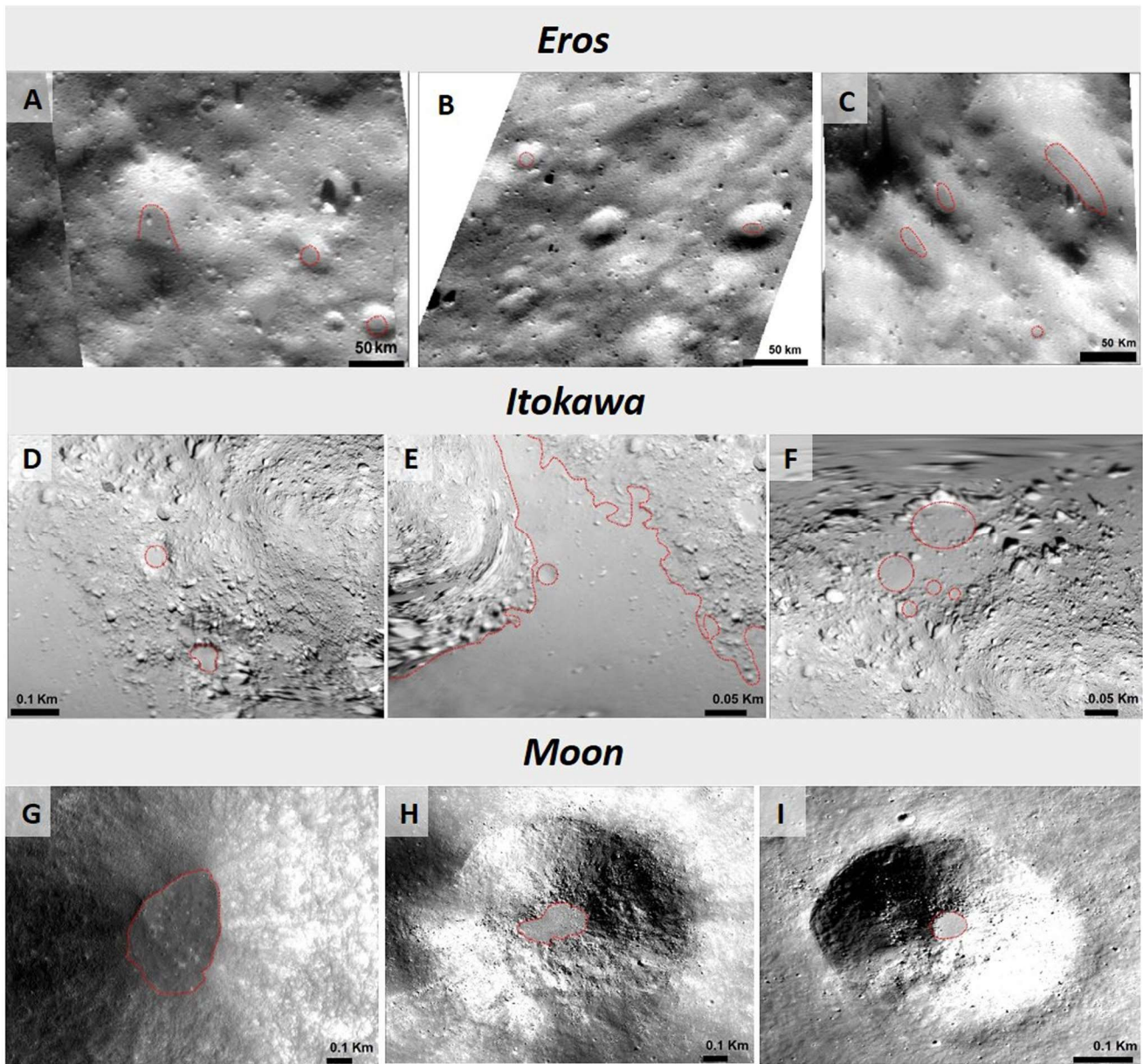
**Plain Language Summary** Ponded landforms are relatively smooth and featureless deposits and are commonly present on dry planetary bodies. The dry regolith of Eros, Itokawa, and the Moon provides ideal conditions for the formation of ponded deposits. They are produced either from the fine-grained regolith substances or impact crater ejecta melt material. Typically, ponded deposits are distributed homogeneously and produce a flat leveled deposit surface. However, due to lack of segregation mechanisms they do not always have an entirely flat topography. The production of ponded deposits relies on geological events that include regolith migration and various mechanisms have been proposed for their formation. In our study, we identify ponded deposits on the surface of Vesta and hypothesize that rare high-amplitude seismic diffusivity and short-lived volatile outgassing were responsible for the material migration and in turn for the production of ponded deposits.

### 1. Introduction

Ponded deposits widely receive attention due to their unusual characteristics on asteroid Eros as revealed by the NEAR Shoemaker mission (Robinson et al., 2001, 2002; Sears et al., 2015). Usually, ponded features are identified within craters. However, there are also a few examples in which ponded features are observed in moderately large regions (Miyamoto, 2014) of a planetary body, for example, the Sagami-hara and Muses-Sea regions (Fujiwara et al., 2006; Saito et al., 2006) on asteroid Itokawa. Due to their smooth appearance, they are called “ponds.” Typically, ponded regions consist of a smooth layer of fine-grained material (less than cm size) (Robinson et al., 2001), partially covering the topography of a crater floor along with boulders of varying sizes or unconsolidated material (Sears et al., 2015) leaving behind a sharp edge of deposition at the walls of a crater depression (Robinson et al., 2001; Veverka et al., 2001). Further, they form a nearly flat or low slope terrain (usually  $\sim 10^\circ$  on Eros) (Cheng et al., 2002) and often have apparent variations with sharp boundaries in albedo relative to the surrounding plains (Robinson et al., 2001). The smooth material is distributed either at the crater floor center and/or is often slightly offset from the geometric center (Robinson et al., 2001) (Figures 1a–1c). The variation in albedo can be due to mineral heterogeneity (Robinson

© 2021 The Authors.

This is an open access article under the terms of the [Creative Commons Attribution-NonCommercial License](https://creativecommons.org/licenses/by-nc/4.0/), which permits use, distribution and reproduction in any medium, provided the original work is properly cited and is not used for commercial purposes.



**Figure 1.** Examples of pond impressions on Eros (a–c), Itokawa (d–f) and the Moon (g–i). The ponded regions are highlighted by red dotted lines. The location of the shown ponds are as follows: (a) long: 175.7°E, lat: 1.61°S; (b) long: 6.56°E, lat: 5.48°S; (c) long: 165.28°E, lat: 3.64°S on Eros; (a) evenly distributed fine material at the crater floor, (b) and (c) identify ponded material at the steepening surface of the crater wall; (d) Komaba crater (long: 102°E, lat: 10°S) and an unnamed flat region; (e) crater like depression present within the large smooth region of Muses Sea and (f) five small circular smooth features located within Uchinoura (long: 40°E, lat: 90°S) on Itokawa. Melt pool exhibiting a smooth surface at the bottom of the crater located at (g) long: 97.5°E, lat: 2.36°N, (h) long: 81.70°E, lat: 32.02°S, (i) long: 235.71°E, lat: 40.6°S on the Moon. The presence of boulders is evident near the ponds' rims in (h) and (i).

et al., 2001), space weathering (Heldmann et al., 2010; Robinson et al., 2001; Sears et al., 2015), or the difference in grain size between the pond regolith and the surrounding region (Heldmann et al., 2010; Robinson et al., 2001). Some of these characteristics of the pond deposits are found not only on Eros but are also identified within large regions (Sagamihara, Muses-Sea) of Itokawa (Fujiwara et al., 2006; Miyamoto et al., 2007; Saito et al., 2006; Yano et al., 2006) (Figures 1d–1f) and small craters on the Moon (Figures 1g–1i) (Hawke & Head, 1977b, 1979; Plescia & Cintala, 2012; Stopar et al., 2012). Overall, ponded regions are noted on planetary bodies with dry brittle regolith and/or low volatile content (Miyamoto et al., 2007; Robinson et al., 2001). However, based on the weathering process, impacts, and regolith material properties of the

**Table 1**  
*Physical Characteristics of the Planetary Objects Discussed in This Study*  
(Murdoch et al., 2015)

Planetary body	Size (km)	Bulk density (kg/m <sup>3</sup> )	Surface acceleration (m/s <sup>2</sup> )
Eros	34.4 × 11.2 × 11.2	2,700	0.0023–0.0056
Itokawa	0.535 × 0.294 × 0.209	1,900	0.000024–0.000086
Moon(dia.)	3,474.8	3,344	1.62
Vesta	572.6 × 557.2 × 446.4	3,500	0.25

different planetary bodies, these geomorphologic appearances may vary and are not necessarily identical in all the identified ponded regions.

Depending on the material properties and identified pond impressions, various geological processes have been suggested as mechanisms to produce ponds on Eros, Itokawa, and the Moon. On Eros, electrostatic levitation and seismic shaking were proposed earlier as a possible formation mechanism for the dust ponds (Cheng et al., 2002; Robinson et al., 2001; Veverka et al., 2001). Electrostatic levitation was proved to be responsible for the mobility of charged particles (Lee, 1996; Roberts et al., 2014; Robinson et al., 2001; Veverka et al., 2001) where as seismic waves induced the segregation to sort grains and produce smooth featureless pond deposits (Cheng et al., 2002; Robinson et al., 2001; Thomas et al., 2002;

Veverka et al., 2001). However, both theories fail to explain the distinct distribution of ponds and significant color variation identified within ponded material (Dombard et al., 2010). Later on, Dombard et al. (2010) proposed the boulder disintegration due to space weathering based on the close proximity of large size boulders (upto ~30 m) with pond deposits. Recent laboratory simulations also suggest the involvement of volatile outgassing as a possible production mechanism for the formation of ponded features on Eros via (a) exogenic volatile-rich meteor impacts or (b) endogenic substances present within subsurface regolith (Sears et al., 2015). Moreover, Eros is a class S asteroid resembling ordinary chondrites (Bell et al., 2002) with the presence of hydrated minerals within chondrites (Grossman et al., 2000; Hutchison et al., 1987). Even though none of the images show direct involvement or geological features of volatile outgassing activity (such as pitted terrains or cracks) on Eros, a possible involvement cannot be excluded.

Similarly, on Itokawa, the Muse-Sea and Sagami-hara regions are composed of unconsolidated granular material that was rearranged post-accumulation (Miyamoto, 2014). As on Eros, it is assumed that the surface of Itokawa experiences a similar process of particle segregation (Saito et al., 2006). Given the small size of Itokawa (Table 1), seismic energy generated through impacts can cause global surface vibrations within the regolith (Miyamoto, 2014) which may result in the rearrangement of unconsolidated material. The smooth ponded regions of Itokawa present within the low gravitational potential (Fujiwara et al., 2006) point toward the gravitational movement of fine particles. Similar to Eros, volatile activity is also suspected as one of the potential mechanisms for the pond formation on Itokawa. The assumption was based on the (a) isotope studies of the Hayabusa returned samples which proved that dehydration occurred during the early history of Itokawa within the region of Muse-Sea (Jin & Bose, 2019), (b) prediction models developed by considering the thermal diffusivity and collision history of Itokawa and the anticipated loss of water within Itokawa regolith at depths of 10 m–1 km during its early history (Jin & Bose, 2019) and (c) the presence of circular depression-like geologic features (Saito et al., 2006) (Figures 1d–1f, highlighted in red) which resemble laboratory-generated depressions formed due to volatile fluidization (Sears et al., 2015).

Unlike Eros and Itokawa, the ponded features identified within craters of the Moon are known as “melt pools” and the majority of them are formed from the melting of impact materials (Hawke & Head, 1977a, 1977b, 1979). Cintala and Grieve (1998) derived a model which predicted that high-velocity impactors (~40 km/s) are capable of producing large volumes of melt that form thin layers in their neighboring regions (Hawke & Head, 1977a, 1977b; Howard & Wilshire, 1975). The ejected melt will then flow to lower elevated regions, forming lobate-like bulge features (Howard & Wilshire, 1975). In such cases, pre-existing topography conditions such as lower height downslope rim crest and evidence of flow margins is required. Nevertheless, only a small percentage of craters (~6%) reveal lobate flow margins and very few craters have low elevated rim crests allowing such drainage (23 out of 69) (Stopar et al., 2014). Thus, the emplacement of melt material requires certain pre-existing surface conditions for the transport of the impact melts which are not always observed. Other than high velocity, near vertical impact velocity models (Cintala & Grieve, 1998; Pierazzo & Melosh, 2000; Plescia & Cintala, 2012) suggests an alternative explanation that does not require any topographic conditions. According to these models, near vertical impactors produce melt that does not spread outside the crater floor but allows the melt to remain within the crater which later creates smooth flat pond surfaces as the temperature decreases (Plescia & Cintala, 2012). The majority of studies focus on melt formation as a possible mechanism to produce ponds on the lunar surface



(Hawke & Head, 1977a, 1977b; Plescia & Cintala, 2012; Stopar et al., 2014), however, given the dusty regolith of the Moon, the formation of ponds via particle levitation cannot be overlooked. Nevertheless, particle levitation requires a higher degree of electric charging to lift and mobilize dust particles on the Moon (Stopar et al., 2014) compared to smaller bodies like Eros due to the larger gravitational pull (Table 1; Thomas et al., 2002). Furthermore, recent data from the Lunar Atmosphere Dust and Environment Explorer (LADEE) do not show any evidence of a dense dust cloud near the lunar surface (Horányi et al., 2015; Szalay & Horányi, 2015). Thus, impact melt production appears to be the most feasible mechanism to explain the formation of ponded features on the surface of the Moon at a global scale.

In a nutshell, multiple mechanisms including electrostatic levitation (Lee, 1996; Robinson et al., 2001), seismic shaking (Robinson et al., 2001), boulder comminution (Dombard et al., 2010), fluidized impact ejecta (Hawke & Head, 1977b) and volatile outgassing (Sears et al., 2015) are possibly responsible for the formation of pond deposits on Eros, Itokawa, and the Moon.

The asteroid Vesta is a dry planetary object (Jaumann et al., 2012) that was rigorously explored by the Dawn mission. Through this mission, a large number of high-resolution data were collected which enabled us to study and understand the surface of Vesta closely. Vesta's surface consists of a low volatile content regolith with a few morphological exceptions such as pitted terrain (Denevi et al., 2012), gully-like features (Scully et al., 2015) and fluidized impact ejecta (Williams, Denevi, et al., 2014; Williams, O'Brien, et al., 2014) of large craters such as Marcia (~58 km in diameter). Vesta's regolith provides an ideal condition for the formation of ponds, which on Eros and Itokawa required a dry environment. In this study, our objective is to identify and characterize the ponded features on the surface of Vesta, including the material properties and surface conditions under which the ponds form. Further, we compare them with numerous possible material migration and regolith sorting mechanisms identified on Eros, Itokawa, and the Moon to understand their formation and explore the detailed morphology of ponded features.

## 2. Methods

### 2.1. Data

For comparison, we adopted the data from previous studies. For Eros, we have used the images collected by the NEAR-Shoemaker spacecraft (Multi-Spectral Imager and Near-Earth Asteroid Rendezvous lander) which has a spatial resolution of ~0.3–0.7 m/pixel. For pond detection, we used geospatial point shapefile data from Robinson et al. (2002). In the case of Itokawa, we used the 0.3 m/pixel imaging mosaic derived from the Gaskell shape model prepared from the Asteroid Multiband Imaging Camera (AMICA) on the Hayabusa mission (Saito et al., 2006). Lastly, for the Moon, the mapped melt pool details are available from Plescia and Cintala (2012). Based on the shared latitude and longitude information, we gathered Lunar Reconnaissance Orbiter Camera (LROC) imaging data of the Moon. The image data has a spatial resolution ranging from 0.1 to 0.9 m/pixel.

For Vesta, we used mosaics from the Low Altitude Mapping Orbit (LAMO) from the Dawn mission's framing camera (Sierks et al., 2011) which has a spatial resolution of ~20 m/pixel (Roatsch et al., 2013). For the topographic information, we overlaid a High-Altitude Mapping Orbit (HAMO) digital terrain model (DTM) with 92 m/pixel lateral spatial resolution (Preusker et al., 2012). The DTM's spatial resolution is coarser than the image resolution, however, given that our smallest craters are 1.4 km in diameter, this is the best available DTM suitable for our analysis. The HAMO DTM is referenced to a best-fit ellipsoid of  $286.3 \times 278.6 \times 223.2$  km (Preusker et al., 2012). On the Moon, melt-like ponds are visible in 25 m/pixel images (Plescia & Cintala, 2012) whereas on Eros smooth ponded features can be identified at 0.5 m/pixel (Robinson et al., 2001), and on Itokawa, they are visible at the 50 m scale in images which have resolutions from 0.3–0.7 m/pixel (Hirata et al., 2009). With similar dry regolith present on Vesta, the high resolution of surface data has successfully enabled us to identify pond deposits.

### 2.2. Criteria for Identification of Pond and Method to Measure Pond Depth

Distinguishing between different types of pond-like landforms can be an arduous task due to their morphologic similarities, especially while using remotely sensed data where confirmation via ground truth is

**Table 2**  
*Summary of Ponded Impressions Identified on Vesta, Eros, Itokawa, and the Moon*

Ponded characteristics on Vesta	Eros	Itokawa	Moon
<b>Type 1 pond deposit</b>			
Fluidized impact ejecta material	✗	✗	✓
Smooth, nearly flat crater floors	✓	✓	✓
Shallow pond depth	✓	✓	✓
Distributed equipotentially within crater floors	✓	✓	✓
Relatively shallow slope	✓	-	✓
<b>Type 2 pond deposit</b>			
Dry fine-grained material	✓	✓	✗
Uneven ponded surface	✗	✓	✗
Material distributed either within crater floors and/or partially extending to the wall	✓	✗	✗
Increase in slope	✓	✓	✓
Pit like impressions	✗	✗	✗
Relatively deep ponds	✗	✗	✗

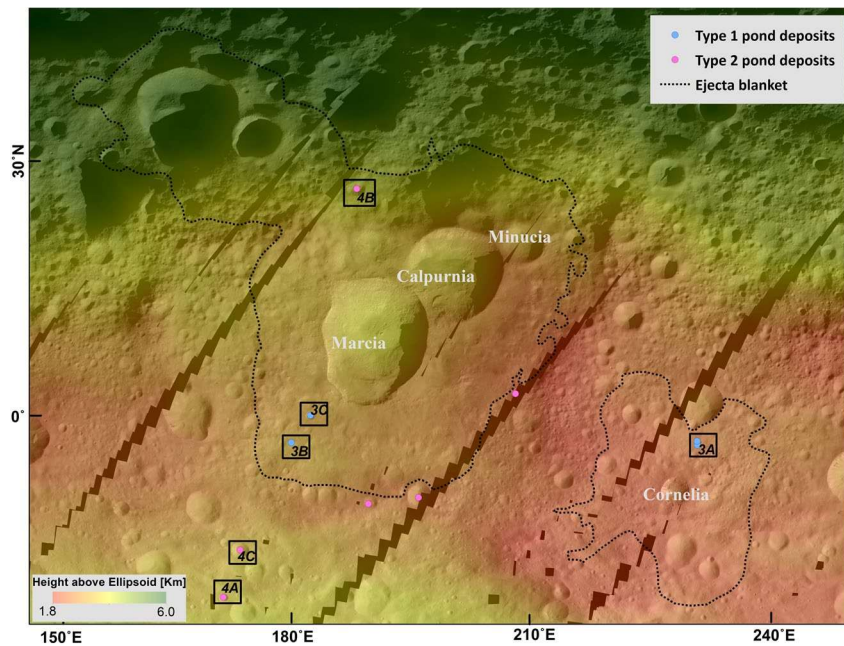
impossible. In such instances, researchers need to rely on the geological context present within the datasets. In our study, we considered neighboring geological conditions and previous studies of ponded features on Eros, Itokawa, and the Moon (Roberts et al., 2014; Robinson et al., 2001; Stopar et al., 2014) to understand the contrast in various morphological characteristics of ponded deposits. In general, dust pond deposits on Eros, Itokawa and melt-pools on the Moon have the following common characteristics, but they are not necessarily present in all the ponded candidates: often both types of deposits (a) have superimposed boulders and loose materials, (b) are in general identified in small craters (<1 km in diameter), (c) have a sharp boundary between the ponded deposit and the crater wall, and (d) are equipotential distributed within the crater floor resulting in a smooth surface (Fujiwara et al., 2006; Roberts et al., 2014; Robinson et al., 2001). However, a key difference between both type of ponds is that the dust deposits on Eros and Itokawa comprise fine dry regolith (with grain sizes of mm to cm on Itokawa and <2 cm on Eros), preferentially present near the equator (observed on Eros) and the majority of them are identified in low gravity regions (Cheng et al., 2002; Fujiwara et al., 2006; Robinson et al., 2001; Saito et al., 2006; Thomas & Robinson, 2005; Veverka et al., 2001). In contrast, the ejecta ponds are not correlated with latitude, longitude, or gravitational regions (Plescia & Cintala, 2012; Stopar et al., 2014) and are formed from the fluidized impact ejecta and/or impact melt of a neighboring crater. In Table 1, we list the observed morphological characteristics of ponded features on Eros, Itokawa, and the Moon. While conducting the survey of ponded candidates on Vesta, we consider the characteristics mentioned in Table 2 as a key for identification and further classify them into two categories namely: type 1 and type 2 pond deposits.

Next, we estimate the approximate depth of the ponded material. For this, we use the DTM and derive the current shape of the crater. We then add a least squares fit of a power function (polynomial fit) to the crater walls and estimate the original crater depth (d). Previously, the polynomial fit method has been used to best estimate the depth of sedimentary infilling within simple bowl-shaped craters on Mars (Savage et al., 2018). The difference between the measured shape from the DTM and the fitted original depth is the ponded material depth.

### 3. Observations and Interpretations

The following sections focus on distinct characteristics of type 1 and type 2 pond deposits on Vesta with concentration to their distribution and morphological evidence. The identified host craters are located within central latitudes (0°–30°N and 0°–25°S) of Vesta. In total, we have identified 10 craters on Vesta which show one or more pond characteristics mentioned in Table 2. These craters have a relatively small diameter (≤11 km) and half of them (5 out of 10) of them are scattered in the southern region of the Marcia (average  $\sim 75.3 \pm 32$  km distance from rim) and northern part of Cornelia crater (2 out of 10 at the average distance

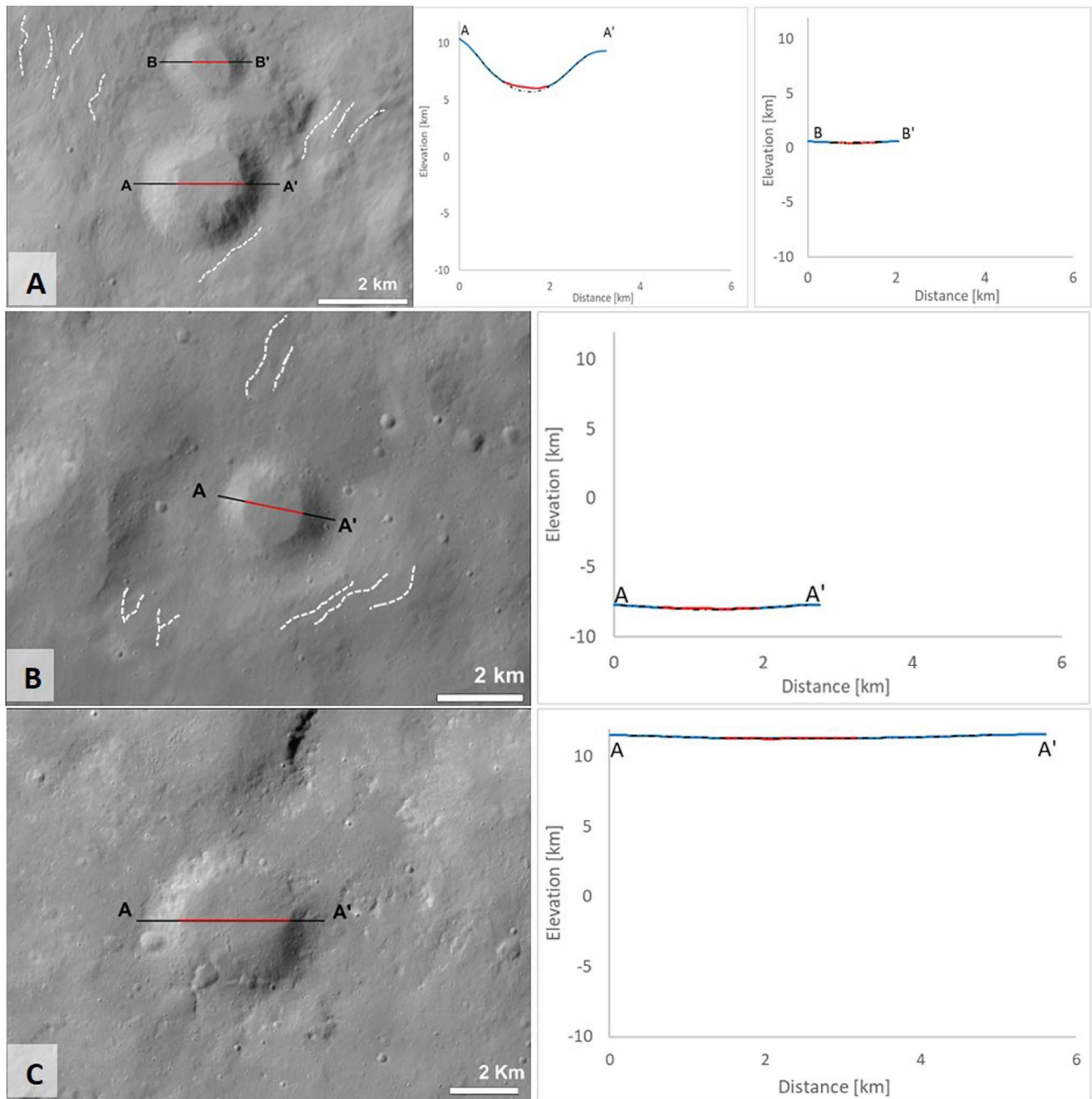




**Figure 2.** Map of ponded crater identified on the surface of Vesta. Black dotted line represents the ejecta blanket of the nearby large craters, derived from the geological map of Vesta by Williams, Denevi, et al. (2014). All type 1 and type 2 pond deposits are observed in and around ejecta blankets. The black boxes indicate the location of areas displayed in Figures 3 and 4. The ponded craters are mapped on a LAMO global mosaic and on a HAMO mosaic (only where high resolution data is not available) on which a HAMO DTM is superimposed (equidistant projection) to understand the surface elevation.

of  $\sim 21.6 \pm 1$  km from the rim (Figure 2). The derived original depth ( $d$ ) to diameter ( $D$ ) ratio of the crater ( $d/D$ ) is  $\sim 0.60$  (by assuming simple bowl-shaped fresh craters). This estimation represents the upper limit of the  $d/D$  ratio of host craters in which ponded features are observed because most of the craters have experienced some degree of degradation but not all the craters show ponded characteristics. Schenk et al. (2021) measured the current  $d/D$  ratio of simple bowl-shaped craters on the Vesta which is  $\sim 0.22$ . The difference in the  $d/D$  ratio of original and current craters can be due to resurfacing events that have been taking place in the past. Note that this is an approximate estimation to understand the variation in pond depth within identified crater candidates.

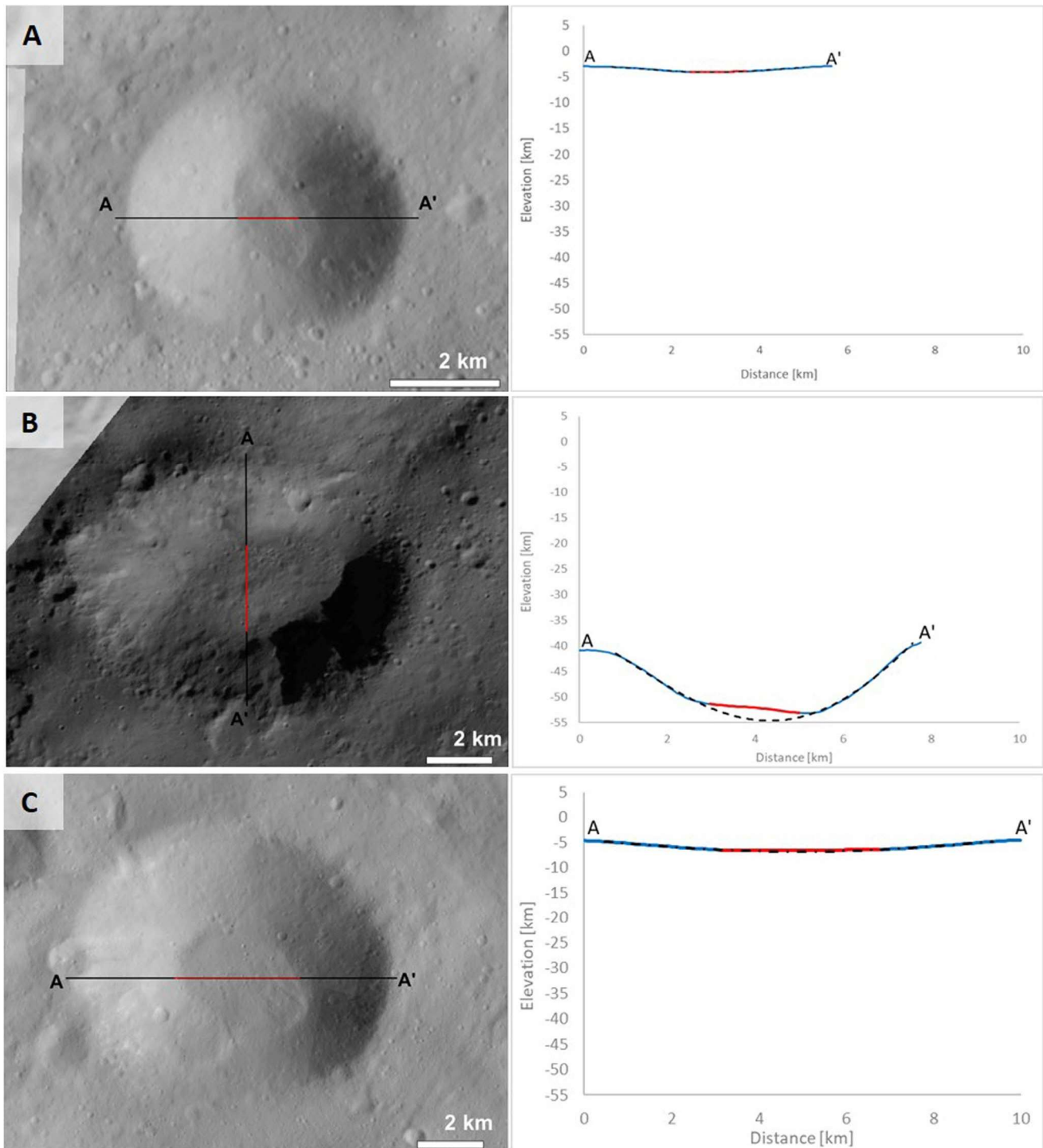
We characterized ponded crater candidates into two categories depending upon their morphology and their position within the craters. Among the identified ponded craters, a few deposits show a shallow slope throughout ( $\leq 15^\circ$ ), have a smooth surface with pond material evenly distributed covering the crater floor, the host craters of these pond deposits are located on relatively low elevated regions (blue dots in Figure 2) and in general present within the vicinity of impact ejecta spread (type 1). Such ponds are shallow in depth (average 0.12 km). So far, we identified four craters that exhibit the above-mentioned morphology (Figures 3a–3c). Based on the topographic profiles, we understand that the material infills the lowest region on the crater interior and gradually builds up toward the crater wall, producing a smooth surface. Similar smooth surfaces also appear outside in the vicinity of these craters (Figures 3a–3c). We notice smooth surfaces in the vicinity (v-shaped cusped toes and furrows highlighted in Figures 3a and 3b), partially broken low-raised rims, and a downslope topography ( $\sim 2.5$  km relief difference) within the host craters' region (Figure 2). Based on this evidence we assume that the material creating the ponds and the neighboring smooth terrain must have originated from the same source. The identified craters in this category are present within the ejecta blanket of nearby larger impact craters (Figure 2). There are a few more small craters observed within ejecta blankets with similar morphology, however, they are not easy to delineate due to lack of strong morphological impressions, unlike the above-mentioned examples. Due to the close proximity of ejecta ponds within Marcia, Calpurnia, Minucia, and Cornelia crater, the combination of impact ejecta and impact melt deposits (Williams, Denevi, et al., 2014) may be the putative source for the ponded deposit



**Figure 3.** Example of type 1 pond deposit on Vesta. (a) two unnamed craters located south of Cornelia crater with their corresponding surface profile (A-A' and B-B'). The ponded deposit is sharply constrained by the pre-existing crater walls. (b) and (c) are two unnamed ejecta pond hosting craters and their corresponding elevation profile. The craters are located south west of Marcia crater at a distance of  $\sim 38.3$  and  $\sim 20$  km from Marcia's crater wall. In the profiles, the blue line denotes the crater shape, red corresponds to the ponded deposit and the black white-dotted line indicates the original shape of the crater. In the images (a) and (b) white dashed lines highlight furrows and v-shaped cusps flow-like impact melt. North is up in all the images.

producing smooth and flat pond surfaces. These pond deposits show all the morphological characteristics similar to 'melt-pools' present on the Moon (Table 2).

Additionally, we found a few ponded features with some different morphological impressions. The ponded deposits within these craters are distributed more heterogeneously, forming an irregular surface with an undulating slope (type 2). In this type, the loose ponded material is located at the base of the crater wall



**Figure 4.** Example of type 2 ponds on Vesta. Crater (a, b, c) and their corresponding elevation profile (right) in which the pond is partially extended at the steep wall of the crater. (b) Based on the topographic information, it is evident that the slope in the central region is not flat indicating that the deposit is not (yet) equipotential distributed. (c) Surface of ponded material identified within an unnamed crater and its topographic information shows a gradual increase in elevation. In all elevation examples, the current crater profile is shown in blue, the pond deposit is highlighted in red and the estimated original crater profile is shown as a black dashed-dotted line. North is up in all the images.

**Table 3**  
*Characteristics of Poned Material on Vesta*

Pond Id	Lat.	Long.	Floor appearance	Crater floor to wall transition	Slope of ponded material	Pond depth (km)	Distinct change in slope from floor to wall	Surface profile direction	Notes
Type 1: Smooth, featureless deposits evenly distributed at the crater floor, shallow slope within deposit material, host craters located at low elevated regions with low relief topography, shallow pond depth, formed from fluidized impact melt.									
(1)	3.77°S	228.34°E	Flat and smooth	Gradual	≤15°	0.21	no	W-E	Smooth in-flow layer distributed equipotentially at the surface, deep bowl-shaped, following crater topography (Figure 3a, bottom)
(2)	3.20°S	228.34°E	Flat and smooth	Gradual	≤15°	--	no	W-E	Partially covering crater floor in simple bowl shape crater with smooth texture (Figure 3a, top)
(3)	3.24°S	179.40°E	Flat and smooth	Sharp	≤15°	0.05	no	NW-SE	Melt material drained from north east and distributed within lower elevated regions of crater, the prominent striation flow patterns are visible in surrounding regions (Figure 3b)
(4)	0.20°S	181.80°E	Flat and smooth	Sharp	≤15°	0.10	no	W-E	Located nearby Marcia impact crater, the low-raised crater rim from north east provide channel to molten material which covers the entire crater floor (Figure 3c)
Type 2: uneven deposit surface infilled with fine grained material, variation in slope within deposit terrain, pond material is partially extended off form the crater floor and often extended up to crater walls, depth of ponded material is higher.									
(5)	10.61°S	189.2°E	Flat	Sharp	≤15°	0.31	no	NW-SE	Material at the floor is flat but the slope increases toward the crater wall
(6)	10.04°S	194.91°E	Uneven	Sharp	0°–31°	0.2	yes	N-S	Partially infilling the crater floor, spread in E-S direction
(7)	2.53°N	206.51°E	Uneven	Sharp	0°–31°	0.1	yes	N-S	Uneven distribution of pond material elevated toward the crater wall in SE direction
(8)	26.5°N	187.68°E	Uneven	Sharp	≤15°	0.22	no	N-S	Irregular pond surface partially covering floor with possible pits (Figure 4b)
(9)	16.1°S	173.30°E	Uneven	Sharp	≤15°	0.23	no	W-E	Two ponded deposits are observed; (a) at the bottom of the crater floor, (b) at the lower flank of SE crater wall (Figure 4c)
(10)	21.59°S	171.29°E	Uneven	Sharp	0°–31°	0.23	no	W-E	Oval shaped pond deposit emplaced at crater floor (Figure 4a)

or partially extending toward the walls from the floor with a gradually increasing slope and/or is unevenly distributed on the crater floor (Figures 4a–4c). These ponded features appear to not have experienced sufficient leveling mechanism to make entirely smooth surfaces, however, the features still possess the main characteristics of ponds mentioned in prior studies (Robinson et al., 2001) (such as pools of fine-grained regolith, partially extending toward crater walls with a sharp boundary with reference to Table 2) (Roberts et al., 2014; Robinson et al., 2001). In general, these ponds are identified inside relatively large craters (5.90–10.05 km) with estimated average pond depths of ~0.21 km. For this group of ponds, the feasible source of ponded material is the migration of loose surface material via seismic shaking and/or emplacement of fine regolith from the subsurface via volatile outgassing. Our identified type 2 ponds on Vesta show some resemblance to ponded craters on Eros and Itokawa (Table 2). Both type 1 and type 2 pond deposits have some different and some overlapping impressions which are summarized in Table 3.



#### 4. Comparison of Vesta Ponds With Those on Eros, Itokawa, and the Moon

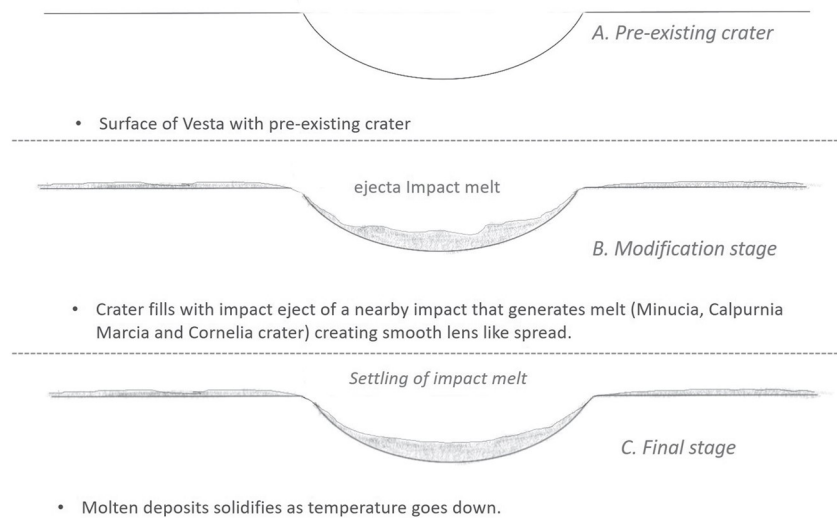
On Vesta, type 1 and type 2 ponds show various degrees of resemblance with ponded deposits on Eros, Itokawa, and the Moon (Table 2). However, ponded features on Eros and Itokawa are produced from fine dust substances whereas similar features are formed from molten and fluidized impact melt material on the surface of the Moon.

On Eros, 334 ponded deposits were identified, but due to limitations in data resolution, only a minority of them (in this Case 55) were analyzed in detail (Robinson et al., 2002). In terms of morphology, there are a few similarities between ponded features of Eros and Vesta, but differences are observed within their geometrical assessments. On Vesta, the majority of ponded craters are identified within similar latitudes as on Eros ( $0^{\circ}$ – $30^{\circ}$ S/N). According to Roberts et al. (2014) out of 55, only 12 ponds have a flat smooth surface ( $\leq 10^{\circ}$  slope) with an equipotential distribution of fine material at the crater floor (Figure 1a) and a shallow depth similar to ejecta ponds on Vesta. On Eros, there are no ejecta ponds. However, in visual interpretation, the smooth surface of dust ponds on Eros appears similar to the smooth surface of ejecta ponds on Vesta. The remaining 43 ponds are identified on steep crater walls or are partially elongated (Figures 1b and 1c), resembling dust ponds on Vesta. Nevertheless, the main difference is the size of the ponds and the potential source of ponded material. In general, the lower limit of the pond diameter is  $>30$  m and is present within craters of  $<1$  km diameter on Eros (Robinson et al., 2001). Further, the ponded deposits infill only a few meters of the original depth of the crater (Robinson et al., 2001) on Eros. Whereas on Vesta, the diameters of ponds range from 0.9 to 6.4 km within larger craters ( $\sim 2$ – $10$  km). The overall pond depth is  $\sim 0.2$  km on Vesta and covers a maximum of up to  $\sim 10\%$  of the crater depth. The smaller size of ponded craters on Eros might be due to the significant size difference and consequently gravitational force between Eros and Vesta. Moreover, the majority of the ponds are present within low gravitational regions on Eros (Robinson et al., 2001, 2002), however, Vesta's gravitational field is comparatively even.

On Itokawa, the surface also shows smooth flat pond regions and depressions. These smooth regions were described as featureless and consisted of a fine regolith layer (Fujiwara et al., 2006; Miyamoto et al., 2007; Saito et al., 2006; Yano et al., 2006). So far 28 craters (out of 38; Hirata et al., 2009) show a morphology that has similar characteristics to dust and ejecta ponds of Vesta. The typical ponded feature on Itokawa includes smooth featureless fully or partially covered crater floors with low raised, brighter rims (Saito et al., 2006) and fine infilling material ( $\sim 6$  cm particle size) (Figures 1d–1f). On Vesta similar characteristics are present within both the category of ponded deposits (such as flat smooth surface within type 1 and fine-grained infilling material within type 2). The identified pond features on Itokawa are more abundant in small craters (0.002–0.134 km in diameter) (Hirata et al., 2009). A strong correlation between color and albedo variation was observed and is possibly sensitive toward the grain sizes within regolith material (Saito et al., 2006). Other than the craters, the Sagami-hara and Muses Sea regions also show smooth featureless ponded deposits (Fujiwara et al., 2006) (Figure 1e) and occupy  $\sim 20\%$  of the total asteroid surface (Hirata et al., 2009; Yano et al., 2006). Nevertheless, unlike Vesta, Itokawa reveals no obvious evidence of type 1 ponds. The overall generation of smooth pond-like impressions involves migration of dry regolith (Fujiwara et al., 2006; Miyamoto et al., 2007; Saito et al., 2006) on Itokawa.

Characteristics of ponded materials were also identified within craters on the Moon (Hawke & Head, 1977a, 1977b; Howard & Wilshire, 1975; Plescia & Cintala, 2012). Previous studies by Howard and Wilshire (1975) reported on the presence of flat featureless ponded material within small craters (diameters of 1–5 km). Fluidized ejecta melt for the production of ejecta ponds was proposed by Hawke and Head (1977a, 1977b). They noted that craters with less than a certain diameter ( $<5$  km) do not possess ponded deposits. However, this study was conducted in relatively low-resolution data. Later on, Plescia and Cintala (2012), used the LROC data set to conduct a global survey of small craters (up to 0.12 km in diameters) and cataloged features as “melt pools.” Stopar et al. (2014) observed similar smooth deposits outside crater rims and concluded that they must be produced from the fluidized ejecta melt. The molten material exhibits flat-floors with a smooth texture, a sharp increase in slope from floor to wall, a heterogeneous distribution of boulders at the rim of the pond, and infilling of the deepest region of the crater floors with molten substances (Figures 1g–1i). We identified similar features as type 1 ponds on Vesta. Depending upon the thickness of pool deposits, boulders, and hummocky material can also be seen partially buried within the melted region on the Moon (Figures 1h and 1i). The identified host craters with ponds on the Moon have





**Figure 5.** Illustration of production of type:1 ponds via emplacement of impact melt. The ejecta ponds on Vesta can be formed via downslope movement of ejecta melt material from neighboring impact crater ejecta. The ejecta infills the lower cavity of the crater and later solidifies.

diameters from 0.12 to 30 km and pool diameters of 0.007–6 km (Plescia & Cintala, 2012). In comparison to Vesta, the impact melt on the Moon is much more prevalent due to higher impactor energies caused by higher velocities of the impactors (40 km/s), derived via theoretical models (French, 1998). So far, the literature predominantly suggests the presence of melt pools on the Moon.

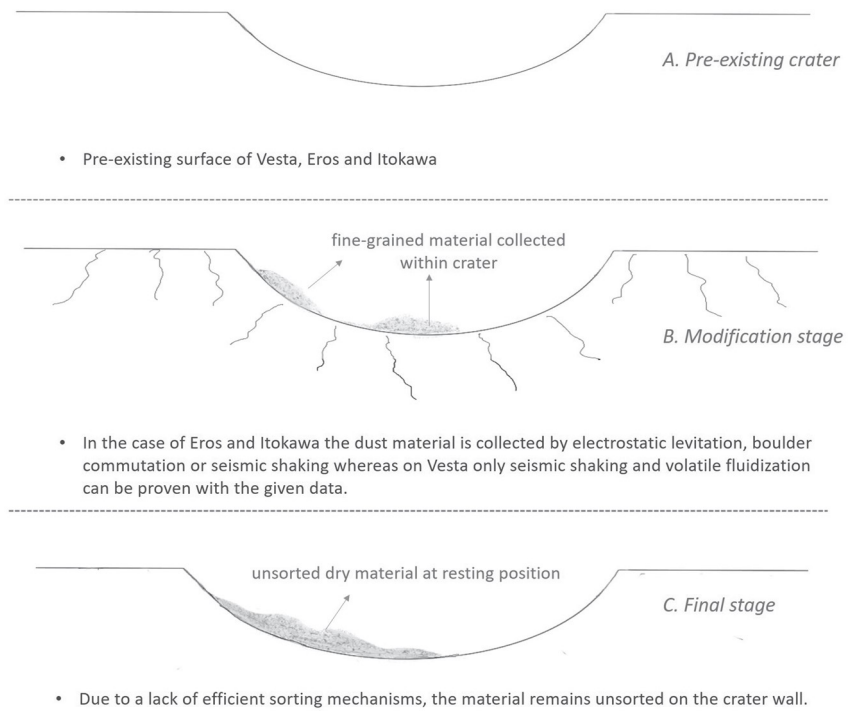
## 5. Hypothesized Processes for the Production of Type 1 and Type 2 Ponds on Vesta

Both the pond deposits on Vesta reveal partially overlapping features with the ponded morphology noted on Eros, Itokawa, and the Moon. However, their formation mechanism and material properties are different. Based on our observation and comparison with ponded characteristics on other planetary objects, we understand that both types of ponds on Vesta must have undergone different formation mechanisms.

Type 1 pond deposits show a flat smooth homogenous distribution of the flow-like impact melt material (Figures 3a and 3b) within the crater floor which is commonly identified on the surface of the Moon. The melt materials are well preserved in and around the vicinity of the impact craters. The craters hosting the ejecta ponds on Vesta are underneath the sheet of the ejecta blanket. They are typically shallow and located within relatively small craters producing a smooth lens-like surface at the bottom of the crater cavity. Similar to ejecta ponds on the Moon, craters hosting type 1 ponds on Vesta too have low raised rims (average ~0.04 km in height) and are located on the lower elevated region which provides ideal topographic conditions for the downslope movements of melts. According to the stratigraphy and age models of the Marcia crater region, the northernmost Minucia crater must be the oldest crater followed by the Calpurnia crater and Marcia (Williams, Denevi, et al., 2014). Geological and spectral evidence gathered from the Dawn data also suggests that the ejecta melt in this region is composed of the impact ejecta of Minucia, Calpurnia, and Marcia (McCord et al., 2012; Williams, Denevi, et al., 2014). Thus, based on the apparent age and the morphological evidence of melt material, we hypothesize that given the close proximity of the ponds to the region that has been identified as melt-rich, the ponds are melted from Marcia, Calpurnia, and Minucia that gathered in pre-existing craters. A similar impact melt infilling process may apply to the ponds identified on the north of Cornelia crater (Figures 2 and 3a). Additionally, the pond-hosting craters are located in lower elevated regions in comparison to Cornelia which makes a possible downslope movement of flow-like impact melt material likely. Due to the similar characteristics of the melt pools of the Moon and type 1

pond deposits on Vesta we name them as “ejecta ponds.” We illustrate the formation mechanism of ejecta ponds with a graphical sketch in Figure 5. Other than the impact melt infilling process, we also consider the near vertical high velocity impact theory proposed for melt pool formation on the Moon. However, given the location of Vesta within the asteroid belt and the comparatively low velocities within the asteroid belt, Vesta has experienced relatively slow impacts ( $\sim 8\text{--}10$  km/s) (O'Brien & Sykes, 2011; Williams, O'Brien, et al., 2014) in comparison to the lunar surface. Thus, direct melt pool formation in near-vertical high speed impacts as suggested on the Moon is unlikely for Vesta. Additionally, if this mechanism was dominant on Vesta, there should be more ponded craters present on the surface of Vesta at a global scale, but that is not the case.

Type 2 shows resemblance with dust deposits of Eros and Itokawa, however, they are often less flat and smooth. Based on the surface morphology and multi-step seismic model results, it was demonstrated that seismic reverberation on Eros and Itokawa is able to destabilize the slope, cause the regolith to move downslope and form pond deposits (Richardson et al., 2004, 2005; Veverka et al., 2001). Thus, we suspect similar processes may account for type 2 pond formation on Vesta. Due to seismic shaking the fine material may drift from parts of the rim and/or the crater wall and serve as a source for the type 2 pond deposit. Once the deposits are transported downslope, the next step is segregation of fine-grained material. However, unlike type 1 pond deposits, type 2 does not show smooth nearly flat pond deposits at the center of the crater floors. Thus, we suggest that after moving downslope, the dusty material did not undergo a sorting process to form a smooth deposit. To support this hypothesis, we compare the process of Vesta with dusty regolith bearing asteroids. On Eros too, few dust pond candidates (approximately 20%) lack the smooth morphology (Roberts et al., 2014). The absence of a smooth pond morphology is possible either due to an insufficient amplitude of seismic shaking and/or the duration of the shaking that might have lasted only to transport the dusty material downslope (Roberts et al., 2014) but not smoothen it. Thus, to understand diffusivity of the impact-induced seismic shaking, a series of numerical shake-table experiments were conducted (Richardson & Kedar, 2013; Richardson et al., 2020). According to the results, the small size impactors (diameter of 4–500 m for Eros and 0.07–0.5 m for Itokawa) are capable of producing global-scale seismic shaking which then diffuses (at the average peak rate of  $\sim 0.5 \pm 0.2$  km<sup>2</sup>/s and  $\sim 0.002 \pm 0.001$  km<sup>2</sup>/s) maximum up to the distance of 20 and 0.62 km on Eros and Itokawa, respectively. Nevertheless, the derived diffusion rate is still of inadequate amplitude to generate a flat-floored pond deposit morphology at a global scale on Eros (Roberts et al., 2014). Given the size of Minucia, Calpurnia, and Marcia craters on Vesta, rare but relatively large-scale impactors (de Elía & Di Sisto, 2011) with similar velocities are expected to generate higher seismic shaking and diffusivity locally. Post-impact seismic energy dispersion may have possibly disturbed the stable conditions and induced the downslope movements of dust. However, to achieve a smooth morphology, separation of grains via segregation would require seismic diffusion for a relatively long time. Since only 6% of the total impactor has a velocity of  $\sim 8$  km/s (Williams, O'Brien, et al., 2014), frequent repetition of high amplitude seismic dispersion is not expected on Vesta. Moreover, the global scale seismic diffusion is applicable to the asteroids with  $\leq 50$  km in diameter, on larger asteroids only local seismic shaking and diffusion are expected (Richardson et al., 2020). Thus, large impacts on the surface of Vesta are not capable of diffusing seismic energy at a global scale. From the above arguments, it is clear that smaller asteroids' surfaces (such as Eros, Itokawa) vibrate more significantly than the larger asteroids (Marchi et al., 2015; Murdoch et al., 2015; Richardson et al., 2004, 2005) for a given impactor size. Additionally, the Small Body Cratered Terrain Evolution Model (SBCTEM) also suggested that at given seismic diffusivity ( $\sim 0.5 \pm 0.2$  km<sup>2</sup>/s), a 0.04 km diameter crater experiences a gradual infilling process and requires energy diffusion for  $\sim 10$  Myr to produce smooth pond morphology on Eros (Richardson & Abramov, 2020). On Vesta, our observed host craters have significantly higher diameters (5.90–10.05 km) which will require even more time along with higher attenuation of seismic diffusivity. Considering the massive size of Vesta and large diameter of pond hosting craters, we suspect rare high-amplitude seismic diffusivity at localized scale might be adequate to transport the material downslope but not able to develop smooth, nearly flat pond deposits due to infrequent large impactors. Another potential mechanism for regolith transport on Vesta is the volatile-induced outgassing of the material from the subsurface (Sears et al., 2015). This process is expected only on planetary bodies which had volatile bearing regolith (Benoit et al., 2003). The volatile-induced fluidization process can be triggered either by the impact that produced the host crater excavating volatile-rich material which subsequently degasses and fluidizes the regolith grains (Sears et al., 2015) or by the implantation of thermal energy via impact that may



**Figure 6.** Illustration of production type 2 ponds via seismic shaking. Two possible mechanisms may be responsible for the production of dust ponds, depending upon the environment of the planetary body. Previous studies explain the involvement of all three mechanisms (electrostatic levitation, seismic shaking or boulder commutation) on the surface of Eros (Cheng et al., 2002; Robinson et al., 2001; Thomas & Robinson, 2005; Veverka et al., 2001) and Itokawa (Fujiwara et al., 2006; Saito et al., 2006). But in the case of Vesta a low degree of seismic shaking and volatile-induced outgassing (illustrated by Sears et al., 2015) is probably responsible for the mobility of fine-grained material into the crater.

release mineral-bound hydroxyl groups (and/or other volatiles). Under laboratory conditions, it has been proven that fluidization by gas flow at subsurface scale lifts the individual grains, resettles them on the surface, and produces fine-grained dust ponds on asteroids (Benoit et al., 2003; Sears et al., 2015). Based on the morphological evidence, a small amount of localized volatile presence is strongly suggested on Vesta (Denevi et al., 2012; Scully et al., 2015). However, they cannot survive for a longer time (Scully et al., 2021). Therefore, type 2 pond formation on Vesta may also be possible via one or more of the above-described mechanisms. Both cases are likely to be relatively quick and the pond material might not experience severe sorting or segregation post-accumulation. This may also lead to a not well-established equipotential alignment of dry pond material. The dry brittle regolith condition of Vesta also provides favorable conditions for electrostatic particle levitation (Lee, 1996; Roberts et al., 2014; Robinson et al., 2001; Veverka et al., 2001) and boulder disintegration (Dombard et al., 2010) which are suggested as a potential mechanism for the formation of dust ponds on Eros. Given the higher gravity, larger size (Table 1; Russell et al., 2012), and high escape velocity ( $\sim 363$  m/s; Veverka et al., 2000) of Vesta, the particle levitation and their segregation is not possible. Next, our mapped type 2 ponds do not reveal any large differences in their surface area and lack the presence of boulders within their depressions at a given resolution. Thus, the boulder disintegration mechanism may not be applied in the case of Vesta. The available data has a different spatial resolution for Vesta, Eros, and Itokawa which may have hindered the analysis and made a direct comparison difficult. It is totally possible that there are Eros and Itokawa like ponds on Vesta, but we simply do not see them. Nevertheless, we can still make a comparison to discuss the different processes. The ponded material of this particular group of craters consists of loose fragmented dust-like dry particles and are closely related to pond deposits on Eros and Itokawa, thus we name them as “dust ponds.”

Both type 1, ejecta pond and type 2, dust ponds are identified within a similar region on Vesta's surface. However, we comprehend that both of them were produced via different mechanisms. Ejecta ponds show flat-

**Table 4**  
*Summary of Possible Geological Processes Responsible for the Production of Ponds on Vesta, Eros, Itokawa, and the Moon*

Geological Process	Vesta	Eros	Itokawa	Moon
Dust pond deposit via volatile outgassing	Likely (this work, e.g. nearby pitted terrains)	Possible, hypothesized under laboratory conditions (Sears et al., 2015), but Eros is a dry S-type asteroid and so far, no direct morphological evidences for volatiles are found	Possible, but unbound volatiles are not present, as this process has been suggested to work for Eros, it should work for Itokawa too	Possible, because volatiles are present in the lunar regolith (Basilevsky et al., 2012), but not reported in literature in relation to ponds
Migration of dust via seismic shaking	Since the surface of Vesta has been heavily bombarded, seismic shaking is possible	Eros' regolith has experienced impacts, due to its small size, seismic waves may propagate through the entire body (Robinson et al., 2001;2004)	Due to seismic shaking granular material may have fallen from higher elevated regions into depressions (Fujiwara et al., 2006).	The surface of the Moon has experienced impacts which have the capacity to generate seismic waves (Plescia and Cintala, 2012)
Material segregation via seismic shaking	Unlikely due to the large size of the body, this phenomenon might not be observable due to limitation in the resolution of the data	Possible (Cheng et al., 2002; Robinson et al., 2001; 2004 ; Thomas et al., 2002; Veverka et al., 2001a)	Smooth terrains likely involve processes for grain-size sorting via seismic shaking initiated by impacts (Fujiwara et al., 2006; Saito et al., 2006)	No evidence of dust sorting mechanism noted using current data.
Material segregation via electrostatic forces	Unlikely due to large distances to be travelled and the topography that would need to be overcome electrostatic charging has not been suggested to be a dominant process either	Pond deposits follow underlying topography because of the low gravity and this mechanism is possible for ponds which are not leveled or flatten (Lee, 1996; Roberts et al., 2014; Robinson et al., 2001; Veverka et al., 2001a)	As this mechanism is possible for Eros, it should also be possible for Itokawa. The fine material may have been levitated but high escape velocity (10-20 cm/s) restrict the particle rearrangement (Miyamoto et al., 2007)	Unlikely due to the high gravitational pull and a lack of evidence for a dust cloud near the lunar surface (Horányi et al., 2015; Stopar et al., 2014; Szalay and Horányi, 2015)
Boulder disintegration	Unlikely because there are not enough large boulders to fill an entire crater pond	Thermally disaggregated boulders have been proposed (Dombard et al., 2010)	This mechanism has not been suggested, but given that it is possible on Eros, it should also be possible on Itokawa	Unlikely because there are not enough large boulders to fill an entire crater pond
Ejecta pond infilling via fluidized ejecta (melt and/or volatiles)	Likely, since impact melt has been observed near ponded craters (Williams et al., 2014b)	Unlikely because melt does not occur in impact craters	Unlikely because melt does not occur in impact craters	Likely, impact melt has been observed near ponded craters (Hawke and Head, 1977a; b; Plescia and Cintala, 2012; Stopar et al., 2014)

Note. The colors represent the likelihood with which the geologic processes occur: Green: possible, Orange: may or may not be possible, and red: highly unlikely.

tened surfaces and are evenly distributed within crater floors whereas dust ponds are unlevelled and present on steep regions of the crater hosting the pond. We interpret that ejecta ponds must have formed via infilling of ejecta from the neighboring large craters (Minucia, Calpurnia, Marcia, and Cornelia) which later solidified as part of the crater evolution process (Figure 5). Whereas for the production of the dust ponds, rare high-amplitude localized seismic diffusion and/or volatile-induced fluidization may be responsible for the transportation of granular material downslope (Figure 6). Nevertheless, given Vesta's size, the transported dust material may not have experienced enough seismic shaking allowing the grainy regolith to remain unlevelled and only partially distributed across the crater floor. As a consequence, the typical smooth surface as observed on Eros or Itokawa may not be achieved in dust ponds on Vesta. In Table 4 we have summarized all possible pond formation mechanisms discussed so far on Vesta, Eros, Itokawa, and the Moon.

## 6. Conclusion

In analogy to investigation on asteroids Eros, Itokawa, and the Moon, we have identified two types of ponded features in craters on Vesta which show some different and some overlapping geomorphologic characteristics. These ponded deposits have experienced different formation mechanisms. Type 1 are ejecta ponds which have a smooth and flat surface with a constant slope and shallow infilling deposits (average  $\sim 0.1$  km). They retain the original shape of the crater and the material is evenly distributed within the crater floor. Crater hosting ejecta ponds are possibly formed by the distribution of impact ejecta of nearby craters (Minucia, Calpurnia, Marcia and Cornelia) on Vesta. They are similar to the melt pools identified on the Moon. The pre-existing topography (e.g., low raised rims and location of host crater in low elevated regions) plays a vital role in channelizing and downslope movement of the melt material. Type 2 are dust ponds that have a few different characteristics (in comparison to type 1 ponds) such as granular pond material, pond deposits with undulating surfaces, often relatively greater depth (average  $\sim 0.2$  km), and sometimes an abrupt change in slope. The type 2 ponded material on Vesta either moved downwards from parts of crater walls via seismic shaking or may have been transferred onto the surface through volatile outgassing. In the case of seismic activity, the energy diffusion is restricted to a local scale due to the large size of Vesta. Additionally, the surface has not experienced large-scale impactors frequently. Thus, a rare high-amplitude of seismic diffusivity is not capable to conduct particle segregation and produce smooth morphology is relatively huge host craters. Similarly, the presence of volatiles on Vesta is observed at a regional scale (Denevi et al., 2012; Scully et al., 2015) but they might have survived for a shorter time (Scully et al., 2021). Therefore, we interpret that type 2 pond material was transported downslope via seismic diffusivity and/or volatile outgassing. However, the transported material might not experience severe sorting or segregation post-accumulation due to rare high amplitude seismic diffusivity and a short span of volatile activity, thus failing to produce the smooth featureless ponded surfaces as observed on Eros and Itokawa.

## Data Availability Statement

Raw images used in this work for Eros (Robinson & Carcich, 2001), Itokawa (Stooke, 2015), and calibrated data from Dawn at Vesta (Nathues et al., 2011) are available at Small Bodies Node of Planetary Data System (PDS). Additionally, we also utilized the pond catalogue of Eros (Roberts, 2021) available at PDS. Derived data products are available via Figshare: Parekh, R. (2021): Formation of ejecta and dust pond deposits on asteroid Vesta (<https://doi.org/10.6084/m9.figshare.16863478.v2>).

## References

- Basilevsky, A., Abdrakhimov, A., & Dorofeeva, V. (2012). Water and other volatiles on the Moon: A review. *Solar System Research*, 46, 89–107. <https://doi.org/10.1134/S0038094612010017>
- Bell, J. F., Izenberg, N. I., Lucey, P. G., Clark, B. E., Peterson, C., Gaffey, M. J., et al. (2002). Near-IR reflectance spectroscopy of 433 Eros from the NIS instrument on the NEAR mission: I. Low phase angle observations. *Icarus*, 155(1), 119–144. <https://doi.org/10.1006/icar.2001.6752>
- Benoit, P., Hagedorn, N., Kracher, A., Sears, D. W. G., & White, J. (2003). *Grain size and density separation on asteroids: Composition of seismic shaking*. LPSC XXXIV.
- Cheng, A. F., Izenberg, N., Chapman, C. R., & Zuber, M. T. (2002). Ponded deposits on asteroid 433 Eros. *Meteoritics and Planetary Science*, 37, 1095–1105. <https://doi.org/10.1111/j.1945-5100.2002.tb00880.x>
- Cintala, M. J., & Grieve, R. A. F. (1998). Scaling impact-melt and crater dimensions: Implications for the lunar cratering record. *Meteoritics & Planetary Science*, 33, 889–912. <https://doi.org/10.1111/j.1945-5100.1998.tb01695.x>

### Acknowledgments

The authors acknowledge the Dawn team for providing data and support. This work is part of the research project "The Physics of Volatile Related Morphologies on Asteroids and Comets". RP and KO would like to gratefully acknowledge the financial support and endorsement from the German Academic Exchange Service (under DLR-DAAD PhD Fellowship) and the DLR Management Board Young Research Group Leader Program by the Executive Board Member for Space Research and Technology. A portion of the work was carried out at the Jet Propulsion Laboratory under contract with NASA. Open access funding enabled and organized by Projekt DEAL.



- de Elía, G., & Di Sisto, R. (2011). Impactor flux and cratering on Ceres and Vesta: Implications for early solar system. *Astronomy & Astrophysics*, 534, A129. <https://doi.org/10.1051/0004-6361/201117543>
- Denevi, B. W., Blewett, D. T., Buczkowski, D. L., Capaccioni, F., Capria, M. T., De Sanctis, M. C., et al. (2012). Pitted terrain on Vesta and implications for the presence of volatiles. *Science*, 338, 246–249. <https://doi.org/10.1126/science.1225374>
- Dombar, A. J., Barnouin, O. S., Prockter, L. M., & Thomas, P. C. (2010). Boulders and ponds on the Asteroid 433 Eros. *Icarus*, 210, 713–721. <https://doi.org/10.1016/j.icarus.2010.07.006>
- French, B. M. (1998). *Traces of catastrophe: A handbook of shock-metamorphic effects in terrestrial meteorite impact structures*. LPI Contribution No. 954 (p. 120). Lunar and Planetary Institute. Retrieved from <https://www.lpi.usra.edu/publications/books/CB-954/CB-954.pdf>
- Fujiwara, A., Kawaguchi, J., Yeomans, D. K., Abe, M., Mukai, T., Okada, T., et al. (2006). The rubble-pile asteroid Itokawa as observed by Hayabusa. *Science*, 312, 1330–1334. <https://doi.org/10.1126/science.1125841>
- Grossman, J. N., Alexander, C. M. O. D., Wang, J., & Brearley, A. J. (2000). Bleached chondrules: Evidence for widespread aqueous processes on the parent asteroids of ordinary chondrites. *Meteoritics and Planetary Science*, 35, 467–486. <https://doi.org/10.1111/j.1945-5100.2000.tb01429.x>
- Hawke, B. R., & Head, J. W. (1977a). Impact melt in lunar crater interiors. In *Presented at the Proceedings of the Lunar and Planetary Science Conference* (p. 415). Retrieved from <http://articles.adsabs.harvard.edu/pdf/1977LPI....8..415H>
- Hawke, B. R., & Head, J. W. (1977b). *Impact melt on lunar crater rims* (p. 815). Pergamon Press, Inc. Retrieved from <http://adsabs.harvard.edu/full/1977iecp.symp..815H>
- Hawke, B. R., & Head, J. W. (1979). *Impact melt volumes associated with lunar craters* (p. 510). Retrieved from <https://ui.adsabs.harvard.edu/abs/1979LPI....10>
- Heldmann, J. L., Conley, C. A., Brown, A. J., Fletcher, L., Bishop, J. L., & McKay, C. P. (2010). Possible liquid water origin for Atacama Desert mudflow and recent gully deposits on Mars. *Icarus*, 206(2), 685–690. <https://doi.org/10.1016/j.icarus.2009.09.013>
- Hirata, N., Barnouin-Jha, O. S., Honda, C., Nakamura, R., Miyamoto, H., Sasaki, S., et al. (2009). A survey of possible impact structures on 25143 Itokawa. *Icarus*, 200, 486–502. <https://doi.org/10.1016/j.icarus.2008.10.027>
- Horányi, M., Szalay, J. R., Kempf, S., Schmidt, J., Grün, E., Srama, R., & Sternovsky, Z. (2015). A permanent, asymmetric dust cloud around the Moon. *Nature*, 522, 324–326. <https://doi.org/10.1038/nature14479>
- Howard, K. A., & Wilshire, H. G. (1975). Flows of impact melt at lunar craters. *Journal of Research of the U. S. Geological Survey*, 3, 237. Retrieved from <https://pubs.usgs.gov/journal/1975/vol3issue2/report.pdf>
- Hutchison, R., Alexander, C. M. O., & Barber, D. J. (1987). The Semarkona meteorite: First recorded occurrence of smectite in an ordinary chondrite, and its implications. *Geochimica et Cosmochimica Acta*, 51(7), 1875–1882. [https://doi.org/10.1016/0016-7037\(87\)90178-5](https://doi.org/10.1016/0016-7037(87)90178-5)
- Jaumann, R., Williams, D. A., Buczkowski, D. L., Yingst, R. A., Preusker, F., Hiesinger, H., et al. (2012). Vesta's shape and morphology. *Science*, 336, 687–690. <https://doi.org/10.1126/science.1219122>
- Jin, Z., & Bose, M. (2019). New clues to ancient water on Itokawa. *Science Advances*, 5, 8106. <https://doi.org/10.1126/sciadv.aav8106>
- Lee, P. (1996). Dust levitation on asteroids. *Icarus*, 124, 181–194. <https://doi.org/10.1006/icar.1996.0197>
- Marchi, S., Chapman, C. R., Barnouin, O. S., Richardson, J. E., & Vincent, J. B. (2015). Cratering on asteroids. In P. Michel, F. E. DeMeo, & W. F. Bottke (Eds.), *Asteroids IV* (pp. 725–744). University of Arizona Press. [https://doi.org/10.2458/azu\\_uapress\\_9780816532131-ch037](https://doi.org/10.2458/azu_uapress_9780816532131-ch037)
- McCord, T. B., Li, J.-Y., Combe, J.-P., McSween, H. Y., Jaumann, R., Reddy, V., et al. (2012). Dark material on Vesta from the infall of carbonaceous volatile-rich material. *Nature*, 491, 83–86. <https://doi.org/10.1038/nature11561>
- Miyamoto, H. (2014). Unconsolidated boulders on the surface of Itokawa. *Planetary and Space Science*, 95, 94–102. <https://doi.org/10.1016/j.pss.2013.06.016>
- Miyamoto, H., Yano, H., Scheeres, D. J., Abe, S., Barnouin-Jha, O., Cheng, A. F., et al. (2007). Regolith migration and sorting on asteroid Itokawa. *Science*, 316, 1011–1014. <https://doi.org/10.1126/science.1134390>
- Murdoch, N., Sanchez, P., Schwartz, S., & Miyamoto, H. (2015). Asteroid surface geophysics. In *Asteroids IV* (pp. 767–792). [https://doi.org/10.2458/azu\\_uapress\\_9780816532131-ch039](https://doi.org/10.2458/azu_uapress_9780816532131-ch039)
- Nathues, A., Sierks, H., Gutierrez-Marques, P., Schroeder, S., Maue, T., Buettner, I., et al. (2011). *DAWN FC2 CALIBRATED VESTA IMAGES V1.0, DAWN-A-FC2-3-RDR-VESTA-IMAGES-V1.0, NASA planetary data System*. Retrieved from <https://sbn.psi.edu/pds/resource/dawn/dwnvfcL1.html>
- O'Brien, D. P., & Sykes, M. V. (2011). The origin and evolution of the asteroid belt—Implications for Vesta and Ceres. *Space Science Reviews*, 163, 41–61. <https://doi.org/10.1007/s11214-011-9808-6>
- Pierazzo, E., & Melosh, H. J. (2000). Melt production in oblique impacts. *Icarus*, 145, 252–261. <https://doi.org/10.1006/icar.1999.6332>
- Plescia, J. B., & Cintala, M. J. (2012). Impact melt in small lunar highland craters. *Journal of Geophysical Research*, 117. <https://doi.org/10.1029/2011JE003941>
- Preusker, F., Scholten, F., Matz, K.-D., Roatsch, T., Jaumann, R., Raymond, C. A., & Russell, C. T. (2012). *Topography of Vesta from Dawn FC stereo images* (pp. EPSC2012–EPSC2428). Retrieved from <http://meetingorganizer.copernicus.org/EPSC2012/EPSC2012-428-1.pdf>
- Richardson, J., Steckloff, J., & Minton, D. (2020). Impact-produced seismic shaking and regolith growth on asteroids 433 Eros, 2867 Šteins, and 25143 Itokawa. *Icarus*, 347, 113811. <https://doi.org/10.1016/j.icarus.2020.113811>
- Richardson, J. E., & Abramov, O. (2020). Modeling the formation of the lunar upper megaregolith layer. *The Planetary Science Journal*, 1(1), 2–19. <https://doi.org/10.3847/psj/ab7235>
- Richardson, J. E., & Kedar, S. (2013). An experimental investigation of the seismic signal produced by hypervelocity impacts. *Lunar and Planetary Science Conference*, 44, 2863.
- Richardson, J. E., Melosh, H. J., & Greenberg, R. (2004). Impact-induced seismic activity on asteroid 433 Eros: A surface modification process. *Science*, 306, 1526–1529. <https://doi.org/10.1126/science.1104731>
- Richardson, J. E., Melosh, H. J., Greenberg, R. J., & O'Brien, D. P. (2005). The global effects of impact-induced seismic activity on fractured asteroid surface morphology. *Icarus*, 179(2), 325–349. <https://doi.org/10.1016/j.icarus.2005.07.005>
- Roatsch, T., Kersten, E., Matz, K.-D., Preusker, F., Scholten, F., Elgner, S., et al. (2013). High-resolution vesta low altitude mapping orbit atlas derived from dawn framing camera images. *Planetary and Space Science*, 85, 293–298. <https://doi.org/10.1016/j.pss.2013.06.024>
- Roberts, J. (2021). *Roberts Eros Ponds Catalog V1.1*. urn:nasa:pds:ast-eros.roberts.ponds-catalog::1.1. NASA Planetary Data System. <https://doi.org/10.26033/4dq-8067>
- Roberts, J. H., Kahn, E. G., Barnouin, O. S., Ernst, C. M., Prockter, L. M., & Gaskell, R. W. (2014). Origin and flatness of ponds on asteroid 433 Eros. *Meteoritics and Planetary Science*, 49, 1735–1748. <https://doi.org/10.1111/maps.12348>
- Robinson, M., & Carcich, B. T. (2001). *NEAR MSI DIM EROS GLOBAL BASEMAPS V1.0, NEAR-A-MSI-5-DIM-EROS/ORBIT-V1.0, NASA Planetary Data System*. Retrieved from [https://arcnav.psi.edu/urn:nasa:pds:context:target:asteroid.433\\_eros/data](https://arcnav.psi.edu/urn:nasa:pds:context:target:asteroid.433_eros/data)

- Robinson, M. S., Thomas, P. C., Veverka, J., Murchie, S., & Carcich, B. (2001). The nature of ponded deposits on Eros. *Nature*, *413*, 396–400. <https://doi.org/10.1038/35096518>
- Robinson, M. S., Thomas, P. C., Veverka, J., Murchie, S. L., & Wilcox, B. B. (2002). The geology of 433 Eros. *Meteoritics & Planetary Sciences*, *37*, 1651–1684. <https://doi.org/10.1111/j.1945-5100.2002.tb01157.x>
- Russell, C. T., Raymond, C. A., Coradini, A., McSween, H. Y., Zuber, M. T., Nathues, A., et al. (2012). Dawn at Vesta: Testing the protoplanetary paradigm. *Science*, *336*, 684–686. <https://doi.org/10.1126/science.1219381>
- Saito, J., Miyamoto, H., Nakamura, R., Ishiguro, M., Michikami, T., Nakamura, A. M., et al. (2006). Detailed images of asteroid 25143 Itokawa from Hayabusa. *Science*, *312*, 1341–1344. <https://doi.org/10.1126/science.1125722>
- Savage, R., Palafox, L., Morris, C. T., Rodriguez, J. J., Barnard, K., Byrne, S., & Hamilton, C. (2018). A Bayesian approach to subkilometer crater shape analysis using individual HiRISE images. *IEEE Transactions on Geoscience*, *56*, 1–5812. <https://doi.org/10.1109/tgrs.2018.2825608>
- Schenk, P., Castillo-Rogez, J., Otto, K. A., O'Brien, D., Bland, M., Hughson, K., et al. (2021). Compositional control on impact crater formation on mid-sized planetary bodies: Dawn at Ceres and Vesta, Cassini at Saturn. *Icarus*, *359*, 114343. <https://doi.org/10.1016/j.icarus.2021.114343>
- Scully, J. E. C., Poston, M., Carey, E., Baker, S., Castillo-Rogez, J., & Raymond, C. (2021). *Testing the hypothesis that curvilinear gullies, lobate deposits and pitted terrain on Vesta and Ceres were formed by short-lived, debris-flow-like processes. LPSC 2021* (p. 2548). Retrieved from <https://www.hou.usra.edu/meetings/lpsc2021/pdf/1252.pdf>
- Scully, J. E. C., Russell, C. T., Yin, A., Jaumann, R., Carey, E., Castillo-Rogez, J., et al. (2015). Geomorphological evidence for transient water flow on Vesta. *Earth and Planetary Science Letters*, *411*, 151–163. <https://doi.org/10.1016/j.epsl.2014.12.004>
- Sears, D. W. G., Tornabene, L. L., Osinski, G. R., Hughes, S. S., & Heldmann, J. L. (2015). Formation of the "ponds" on asteroid (433) Eros by fluidization. *Planetary and Space Science*, *117*, 106–118. <https://doi.org/10.1016/j.pss.2015.05.011>
- Sierks, H., Keller, H. U., Jaumann, R., Michalik, H., Behnke, T., Bubenhausen, F., et al. (2011). The dawn framing camera. *Space Science Reviews*, *163*, 263–327. <https://doi.org/10.1007/s11214-011-9745-4>
- Stooke, P. (2015). *Stooke small bodies maps V3.0. MULTI-SA-MULTI-6-STOOKEMAPS-V3.0. NASA Planetary Data System*. Retrieved from <https://sbn.psi.edu/pds/resource/stookemaps.html>
- Stopar, J., Hawke, B., Robinson, M., Denevi, B., & Giguere, T. (2012). Distribution, occurrence, and degradation of impact melt associated with small lunar craters. *Lunar and Planetary Science Conference*, 1645. Retrieved from <https://www.lpi.usra.edu/meetings/lpsc2012/pdf/1645.pdf>
- Stopar, J. D., Hawke, B. R., Robinson, M. S., Denevi, B. W., Giguere, T. A., & Koeber, S. D. (2014). Occurrence and mechanisms of impact melt emplacement at small lunar craters. *Icarus*, *243*, 337–357. <https://doi.org/10.1016/j.icarus.2014.08.011>
- Szalay, J. R., & Horányi, M. (2015). The search for electrostatically lofted grains above the Moon with the Lunar Dust Experiment. *Journal of Geophysical Research Letters*, *42*, 5141–5146. <https://doi.org/10.1002/2015gl064324>
- Thomas, P. C., Prockter, L., Robinson, M., Joseph, J., & Veverka, J. (2002). Global structure of asteroid 433 Eros. *Journal of Geophysical Research Letters*, *29*, 1408–1411. <https://doi.org/10.1029/2001gl014599>
- Thomas, P. C., & Robinson, M. S. (2005). Seismic resurfacing by a single impact on the asteroid 433 Eros. *Nature*, *436*, 366–369. <https://doi.org/10.1038/nature03855>
- Veverka, J., Robinson, M., Thomas, P., Murchie, S., Bell, J. F., Izenberg, N., et al. (2000). NEAR at Eros: Imaging and spectral results. *Science*, *289*, 2088–2097. <https://doi.org/10.1126/science.289.5487.2088>
- Veverka, J., Thomas, P. C., Robinson, M., Murchie, S., Chapman, C., Bell, M., et al. (2001). Imaging of small-scale features on 433 Eros from NEAR: Evidence for a complex regolith. *Science*, *292*, 484–488. <https://doi.org/10.1126/science.1058651>
- Williams, D. A., Denevi, B. W., Mittlefehldt, D. W., Mest, S. C., Schenk, P. M., Yingst, R. A., et al. (2014). The geology of the Marcia quadrangle of asteroid Vesta: Assessing the effects of large, young craters. *Icarus*, *244*, 74–88. <https://doi.org/10.1016/j.icarus.2014.01.033>
- Williams, D. A., O'Brien, D. P., Schenk, P. M., Denevi, B. W., Carsenty, U., Marchi, S., et al. (2014). Lobate and flow-like features on asteroid Vesta. *Planetary and Space Science*, *103*, 24–35. <https://doi.org/10.1016/j.pss.2013.06.017>
- Yano, H., Kubota, T., Miyamoto, H., Okada, T., Scheeres, D., Takagi, Y., et al. (2006). Touchdown of the Hayabusa spacecraft at the muses sea on Itokawa. *Science*, *312*, 1350–1353. <https://doi.org/10.1126/science.1126164>

## 2.2 Volatile Morphologies Examined Using Laboratory Experiments

The following three publications were written by D. Haack and focus on the evolution of morphologic features formed of volatile-rich comet analogues under sublimation conditions in the laboratory. The laboratory work has been performed by D. Haack within the CoPhyLab framework (Kreuzig et al., 2021) at the University of Braunschweig. Prior to the implementation of this work, I had developed the idea as part of the junior research group.

The articles are based on each other with Haack et al. (2020) focussing on the determination of an adequate cometary regolith analogue and its tensile strength. Haack et al. (2021a) then investigates the morphologic evolution when placing such analogue materials under sublimation conditions in the laboratory. Finally, Haack et al. (2021b) investigates the effect that organic materials, common on comets, have on the experiments.

Haack et al. (2020) introduce the laboratory setup and analogue materials used in the subsequent publications. Next to a chemical description of the analogue materials including angular silica, spherical fly ash and spherical water ice particles, the article also shows size frequency distributions. Two component mixtures of these materials were shaped into 2.5 cm sized cylinders to perform Brazilian disk tests. This test allows the calculation of the tensile strength of a material by measuring the maximum force exerted through a piston onto the disk at the point of breaking. By combining two different analogue materials at a time in various mixing ratios, the research finds that the tensile strength is dominated by the component with the higher tensile strength. It increases with decreasing particle size, increasing temperature and increasing angularity.

Haack et al. (2021a) subsequently used the dust-ice mixtures characterized in Haack et al. (2020) and created 2.5 cm wide cylinders. These cylinders were placed in a cooled vacuum chamber and irradiated with a solar simulator to simulate an active cometary environment. After discussing the spatial scaling of such laboratory experiments to real comets (e.g. the lower gravitational acceleration on the comet is compensated by a higher energy input and smaller particle sizes in the laboratory), the article describes the evolution of the cliff-like morphology in the laboratory. The research shows that the morphologic evolution is dependent on the dust to ice mixing ratio and the insolation direction. While large abundances of ice in the analogue material (66 vol%) result in exotic morphologies and constant alterations, lower ice abundances (20-25 vol%) yield episodic morphologic changes. Continuous outgassing and morphologic changes were

## 2 Synergy of Conducted Research

observed for medium amounts of ice (33-50 vol%) in the analogue material. Collapses of walls were only observed when the insolation was directed vertically onto the sample.

Haack et al. (2021b) repeated the setup from Haack et al. (2021a) but added organic materials including glycerine and sodium acetate in their analogue materials. Such materials, which can be found on comets, have an adhesive effect that can influence the morphologic evolution when volatiles are sublimating. The experiments show that fractures form on the sample surface as a result of volatile sublimation, but collapses and particle ejections as observed in Haack et al. (2021a) could not be recorded. This indicates that the presence of organics on comets may have an effect on the morphologic evolution of their surfaces.

The three articles focussing on laboratory work can be cited as:

- Haack, D., Otto, K. A., Gundlach, B., Kreuzig, C., Bischoff, D., Kührt, E., & Blum, J. (2020). Tensile Strength of Dust-ice Mixtures and their Relevance as Cometary Analog Material. *Astronomy & Astrophysics*, *642*, A218. <https://doi.org/10.1051/0004-6361/202037763>.
- Haack, D., Lethuillier, A., Kreuzig, C., Feller, C., Gundlach, B., Pommerol, A., Blum, J., & Otto, K. A. (2021a). Sublimation of Ice-dust Mixtures in Cooled Vacuum Environments to Reproduce Cometary Morphologies. *Astronomy & Astrophysics*, *649*, A35. <https://doi.org/10.1051/0004-6361/202140435>.
- Haack, D., Kreuzig, C., Gundlach, B., Blum, J., & Otto, K. A. (2021b). Sublimation of Organic-rich Comet Analog Materials and their Relevance in Fracture Formation. *Astronomy & Astrophysics*, *653*, A153. <https://doi.org/10.1051/0004-6361/202142069>.

**2.2.1 Haack et al. (2020)**

Haack, D., Otto, K. A., Gundlach, B., Kreuzig, C., Bischoff, D.,  
Kührt, E., & Blum, J. (2020). Tensile Strength of Dust-ice Mixtures  
and their Relevance as Cometary Analog Material. *Astronomy &  
Astrophysics*, 642, A218.  
<https://doi.org/10.1051/0004-6361/202037763>.

The laboratory work comprised in this article has been conducted by D. Haack. I provided the initial idea to this project and together with E. Kührt established the collaboration with the CoPhyLab network. B. Gundlach, C. Kreuzig, D. Bischoff and J. Blum are collaborators at the University of Braunschweig who provided the equipment and trained D. Haack to use the facilities. I helped choosing the ice-dust mixing ratios and interpreting and illustrating the data. I provided feedback on the suitability of fly ash as cometary analogue material and produced data for Figure 2. All authors assisted with the data interpretation and with refining the manuscript.



# Tensile strength of dust-ice mixtures and their relevance as cometary analog material

David Haack<sup>1</sup>, Katharina Otto<sup>1</sup>, Bastian Gundlach<sup>2</sup>, Christopher Kreuzig<sup>2</sup>, Dorothea Bischoff<sup>2</sup>, Ekkehard Kührt<sup>1</sup>, and Jürgen Blum<sup>2</sup>

<sup>1</sup> Institut für Planetenforschung, Deutsches Zentrum für Luft- und Raumfahrt (DLR), Berlin, Germany  
e-mail: David.Haack@dlr.de

<sup>2</sup> Institut für Geophysik und Extraterrestrische Physik, Technische Universität Braunschweig, Braunschweig, Germany

Received 18 February 2020 / Accepted 2 September 2020

## ABSTRACT

**Aims.** The tensile strength of granular matter is of great importance to our understanding of the evolution of comets and to our attempts to reproduce processes on cometary surfaces in laboratory experiments. In this work, we investigate the tensile strength of three different materials and their mixtures, which can be used as cometary analog materials in the laboratory.

**Methods.** We used two types of siliceous dusts and granular water ice whose polydisperse particles were either angular or spherical. Our samples were cooled to below 150 K to better simulate the conditions of a cometary surface and to avoid thermal alteration of the material. We used the Brazilian disk test method to exert stress on the cooled samples and determine the tensile strength at the moment the samples broke.

**Results.** We find that the tensile strength of two component mixtures is strongly dominated by the component with the higher tensile strength. The materials made of mostly angular dust particles have a lower filling fraction, but a higher tensile strength compared to materials made of spherical particles. Furthermore, the tensile strength of the cooled components is substantially lower than the tensile strength of the same components at room temperature. This implies that the surface energy of the investigated materials at low temperatures is significantly lower than previously assumed.

**Key words.** comets: general – methods: laboratory: solid state – planets and satellites: formation

## 1. Introduction

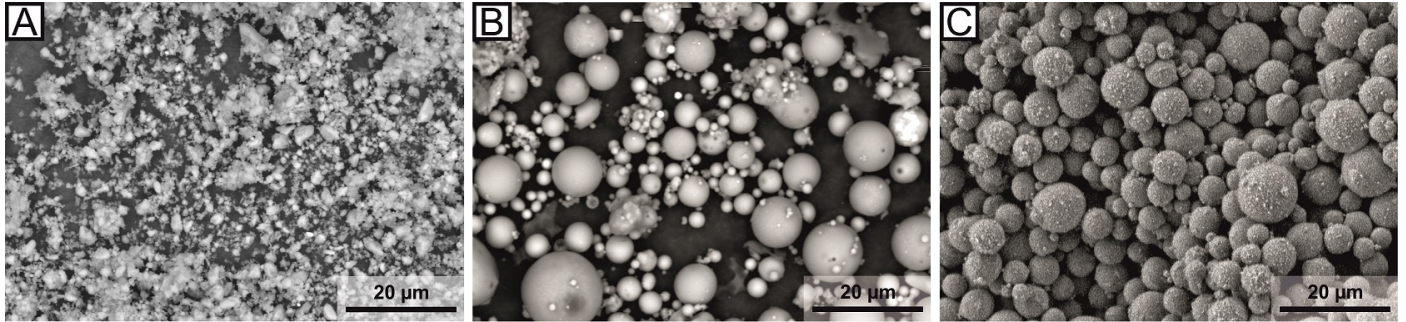
Despite visits of recent space missions to comets (e.g., ESA's Rosetta mission and NASA's Deep Impact mission), the activity of comets is not yet well understood. Direct observations and laboratory experiments on Earth have shown that cometary surfaces are very active when approaching the Sun. Near-surface volatiles enter the gas phase through sublimation and drag non-volatile particles with them (Kührt & Keller 1994; Gundlach et al. 2015; Keller et al. 2017). Through this process a comet loses material during each orbit until it finally extinguishes. In the 1990s sublimation experiments with dust-ice mixtures were performed as part of the KOSI (KOMetenSIMulation) project to simulate and understand these cometary surface processes (e.g., Grün et al. 1989, 1993; Lämmerzahl et al. 1995). However, these experiments are not suitable and were not designed to understand complex morphologies such as cliffs, cracks, or mass movements that have only later been observed on 67P/Churyumov-Gerasimenko (Thomas et al. 2015; Pajola et al. 2016; El-Maarry et al. 2019). The composition and grain size of the material, interparticle forces, and porosity are of fundamental importance in processes that form these morphologies. These parameters find their macroscopic expression in the tensile strength of the comet-forming materials and determine whether cliffs, cracks, or boulders can form on the surface of a comet (El-Maarry et al. 2015; Groussin et al. 2015; Vincent et al. 2016).

In this work we examined the suitability of different components and their mixtures as cometary analogs with respect to their tensile strength. According to the Johnson-Kendall-Roberts

(JKR) theory from Johnson et al. (1971) the tensile strength is linearly dependent on the surface energy of a material. This approach is suitable to calculate the surface energy of granular materials made of spheres and to compare liquid nitrogen cooled samples and uncooled samples of previous works (Kimura et al. 2015). The tensile strength of granular matter is also dependent on the number of mutual contacts of individual particles. This number transfers into the macroscopic value of the filling fraction and describes how much free space is in a volume filled with particles.

To realize the analyses, the Brazilian disk test is an established method to measure the tensile strength of a material (Meisner et al. 2012; Li & Wong 2013). In this test, pressure is applied to cylindrical samples until they break. The pressure exerted in the moment of the breakup refers to the tensile strength and can be analyzed. So far, using the Brazilian disk test method, the tensile strength has only been measured for the pure components from which a comet could be formed, for example, water ice, or dust with a tensile strength of a few kilopascals (Gundlach et al. 2018a; Steinpilz et al. 2019) or granular organic materials (Bischoff et al. 2020). In this study, we present Brazilian disk test measurements of mixtures of different components that could be considered as cometary analog materials and show their dependence on particle shape, tensile strength, filling fraction, and surface energy. With the data obtained from these measurements, numerical models simulating granular matter on comets (Kappel et al. 2020) can be improved or calibrated.

A major challenge to design Earth-based experiments and to find suitable analog materials is to overcome Earth's gravity that



**Fig. 1.** Images of particles used in this work taken with an electron microscope. *Panel A:* angular silica particles, *panel B:* spherical fly ash particles, and *panel C:* spherical water ice particles at the same scale are shown.

usually is orders of magnitude larger than comets. On a comet gravity plays a minor role in solidity, which is dominated by the cohesion of its components (Scheeres et al. 2010; Skorov & Blum 2012; Sánchez & Scheeres 2014). In order to achieve a regime dominated by cohesion in the laboratory, the used particles have to be very small. When the particle radius is less than  $50\ \mu\text{m}$ , the amount of mutual particle contacts in a given volume produces cohesive forces that exceed gravity (Bischoff et al. 2019). Thus, to produce cometary analog materials whose mechanical properties are dominated by cohesion, particle sizes in the laboratory must be on the order of a few microns. We selected the three materials water ice, silica, and fly ash with particle sizes in this range, but different particle shapes, and we analyzed their influence on filling fraction, tensile strength, and surface energy of a sample.

In recent years, experiments with vacuum sublimation chambers were used to simulate space conditions to investigate the evolving surfaces of dust-volatile mixtures (Poch et al. 2016a,b; Kaufmann & Hagermann 2018). As part of the Cometary Physics Laboratory (CoPhyLab) project, we aim to support these and similar experiments by studying various siliceous dust and water ice mixtures not only for their tensile strength but also their suitability as cometary analog materials. In addition to the influence of different materials and low temperatures, we investigate how spherical and angular grain shapes affects the tensile strength. The results contribute to a better understanding of the formation of the observed morphologies on a surface of the comet.

Motivated to find suitable cometary analog materials, we describe sample preparation and experimental setup in Sect. 2 and present the determined filling fractions, tensile strengths, and surface energies in Sect. 3. These results are discussed in Sect. 4 and finally summarized in Sect. 5.

## 2. Methods

### 2.1. Sample preparation

We conducted three series of experiments with samples that were composed of two of three materials in varying mixing ratios. The first mixture comprised water ice spherules and angular silica (icy spherical-angular mixture), the second comprised water ice spherules and fly ash (icy spherical-spherical mixture), and the third mixture included fly ash and silica (dry spherical-angular mixture). We used these mixtures to test the dependence of the tensile strength on the ice content of the mixture and the shape of the involved particles. We picked these three materials to simulate the different components of a comet. Silica or fly ash represent the siliceous dust content of a comet and the water ice represents its volatile component. Furthermore, with angular

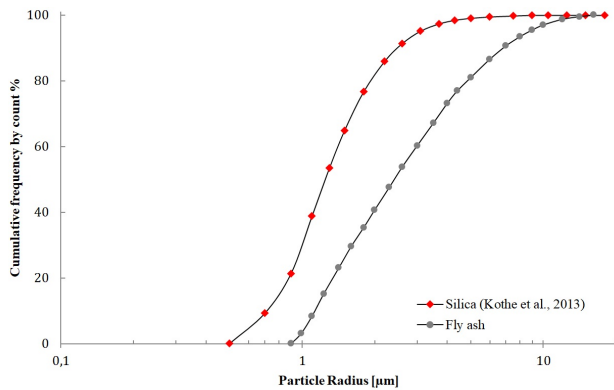
**Table 1.** Characteristics and chemical composition of individual components mixed to simulate cometary materials.

	Silica	Fly ash	Water ice
Particle shape	Angular	Spherical	Spherical
Particle radius [ $\mu\text{m}$ ]	1.3 <sup>(*)</sup>	$2.43 \pm 1.41$	$2.38 \pm 1.11$
Density [ $\text{g cm}^{-3}$ ]	2.65	1.91	0.93
Compd %			
SiO <sub>2</sub>	100.00	59.20	
Al <sub>2</sub> O <sub>3</sub>		27.90	
FeO		3.86	
CaO		3.62	
K <sub>2</sub> O		2.67	
MgO		1.51	
TiO <sub>2</sub>		1.40	
Na <sub>2</sub> O		0.68	
H <sub>2</sub> O			100.00

**Notes.** <sup>(\*)</sup>Specifications for silica given by the manufacturer: 99% of particles have radii between  $0.5\ \mu\text{m}$  and  $10\ \mu\text{m}$  and 80% of particles between  $1\ \mu\text{m}$  and  $5\ \mu\text{m}$ . This size distribution was analyzed and fitted by a log-normal distribution by Kothe et al. (2013).

silica and spherical fly ash we were able to study the influence of different particle shapes on the tensile strength. All three components (silica, fly ash, and water ice) had a comparable average grain size (Fig. 1, Table 1). Notably, the grain size distribution of fly ash is wider than that of silica (Fig. 2).

In order to investigate the tensile strength of ice-dust mixtures, we used silica and fly ash as the dusty component of a cometary regolith and combined these in two-component mixtures with water ice. The first dusty component was silica with polydisperse particles of highly angular shape and with the physical and chemical properties shown in Table 1. The second dusty component was fly ash with polydisperse particles of approximately spherical shape. This material is a mixture of mostly SiO<sub>2</sub> and Al<sub>2</sub>O<sub>3</sub> (Table 1). To constrain the particle size distribution, the fly ash was sieved to a maximum particle diameter of  $25\ \mu\text{m}$ . Another advantage of fly ash is that it is inexpensive and available in large quantities. It must be noted that fly ash may contain minor amounts of magnetic components. These magnetic particles are not spherical and, at more than  $25\ \mu\text{m}$ , much larger than the majority of the fly ash particles. Before our experiments



**Fig. 2.** Cumulative size distributions of dust particles. Irregularly shaped silica particles are indicated as red diamonds and spherical fly ash particles as gray dots. The grain size distribution of fly ash is wider than that of silica.

started, these components were largely removed by sieving and remained in negligible quantities in the samples. Electron microscopic comparisons of non-sieved and sieved fly ash confirmed the removal of these particles. Furthermore, the samples were not exposed to strong electromagnetic fields during the experiment, which could have an influence on the fracture behavior of the samples. Therefore, we neglected potential magnetic behavior of these particles in our analysis. The volatile component was water ice with particles of spherical shape. To produce the water ice particles, mist from a water droplet dispenser was sprayed into a Dewar vessel filled with liquid nitrogen (Gundlach et al. 2018a). The water droplets instantaneously froze and sank to the bottom of the liquid. The result was a suspension of polydisperse spherical ice particles in liquid nitrogen.

To determine the amount of water ice in the Dewar vessel we used Archimedes' principle. We measured the weight of a certain volume of pure liquid nitrogen and the weight of the same volume of liquid nitrogen with suspended water ice. The weight difference between both measurements and the known density of liquid nitrogen and water ice allowed us to calculate the mass of water ice in the Dewar vessel. The amount of the used dust was directly measured with a scale.

The usage of liquid nitrogen as a coolant also simulated the required temperature conditions of a comet (Kührt 1984) and prevented sintering of the ice particles (Kuroiwa 1961; Thomas et al. 1994; Gundlach et al. 2018b) in the samples and the experimental setup. Otherwise, sintered ice particles would result in unrealistically high values for the tensile strength.

To produce the icy spherical-angular and the icy spherical-spherical mixtures predefined amounts of either silica or fly ash were added into the Dewar vessel filled with liquid nitrogen and the known amount of water ice spherules. To get the exact mixing ratios, the amounts of used silica and fly ash were measured with a scale. The two types of particles and the liquid nitrogen were mixed manually with a ladle until all particles were in suspension. We then immediately removed material with the ladle from the Dewar vessel and filled it into the cylindrical steel mold while the particles were still in suspension. Given the difficulties in preparation and the fragility of the material involved this is the currently best method to mix the particles sufficiently well. The dry spherical-angular mixture was also prepared in liquid nitrogen to maintain consistency during sample preparation and the experiment.

The mixtures of particles and liquid nitrogen were then filled into a precooled steel mold with an inner diameter of 26 mm.

After the evaporation of the liquid nitrogen, cylindrical samples were pressed by manually pushing a stamp down onto the material. To maintain consistency, a lid was placed over the stamp and the experimenter pressed onto the lid with his full body weight for 5 s. Given that the weight of the experimenter was constant over the experiment series time frame, this method allowed for a reliable and reproducible implementation of 1.2 MPa to the cylindrical sample. However, to reflect variations in weight due to clothing and other natural fluctuations, we assumed an error of 0.05 MPa. At the end of the preparation process, and while still inside the mold, the length and mass of each sample were determined to calculate the filling fraction. The cylindrical samples were subsequently used to measure the tensile strength of the mixtures with the Brazilian disk test (details next section).

## 2.2. Brazilian disk test

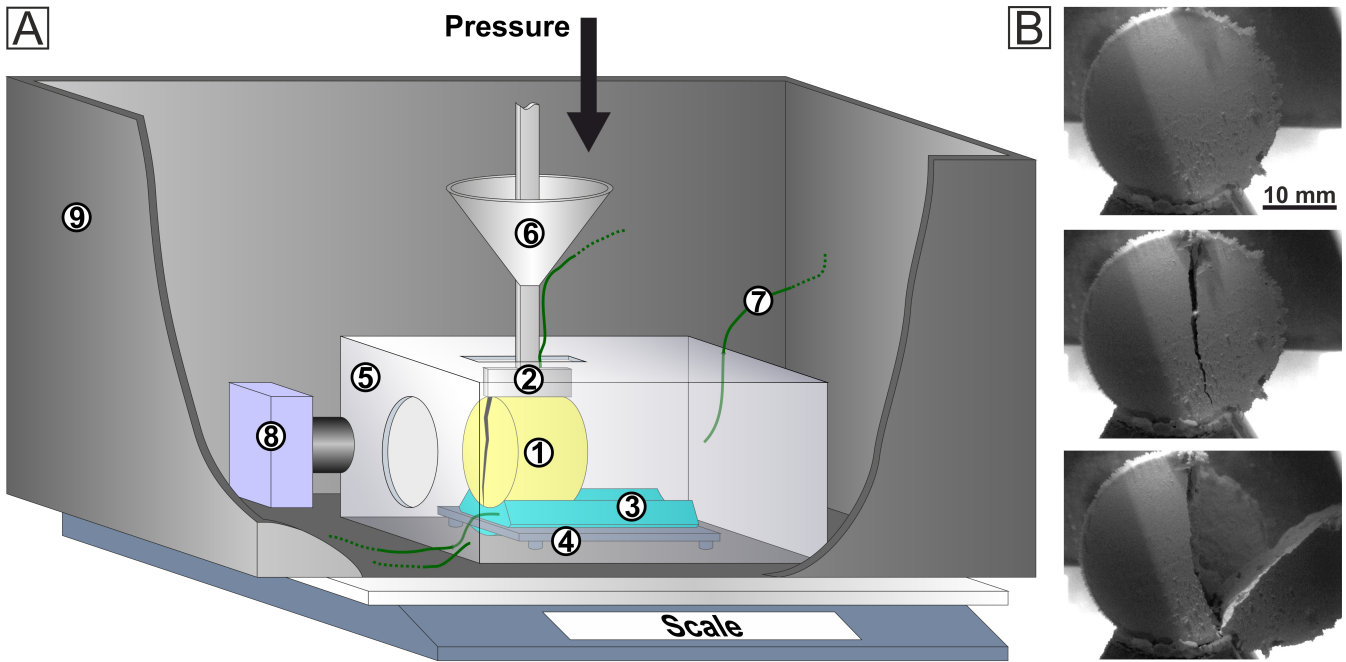
Initially, the atmosphere in a precooled polystyrene box was replaced by the evaporation of liquid nitrogen to provide minimal air humidity during the measurement. The samples produced in Sect. 2.1 were horizontally placed in this polystyrene box while still in the cylindrical pressing mold. Then the detachable pressing mold was removed so that the now free sample rested on a sample holder inside the polystyrene box (Fig. 3A). A metal box (cooling shield) was placed around the sample on its holder to keep it at constantly low temperatures. To ensure this, the sample holder and cooling shield were stored in liquid nitrogen and placed inside the polystyrene box directly before the measurement. Thermocouple sensors monitored the temperatures of the sample holder, cooling shield, and atmosphere inside the cooling shield and ensured constant low temperatures of less than 150 K. This temperature is necessary to prevent sintering of the water ice particles before and during the measurement (Kuroiwa 1961; Gundlach et al. 2018a,b). The cooling shield also reduced the formation of frost on the sample surface from atmospheric moisture that could penetrate the box during the measurement. A camera was installed in front of the sample to record the experimental process.

Through a narrow slit in the cooling shield, an actively cooled piston (1 × 30 mm) was used to apply pressure on the full length of the cylindrical surface of the horizontal sample (Fig. 3A). The pressure was continuously increased by lowering the piston with a motor that descends at a constant speed of 0.05 mm s<sup>-1</sup>. The polystyrene box with the entire precooled experimental setup inside was placed on a scale to record the weight and thus the exerted force. The increasing force transforms into a stress on the sample. The stress at which the sample broke longitudinally in two similar sized half-cylinders was determined (Figs. 3B and 4) and reflects the tensile strength  $\sigma$  of the sample material by

$$\sigma = \frac{2F}{\pi DL}. \quad (1)$$

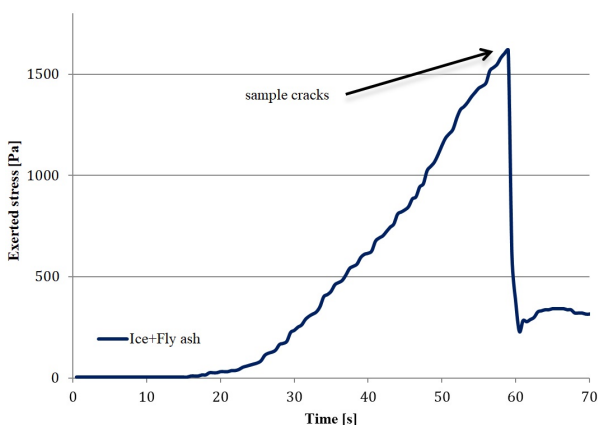
In this equation,  $F$  is the force applied to the cylindrical sample in the moment of breakup,  $D$  is the sample diameter of 26 mm, and  $L$  the length of the sample, which slightly varied for each sample with an average of 25 mm. Simultaneously, images of the samples and evolving cracks were taken with the camera (Fig. 3B) for visual reference of the quality of each individual experiment. As a consequence of the low strength of the involved materials and the challenges arising when handling equipment cooled with liquid nitrogen, this method is very delicate and requires practice; therefore not every experiment resulted in a





- 1) Sample
- 2) Piston
- 3) Section of pressing mold
- 4) Sample holder
- 5) Metal cooling shield
- 6) Reservoir with liquid nitrogen to cool the piston
- 7) Temperature sensors (piston, sample holder, cooling shield, atmosphere inside cooling shield)
- 8) Camera
- 9) Polystyrene box

**Fig. 3.** (A) Schematic and not to scale diagram of the Brazilian disk test. The sample (yellow) rests on a section of the mold in a sample holder and is surrounded by a metal cooling shield. These parts were kept in liquid nitrogen until the moment of measurement. A narrow piston descends onto the sample and generates a crack when the force is sufficient. The corresponding mass to the force is measured by a scale. (B) An image series to illustrate the sample size and the crack evolution in a sample.



**Fig. 4.** Example of a typical pressure curve for a water ice-fly ash mixture in the volume ratio 1:1. The descent of the piston increases the stress on the sample and weight on the scale. The tensile strength is the maximum stress reached at the moment when the sample breaks.

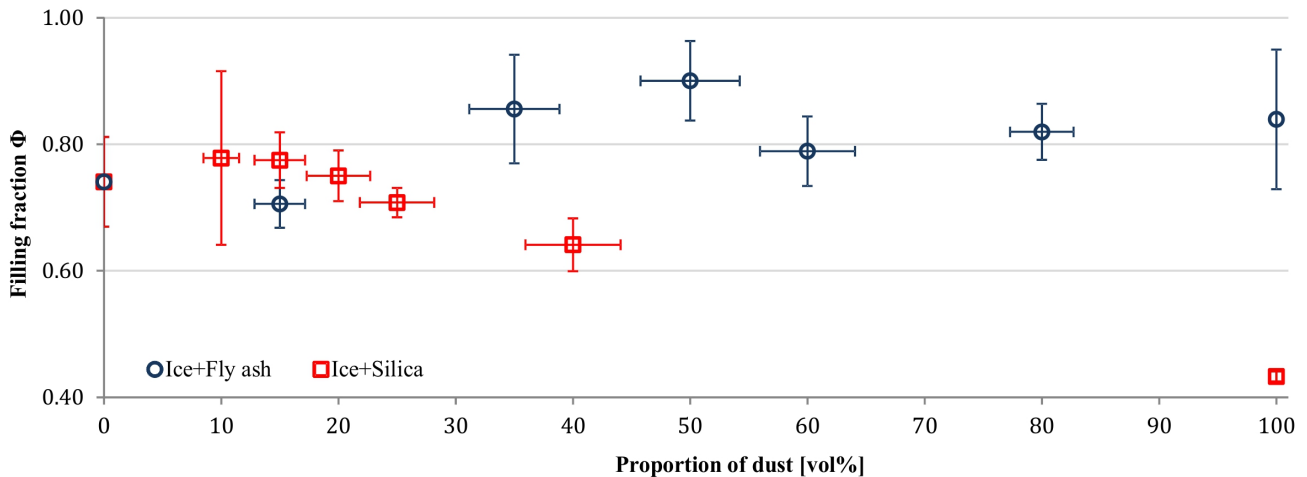
satisfying measurement. Only samples that showed a clear and central break along their longitudinal axis were used for the analyses (Fig. 3).

### 3. Results

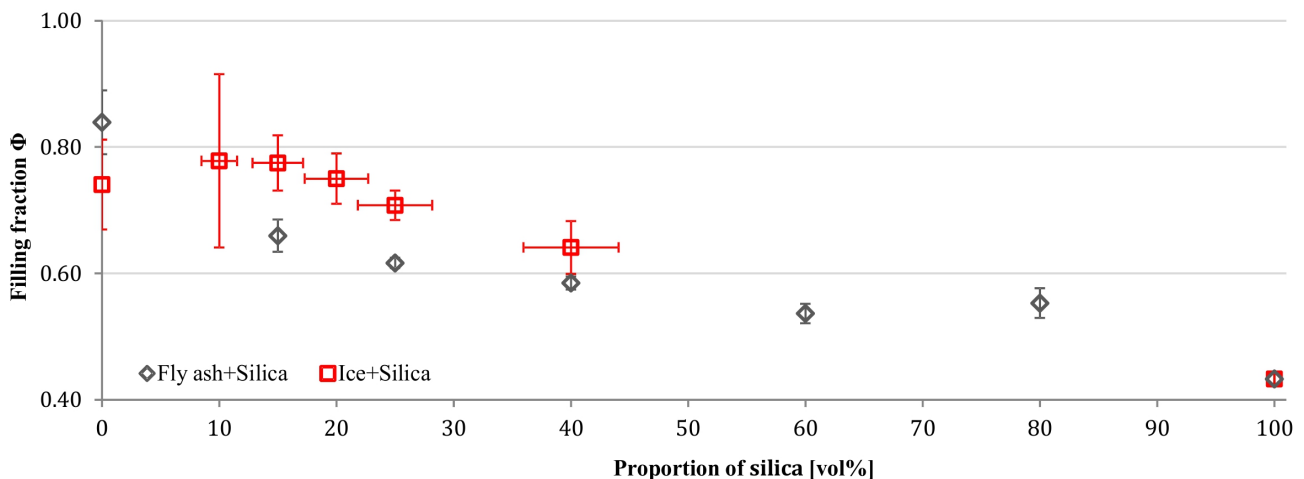
#### 3.1. Filling fraction

The mass and volume of the samples were measured to determine the bulk density of the samples before applying the above-described Brazilian disk test on the samples. With the known densities of the dust and ice particles, the filling fraction  $\Phi$  of the samples was calculated by dividing bulk density by particle densities. We determined the average filling fraction of the individual components (water ice, silica, and fly ash) and of their two-component mixtures in various ratios.

Samples made of pure spherical water ice particles had an average filling fraction of  $\Phi = 0.74$ , which means that 74% of the space is filled with ice particles (Fig. 5). For different icy spherical-spherical mixtures (water ice and fly ash) the average filling fraction varied as the proportion of fly ash was increased, but a clear trend could not be observed (Sect. 4.1). The average filling fraction for pure fly ash was  $\Phi = 0.84$ . For different icy spherical-angular mixtures (water ice and silica) the filling fraction decreased significantly when the proportion of silica exceeded 25 vol%. With higher silica content the pore space between the particles increased up to a filling fraction of  $\Phi = 0.43$  for pure silica dust (Sect. 4.1).



**Fig. 5.** Filling fractions of different ice-dust mixtures with varying amounts of ice. The value for pure ice is shown at 0 vol% on the left and for pure dust at 100 vol% on the right. The error of the ice-dust mixing ratio stems from the uncertainty of the ice mass determination. Spherical water ice particles mixed with spherical fly ash particles are shown as blue circles and mixtures containing angular silica particles as red squares. The number of investigated proportions is different for the two types of mixtures.



**Fig. 6.** Filling fractions of angular silica particles mixed with varying amounts of spherical ice particles (red squares) and spherical fly ash particles (gray diamonds). The values for pure spherical particles are shown at 0 vol% on the left and for pure angular silica particles at 100 vol% on the right. The number of investigated proportions is different for the two types of mixtures.

To investigate the influence of particle shape on the filling fraction, we prepared dry spherical-angular mixtures including silica and fly ash without any ice. In this case the filling fraction dropped monotonously from the value of pure fly ash to the value of pure silica (Fig. 6).

### 3.2. Tensile strength

For each cylindrical sample used in the Brazilian disk test, we recorded the load exerted by the slowly sinking piston onto the disk. The measured weight rose as the piston contacted the sample and dropped abruptly at the moment the samples cracked (Fig. 4). Equation (1) was used to calculate the tensile strength from the measured maximum force at the moment of breakup (Figs. 3 and 4). For each mixing ratio of ice and dust approximately nine individual measurements were analyzed and averaged. First, the tensile strength of pure ice samples was determined to be  $\sigma = 1800$  Pa (Fig. 7). The addition of only 10 vol% angular silica to the ice resulted in an increase of the tensile strength to  $\sigma = 5400$  Pa. With a further increase of the

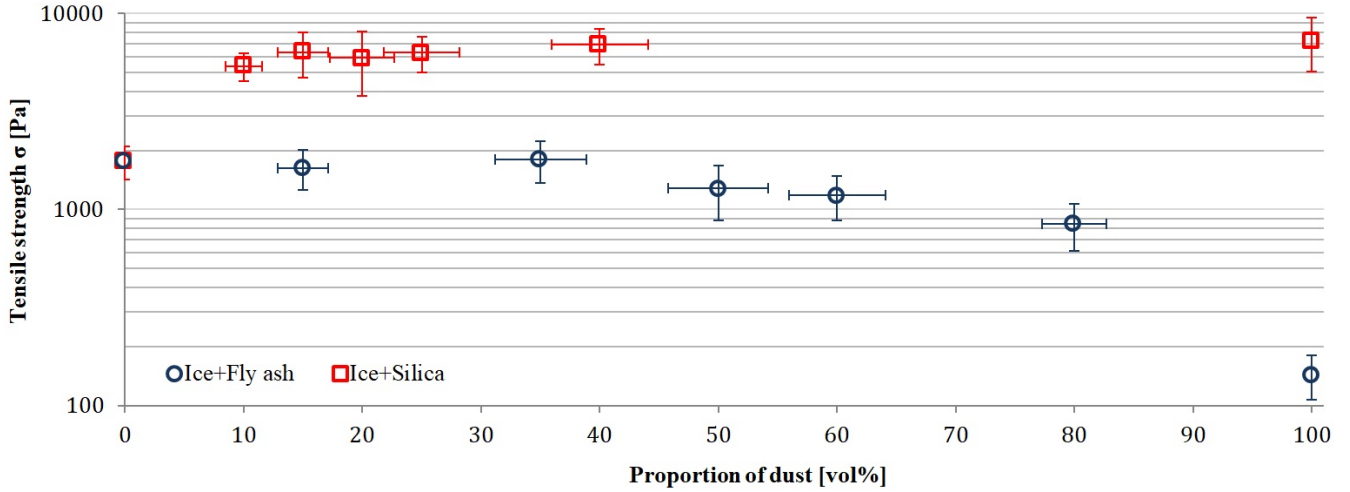
angular silica content the tensile strength increased slowly to  $\sigma = 7300$  Pa, which is the value of pure angular silica.

The same procedure was repeated for ice-fly ash mixtures. With increasing proportions of spherical fly ash the tensile strength of the samples decreased slightly. At a fly ash content of more than 80 vol% the tensile strength started to decrease significantly and reached its minimum at  $\sigma = 140$  Pa for pure spherical fly ash.

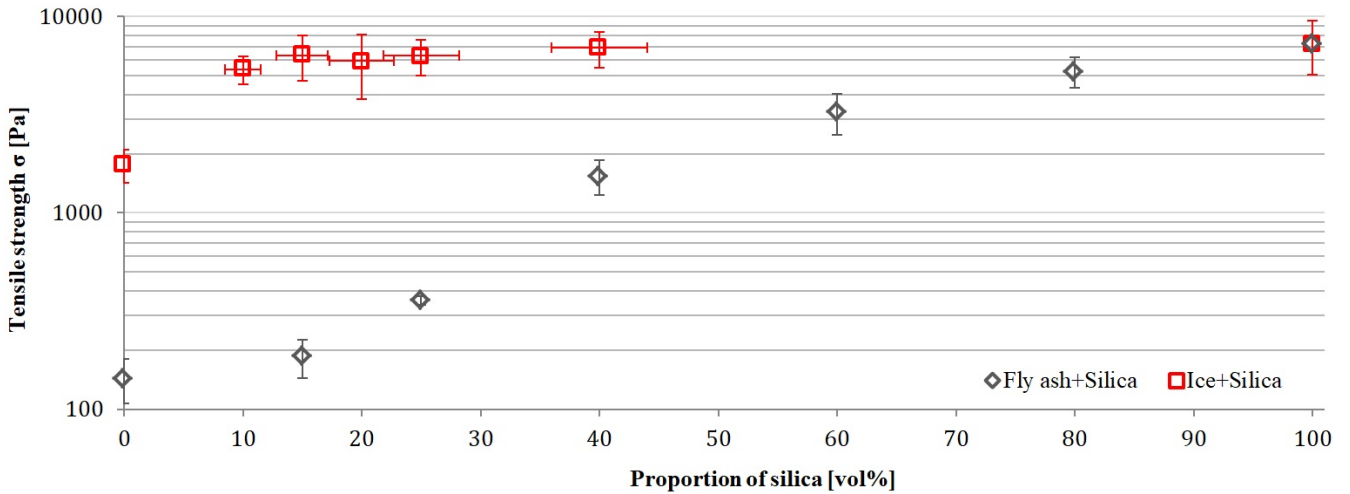
A comparison of pure components with their mixtures shows that the tensile strength of mixtures is dominated by the component with the higher tensile strength. The tensile strength of the whole mixture starts to decrease when the proportion of the component with the lower tensile strength exceeds 80–85 vol%. Then, the tensile strength of the mixture decreases to the value of the component with the lower tensile strength.

To analyze the influence of the particle shape on the tensile strength, we conducted Brazilian disk tests with dry mixtures of angular silica and spherical fly ash. In contrast to samples with water ice, the tensile strength of dry samples increases steadily toward the value of pure silica with increasing amounts





**Fig. 7.** Tensile strength  $\sigma$  of different ice-dust mixtures. The value for pure ice is shown at 0 vol% on the left and for pure dust at 100 vol% on the right. Mixtures of spherical water ice particles and spherical fly ash particles are represented as blue circles and mixtures containing angular silica particles as red squares. The number of investigated proportions is different for the two types of mixtures.



**Fig. 8.** Tensile strength  $\sigma$  of spherical particles mixed with angular particles. The tensile strength values for pure spherical particles are shown at 0 vol% on the left and for pure angular silica particles at 100 vol% on the right. The number of investigated proportions is different for the two types of mixtures.

of angular particles (Fig. 8). The angular silica component in the dry spherical-angular mixture has a less dominant effect on the tensile strength compared to the icy spherical-angular mixture. The tensile strength of the dry mixture increases consistently above 25 vol% silica in the mixture. This increase spans over wider range of mixing ratios compared to the icy silica mixture for which the tensile strength increases abruptly at 10% silica content.

### 3.3. Surface energy

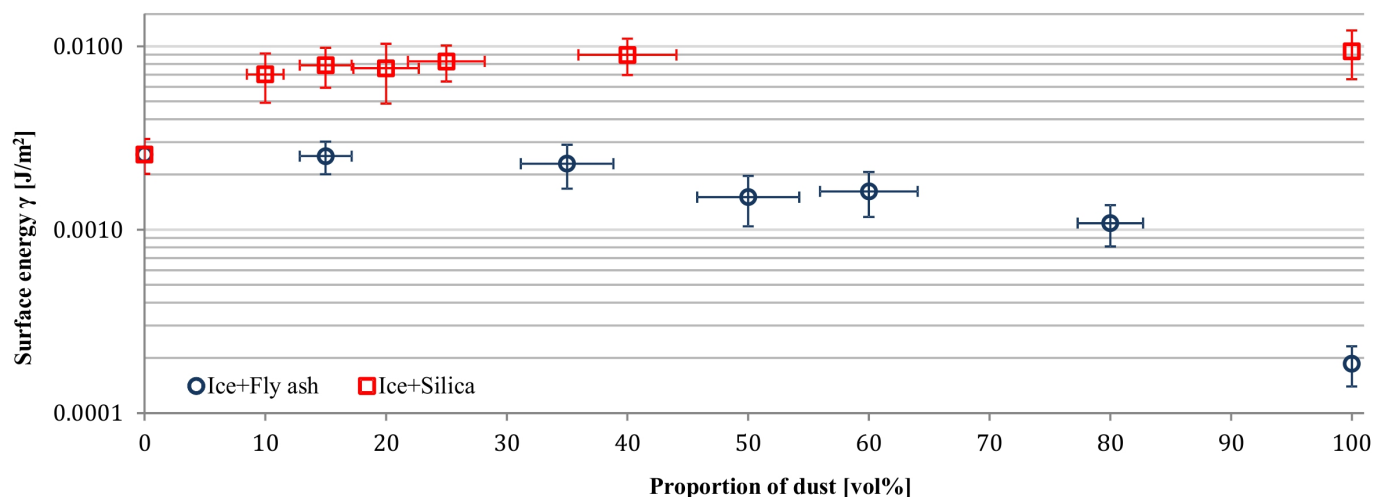
Assuming that during the Brazilian disk test in the moment of crack formation all cohesive bonds between the particles break simultaneously, the upper limit of the tensile strength  $\sigma$  can be calculated with the formula of Blum et al. (2006) as follows:

$$\sigma = \frac{3N_C\Phi\gamma}{8r}. \quad (2)$$

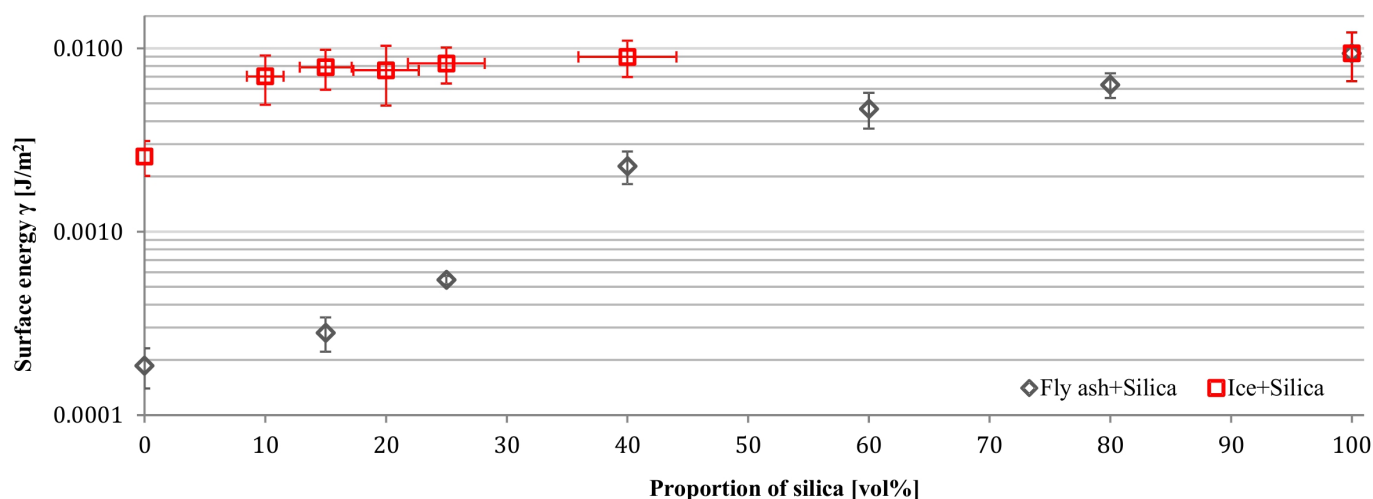
This equation is derived from the JKR theory (Johnson et al. 1971) and used to calculate the specific surface energy  $\gamma$  of the

sample material. The quantity  $\Phi$  is the filling fraction (Sect. 3.1) and  $r$  is the particle radius. We used the average particle radius as our mixtures were polydisperse. The coordination number  $N_C$  is the average number of contacts per particle. Following Murphy (1982), Yang et al. (2000), and Gundlach et al. (2018a), a value between 5 and 7 is reasonable and thus we adopted the value of 6 in this equation. Accordingly, the endmembers of 1 and 12 contacts per particle would result in a sixth and twice the tensile strength value, respectively. The exact coordination number is of minor importance in this equation, since a variation between 5 and 7 has little influence on the calculated trend of the surface energy.

For samples composed of pure water ice and temperatures below 150 K the surface energy was calculated to be  $\gamma = 0.0026 \text{ J m}^{-2}$ . In the icy spherical-spherical mixture including fly ash and water ice, the surface energy does not change considerably with increasing proportions of fly ash at low fly ash proportions. When the proportion of fly ash exceeds 80 vol%,  $\gamma$  decreases and reached very low values of  $\gamma = 0.00019 \text{ J m}^{-2}$  for pure fly ash (Fig. 9).



**Fig. 9.** Surface energy  $\gamma$  of different ice-dust mixtures. The value for pure ice is shown at 0 vol% on the left and for pure dust at 100 vol% on the right. Mixtures of water ice particles and spherical fly ash particles are indicated as blue circles and mixtures containing angular silica particles as red squares. The number of investigated proportions is different for the two types of mixtures.



**Fig. 10.** Surface energy  $\gamma$  of different spherical particles mixed with angular particles. The values for pure spherical particles (fly ash indicated as gray diamonds and water ice indicated red squares) are shown at 0 vol% on the left and for pure angular silica particles at 100 vol% on the right. The number of investigated proportions is different for the two types of mixtures.

When angular silica is added to the water ice the surface energy increases rapidly to the value of pure angular silica. The calculated surface energy of pure angular silica is  $\gamma = 0.0094 \text{ J m}^{-2}$  and thus higher compared to water ice and fly ash in particular (Figs. 9 and 10). Because of the direct dependence on the tensile strength, the trend of the surface energy at varying mixing ratios is very similar.

## 4. Discussion

### 4.1. Filling fraction

As observed in experiments by Omura & Nakamura (2017), our samples of primary angular particles trend toward having a lower filling fraction compared to those of spherical particles (Figs. 5 and 6). Rogers & Head (1961) found that the more irregular polydisperse particles are, the lower the filling fraction of a sample. Since the silica used consists of the most irregular grains of the three compounds (Table 1), the lower filling fraction of

silica-rich samples can be explained. This may be caused by increased interparticle friction between angular particles. The angular shape of silica particles may cause restricted rotation and translation against each other. In contrast, the spherical fly ash particles are more mobile than silica particles and can roll into voids upon exerted pressure (Heim et al. 1999; Schellart 2000). As the proportion of angular silica particles in the mixtures exceeds 20 vol%, more of these particles contact each other and interlock without rearranging. Consequently, the space between particles is less effectively filled and the filling fraction decreases. In contrast to angular-spherical mixtures the filling fraction of spherical-spherical mixtures remained rather stable for all mixing ratios. The filling fraction varied around 0.8 with a deviation of 0.07 in all analyzed spherical-spherical mixing ratios (Fig. 5). In these samples, the size and shape of the two particle types were very similar and so were the filling fractions of their mixtures. Therefore, the arrangement of the particles was similar in all samples. The variations of the filling fraction of the spherical-spherical samples may be the result of the sample preparation procedure. Despite all the care taken, it cannot

be ruled out for all series of measurements that minor variations occurred in the pressure applied to press the disk. This uncertainty was reduced by standardizing the sample preparation and by repeating the measurement many times. However, since the pressing of the disk was done manually, some variations are unavoidable.

#### 4.2. Tensile strength

The tensile strength of samples mixed of two different components does not change linearly with the proportions of the components. The component with the higher tensile strength dominated the tensile strength of the whole sample until its proportion was significantly lower than that of the material with lower tensile strength. In our icy spherical-angular experimental series the silica ( $\sigma = 7300$  Pa) had a higher tensile strength compared to water ice ( $\sigma = 1800$  Pa). In this series the angular silica particles determined the tensile strength of the sample when its content exceeded 15 vol% mixed with spherical water ice particles (Fig. 7). On the other hand, in the icy spherical-spherical series, the tensile strength of water ice was higher than that of fly ash. In this case, water ice dominated the tensile strength of the sample until its proportion decreased below 20 vol%. We explain this threshold of about 15–20 vol% that too few particles with high surface energy are present and do not connect to each other directly. Starting from a pure ice sample, a critical number of dust particles is required to cause a significant change in tensile strength. This number depends on the coordination number and the particle shape. Powell (1979) has shown that this value is 18 vol% for monodisperse spheres in random packing, which is in good agreement with our measurements. This observation is described by the percolation theory and the minimum of particles that must be added to achieve an effect is called critical volume fraction. When the concentration of high surface energy particles is above this critical volume fraction, these particles dominate the cohesion of the whole mixture and the surface energy on the microscopic scale translates into a high tensile strength on the macroscopic scale. If the concentration of particles with high surface energy is lower, the cohesion quickly decreases to the value of the component with the lower surface energy.

The tensile strength of samples containing angular silica particles is significantly higher compared to those samples that mainly consist of spherical particles. In Sect. 4.1 we described that an increasing content of angular particles corresponds to a decreased filling fraction of a sample. A lower filling fraction results in a lower number of mutual particle contacts and should lead to lower cohesive forces (Blum et al. 2006). However, this effect could be superimposed by the smaller size of silica particles, which are only about half as large as fly ash and ice particles (Fig. 2; Table 1). Despite the lower filling fraction, there are more silica particles per sample volume and thus more particle-particle bonds. This would increase the tensile stress of a sample (Sánchez & Scheeres 2014). Additionally, interlocking and higher friction due to increased tensile or shear forces between angular particles (Schellart 2000) may increase the tensile strength of silica-rich samples. Therefore, both the particle size and shape may be attributed to the higher tensile strength of materials rich in angular silica particles. With our experimental setup we can determine the sum of these effects. However, it is not suitable for the quantitative determination of these individual effects. This is not necessary either because we want to find out which easy to obtain material is better suited to produce comet analog material with the lowest possible tensile strength.

#### 4.3. Surface energy

In the past, multiple laboratory experiments with different approaches and environmental conditions have been performed to determine the surface energy of silica (Kimura et al. 2015). It has been shown that the surface energy of silica at elevated temperatures (e.g., Fournel et al. 2012; Li 2013) tends to be about one order of magnitude higher than at room temperature (e.g., Heim et al. 1999; Leroch & Wendland 2012). Our results show that this trend continues for low temperatures. Below 150 K our silica-rich samples show a surface energy of  $\gamma = 0.0094$  J m<sup>-2</sup> that is almost one order of magnitude lower compared to values at room temperature (e.g., Kimura et al. 2015). However, our found surface energy is probably too high as a result of friction between the angular particles that may interlock. The particles can only be separated by the effort of an additional force that could be interpreted as increased geometric cohesion.

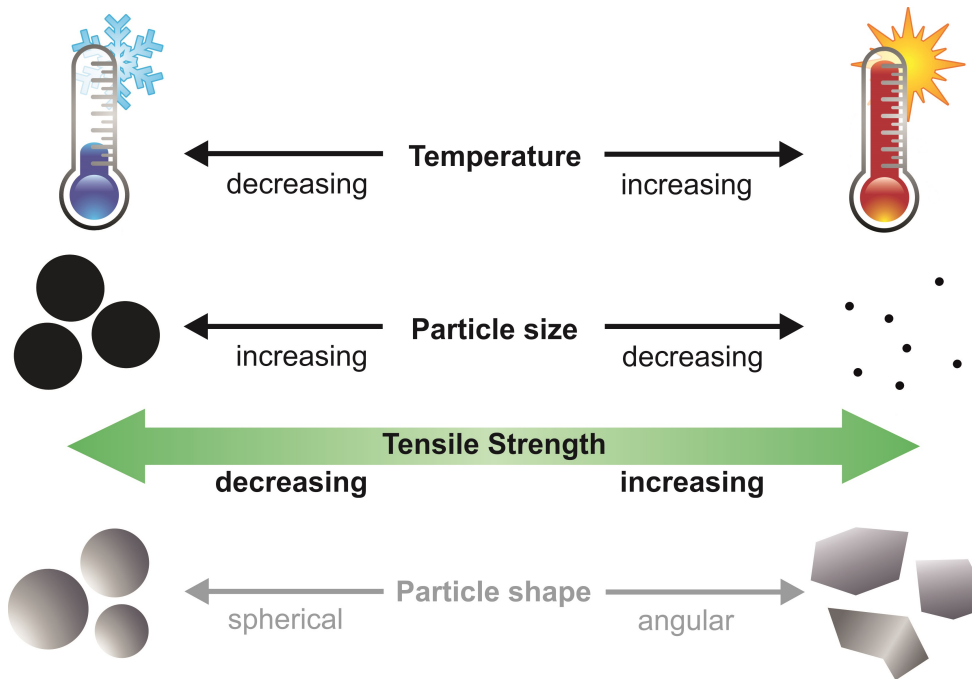
The fly ash, on the other hand, which consists of about 60% SiO<sub>2</sub>, has a surface energy of  $\gamma = 0.00019$  J m<sup>-2</sup> at 150 K. This value for the surface energy of cooled spherical fly ash is about two orders of magnitude lower than in experiments performed with uncooled samples of pure silica (Kimura et al. 2015; Gundlach et al. 2018a). It is unlikely that same types of intermolecular forces lead to strongly different surface energies of silica and fly ash, since their chemical composition is about 60% identical (Table 1). This would be further indication that the determined surface energy of angular silica is too high.

The surface energy of water ice follows the same decreasing trend. It drops significantly from  $\gamma = 0.065$  J m<sup>-2</sup> for samples below freezing point (Ketcham & Hobbs 1969) to  $\gamma = 0.0026$  J m<sup>-2</sup> below 150 K in our experiments. This value was also found by Musiolik & Wurm (2019). With such low surface energy values at low temperatures it is possible to provide water ice-fly ash mixtures as cometary analogs whose tensile strength is well below the tensile strength of uncooled analog materials (Gundlach et al. 2018a; Steinpilz et al. 2019; Bischoff et al. 2020).

#### 4.4. Possible error sources

It should be noted that Eq. (2) is derived from JKR theory (Johnson et al. 1971), which is only valid for spherical particles. Angular silica particles are a more complex material, in which the edges of the particles can be assumed to be particles with very small radii of curvature and their flat sides correspond to very large radii of curvatures. Therefore, the distribution of effective particle sizes derived from the radii of curvature in an angular granular medium varies significantly. This assumed average grain size may result in errors in the derived surface energy.

During the experiments, the samples were cooled down to temperatures <150 K, which prevented sintering of water ice particles (Kuroiwa 1961). As a result, an increase of the tensile strength of the sample material by sinter necks between water ice particles could be avoided. Therefore, the strength of the samples was determined by the cohesion of directly neighboring particles and the particle shape. However, partial sintering of the sample surface cannot be completely ruled out. Air humidity may penetrate into the cooled polystyrene box, reach under the cooling shield, and may have crystallized on the surface of the samples. This would create a stiff connection between individual particles at the disk surface. However, this process probably had only a negligible influence on the measurement. The measurement of the tensile strength lasted only two to three minutes and to avoid atmospheric moisture the atmosphere in the polystyrene box was



**Fig. 11.** Schematic overview of parameters affecting the tensile strength of granular matter in our experiments. Higher temperatures and smaller particle sizes increase the tensile strength of a material. A dependence of the tensile strength on the grain shape can be assumed, but cannot be determined with our measurements.

made up of evaporated liquid nitrogen. Therefore, the nitrogen atmosphere in the box was colder and heavier than air and did not readily mix with it.

Another factor that could influence the results of the tensile strength measurements is the hydrophilicity of amorphous silica. Air humidity could reach the used silica dust before the sample preparation and probably accumulated on its surface. The bonding of water molecules or silanol groups on the particle surface would be the consequence and could decrease the surface energy of the individual particles (Steinpilz et al. 2019). With an increased availability of moisture, a thin layer of water could form around dust particles. Cooled down, this water would freeze and the particles would be indistinguishable from water ice particles in terms of surface energy and tensile strength. To avoid this effect the silica used in our experiments was always stored in tightly closed containers, which were only opened briefly for gaining sample components. However, the formation of silanol groups on the particle surfaces cannot be ruled out completely. No measurements however give any hint of this effect, especially since we observed an significantly increased tensile strength of silica-rich samples compared to fly ash-rich samples. Even if the tensile strength would be reduced by the hydrophilicity of silica, it is still much higher than that of samples with fly ash and therefore less suitable to produce samples with low tensile strength.

## 5. Conclusions

We conducted three series of Brazilian disk test measurements to analyze the tensile strength of samples composed of different cometary analog materials. For this we combined two of the three components: spherical water ice, spherical fly ash particles, or angular silica particles at sizes of few microns. We cooled these materials to temperatures below 150 K. The samples of these series were combinations of (a) icy spherical-angular particles, (b) icy spherical-spherical particles, and (c) dry spherical-angular particles. We conclude that below 150 K the tensile strength and the derived surface energy of silica, fly

ash, and water ice mixtures are generally much lower than at room temperature (Kimura et al. 2015; Gundlach et al. 2018a).

At temperatures below 150 K the tensile strength of the sample mixtures was strongly dependent on the amount of ice mixed within the sample and on the particle geometry (Fig. 11). We suspect that the friction between angular particles increases, but we cannot quantify this effect with our experiment. This and the mean grain radius of  $1.3 \mu\text{m}$  of pure silica particles lead to the tensile strength of  $\sigma = 7300 \text{ Pa}$  at a filling fraction of  $\Phi = 0.43$ . A direct calculation of the surface energy with JKR based Eq. (2) was not feasible in this case, since the particles were not spherical and the friction between particles may distort the tensile strength of the sample. Therefore, the surface energy values for angular silica particles (Figs. 9 and 10) must be interpreted with caution and could be too high.

The second dust component was fly ash, which consists of about 60%  $\text{SiO}_2$  and is composed of spherical particles with a mean radius of  $r = 2.43 \mu\text{m}$  (Table 1). Our samples of pure cooled fly ash have a filling fraction of  $\Phi = 0.84$  and a low tensile strength of  $\sigma = 140 \text{ Pa}$ . That corresponds to a surface energy of  $\gamma = 0.00019 \text{ J m}^{-2}$  and is about two orders of magnitude smaller than pure silica at room temperature (e.g., Kimura et al. 2015). In the samples, which are mainly composed of spherical particles, these particles can easily pass each other by rolling. Hence, the surface energy of the material can be calculated more directly from the tensile strength with Eq. (2).

The properties of pure water ice samples were determined to  $\sigma = 1800 \text{ Pa}$  and  $\gamma = 0.0026 \text{ J m}^{-2}$  at 150 K. These values for tensile strength and surface energy are significantly higher compared to values of fly ash particles. Owing to their spherical shape the ice particles were also not affected by interlocking. Therefore, the tensile strength of the samples was used to calculate the surface energy of water ice.

When two of the three analog materials were mixed, the component with the higher tensile strength dominated the tensile strength of the whole sample. As soon as the abundance of the material with the lower surface energy exceeds 80 vol%, the tensile strength of the mixture decreases quickly toward the value of the component with this lower tensile strength (Fig. 7). At that



mixing ratio, there are too few direct connections between particles with higher attractive interparticle forces to significantly increase the tensile strength of the whole sample.

Our experiments showed that fly ash can be used as suitable analog material for cometary dust in the laboratory. As a consequence of the very low surface energy of fly ash, samples with a tensile strength of few hundred Pascals and less can be easily produced. This is in the range of the tensile strength of cometary material, as estimated for comet 67P/Churyumov-Gerasimenko (Groussin et al. 2015; Attree et al. 2018). In contrast to angular silica particles, the spherical shape of the fly ash and water ice particles prevents interlocking. This significantly reduces the friction between the particles so that cohesion remains the dominant force between single particles. Therefore, the spherical shape of fly ash and water ice particles in the laboratory is advantageous to produce samples with very low tensile strength. If more than 20 vol% water ice is mixed as a volatile material to fly ash, the tensile strength increases rapidly to the value of pure water ice. Assuming that comets can be described as icy dirt balls (Keller 1989; Pätzold et al. 2016), this effect can be reduced when the ice content in the samples is kept low. The result is a mixture whose tensile strength is still a few hundred Pascals and would be a good analog material for comets in the laboratory.

In the laboratory the small particle diameter of a few microns increases the cohesion of the samples, which exceeds the influence of gravity (Bischoff et al. 2019). We used the ratios of these cohesive and gravitational force in the laboratory and on 67P/Churyumov-Gerasimenko (Bischoff et al. 2019) to estimate the particle size on a comet we are able to simulate with our micron-sized particles in the laboratory. We found that centimeter-sized aggregates (Güttler et al. 2010, 2019; Blum et al. 2014) in the gravitational field of a comet can be scaled down to few micron-sized particles in the laboratory (Scheeres et al. 2010; Durda et al. 2014).

*Acknowledgements.* This work was carried out in the framework of the CoPhyLab project funded by the D-A-CH programme (GU 1620/3-1 and BL 298/26-1/SNF 200021E 177964 / FWF I 3730-N36). The research project “The Physics of Volatile-Related Morphologies on Asteroids and Comets” is funded by the DLR Management Board Young Research Group Leader Programme and the Executive Board Member for Space Research and Technology. We gratefully acknowledge their financial support and endorsement. Many thanks to I. Büttner from DLR Berlin for sieving the fly ash, to U. Altenberger from the University of Potsdam for providing SEM images of fly ash and silica and to M. Neuhaus for providing images of ice particles.

## References

- Attree, N., Groussin, O., Jorda, L., et al. 2018, *A&A*, 611, A33
- Bischoff, D., Gundlach, B., Neuhaus, M., & Blum, J. 2019, *MNRAS*, 483, 1202
- Bischoff, D., Kreuzig, C., Haack, D., Gundlach, B., & Blum, J. 2020, *MNRAS*, 497, 2517
- Blum, J., Schrapler, R., Davidsson, B. J. R., & Trigo-Rodriguez, J. M. 2006, *ApJ*, 652, 1768-81
- Blum, J., Gundlach, B., Mühle, S., & Trigo-Rodriguez, J. M. 2014, *Icarus*, 235, 156
- Durda, D. D., Sanchez, P., Fischer, A., et al. 2014, *Lunar Planet. Sci. Conf.*, 45
- El-Maarry, M. R., Thomas, N., Gracia-Berná, A., et al. 2015, *Geophys. Res. Lett.*, 42, 2015GL064500
- El-Maarry, M. R., Groussin, O., Keller, H. U., et al. 2019, *Space Sci. Rev.*, 215, 36
- Fournel, F., Continni, L., Morales, C., et al. 2012, *J. Appl. Phys.*, 111, 104907
- Grün, E., Bar-Nun, A., Benkhoff, J., et al. 1989, *IAU Colloquium*, 116, 277
- Grün, E., Gebhard, J., Bar-Nun, A., et al. 1993, *J. Geophys. Res. Planets*, 98, 15091
- Groussin, O., Jorda, L., Auger, A.-T., et al. 2015, *A&A*, 583, A32
- Güttler, C., Blum, J., Zsom, A., Ormel, C. W., & Dullemond, C. P. 2010, *A&A*, 513, A56
- Güttler, C., Mannel, T., Rotundi, A., et al. 2019, *A&A*, 630, A24
- Gundlach, B., Blum, J., Keller, H. U., & Skorov, Y. V. 2015, *A&A*, 583, A12
- Gundlach, B., Ratte, J., Blum, J., Oesert, J., & Gorb, S. N. 2018a, *MNRAS*, 479, 5272
- Gundlach, B., Schmidt, K. P., Kreuzig, C., et al. 2018b, *MNRAS*, 479, 1273
- Heim, L.-O., Blum, J., Preuss, M., & Butt, H.-J. 1999, *Phys. Rev. Lett.*, 83, 3328
- Johnson, K. L., Kendall, K., Roberts, A. D., & Tabor, D. 1971, *Proc. R. Soc. London A Math. Phys. Sci.*, 324, 301
- Kappel, D., Sachse, M., Haack, D., & Otto, K. A. 2020, *A&A*, 641, A19
- Kaufmann, E., & Hagermann, A. 2018, *Icarus*, 311, 105
- Keller, H. U. 1989, *ESA SP*, 302, 39
- Keller, H. U., Mottola, S., Hviid, S. F., et al. 2017, *MNRAS*, 469, S357
- Ketcham, W. M., & Hobbs, P. V. 1969, *Phil. Mag. J. Theor. Exp. Appl. Phys.*, 19, 1161
- Kührt, E. 1984, *Icarus*, 60, 512
- Kührt, E., & Keller, H. U. 1994, *Icarus*, 109, 121
- Kimura, H., Wada, K., Senshu, H., & Kobayashi, H. 2015, *ApJ*, 812, 67
- Kothe, S., Blum, J., Weidling, R., & Güttler, C. 2013, *Icarus*, 225, 75
- Kuroiwa, D. 1961, *Tellus*, 13, 252
- Leroch, S., & Wendland, M. 2012, *J. Phys. Chem. C*, 116, 26247
- Li, D.-I. 2013, *J. Zhejiang Univ. Sci. C*, 14, 244
- Li, D., & Wong, L. N. Y. 2013, *Rock Mech. Rock Eng.*, 46, 269
- Lämmerzahl, P., Gebhard, J., Grün, E., & Klees, G. 1995, *Planet. Space Sci.*, 43, 363
- Meisner, T., Wurm, G., & Teiser, J. 2012, *A&A*, 544, A138
- Murphy, W. F. 1982, PhD thesis, Stanford University, USA
- Musioli, G., & Wurm, G. 2019, *ApJ*, 873, 58
- Omura, T., & Nakamura, A. M. 2017, *Planet. Space Sci.*, 149, 14
- Pajola, M., Oklay, N., Forgia, F. L., et al. 2016, *A&A*, 592, A69
- Pätzold, M., Andert, T., Hahn, M., et al. 2016, *Nature*, 530, 63
- Poch, O., Pommerol, A., Jost, B., et al. 2016a, *Icarus*, 266, 288
- Poch, O., Pommerol, A., Jost, B., et al. 2016b, *Icarus*, 267, 154
- Powell, M. J. 1979, *Phys. Rev. B*, 20, 4194
- Rogers, J. J. W., & Head, W. B. 1961, *J. Sediment. Res.*, 31, 467
- Scheeres, D., Hartzell, C., Sánchez, P., & Swift, M. 2010, *Icarus*, 210, 968
- Schellart, W. P. 2000, *Tectonophysics*, 324, 1
- Skorov, Y., & Blum, J. 2012, *Icarus*, 221, 1
- Sánchez, P., & Scheeres, D. J. 2014, *Meteorit. Planet. Sci.*, 49, 788
- Steinpilz, T., Teiser, J., & Wurm, G. 2019, *ApJ*, 874, 60
- Thomas, H., Ratke, L., & Kochan, H. 1994, *Adv. Space Res.*, 14, 207
- Thomas, N., Sierks, H., Barbieri, C., et al. 2015, *Science*, 347, aaa0440
- Vincent, J.-B., Oklay, N., Pajola, M., et al. 2016, *A&A*, 587, A14
- Yang, R. Y., Zou, R. P., & Yu, A. B. 2000, *Phys. Rev. E*, 62, 3900



**2.2.2 Haack et al. (2021a)**

Haack, D., Lethuillier, A., Kreuzig, C., Feller, C., Gundlach, B., Pommerol, A., Blum, J., & Otto, K. A. (2021a). Sublimation of Ice-dust Mixtures in Cooled Vacuum Environments to Reproduce Cometary Morphologies. *Astronomy & Astrophysics*, *649*, A35.  
<https://doi.org/10.1051/0004-6361/202140435>.

The laboratory work comprised in this article has been conducted by D. Haack. I provided the initial idea to this project established the collaboration with the CoPhyLab network. A. Lethuillier, C. Kreuzig, B. Gundlach and J. Blum are collaborators at the University of Braunschweig who provided the equipment and trained D. Haack to use the facilities. C. Feller and A. Pommerol provided feedback on the project. I helped establishing mixing ratios and the scaling relations and describing the morphologic evolution of the samples. I also produced and assembled data for Figures 1 and 7 and provided feedback on the comparability of cometary and laboratory morphologies. All authors assisted with the data interpretation and with refining the manuscript.

# Sublimation of ice-dust mixtures in cooled vacuum environments to reproduce cometary morphologies<sup>★</sup>

David Haack<sup>1</sup>, Anthony Lethuillier<sup>2</sup>, Christopher Kreuzig<sup>2</sup>, Clément Feller<sup>3</sup>, Bastian Gundlach<sup>2</sup>, Antoine Pommerol<sup>3</sup>, Jürgen Blum<sup>2</sup>, and Katharina Otto<sup>1</sup>

<sup>1</sup> Institut für Planetenforschung, Deutsches Zentrum für Luft- und Raumfahrt (DLR), Berlin, Germany  
e-mail: david.haack@dlr.de

<sup>2</sup> Institut für Geophysik und Extraterrestrische Physik, Technische Universität Braunschweig, Braunschweig, Germany

<sup>3</sup> Physikalisches Institut, Universität Bern, Bern, Switzerland

Received 28 January 2021 / Accepted 22 March 2021

## ABSTRACT

**Aims.** The morphology of cometary surfaces can provide important information to constrain the composition and evolution of comets. In this work, we investigate the sublimation behavior of comet analog materials and how the sample composition affects the evolution of morphological features in laboratory experiments. In our experiments, we used dust ice mixtures as analog material to form observed cometary morphologies.

**Methods.** We used ice-dust mixtures in different mixing ratios as cometary analog material. In order to obtain realistic results, we scaled the expected cohesive and gravitational forces on comets to laboratory conditions. The samples were placed in a vacuum sublimation chamber and permanently cooled down to temperatures below 150 K to simulate the space environment. In the experiment, the samples were insolated with a light source from two different directions and alterations on the surface were recorded with a camera.

**Results.** We find that the morphology of sublimation residues of ice-dust mixtures is strongly dependent on the ice-dust ratio as well as the insolation direction. High amounts of ice cause constant surface alteration and lead to exotic morphologies. Low amounts cause fewer and more episodic surface changes during its sublimation. Collapse events resulting in irregular and very rough surfaces occur during horizontal insolation.

**Key words.** comets: general – methods: laboratory: solid state – planets and satellites: formation

## 1. Introduction

In the past, several space missions have been sent to comets to study their properties at a close range (e.g., ESA's Rosetta mission and NASA's Deep Impact mission). Despite these visits, the activities on the surface of comets are still not well understood. Satellite-based observations have shown that the surfaces of comets become very active as they approach the Sun (Snodgrass et al. 2013; Gulkis et al. 2015; Sierks et al. 2015) by which we mean the occurrence of sublimation-driven outgassing events. The main process responsible for this activity is the sublimation of volatiles in a shallow subsurface region of a comet. It is caused by the direct radiation of solar energy onto surfaces in an air-less environment. Since comets also consist of non-volatile minerals, salts, and organic substances, volatile-depleted residues remain after the sublimation of the ices. The pressure drag of sublimating volatiles detaches volatile and nonvolatile particles and gas drag transports them away from the surface (Kührt & Keller 1994; Gundlach et al. 2015; Keller et al. 2017; Bischoff et al. 2019). In this way, a comet loses material with each orbit around the Sun and diverse morphological features form at its surface. Based on Rosetta data, the tensile strength was estimated from overhangs (Groussin et al. 2015; Attree et al. 2018), fractures were proposed to be related to desiccation processes (El-Maarry et al. 2015), and boulder size frequency

distributions were used as indicators of evolutionary processes (Pajola et al. 2015, 2016a,b). To enhance our understanding of these sublimation-driven processes, the morphologies of the cometary surfaces as well as the morphologies developing under laboratory conditions need to be further examined. Chemical composition, grain size, porosity, and gravitational and cohesive forces between individual particles decisively determine how the surface of a comet develops. Therefore, the comparison of morphological features in the laboratory with those at a comet's surface may provide information about its composition and could constrain the evolutionary history of comets.

The KOSI laboratory experiments in the 1990s simulated and studied sublimation processes that were expected on the surfaces of comets (e.g., Grün et al. 1989, 1993; Lämmerzahl et al. 1995). In a sublimation chamber, mixtures of water ice and nonvolatile analog materials were illuminated by an energy source and the changes in the samples' surfaces were analyzed. After prolonged insolation of the samples, an ice-free cover layer formed, which protected deeper layers from warming up and it prevented further activity.

Cometary science got a recent boost with the Rosetta mission. Since the spacecraft reached comet 67P/Churyumov-Gerasimenko (hereafter 67P), we obtained detailed images of its surface and improved our knowledge of organic materials on a comet (Capaccioni et al. 2015; Goesmann et al. 2015; Raponi et al. 2020). However, in order to properly interpret the morphologies displayed in Rosetta images, an understanding of the nucleus composition, in particular its dust-to-ice ratio, is vital.

<sup>★</sup> Movies associated to Figs 6 and 8 are available at <https://www.aanda.org>

Therefore, analog studies with vacuum sublimation chambers have been increasingly dedicated to the development of specific morphologic features. The Simulation Chamber for Imaging the Temporal Evolution of Analogue Samples (SCITEAS; Pommerol et al. 2015) allowed monitoring and photometric analyses of volatile-rich samples during the process of sublimation. The chamber provided temperatures and low pressure comparable to conditions on comets for low heliocentric distances. With this chamber, Poch et al. (2016a,b) investigated the influence of organic materials and mineral components on the sublimation behavior of water ice. The presence of organic material results in significant textural differences on the sample's surface after sublimation of the volatiles. Samples with refractory grains included in the ice matrix (intra-mixtures) produced very porous (foam-like) and highly cohesive structures. On the other hand, when the components were mixed with each other as pure particles (inter-mixtures), more compact and less cohesive residuals at the surface of the samples formed (Poch et al. 2016a,b). However, the concentrations of nonvolatile components in the initial sample mixtures were very low with up to one mass percent and, therefore, they are not representative of realistic cometary regoliths. Additionally, the arrangement of the samples in molds was not suitable to allow vertical mass transport. This is why the samples could not reproduce the observed morphologies of a cometary surface. Other experiments by Kaufmann & Hagermann (2018) were used to analyze the influence of carbon black on the sublimation of icy surfaces. They verified the hardening of a subsurface layer as described by Kochan et al. (1989) and Kossacki et al. (1997) and the development of an ice-depleted cover with a very low density. Most of these experiments were conducted using a very high and possibly unrealistic volatile content of >90 wt.%. Experiments focusing on the development and evolution of morphologies using a more realistic dust-to-ice ratio are conducted in this work.

Previous experimental work has shown that at temperatures of 150 K and below, the tensile strength of water ice is much lower than previously expected (Gundlach et al. 2018a; Musiolik & Wurm 2019). Haack et al. (2020) extended these experiments and investigated different mixtures of dust and water ice for their suitability as comet analogs and found that the tensile strength of a mixture is dominated by the component with the highest tensile strength. In this work, we use these mixtures to study the morphological evolution of samples in a vacuum sublimation chamber with the aim of reproducing basic morphological structures observed at the surface of 67P. In our experiments, we insulated samples, which were composed of water ice and non-volatile dust particles in different ratios. We took advantage of the very low tensile strength of spherical water ice and fly ash particles that are mixed together and cooled below 150 K (Haack et al. 2020; Kappel et al. 2020). We also allowed vertical and horizontal mass transport of the sample material by the omission of lateral sample boundaries. The intensity of the insolation was varied and the angle of incidence could be set either vertical or horizontal relative to the surface of the sample. We focused on the conditions under which the sublimation of water ice starts to significantly change the sample texture. Alterations of the sample morphology were analyzed and checked for their relevance with respect to cometary surfaces. We find that the resulting morphological features are dependent on the composition of the samples.

Motivated by reproducing the morphology of cometary surfaces with analog materials, we describe scaling of cometary environments to the laboratory and experimental setup in Sect. 2.

**Table 1.** Characteristics and chemical composition of components used to simulate cometary materials.

	Water ice	Fly ash
Particle shape	Spherical	Spherical
Particle radius ( $\mu\text{m}$ )	$2.38 \pm 1.11$	$2.43 \pm 1.41$
Density ( $\text{g cm}^{-3}$ )	0.93	2.25
Compd%		
H <sub>2</sub> O	100.00	
SiO <sub>2</sub>		59.20
Al <sub>2</sub> O <sub>3</sub>		27.90
Metal oxides		12.90

**Notes.** The properties and chemical composition of the particles were measured using an electron microscope before starting the experiments.

In Sect. 3, we present our results and discuss them in Sect. 4. Finally, our analyses are summarized in Sect. 5.

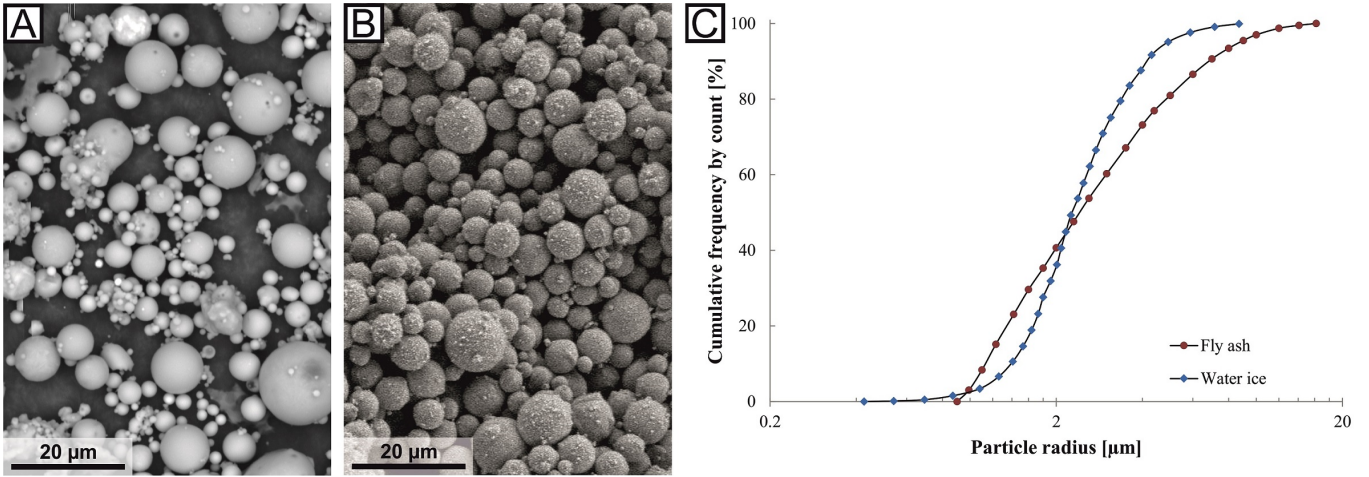
## 2. Methods

### 2.1. Selection of materials

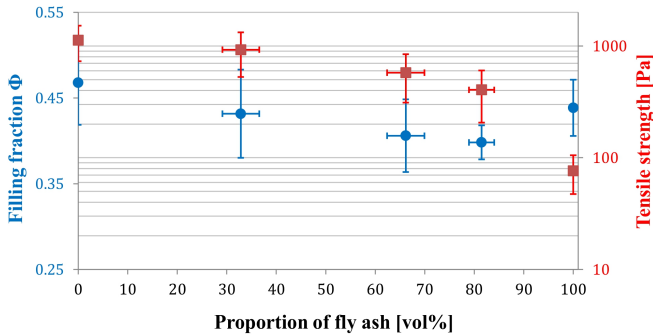
We decided to investigate comet analog materials consisting of binary mixtures of a volatile and a refractory component. This not only keeps the complexity of the experiments within limits but also allowed us to investigate the influence of individual parameters on the morphology after sublimation (e.g., dust-ice ratio, insolation direction).

We used polydisperse water ice spheres with an average radius of 2.4  $\mu\text{m}$  (Table 1) as the volatile component of the analog material. This is a first grade approximation since H<sub>2</sub>O dominates the amount of volatile materials in 67P (Hässig et al. 2015). Other volatiles such as CO<sub>2</sub> or CO account for only up to 15 mass% abundance relative to H<sub>2</sub>O (Bockelée-Morvan et al. 2016; Lauter et al. 2018; Biver et al. 2019). Even when H<sub>2</sub>O dominates, CO<sub>2</sub> and CO ices might play key roles in the activity at large heliocentric distances where water does not sublimate. Our approximation is a first step and other ices will be introduced in future work to see if this makes differences or not.

We used dust as refractory material, whereby a compromise between physical and chemical accuracy had to be found. We decided to use spherical fly ash particles. These have the advantage of not consisting of pure amorphous SiO<sub>2</sub> as in previous experiments, but rather they correspond to the more mineralic composition of plagioclase (Table 1). The fly ash particles are polydisperse and of a similar size as the water ice particles used (Fig. 1). Additionally, it is possible to produce samples with a very low tensile strength with these spherical particles (Haack et al. 2020) to simulate the low tensile strength of cometary materials (Groussin et al. 2015; Attree et al. 2018). The filling fraction of the samples describes how much free space is in a volume filled with particles and is with  $\sim 0.4$  (Fig. 2) higher than observations of 67P suggest (Groussin et al. 2015; Attree et al. 2018; O'Rourke et al. 2020). In the experiment, the higher filling fraction would lead to more interparticle bonds and thus a higher tensile strength. However, this effect may be reduced by the spherical shape of the particles that reduces interlocking of realistically angular particles and would compensate for their limited freedom of movement (Haack et al. 2020; Kappel et al. 2020). Although olivine and pyroxene may be more suitable cometary refractory analog materials, the difficulties in acquiring these materials in a micrometer-sized spherical shape



**Fig. 1.** Electron-microscopy images and size distribution of the particles used in our experiments. The images of spherical fly ash in *panel A* and water ice particles in *panel B* are at the same scale (modified from Haack et al. 2020). *Panel C* presents the comparable cumulative size distributions of fly ash (red dots) and water ice (blue diamonds).



**Fig. 2.** Filling fractions and tensile strengths of different water ice-fly ash mixtures. Pure ice corresponds to 0 vol% on the left, and the respective pure fly ash to 100 vol% on the right. The error of the water ice-fly ash mixing ratio originates from the uncertainty as to the ice mass determination.

were disproportionate for this work. Angular particles, however, would greatly increase the tensile strength of the samples (Haack et al. 2020) and could prevent the alteration of the sample morphology during the sublimation experiment.

Organic materials are also important components of comets (Sandford et al. 2006; Capaccioni et al. 2015; Goesmann et al. 2015; Raponi et al. 2020). However, in this series of experiments, we have omitted organic components in order to cap the complexity of our experiments to be able to attribute a change in morphology to the variation of one individual parameter. The results can be used as a basis for further experiments with more complex sample compositions.

## 2.2. Particle scaling

A major challenge with experiments in the laboratory is Earth's gravitational acceleration, which is higher, by order of magnitudes, than the  $\sim 2 \times 10^{-4} \text{ m s}^{-2}$  of comet 67P (Agarwal et al. 2016). Therefore, particles at the surface of the comet are subject to much less gravity and the importance of cohesion between particles is significantly increased (Scheeres et al. 2010; Skorov & Blum 2012; Sánchez & Scheeres 2014). Bischoff et al. (2019) present a model according to which decimeter-sized particles on the surface of 67P are subject to approximately equal cohesive and gravitational forces. Between particles smaller than

this threshold, the cohesion is dominant; for larger particles, gravity becomes more important. Previous studies have suggested that comets are formed of up to centimeter-sized pebbles (Zsom et al. 2010; Blum et al. 2014, 2017; Kretke & Levison 2015; Fulle et al. 2016; Lorek et al. 2018). Therefore, cohesive forces should dominate on a comet. To simulate processes in the laboratory that are comparable to processes on cometary surfaces, a way to reduce the influence of gravity compared to cohesive forces on the experiment must be found. According to Bischoff et al. (2019), on Earth, the threshold between gravitational and cohesive dominance is a particle radius of  $\sim 35 \mu\text{m}$ . To significantly reduce the relative importance of gravity and to ensure the dominance of cohesive inter-particle forces, the particle radius used in the experiment must be significantly below this size. Water ice and fly ash particles fulfill this criterion, but their cohesion with respect to 67P must be determined.

Images obtained during the Rosetta mission at 67P show complex morphologies, such as cliffs, cracks, or mass movements (Thomas et al. 2015b; Pajola et al. 2016b; El-Maarry et al. 2019), which are morphologically similar to those on Earth. This could indicate that between particles the ratio of cohesive forces and the comet's gravity is comparable to the ratio between these forces on Earth, even if they differ greatly in absolute numbers. If the cohesion forces on a comet were much more dominant than on Earth, exotic structures such as extreme overhangs or cave-like structures could be expected at the comet's surface, which would collapse immediately under Earth's gravity if made of the same material. On the other hand, if gravity was much more dominant, the observed cliffs and boulders would be unstable (Kappel et al. 2020) and the comet's surface would be much smoother in general. Using this approach, Groussin et al. (2015) have suggested that the ratio of cohesive and gravitational forces at 67P corresponds to that of weak rocks on Earth on a macroscopic scale. We use this suggestion and assume that the ratio between gravity and cohesion on 67P and on Earth is comparable and thus as follows:

$$\frac{F_{G_{67P}}}{F_{C_{67P}}} \approx \frac{F_{G_{\text{Earth}}}}{F_{C_{\text{Earth}}}}. \quad (1)$$

With given gravitational forces

$$F_G = \frac{4}{3}\pi r^3 \rho g \quad (2)$$



of particles on 67P and Earth and the known cohesion

$$F_C = 3\pi r\gamma \quad (3)$$

of particles used in the laboratory (Haack et al. 2020), we were able to estimate the corresponding particle size on 67P. In these equations,  $r$  is the reduced radius of the particles,  $\rho$  is the particle density,  $g$  is the gravity acceleration, and  $\gamma$  is the surface energy per unit area. In our experiments, we used mixtures of water ice and fly ash particles with a mean radius of about 2.4  $\mu\text{m}$  (Table 1). According to the used approximation, the water ice and fly ash particles in the experiments reflect millimeter-sized particles on 67P. This agrees well with the model of Bischoff et al. (2019) and is in line with the size of hypothesized pebbles of which comets may have been formed initially (Lorek et al. 2016; Blum et al. 2017). Transferred to macroscopic scales, a 2.5 cm high sample in the sublimation chamber would represent a 10 m-high object on 67P.

### 2.3. Energy scaling

The scaling of the particle size in the laboratory was intended to increase cohesive inter-particle forces with respect to gravity. As a result, the force that is required to separate the particles from each other and to change the sample morphology was also increased compared to the actual inter-particle cohesive force on the comet. In our experiments, this separating force is the near-surface pressure drag, caused by the vapor pressure of sublimating water ice. To transport single particles or larger aggregates away from their initial positions on the sample's surface, the pressure drag has to exceed the cohesive forces between the particles. Therefore, the applied energy to create the pressure drag in the experiment must be scaled with the particle cohesion to simulate realistic pressure drag-cohesion ratios.

As a first step, we estimated the surface temperature of 67P as a function of its heliocentric distance. The energy balance of insolation and sublimation is given by the Stefan–Boltzmann law plus a term for the sublimation heat flux, derived from Hertz–Knudsen (Kührt & Keller 1994)

$$\frac{C_s}{R^2}(1-a) = \epsilon\sigma T^4 + \frac{H P_v(T)}{\sqrt{2\pi k_B \frac{T}{m}}}. \quad (4)$$

In this equation, the following notation is used:

$C_s$	solar constant,
$R$	heliocentric distance,
$a$	albedo,
$\epsilon$	emissivity,
$\sigma$	Stefan–Boltzmann constant,
$T$	temperature,
$H$	latent sublimation heat,
$P_v$	vapor pressure,
$k_B$	Boltzmann constant, and
$m$	molecule mass.

As a second step, we assumed equal ratios of pressure drag  $F_D$  and cohesion  $F_C$  for 67P and in the laboratory and thus follow:

$$\frac{F_{D67P}}{F_{C67P}} \approx \frac{F_{D\text{Earth}}}{F_{C\text{Earth}}}. \quad (5)$$

The pressure drag  $F_D$  results from the vapor pressure (Panale & Salvail 1984; Gundlach et al. 2011) on the particle cross section

$$F_D = \pi r^2 3.56 \times 10^{12} \text{ Pa} \exp\left\{\frac{-6142 \text{ K}}{T}\right\}. \quad (6)$$

With the particle radius  $r$  of the analog material, the calculated surface temperature  $T$  of 67P from step one, and the cohesion of 67P and the samples, we determined the temperature-dependent gas drag in the laboratory.

The fly ash albedo  $a$  was determined to be 0.35 on average in previous measurements. This value was also used as an approximation for the ice-dust mixtures, since the albedo of an ice-bearing sample is mainly determined by the dust component (Chýlek et al. 1983; Clark & Lucey 1984; Oehler & Neukum 1991). Thus the generally low albedo of 67P of 0.06 (Ciarniello et al. 2015) was considered in this scaling and compensated for by a higher energy input. Then we used the temperature derived in Eq. (4) to calculate the insolation intensity in the laboratory.

For our spherical water ice particles, which are mixed with dust particles, we estimated an insolation flux of  $\sim 1$  solar constant in the laboratory to simulate a heliocentric distance of 4 AU in our experiments. This was approximately the distance to the Sun, when the Rosetta spacecraft reached 67P and monitored activity at the surface (Tubiana et al. 2015). The maximum of solar radiation to the surface of 67P is reached at its perihelion at 1.24 AU. This would transform into an insolation flux of about 33.6 solar constants in the laboratory to simulate the cohesion-pressure drag ratio. However, this insolation flux was not feasible with our experimental setup.

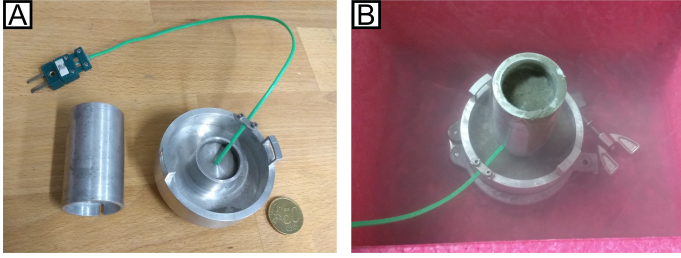
### 2.4. Sample preparation

We conducted a series of sublimation experiments with samples that were composed of water ice and fly ash in different mixing ratios (Haack et al. 2020). These were inter-mixtures, which means that individual particles consisting of a single component were mixed together. Water ice spherules represent the volatile content of a comet and fly ash particles represent the refractory dust components. These mixtures were used to test the dependence of the sublimation of a sample on (a) the ice-dust ratio of the mixture and (b) the direction of the insolation flux.

The water ice particles were produced with a water droplet dispenser that sprays mist into a Dewar vessel filled with liquid nitrogen (Gundlach et al. 2018b; Haack et al. 2020). The water droplets freeze, forming a suspension of polydisperse spherical water ice particles and liquid nitrogen, and they eventually sink down to the bottom of the Dewar vessel. The amount of water ice in the suspension was determined by using Archimedes' principle. The weights of a defined volume of pure liquid nitrogen and of liquid nitrogen with suspended water ice were measured. The densities of liquid nitrogen and water ice are known and allowed the calculation of the mass of water ice in the suspension from the weight difference between both components. Fly ash was directly weighed with a scale.

We produced five different ice-dust mixtures (66, 50, 33, 25, and 20 vol% water ice) by adding predefined amounts of dust into the suspension of liquid nitrogen and a known amount of water ice. This corresponds to dust-ice mass ratios of  $\sim 1.2, 2.4, 4.8, 7.3,$  and  $9.7$ , similar to those expected for the nucleus of a comet (Rotundi et al. 2015; Herique et al. 2017; Fulle et al. 2017, 2018; Pätzold et al. 2018). The liquid nitrogen, water ice, and dust particles were mixed manually with a ladle to obtain a homogeneous suspension. Then, the mixtures were filled into a metal cylinder with an inner diameter of 25 mm, which was placed vertically on a permanently nitrogen-cooled sample holder (Fig. 3). The viscosity of the mixture in the cylinder was high enough that ice and dust could no longer segregate due to their different densities. The liquid nitrogen as a coolant was necessary to prevent sintering of the ice particles (Kuroiwa 1961; Gundlach et al. 2018a).





**Fig. 3.** Preparation of the samples. *Panel A:* metal cylinder (left) and sample holder (right) that were used to prepare the samples. The green cable with the connector belongs to one of the thermocouple sensors, which was used to monitor the sample temperature during the experiment. *Panel B:* the metal cylinder was plugged onto the sample holder and filled with a suspension of liquid nitrogen, water ice, and dust particles. To ensure that the setup was constantly cooled while the liquid nitrogen evaporated from the sample mixture, the outer volume of the sample holder was also filled with liquid nitrogen.

Without cooling during the sample preparation, stiff sinter necks could form between ice particles and would lead to higher values for the tensile strength of the sample materials. After the liquid nitrogen of the suspension slowly evaporated from inside the metal cylinder, the cylinder was carefully lifted up. As a result a cylindrical sample of water ice and dust remained on the sample holder. Its diameter was the same as the inner diameter of the cylinder (25 mm) and the height varied between 20 mm and 25 mm. A slow and steady evaporation of the liquid nitrogen was necessary to avoid the formation of cavities within the sample and to reduce their formation at the contact surface with the cylinder. During the preparation, the samples were not mechanically compressed and were held together by their own cohesion. After removing the metal cylinder, the cooled sample holder with the sample on top was quickly placed into the precooled vacuum sublimation chamber and ready for the sublimation experiment.

### 2.5. Tensile strength

Before we started the sublimation experiments, we performed a series of measurements to determine the tensile strength of the samples. We prepared 15 samples, each of various ice-dust mixtures in the manner described above, and made sure that all nitrogen had evaporated from the samples. We then determined their weight and volume and were able to calculate the filling fraction  $\Phi$  of the samples. We started with a water ice content of 100 vol% and reduced it to 0 vol%. The filling fractions of all investigated mixing ratios were between 0.40 and 0.46 (Fig. 2). According to Blum et al. (2006), the upper limit of the tensile strength  $\sigma$  of granular matter is

$$\sigma = \frac{9\Phi\gamma}{4r}. \quad (7)$$

With the values for the surface energy  $\gamma$  of water ice-fly ash mixtures at liquid nitrogen temperatures (Haack et al. 2020) and the particle radius  $r$ , we could determine the tensile strength of the samples. Since pure water ice or fly ash are not suitable as comet analog material, we used mixtures with a water ice content between 66 vol% and 20 vol% for the sublimation experiments. This gave tensile strengths of water ice-fly ash mixtures between  $930 \pm 60$  Pa and  $400 \pm 10$  Pa, respectively (Fig. 2).

### 2.6. Sublimation experiments

For our experiments, we used a cylindrical vacuum sublimation chamber with an inner diameter of 25 cm and a height of 80 cm

(Fig. 4). Before the start of the experiment, the chamber was closed, cooled down to about 110 K, and flooded with argon. The argon ensured the absence of atmospheric moisture inside the chamber when it was opened to place the sample inside. To ensure constantly low sample temperatures, which are similar to those of a comet (Kührt 1984), and to prevent thermal background radiation, an actively cooled shield system was used. This cooling shield is a rectangular metal housing with a side length of 10 cm and with a firm connection to a circuit for continually circulating liquid nitrogen. The cooling shield is coated black on the inside to prevent reflections and has two windows for insolation and observation of the sample inside (Fig. 4).

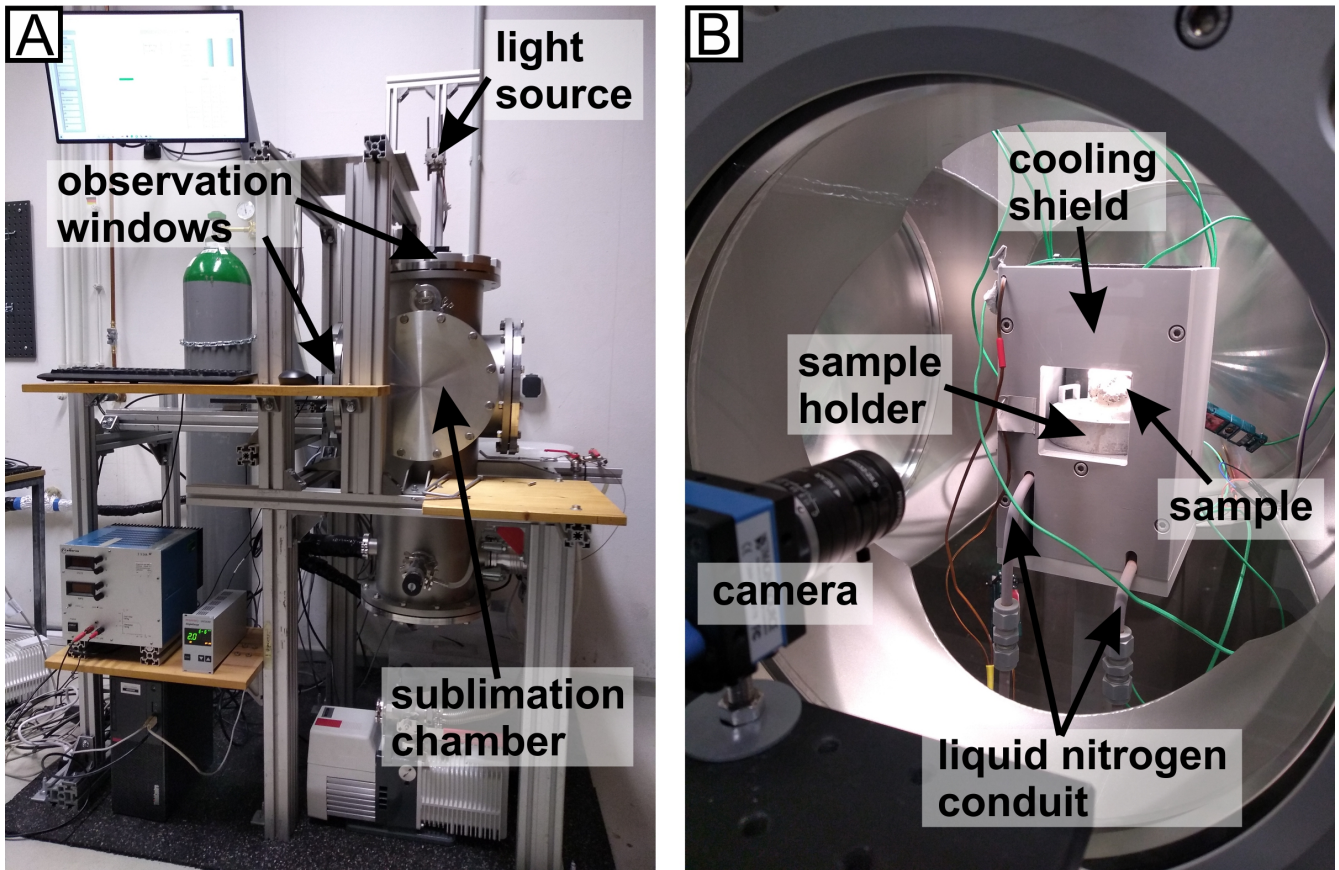
Immediately after preparation, the sample was placed inside the cooling shield. Thereby, the sample holder was firmly screwed to the cooling shield and temperature sensors were connected to the sample holder. Subsequently, the chamber was closed and the atmospheric pressure inside was reduced to  $\sim 10^{-7}$  mbar. To ensure that the measurements were performed in a controlled environment, the pressure inside the chamber and the temperature at four positions (sample, cooling shield top and bottom, and nitrogen input) were monitored in parallel (Fig. 5). From the beginning of the placement of the sample, a camera with a resolution of  $3000 \times 2000$  pixels was focused at the sample through a window in the sublimation chamber and monitored the sample at a rate of one image per second.

After the pressure inside the chamber had reached its operating value of  $\sim 10^{-7}$  mbar, we started to insulate the sample. We used a halogen lamp with variable intensity and a simple mirror and lens system to focus the light on the sample. We also distinguished between insolation vertically to the top of the sample or horizontally to the side. This was implemented to investigate possible differences in material transport. During the experiments, the light source insulated the samples constantly in one direction.

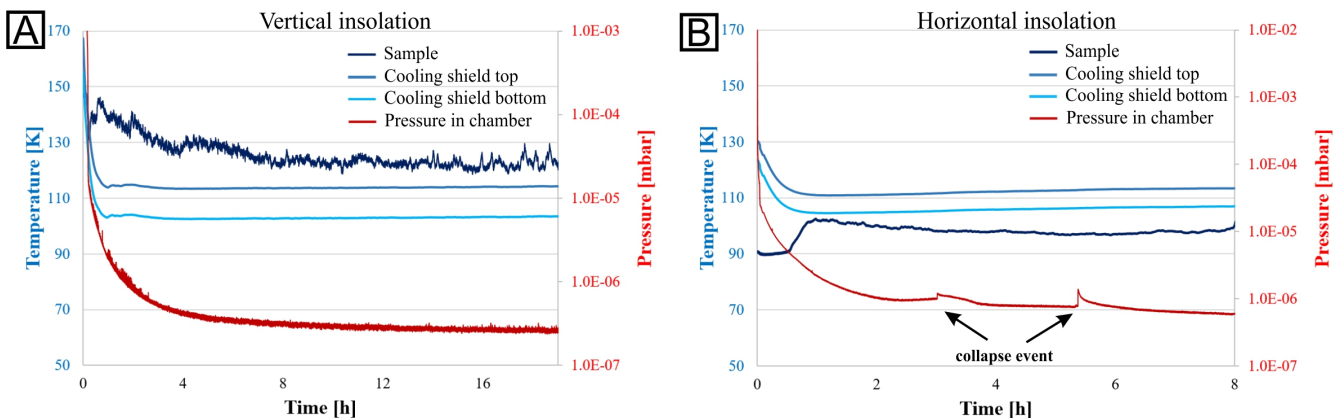
In a first series of experiments, we combined different mixing ratios with horizontal or vertical insolation. For this series of measurements, we chose an insolation flux of  $\sim 1$  solar constant, which corresponds to a heliocentric distance of 4 AU, following the scaling relations. In a second series of experiments, we increased the insolation flux to about 3 solar constants, which represents a heliocentric distance of 3.1 AU. The insolation of a sample lasted up to 20 h. After that time, the active cooling had to be stopped to replenish the liquid nitrogen supply. At the end of the experiment, the degree of alteration of the samples' surface was analyzed via the camera observations and related to different material compositions and levels and directions of insolation.

## 3. Results

The experiments of the first series with an insolation flux of about 1 solar constant (corresponding to a heliocentric distance of 4 AU) resulted in no visible alterations of the samples' morphology. Even the samples with the highest fraction of 66 vol% water ice showed no signs of activity under horizontal or vertical insolation, respectively. The samples were removed from the sublimation chamber after about 20 hours. The strength of the samples had increased significantly. They could be gripped with crucible tongs without damaging them. More detailed measurements of the exact tensile strength, porosity, among others, were not feasible because the room temperature and humidity in the laboratory were too high. As a result, frost immediately formed on the surface of the samples and additional sintering of the particles could not be avoided (Kuroiwa 1961), which



**Fig. 4.** Setup of the sublimation experiments. *Panel A:* cylindrical vacuum sublimation chamber with two observation windows. One is located on the top and one on the lateral side of the chamber. In the configuration shown, the light enters the chamber from above. *Panel B:* view through the lateral observation window into the inside of the vacuum sublimation chamber. The sample holder is firmly attached to the cuboid cooling shield. The object visible inside the cooling shield is the sample insulated from above. The green cables in the chamber belong to the different temperature sensors that monitor the temperature of the sample and the experimental setup. A camera is directed at the sample from outside.



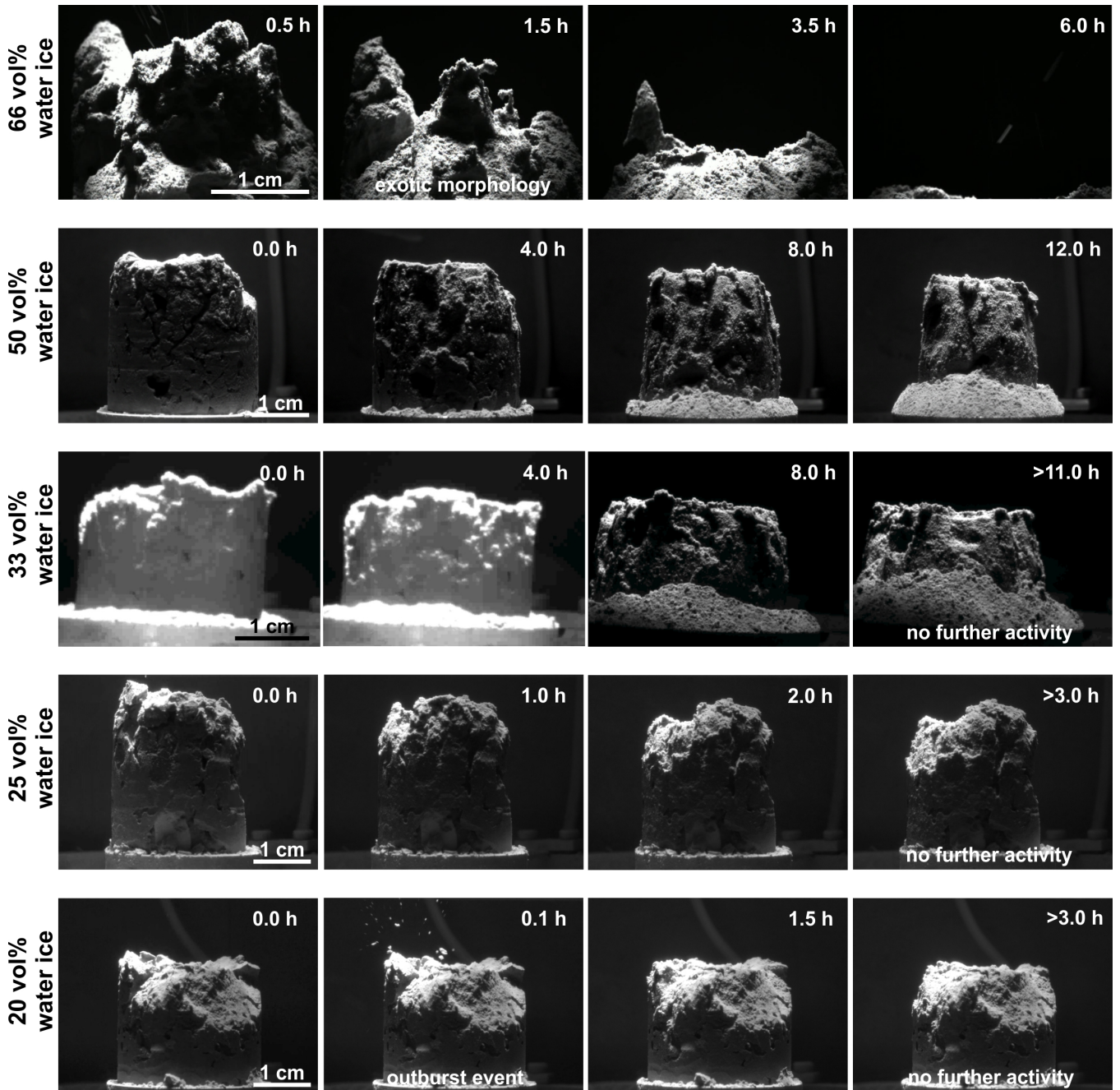
**Fig. 5.** Two examples of the monitored pressure and temperatures in the chamber for two samples with 25 vol% water ice, each. The recordings were made every second from the beginning of the experiment to its end. *Panel A:* the insolation with  $\sim 3$  solar constants was vertical from above. When the sublimation activity of the sample stopped after about 3 h, the pressure and temperatures remained stable until the end of the experiment. *Panel B:* the insolation was horizontal from the side. The temperatures of the sample and setup remained approximately stable. The pressure curve shows two short-term increases after 3 and 5.5 h, which can be attributed to two collapse events on the sample. The sample temperature increased at  $\sim 0.5$  h after the remainder of liquid nitrogen vaporized from the sample.

would have falsified possible measurement results. After heating up the sample remains to room temperature, it was observed that the subsequently melting ice in the interior of the samples was preserved and did not sublimate.

The second series of experiments with an insolation flux of  $\sim 3$  solar constants, which correspond to 3.1 AU, resulted in a

broad variety of activities at the samples' surfaces. In addition to different ice-to-dust ratios, vertical and horizontal insolation resulted in different surface activities during the observation periods. The temperature and pressure inside the cooling shield were monitored continuously. In all measurements, the internal sample temperature remained below 150 K and short-term





**Fig. 6.** Five vertically insulated samples with different dust-to-water ice ratios at an insolation rate of  $\sim 3$  solar constants. The image series show how the sublimation activity reduces with a decreasing water ice content (online movies). At a 66 vol% water ice content, several ejected particles are visible as elongated bright dashes (in the panels with a timestamp of 0.5 h and 6.0 h) and the whole sample has disappeared after about 6 h of continuous sublimation. The series of pictures with a 33 vol% and 50 vol% water ice content show the erosion of lateral surfaces, the formation of a talus, and the granular structure of the sample material. The first two images of the series with 33 vol% water ice appear brighter because the filter in front of the camera, which reduces the brightness, was not installed and was added during the experiment. The shape of the samples with a 25 vol% and 20 vol% water ice content changed rather in single events (ejections) and did not experience any further visible changes after about 3 h (see Fig. 5A).

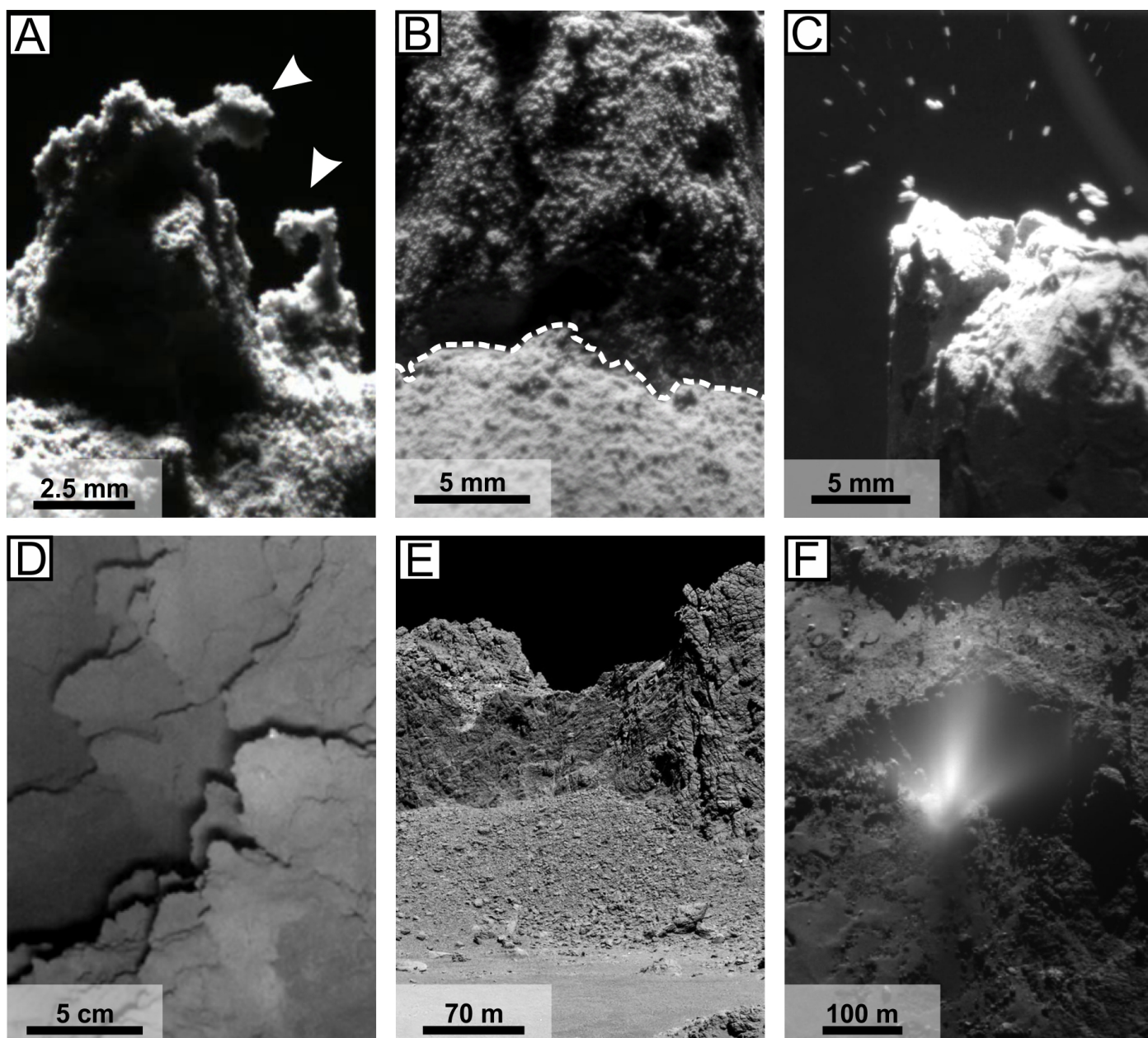
changes in pressure could be attributed to events that changed the sample's surface (Fig. 5).

### 3.1. Vertical insolation

We analyzed samples with a 66–20 vol% water ice content under vertical insolation flux of  $\sim 3$  solar constants. The results could be summarized into three groups, depending on their ice contents.

#### 3.1.1. 66 vol% water ice content

We started the experiments with a high water ice content of 66 vol%. Most noticeable was a fast and intense reshaping of the sample's surface. The sublimating water ice created a permanent and distinctly visible stream of particles that detached from the surface and were ejected away from the sample (Fig. 6). No ice-free layer of dust was able to form at any insulated area of the sample. A change in the albedo could not be observed either. As



**Fig. 7.** Comparison between laboratory results and observations on 67P. *Panels A–C* show details of different vertically illuminated samples from Fig. 6 during the phase of active sublimation in the laboratory. *Panels D–F* show images of the in situ surface of comet 67P to compare them with the corresponding lab results. *Panel A:* exotic morphology of the sample with a 66 vol% water ice content. The arrows indicate extreme overhangs, which did not collapse immediately. *Panel B:* shown is an enlarged section of the sample with a 50 vol% water ice content. The dotted line separates the sample wall (upper area) from the talus of loose debris (lower area). The granular structure of the sample material is clearly visible. The micrometer-sized individual particles (see Fig. 1) form aggregates of up to 1.5 mm in size and frequently remain intact when they detach from the sample and accumulate on the talus. This image represents the granular structure of all investigated samples. *Panel C:* the sample with a 20 vol% water ice content in the early phase of the experiment. Several fragments up to a millimeter in size were detached from the sample’s surface and ejected in single outburst events. *Panel D:* a detailed image of the surface of 67P taken by the Philae lander. It shows the actual surface of 67P without extreme overhangs as seen in panel A (ROLIS image derived from Schröder et al. (2017)). *Panel E:* a cliff on the comet with a talus of debris material that is reminiscent of laboratory results in panel B. *Panel F:* an outburst plume at the surface of 67P. Agarwal et al. (2016) describe meter-sized boulders that were ejected during these outbursts. Image credits: ESA/Rosetta/MPS for OSIRIS Team MPS/UPD/LAM/IAA/SSO/INTA/UPM/DASP/IDA.

a result, fresh sample material was always present on the surface and was exposed to progressive sublimation. The texture of the sample material appeared granular with a grain size in the submillimeter range. The observed grains were larger than the initially used ice and fly ash particles, which accumulated in these larger aggregates. After about six hours, the constant sublimation process had progressed so far that all water ice had

sublimated from the sample and the majority of refractory dust was transported away.

During the evolution of the surface exotic structures, spikes, and extreme overhangs formed, which only collapsed after most of the material had been transported away (Fig. 7). These roughly horizontal overhangs reflect the dominance of cohesive forces compared to gravity within the sample material.



### 3.1.2. 50 vol% and 33 vol% water ice content

As the water ice content of the samples decreased to 50 vol% and 33 vol%, the kinetics of surface alteration decreased significantly. At the beginning of the sublimation experiments, particles were continuously ejected from the sample. But the particle ejection frequency and transport range were significantly reduced, compared to samples with a 66 vol% ice content. Unfortunately, the setup did not allow us to quantify this more precisely. After 15–20 min, the phase of active ejection of particles ended for both samples. Material, which was detached from the sample's surface, predominantly fell down because of gravity. The alterations of the samples were mainly limited to their vertical walls. This led to a continuous decrease in the sample's diameter. The loose and ice-depleted material accumulated around the base of the sample and formed a talus of debris (Figs. 6 and 7). This talus consisted of aggregates up to 0.5 mm in size, consisting of dust particles and small amounts of water ice. The granular structure visible at the talus could also be observed directly in the ice-dust mixture on the sample's surface. Some aggregates reached sizes of up to 1.5 mm, but decayed into smaller fragments as soon as they fell off the sample's surface. In the submillimeter range, the surface appeared very rough. With the particle scaling from Sect. 2.1, the observed aggregates would correspond to boulders of some decimeters on the surface of 67P. In contrast to the diameter, the height of the two samples remained stable. At the end of the experiments, a thin layer of dust was observed on the horizontal surface layer of the samples.

The morphological development that both samples underwent seems to be comparable, but it proceeded on different timescales. The surface of the sample with 50 vol% water ice changed continuously until the end of the experiment. In contrast, the evolution of the sample with 33 vol% water ice slowed down noticeably and came to an end after 11 h. Although the sample was observed for another 7 h, no further alterations on the surface were observed.

After the remains of the samples were removed from the sublimation chamber, large amounts of water ice were noticed in the center of the remaining samples and some amounts were in the talus material. Additionally, the ice-rich center of the remaining samples was significantly solidified, compared to the start of the experiments, when the samples were extremely fragile. With our setup, it was not possible to determine the amount of ice in the remaining material because it began to thaw after it was removed from the chamber.

### 3.1.3. 25 vol% and 20 vol% water ice content

The samples with a water ice content of 25 vol% and 20 vol% showed a very similar development. Ejected particles were observed in the first minutes of the experiments and then only sporadically. Samples with both mixing ratios lost limited amounts of material at their directly insulated top surface. A visible loss of material on the lateral surfaces could not be observed. The constant low pressure in the chamber also shows that the sample did not lose any further volatile material after the end of the limited surface erosion (Fig. 5A).

A few minutes after the beginning of the experiment with the 20 vol% water ice sample, some major outburst events from the top surface were observed. A large number of up to millimeter-sized fragments detached and were transported away explosively (Fig. 7). However, these outburst events were limited to the initial phase of the experiment and did not occur during its further course. Fresh sample material became visible where alterations on the sample's surface occurred. It appeared very

similar to the other mixtures and showed a granular structure in the submillimeter range.

Even after prolonged insolation, no further surface changes were observed in either sample type after 3 h. Comparable to the samples with a higher ice content, the remains of the samples kept their ice content and were strongly solidified when they were removed from the sublimation chamber.

## 3.2. Horizontal insolation

Analog to experiments with vertical insolation, we analyzed samples with a 66–20 vol% water ice content under horizontal insolation flux of  $\sim 3$  solar constants.

### 3.2.1. 66 vol% water ice content

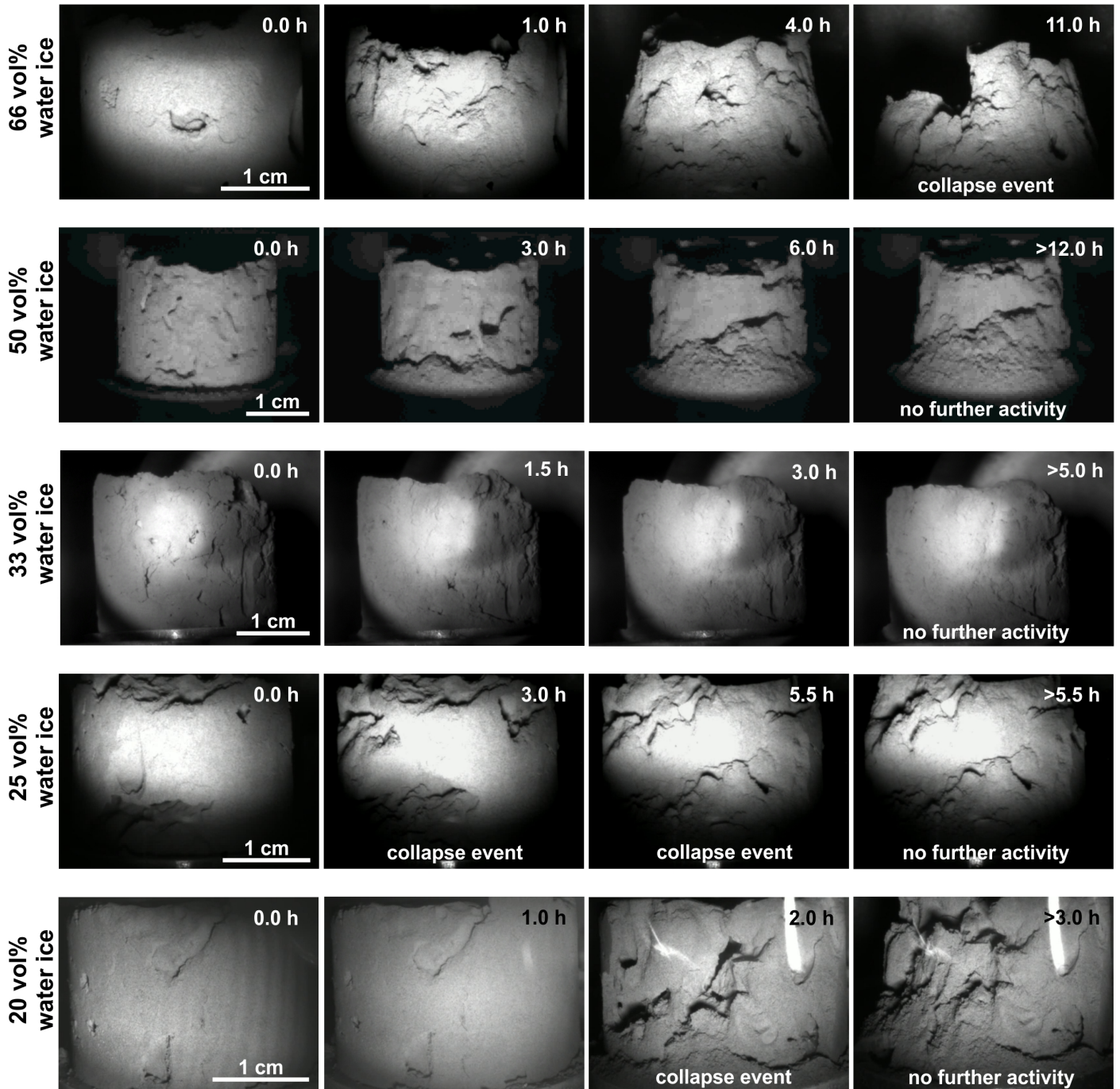
At the beginning of the insolation, the sample with a 66 vol% water ice content showed intense activity at its surface. Particles and macroscopic aggregates in the submillimeter range detached from the sample and were ejected from its surface. During this process, the vertical and smooth surface of the sample evolved to an irregularly rough surface and a thin layer of dust did accumulate. During this process the activity decreased continuously, and particles and aggregates were ejected less frequently and less far. After about 4 h, the initially vertical sample wall was tilted and showed only sporadic signs of morphologic alterations. At that time, the sample had lost more than half of its initial material. After an additional 7 h in the sublimation chamber and with a nearly unchanged morphology, the upper part of the sample collapsed spontaneously. The sample material that remained created a cliff-like structure (Fig. 8). The debris accumulated at the base of the sample and decayed into fine dust and aggregates whose grain size did not exceed one millimeter. When trying to examine the remaining sample material at the end of the experiment, we found that the debris appeared almost free of water and the slightest vibration or air-draft would immediately change the position and shape of the remains. Within the "cliff" and at the bottom of the sample, a substantial amount of water ice was still present. However, it could not be determined whether the total ice-to-dust ratio had changed significantly within the remaining sample material.

### 3.2.2. 50 vol% and 33 vol% water ice content

At the start of the insolation of the sample with 50 vol% ice and dust, respectively, a significant number of particles were ejected from the surface. After a few minutes, the distance covered by the particles decreased significantly and they accumulated at the base of the sample. Over the course of the experiment, a talus of debris grew on the insulated side of the sample (Fig. 8). The degree of activity and number of ejected particles remained relatively constant for the first 6 h, then activity slowed down significantly and came to an end after a total of 12 h. At that time, the accumulated debris material covered approximately the lower half of the sample. The upper half of the sample appeared to be covered by a thin layer of ice-depleted dust, but underneath this layer the original ice-dust ratio was preserved. The height of the sample and the side facing away from the light remained unchanged throughout the experiment.

The results of the experiment with 33 vol% ice strongly resemble the ones of the experiment with 50 vol% ice. However, the talus of accumulated material at the foot of the sample developed significantly less and the alterations on the sample's surface came to a complete end after 5 h.





**Fig. 8.** Evolution of the five different ice-dust mixtures with horizontal insolation. The occurrence of collapse events with different sample compositions is noticeable ([online movies](#)). Samples with a 33 vol% and 50 vol% water ice content show a continuous alteration of their shape until the end of the sublimation activity and formation of talus at their base. At a 25 vol% and 20 vol% water ice content, single events occurred in the form of cliff collapses exposing fresh material on the surface (see Fig. 5B). After 5.5 h and 3 h, respectively, no further alterations on the surface were visible. The bright areas in the upper right corner of the images with 20 vol% water ice are reflections of a light source in the laboratory on the observation window of the sublimation chamber.

The morphological development of these two samples is very similar to results with vertical insolation. Samples of both series of experiments showed the same granular structure and a talus formed for both types at their base.

### 3.2.3. 25 vol% and 20 vol% water ice content

The sample with a 25 vol% water ice content showed little ejection activity at the beginning, which came to an end after a few

minutes. The sample morphology did not change continuously as observed on previous samples, but two collapse events occurred. The first one after 3 h was limited to a small area, but during the second one after 5.5 h the whole insolated area collapsed. Both events can be read off well from the changes in the pressure curve (Figs. 5 and 8), because fresh volatile-containing material was exposed to the surface. This led to an increase in sublimation activity for about 40 min. After the second collapse, the surface of the sample was significantly roughened and became irregular

and ejection activity occurred again, and it decreased after about 30 min. From that point on, the morphology of the sample did not alternate until the end of the experiment.

The sample with 20 vol% water ice evolved similarly to that with a 25 vol% water ice content. At the start of the experiment, only a few particles were ejected from the insulated side. After about 2 h, this side collapsed and left a significantly irregular surface. After some subsequent minor alterations of the sample morphology, no additional changes were observed for the remainder of the experiment.

## 4. Discussion

The following sections discuss the grouped results of experiments with an insolation flux of about three solar constants (3.1 AU). Experiments with about 1 solar constant (4 AU) showed no surface alteration and are not discussed.

### 4.1. Vertical insolation

#### 4.1.1. 66 vol% water ice content

Samples with a water ice content of 66 vol% are similar in porosity (0.56) and density ( $0.57 \text{ g cm}^{-3}$ ) to 67P (Hornung et al. 2016; Langevin et al. 2017; Pätzold et al. 2018). However, the morphological features and the speed at which these were formed indicate that the high content of volatiles is unlikely to be present at the surface of 67P. The vapor pressure of the sublimating ice entrained all the detached dust particles, so that no ice-depleted cover layer could form. On the entire surface of the sample, fresh and ice-rich material was exposed for the full duration of the observation. This is in contradiction to Deep Impact and Rosetta observations, which showed discrete patches of volatile-rich material on an overall ice-depleted surface (Sunshine et al. 2006; Capaccioni et al. 2015). Furthermore, the high water ice content significantly increases the tensile strength of the sample (Haack et al. 2020). This results in the formation of exotic structures on the sample's surface that do not resemble the 67P morphology (Fig. 7). Extreme overhangs and nearly horizontal spikes with material accumulations at their free ends are an expression of very high cohesion between the particles, which was not observed on a comet. This experiment provides further indication that the near-surface composition of comets is dominated by refractory materials and not by volatile ices (Herique et al. 2017; Fulle et al. 2018; Pätzold et al. 2018).

#### 4.1.2. 50 vol% and 33 vol% water ice content

The increased dust content in samples with a 50 vol% and 33 vol% water ice content reduced the sublimation activity significantly. After 15–20 min, a layer of dust had formed on the horizontal top of the samples and prevented fresh ice from being insulated. Therefore, the height of the samples decreases only slightly during these experiments. This process was already observed in earlier experiments (e.g., Grün et al. 1993; Kührt & Keller 1994; Lämmerzahl et al. 1995) and could be a source of dust that covers substantial parts of the surface of 67P (Thomas et al. 2015a; Lai et al. 2016). It must be noted that significant amounts of dust are redeposited on 67P and substantial dust blankets do not have to have formed in situ on the comet's surface (Kramer & Noack 2015; El-Maarry et al. 2016; Lai et al. 2017; Cambianica et al. 2020).

The material loss of the samples occurred mainly on their vertical surfaces and made the granular structure of the samples visible. These grains can easily be removed against cohesion

and gravity via pressure drag forces and their size scaling to cometary conditions can be reproduced very well in in situ observations of millimeter- to decimeter-sized particles of 67P (Mottola et al. 2015; Rotundi et al. 2015; Fulle et al. 2016; Ott et al. 2017). In fact, the surface structure also resembles in situ observations from Rolis on Philae. Schröder et al. (2017) and Otto et al. (2020) describe the morphology of the cometary material on an actual millimeter scale. Our experiments are scaled to larger sizes, but the in situ images show cohesive material which we also produced. Despite the vertical walls not being directly insulated in our setup, the small amount of energy that reached the vertical walls was sufficient to sublimate the ice, which has a higher surface energy than fly ash (Haack et al. 2020) and acts as “glue.” Diffuse reflections from inside the chamber were unlikely due to the black coating of the inner cooling shield. With the reduced amount of ice, the tensile strength of the sample material decreased and ice-depleted material detached from the surface. Due to the high incidence angle at which the vertical surfaces were insulated, the incoming energy was not sufficient at ejecting the dust particles and aggregates as well as the talus that formed around the sample. Over time, the diameter of the sample decreased while its height remained mostly constant. This process has been suggested to be at work on 67P by Vincent et al. (2016).

This shows that the durability of an insulated object on a cometary surface depends not only on its material, but also on its shape if some illumination directions are obstructed. At vertical walls, the formation of stable dust layers is limited, so that local morphological features (boulders, cliffs, etc.) on a comet's surface can become the starting point of regressive erosion. With these two experimental setups, we could reproduce retreating scarps and boulder movements at taluses observed on comets 9P or 67P (e.g., Thomas et al. 2013; El-Maarry et al. 2017). The erosion only comes to rest when irregular surfaces are smoothed and covered by an ice-depleted layer of dust. This could be reproduced in the sample with 33 vol% water ice when after about 11 h substantial parts of the lateral surface were covered by the talus and enough dust had accumulated on the meanwhile nonvertical surfaces to prevent progressive erosion.

In 67P, fractures evolved within the cometary material to a length of up to several hundred meters (El-Maarry et al. 2015; Poulet et al. 2016) and formed networks of polygons. These polygons are predominantly 1–5 m in width, but they can exceed 13 m (Auger et al. 2018). They form when a near-surface layer is hardened by the sublimation and condensation of volatile materials (Spohn et al. 2015; Knapmeyer et al. 2018), and tensions can build up in the hardened layer. After the sublimation experiments, we observed the hardening of the samples' interiors, but we did not simulate diurnal cycles. Therefore, the samples were not exposed to a temperature-dependent volume change and subsequent mechanical stress. This may have prevented the formation of crack systems.

It is also possible that the samples in the laboratory were too small to develop a stress field sufficient to create visible fractures in the samples.

#### 4.1.3. 25 vol% and 20 vol% water ice content

The granular structure of the sample material with 25 vol% and 20 vol% water ice appeared to be very similar to that of samples with a higher water ice content. However, the small changes in the morphology of the samples show that the vapor pressure was no longer sufficient to continuously detach and eject particles (Finson & Probst 1968; Farnham et al. 2007). The high

dust content prevents a simple escape of gaseous water, so that a higher vapor pressure can build up near the sample's surface. This pressure is eventually released in an outburst event, entraining substantial parts of the surface. This could be interpreted as an analogous process of spontaneous jet formation on the rough surface of 67P (Tubiana et al. 2015; Vincent et al. 2015a,b). In the experiment, this process is suppressed after a few minutes by a cover layer of dust, which protected the underlying water ice from sublimation (see Grün et al. 1993; Kührt & Keller 1994).

This series of experiments showed that the type of sublimation activity and the morphologic appearance of the erosion process are depended on the volatile content. When the volatile content is large, the mass loss is fast but continuous (Fig. 6). As the dust content increases, the mass loss per time decreases and single but larger ejection events occur. This shows that sublimation activity is not necessarily a slow and continuous process, just as observed for 67P (Tubiana et al. 2015; Vincent et al. 2016). It is possible to suggest that the different outburst and activity patterns on 67P could also be attributed to a heterogeneous volatile content in the comet's material with the jet occurring in potentially more dust-rich areas. Vincent et al. (2016) actually attribute outbursts to areas with steep scarps. We find that the spatial distribution of outburst locations on the nucleus correlates well with morphological region boundaries, especially areas marked by steep scarps or cliffs.

#### 4.2. Horizontal insolation

Analog to the experiments with vertical insolation, the ice-dust mixtures were insolated horizontally in a series of sublimation experiments. Despite their identical composition, the morphology of the samples developed differently than under vertical insolation.

##### 4.2.1. 66 vol% water ice content

The sample with 66 vol% water ice showed a similarly high sublimation activity at the beginning of the experiment as under vertical insolation, but this activity decreased after a short time. The vertical wall quickly lost material, became very rough, and eroded more rapidly at the free surface at the top. Therefore, a thin layer of dust could more easily form on less intensively insolated areas. This prevented rapid and complete material loss. After 4 h, a thin dust layer had formed and only a few particles and aggregates were ejected. Due to the generally low dust content in the sample, the dust layer accumulated slowly, but was sufficient to prevent the complete sublimation of the ice.

After 11 h in the chamber, the upper part of the sample collapsed (Fig. 8). This shows that despite the thin protective dust layer, water sublimated from the sample material below. A comparable process of sublimation of volatiles through the porous mantle of cometary nuclei was reviewed by Belton (2010) and observed on 67P (Oklay et al. 2016). However, the collapse of the sample seems unexpected because remaining water ice in the sample would act as an adhesive. During experiments with vertical insolation, aggregates detached from the sample wall and scaled to a few centimeters to decimeters on a comet. In contrast, the cliff collapse under horizontal insolation in the laboratory would scale to several meters on a comet. In this size range, gravity plays a more important role in the laboratory and on the comet (Sánchez & Scheeres 2014; Bischoff et al. 2019) and subsequently the ice-depleted cliff collapsed under its own weight.

A further explanation for the reduced sublimation rate compared to vertical insolation could be found in the sample preparation phase. It cannot be completely excluded that at the moment

the sample was placed in the chamber, its surface temperature increased above 150 K and the superficial ice particles started to sinter (Kuroiwa 1961; Gundlach et al. 2018a). This would have greatly increased the tensile strength of the sample material and made changes in morphology more difficult. In this case, the cliff collapse would have been unlikely.

##### 4.2.2. 50 vol% and 33 vol% water ice content

As under vertical insolation, the samples with a 50 vol% and 33 vol% water ice content altered comparable to continuously receding cliffs and they formed taluses of debris as observed for cometary nuclei (Farnham et al. 2013; Vincent et al. 2015a,b). However, the timescales on which this occurred were different. Due to direct horizontal insolation of the lateral sample's surface, the sublimation phase was more intense but it slowed down much earlier. This resulted in a faster development of the ice-reduced talus and dust layer. They covered substantial areas of the surface much earlier and prevented further sublimation activity such as the ejection of particles. This explains the paradox that despite direct insolation, the sample became inactive more quickly.

The fact that the samples tended to lose material rather continuously than in larger cliff collapses could be due to their water ice content, which increases the tensile strength (Haack et al. 2020). Also the random internal structure of the individual samples may prevent collapses.

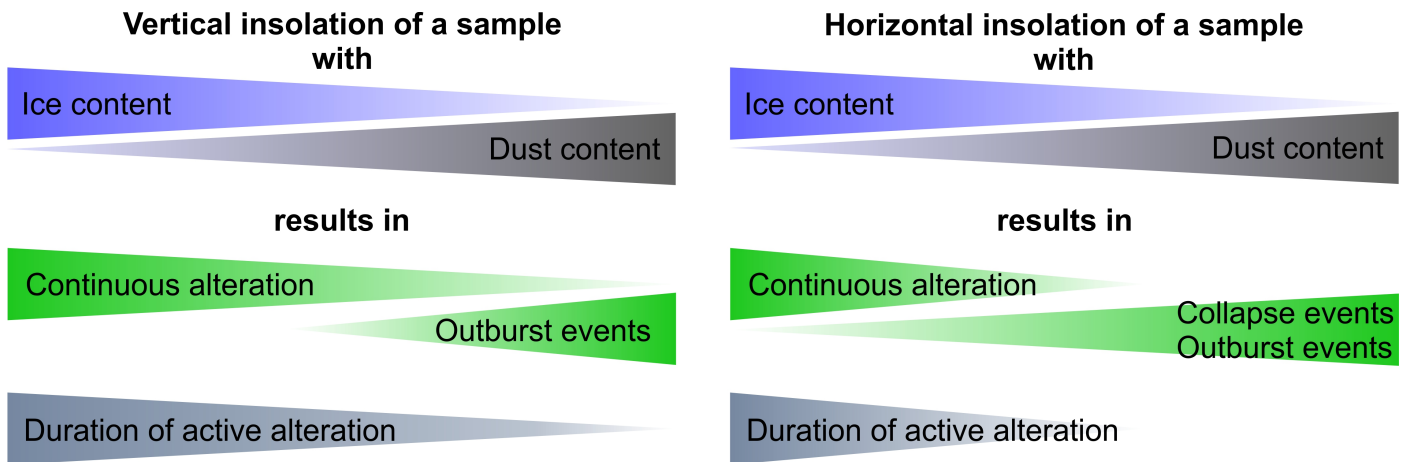
##### 4.2.3. 25 vol% and 20 vol% water ice content

The morphological development of the samples with only 25 vol% and 20 vol% water ice was different compared to that with the same volatile content but insolated vertically. The cliff collapses occurred after the insolated area became unstable due to the loss of water by sublimation (Belton 2010). This could not be observed on horizontal surfaces because vertical mass transport is not possible. Therefore, the mass loss of even volatile-depleted samples was enhanced under horizontal insolation compared to vertical insolation. The reactivated release of volatiles after collapse events corresponds to the observations of 67P where cliff collapses and other mass wasting processes are linked to the local formation of gas jets (Steckloff et al. 2016; Oklay et al. 2016; Vincent et al. 2016). As the activity of the sample ended, its surface appeared very similar to the rough surface of 67P in close-up images (e.g., Vincent et al. 2015a,b; Schröder et al. 2017).

At the end of the experiments, the final morphologies of the different samples were comparable when insolated horizontally. The stable remains of the samples displayed very rough and irregular surfaces, while the fine-grained debris material formed a talus at the bottom of the sample. However, the formation processes were different: from a longer lasting and uniform sublimation activity of samples with high volatile content to an event-dominated and faster ending activity of samples with low volatile content. Since continuous and thus high sublimation rates would let a comet decay quickly and observations of 67P would suggest episodic activity (Tubiana et al. 2015; Steckloff et al. 2016; Vincent et al. 2016), a low near-surface ice content up to 20 vol% seems plausible on a comet.

Despite many similarities between morphologies of laboratory experiments and in situ observations, it must be noted that our comet analog material is a rough approximation of the actual cometary material. Thus, in our setup we completely abstained from using organic materials (Capaccioni et al. 2015; Goesmann et al. 2015; Fulle et al. 2017). However, their influence on the





**Fig. 9.** Schematic and qualitative overview of parameters affecting the alteration of the sample's surfaces in the experiment. Vertical insolation and high ice content result in a more continuous alteration and increase its duration. Horizontal insolation and high dust content result more often in spontaneous outburst and collapse events and decrease the overall duration of active surface alteration.

development of cometary surfaces cannot be underestimated and must be analyzed in future experiments.

None of the sublimation experiments with an insolation flux of  $\sim 1$  solar constant resulted in visible changes in the sample's surfaces. According to our scaling, this insolation flux corresponds to a heliocentric distance of the comet of  $\sim 4$  AU and at this distance 67P already showed activity on its surface (Tubiana et al. 2015). For this discrepancy, the following two explanations are possible. (1) The scaling is not sufficiently accurate and the required energy for a simulated heliocentric distance of the comet was underestimated. (2) The sample mixture does not reflect the composition of a comet accurately enough.

Since the physical correlation between sublimation and van der Waals related cohesion have been well described in previous publications as the main suppressor of cometary activity (Chokshi et al. 1993; Kührt & Keller 1994; Scheeres et al. 2010; Skorov & Blum 2012), it is most likely that the reason for the negative results lies within the sample mixture. The increased albedo and the absence of other volatiles and organic material in the laboratory are major differences to the composition of comets possibly reducing the laboratory cometary activity. Nevertheless, the influence of the albedo on the required energy in the laboratory was taken into account in Eq. (4).

A probable explanation for cometary activity at large heliocentric distances is the presence of  $\text{CO}_2$ , CO, and other super-volatile ices (Bockelée-Morvan & Biver 2017; Läuter et al. 2018; Gundlach et al. 2015), which start to sublimate at lower temperatures. Since we only used water ice as volatile, this could shift the sublimation activity of the samples to higher insolation fluxes. Additionally, it is conceivable that the presence of organic material in 67P favors the absorption of energy due to their dark color (Ciarniello et al. 2015) and allows ices to sublimate faster on the comet.

## 5. Conclusions

The insolation flux required to generate sublimation activity on a sample and thus a cometary surface depends on its content of different volatile materials. Using water ice as the only volatile, it was not possible to generate activity at a distance equivalent to about 4 AU in the laboratory. However, at a simulated heliocentric distance of 3.1 AU, pronounced activity could be generated.

All of the prepared sample mixtures presented a similar granular structure. The dust and ice particles, which were used as analog materials, formed submillimeter- to millimeter-sized aggregates. These aggregates would correspond to centimeter- to decimeter-sized pebbles on 67P and simulate the predicted granular structure of the comet (Fulle et al. 2016; Blum et al. 2017; Pajola et al. 2016a).

The volatile content of the sample has a major influence on the type of sublimation activity (Fig. 9). Volatile-rich samples are subject to the generally continuous and rapid loss of ice and dust. Due to the low dust content, no uppermost layer of dust forms, or only slowly, which would prevent extensive sublimation by covering fresher material. Simultaneously, the high water ice content increases the tensile strength (Haack et al. 2020) and allows the formation of exotic morphologies such as spikes or extreme overhangs.

When the amount of dust in the samples increases, the activity comes to an earlier end due to an evolving protective layer of dust. At the same time, the activity gets a more episodic character resulting in outburst events or cliff collapses. The resulting water-depleted deposits are less cohesive, but they form very irregular and more stable surfaces compared to volatile-rich materials.

The shape of the surface features and the angle at which they are insolated can partly compensate for the effects of different volatile content. Under vertical insolation, layers of dust can form on horizontal surfaces. These layers remain stable due to reduced gravitational transport processes. Thus the underlying, possibly volatile-rich material remains unaffected by sublimation and the height of a sample or an area on a comet remains largely constant.

This changes with the horizontal insolation of features that allow material to fall down (scarps, pits, etc.). If an ice-depleted layer forms on a steep wall, it collapses when its weight exceeds its cohesion and exposes fresh volatile-containing material. This process can repeat episodically and lead to regressive erosion along a scarp. In this geometry, Earth's gravity helps to get rid of desiccated dust mantles. This could perhaps mimic the aerodynamic drag of the escaping gas with the loosened dust bodies on the surface.

The erosion comes to an end when the initial scarp develops an irregular or rough shape that no longer permits vertical mass transport. Additionally, the formation of a talus of debris can



cover substantial parts of the original morphological feature and protect it from further erosion. This was typical for mixtures with a moderate water ice content.

Our investigations suggest that a volatile content of more than 50 vol% (<2.4 dust-to-ice mass ratio) in the outer layers of 67P is unlikely since the morphological features generated in the laboratory and high sublimation rates were not found in 67P. Due to the generally low activity of samples with a volatile content of 25 vol% (>7.3 dust-to-ice mass ratio) and less, these values are also unlikely, but they cannot be excluded completely. Our experiments based on the morphologic evolution of surface structures suggest that near the surface, a comet possesses dust-to-ice ratios between these limits. The results obtained in the laboratory are most consistent with observations and predictions for 67P (Herique et al. 2017; Fulle et al. 2018; Pätzold et al. 2018). However, further experiments are necessary to study, in more detail, the influence of organic matter on the morphological development of cometary surfaces.

*Acknowledgements.* This work was carried out in the framework of the CoPhyLab project funded by the D-A-CH programme (GU 1620/3-1 and BL 298/26-1/SNF 200021E 177964/FWF I 3730-N36). The research project “The Physics of Volatile-Related Morphologies on Asteroids and Comets” is funded by the DLR Management Board Young Research Group Leader Programme and the Executive Board Member for Space Research and Technology. We gratefully acknowledge their financial support and endorsement. Many thanks to I. Büttner from DLR Berlin for sieving the fly ash, to U. Altenberger from the University of Potsdam for providing SEM images and chemical analysis of fly ash and to M. Neuhaus for providing images of ice particles.

## References

- Agarwal, J., A’Hearn, M. F., Vincent, J.-B., et al. 2016, *MNRAS*, 462, S78
- Attree, Groussin, O., Jorda, L., et al. 2018, *A&A*, 611, A33
- Auger, A.-T., Groussin, O., Jorda, L., et al. 2018, *Icarus*, 301, 173
- Belton, M. J. 2010, *Icarus*, 210, 881
- Bischoff, D., Gundlach, B., Neuhaus, M., & Blum, J. 2019, *MNRAS*, 483, 1202
- Biver, Bockelée-Morvan, D., Hofstadter, M., et al. 2019, *A&A*, 630, A19
- Blum, J., Schrapler, R., Davidsson, B. J. R., & Trigo-Rodríguez, J. M. 2006, *ApJ*, 652, 1768
- Blum, J., Gundlach, B., Mühle, S., & Trigo-Rodríguez, J. M. 2014, *Icarus*, 235, 156
- Blum, J., Gundlach, B., Krause, M., et al. 2017, *MNRAS*, 469, S755
- Bockelée-Morvan, D., & Biver, N. 2017, *Phil. Trans. Roy. Soc. A: Math. Phys. Eng. Sci.*, 375, 20160252
- Bockelée-Morvan, D., Crovisier, J., Erard, S., et al. 2016, *MNRAS*, 462, S170
- Cambianica, P., Fulle, M., Cremonese, G., et al. 2020, *A&A*, 636, A91
- Capaccioni, F., Coradini, A., Filacchione, G., et al. 2015, *Science*, 347, aaa0628
- Chokshi, A., Tielens, A. G. G. M., & Hollenbach, D. 1993, *ApJ*, 407, 806
- Chýlek, P., Ramaswamy, V., & Srivastava, V. 1983, *J. Geophys. Res.: Oceans*, 88, 10837
- Ciarniello, M., Capaccioni, F., Filacchione, G., et al. 2015, *A&A*, 583, A31
- Clark, R. N., & Lucey, P. G. 1984, *J. Geophys. Res.: Solid Earth*, 89, 6341
- El-Maarry, M. R., Thomas, N., Gracia-Berná, A., et al. 2015, *Geophys. Res. Lett.*, 42, 5170
- El-Maarry, M. R., Thomas, N., Gracia-Berná, A., et al. 2016, *A&A*, 593, A110
- El-Maarry, M. R., Groussin, O., Thomas, N., et al. 2017, *Science*, 355, 1392
- El-Maarry, M. R., Groussin, O., Keller, H. U., et al. 2019, *Space Sci. Rev.*, 215, 36
- Farnham, T., Wellnitz, D., Hampton, D., et al. 2007, *Icarus*, 187, 26
- Farnham, T., Bodewits, D., Li, J.-Y., et al. 2013, *Icarus*, 222, 540
- Finson, M. J., & Probst, R. F. 1968, *ApJ*, 154, 327
- Fulle, M., Della Corte, V., Rotundi, A., et al. 2016, *MNRAS*, 462, S132
- Fulle, M., Della Corte, V., Rotundi, A., et al. 2017, *MNRAS*, 469, S45
- Fulle, M., Blum, J., Green, S. F., et al. 2018, *MNRAS*, 482, 3326
- Goesmann, F., Rosenbauer, H., Bredehöft, J. H., et al. 2015, *Science*, 349, aab0689
- Groussin, O., Jorda, L., Auger, A.-T., et al. 2015, *A&A*, 583, A32
- Grün, E., Bar-Nun, A., Benkhoff, J., et al. 1989, *Int. Astron. Union Colloq.*, 116, 277
- Grün, E., Gebhard, J., Bar-Nun, A., et al. 1993, *J. Geophys. Res.: Planets*, 98, 15091
- Gulkis, S., Allen, M., von Allmen, P., et al. 2015, *Science*, 347, aaa0709
- Gundlach, B., Skorov, Y., & Blum, J. 2011, *Icarus*, 213, 710
- Gundlach, B., Blum, J., Keller, H. U., & Skorov, Y. V. 2015, *A&A*, 583, A12
- Gundlach, B., Ratte, J., Blum, J., Oesert, J., & Gorb, S. N. 2018a, *MNRAS*, 479, 5272–5287
- Gundlach, B., Schmidt, K. P., Kreuzig, C., et al. 2018b, *MNRAS*, 479, 1273
- Haack, D., Otto, K. A., Gundlach, B., et al. 2020, *A&A*, 642, A218
- Hässig, M., Altwegg, K., Balsiger, H., et al. 2015, *Science*, 347, aaa0276
- Herique, A., Kofman, W., Beck, P., et al. 2017, *MNRAS*, 462, S516
- Hornung, K., Merouane, S., Hilchenbach, M., et al. 2016, *Planet. Space Sci.*, 133, 63
- Kappel, D., Sachse, M., Haack, D., & Otto, K. A. 2020, *A&A*, 641, A19
- Kaufmann, E., & Hagermann, A. 2018, *Icarus*, 311, 105
- Keller, H. U., Mottola, S., Hviid, S. F., et al. 2017, *MNRAS*, 469, S357
- Knapmeyer, M., Fischer, H.-H., Knollenberg, J., et al. 2018, *Icarus*, 310, 165
- Kochan, H., Roessler, K., Ratke, L., et al. 1989, in *ESA SP, 302, Physics and Mechanics of Cometary Materials*, eds. J. J. Hunt, & T. D. Guyenne, 115
- Kossacki, K., Kömle, N., Leliwa-Kopystyński, J., & Kargl, G. 1997, *Icarus*, 128, 127
- Kramer, T., & Noack, M. 2015, *ApJ*, 813, L33
- Kretke, K., & Levison, H. 2015, *Icarus*, 262, 9
- Kührt, E. 1984, *Icarus*, 60, 512
- Kührt, E., & Keller, H. U. 1994, *Icarus*, 109, 121
- Kuroiwa, D. 1961, *Tellus*, 13, 252
- Lai, I. L., Ip, W. H., Lee, J. C., et al. 2016, in *AGU Fall Meeting Abstracts*, P43A-2087
- Lai, I.-L., Ip, W.-H., Su, C.-C., et al. 2017, *MNRAS*, 462, S533
- Lämmerzahl, P., Gebhard, J., Grün, E., & Klees, G. 1995, *Planet. Space Sci.*, 43, 363
- Langevin, Y., Hilchenbach, M., Vincendon, M., et al. 2017, *MNRAS*, 469, S535
- Läuter, M., Kramer, T., Rubin, M., & Altwegg, K. 2018, *MNRAS*, 483, 852
- Lorek, Gundlach, B., Lacerda, P., & Blum, J. 2016, *A&A*, 587, A128
- Lorek, S., Lacerda, P., & Blum, J. 2018, *A&A*, 611, A18
- Mottola, S., Arnold, G., Grothues, H.-G., et al. 2015, *Science*, 349, aab0232
- Musioli, G., & Wurm, G. 2019, *ApJ*, 873, 58
- Oehler, A., & Neukum, G. 1991, *Geophys. Res. Lett.*, 18, 253
- Oklay, N., Vincent, J.-B., Fornasier, S., et al. 2016, *A&A*, 586, A80
- O’Rourke, L., Heinisch, P., Blum, J., et al. 2020, *Nature*, 586, 697
- Ott, T., Drolshagen, E., Koschny, D., et al. 2017, *MNRAS*, 469, S276
- Otto, K. A., Matz, K.-D., Schröder, S. E., et al. 2020, *MNRAS*, 500, 3178
- Pajola, Vincent, Jean-Baptiste, Güttler, Carsten, et al. 2015, *A&A*, 583, A37
- Pajola, M., Lucchetti, A., Fulle, M., et al. 2016a, *MNRAS*, 469, S636
- Pajola, M., Oklay, N., Forgia, F. L., et al. 2016b, *A&A*, 592, A69
- Panale, F. P., & Salvail, J. R. 1984, *Icarus*, 60, 476
- Pätzold, M., Andert, T. P., Hahn, M., et al. 2018, *MNRAS*, 483, 2337
- Poch, O., Pommerol, A., Jost, B., et al. 2016a, *Icarus*, 266, 288
- Poch, O., Pommerol, A., Jost, B., et al. 2016b, *Icarus*, 267, 154
- Poulet, F., Lucchetti, A., Bibring, J.-P., et al. 2016, *MNRAS*, 462, S23
- Pommerol, A., Jost, B., Poch, O. et al. 2015, *Planet. Space Sci.*, 109, 106
- Raponi, A., Ciarniello, M., Capaccioni, F., et al. 2020, *Nat. Astron.*, 5, 500
- Rotundi, A., Sierks, H., Della Corte, V., et al. 2015, *Science*, 347, aaa3905
- Sandford, S. A., Aléon, J., Alexander, C. M. D., et al. 2006, *Science*, 314, 1720
- Scheeres, D., Hartzell, C., Sánchez, P., & Swift, M. 2010, *Icarus*, 210, 968
- Schröder, S., Mottola, S., Arnold, G., et al. 2017, *Icarus*, 285, 263
- Sierks, H., Barbieri, C., Lamy, P. L., et al. 2015, *Science*, 347, aaa1044
- Skorov, Y., & Blum, J. 2012, *Icarus*, 221, 1
- Sánchez, P., & Scheeres, D. J. 2014, *Meteor. Planet. Sci.*, 49, 788
- Snodgrass, C., Tubiana, C., Bramich, D. M., et al. 2013, *A&A*, 557, A33
- Spohn, T., Knollenberg, J., Ball, A. J., et al. 2015, *Science*, 349, aab0464
- Steckloff, J. K., Graves, K., Hirabayashi, M., Melosh, H. J., & Richardson, J. E. 2016, *Icarus*, 272, 60
- Sunshine, J. M., A. Hearn, M. F., Groussin, O., et al. 2006, *Science*, 311, 1453
- Thomas, P., A’Hearn, M., Belton, M., et al. 2013, *Icarus*, 222, 453, stardust/EPOXI
- Thomas, N., Davidsson, B., El-Maarry, M. R., et al. 2015a, *A&A*, 583, A17
- Thomas, N., Sierks, H., Barbieri, C., et al. 2015b, *Science*, 347, aaa0440
- Tubiana, Snodgrass, C., Bertini, I., et al. 2015, *A&A*, 573, A62
- Vincent, J.-B., Bodewits, D., Besse, S., et al. 2015a, *Nature*, 523, 63
- Vincent, J.-B., Oklay, N., Marchi, S., Höfner, S., & Sierks, H. 2015b, *Planet. Space Sci.*, 107, 53
- Vincent, J.-B., A’Hearn, M. F., Lin, Z.-Y., et al. 2016, *MNRAS*, 462, S184
- Zsom, Ormel, C. W., Güttler, C., Blum, J., & Dullemond, C. P. 2010, *A&A*, 513, A57

**2.2.3 Haack et al. (2021b)**

Haack, D., Kreuzig, C., Gundlach, B., Blum, J., & Otto, K. A. (2021b). Sublimation of Organic-rich Comet Analog Materials and their Relevance in Fracture Formation. *Astronomy & Astrophysics*, 653, A153. <https://doi.org/10.1051/0004-6361/202142069>.

The laboratory work comprised in this article has been conducted by D. Haack. I provided the initial idea of investigation morphologic evolution of sublimating analogue materials and established the collaboration with the CoPhyLab network. C. Kreuzig, B. Gundlach and J. Blum are collaborators at the University of Braunschweig who provided the equipment and trained D. Haack to use the facilities. I helped choosing the organic materials and mixing ratios. I contributed to interpreting the fracture formation and the morphologic evolution of the samples. I also assembled data for Figure 4 and provided feedback on the comparability of cometary and laboratory morphologies. All authors assisted with the data interpretation and with refining the manuscript.

# Sublimation of organic-rich comet analog materials and their relevance in fracture formation<sup>★</sup>

David Haack<sup>1</sup>, Christopher Kreuzig<sup>2</sup>, Bastian Gundlach<sup>2</sup>, Jürgen Blum<sup>2</sup>, and Katharina Otto<sup>1</sup>

<sup>1</sup> Institut für Planetenforschung, Deutsches Zentrum für Luft- und Raumfahrt (DLR), Berlin, Germany  
e-mail: david.haack@dlr.de

<sup>2</sup> Institut für Geophysik und Extraterrestrische Physik, Technische Universität Braunschweig, Braunschweig, Germany

Received 23 August 2021 / Accepted 6 September 2021

## ABSTRACT

**Aims.** The morphology of cometary nuclei is the result of an ongoing evolution and can provide valuable information to constrain the composition of comets. In our laboratory experiments we investigated the morphological evolution of comet analog materials, which consist of volatile, dust, and organic components. The laboratory results are aimed to help understand the evolution of cometary surfaces.

**Methods.** We used spherical particles of fly ash and mixtures of ice, glycine, and sodium acetate as analog materials in different mass ratios to reproduce observed cometary morphologies. The cohesive and gravitational properties in the laboratory are scaled to cometary conditions to draw meaningful conclusions from the experimental results. The samples were placed in a vacuum sublimation chamber, cooled down to below 150 K, and were insolated with an external light source. To analyze the morphology of the samples, a camera was used to monitor the alterations of the surface.

**Results.** Organic components in volatile-rich samples can have a distinct adhesive effect after the volatiles sublimate. During the sublimation process the sample volume decreases and fractures form on the sample surface. Due to the stability of the remaining volatile-depleted material, significant cliff collapses or ejected particles were not observed in the laboratory.

**Key words.** comets: general – methods: laboratory: solid state – planets and satellites: formation

## 1. Introduction

Comets are primordial objects from the early days of the Solar System. Due to their origin from the outer Solar System beyond the ice lines of volatile materials (Dodson-Robinson et al. 2009), they have been subject to no or only minor alterations since their formation and thus are archives with information about the early Solar System. This makes them interesting targets for space missions that have studied comets at close range since the mid-1980s (e.g., ESA's Giotto and Rosetta missions and NASA's Stardust and Deep Impact missions). Even with these missions, the processes leading to the formation of comets and their evolution are not yet fully understood (Weissman et al. 2020). Which amounts of volatile and nonvolatile materials are present in a cometary nucleus and which processes alter a comet's surface as it approaches the Sun are still the subject of investigation (Gulkis et al. 2015; Sierks et al. 2015). The sublimation of volatile components, such as CO, CO<sub>2</sub>, or H<sub>2</sub>O (Hässig et al. 2015; Läuter et al. 2018; Biver et al. 2019), is caused by the insolation of solar energy to the surface and the heat transfer to the shallow subsurface of a comet in an airless environment. During this process, layers of nonvolatile mineralic and organic components (Capaccioni et al. 2015; Goesmann et al. 2015; Raponi et al. 2020) accumulate at the surface and can be redeposited or transported away by the gas drag of continuously sublimating volatiles (Kührt & Keller 1994; Gundlach et al. 2015, 2020; Keller et al. 2017; Bischoff et al. 2019). With each orbit around the Sun, a comet loses more material via progressive erosion

(Thomas et al. 2015a) and a variety of morphologies are formed on its surface, such as cliffs, fractures, and rocky or flat areas (Thomas et al. 2015b; Pajola et al. 2016; El-Maarry et al. 2019). The appearance of morphological features are determined by the chemical composition, grain size, porosity, and cohesive and gravitational forces of the comet's nucleus. Therefore, the reproduction and analysis of cometary morphologies in the laboratory may provide information about the composition and evolutionary history of comets in space.

Laboratory experiments, such as the KOSI (KOMetenSimulation) project in the 1990s, have studied sublimation processes that are expected to take place on comets (Grün et al. 1989, 1993; Lämmerzahl et al. 1995). As part of the KOSI project, a sample container was filled with mixtures of nonvolatile analog materials and ices and was placed in a sublimation chamber. After the samples were insolated with an energy source, an ice-free layer formed on their surfaces, preventing energy transport to underlying layers and further sublimation processes after a few hours. With the Rosetta mission and its landing module Philae, cometary science and laboratory analog experiments increasingly came into focus. The measurements and detailed images of comet 67P/Churyumov-Gerasimenko (hereafter 67P) provided by the spacecraft significantly increased our knowledge of comets. Nevertheless, the influence of detected volatiles, organic compounds, and their abundances (e.g., Hässig et al. 2015; Läuter et al. 2018; Capaccioni et al. 2015; Raponi et al. 2020) on the evolution of the comet remains a research objective vital to the interpretation of cometary surfaces.

In order to more precisely determine the properties of materials that could be considered for analog experiments, several

<sup>★</sup> Movies are available at <https://www.aanda.org>

series of measurements have been performed. It was found that the tensile strength of water ice at temperatures below 150 K is much lower than expected (Gundlach et al. 2018b; Musiolik & Wurm 2019). This temperature limit should not be exceeded in the experiment; if so, water ice particles start to sinter and stiff connections form between the particles (Kuroiwa 1961; Gundlach et al. 2018a). Furthermore, it was shown that spherical particles could produce samples whose low tensile strengths and filling factors are closer to those of comets than of samples made of angular particles (Haack et al. 2020). The filling factor describes the ratio of a volume filled with particles. Besides applications in the laboratory, these findings were also used to calibrate numerical models of comet simulations (Kappel et al. 2020).

Analog experiments with the Simulation Chamber for Imaging the Temporal Evolution of Analogue Samples (SCITEAS; Pommerol et al. 2015) allowed photometric studies and visual observation of sublimating sample surfaces at temperatures and pressures similar to those expected on the surface of comets at low heliocentric distances. Poch et al. (2016a,b) used SCITEAS to investigate the influence of organic and mineralic components on the sublimation behavior of water ice. They found that the texture of the residuals after sublimation of the ice differed significantly depending on whether the nonvolatile components were included in the ice matrix (intra-mixtures) or were added as pure substances to pure ice particles (inter-mixture). The residuals of intra-mixtures were extremely porous and foam-like, and cohesive large flakes sometimes ejected from the surface. Inter-mixtures formed more compact and less cohesive residuals on the sample surface during the sublimation process. However, the aim of these experiments was not to realistically reproduce cometary morphologies. Therefore, the amount of nonvolatile materials accounted for less than one percent by mass in the mixtures and was not representative of cometary regolith. Kaufmann & Hagermann (2018) conducted sublimation experiments with water ice and carbon black and, like Poch et al. (2016b), observed a solidified subsurface layer under an ice-depleted and low-density cover layer. This suggests the subsurface hardening of volatile-rich and porous materials due to sublimation and recondensation (Kochan et al. 1989; Kossacki et al. 1997).

Most of these experiments were not aimed at reproducing cometary morphologies and were performed with volatile contents of >90 vol%, which are atypical for comets. To produce more realistic morphologies in the laboratory, Haack et al. (2021) performed sublimation experiments with more representative dust-ice ratios. They used fly ash (a by-product of industrial coal combustion) as the mineralic dust component and water ice particles as the volatile. The amount of ice in the sample material ranged between 66 vol% and 25 vol%, as presumed for comets (Herique et al. 2017; Fulle et al. 2018; Pätzold et al. 2018). In addition, they allowed horizontal and vertical mass transport of the sample material and found that the resulting sublimation activities and morphologies depend on the insolation angle in addition to the volatile content.

We decided to expand on previous experiments with refractory fly ash and volatile water ice (Haack et al. 2020, 2021) and added organic components as analog materials to the mixtures. The organic components consisted of sodium acetate and glycine in equal parts per mass, which are confirmed on 67P and are nonvolatile materials under our experimental conditions. Based on the findings of the Rosetta satellite mission and laboratory measurements, we prepared sample mixtures of volatile and nonvolatile materials in different ratios as plausible on a

comet (Choukroun et al. 2020; Haack et al. 2021). For this, we took advantage of the low tensile strength of granular matter composed of spherical particles at temperatures below 150 K (Gundlach et al. 2018b; Haack et al. 2020). The aim of the experiments is to investigate the influence of organic components on the sublimation activity and the evolution of the sample morphology and to analyze the results for their relevance with respect to cometary surfaces.

## 2. Methods

### 2.1. Selection of materials

As in previous sublimation experiments (Haack et al. 2021), polydisperse fly ash spheres, with an average radius of about 2.4  $\mu\text{m}$  and a density of 2.25  $\text{g cm}^{-3}$ , were used as a refractory dust analog. This material is a compromise between physical and chemical accuracy of dust on a comet. Fly ash corresponds to the mineralic composition of plagioclase (Haack et al. 2021) and is therefore more representative of a mineralic component of a comet compared to particles of pure  $\text{SiO}_2$ . Due to their spherical shape, mutual particle interlocking is prevented. Furthermore, it is possible to produce samples with a very low tensile strength in the laboratory (Haack et al. 2020; Kappel et al. 2020) to simulate the physical properties of cometary materials (Groussin et al. 2015; Attree et al. 2018a). The minerals olivine and pyroxene would be more accurate chemical analogs, but micrometer-sized particles of these minerals are only available with an angular shape. This would result in a drastic increase in the tensile strength of the sample material (Haack et al. 2020) and could reduce or prevent the alteration of the sample surface during the experiments.

As volatile analog material, we used polydisperse water ice spheres with an average radius of about 2.4  $\mu\text{m}$ . Water ice dominates the volatile materials on 67P (Hässig et al. 2015) and was used as a first grade approximation of the volatile component of a comet. Other volatiles, such as CO or  $\text{CO}_2$ , contribute 15 mass% to the amount of volatile materials on 67P (Bockelée-Morvan et al. 2016; Läuter et al. 2018; Biver et al. 2019) and may play an important role in the evolution of a comet but were omitted to limit the complexity of the experiments. This is a reasonable limitation because in our experiments we simulated cometary conditions in which the sublimation of water may predominate since CO or  $\text{CO}_2$  are more volatile and would already be sublimated in the simulated scenario. However, the influence of other ices on the activity of a simulated comet should be studied in future experiments.

The additional third component should be a combination of organic materials that is nonvolatile both on a cometary surface and under experimental conditions. Since the composition of the organic components of a comet is very complex (Capaccioni et al. 2015; Goesmann et al. 2015; Altwegg et al. 2017), we had to limit the number of organic components in our experiments to a few materials that may represent the chemical properties of a large variety of organic materials on a comet. We used a combination of sodium acetate ( $\text{NaCH}_3\text{COO}$ ) and glycine ( $\text{C}_2\text{H}_5\text{NO}_2$ ) in equal amounts, which are confirmed as components of 67P (e.g., Elsila et al. 2009; Altwegg et al. 2016; Rubin et al. 2019; Schuhmann et al. 2019). Sodium acetate represents organic ions and salts, and glycine is a simple amino acid and stands for a group of organic components that can potentially form larger and complex molecules. This selection of organic analog materials is very limited and cannot reflect the complexity of organic materials on a comet; however, this was inevitable since the



actual composition of organic components on a comet is not fully understood and we had to limit the complexity of the experiments. Other combinations of organic materials could be conceivable, but a limited selection would generally not be able to simulate the complete variety of organic material on a comet. An additional reason for the chemical limitation was the feasibility of the experiments in terms of the components' toxicity. The nonvolatile character of the organic components was confirmed in previous measurements with the same experimental setup.

We omitted the usage of additional materials to reduce the sample's albedo. This is not realistic because comets have a very low albedo (Keller et al. 1986; Ciarniello et al. 2015) and absorb insolated radiation much better than the analog material. However, this effect was taken into account in the energy scaling (see Haack et al. 2021) and led to increased insolation rates in the laboratory. This allowed the direct comparison of the obtained results with previous sublimation experiments without organic components (Haack et al. 2021), where all samples had an albedo of  $\sim 0.35$ . This decision also kept the complexity of the experiment within limits and reduced the number of possibly interfering effects at the sample's surfaces.

## 2.2. Sample preparation

To keep the results comparable to those of previous experiments, the sample preparation method was adapted from Gundlach et al. (2018b) and Haack et al. (2020). Water mist was generated with a droplet dispenser and sprayed into a Dewar vessel containing liquid nitrogen. The droplets froze in the liquid nitrogen to form polydisperse spherical ice particles and sank to the bottom of the container.

We modified this method: the droplet dispenser was filled with an aqueous solution of the organic molecules instead of pure water. For this, sodium acetate and glycine were mixed in equal mass ratios (hereafter referred to as organics) and completely dissolved in water. In order to study the influence of different ratios of organic materials and water, two solutions were prepared, with the organic-to-water mass ratios of 10:100 and 5:100.

The resulting particles in the Dewar vessel consisted of organic components enclosed in an ice matrix. The advantage of this method was that the pure organic analog materials did not have to be shaped into micrometer-sized spheres to be comparable to fly ash and water ice particles. In addition, Hadraoui et al. (2019) suggested that glycine embedded in a sublimating ice matrix reproduces the emitted glycine detected in the coma of 67P most realistically.

Archimedes' principle was used to determine the amount of organic-bearing ice particles in the Dewar vessel. The weights of the same volumes of pure liquid nitrogen and of the liquid nitrogen-ice suspension were measured. Using the weight difference of the two measurements and the known densities of liquid nitrogen and ice (Table 1), the mass of ice in the Dewar vessel was calculated. After the amount of ice particles in the vessel was determined, a scale was used to add predefined amounts of fly ash to the suspension. The relative amounts of ice to fly ash were selected between 20 and 40 mass%; they correspond to the ratios estimated for the nucleus of 67P (Herique et al. 2017; Fulle et al. 2018; Pätzold et al. 2018) and are comparable to those of the sublimation experiments carried out by Haack et al. (2021).

A cylindrical metal mold was filled with the suspensions of organic-bearing ice, fly ash, and liquid nitrogen in the Dewar vessel, which were thoroughly mixed. The mold had an inner diameter of 25 mm and was placed vertically on a metal sample

**Table 1.** Molar mass and density of components used to simulate cometary materials.

	Molar mass (g mol <sup>-1</sup> )	Density (g cm <sup>-3</sup> )
Fly ash		2.25
H <sub>2</sub> O (ice)	18.02	0.93
NaCH <sub>3</sub> COO	82.03	1.52
C <sub>2</sub> H <sub>5</sub> NO <sub>2</sub>	75.07	1.60
N <sub>2</sub> (liquid)	28.01	0.807

holder (see Haack et al. 2021). The mold and sample holder were cooled with liquid nitrogen before the sample mixture was added in. As the nitrogen of the suspension slowly evaporated, only the ice-organic and fly ash particles remained in the cylinder. When the nitrogen had completely evaporated, the cylindrical mold was removed from the sample holder, uncovering solid but extremely porous samples (Haack et al. 2021) with the diameter of the mold. The samples were immediately placed in the vacuum sublimation chamber prepared for the measurement. This procedure ensured that the sample temperature did not exceed 150 K and prevented sintering of the ice particles.

To determine the cohesive force between the organic-bearing ice particles, their tensile strength and surface energy were determined with other samples of the same mixture before the sublimation experiments. For this purpose, the Brazilian disk test method was used, as described in previous experiments (Gundlach et al. 2018b; Bischoff et al. 2020; Haack et al. 2020). With a particle radius,  $r$ , of 2.4  $\mu\text{m}$  and a filling factor,  $\Phi$ , of 0.46, the tensile strength of ice with 10 mass% organics at 150 K amounts to  $1300 \pm 250$  Pa, compared to  $1100 \pm 210$  Pa for pure water ice (Haack et al. 2020). Following Blum et al. (2006), the upper limit for the surface energy,  $\gamma$ , is

$$\gamma = \frac{4r\sigma}{9\Phi}. \quad (1)$$

With the values of the tensile strength,  $\sigma$ , the surface energy of the used organic-rich ice is  $0.0029 \pm 0.0006$  J m<sup>-2</sup>, compared to  $0.0026 \pm 0.0005$  J m<sup>-2</sup> for pure water ice (Haack et al. 2020). These values are the same within measurement error, and therefore we can use the previous values of tensile strength and surface energy from Haack et al. (2020) for further calculations of different organic-bearing ice-dust mixtures.

In previous measurements, the albedo of fly ash was determined to be 0.35. This value was also assumed for our sample mixtures since the albedo of ice-bearing mixtures is mainly determined by the dust component (Chýlek et al. 1983; Clark & Lucey 1984; Oehler & Neukum 1991).

## 2.3. Scaling to cometary conditions

To obtain meaningful results from the experiments, the conditions in the laboratory must be scaled to the conditions on a comet. The most important difference between the two environments is the gravity that is by orders of magnitudes higher in the laboratory compared to the  $\sim 2 \times 10^{-4}$  m s<sup>-2</sup> on comet 67P (Agarwal et al. 2016). To solve this problem, we used the same scaling for particle size as for the experiments described in Haack et al. (2021). The scaling relates the ratios of gravity and particle-size-dependent cohesion in the laboratory and on 67P. With known gravity  $F_G = \frac{4}{3}\pi r^3 \rho g$  and cohesion  $F_C = 3\pi r \gamma$  in the

laboratory (Haack et al. 2020) and the known gravity on 67P, the corresponding cohesion and thus particle size on the comet can be estimated with

$$\frac{F_{G_{67P}}}{F_{C_{67P}}} \approx \frac{F_{G_{Earth}}}{F_{C_{Earth}}}. \quad (2)$$

In these equations,  $r$  is the particle radius,  $\rho$  is the particle density,  $g$  is the gravitational acceleration, and  $\gamma$  is the surface energy. According to the determined values of the surface energy and the scaling of Haack et al. (2021), the fly ash and organic-rich ice particles with a radius of  $\sim 2.4 \mu\text{m}$  represent millimeter-sized particles on 67P. This is in line with the size of hypothesized pebbles, which may have initially formed comets (Blum et al. 2014, 2017; Fulle et al. 2016; Lorek et al. 2016, 2018). On a macroscopic scale, a 2.5 cm object in the laboratory would correspond to an object of about 10 m in size on 67P. This could be a cliff, a large boulder, or other morphological features on the comet (Thomas et al. 2015b; Pajola et al. 2016; El-Maarry et al. 2019) that would be subject to progressive alteration by the sublimation of volatile materials.

After increasing the cohesive forces by reducing the particle size, the insolated energy in the experiment had to be adapted to reflect realistic cometary conditions. The insolated energy heats the ice at the surface, which sublimates and creates a near-surface vapor pressure according to the Clapeyron–Clausius equation  $P_v = Ae^{-B/T}$ , where  $T$  is the temperature of the ice and  $A$  and  $B$  are constants with values  $A = 3.56 \times 10^{12} \text{ Pa}$  and  $B = 6142 \text{ K}$  for water ice (Fanale & Salvail 1984). The vapor pressure acts on the particle cross section and creates a pressure drag,  $F_D = \pi r^2 P_v$ , on the particles of the sample, where  $r$  is the particle radius. When the  $F_D$  on the particles exceeds their cohesion,  $F_C$ , individual particles or particle aggregates detach from the sample's surface and can be transported away. To compare this process in the laboratory with 67P, this scaling relates the ratios of insolation-dependent pressure drag and particle cohesion of the sample and on 67P as described in Haack et al. (2021) and follows

$$\frac{F_{D_{67P}}}{F_{C_{67P}}} \approx \frac{F_{D_{Earth}}}{F_{C_{Earth}}}. \quad (3)$$

This second scaling ensures that the insolated energy on the sample surface is sufficient to sublimate the water ice and can be related to the corresponding insolation rate on 67P.

When Rosetta reached 67P and monitored activity on its surface, the comet had a heliocentric distance of about 4 AU (Tubiana et al. 2015). According to the energy scaling, this distance can be simulated with  $\sim 1$  solar constant in the laboratory. When 67P reaches its perihelion at 1.24 AU, the solar insolation reaches its maximum. This insolation flux would transform to about 33.6 solar constants in the laboratory (Haack et al. 2021). However, the experimental setup was not built to provide this amount of energy. With the solar simulator used in our experiments, a maximum insolation rate of 1.9 solar constants was reachable. This corresponds to a heliocentric distance of 3.6 AU for 67P. Activity has already been observed on the surface of 67P at this distance (Snodgrass et al. 2013; Tubiana et al. 2015).

#### 2.4. Sublimation experiments

The experiments were performed in the vacuum sublimation chamber, which was also used in Haack et al. (2021). Before the sample was placed, the chamber was cooled to about 110 K and flooded with argon to prevent atmospheric moisture from

**Table 2.** Mass ratios of the sample mixtures used: relative mass ratios of organics, ice, and dust used for various sample mixtures in the sublimation experiments.

	Organics	Ice	Dust (vol%)
Organic free reference	0	100	500 (67)
	5	100	300 (59)
Low organic content	5	100	500 (70)
	5	100	700 (77)
High organic content	10	100	300 (62)
	10	100	500 (73)
	10	100	700 (79)

**Notes.** The ice fraction was normalized to 100 for ease of reference. The dust volume with respect to the bulk material is given in parentheses.

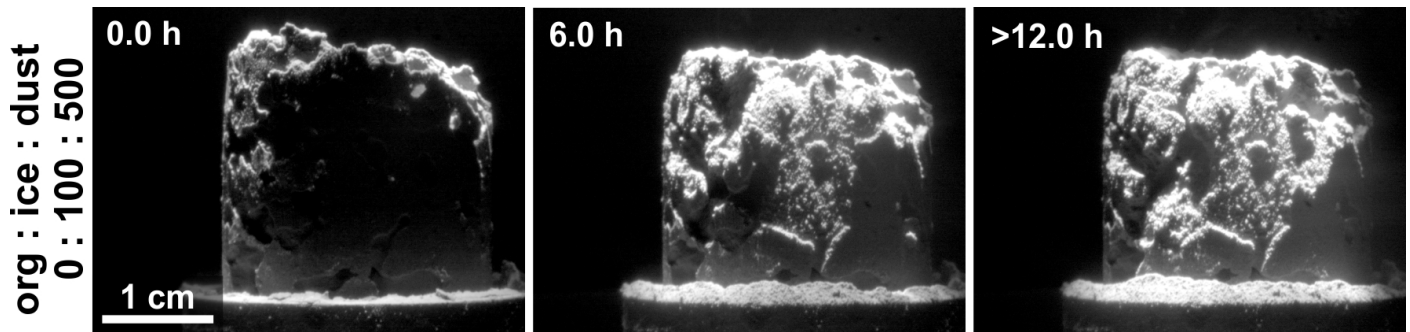
entering the chamber when it was opened for sample insertion. The sample holder, with the sample on top, was firmly mounted inside a cooling shield within the chamber and connected to temperature sensors. The cooling shield was a rectangular metal housing, with a side length of 10 cm, which was actively cooled with liquid nitrogen throughout the duration of the experiments. It has two openings, one on its top to allow insolation of the sample from above and one on its side surface for visual observation of the sample (see Fig. 4 in Haack et al. 2021). This mitigated the alteration of the samples by background thermal radiation during the experiments.

After the mounting of the sample holder, the chamber was closed immediately and the pressure and temperature inside were reduced to  $\sim 10^{-7}$  mbar and below 150 K, respectively, to simulate conditions similar to those of a comet (Kührt 1984). When pressure and temperature reached operating values, a solar simulator was used to insolate the sample vertically from above with an insolation flux of 1.9 solar constants. According to the energy scaling, this corresponds to a heliocentric distance of about 3.6 AU. To verify the temperature stability during the experiments, temperature sensors were used to monitor the sample and the cooling shield. A camera with a  $3000 \times 2000$  pixel sensor was focused at the sample through a side window of the sublimation chamber and captured images ( $25 \mu\text{m}$  per pixel) at a frame rate of one image per second.

Two series of experiments with three measurements each were performed with two different fixed organic-ice mass ratios, 5:100 and 10:100. The subsequently added amount of dust led to 300:100, 500:100, and 700:100 mass ratios with respect to ice for both series (Table 2). This represents ice-dust ratios as suggested by observations on 67P (Herique et al. 2017; Fulle et al. 2017, 2018) and by laboratory experiments (Haack et al. 2021). A reference measurement was performed without organics to directly infer the influence of organics on the evolution of the sample morphology. The insolation stopped after a maximum of 20 h of measurements, when the supply of liquid nitrogen to cool the sublimation chamber had to be replenished. At the end of the experiment, the images taken with the camera were analyzed in terms of the degree of alterations on the sample surface with respect to the sample compositions.

### 3. Results

To obtain a reference measurement of organic-free material, a sample with an ice-dust mass ratio of 100:500 was placed in the



**Fig. 1.** Sublimation experiment without organic components as reference. It was performed to obtain a reference to samples with organic components. The series shows how the surface of a sample with an ice-dust mass ratio of 100:500 evolves under a vertical insolation of 1.9 solar constants. The shape of the sample altered as material detached and fell off the lateral surfaces as individual grains or local cliff collapses. No further surface alterations were observed after 12 h. A time lapse of the evolution is available as an [online](#) movie.

chamber. With vertical insolation, particles were only sporadically ejected from the top in the first minutes of the experiment. Significant surface alteration was limited to the vertical surface. Material detached from the vertical side wall and fell down due to gravity. In this process, larger areas of the wall collapsed repeatedly. This altered the shape of the sample from cylindrical to more conical, with decreasing diameter toward the top (Fig. 1). A difference between the albedo of ice-depleted and fresh material could not be detected.

Areas where fresh material was exposed to the sample surface appeared very rough, with a granular texture in the sub-millimeter range. The detached material accumulated directly at the base of the sample as ice-depleted granular dust. The surface alteration rate decreased throughout the experiment, and after about 12 h the activity came to an end. Unfortunately, the experimental setup was not designed to monitor mass loss during the experiments, so the results were limited to visual observations.

By the end of the experiment, an ice-depleted non-cohesive dust layer had formed on the remaining sample material, and large amounts of ice were observed in the center of the remains. The remaining ice-rich material had solidified significantly compared to the sample material at the start of the experiment. However, with the setup used, it was not possible to determine the exact amount of remaining ice and the sample's tensile strength because frost formed on the sample immediately after it was removed from the sublimation chamber and the ice began to thaw.

### 3.1. Low organic content

We started the first series of measurements with an organic-ice-dust mass ratio of 5:100:300 and increased the dust content in two steps, to 5:100:500 and 5:100:700, respectively. In all measurements the reduction of the samples' volume was most noticeable as the ice sublimated (Fig. 2). No solid material detached in the form of ejected particles or cliff collapses, and we did not observe any transport away from the surface via other mass movement processes. As a result, none of the three samples produced visible areas where fresh material was exposed to the surface. In contrast to organic-free ice-dust mixtures, material loss from all organic-bearing samples appeared to be caused by sublimating ice only. On the lateral surface of the sample with the lowest dust content (5:100:300), the sample volume decreased and short fractures of 2–3 mm formed during the sublimation phase. This process slowed down during the experiment, and no further change was observed after 12 h. With

increasing dust content and a correspondingly lower amount of organic-rich ice, the formation of fractures became less evident. On the sample surface with the lowest content of the organic-rich ice (5:100:700), no distinct fractures could be observed. On this sample, the surface alteration was generally less significant and stopped after 8 h.

At the end of the experiment, the sample residues were removed from the sublimation chamber and a mantle of ice-depleted material a few millimeters thick was observed. The mantle material was extremely porous and fragile but preserved its shape after the ice had sublimated. In contrast to the organic-free reference experiment, the ice-depleted material did not decay into granular dust under the influence of gravity. The ice-depleted mantle covered the sample center, where ice remained preserved. As observed in the organic-free reference sample and in previous sublimation experiments (e.g., [Poch et al. 2016b](#); [Kaufmann & Hagermann 2018](#); [Haack et al. 2021](#)), the ice-containing sample center was significantly solidified compared to the start of the experiment. No change in albedo before and after the experiment was detected on the side wall of any of the three samples.

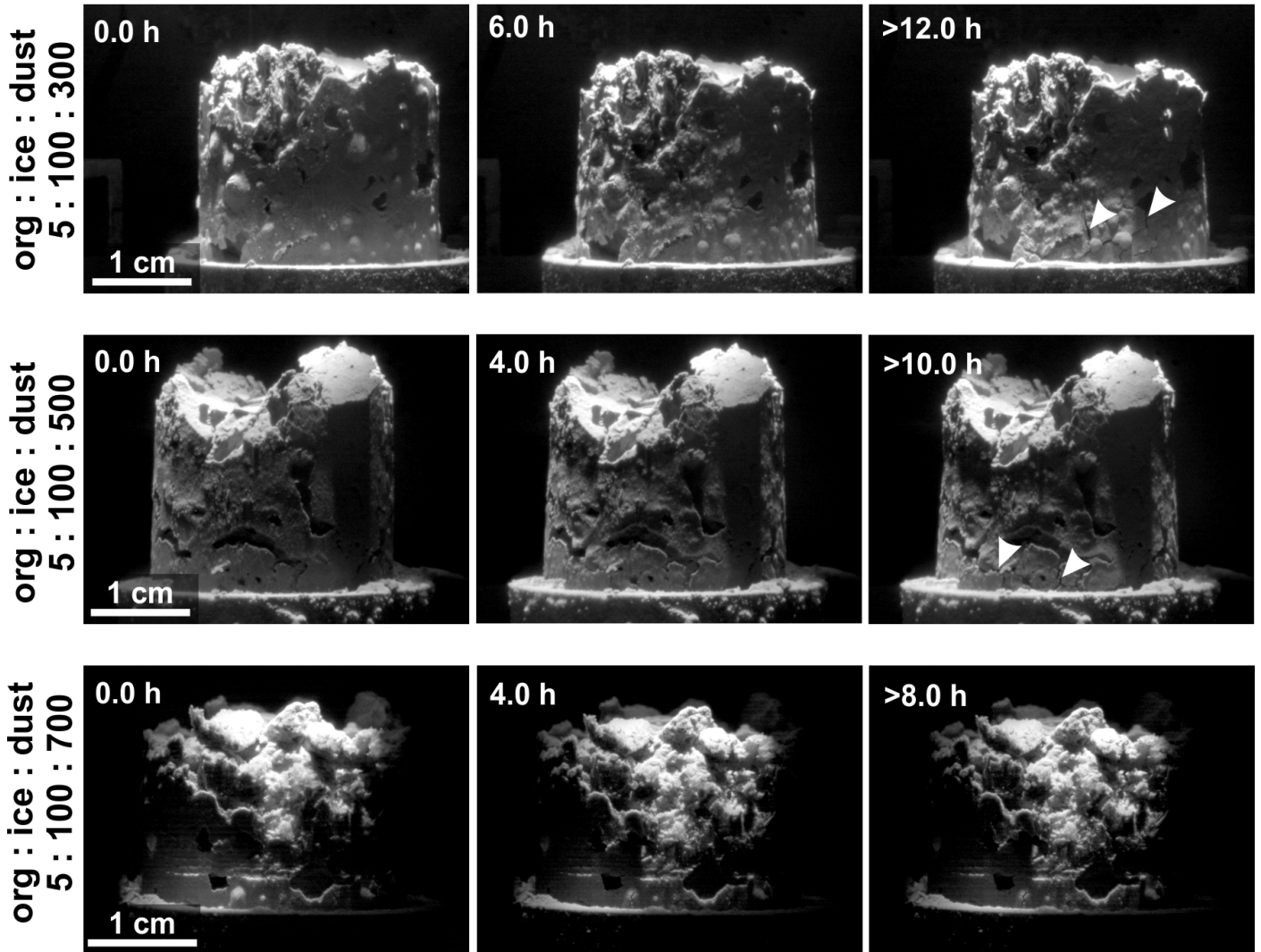
### 3.2. High organic content

In the second series of measurements, the mass of organic material was doubled with respect to the amount of water ice. The mass ratios of dust were increased in three steps and were comparable to those of the first series of measurements (Table 2). The vertical insolation of 1.9 solar constants remained unchanged.

The samples of this measurement series presented a volume loss, which appeared qualitatively increased compared to samples with lower organic content (Fig. 3). No mass transport of solid material away from the surface was observed in any of the three samples. In the course of the experiments, distinct fractures developed on the lateral side of the samples. These fractures were more pronounced than in experiments with lower organic content, frequently exceeded 5 mm in length, and formed poorly developed networks. The angles at which they intersected were variable. The fractures evolved most distinctly, and the apparently highest volume loss was observed on the sample with the lowest dust content (10:100:300). The phase of observable surface alteration for this sample with the lowest dust content ended after about 12 h.

In contrast to the first series, the sample with the highest dust content (10:100:700) also showed significant fracturing. However, the volume decrease was reduced and less rapid compared





**Fig. 2.** Three vertically insulated samples with different organic-to-ice-to-dust mass ratios at an insolation rate of 1.9 solar constants. The image series show the alterations of the sample surfaces as a function of increasing dust content ([online movies](#)). The decreasing sample volume and formation of fractures (some marked with arrows) is most evident at a component mass ratio of 5:100:300 and reduces significantly with increasing dust content. The surface-altering activity of the first sample comes to an end after 12 h. The following series show the dust-dependent reduction of the surface alterations and the timescales on which they occur. At a maximum relative dust amount of 5:100:700 per mass, the duration of visible sample alteration is reduced to 8 h.

to samples with lower dust content. The phase of visible surface alteration of the sample with the highest dust content came to an end after about 6 h. The comparison between the two series of measurements showed that the duration of the observable surface alteration depends predominantly on the dust content and not on the amount of the organic component. An increased dust content generally leads to reduced phases of surface alteration.

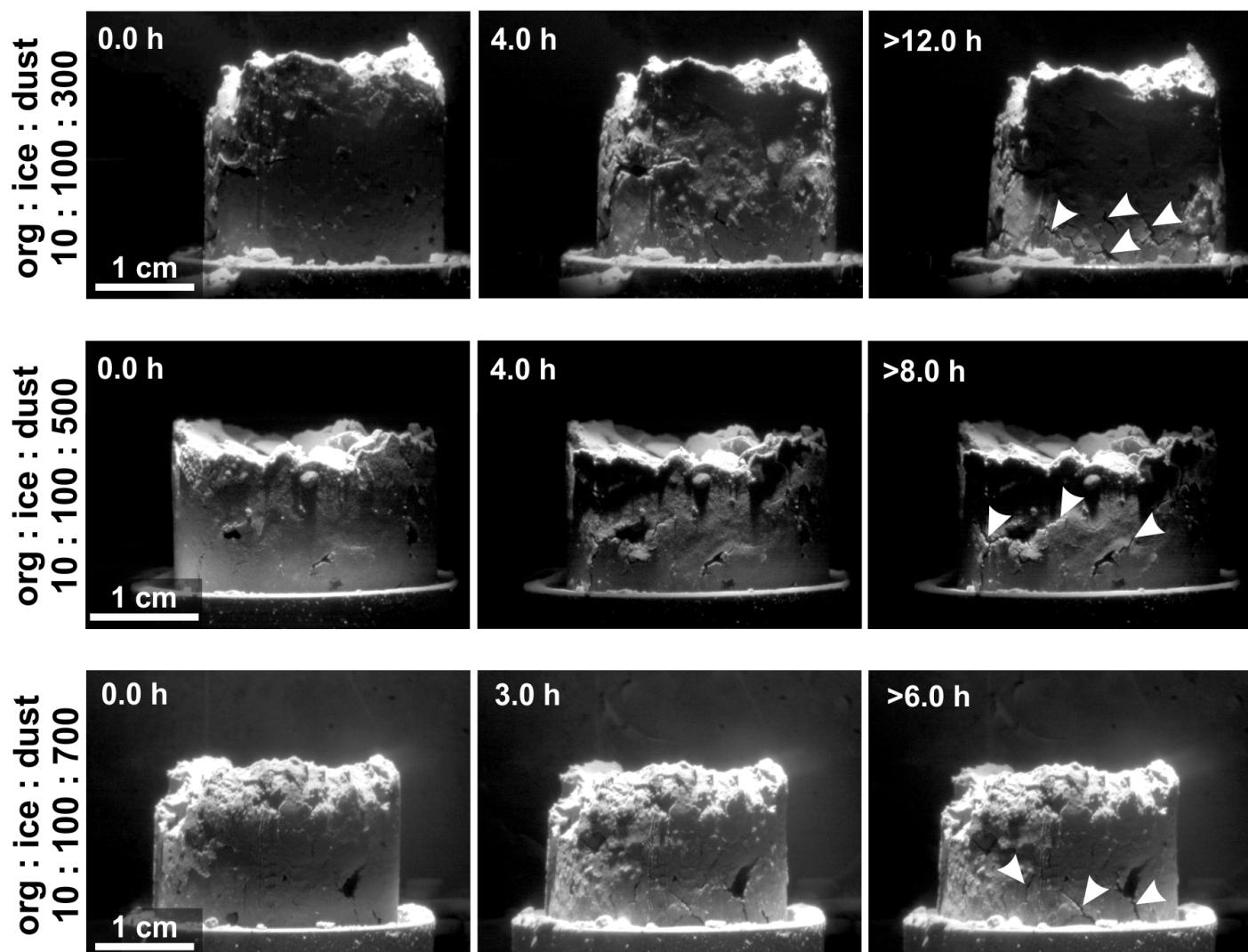
After the remains of the samples were removed from the sublimation chamber at the end of the experiments, an ice-depleted mantle on the surface, which enveloped an ice-rich core, was observed. This is in analogy to the results of the experiments with low organic content. The thickness of the mantle at the side surfaces reduced from more than 3 millimeters to about 1 millimeter as the dust content of the samples increased. Despite its high porosity, the mantle material was cohesive enough that fragments could be manually removed without disintegrating into granular dust. No change in the albedo of the sample materials before and after the experiments was observed.

The results of organic-rich sublimation experiments differ significantly from those without organics. The observed activities and morphologies at the sample surfaces are less diverse (no cliff collapses, outbursts etc.) and less dependent on the volatile content compared to the alterations of samples without organics (Fig. 1; see also [Haack et al. 2021](#)). In all observed samples, the surface alterations were dominated by volume loss and fracture formation that proceeded continuously with no distinct individual events.

#### 4. Discussion

The observations obtained with the organic-free reference measurement are in line with those presented by [Haack et al. \(2021\)](#), even though the insolation flux is somewhat reduced compared to the previous experiments. The test shows that, with our experimental setup, a sample without organic components loses substantial amounts of nonvolatile material and is subject to





**Fig. 3.** Evolution of three sample surfaces with high organic content under vertical insolation. The reduction in the sample volume and the formation of fractures (some marked with arrows) can be observed in all three image series ([online](#) movies). This surface evolution is most distinctly observable in the top series, with an organic-to-ice-to-dust mass ratio of 10:100:300, whose phase of activity ended after 12 h. The degree of surface alteration and its duration decreased with increasing amounts of the dust component and ended after 8 and 6 h, respectively.

a significantly different morphological evolution than samples with organics.

At 150 K, the addition of glycine and sodium acetate to water ice in a mass ratio of 10:100 only increases the surface energy of the ice particles within the measurement inaccuracy of the surface energy of pure water ice. We assume that this difference between organic-to-ice mixtures of 5:100 and pure ice is even smaller and cannot be determined with sufficient accuracy because of the limitations of the Brazilian disk test method. Therefore, we extrapolated the average surface energies of mixtures of dust, ice, and organics by using the values of previous Brazilian disk tests with ice-dust mixtures without organics (Haack et al. 2020) to estimate the tensile strength of each sample material.

The volume fractions of dust in the samples with different mixing ratios range from about 60 vol% for the lowest dust content (X:100:300) to almost 80 vol% for the highest dust content (X:100:700; Table 2). The different amounts of organics have only a minor influence on the various volume fractions of the sample mixtures because of their small share in the total mass of the samples. With the sample's filling factor of 0.41

(Haack et al. 2021), the tensile strength values of the samples were calculated and range between 540 Pa for the lowest and 360 Pa for the highest dust content. This is somewhat above the high end predicted for materials on 67P by Groussin et al. (2015). Other estimates give an even lower strength of only a few pascals for cometary material (Attree et al. 2018a; O'Rourke et al. 2020). Since the size scaling is based on the comparison of cohesion on 67P and in the laboratory, it should be considered with caution. However, it is not unrealistic since hypothetical samples with a filling factor between 0.15 and 0.37, as assumed for 67P (Fulle et al. 2016; Pätzold et al. 2016; Herique et al. 2019), would have a calculated tensile strength equivalent to that given by Groussin et al. (2015). With the method of sample preparation used, such low filling factors are not achievable. Therefore, the tensile strength in the laboratory is higher compared to on 67P.

#### 4.1. Low organic content

In contrast to samples of previous sublimation experiments that investigated pure dust-ice mixtures, the samples with added organic components showed no broad diversity in their

morphological evolution with respect to their variable volatile content. The two observed types of alterations were the reduction in the sample volume and the formation of fractures on the surface.

The volume reduction can be explained by the sublimation of the water ice. The organic components in the ice matrix (intra-mixture) remained in the sample after the sublimation of the ice and adhesively kept the dust particles in contact with one another. It is unlikely that significant amounts of organic material was transported away with the sublimating ice. Otherwise, analogous to the sample without organic components, the dust particles would have detached from the sample surface and fallen down (Fig. 1).

However, the effect of the organic material as a “glue” (Bischoff et al. 2020) holding the dust particles together remained sufficient to compensate for the loss of volatiles. Ice, with its higher surface energy compared to dust (Kimura et al. 2015; Gundlach et al. 2018b; Haack et al. 2020), prevents disintegration of the sample before its sublimation. After sublimation, a mixture of dust and organics remains, the tensile strength of which is higher than that of pure dust. Therefore, after the sublimation of the ice, the organic-rich samples do not disintegrate into individual dust particles, in contrast to what was observed in the reference measurement without organics and as described in Haack et al. (2021). The resulting free space was partially refilled by the remaining dust particles, which caused the samples to shrink. The observation that the ice-depleted material did not form a foam-like texture (Poch et al. 2016b) is probably due to the fact that the fraction of nonvolatile materials was much higher in our experiments. The reduced volume loss of samples with increased dust content can be explained by the lower ice content, which creates less free space after sublimation.

The reduced duration of sublimation activity results from the faster development of ice-depleted mantle material as the dust content of individual samples increases. The mantle protects underlying ice-containing layers from insolation and thus from further sublimation. A comparable process was already observed in previous experiments (e.g., Grün et al. 1993; Lämmerzahl et al. 1995; Haack et al. 2021), where an ice-depleted layer was formed of loose dust but not of cohesive material, unlike in our experiments.

The decrease in volume during sublimation created tensile stresses in the ice-depleted mantle and led to the formation of contraction cracks. This process is comparable to drying shrinkage due to the loss of volatiles and the formation of desiccation cracks on Earth (Peron et al. 2009; Sima et al. 2014). Desiccation is also one of the proposed processes responsible for the formation of fractures on comets (El-Maarry et al. 2015; Poulet et al. 2016). However, in the samples with a low content of organics, the fractures were only a few millimeters long, mostly isolated, and did not form networks. This could indicate that the amount of organic adhesive between the dust particles was sufficient to keep them attached to the original sample but allowed limited movement of the dust particles into the evolving free space. Accordingly, the ice-depleted material had a degree of plasticity that reduced the formation of fractures and prevented fractures altogether in the case of high dust contents. Another explanation for the absence of distinct fracture networks could be the limited surface area of the samples, which prevented the formation of extended fracture patterns.

Another process that can create fractures on the surface of a comet is repeated thermal contraction and expansion (El-Maarry et al. 2015; Spohn et al. 2015; Auger et al. 2018; Attree et al. 2018b). This is a slow process, requires periodical cycles of

insolation, and produces polygonal patterns typical in periglacial landscapes on Earth (French 2017). In the laboratory, however, we did not perform insolation cycles and thus did not trigger any periodic thermal contraction or expansion. This explanation for the origin of fractures is therefore not applicable for our experiments. The formation of fractures by tectonics and compressive stress is conceivable on comets (Thomas et al. 2015b; Franceschi et al. 2020) but can be excluded in our laboratory experiments.

The formation of an ice-rich layer below the ice-depleted mantle can be explained by the recondensation and/or sintering of ice (Spohn & Benkhoff 1990; Thomas et al. 1994; Seiferlin et al. 1995; Kossacki et al. 2015). This process has been observed many times in previous sublimation experiments (e.g., Grün et al. 1993; Poch et al. 2016b; Kaufmann & Hagermann 2018) and is likely on 67P (Spohn et al. 2015; Lethuillier et al. 2016; Knapmeyer et al. 2018; Gundlach et al. 2020). In this process, water vapor migrates from near-surface layers deeper into the sample and recondenses there into a solid material (Kührt & Keller 1994; Gundlach et al. 2020). Additionally, a temperature increase in near-surface layers due to insolated energy can trigger the sintering of ice particles (Gundlach et al. 2018a). In these cases, stiff connections of ice form between the particles and significantly increase the tensile strength of the material (Kuroiwa 1961; Gundlach et al. 2018a). Nevertheless, due to the reduced formation of fractures in this series of measurements, comparison with fracture-related morphologies of 67P is of limited significance.

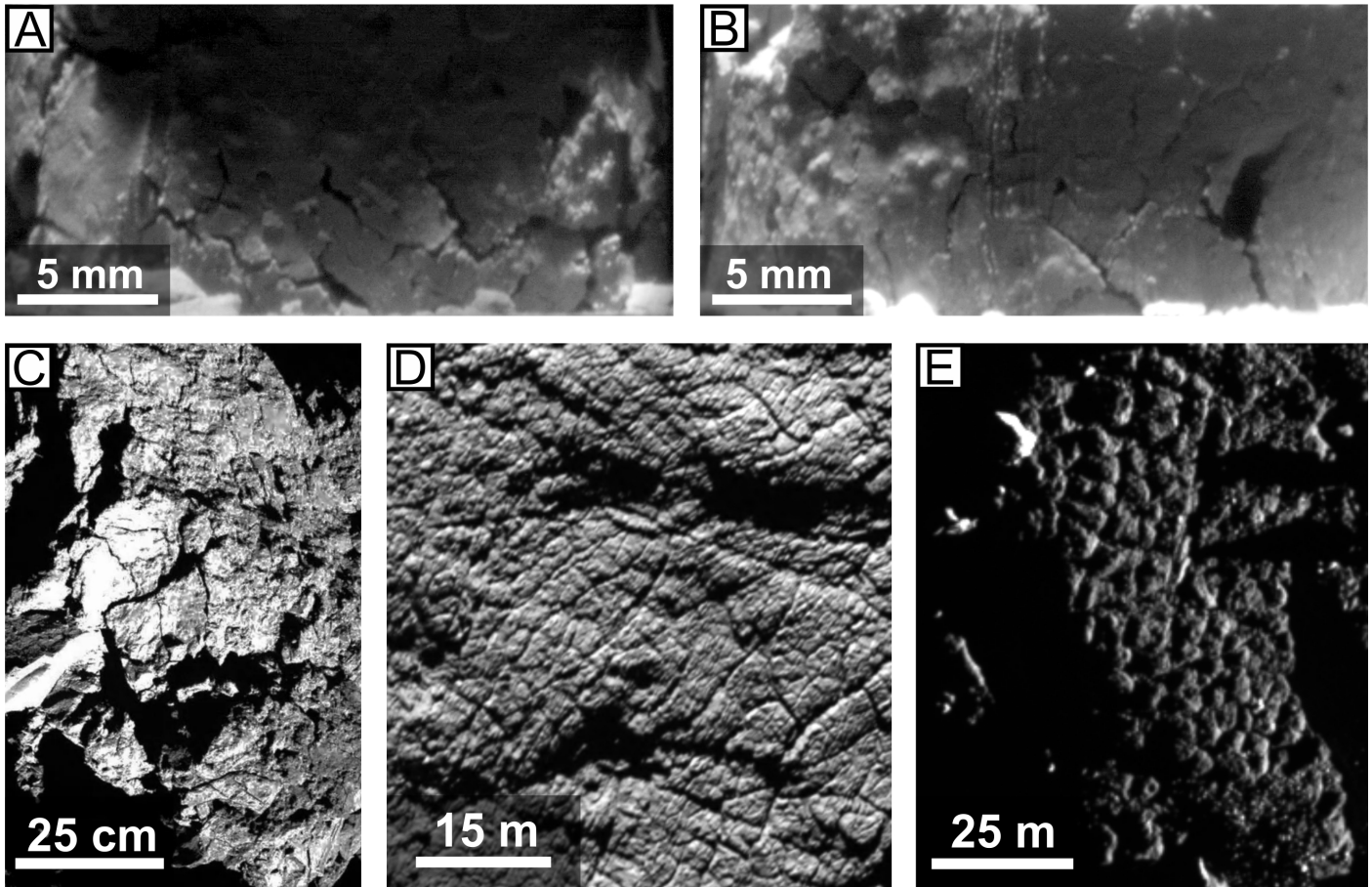
#### 4.2. High organic content

The doubled amount of organics in the second series of measurements enhanced the decrease in the sample volume and enhanced the formation of irregularly shaped fractures as the ice sublimated. The duration of the active phase of sample alteration was comparable to that of the first series with respect to the same ice-dust ratios. Due to the limitations of the experimental setup, the physical properties of the remaining material could not be measured after the experiment, so the analysis could only be done using the images taken by the camera (Fig. 3). Therefore, direct comparison of volume changes of different samples should be treated with caution since the whole sample was not observed and misperceptions could occur due to the camera’s perspective. However, it is clear that the visually increased volume loss and intensified formation of fractures on the surface differ significantly compared to the first series. A possible explanation is increased inter-particle forces due to the higher organic content acting as an adhesive. The higher inter-particle forces would reduce the mobility of the particles and tend to make the mantle material less plastic compared with the low organics scenario (Valverde et al. 1998; Gröger et al. 2003). The consequence would be an increased formation of tensile fractures due to the volume loss. This process is comparable to the formation of desiccation cracks on Earth (Rayhani et al. 2008; Peron et al. 2009; Sima et al. 2014), which occur in a cohesive material due to the loss of volatiles.

As in the first series with low organic content, the possibility that the fractures result from thermal stress can be excluded. Such a possibility is contradicted by the fact that no periodically changing insolation was realized and that a large number of fractures occurred on the side surfaces of the samples, which were insolated only at very high angles of incidence.

Evolved networks of intersecting fractures are known to have been caused by terrestrial desiccation processes and on 67P may have been caused by thermal stresses (Spohn et al. 2015;





**Fig. 4.** Comparison of fractures generated in the laboratory (*panels A and B*) and observed on 67P (*panels C–E*). *Panel A*: close-up of the sample with the lowest dust fraction (10:100:300) from Fig. 3. Distinct and irregularly shaped fractures form a poorly developed network on the side wall of the sample. *Panel B*: enlarged section of the sample with the highest dust content (10:100:700) from Fig. 3. The length and pattern of evolving fractures are comparable to those on samples with lower dust content, but they are significantly narrower. *Panel C*: detailed image of fractures on the surface of 67P, taken by the Philae lander. Several irregular cracks are visible on a rough and dust-free surface. The fracture patterns correspond most closely to those on panel B. Image credit: ESA/Rosetta/Philae/CIVA. *Panel D*: fracture network on the surface of 67P. The fractures form a pattern of polygons with widths of up to 5 m. *Panel E*: evolved polygonal structures, caused by fractures on the surface of 67P. Image credits: ESA/Rosetta/MPS for OSIRIS Team MPS/UPD/LAM/IAA/SSO/INTA/UPM/DASP/IDA.

Auger et al. 2018; Attree et al. 2018b; El-Maarry et al. 2015, 2019), although none formed here. Occasionally, fractures intersected, but not at a preferred angle typical of polygonal fracture networks (Peron et al. 2009; Auger et al. 2018; French 2017). However, it cannot be excluded that the observed fractures represent an early stage of a slowly forming network or that polygonal networks could form in the analog material if the sample's surface area or the insolation rate were increased. These considerations suggest that polygonal networks do not necessarily have to be restricted to the near-surface hardened layer of a comet (Kochan et al. 1989; Kossacki et al. 2015; Spohn et al. 2015). Taking the size scaling of the laboratory experiments into account, irregular meter-sized desiccation cracks may form on a comet due to volatile loss (Poulet et al. 2016), while large polygonal networks could be generated by thermal stresses due to diurnal heating periods (e.g., Spohn et al. 2015; Auger et al. 2018; Attree et al. 2018b, see our Fig. 4).

As described in Sect. 4.2, larger and more numerous fractures were formed in volatile-rich samples. In parallel, the period of visible surface alteration and the thickness of the ice-depleted mantle are increased. This could indicate that fractures in volatile-rich samples propagate deeper into the material, where exposed volatiles also start to sublimate. This could cause

existing fractures to propagate farther or new fractures to form. On a comet, these propagating fractures could locally increase the sublimation activity and lead to outgassing events (Skorov et al. 2016; Vincent et al. 2016; Höfner et al. 2017).

In all our experiments, water ice was the only volatile used. As mentioned in Sect. 2.1, water dominates the amount of all volatiles on 67P (e.g., Hässig et al. 2015; Läuter et al. 2018; Biver et al. 2019), and the potential sublimation and recondensation of CO<sub>2</sub> does not result in a substantial solidification of a subsurface crust, since individual CO<sub>2</sub> crystals do not form bridges to H<sub>2</sub>O crystals (Kochan et al. 1989). Therefore, water ice is expected to be the dominant volatile in the upper centimeters of the comet surface (Filacchione et al. 2016; Gundlach et al. 2020). Nevertheless, the influence of other volatiles on the evolution of a comet cannot be underestimated and remains a subject of investigation for future experiments.

The absence of collapse events or ejected fragments (Tubiana et al. 2015; Vincent et al. 2015a,b, 2016) from the sample surface could indicate that the sample mixtures do not simulate the actual composition of a comet accurately enough. It is also conceivable that an increased and periodically changing insolation in combination with the low albedo of a comet (Keller et al. 1986; Ciarniello et al. 2015) could have a significant effect on

the evolution of the patterns and depths of fracture systems in future experiments.

## 5. Conclusions

A number of sublimation experiments were performed with samples containing variable amounts of organic, volatile, and dust components. The focus of the experiments was to study samples that contain the organic molecules glycine and sodium acetate (Elsila et al. 2009; Altwegg et al. 2016; Rubin et al. 2019; Schuhmann et al. 2019). Comparison with organic-free sample material showed that an insolation flux of 1.9 solar constants, equivalent to a simulated heliocentric distance of 3.6 AU, was sufficient to sublimate the near-surface volatile water component and to alter the sample surface. The addition of a few mass percent of organic material to a volatile-rich sample fundamentally changes the evolution of the sample morphology. The evolution of sample surfaces with organics was characterized by a loss of volume and the formation of fractures at the surface. These fractures were compared with those on 67P (Spohn et al. 2015; El-Maarry et al. 2015; Poulet et al. 2016; Auger et al. 2018) and discussed with respect to their relevance to fracture formation on 67P.

The volatile content of the samples had a distinct influence on the duration of the surface alteration and on the degree of volume loss. The alteration of ice-rich samples lasted longer than that of samples with initially lower amounts of ice, and the former qualitatively lost more of their volume. These processes became less distinct with an increasing dust content of the samples. At the end of the experiments the thickness of ice-depleted material on the top and side surfaces was significantly higher for samples with initially high ice content compared to samples with lower ice content. This mantle prevented sublimation of ice from the sample center, and with increasing mantle thickness the surface alteration came to an end. The mantle material was extremely porous but was stable enough not to disintegrate into individual dust particles when mechanically stressed after the experiment. The nonvolatile organic components remained in the sample and acted as an adhesive between the individual dust particles, consolidating the ice-depleted material. The more organic material initially added to the sample, the more stable the ice-reduced mantle appeared.

In ice-depleted mantles with initially high organic content, the dust particles were less mobile compared to samples with low organic content. As a result, the mantle material became less plastic. The loss of sublimating ice caused the mantle material to contract, resulting in near-surface tensile stresses and the formation of fractures. These fractures propagated farther into the sample's subsurface as sublimation of the ice continued. This allowed further sublimation of ice from subsurface layers, which presumably would be protected from sublimation by a fracture-free mantle. The fractures in the experiment remained mostly separated from one another and did not form polygonal structures as observed on 67P (El-Maarry et al. 2015, 2016; Auger et al. 2018). However, this could be a result of the limited dimensions of the experimental setup. With a larger sample surface and a more intense insolation, the formation of polygonal structures due to volatile loss cannot be excluded. We conclude that the formation of fractures and, possibly, networks on a comet is not necessarily limited to a hardened subsurface layer and its diurnal thermal contraction (Spohn et al. 2015; Auger et al. 2018; Attree et al. 2018b). On meter scales, fractures on a comet could also result from the loss of sublimating volatiles, comparable to desiccation processes on Earth.

In our experiments we used nonvolatile-to-volatile ratios from 3 to 7 per mass, as inferred on 67P (Herique et al. 2017; Pätzold et al. 2018; Fulle et al. 2017, 2018) and confirmed in previous sublimation experiments (Haack et al. 2021). In future experiments, our restriction to glycine and acetate as organic analogs could be extended to other organic materials detected on 67P. Also, further experiments are necessary to investigate the influence of other volatiles, such as CO<sub>2</sub>, the influence of increased insolation flux, and the influence of a drastically reduced albedo on the morphological evolution of cometary surfaces.

*Acknowledgements.* This work was carried out in the framework of the CoPhyLab project funded by the D-A-CH programme (GU 1620/3-1 and BL 298/26-1/SNF 200021E 177964/FWF I 3730-N36). The research project "The Physics of Volatile-Related Morphologies on Asteroids and Comets" is funded by the DLR Management Board Young Research Group Leader Programme and the Executive Board Member for Space Research and Technology. We gratefully acknowledge their financial support and endorsement. Many thanks to I. Büttner from DLR Berlin for sieving the fly ash and to U. Altenberger from the University of Potsdam for providing SEM images and chemical analysis of fly ash.

## References

- Agarwal, J., A'Hearn, M. F., Vincent, J.-B., et al. 2016, *MNRAS*, **462**, S78
- Altwegg, K., Balsiger, H., Bar-Nun, A., et al. 2016, *Sci. Adv.*, **2**, e1600285
- Altwegg, K., Balsiger, H., Berthelier, J., et al. 2017, *MNRAS*, **469**, S130
- Attree, N., Groussin, O., Jorda, L., et al. 2018a, *A&A*, **611**, A33
- Attree, N., Groussin, O., Jorda, L., et al. 2018b, *A&A*, **610**, A76
- Auger, A.-T., Groussin, O., Jorda, L., et al. 2018, *Icarus*, **301**, 173
- Bischoff, D., Gundlach, B., Neuhaus, M., & Blum, J. 2019, *MNRAS*, **483**, 1202
- Bischoff, D., Kreuzig, C., Haack, D., Gundlach, B., & Blum, J. 2020, *MNRAS*, **497**, 2517
- Biver, Bockelée-Morvan, D., Hofstadter, M., et al. 2019, *A&A*, **630**, A19
- Blum, J., Schrapler, R., Davidsson, B. J. R., & Trigo-Rodríguez, J. M. 2006, *ApJ*, **652**, 1768-81
- Blum, J., Gundlach, B., Mühle, S., & Trigo-Rodríguez, J. M. 2014, *Icarus*, **235**, 156
- Blum, J., Gundlach, B., Krause, M., et al. 2017, *MNRAS*, **469**, S755
- Bockelée-Morvan, D., Crovisier, J., Erard, S., et al. 2016, *MNRAS*, **462**, S170
- Capaccioni, F., Coradini, A., Filacchione, G., et al. 2015, *Science*, **347**, aaa0628
- Chylek, P., Ramaswamy, V., & Srivastava, V. 1983, *J. Geophys. Res.: Oceans*, **88**, 10837
- Choukroun, M., Altwegg, K., Kührt, E., et al. 2020, *Space Sci. Rev.*, **216**, 44
- Ciarniello, M., Capaccioni, F., Filacchione, G., et al. 2015, *A&A*, **583**, A31
- Clark, R. N., & Lucey, P. G. 1984, *J. Geophys. Res.: Solid Earth*, **89**, 6341
- Dodson-Robinson, S. E., Willacy, K., Bodenheimer, P., Turner, N. J., & Beichman, C. A. 2009, *Icarus*, **200**, 672
- El-Maarry, M., Thomas, N., Gracia-Berná, A., et al. 2015, *Geophys. Res. Lett.*, **42**, 5170
- El-Maarry, M., Thomas, N., Gracia-Berná, A., et al. 2016, *A&A*, **593**, A110
- El-Maarry, M. R., Groussin, O., Keller, H. U., et al. 2019, *Space Sci. Rev.*, **215**, 36
- Elsila, J. E., Glavin, D. P., & Dworkin, J. P. 2009, *Meteoritics Planet. Sci.*, **44**, 1323
- Fanale, F. P., & Salvail, J. R. 1984, *Icarus*, **60**, 476
- Filacchione, G., De Sanctis, M. C., Capaccioni, F., et al. 2016, *Nature*, **529**, 368
- Franceschi, M., Penasa, L., Massironi, M., et al. 2020, *Proc. Natl. Acad. Sci. U.S.A.*, **117**, 10181
- French, H. M. 2017, *The Periglacial Environment* (John Wiley & Sons)
- Fulle, M., Della Corte, V., Rotundi, A., et al. 2016, *MNRAS*, **462**, S132
- Fulle, M., Della Corte, V., Rotundi, A., et al. 2017, *MNRAS*, **469**, S45
- Fulle, M., Blum, J., Green, S. F., et al. 2018, *MNRAS*, **482**, 3326
- Goesmann, F., Rosenbauer, H., Bredehöft, J. H., et al. 2015, *Science*, **349**
- Gröger, T., Tüzzin, U., & Heyes, D. M. 2003, *Powder Technol.*, **133**, 203
- Groussin, O., Jorda, L., Auger, A.-T., et al. 2015, *A&A*, **583**, A32
- Grün, E., Bar-Nun, A., Benkhoff, J., et al. 1989, *Int. Astron. Union Colloquium*, **116**, 277
- Grün, E., Gebhard, J., Bar-Nun, A., et al. 1993, *J. Geophys. Res.: Planets*, **98**, 15091
- Gulkis, S., Allen, M., von Allmen, P., et al. 2015, *Science*, **347**, aaa0709
- Gundlach, B., Blum, J., Keller, H. U., & Skorov, Y. V. 2015, *A&A*, **583**, A12
- Gundlach, B., Ratte, J., Blum, J., Oesert, J., & Gorb, S. N. 2018a, *MNRAS*, **479**, 5272



- Gundlach, B., Schmidt, K. P., Kreuzig, C., et al. 2018b, *MNRAS*, 479, 1273
- Gundlach, B., Fulle, M., & Blum, J. 2020, *MNRAS*, 493, 3690
- Haack, D., Otto, K. A., Gundlach, B., et al. 2020, *A&A*, 642, A218
- Haack, D., Lethuillier, A., Kreuzig, C., et al. 2021, *A&A*, 649, A35
- Hadraoui, K., Cottin, H., Ivanovski, S. L., et al. 2019, *A&A*, 630, A32
- Hässig, M., Altwegg, K., Balsiger, H., et al. 2015, *Science*, 347, aaa0276
- Herique, A., Kofman, W., Beck, P., et al. 2017, *MNRAS*, 462, S516
- Herique, A., Kofman, W., Zine, S., et al. 2019, *A&A*, 630, A6
- Höfner, S., Vincent, J.-B., Blum, J., et al. 2017, *A&A*, 608, A121
- Kappel, D., Sachse, M., Haack, D., & Otto, K. A. 2020, *A&A*, 641, A19
- Kaufmann, E., & Hagermann, A. 2018, *Icarus*, 311, 105
- Keller, H. U., Arpigny, C., Barbieri, C., et al. 1986, *Nature*, 321, 320
- Keller, H. U., Mottola, S., Hviid, S. F., et al. 2017, *MNRAS*, 469, S357
- Kührt, E. 1984, *Icarus*, 60, 512-21
- Kührt, E., & Keller, H. U. 1994, *Icarus*, 109, 121
- Kimura, H., Wada, K., Senshu, H., & Kobayashi, H. 2015, *ApJ*, 812, 67
- Knapmeyer, M., Fischer, H.-H., Knollenberg, J., et al. 2018, *Icarus*, 310, 165
- Kochan, H., Roessler, K., Ratke, L., et al. 1989, in *ESA SP 302, Physics and Mechanics of Cometary Materials*, eds. J. J. Hunt & T. D. Guyenne, 115
- Kossacki, K., Kömle, N., Leliwa-Kopystyński, J., & Kargl, G. 1997, *Icarus*, 128, 127
- Kossacki, K. J., Spohn, T., Hagermann, A., Kaufmann, E., & Kührt, E. 2015, *Icarus*, 260, 464
- Kuroiwa, D. 1961, *Tellus*, 13, 252
- Lämmerzahl, P., Gebhard, J., Grün, E., & Klees, G. 1995, *Planet. Space Sci.*, 43, 363-73
- Läuter, M., Kramer, T., Rubin, M., & Altwegg, K. 2018, *MNRAS*, 483, 852
- Lethuillier, A., Le Gall, A., Hamelin, M., et al. 2016, *A&A*, 591, A32
- Lorek, S., Gundlach, B., Lacerda, P., & Blum, J. 2016, *A&A*, 587, A128
- Lorek, S., Lacerda, P., & Blum, J. 2018, *A&A*, 611, A18
- Musiolik, G., & Wurm, G. 2019, *ApJ*, 873, 58
- Oehler, A., & Neukum, G. 1991, *Geophys. Res. Lett.*, 18, 253
- O'Rourke, L., Heinisch, P., Blum, J., et al. 2020, *Nature*, 586, 697
- Pajola, M., Oklay, N., Forgia, F. L., et al. 2016, *A&A*, 592, A69
- Pätzold, M., Andert, T., Hahn, M., et al. 2016, *Nature*, 530, 63
- Pätzold, M., Andert, T. P., Hahn, M., et al. 2018, *MNRAS*, 483, 2337
- Peron, H., Laloui, L., Hueckel, T., & Bo Hu, L. 2009, *Eur. J. Environ. Civil Eng.*, 13, 869
- Poch, O., Pommerol, A., Jost, B., et al. 2016a, *Icarus*, 266, 288
- Poch, O., Pommerol, A., Jost, B., et al. 2016b, *Icarus*, 267, 154
- Pommerol, A., Jost, B., Poch, O., et al. 2015, *Planet. Space Sci.*, 109–110, 106
- Poulet, F., Lucchetti, A., Bibring, J.-P., et al. 2016, *MNRAS*, 462, S23
- Raponi, A., Ciarniello, M., Capaccioni, F., et al. 2020, *Nat. Astron.*, 5, 500
- Rayhani, M., Yanful, E., & Fakher, A. 2008, *Eng. Geol.*, 97, 25
- Rubin, M., Altwegg, K., Balsiger, H., et al. 2019, *MNRAS*, 489, 594
- Schuhmann, M., Altwegg, K., Balsiger, H., et al. 2019, *ACS Earth Space Chem.*, 3, 1854
- Seiferlin, K., Spohn, T., & Benkhoff, J. 1995, *Adv. Space Res.*, 15, 35
- Sierks, H., Barbieri, C., Lamy, P. L., et al. 2015, *Science*, 347, aaa1044
- Sima, J., Jiang, M., & Zhou, C. 2014, *Comput. Geotech.*, 56, 168
- Skorov, Y., Rezac, L., Hartogh, P., Bazilevsky, A., & Keller, H. 2016, *A&A*, 593, A76
- Snodgrass, C., Tubiana, C., Bramich, D. M., et al. 2013, *A&A*, 557, A33
- Spohn, T., & Benkhoff, J. 1990, *Icarus*, 87, 358
- Spohn, T., Knollenberg, J., Ball, A. J., et al. 2015, *Science*, 349
- Thomas, H., Ratke, L., & Kochan, H. 1994, *Adv. Space Res.*, 14, 207
- Thomas, N., Davidsson, B., El-Maarry, M. R., et al. 2015a, *A&A*, 583, A17
- Thomas, N., Sierks, H., Barbieri, C., et al. 2015b, *Science*, 347, aaa0440
- Tubiana, C., Snodgrass, C., Bertini, I., et al. 2015, *A&A*, 573, A62
- Valverde, J. M., Ramos, A., Castellanos, A., & Keith Watson, P. 1998, *Powder Technol.*, 97, 237
- Vincent, J.-B., Bodewits, D., Besse, S., et al. 2015a, *Nature*, 523, 63
- Vincent, J.-B., Oklay, N., Marchi, S., Höfner, S., & Sierks, H. 2015b, *Planet. Space Sci.*, 107, 53
- Vincent, J.-B., Oklay, N., Pajola, M., et al. 2016, *A&A*, 587, A14
- Weissman, P., Morbidelli, A., Davidsson, B., & Blum, J. 2020, *Space Sci. Rev.*, 216, 1

## **2.3 Volatile Morphologies Examined Using Discrete Element Method Modelling**

This section includes two articles focussing on DEM modelling written by D. Kappel and M. Sachse. They discuss the dynamic evolution of morphologic features formed of a mixture of polydisperse dust and ice DEM particles. These particles represent dust and ice through different physical properties similar to the analogue materials used in the laboratory investigations described in Section 2.2. The overarching aim is to extract physical properties of cometary regolith constrained by morphologic features and their evolution. Prior to the implementation of this work, I had developed the idea as part of the junior research group.

The articles are based on each other with Kappel et al. (2020) establishing the framework of the simulations. This publication includes a variety of parameter studies that were necessary to adequately describe cometary regolith. Sachse et al. (2022) subsequently builds on and expands this study to the process of particle redistribution on comets (Keller et al., 2017).

Kappel et al. (2020) introduce the physics behind the DEM code (e.g. the contact model, particle scaling, inter-particle friction, cohesion and bonds). Considering a two component mixture of polydisperse dust and ice particles, they determined a working set of parameters that enabled the simulation of realistic morphologies and their evolution on comet 67P. Constraints on the physical parameters were derived by simulating events on 67P, such as boulders dropping from a plateau and cliffs collapsing under gravity, and adjusting the code to match the simulated to the observed morphologies on 67P. The study finds that the simulated cometary material has a tensile strength on the order of 1–10 Pa and that a high particle friction, possibly caused by rough and angular particles, is necessary to reproduce the brittleness of the observed cometary material. It also finds that heterogeneities and/or structural defects, possibly caused by the uneven distribution or sublimation of ice, are necessary to enable cliff collapses.

The article by Sachse et al. (2022) focuses on the formation mechanism of aeolian-like features on 67P. In particular the work investigates wind tail-like features that occur as a deposit of fine grained regolith behind boulders. Occasionally, a moat in front of a boulder with a wind tail can also be observed. After a morphologic description of the aeolian-like features on 67P, the article describes a DEM simulation investigating their formation. The simulation consists of a boulder embedded in a particle bed impinged by a volatile-driven particle stream. The simulation explores the effect of different model parameters (e.g. boulder shape and particle sizes, friction and Young's modulus) on the

## 2 Synergy of Conducted Research

morphology of the developing wind tails and moats. The research shows that the density of particles near the surface mobilized through volatile sublimation has to be on the order of  $10^{-6}$ – $10^{-4}$  kg/m<sup>3</sup> and the mass required to recreate the observed morphology on 67P sums up to about 250 kg/m<sup>2</sup>.

The two DEM focused articles can be cited as:

- Kappel, D., Sachse, M., Haack, D., & Otto, K. A. (2020). Discrete Element Modeling of Boulder and Cliff Morphologies on Comet 67P/Churyumov-Gerasimenko. *Astronomy & Astrophysics*, 641(A19), 1–22. <https://doi.org/10.1051/0004-6361/201937152>.
- Sachse, M., Kappel, D., Tirsch, D., & Otto, K. A. (2022). Discrete Element Modeling of Aeolian-like Morphologies on Comet 67P/Churyumov-Gerasimenko. *Astronomy & Astrophysics*, 662(A2), 1–15. <https://doi.org/10.1051/0004-6361/202141296>.

### 2.3.1 Kappel et al. (2020)

Kappel, D., Sachse, M., Haack, D., & Otto, K. A. (2020). Discrete Element Modeling of Boulder and Cliff Morphologies on Comet 67P/Churyumov-Gerasimenko. *Astronomy & Astrophysics*, 641(A19), 1–22. <https://doi.org/10.1051/0004-6361/201937152>.

The research leading to this publication was led by D. Kappel. I devised the concept of this project, namely using morphologic features to constrain the volatile content in cometary regoliths, here the regolith of comet 67P. I provided information on the morphologic features considered in this work (e.g. cliffs and boulders) and generated Figure 1. M. Sachse supported the choice of input data, simulations and data interpretation, while D. Haack provided feedback on the tensile strength simulations based on his laboratory work (Haack et al., 2020). All authors assisted with refining the manuscript.



# Discrete element modeling of boulder and cliff morphologies on comet 67P/Churyumov-Gerasimenko

D. Kappel<sup>1,2</sup>, M. Sachse<sup>2</sup>, D. Haack<sup>2</sup>, and K. A. Otto<sup>2</sup>

<sup>1</sup> Institute of Physics and Astronomy, University of Potsdam, Karl-Liebknecht-Str. 24–25, 14476 Potsdam, Germany  
e-mail: [dakappel@uni-potsdam.de](mailto:dakappel@uni-potsdam.de)

<sup>2</sup> Institute of Planetary Research, German Aerospace Center (DLR), Rutherfordstr. 2, 12489 Berlin, Germany

Received 20 November 2019 / Accepted 10 July 2020

## ABSTRACT

**Context.** Even after the Rosetta mission, some of the mechanical parameters of comet 67P/Churyumov-Gerasimenko's surface material are not yet well constrained. These parameters are needed to improve our understanding of cometary activity or for planning sample return missions.

**Aims.** We study some of the physical processes involved in the formation of selected surface features and investigate the mechanical and geometrical parameters involved.

**Methods.** Applying the discrete element method (DEM) in a low-gravity environment, we numerically simulated the surface layer particle dynamics involved in the formation of selected morphological features. The material considered is a mixture of polydisperse ice and dust spheres with inter-particle forces given by the Hertz contact model, translational friction, rolling friction, cohesion from unsintered contacts, and optionally due to bonds from ice sintering. We determined a working set of parameters that enables the simulations to be reasonably realistic and investigated morphological changes due to modifications thereof.

**Results.** The selected morphological features are reasonably well reproduced using model materials with a tensile strength on the order of 1–10 Pa. Increasing the diameters of the spherical particles decreases the material strength, and increasing the friction leads to a more brittle but somewhat stronger material. High friction is required to make the material sufficiently brittle to match observations, which points to the presence of very rough, even angular particles. Reasonable seismic activity does not suffice to trigger the collapses of cliffs without material heterogeneities or structural defects.

**Conclusions.** DEM modeling can be a powerful tool to investigate mechanical parameters of cometary surface material. However, many uncertainties arise from our limited understanding of particle shapes, spatial configurations, and size distributions, all on multiple length scales. Further numerical work, in situ measurements, and sample return missions are needed to better understand the mechanics of cometary material and cometary activity.

**Key words.** comets: general – comets: individual: 67P/Churyumov-Gerasimenko – methods: numerical

## 1. Introduction

Remote sensing data of cometary nuclei have revealed a wealth of morphologic features that cover the surfaces of comets (Sunshine et al. 2016; El-Maarry et al. 2019). These include features unique to comets, such as pits (Vincent et al. 2015) and quasi-circular depressions (Brownlee et al. 2004), but they also encompass features known from other planetary bodies, such as mass-wasting deposits (Thomas et al. 2015a), boulder fields (Pajola et al. 2015), and sedimentary deposits (Thomas et al. 2015b). Morphologic features and the processes that form them are manifestations of the mechanical properties of the cometary material under the influence of a relatively low surface acceleration ( $\sim 2 \times 10^{-4} \text{ m s}^{-2}$ , Groussin et al. 2015), an effect of cohesive forces that is more pronounced than in our natural terrestrial environment (Scheeres et al. 2010), and the activity generated by sublimation of ices at smaller heliocentric distances. These features have the potential to reveal information on the mechanical properties of the cometary material which is indispensable for a wide range of research involving the modeling of activity, outbursts, thermal alterations, and potential sample-return techniques.

The mechanical properties of the most thoroughly studied comet 67P/Churyumov-Gerasimenko (hereafter 67P) have been

investigated by a variety of instruments onboard the Rosetta spacecraft and its lander Philae. The nucleus of 67P measures approximately 4.3 km by 4.1 km at its longest and widest dimensions, respectively, and consists of a larger and a smaller lobe connected by a narrower neck (Sierks et al. 2015). The evaluation of in situ data acquired on the nucleus surface (Knapmeyer et al. 2018; Spohn et al. 2015) and of remote sensing data from kilometer-scale (Sierks et al. 2015; Capaccioni et al. 2015; Fornasier et al. 2015) and centimeter-scale (Mottola et al. 2015; Bibring et al. 2015) distances have revealed the presence of highly complex processes shaping the comet's surface and near subsurface. For example, the southern hemisphere of comet 67P is mainly composed of bare consolidated material while the northern hemisphere is extensively covered by airfall particles (El-Maarry et al. 2015, 2016, 2017). This dichotomy is caused by inhomogeneous energy input introduced by seasonal effects, which result in higher erosion rates in the south and airfall particle deposition in the north (Keller et al. 2015, 2017).

The consolidated surface layer mainly observed in 67P's southern hemisphere is probably extremely tough with a uniaxial compressive strength of  $>2 \text{ MPa}$  (Spohn et al. 2015), presumably as a result of sintering of water ice components of the surface layer material, but the compressive strength of the granular airfall material covering the northern hemisphere is only  $\sim 1\text{--}3 \text{ kPa}$

with a shear strength of 4–30 Pa (Biele et al. 2015; Groussin et al. 2015; Basilevsky et al. 2016). The size and arrangement of fracture polygons on the consolidated surfaces also hint at a strength in the MPa range (Auger et al. 2018). The thickness of a sintered layer is related to the diurnal and seasonal thermal skin depths, which are of the order of 1–2 cm and 1 m, respectively (Gulkis et al. 2015). In agreement with these findings, the accelerometers onboard the Philae lander measured the thickness of the consolidated layer at the Abydos landing site, and a value of 10–50 cm was retrieved (Knapmeyer et al. 2018). Below this layer, the cometary material is assumed to be unaffected by insolation and should therefore be pristine (Groussin et al. 2015). Observations by Rosetta seem to suggest that the pristine bulk cometary material is composed of small pebbles ranging from millimeter to centimeter scales (Fulle et al. 2016; Blum et al. 2017). These pebbles are built of individual, smaller, micron-scale dust grains (Fulle et al. 2015; Mannel et al. 2016) and volatiles that may sublime when close to the sufficiently illuminated comet surface (Blum et al. 2017).

Estimates of the tensile strength of the pristine cometary material on a larger scale have been derived from geometrical dimensions of overhangs in the presence of the local surface acceleration and are found to be on the order of 10 Pa (Groussin et al. 2015; Attree et al. 2018). Additional estimates based on stresses introduced by the self-gravity of the whole bilobed comet reveal a comparable internal strength between 10 Pa and 70 Pa (Hviid et al. 2016, Hviid et al., priv. comm.). The tensile strength could also be constrained by the Deep Impact cratering experiment on comet Tempel 1 and has been reported to be less than 12 kPa (Holsapple & Housen 2007).

Further mechanical properties of the consolidated surface material on 67P have been derived with the accelerometers onboard the Philae lander, which allow a confinement of the shear modulus to 3.6–346 MPa and of Young’s modulus to 7.2–980 MPa (Knapmeyer et al. 2018). The average density of 67P was determined as  $\sim 0.5 \text{ g cm}^{-3}$  (Jorda et al. 2016; Preusker et al. 2017) leading to a bulk porosity of 70–75% assuming a dust-to-ice-mass ratio of  $4 \pm 2$  (Rotundi et al. 2015), which is highly comparable to the porosity of 75–85% inferred from CONSERT radar measurements (Kofman et al. 2015).

Despite the low strength, density, and gravitational acceleration on cometary surfaces, the strength-to-gravity ratio is similar to that of weak rocks on Earth (e.g. siltstone) (Groussin et al. 2015). Therefore, well-known gravitationally influenced processes on Earth, such as cliff collapses and the subsequent deposition of boulders on intermediate slopes, are also abundant on 67P (Fig. 1). In particular, the recent collapse of the Aswan cliff on 67P has attracted much attention because it revealed pristine material enriched in water ice at the freshly exposed escarpment (Pajola et al. 2017). The collapse of the approximately 134-m-high cliff generated talus material and debris, which comprises a large number of boulders (Pajola et al. 2017; Pajola et al. 2016). The largest boulder has a size of 25.5 m and is located on a relatively flat slope of less than  $10^\circ$ . Generally, the sizes of deposited boulders on 67P decrease with increasing slope (Pajola et al. 2016; Groussin et al. 2015), and the largest boulders are located in the comet’s gravitational lows (Imhotep and Hapi morphological regions; Thomas et al. 2015a) with diameters up to about 50 m. Boulders located in the neck region of 67P (Hapi region) possibly dropped from a maximum height of approximately 900 m (Thomas et al. 2015a). The survival of these relatively large boulders from falls of such heights again constrains the mechanical properties of the involved material.

Due to the limited temporal coverage of observations at given surface locations, dynamical processes like cliff collapses have not been observed themselves, but in the best cases observations were made before and after they happened. Other processes causing slow but continuous changes of the local surface morphology like dust movement (dunes, aeolian-like structures, burying or excavation of consolidated structures by dust) or the development of fracture networks have mainly been observed with long time gaps.

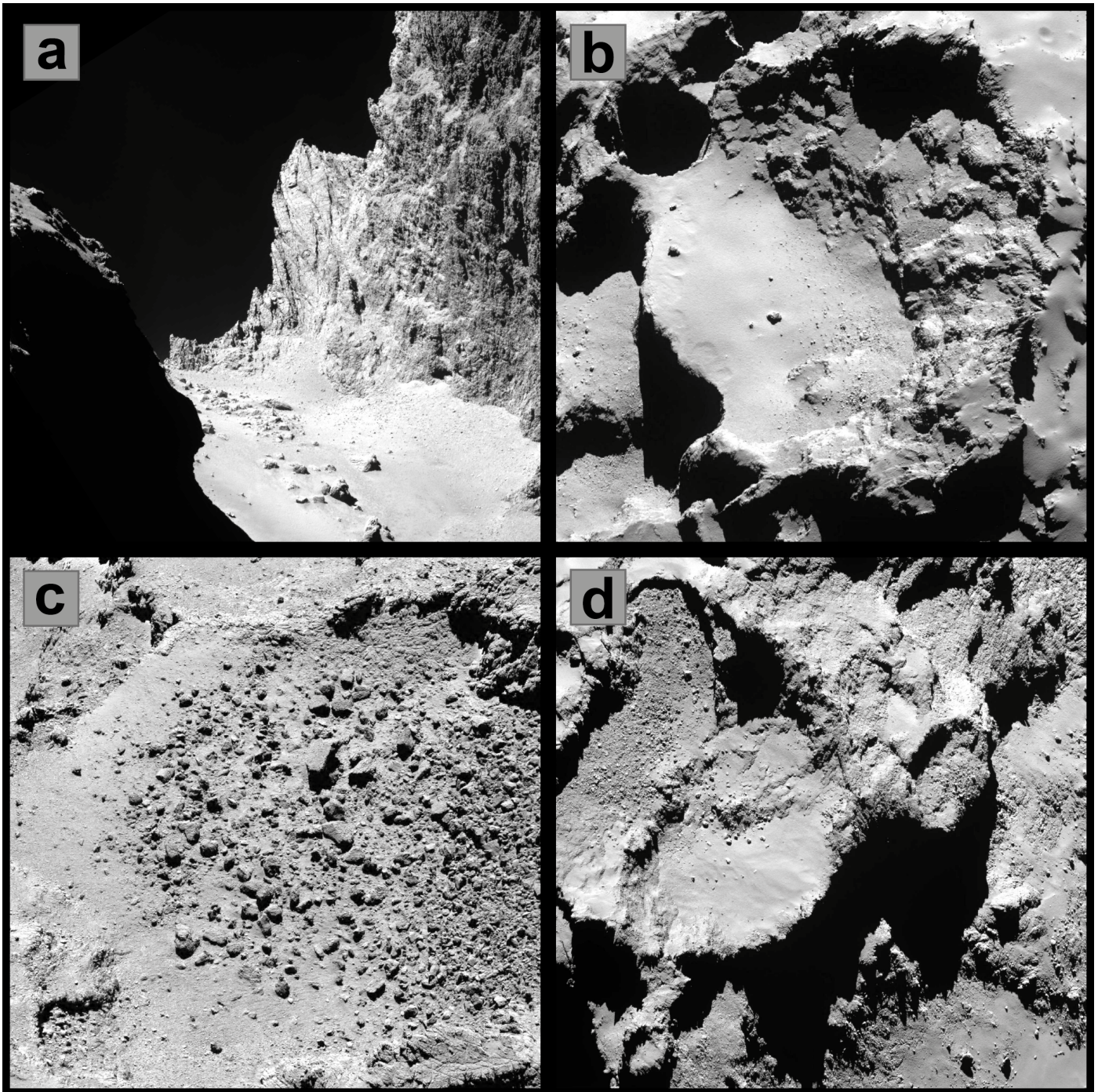
To complement the available measurements and improve our general understanding of the mechanical properties and dynamic processes on comets, numerical simulations can help to constrain some of the micro- and macro-mechanical parameters, for example by excluding certain parameter ranges or combinations incompatible with the development of various observed morphological features. The discrete element method (DEM) is a widely accepted method for modeling granular and discontinuous materials that consist of separate, discrete particles, a well-suited analog for the pebbles assumed to make up the pristine cometary material.

The DEM has also been used to simulate the dynamics of atoms and molecules, granular matter, bulk materials, and rocks. In the field of planetary science, DEM modeling has been used to study the formation, evolution, and surface properties of planetary bodies, including small bodies with weak surface materials and at low gravity such as asteroids and comets. For example, it has been used to simulate impact processes on the asteroids Eros and Itokawa to explain the origin of exposed boulders on their surfaces via the Brazil nut effect (Tancredi et al. 2012), the removal of surface materials on asteroids by strong centrifugal forces resulting from rapid rotation (Hirabayashi et al. 2015), and catastrophic collisional disruptions of planetesimals and reaccumulation of their fragments to explain the formation and the bilobate shape of several comets including 67P (Schwartz et al. 2018). The DEM has also been used to address engineering problems such as hopping mechanisms to relocate landers on asteroids (Cheng et al. 2019) and techniques to sample material from asteroid surfaces (Cheng et al. 2017). However, DEM modeling has not yet been widely used to study the surface morphology or mechanical properties of cometary material – a material in a low-gravity environment that, in addition to dust, consists of ices, and where the ices may form sinter bonds and sublime.

Our overall aim in studying the mechanical properties of cometary surfaces and nuclei is to provide reliable data needed to understand the development of the coma (e.g., dust lifting), to assess the impact scenarios on the nucleus itself or of a comet on the Earth for example, to design mitigation schemes to change a comet’s ephemerides to avoid the latter, to design sample-return procedures (Squyres et al. 2018; Küppers et al. 2009), and so on. Depending on whether the nucleus is a so-called rubble pile with or without large voids or a mechanically homogeneous dust–ice mixture, mechanical interactions can turn out very differently. In the same way, it can make a large difference if the nucleus has a tough meter-scale surface layer that extends globally or is locally confined, has large tough or weak boulders, or is entirely built from fluffy particle agglomerates. This can render a sample-return procedure unsuccessful or can decide which method is to be employed for an ephemerides modification required to prevent a potential impact on Earth.

In particular, we investigate in the present work the dropping of larger boulders from small heights and collapses of cliffs. For this purpose, we aim to reproduce such events with DEM modeling of corresponding suitable simulation scenarios using the





**Fig. 1.** Examples of morphologic features on comet 67P as imaged by the OSIRIS narrow-angle camera (Keller et al. 2007). (a) Hathor cliff with boulders accumulating at the airfall-covered foot of the cliff. The consolidated tough material of the cliff supports an escarpment height of about 900 m. The largest boulders are approximately 50 m across. (b) Pre-collapse Aswan plateau and cliff site with smooth airfall deposits, consolidated wall material, and debris with boulders at the cliff foot (*center left*). The shadowed pit in the top left of the image is approximately 200 m across. (c) Foot of a collapsed debris field populated with boulders up to 10–15 m across. (d) Debris deposits superimposing an apparently smooth region of small airfall particles. Bare consolidated and airfall-covered terrains alternate spatially. The boulder deposit in the upper left and the airfall-covered plateau in the center of the image are each approximately 500 m wide. Figure tags: (a) NAC\_2014-09-29T08.52.08.332Z\_ID30\_1397549001\_F41, (b) NAC\_2014-09-29T16.10.04.817Z\_ID30\_1397549000\_F16, (c) NAC\_2016-08-03T07.28.34.758Z\_ID30\_1397549000\_F22, (d) NAC\_2014-09-13T23.29.22.367Z\_ID30\_1397549001\_F41. Credits: ESA/Rosetta/MPS for OSIRIS Team MPS/UPD/LAM/IAA/SSO/INTA/UPM/DASP/IDA.

example of comet 67P. Since the modeling cannot capture the full real-world complexity, our immediate aim is to study some of the physical processes involved in the formation of these features and to find a working set of parameters that enables the

simulations to be reasonably realistic. The simulation scenarios are then used as starting points for parameter sensitivity studies to constrain mechanical properties, contact forces, particle sizes, and so on, of the surface-layer material.



In Sect. 2 we provide details of our numerical DEM modeling. The basic investigated simulation scenarios are introduced in Sect. 3, and the simulation outcomes and changes when varying their setups are presented and discussed in Sect. 4. Finally, conclusions and an outlook are given in Sect. 5.

## 2. Numerical modeling

The dynamics of the granular cometary surface material are modeled with the open-source DEM simulation code LIGGGHTS (Kloss et al. 2012) which is capable of parallel processing. Generally, we assume the particles to be represented by polydisperse spheres consisting either of dust or of water ice. The spheres interact according to the Hertz contact model (Sect. 2.1) and additionally are subject to translational friction (Sect. 2.1), rolling friction (Sect. 2.2), and ambient surface acceleration. In addition to unsintered cohesive contacts (Sect. 2.3), bonds from ice sintering can be introduced (Sect. 2.4) that break when the interparticle stresses exceed certain threshold values. This way, we can also model the hard consolidated terrain that was found in many places on the surface of 67P and may result from water-ice sintering. To enable the simulation of macroscopic scenarios with relatively small particles, we apply the coarse-graining technique (Bierwisch et al. 2009) (Sect. 2.5). Table 1 provides an overview of the employed symbols and typing notations.

### 2.1. Hertz contact model

Using the discrete element method (Cundall & Strack 1979) to model the dynamics of granular matter, Newton's equations of motion,

$$\begin{aligned} m_i \dot{\mathbf{v}}_i &= \mathbf{F}_i \\ \underline{I}_i \dot{\boldsymbol{\omega}}_i &= \mathbf{M}_i, \end{aligned} \quad (1)$$

have to be solved for  $N$  particles with masses  $m_i$ , inertia tensors  $\underline{I}_i$ , center of mass positions  $\mathbf{r}_i$ , velocities  $\mathbf{v}_i$ , angular velocities  $\boldsymbol{\omega}_i$ , forces  $\mathbf{F}_i$ , and torques  $\mathbf{M}_i$ , where subscript  $i$  is a counting index with  $i \in \{1, \dots, N\}$ . The solution is performed by explicit time integration with fixed time-step  $\Delta t$  using the velocity Verlet method (Swope et al. 1982) that achieves a global error of order two,

$$\begin{aligned} \mathbf{r}_i(t + \Delta t) &= \mathbf{r}_i(t) + \mathbf{v}_i(t) \Delta t + \frac{\mathbf{F}_i(t)}{2m_i} \Delta t^2 \\ \mathbf{v}_i(t + \Delta t) &= \mathbf{v}_i(t) + \frac{\mathbf{F}_i(t) + \mathbf{F}_i(t + \Delta t)}{2m_i} \Delta t \\ \boldsymbol{\omega}_i(t + \Delta t) &= \boldsymbol{\omega}_i(t) + \frac{\underline{I}_i^{-1} [\mathbf{M}_i(t) + \mathbf{M}_i(t + \Delta t)]}{2} \Delta t. \end{aligned} \quad (2)$$

The net force  $\mathbf{F}_i$  acting on a given particle can be written as a sum of external forces  $\mathbf{F}_{\text{ext},i}$  and of forces arising from interactions with other particles  $\mathbf{F}_{ij}$ ,

$$\mathbf{F}_i = \mathbf{F}_{\text{ext},i} + \sum_{j \neq i} \mathbf{F}_{ij}. \quad (3)$$

Here, we only consider the force due to the surface acceleration of the nucleus,  $\mathbf{F}_{\text{ext},i} = m_i \mathbf{g}$ , and mechanical forces between contacting particles as listed in the introduction paragraph of Sect. 2. In particular, we do not consider gravity between particles, solar radiation pressure, or electrostatic forces.

**Table 1.** Symbols.

Symbol	Unit	Description
$\bar{A}$	m <sup>2</sup>	Area of sinter bond cross section
$cg$	1	Coarse-graining factor
$C_r$	1	Rolling viscous damping coeff.
$e_r$	1	Coefficient of restitution
$E$	Pa	Young's modulus
$F$	N	Force
$F_c$	N	Cohes. force from unsint. contacts
$F_{c,a}$	N	Asperity cohesive force
$F_H$	N	Hertz contact force
$g$	m s <sup>-2</sup>	Ambient surface acceleration
$i_c$	1	Index of cumulative power law
$I$	kg m <sup>2</sup>	MOI of particle
$\bar{I}$	m <sup>4</sup>	MOI of sinter bond cross section
$\bar{J}$	m <sup>4</sup>	Polar MOI of sinter bond cross sect.
$k$	N m <sup>-1</sup>	Elastic stiffness
$m$	kg	Mass
$M$	N m	Torque
$\mathbf{n}$	m	Normal vector
$r$	m	Position
$R_a$	m	Radius of surface asperity
$R$	m	Particle radius
$S_c$	1	Surface cleanliness
$t$	s	Time (not as subscript)
$t_c$	m	Min. distance between surfaces
$\Delta U$	m	Position increment
$v$	m s <sup>-1</sup>	Velocity
$\gamma_n$	N s m <sup>-1</sup>	Normal damping parameter
$\gamma_t$	N s m <sup>-1</sup>	Tangential damping parameter
$\delta_n$	m	Normal overlap distance
$\delta_t$	m	Tangential displacement
$\eta_r$	1	Rolling viscous damping ratio
$\Delta\theta$	rad	Rotation increment
$\dot{\theta}_r$	rad s <sup>-1</sup>	Relative rolling angular velocity
$\bar{\lambda}$	1	Sinter bond radius scaling
$\mu$	1	Translational friction coefficient
$\mu_r$	1	Rolling friction coefficient
$\nu$	1	Poisson's ratio
$\rho$	kg m <sup>-3</sup>	Particle solid mass density
$\sigma$	N m <sup>-2</sup>	Tensile stress
$\tau$	N m <sup>-2</sup>	Shear stress
$\phi$	1	Volume filling factor
$\omega$	J m <sup>-2</sup>	Surface energy density (no subscr.)
$\omega$	rad s <sup>-1</sup>	Angular velocity (with subscript)

**Notes.** Additional subscripts n, t, and r are for normal and tangential components and rotational parameters, respectively, and  $i$  and  $j$  are counting-indices for different particles. Overlines indicate sinter bond properties, and an additional superscript asterisk indicates effective versions of a quantity computed from the properties of the two contact partners. Vectorial quantities are typed in bold, their absolute values and other scalars are not, and tensors are indicated by an underscore. "MOI" stands for "moment of inertia".

In order to efficiently check for interactions between particles, neighbor lists, which store all particle pairs within a given cutoff distance, are used and only updated after several time-steps. Typically, the larger the cutoff distance, the less often



neighbor lists need to be updated, but at every time-step more pairs must be checked for possible interactions. The time-steps were set to be just shorter than 10% of the minimum of Rayleigh time and Hertz time, which proved to lead to a stable time integration, but exemplarily we also test 3%.

The Hertz (H) contact force between two particles is computed as the sum of the normal (n) and tangential (t) forces at the contact point (Kloss et al. 2012),

$$\mathbf{F}_H = \mathbf{F}_n + \mathbf{F}_t, \quad (4)$$

with

$$\begin{aligned} \mathbf{F}_n &= k_n \delta_n \mathbf{n} - \gamma_n \mathbf{v}_n \\ \mathbf{F}_t &= k_t \delta_t - \gamma_t \mathbf{v}_t, \end{aligned} \quad (5)$$

which is a nonlinear spring-dashpot model consisting of an elastic (Hertz 1882) and a viscous/dissipative part.  $k_n$  and  $k_t$  are the elastic parameters for normal and tangential contact, and  $\gamma_n$  and  $\gamma_t$  the normal and tangential damping parameters that govern the damping forces resulting at the relative normal and tangential velocities of the surfaces at the contact point,  $\mathbf{v}_n$  and  $\mathbf{v}_t$ , which are given by

$$\begin{aligned} \mathbf{v} &= (\dot{\mathbf{r}}_i - \boldsymbol{\omega}_i \times R_i \mathbf{n}) - (\dot{\mathbf{r}}_j + \boldsymbol{\omega}_j \times R_j \mathbf{n}) \\ \mathbf{v}_n &= (\mathbf{v} \cdot \mathbf{n}) \mathbf{n} \\ \mathbf{v}_t &= \mathbf{v} - \mathbf{v}_n, \end{aligned} \quad (6)$$

and where

$$\mathbf{n} = \frac{\mathbf{r}_i - \mathbf{r}_j}{|\mathbf{r}_i - \mathbf{r}_j|}, \quad (7)$$

is the unit vector in the contact normal direction. For improved readability, we typically suppress double indexes  $ij$  indicating quantities associated to a particle pair.

The normal overlap  $\delta_n$  of two particles is defined as the sum of their nominal radii,  $R_i$  and  $R_j$ , minus the distance between their center positions  $\mathbf{r}_i$  and  $\mathbf{r}_j$ ,

$$\delta_n = R_i + R_j - |\mathbf{r}_i - \mathbf{r}_j|, \quad (8)$$

or zero in case there is no overlap. The tangential displacement  $\delta_t$  is computed by integrating the relative tangential velocity of the surfaces at the contact point,  $\mathbf{v}_t$ , from the time at which the contact was initiated to the current time,

$$\delta_t^* = \sum_i \mathbf{v}_t(t_i) \Delta t, \quad (9)$$

and projecting this path onto the current contact plane,

$$\delta_t = \delta_t^* - (\delta_t^* \cdot \mathbf{n}) \mathbf{n}. \quad (10)$$

The tangential displacement is truncated to fulfill the Coulomb friction law,  $F_t \leq \mu F_n$ , with translational friction coefficient  $\mu$  such that  $\mu F_n$  is the maximum tangential force before the particles begin to slide over each other.

From the coefficient of restitution  $e_r$  ( $0 < e_r \leq 1$ ), which is defined as the ratio of the final to the initial relative velocity between two particles after they collide, Young's modulus  $E$ , and Poisson's ratio  $\nu$ , the coefficients in Eq. (5) are computed as (Di Renzo & Di Maio 2004).

$$\begin{aligned} k_n &= \frac{2}{3} S_n \\ \gamma_n &= -2 \sqrt{\frac{5}{6}} \beta \sqrt{S_n m^*} \geq 0 \\ k_t &= S_t \\ \gamma_t &= -2 \sqrt{\frac{5}{6}} \beta \sqrt{S_t m^*} \geq 0, \end{aligned} \quad (11)$$

where the notation  $\geq 0$  indicates terms that are non-negative because of the minus sign, and the intermediate quantities are

$$\begin{aligned} S_n &= 2 E^* \sqrt{R^* \delta_n} \\ S_t &= 8 G^* \sqrt{R^* \delta_n} \\ \beta &= \frac{\log(e_r)}{\sqrt{\log^2(e_r) + \pi^2}} \leq 0 \\ \frac{1}{m^*} &= \frac{1}{m_i} + \frac{1}{m_j} \\ \frac{1}{R^*} &= \frac{1}{R_i} + \frac{1}{R_j} \\ \frac{1}{E^*} &= \frac{1 - \nu_i^2}{E_i} + \frac{1 - \nu_j^2}{E_j} \\ \frac{1}{G^*} &= \frac{2(2 - \nu_i)(1 + \nu_i)}{E_i} + \frac{2(2 - \nu_j)(1 + \nu_j)}{E_j}. \end{aligned} \quad (12)$$

Here,  $E^*$  is the effective Young's modulus,  $G^*$  the effective shear modulus,  $m^*$  the effective mass, and  $R^*$  the effective radius. We note that there is a mistake in the definition of  $G^*$  in Di Renzo & Di Maio (2004), which was corrected in Di Renzo & Di Maio (2005).

Young's modulus ranges from 6 to 15 GPa from 273 to 133 K for water ice (see Mellon 1997 and citations therein Gold 1958; Hobbs 1974), and for example has a value of  $(78 \pm 19)$  GPa for basaltic rock mass (Schultz 1995) as proxy for our dust. However, using such high values in our simulations would require very small time-steps to resolve the Hertz collisions, and consequently very long computation times. However, Bierwisch et al. (2009) verified that  $E$  (or rather  $E/(1 - \nu^2)$ ) can be reduced to significantly smaller values (in the order of  $\geq 10^7$  Pa) without substantially affecting the simulation outcomes, and cited Martin & Bordia (2008) for the observation that a realistic value is important only if an external pressure is applied, the latter being negligible in our scenarios. We therefore take  $E = 10^8$  Pa for both water ice and dust particles. For Poisson's ratio, Schultz (1995) gave a value of  $0.25 \pm 0.05$  for basaltic rock mass, and Mellon (1997) cited values between 0.1 and 0.3 for most rocks (Haas 1989) and around 0.4 for water ice at Martian temperatures (Hobbs 1974). We set the Poisson's ratio for both our ice and dust particles to  $\nu = 0.3$ . Finally, the coefficient of restitution generally depends on impact speed. However, since the relative velocities of neighboring particles differ only slightly, we assume  $e_r = 0.3$ , independent of impact speed, an intermediate value typical at normal-impact velocities of around  $2 \text{ cm s}^{-1}$  (Brilliantov et al. 1996). Additionally, we perform simulations with  $e_r = 0.1$  and 0.8 to investigate the effect of this parameter.

## 2.2. Rolling friction

As reviewed by Ai et al. (2011), causes of rolling resistance include aspherical particle shapes, plastic deformation, viscous

hysteresis, and adhesion. [Ai et al. \(2011\)](#) classified rolling resistance models into four different types from A to D. In Model A, a constant torque is directed against the relative rotation between two particles in contact. Although this dissipates kinetic energy, as desired, after settling of a particle assembly there remains residual energy that is dependent on the time discretization of the simulation because of a remaining torque with constant magnitude whose direction is alternating at every time-step. This can destabilize (pseudo-) static particle configurations (piles). In Model B (viscous type), rolling friction is parameterized as being proportional to angular velocity. This model properly dissipates kinetic energy, but the formation of (pseudo-) static piles requires an additional static torque. [Ai et al. \(2011\)](#) immediately dismissed contact-independent Model D, in which torque depends on the absolute- rather than the relative rotation or rotational velocity. This can lead to different torques being applied to each of the two particles in contact, which violates the conservation of angular momentum. Hence, we apply Model C, an elastic-plastic spring-dashpot model (EPSD). Here, the presence of both dynamic and static torques leads to kinetic energy dissipation and can support the packing structure in (pseudo-) static configurations, while it also avoids unphysical Model-A-type residual oscillations.

The equations governing Model C can be found in [Ai et al. \(2011, Sect. 5.3\)](#) and are here recited for later reference in [Sect. 2.5](#). The rolling resistance torque at time  $t$ ,

$$M_r(t) = M_r^k(t) + M_r^d(t), \quad (13)$$

consists of a spring torque  $M_r^k$  and a viscous damping torque  $M_r^d$ .

The spring torque after time increment  $\Delta t$  is

$$M_r^k(t + \Delta t) = \min(M_r^k(t) + \Delta M_r^k(t), M_r^m), \quad (14)$$

with spring torque increment

$$\Delta M_r^k(t) = -k_r \Delta \theta_r \quad (15)$$

and limiting spring torque

$$M_r^m = \mu_r R^* F_n, \quad (16)$$

which is achieved at the full mobilization rolling angle  $\theta_r^m = M_r^m/k_r$ , where the particles begin to slide over each other. Here,  $\mu_r$  is the rolling friction coefficient, and  $k_r$  is the rolling stiffness, which is calculated in LIGGGHTS ([DCS Computing GmbH 2016](#)) as

$$k_r = 2.25 \frac{1}{\text{rad}} k_n \mu_r^2 R^{*2}. \quad (17)$$

The viscous damping torque  $M_r^d$  after time increment  $\Delta t$  is

$$M_r^d(t + \Delta t) = -C_r \dot{\theta}_r, \quad (18)$$

in cases where  $|M_r^k(t + \Delta t)| < M_r^m$ , and zero in cases of full mobilization  $|M_r^k(t + \Delta t)| = M_r^m$ , where  $\dot{\theta}_r$  is the relative rolling angular velocity between the two particles in contact. The rolling viscous damping coefficient  $C_r$  can be expressed as

$$C_r = 2 \eta_r \sqrt{k_r} \left( \frac{1}{I_i + m_i R_i^2} + \frac{1}{I_j + m_j R_j^2} \right)^{-1/2}, \quad (19)$$

where  $\eta_r$  is the rolling viscous damping ratio, and  $I_i$  and  $I_j$  are the moments of inertia of the two contacting particles.

In our simulations, we have to set the rolling friction coefficient  $\mu_r$  and rolling viscous damping ratio  $\eta_r$  as unitless non-negative parameters that define the magnitudes of the spring and the viscous damping torques. For numerical tests, [Ai et al. \(2011\)](#) used values up to 0.8 for  $\mu_r$  and up to 1.5 for  $\eta_r$ , but as in translational friction, larger values are possible on physical grounds, as can be seen when considering the effective rolling friction between cog wheels for example. We use rolling friction also as a computationally inexpensive proxy for complex particle shapes.

### 2.3. Unsintered cohesive contacts

A particle is additionally subject to forces arising from the mere contact with or close proximity to another particle (van-der-Waals inter-particle force), which we here denote as cohesive forces from unsintered contacts. In particular, these forces do not include forces due to bonds resulting from ice sintering, and in contrast to sinter bond forces ([Sect. 2.4](#)), they do not depend on the rotational deviation from the initial state at which a contact between two particles was established.

The Johnson-Kendall-Roberts (JKR) model ([Johnson et al. 1971](#)) is widely applied to describe cohesive forces between unsintered spherical particles, but it is numerically not very efficient and also predicts significant forces even when the sphere centers are separated by distances exceeding the sum of their nominal radii, which makes it cumbersome to use in LIGGGHTS. Since the real-world cohesive forces are not exactly known for cometary particles and also depend on particle shape, roughness, cleanliness of the particles (see below), and other parameters we cannot control, we apply the numerically much simpler Derjaguin-Muller-Toporov (DMT) model ([Muller et al. 1983](#)). The DMT cohesive force,

$$F_c = -2\pi R^* \omega, \quad (20)$$

is independent of the Hertz-overlap, and applies as long as the spheres are nominally in contact, that is, the sphere center distance does not exceed the sum of the nominal particle radii. This force is also the value of the pull-off force defined as the force required to separate the surfaces ([Barthel 2008](#)). Here,  $\omega$  is the surface energy density (or rather half the sum of the surface energy densities of the contacting partners), which is tabulated in the literature for various materials. We take  $\omega = 0.028 \text{ J m}^{-2}$  from the direct measurements by [Heim et al. \(1999\)](#). This value has been determined by pull-off force measurements of micron-sized silica spheres and is valid for the DMT model. Furthermore,  $\omega$  for the JKR model is four-thirds of this value. We note that [Heim et al. \(1999\)](#) used a different definition of the surface energy density: their  $\gamma$  in the pull-off force  $-4\pi R^* \gamma$  corresponds to  $\omega/2$ . The different surface energy density measurements for silica spheres reviewed by [Kimura et al. \(2015\)](#) scatter over two orders of magnitude, with the value given by [Heim et al. \(1999\)](#) being more representative of the lower end. This value is compatible with recent results from Brazilian disc test measurements ([Gundlach et al. 2018](#)) that additionally suggest the surface energy density of pure water ice spheres to be similar. Since the particles present in the surface layer of comet 67P are most certainly not perfectly spherical, a reduced cohesion can be expected ([Fuller & Tabor 1975; Leite et al. 2012](#)); see below for further details.

Another approach to describe cohesion from unsintered contacts was presented by [Scheeres et al. \(2010\)](#), where the cohesive force for particles on asteroids is explicitly given in terms of

the surface cleanliness,  $S_c = \Omega/t_c$ , the ratio of the diameter of an oxygen molecule,  $\Omega \sim 1.5 \times 10^{-10}$  m, to the minimum inter-particle distance between two surfaces,  $t_c$ . The resulting force is then estimated as  $F_c = -0.036 \text{ J m}^{-2} S_c^2 R^*$  (Scheeres et al. 2010), where the proportionality factor follows from a Hamaker constant of  $A = 4.3 \times 10^{-20}$  J and Eq. (27) by Scheeres et al. (2010),  $F_c = -A S_c^2 R^*/(48 \Omega^2)$ . The motivation of a formulation in terms of the surface cleanliness is given by the fact that two surfaces cannot come in close contact in terrestrial environments, because they are contaminated by atmospheric gas molecules. This leads to a decrease in the attractive force ( $S_c \sim 0.1$ ). In space environments, the contamination is smaller, and stronger forces can be expected ( $S_c \rightarrow 1$ ). Scheeres et al. (2010) also recited results by Castellanos (2005), who experimentally investigated the effect of surface asperities of particles with typical asperity radius  $R_a$ , where  $R_a < R$ . In this case, or when the particles are covered by smaller particles of radius  $R_a$ , the forces scale with  $R_a$  instead of  $R^*$ , i.e.,  $F_{c,a} \sim F_c R_a/R^*$  (Scheeres et al. 2010). Comparing with the plain DMT cohesive force, one can write  $F_c = -2\pi \omega R^* = -0.036 \text{ J m}^{-2} S_c^2 R^*$ , which translates to  $S_c = 1.56$ , and on the other hand we have  $F_{c,a} \sim -2\pi R^* (\omega R_a/R^*)$ .

In conclusion, for the cohesive forces from unsintered contacts we apply DMT theory with  $\omega$  from Heim et al. (1999), but regard this as an upper limit. For complex-shaped particles, we assume  $R_a/R^*$  to be on the order of 0.1–1.0. In our simulations, we therefore have to also investigate the effect of the DMT cohesive force being reduced by a certain factor; see also discussion in Sect. 4.1. Finally, Scheeres et al. (2010) investigated the relative importance of the physical forces acting on particles on the surface of small Solar System bodies. Applying the findings of these latter authors to the situation in our 67P simulation scenarios, self-gravity, solar radiation pressure, and electrostatic forces away from the terminator can be neglected compared to cohesive forces from unsintered contacts and to ambient surface acceleration.

## 2.4. Parallel bonds

As reviewed by Blackford (2007), when particles containing water ice are in contact over longer time-spans, they sinter, that is, necks form between them that grow with time, resulting in rigid bonds. This is even the case in the absence of pressure or melting, and can also take place without water vapor transport simply by surface or volume diffusion of water-ice molecules in the solid material. Water-ice sintering is only efficient when the absolute temperature is warmer than about 60% of the melting point (Blackford 2007, Fig. 11; reprinted from Maeno & Ebinuma 1983). The dominant processes are surface diffusion and vapor transport, the former being more efficient for colder temperatures and small sinter necks (Blackford 2007, Fig. 10; reprinted from Maeno & Ebinuma 1983). Regarding the diurnal and seasonal illumination cycles and the heat diffusion from the illuminated surface into deeper layers, the maximum sintering rate occurs at the surface down to a few thermal skin depths, where the ice experiences the highest temperatures (Molaro et al. 2019). In the case of 67P, we therefore expect the most and strongest sinter bonds to occur within the topmost layer on the scale of centimeters (diurnal) to meters (seasonal), considering the thermal inertia of about  $10\text{--}50 \text{ J K}^{-1} \text{ m}^{-2} \text{ s}^{-1/2}$  inferred from measurements of the MIRO instrument aboard Rosetta (Gulkis et al. 2015). However, in the uppermost layers, sublimation of volatiles is also efficient leading to desiccation and thus fewer or weaker sinter bonds, at least partly balanced by recondensation

during night, all of which potentially leads to a complex sinter bond and strength pattern with depth.

We apply the parallel bonds model by Potyondy & Cundall (2004) in our DEM framework to simulate the inter-particle forces resulting from such sinter bonds. Our implementation is based on the LIGGGHTS-WITH-BONDS package (Richter 2015), which is a beta version aimed at implementing the cited parallel bonds model. Such bonds are initially formed in the simulation when the surfaces of two particles are closer than a fraction of their mean radius and break when the inter-particle stresses exceed certain threshold values. We do not switch off the cohesive forces from the unsintered contacts when a sinter bond is formed because for a very weak sinter bond for example (immediately after its initial formation in case of real material) this would otherwise actually lead to an abrupt decrease of the inter-particle force, which we judge to be unrealistic and which is numerically unstable. In the other extreme, in case of a very strong sinter bond, a numerically still active cohesive force due to unsintered contacts does not significantly affect the result and incurs only minor computational overheads. Once broken, we do not let a sinter bond form again because the timescale for sintering is assumed to far exceed the simulated time-span. Potyondy & Cundall (2004) pointed out that on the microscopic level, parallel bonds exclusively break in case of tension between particles, not in case of compression. Macroscopic compressional fracturing of the material is caused by bond breakage due to lateral tension between particles resulting from the macroscopic compression. We note that LIGGGHTS-WITH-BONDS has to be modified in this regard to correctly implement Eq. (16.1) from Potyondy & Cundall (2004).

Potyondy & Cundall (2004) regarded a parallel bond between two bonding partners as a beam in classical theory of elasticity. The bond cement has mechanical properties that we take – in the absence of more detailed knowledge – to coincide with those of the bonded spheres themselves (motivated by the sintering being a result of the redistribution of the sphere material; at least of the water-ice part of it). In particular, this applies to Young’s modulus  $\bar{E} = E$  and Poisson’s ratio  $\bar{\nu} = \nu$ , where the overlines indicate parameters of the bond cement as opposed to parameters of the spheres. Following Silbert et al. (2001), we set the ratio between normal and shear stiffness  $\bar{k}_n/\bar{k}_t = 7/2$ . Additional bond properties include the bond radius  $\bar{R} = \bar{\lambda} \min(R_i, R_j)$ , with the radii  $R_i$  and  $R_j$  of the bonded spheres and parameter  $\bar{\lambda}$  scaling the bond radius, and the tensile and shear strengths of the bond cement,  $\bar{\sigma}$  and  $\bar{\tau}$ , respectively. To reduce the parameter space, we take  $\bar{\tau} = \bar{\sigma}$  and verified that the choice  $\bar{\tau} = 0.3 \bar{\sigma}$  leads to very similar simulation outcomes, which is related to the observation that most bonds in our simulations break due to normal stress. Assuming a bond state intermediate between barely ( $\bar{\lambda} \ll 1$ ) and completely sintered ( $\bar{\lambda} = 1$ ), we set  $\bar{\lambda} = 0.1$ . Mellon (1997) recited values of  $\bar{\sigma}$  between 1 and 2 MPa for water ice, and a moderately wider range for polycrystalline ice samples or frozen soils, all depending on strain rate, temperature, and sample size. Given the uncertainties, we use a reasonable generic value of  $\bar{\sigma} = 10^6$  Pa.

The force  $\bar{\mathbf{F}}$  and moment  $\bar{\mathbf{M}}$  carried by the parallel bond are computed as the sums of their normal (n) and tangential (t) components with respect to the contact plane,

$$\begin{aligned}\bar{\mathbf{F}} &= \bar{F}_n \mathbf{n} + \bar{F}_t \mathbf{t} \\ \bar{\mathbf{M}} &= \bar{M}_n \mathbf{n} + \bar{M}_t \mathbf{t},\end{aligned}\quad (21)$$



which are initialized to zero at bond formation and are then integrated from their increments

$$\begin{aligned}\Delta\bar{F}_n &= \bar{k}_n \bar{A} \Delta U_n \\ \Delta\bar{F}_t &= -\bar{k}_t \bar{A} \Delta U_t \\ \Delta\bar{M}_n &= -\bar{k}_t \bar{J} \Delta\theta_n \\ \Delta\bar{M}_t &= -\bar{k}_n \bar{J} \Delta\theta_t.\end{aligned}\quad (22)$$

Here,  $\Delta U_n$  is the increment of the sphere overlap taking into account changes in both sphere center positions and sphere radii, and  $\Delta U_t$  is the increment of the tangential displacement taking into account both rotation and sphere center positions.  $\Delta\theta_n$  and  $\Delta\theta_t$  are the relative rotational increments of twisting and bending. The tangential components in Eq. (22) have to be rotated before summation to account for orientation changes of the contact plane.  $\bar{A}$ ,  $\bar{I}$ , and  $\bar{J}$  are the area, moment of inertia, and polar moment of inertia of the parallel bond cross-section, respectively. For cylindrical bonds with radius  $\bar{R}$ , these quantities are  $\bar{A} = \pi \bar{R}^2$ ,  $\bar{I} = \pi \bar{R}^4/4$ , and  $\bar{J} = \pi \bar{R}^4/2$ .

Motivated by classical beam theory, Potyondy & Cundall (2004, Eq. (18)) defined

$$\begin{aligned}\bar{k}_n &= \frac{\bar{E}}{R_i + R_j} \\ \bar{k}_t &= \frac{\bar{k}_n}{k_n/k_t}.\end{aligned}\quad (23)$$

With these definitions, the particle size dependence of the macroscopic elastic properties of an example material was demonstrated by these latter authors in several 3D simulations to become only minor. For each of our simulation scenarios that involves parallel bonds, we exemplarily check the influence of the particle size (or rather of the coarse-graining factor discussed in Sect. 2.5) on the macroscopic behavior.

A parallel bond breaks when the maximum tensile stress  $\bar{\sigma}^{\max}$  acting on the beam-analog of the bond exceeds the bond's tensile strength  $\bar{\sigma}$ , or when the maximum shear stress  $\bar{\tau}^{\max}$  exceeds the bond's shear strength  $\bar{\tau}$ , where, according to Potyondy & Cundall (2004, Eq. (16)),

$$\begin{aligned}\bar{\sigma}^{\max} &= \frac{-\bar{F}_n}{\bar{A}} + \frac{|\bar{M}_t| \bar{R}}{\bar{I}} \\ \bar{\tau}^{\max} &= \frac{|\bar{F}_t|}{\bar{A}} + \frac{|\bar{M}_n| \bar{R}}{\bar{J}}.\end{aligned}\quad (24)$$

## 2.5. Particle sizes and coarse-graining

The particle sizes affect the interparticle forces. For instance, the DMT cohesive force (Eq. (20)) increases linearly with particle size (Muller et al. 1983). In the same way, forces due to sinter bonds in the model of Potyondy & Cundall (2004) depend on the radius of the smallest particle of the bond pair. In case of monodisperse spheres, the interparticle forces are degenerated, causing objects made of such particles to disintegrate quite homogeneously around a specific macroscopic force threshold. For example, a dropped boulder either completely disintegrates or remains undamaged, with a very narrow transition range and depending on the external forces acting on the body. To achieve a more realistic behavior, with only parts of the object disintegrating, polydisperse particles are used in our models. Using just two

or three different particle radii still leads to a bond force degeneration, since it is quite likely that at least one of the two bonded partners is of the typically more frequent small size resulting in a degeneration of bond radius  $\bar{R}$ . Because of the way types of particles and their properties are implemented in LIGGGHTS, we cannot use a continuous size distribution without larger code changes. Therefore, we use a discrete particle size distribution with eight different equally spaced radii, but the impact of using more bins is tested as well. We note that due to modeling complexity and the limited available computational resources, we do not investigate the presence of small interstitial particles partially filling the voids between the larger particles and their potential cohesive effects.

The cumulative particle size distribution is set to follow a power-law with index  $i_c$  such that the number of particles with radius larger than  $R$  is proportional to  $R^{-i_c}$ . Mottola et al. (2015) reported ROLIS measurements for Agilkia, the initial touchdown site of the Philae lander, exhibiting values of  $i_c$  in the range from 2.2 to 3.5. We note that the exponent of the corresponding differential size distribution is  $i_c + 1$ , and that of the incremental size distribution with logarithmic radius increments is  $i_c$  (Colwell 1993). Here,  $i_c = 2$  translates to a uniform mass distribution with respect to particle radius. Since the number of particles in a DEM simulation is limited by the available computational resources, with our scenarios typically comprising on the order of  $10^4$ – $10^6$  particles, the minimum particle size is limited by the volume that needs to be filled. Similarly, the maximum particle size is limited by the spatial extent of the simulation domain, but typically we use a much smaller maximum particle size than that because the steep particle size distribution requires a low ratio between the radii of the largest and the smallest particles to ensure a statistically representative number of large particles. In our simulations, we use  $i_c = 2.5$ , and the ratio between the radii of the largest and the smallest particle is 2, meaning that eight of the smallest particles have the same mass as one of the largest ones.

Our simulation scenarios have typical dimensions of 1–100 m, often leading to a prohibitively large number of particles when we assume particle radii in the reasonable range of millimeters to centimeters. This is why we apply the coarse-graining scheme of Bierwisch et al. (2009), where instead of the physical particles, an effective medium of computational parcels is considered, each parcel representing groups of several particles. The coarse-graining factor  $cg$  scales the radius of the computational parcels relative to the radius of the original particles. Bierwisch et al. (2009) argued that in order to obtain simulation results that are statistically similar between the scaled and the unscaled system, the model parameters of the computational parcels have to be scaled in such a way that the energy density and evolution of energy density are the same as for the unscaled system. Applying coarse-graining, we can save computational resources by reducing the number of particles that have to be considered, enabling the simulation of macroscopic scenarios with small particles. In addition, we can better manage different size scales of the respective scenarios when comparing mechanical parameters between them.

We now investigate the scaling of the volume densities of gravitational potential energy, potential energy in unsintered and sintered cohesive contacts, and translational and rotational kinetic energy, all with respect to the coarse-graining factor  $cg$ . In the following, scaled quantities are indicated by a prime, and the unscaled ones are written without prime. The radius of a computational parcel is scaled as  $R' = cg R$ .



Consider  $N$  spherical particles with solid mass density  $\rho$ , radii  $R_i$ , and masses  $m_i = 4/3 \pi R_i^3 \rho$  experiencing ambient surface acceleration  $g$  in a volume  $V$ . Additionally, we assume that the considered volume is sufficiently small that kinematic quantities such as particle speed  $v_i = |\mathbf{v}_i|$  and vertical position  $z_i$  are approximately the same ( $v$  and  $z$ ) for all particles in this volume. Following the arguments of Bierwisch et al. (2009), the density of the gravitational potential energy  $U$ ,

$$\frac{U}{V} = \frac{\sum_i m_i g z_i}{V} \sim \rho \phi g z, \quad (25)$$

where the sum is taken over all particles in the volume  $V$ , is independent of  $cg$  when the solid mass density  $\rho$  and the filling factor  $\phi = \sum_i 4/3 \pi R_i^3 / V$  are constant, i.e.  $\rho' = \rho$  and  $\phi' = \phi$ . This means that, when leaving  $\rho$  constant, we have to ensure that  $\phi$  is unaffected by the scaling, which is the case when we leave the particle size distribution normalized with respect to the minimum particle radius unchanged.

The density of the translational kinetic energy  $K$  reads

$$\frac{K}{V} = \frac{\sum_i m_i v_i^2}{2V} \sim \rho \phi \frac{v^2}{2}, \quad (26)$$

where, because the solid mass density and the filling factor are constant, we have to ensure that the velocities are unaffected by the scaling. Then, gain and loss of kinetic energy are given by the surface acceleration, which is independent of particle size, and by collisions between particles governed by the Hertz contact law. For two contacting particles, Eq. (5a) can be written as

$$m^* \ddot{\delta}_n = k_n \delta_n - \gamma_n \dot{\delta}_n, \quad (27)$$

with the effective mass

$$m^* = \frac{m_i m_j}{m_i + m_j} = \frac{4\pi R_i^3 \rho \beta^3}{3(1 + \beta^3)}, \quad (28)$$

where  $\beta = R_j/R_i$  is the ratio of the radii of the colliding particles. Inserting Eq. (28) into Eq. (27) and using dimensionless variables  $\delta_n^\dagger = \delta_n/R_i$  and  $t^\dagger = t v_0/R_i$  with a reference velocity  $v_0$ , Eq. (27) reads

$$\frac{4\pi}{3} \frac{\beta^3}{1 + \beta^3} \ddot{\delta}_n^\dagger = \frac{k_n}{R_i \rho v_0^2} \delta_n^\dagger - \frac{\gamma_n}{R_i^2 \rho v_0} \dot{\delta}_n^\dagger. \quad (29)$$

A dimensional analysis shows that the velocities are independent of  $cg$  when  $\beta$  is constant, i.e.  $\beta' = \beta$ , and when  $k_n' = cg k_n$  and  $\gamma_n' = cg^2 \gamma_n$ . This scaling is already fulfilled by way of Eqs. (11) and (12) when leaving Young's modulus constant, i.e.  $E' = E$ . Similar scaling considerations for the density of the rotational kinetic energy show that the tangential coefficients  $k_t$  and  $\gamma_t$  as defined by Eq. (11) do not need to be additionally scaled either.

The cohesive potential energy density in the DMT model, using Eq. (20), reads

$$\frac{\sum_i F_c \delta_n}{V} = - \frac{\sum_i 2\pi R^* \omega \delta_n}{V} \sim \frac{\beta}{1 + \beta} \frac{\omega}{R_i} \delta_n^\dagger, \quad (30)$$

with the effective radius

$$R^* = \frac{R_i R_j}{R_i + R_j} = \frac{R_i \beta}{1 + \beta}, \quad (31)$$

and where the sum is taken over all contact partner pairs in the volume  $V$ . Here, we exploit the fact that the parcel number in

the volume  $V$  scales with  $cg^{-3}$ , when the particle size distribution normalized with respect to the minimum particle radius is unchanged. Since  $\beta$  is constant, the DMT cohesive potential energy density is independent of  $cg$  when  $\omega' = cg \omega$ .

A dimensional analysis of Eqs. (16)–(19) shows that the rolling friction coefficient  $\mu_r$  and rolling viscous damping ratio  $\eta_r$  are not scaled with  $cg$ .

Similarly, the potential energy density of a sinter bond, using Eqs. (22) and (23),

$$\begin{aligned} \frac{\sum_i \Delta \bar{F}_n \Delta U_n}{V} &= \frac{\sum_i \bar{k}_n \bar{A} \Delta U_n^2}{V} = \frac{\sum_i \frac{\bar{E}}{R_i + R_j} \pi \bar{R}^2 \Delta U_n^2}{V} \\ &\sim \frac{[\min(1, \beta)]^2 \bar{E} \Delta U_n^2}{1 + \beta R_i^2}, \end{aligned} \quad (32)$$

is independent of  $cg$  when the Young's modulus  $\bar{E}$  of the bond cement is constant, i.e.  $\bar{E}' = \bar{E}$ , because  $\beta$  is constant and both the increment of the sphere overlap  $\Delta U_n$  and the parcel radius  $R_i$  scale with  $cg$ . In addition, Eqs. (24) imply that  $\bar{\sigma}^{\max}$  and  $\bar{\tau}^{\max}$  do not scale with  $cg$ , which is why the tensile and shear strengths of sinter bond,  $\bar{\sigma}$  and  $\bar{\tau}$ , respectively, are also not scaled. In other words, the definition of  $\bar{k}_n$  and  $\bar{k}_t$  according to Eqs. (23), intended by Potyondy & Cundall (2004) to minimize the particle size dependence of the macroscopic elastic properties, ensures that our simulations become almost statistically independent of  $cg$ .

In conclusion, velocities scale with  $cg^0$ , parcel radii with  $cg^1$ , forces with  $cg^2$ , and torques with  $cg^3$ . Moreover, we deduce that the time-steps in the simulation scale with  $cg$ . This implies that for a given simulation volume to be filled with computational parcels, and for a given span of real time, the required computer memory scales with  $cg^{-3}$ , whereas the processing time scales with  $cg^{-4}$ . All the scalings are automatically fulfilled by the parameter definitions recited in Sects. 2.1–2.4, once parcel radii and the surface energy density  $\omega$  are scaled with  $cg$ , and for numerical efficiency, the time-steps can also be scaled with  $cg$ , whereas the cutoff distance for building the neighbor lists (see Sect. 2.1) has to be scaled with  $cg$  for numerical stability. No other of the remaining physical parameters that we have to set in our DEM simulations ( $\rho, \phi, g, E = \bar{E}, v = \bar{v}, e_r, \mu, \mu_r, \eta_r, \bar{k}_n/\bar{k}_t, \bar{\lambda}, \bar{\sigma} = \bar{\tau}, i_c$ ) is scaled with  $cg$ .

We would like to point out that these are only first-order scaling rules, and in practice, corrections may be necessary to achieve a comparable morphologic behavior between the scaled and the unscaled system. In particular, working with a certain size distribution for computational parcels does not mean that the physical particles follow this size distribution. Also, this approach neglects interparticle collisions and energy and momentum dissipation within a given computational parcel; see Radl et al. (2011) for comparison. Therefore, we always exemplarily check whether the morphologic features of the simulation results are indeed mostly unaffected when  $cg$  is varied within a reasonable range. In cases where it is not possible due to insufficient computational resources to compare to full-resolution results, we compare results for different coarse-graining factors as widely separated as half an order of magnitude. Depending on particle size and the scenario dimensions, we use coarse-graining factors typically on the order of 1–100. For convenience, we use the terms ‘‘particle’’ and ‘‘parcel’’ interchangeably in the following when referring to simulations. Indeed, all our simulations are performed with parcels, even when coarse-graining is switched off, which is accomplished by setting  $cg = 1$ . Physical 67P particles are explicitly referred to as ‘‘particles’’.

### 3. Simulation scenarios

We consider two different simulation scenarios that are related to observations on comet 67P by Rosetta: the stability of boulders and the collapse of cliffs. A third scenario serves to estimate the tensile strength for our model materials for direct comparison to estimates derived from Rosetta measurements. The simulation outcomes are presented and discussed in Sect. 4.

#### 3.1. Boulder stability

We start with the requirement that boulders of sizes observed on the nucleus surface have to be stable without collapsing under their own weight or when falling from smaller (e.g. during cliff collapses) or greater (from the coma) heights. For this purpose, we assume a large spherical boulder to be made up of small particles and investigate conditions for it to be reasonably stable when being dropped from small altitudes above a hard surface.

Our boulders are 2 m in diameter and made up of a mixture of two types of particles that consist of different materials: either dust or water ice. For simplicity, the particle types are assumed to differ only in their mass density (dust:  $2000 \text{ kg m}^{-3}$ , ice:  $920 \text{ kg m}^{-3}$ ) and their ability to form bonds from sintering (dust–dust: no bonds, ice–dust: no bonds, ice–ice: bonds) as the conditions on the comet allow only the sintering of ice. In particular, it is assumed that both particle types have the same size distribution, mechanical parameters, and surface energy density of unsintered cohesive contacts. The latter assumption is motivated by recent laboratory experiments with dust and ice particles at low temperatures (Gundlach et al. 2018). We simulate boulders made up of pure dust and of two dust-ice mixtures with a dust-to-ice volume ratio (ice volume fraction) of 2:1 (33%), and 1:1 (50%), respectively. The macroscopic porosity of the material is prepared between 63 and 73% depending on the ice content in order to achieve a bulk density of the boulder that is similar to the global mean value of  $538 \text{ kg m}^{-3}$  for comet 67P (Preusker et al. 2017).

As a typical impact velocity of the boulder, we take the free-fall velocity from 30 m above the surface, which is about  $0.1 \text{ ms}^{-1}$  for a typical surface acceleration on 67P of  $1.8 \times 10^{-4} \text{ ms}^{-2}$  calculated as the median over all facets of the 67P shape model (Preusker et al. 2017). We simulated vertical impacts as well as oblique impacts with an impact angle of  $30^\circ$  (measured from the normal to the surface). Since we did not observe major morphological differences between results for these impact conditions, we only show oblique impacts as they lead to a better visual separation of the post-impact boulder fragments than vertical impacts.

The simulation is composed of two parts – the construction of the spherical boulder, and its impact on the surface. It starts by loosely filling a large sphere with noncontacting randomly sized and positioned particles. This particle cloud is then compacted to the desired level by equally accelerating all particles in the direction of the particles' center of mass. As the particles converge towards this point, they collide with each other and dissipate their kinetic energy. By changing the particles' initial velocity and (temporarily) the interparticle contact parameters, we can control the bulk mass density and porosity of the emerging boulder. After settling, excess particles outside the intended boulder diameter are removed, and contacting particles capable of sintering are bonded. Settling of the particles is ensured after every preparation step, and we verify that the prescribed size distribution, mixing ratio, porosity, bulk mass density, and homogeneity have indeed been achieved after the preparation

phase. The boulder is then moved to a position directly above the surface and instantaneously accelerated to its impact velocity by setting the velocity of all particles to that value. The simulation is run until the boulder or its fragments have settled after the primary impact. An example of the *boulder stability* scenario is shown in Fig. 2.

This simple scenario is suited to study the effects of changing the material composition (ice content) of the boulder and the particle properties including size distribution, mechanical parameters, surface energy density, and so on, which is information that can be used for setting up the more complex *cliff collapse* scenario (Sect. 3.2).

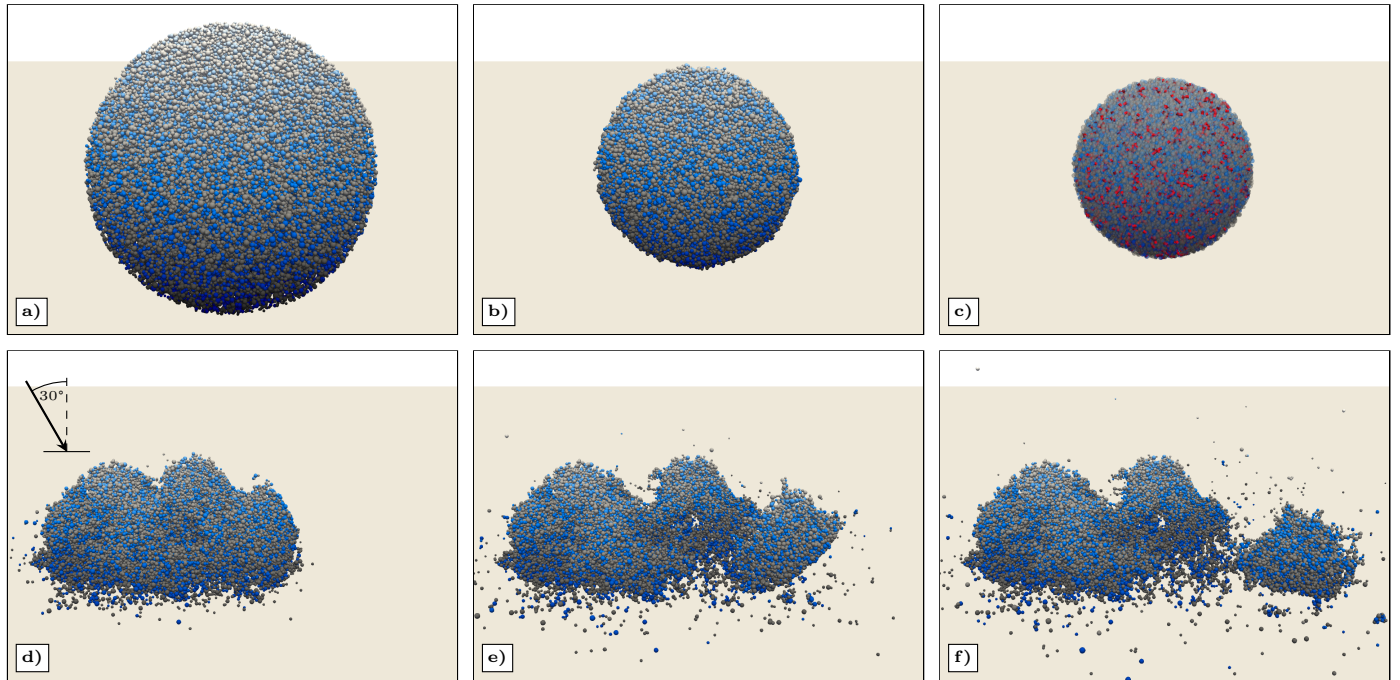
#### 3.2. Cliff collapse

Cliff and overhang collapses have been observed on 67P, and their debris is abundant on the nucleus surface (Pajola et al. 2017; Vincent et al. 2016; Groussin et al. 2015). We develop a corresponding simulation setup starting with the results from the *boulder stability* scenario (Sect. 3.1).

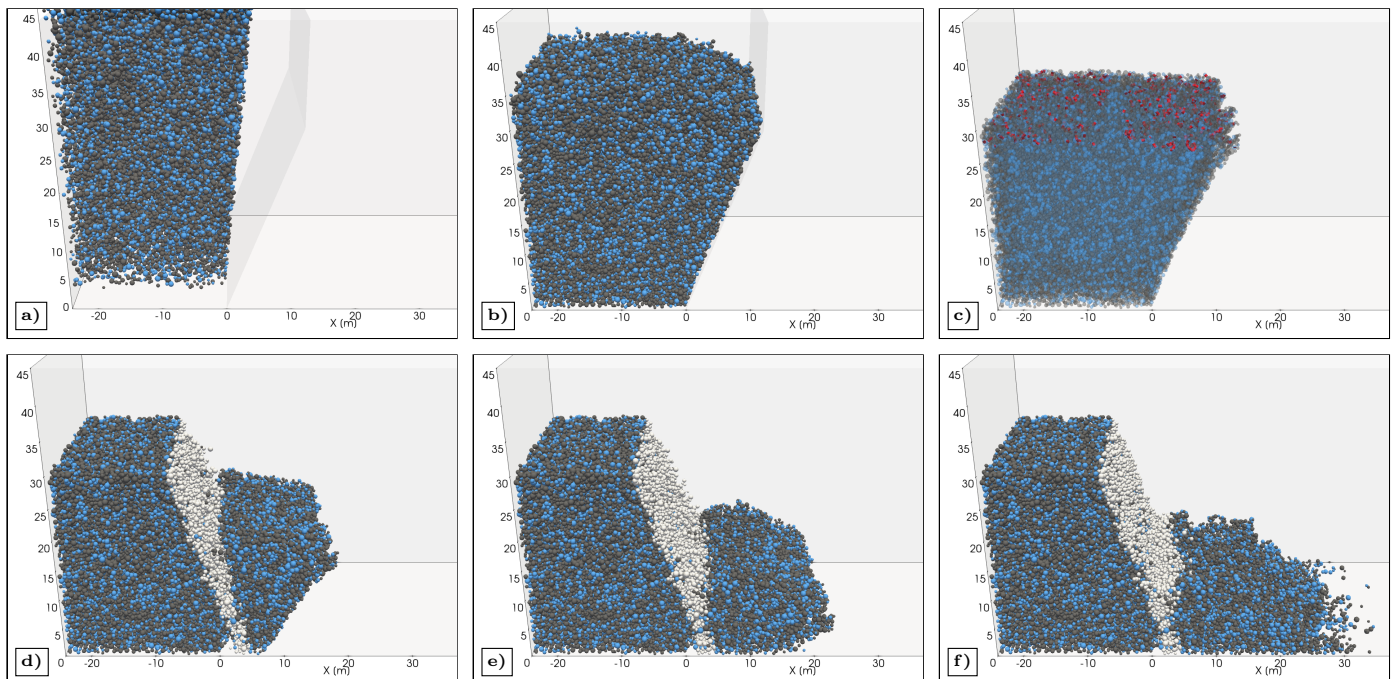
Motivated by a survey of 20 overhanging cliffs on 67P in Attree et al. (2018), our cliff is set to be 30 m high and has an overhang with an angle of  $10^\circ$ ,  $20^\circ$ , or  $30^\circ$ , respectively. The material is a mixture of dust and ice particles identical to the material used for the boulders. It is assumed that the collapse is made possible by a weakness in the cliff material that cannot withstand significantly more stress than the pressure exerted by 67P's surface acceleration. This weakness could result from natural variations in the material composition or from structural defects, in particular cracks caused for example by thermal fracturing or by material loss or sinter bond annihilation due to sublimation. The collapse of a barely stable cliff could then be triggered by the crack expanding beyond a critical threshold, or by low seismic activity, for example due to impacts (Richardson et al. 2005) of small interplanetary meteoroids or of boulders falling from the coma, or due to tidal and self-gravity stresses of the nonspherical nucleus and stresses induced by changes of the rotation period of the comet due to nongravitational forces (Hviid et al. 2016; Matonti et al. 2019).

The simulation starts by inserting noncontacting randomly sized and positioned particles with a given downward velocity above a cliff-shaped region confined by walls. As the particles fall down, they gradually fill the space between the cliff walls from the bottom to the top. By changing the insertion velocity and (temporarily) the interparticle contact parameters, we can control the bulk mass density and porosity of the emerging cliff. After settling, excess particles beyond the given cliff height are removed, and particles capable of sintering are bonded, but only in the top layer (3 m) to account for the fact that sintering is most efficient near the surface (see Sect. 2.4). Finally, the wall supporting the overhang is removed and the collapse of the cliff is triggered. The simulation is run until the particles forming the debris pile have settled. An example of the *cliff collapse* scenario is shown in Fig. 3.

Seismic shaking as the collapse trigger is implemented by moving the remaining walls (bottom, back, and sides) along the main coordinate directions with velocities that follow sine functions with certain frequencies, amplitudes, and phases that differ between the directions. These vibrations are transferred by the wall–particle forces to the particles in direct contact with the walls and from there travel further into the cliff material. High frequencies are dissipated more efficiently than lower ones, while overly low frequencies do not lead to significant stresses in the cliff material. Hence, a certain intermediate frequency range



**Fig. 2.** Construction and simulated drop of a sintered two-meter-sized boulder made up of a 2:1 dust–ice mixture (34 000 computational parcels) from 30 m above the surface (beige-colored plane) of comet 67P. Oblique impact with impact speed of  $0.1 \text{ m s}^{-1}$  and impact angle of  $30^\circ$  measured from the normal to the surface. *Top row:* construction of the boulder. (a) Loose filling of a large sphere with noncontacting randomly sized and positioned dust (gray spheres) and ice (blue spheres) particles. (b) Compaction of the boulder to the bulk mass density and porosity of comet 67P. (c) Removal of particles outside the intended boulder diameter and formation of sinter bonds (thick red bars) between ice particles. *Bottom row:* (d–f) Several stages after impacting the surface of 67P; sinter bond representation is omitted for clarity. Lighter shades of gray or blue visualize a higher topography. In case (c), the material is visualized partly transparent.



**Fig. 3.** Construction and simulated collapse of a 30-m-high cliff made up of a 2:1 dust–ice mixture (65 000 computational parcels) with a sintered top layer of 3 m thickness. *Top row:* construction of the cliff. (a) Loose filling of a region confined by walls with noncontacting randomly sized and positioned dust (gray spheres) and ice (blue spheres) particles. (b) Compaction of the cliff to the bulk mass density and porosity of comet 67P. (c) Removal of particles beyond the given cliff height, formation of sinter bonds (thick red bars) between ice particles in the top layer of the cliff, and removal of the wall supporting the overhang. *Bottom row:* (d–f) Several stages after triggering the collapse. Representation as in Fig. 2. Particles in white are from the initial crack region.



is the most effective as a collapse trigger. Regarding the vibration amplitudes, overly small values have no effect, whereas very large ones completely disintegrate the cliff in an unrealistic way, necessitating a balanced choice as for the frequencies.

The pre-collapse dimensions of the cliff, considering it has to support itself before initiating the collapse trigger, and the post-collapse boulder size distribution and angle of repose can provide us with constraints on mechanical parameters. This scenario also permits the study of collapse triggers.

### 3.3. Tensile strength test

This additional scenario serves to estimate the tensile strength for our model materials for direct comparison to estimates derived from Rosetta measurements. The microscopic parameters (particle size distribution and geometrical configuration, surface energy density, friction coefficients, etc.) manifest in a macroscopic strength of the material. To determine the strength of our model materials, we perform a numerical simulation of a tensile strength test, where an elongated material sample is pulled to its breaking point. In our test, we prepare a cylinder of 5 cm (diameter)  $\times$  10 cm (height) in dimension consisting of a sufficient number of small particles to avoid significant boundary effects. This is mounted in a clamp (a wall with the shape of a truncated cone) with its flat top side, while a gradually increasing force is pulling on the flat bottom side of the cylinder. We monitor the forces experienced by the clamp. Mediated by the cylinder material, the force registered at the clamp corresponds to the one applied at the bottom. It increases as long as the cylinder is intact, but rapidly decreases as soon as the cylinder breaks apart. The force at the breaking point normalized over the cylinder's cross-sectional area is defined as the material's tensile strength, which we can calculate from our model readings in order to compare it to the values of the real cometary material recited in Sect. 1 and to laboratory measurements of cometary analog materials.

## 4. Results and discussion

In this section we report and discuss the outcomes of our simulations for the basic scenarios, and the changes that occur when modifying the setup or varying the parameters.

### 4.1. Boulder stability

Before starting the actual dropping simulations, we investigated boulders resting on the surface and found them to be stable (except for small deformations around the contact at the bottom) up to diameters exceeding that of the largest boulders observed on the surface of 67P ( $\sim 50$  m).

For each material composition, we then simulated drops of boulders made up of particles respecting the relative size distribution from Sect. 2.5 scaled to cover six different diameter ranges: 0.2–0.4 mm, 0.4–0.8 mm, 1–2 mm, 2–4 mm, 4–8 mm, and 10–20 mm, in total covering about two orders of magnitude, with a corresponding opposite effect on stability. For each case, we performed simulations with three distinct levels of friction: one with low to medium friction (triple of friction coefficients  $\mu/\mu_r/\eta_r$  of 0.8/0.2/0.3, adopted from Ai et al. 2011), one with high friction (coefficients 1.0/1.0/1.0), and one with very high friction (coefficients 2.0/2.0/2.0). High friction levels can be used as a proxy to describe interlocking between complex-shaped particles. For the dust–ice mixtures, we performed all simulations twice, either with or without sintering of the ice particles. In total, and with additionally probing the

influence of other parameters, such as for example the boulder size and impact conditions, we performed over 100 different boulder drops each made up of 30 000–40 000 computational parcels and always taking about 200 CPU-core hours of processing time. As we cannot show all of them here, we have selected a limited set that still captures the main effects of changing the various model parameters. Figure 4 shows the influence of friction and particle size for boulders made of pure dust, and Figs. 5 and 6 show the effect of friction, ice sintering, and particle size for boulders made of the 2:1 and the 1:1 dust-to-ice mixture, respectively.

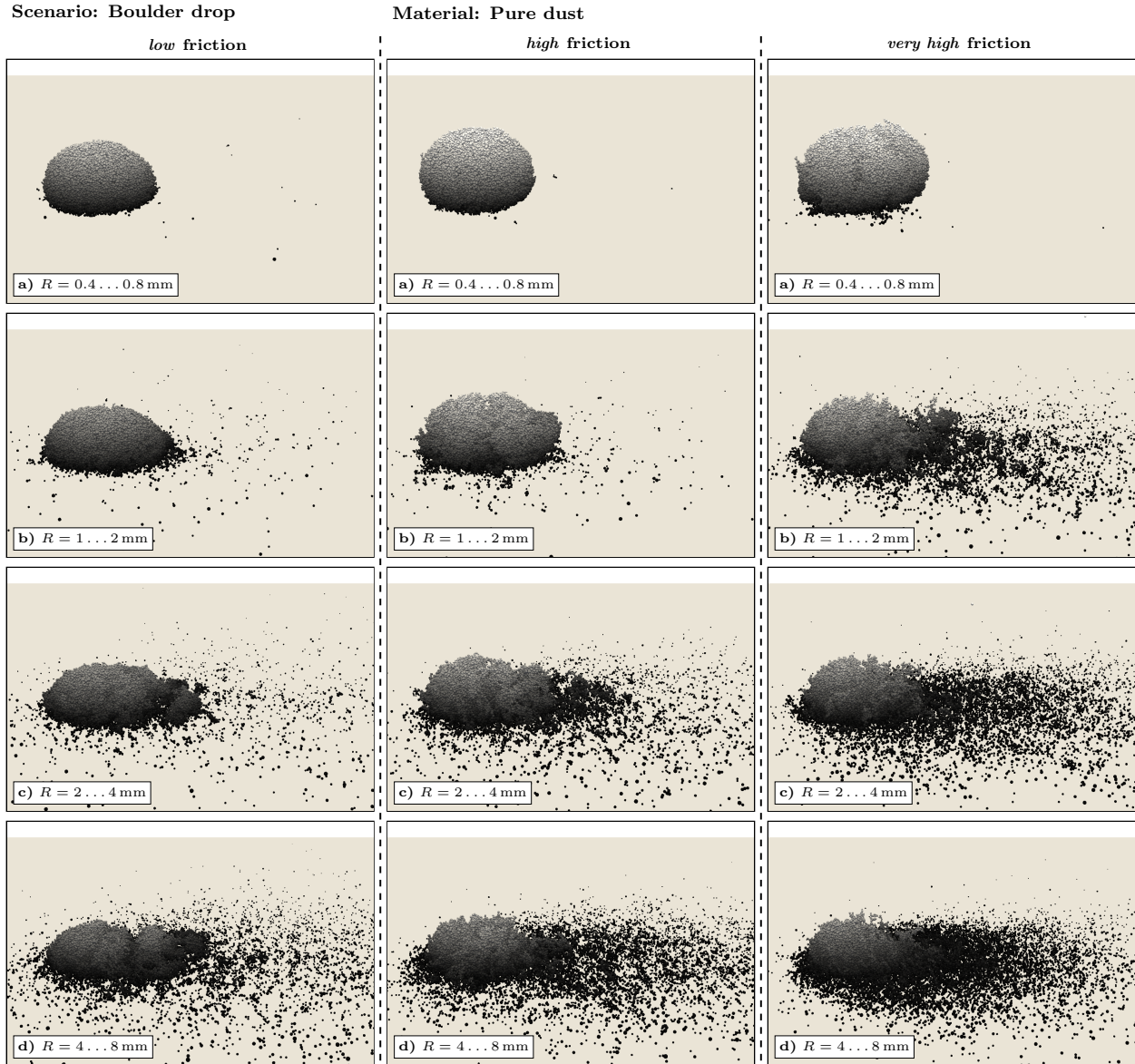
We exemplarily investigated moderate changes in the coarse-graining factor  $cg$  (increase by up to half an order of magnitude compared to our respective highest-resolution level). While the details of, for instance, the fragmentation (location and shape of cracks, exact number of fragments, spatial arrangement of debris pile) can be quite different, the general trend in the morphologic behavior (complete disintegration, breakage into large/small fragments, undamaged) and observables like settling time, extent of debris field, or macroscopic pressure at impact point are largely preserved. Since the precise geometric arrangement of the computational parcels slightly changes with  $cg$ , the simulation outcomes have to be interpreted within tolerances given by slight changes in the geometric arrangements at unchanged  $cg$ . This can give rise to a behavior of deterministic chaos. Starting for example with a different realization of the random parcel initialization, the parcel that first contacts the bottom plane is different, as is the configuration of its neighbors, which can lead to a different simulation outcome, a situation reminiscent of the nonlinear properties of the real particle ensemble. However, we have to avoid overly coarse resolutions to keep the fraction of parcels that are at the boundaries of the boulder or its fragments low. At extremely low resolution, where almost all parcels are at or close to the boundaries, the simulation outcome is completely meaningless.

When impacting the surface, the boulder has to withstand the forces arising in the collision as well as the surface acceleration of the nucleus. In general, the boulder remains undamaged after impact when the interparticle forces (from unsintered and sintered cohesive contacts) are set too strong, whereas it totally disintegrates upon impact when they are set too weak. A reasonable behavior somewhere in between would cause the boulder to break up into large fragments with some debris, or lead to partial damage of the main body with some smaller parts broken off.

*Without sinter bonds.* When the simulation is run without sinter bonds between the ice particles, the boulder is held together by cohesive forces from unsintered contacts only. This simpler case is suited to studying the effects of changing the particle size distribution and the mechanical properties of the particles separately from the properties of the sinter bonds.

The inability of the ice particles to form sinter bonds implies that the only remaining difference between both particle types is their mass density, and varying the ice content of the material requires a change of porosity to maintain the desired bulk density of the boulder of about  $0.53 \text{ g cm}^{-3}$ . For our two limiting cases of pure dust and the 1:1 dust–ice mixture, with a solid mass density of  $2000 \text{ kg m}^{-3}$  and  $1460 \text{ kg m}^{-3}$ , the required porosity of the material is 73 and 63%, respectively. The larger filling factor of the ice-rich boulder means that the particles are more closely packed and on average in contact with more neighboring particles. For our porous materials, a particle typically adjoins only two or three neighbors, corresponding to a mean coordination number between 2.1 for pure dust and 2.9 for the 1:1 dust–ice





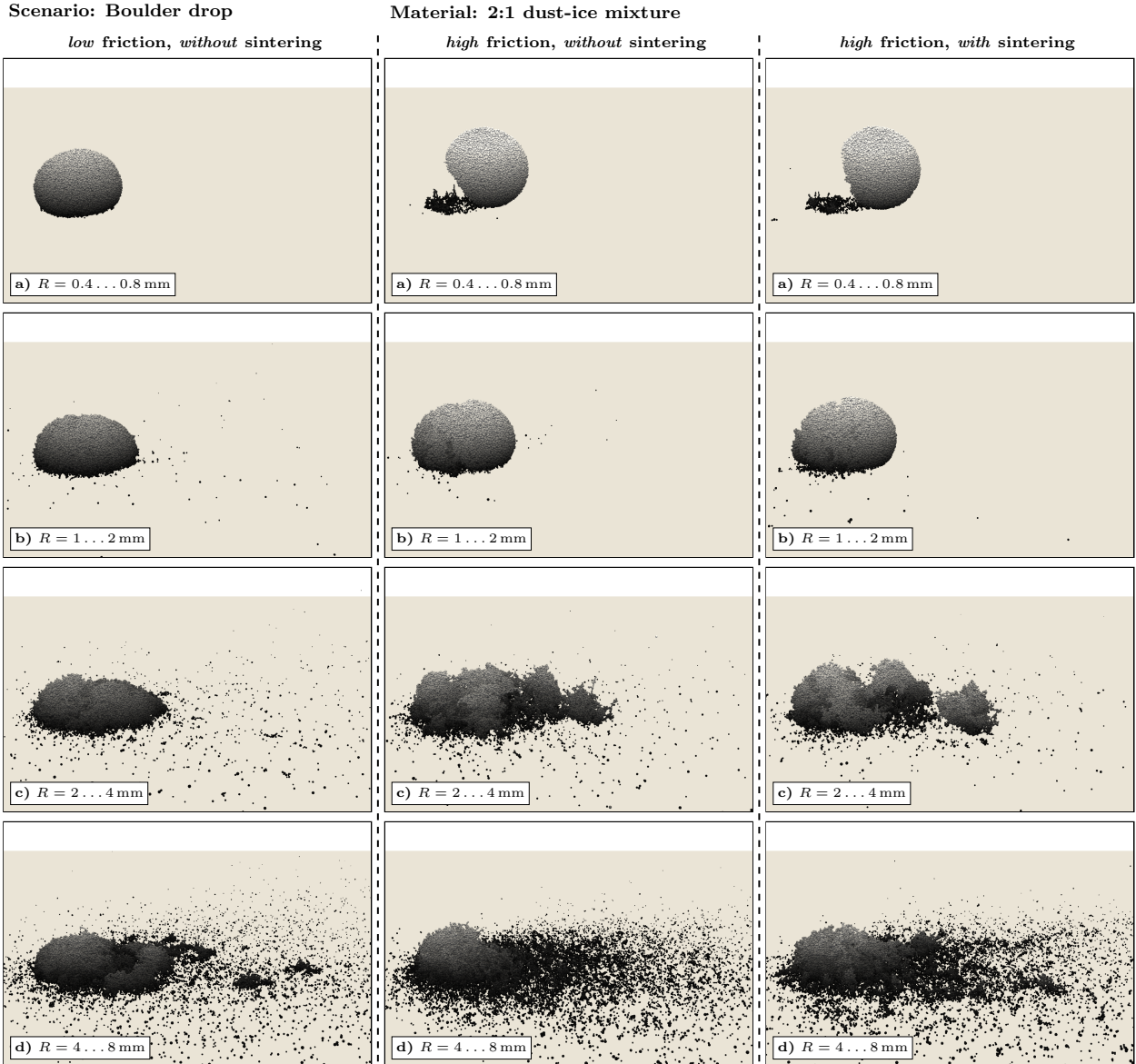
**Fig. 4.** Post-impact morphology of dropped two-meter-sized boulders made up of dust particles from different size ranges (*rows*). Impact conditions and graphical representation as in Fig. 2, but the indication of the particle type (water ice vs. dust) by colors is omitted for clarity here and in the following. *Left column:* low friction. *Mid column:* high friction. *Right column:* very high friction.

mixture. This translates to a higher strength of the ice-rich boulder, but this effect is generally small, and, compared to other factors influencing the boulder's stability, it is too small to constrain the ice content of the material by matching the simulation outcomes to the observed morphologies, all other parameters equal.

A larger, clearly noticeable effect on the stability of the boulders is observed when changing the particle size distribution. In general, objects made up of larger spherical particles are less stable. More precisely, the strength of the material scales inversely with particle size ( $\propto R^{-1}$ ), because the number of contacts between two particle layers scales with  $R^{-2}$ , while the DMT cohesive force of a single contact scales with  $R$  (Eq. (20)). This means that increasing the particle size by one order of magnitude decreases the strength of the boulder by a factor of ten. An equivalent effect can be produced by leaving the sizes but assuming the particles have surface asperities with typical asperity radii  $R_a$  of one tenth of the sphere radii (see Sect. 2.3).

As discussed above, we are restricted to a limited particle size range in our simulations, with the ratio between the radii of the largest and the smallest particle being generally set to two. We found that when doubling the largest particle radius while keeping the smallest one, the size distribution index, and the bin size (thus using 22 size bins), the material strength decreases (morphologically comparable to the case with a ratio of two with all radii multiplied by a factor in the order of 1.5) in our boulder stability scenario (1:1 dust-to-ice ratio, high friction, no sintering). This suggests that, even though the material becomes stronger when extending the size range towards smaller particles, there is a certain effective particle radius between the smallest and the largest radii around which the size range can be (in a suitable and moderate way) extended without major morphological impact: The increased strength from adding smaller particles is compensated by adding larger particles.

Using an additional simulation, we verified that the relatively small number of eight particle size bins we generally use



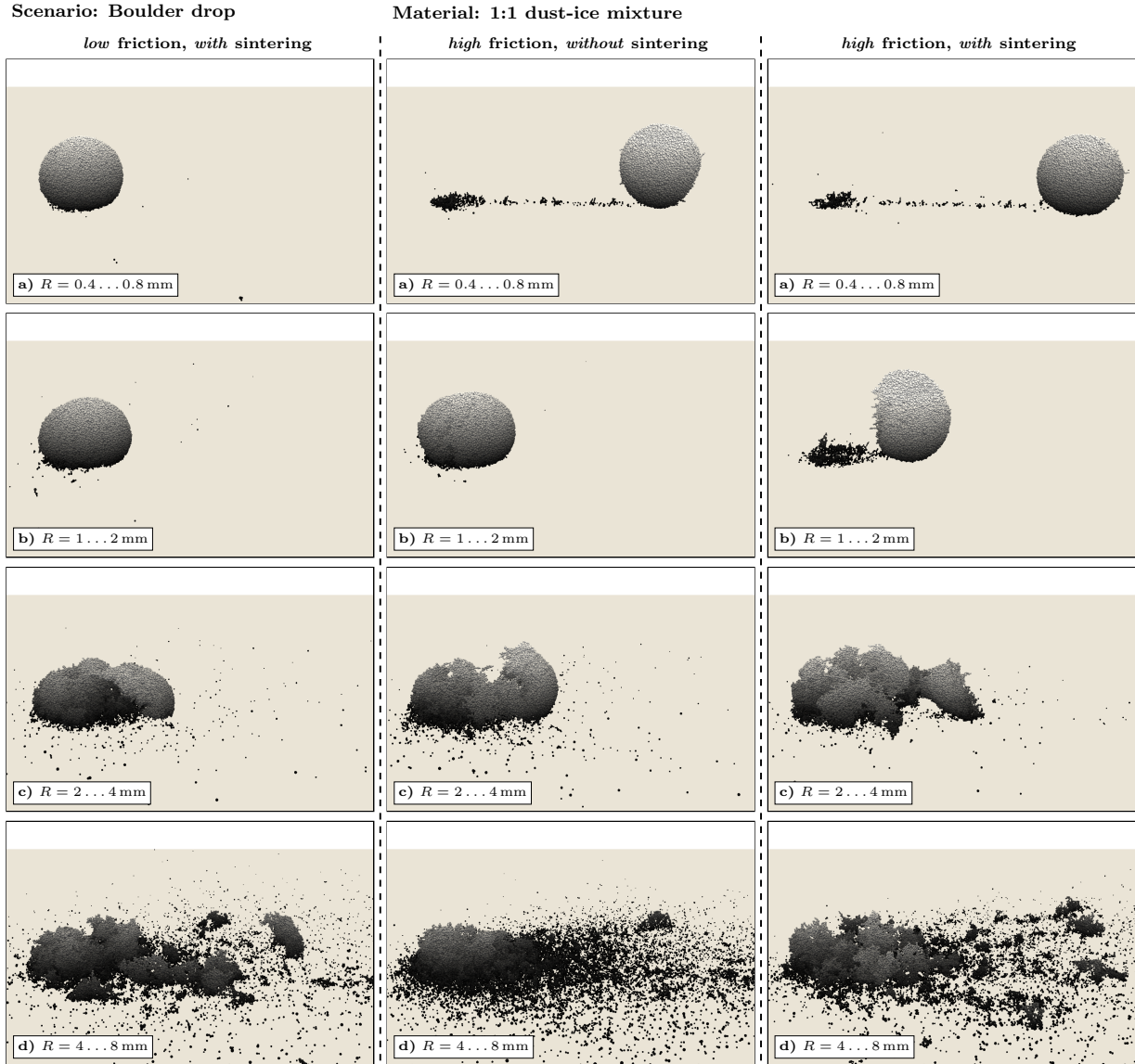
**Fig. 5.** Post-impact morphology of dropped two-meter-sized boulders made up of a 2:1 dust-ice mixture of particles from different size ranges (*rows*) and under different friction and sintering conditions (*columns*). Impact conditions and graphical representation as in Fig. 4.

in the present paper is not critical to our results. Keeping the largest and the smallest particle size and the size distribution index but utilizing 22 instead of eight bins yielded morphologically equivalent simulation outcomes. In the same way, a smaller time-step of 3% instead of 10% of the minimum of Rayleigh time and Hertz time resulted in morphological equivalence as well as unchanged settling time.

In addition to our reference value of 0.3 for the coefficient of restitution  $e_r$ , we also performed simulations with  $e_r$  set to 0.1 and 0.8, respectively, to investigate the sensitivity to this parameter. Higher coefficients of restitution led to a larger amount of small debris but only moderate morphological changes to the large fragments. Additionally, all fragments were distributed over a larger surface area. Similarly, an additional simulation with a Young's modulus of 1 GPa, which is ten times the nominal value in our other simulations, had a longer settling time and showed a higher degree of fragmentation, corresponding to a lower level of internal energy dissipation. In both of these cases, the resulting morphology was similar to that associated

with boulder drops from higher altitudes or boulders made up of constituents that have a Young's modulus of 0.1 GPa but are twice as large.

Our simulations show that boulders made up of sub-millimeter-sized or smaller particles remain more or less undamaged after impact, while boulders made up of centimeter-sized or larger particles totally disintegrate upon impact. We note that some boulders on 67P have been observed to be particularly stable; it is believed that some have even bounced over the surface several times before finally coming to a rest (Vincent et al. 2019). Boulders made up of millimeter-sized particles show a plausible behavior that is somewhere between the no-damage and the total-disintegration cases. At the lower end of this size range, the boulder is deformed from its initially spherical shape into an oblate shape with only small amounts of material being broken off. For gradually larger constituents, the boulder can break apart into several large fragments, or an increasingly larger fraction of material is broken off and dispersed into gradually smaller fragments over a larger area, forming a debris field. This debris field



**Fig. 6.** Post-impact morphology of dropped two-meter-sized boulders made up of a 1:1 dust-ice mixture of particles from different size ranges (*rows*) and under different friction and sintering conditions (*columns*). Impact conditions and graphical representation as in Fig. 4.

is relatively flat and resembles a continuous layer of similarly sized small boulder fragments. We attribute this lack of larger fragments in the debris field to the structural homogeneity of the boulder in the absence of sinter bonds. When the index  $i_c$  of the power-law is set to a larger (steeper) value, the number of smaller particles is increased with respect to the number of larger ones, which translates to a higher strength and thus to more stability.

Translational friction and rolling friction also hamper the boulder’s deformation and disintegration, but their effect on the stability of the boulder is smaller than that of the particle size distribution. More importantly, friction affects the elasticity of the boulder and the roughness of the post-impact morphology. Low friction leads to a weaker and more elastic boulder that is easier to deform and features a smoother post-impact morphology. High friction leads to a stronger but more brittle boulder that is harder to deform, but if it is deformed, it “breaks” and features a sharper-edged post-impact morphology.

Finally, we investigated the behavior when the properties of the bottom surface impacted by the boulder are moderately

altered. We find that a very dissipative surface (e.g., some tough material covered with a layer of finer debris) with a restitution coefficient of 0.1 instead of our reference value 0.3 does not lead to significant morphological changes. The same applies for the Young’s modulus of the bottom surface decreased by one order of magnitude (i.e.,  $E = 10^7 \text{ Pa}$ ).

Our results suggest that the constituents of the cometary surface material, if spherical, have diameters mostly on the order of  $10^{-3} \text{ m}$  for a surface energy density of  $\omega = 0.028 \text{ J m}^{-2}$ . For a lower or higher surface energy density, the constituent sizes of stable boulders have to be scaled by the same factor to maintain the strength of the boulder and observe the same post-impact morphology as before. The breaking of boulders into large fragments requires high levels of friction, which suggests that cometary particles are probably not all spherical but at least partly highly angular or very rough. This also translates to weaker interparticle cohesive forces (asperity effect, Sect. 2.3), which has to be compensated by a correspondingly smaller particle size to again arrive at the same morphology. These observations can be carried over when heterogeneities are



allowed by introducing locally more stable regions (e.g., smaller or less rough particles, higher coordination number).

*With sinter bonds.* In this case, ice particles can form sinter bonds between each other, which hold the boulder together in addition to cohesive forces from unsintered contacts, and whose number depends on the ice content of the material. This more complicated case is therefore suited to studying the effect of the ice content and the sinter bond properties.

We can measure the number of broken sinter bonds referred to the number of intact ones before impact. A morphologically reasonable behavior is associated to a sinter-bond-break ratio on the order of typically 10 to 50%. Total disintegration (100%) and total stability (0%) may both occur in reality on the nucleus due to local variations in the material of the comet. However, here we focus on cases with partial damage because they are subprocesses of larger scenarios, in particular of cliff collapses (Sect. 4.2), which is why we take the 30-m-free-fall velocity as reference for the *boulder stability* scenario.

To estimate the influence of ice sintering on the dust-ice mixtures used in our simulations, we calculate the fraction of sintered contacts when the ice particles are distributed homogeneously in the boulder. This number does not scale linearly with the ice content as a higher ice content reduces the average distance between two ice particles and thus increases the probability of ice particles being in contact with each other, in addition to the higher number of ice particles in general. For an ice volume fraction  $x = V_{\text{ice}}/V \approx N_{\text{ice}}/N$  and a coordination number  $CN$ , an ice particle is on average in contact with  $x \cdot CN$  other ice particles. This results in a total of  $x \cdot CN \cdot N_{\text{ice}}/2$  (division by two to not count contacts twice) sinter bonds in addition to a total of  $CN \cdot N/2$  unsintered cohesive contacts in the boulder (we reiterate that we do not switch off cohesion from unsintered contacts when a sinter bond is formed). The fraction of contacts that are additionally sintered is therefore  $x^2$ . For our dust-to-ice volume ratios (ice volume fraction) of 2:1 (33%) and 1:1 (50%), this gives a fraction of 11% and 25% of sintered contacts, respectively, suggesting a rapidly decreasing influence of ice sintering for increasingly ice-poor materials.

Our simulations confirm a relatively small influence of ice sintering for homogeneous boulders with a dust-to-ice volume ratio higher than 2:1. The bond network of sintered ice particles can be pictured as a skeleton with other particles attached to it. For a lower ice content, this structure is more fragile as individual clusters of ice particles in the boulder are connected by just a few easily breakable sinter bonds (in addition to the unsintered background), or not connected at all. For a 1:1 dust-to-ice volume ratio, the debris fields of dropped sintered boulders show a strong clustering of ice particles compared to the homogeneous and flat debris fields of unsintered boulders. In addition, and similar to the effect of high friction, a sintered boulder is more rigid and more brittle; it deforms less, but if it does, it rather “breaks” into more fragments that are clearly distinguishable.

Using an additional simulation, we investigated the effect of bulk mass density and porosity on the stability of sintered boulders. In this simulation, we prepared a material with a larger bulk mass density of about  $800 \text{ kg m}^{-3}$ , which corresponds to a lower porosity of about 45% for our 1:1 dust-to-ice mixture. As expected, the sintered, less-porous boulder was noticeably stronger and more brittle, which can be attributed to the higher coordination number of the particles resulting in a larger number of bonds.

Both friction and sintering have the effect of increasing the strength and the brittleness of the material. However, if no debris

field is present after the impact, the post-impact morphologies can be quite similar and difficult to distinguish from one another. If a debris field is present, the effects of high friction, and of additional sinter bonds and low friction, can be clearly distinguished based on the clustering of the debris. For a 2:1 dust-to-ice volume ratio, the influence of sintering is noticeably weaker but still recognizable. For even higher dust-to-ice volume ratios, the influence of sintering is too small to reliably distinguish between a sintered and an unsintered boulder solely based on morphology. On the basis of the clustering in the debris fields and the angularity of boulders imaged on the surface of 67P, our numerical results again suggest that the friction coefficients of the surface material can be comparatively high in places, and additionally that sintering of ice can play an important role for materials with an ice content larger than 67P’s global mean. However, it has to be kept in mind that the way dust and ice interact on 67P is much more complicated than we are able to model within the limits of our simulation setups.

#### 4.2. Cliff collapse

For the *cliff collapse* scenario, we now focus on the particle sizes associated with intermediate levels of fragmentation and the set of high-friction-level coefficients ( $\mu/\mu_r/\eta_r = 1.0/1.0/1.0$ ) that led to the overall best boulder stability simulation outcomes. Since the dimensions of the present scenario are larger by an order of magnitude, the coarse-graining factor has to be set to a correspondingly larger value.

*Trigger mechanisms.* Following Richardson et al. (2005), we can calculate a rough estimate for the seismic amplitude generated by large boulders falling from the coma and re-impacting the nucleus of 67P. For impacts in direct proximity to the cliff, the dissipation of seismic energy can be neglected even for the highly porous cometary material. At a distance of 100 m from the cliff, using a seismic efficiency factor at the lower end of the literature values ( $10^{-6}$ ) and assuming an impact with escape velocity ( $1 \text{ m s}^{-1}$ ), seismic amplitudes of 1, 10, and 100 times the typical surface acceleration of 67P ( $2 \times 10^{-4} \text{ m s}^{-2}$ ) are generated by impacting boulders with diameters of 2 m, 8 m, and 40 m, respectively. As the largest objects orbiting 67P are a few meters in size (Bertini et al. 2015), we estimate a reasonable seismic amplitude to be on the order of  $10^{-3} \text{ m s}^{-2}$ . For high seismic frequencies, the damage to the particle block in our scenario is concentrated near the walls. Decreasing the frequency, the skin depth of the damage increases. We use frequencies of about 1 Hz, which have been measured to dominate the spectrum of seismic activity on Earth and Mars, but also on less consolidated bodies such as asteroids (Teanby & Wookey 2011; Richardson et al. 2005).

Obliging the cliff to be statically self-sustained, and without resorting to fine-tuning of the parameters, we find that low-level seismic activity does generally not suffice to trigger the collapse of a cliff with a sintered top layer and no weaknesses. To still force a collapse in this situation, the seismic activity has to be increased to unreasonably high levels. Weaknesses in the cliff that make it more susceptible to low-level activity could result from natural variations in the material composition or from structural defects.

The strength of the cliff material is a consequence of unsintered cohesive frictional contacts and sinter bonds between the particles, and the resulting inter-particle forces depend on the particles’ properties. Natural variation in the strength, and partially in the friction, could be caused for example by locally



varying particle sizes or shapes, porosity, or composition. As discussed in Sect. 4.1, objects made of larger particles are weaker, since the strength of the material scales inversely with particle size. A local enhancement of large particles, for example, will then lead to a material that is weaker than the surroundings. Similarly, natural variations in the strength from sintering can result from a heterogeneous distribution of the ice, or from differences in the thermal history and thus the sinter bond radius factor  $\bar{\lambda}$  (Sect. 2.4). Since the ice content limits the number density of sinter bonds in the material, for instance a local reduction of it will then provide less strength from sintering leading to a material that is overall weaker than the surroundings. In any case, we aim to set the conditions in a way that the (homogeneous) cliff is barely stable after the removal of the wall supporting the cliff's overhang. A subsequent low-level seismic activity then suffices to trigger the collapse. This is motivated by the consideration that overly weak material could never have formed a cliff in the first place, and overly strong material is excluded by the limited overhang angles observed on the nucleus; see Attree et al. (2018) for comparison.

As an alternative to constructing heterogeneous cliffs, we can artificially induce a crack in the material, such that the cliff face is less strongly connected to the rest of the cliff (the “cliff body”). When the crack is deep enough, low-level seismic activity can initiate the collapse. When the crack continues to expand even further into the cliff, the collapse can be triggered solely by the comet's low gravity without additional forcing by seismic activity. The presence of a distinct crack was in fact observed before the Aswan cliff collapse (Pajola et al. 2017) with the crack becoming the new post-collapse cliff face. This leads us to choose this mechanism in our simulations. It may also be possible that not a single large crack is present, but many localized micro-cracks instead. However, this has the same effect of weakening the connection between cliff face and body, and therefore, as a proxy, we implement this situation as well by inducing a single distinct crack.

Triggering the cliff collapse by creating a crack leaves us also more options to vary the material properties in order to obtain debris with a boulder size distribution and angle of repose that can be matched to the ones observed in nature. The real-world formation of such a crack or weakened region has been discussed by Pajola et al. (2017) and could be related to the formation of thermally induced cracks followed by widening and deepening of these cracks by sublimation.

In the simulations, we induce the crack by changing the properties between the particles in a certain region (a tilted narrow box completely crossing the layer with sinter bonds and extending a certain distance further down into the unsintered domain) to a different type. Sinter bonds between particles of this type are so weak that they immediately break after the type change. To mimic the actual spatial separation that has been observed in the Aswan pre-collapse crack, we also remove the cohesive forces from unsintered contacts in this crack region. Immediately after that, the pressure exerted by the cliff face onto the unchanged underlying material overcomes the forces that bind the cliff face to the body. The cliff face slides down, and, mediated by the disintegrating cliff base, impacts the bottom wall of the simulation domain, in this process also eroding the new cliff face to some extent. The cohesionless particles (represented in white in Fig. 3) trickle down in the crack region and partly serve as lubricant that eases the downslope of the cliff face.

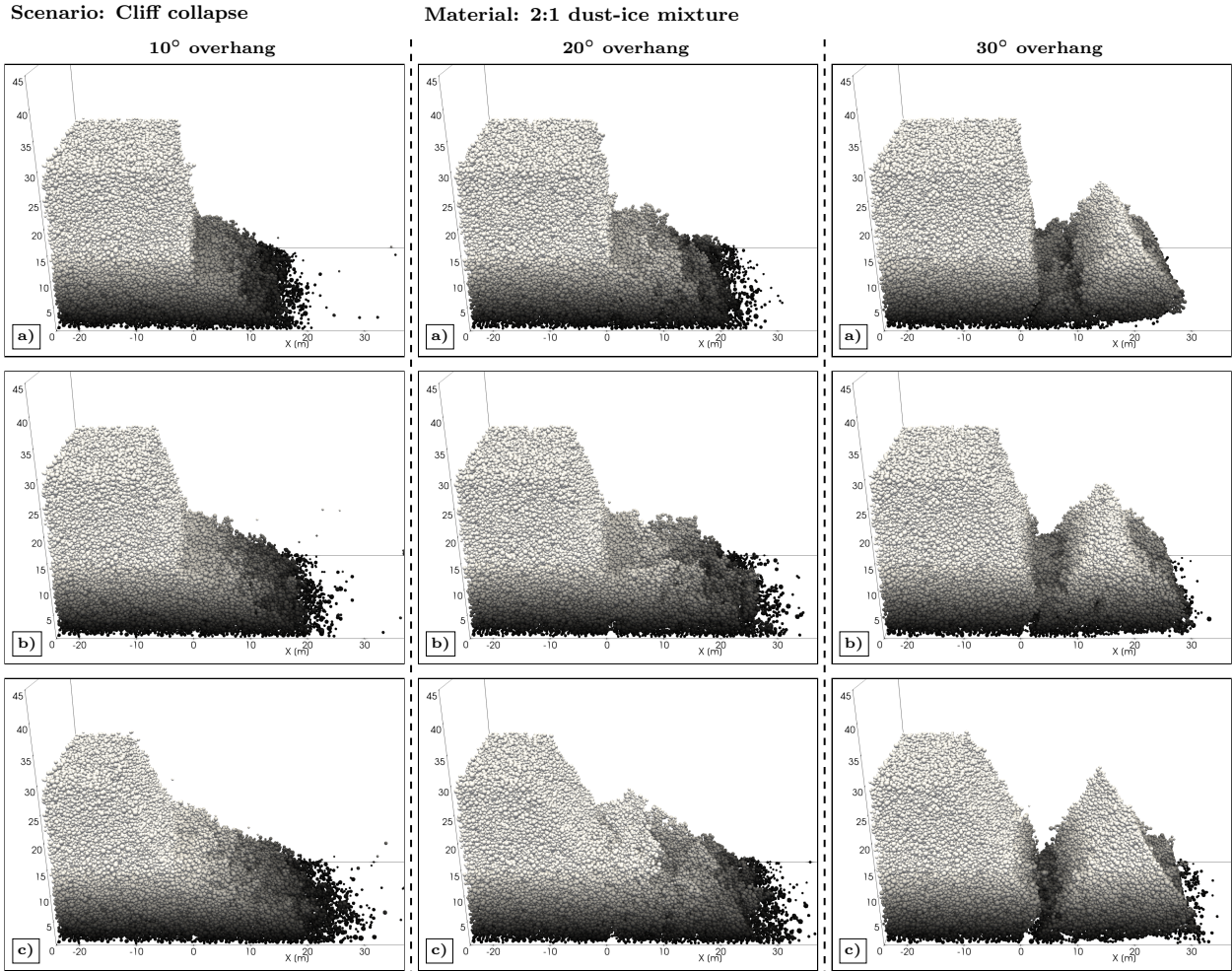
**Collapse.** We simulated the collapses of cliffs that have an overhang of  $10^\circ$ ,  $20^\circ$ , or  $30^\circ$ , motivated by the above-mentioned

survey of overhangs on 67P by Attree et al. (2018), and that have an oppositely oriented crack with a tilt angle of  $10^\circ$ ,  $20^\circ$ , or  $30^\circ$ , respectively. Each cliff is made up of 60 000–70 000 computational parcels. At the low surface acceleration on 67P, the free-fall time from 30 m above the surface is about 10 min, and the collapse of the cliff, including the settling of the debris, takes up to one hour in real time. The post-collapse morphologies of these cases are shown in Fig. 7. In these simulations, the constituent sizes are chosen such that the cliffs are barely stable before triggering the collapse, which requires smaller particles for steeper overhangs, in this way also giving us the opportunity to investigate the influence of the material strength. Due to this setup, the strength of the cliff material increases from left to right (particle diameters 6–12 mm, 4–8 mm, and 2–4 mm) in Fig. 7, and thus the amount of damage after impacting the bottom decreases, from a cliff face that largely disintegrates (left column) to a cliff face that is nearly undamaged (right column). Again, the results can be carried over when allowing heterogeneities by introducing locally stronger material.

After sliding down and impacting the bottom, different simulation outcomes can occur, which mainly depend on the strength of the cliff material. If the material is relatively weak (left column of Fig. 7), the cliff face largely disintegrates upon impact, such that it is broken into relatively fine fragments, which form a smooth debris pile with a uniform angle of repose. If the material is stronger (mid column of Fig. 7), the cliff face only weakly disintegrates upon contact with the bottom, such that large boulders can be found to protrude out of the debris pile, whose angle of repose can only be determined as a mean value. If the material is very strong (right column of Fig. 7), the cliff face can either tilt forward or backward as its almost undamaged base is held rather firmly in contact with the bottom surface by friction. If the cliff face tilts away from the rest of the cliff (i.e., “forward”), it hits the bottom with its full former front face, which can lead to an abrupt partial disintegration of the former face upon impact. If the cliff face tilts backward, it continues to slide down the rest of the cliff until it comes to rest. In this latter case, the cohesionless particles and the debris on which the cliff face slides serve as lubricant. In contrast to the abrupt disintegration upon impact on the bottom in the forward-tilting case, the backward case leads to a gradual crumbling during the process of sliding down. The simulation outcome mainly depends on the initial slopes of the (forward-oriented) overhang and of the (backward-leaning) crack, which determine the balance of the cliff face that, when seen from the side, looks like a triangle standing on one of its corners; see Fig. 7. If the crack is at a steeper angle than the overhang, the cliff will rather tilt forward, and in the opposite case, it will tilt backward.

Comparing to morphologies observed on 67P and assuming homogeneous pre-collapse material, our numerical results suggest that most debris fields associated with collapses of cliffs probably originate from not overly strong material and thus from not overly steep overhangs. However, the 67P observations are also compatible with a heterogeneous origin or the occurrence of pre-collapse micro-cracks.

**Aswan cliff collapse.** One particular cliff collapse that has been imaged by Rosetta's OSIRIS camera (Keller et al. 2007) before and after the event is that of the Aswan cliff (Pajola et al. 2017). It appears that this cliff has a relatively upright face in the lower half and, before the recent collapse, had a moderately steep overhang in the upper half. The amount of debris found at the foot of the cliff exceeds the volume estimated to have collapsed during this particular event indicating previous and ongoing

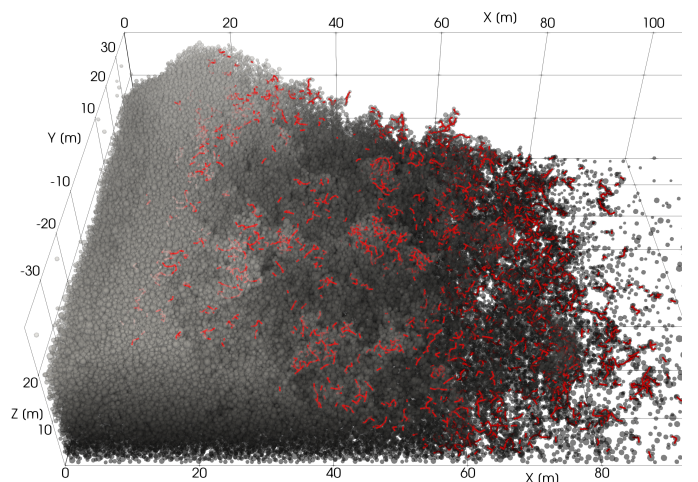


**Fig. 7.** Post-collapse morphology of a 30-m-high cliff made up of a high-friction 2:1 dust-ice mixture with a 3-m-thick sintered top layer for three different tilt angles of the overhang (*columns*) and of the crack (*rows*), respectively, (a) 10°, (b) 20°, (c) 30°. Steeper overhangs require a higher strength to be stable before triggering the collapse. Graphical representation as in Fig. 4.

erosion. Boulders with diameters between about 1 m and 10 m have been observed in the debris pile; they follow a cumulative power-law size distribution with index  $i_c = 3.6$  (Pajola et al. 2017), which is in the range of indexes expected for gravitational events triggered by sublimation or thermal fracturing (Pajola et al. 2015).

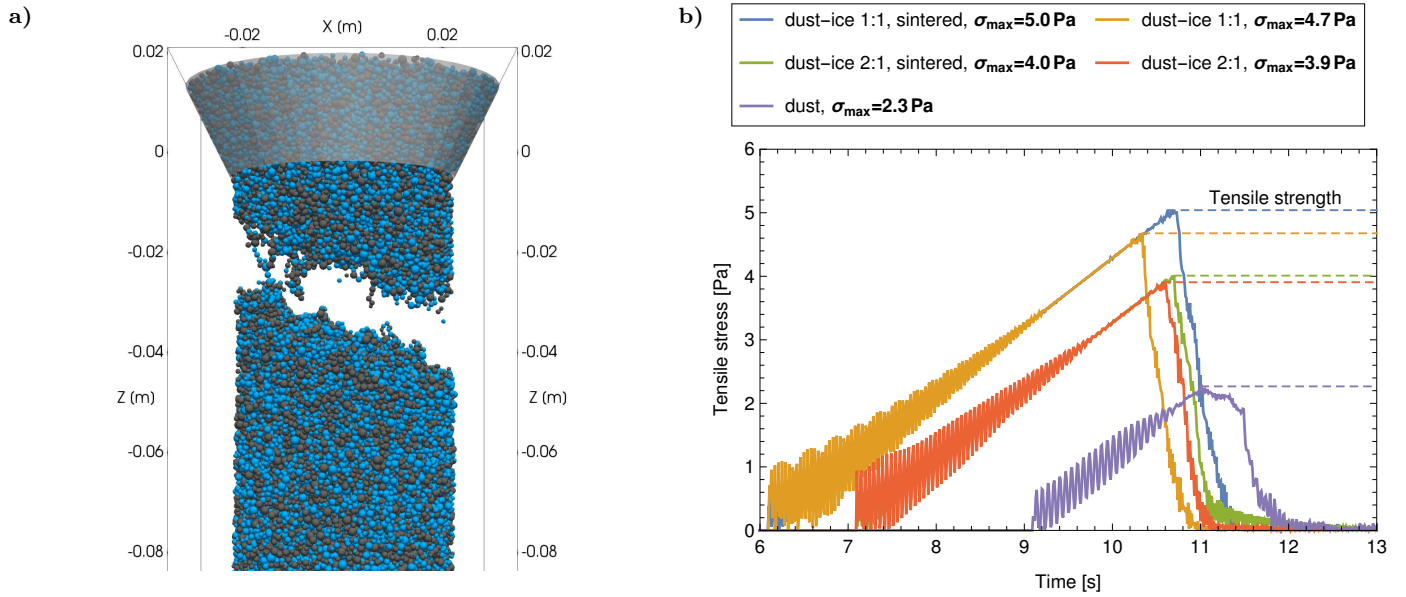
We simulate a cliff with a geometry similar to that of the Aswan cliff before its collapse. It is set to be 130 m high with an overhang of 20°, while the crack starts at half the cliff height with an opposite tilt angle of 10°. For a scenario as large as this, the limited number of parcels in our previous simulations would make it difficult to resolve boulders of the mentioned size. Therefore, we have performed a spatially highly resolved simulation using parallel processing. The cliff's upper half with the overhang is composed of about 270 000 computational parcels, the smallest of which are 0.6 m in diameter, while the cliff's lower half, which does not participate in the collapse, is built of wall elements to save computational resources.

The post-collapse morphology of this simulation is shown in Fig. 8. We have chosen constituent sizes (particle diameters 3–6 mm) such that the cliff is barely stable before triggering the collapse. This leads to a relatively smooth debris pile with some protruding boulders, which resembles the morphology of the debris observed beneath the Aswan cliff. In our simulation, the pile reaches its maximum height of 28 m not directly at the



**Fig. 8.** Detailed view of the post-collapse morphology for the Aswan cliff collapse case. The pre-collapse cliff is made up of a 1:1 dust-ice mixture with a five-meter-thick sintered top layer. It is 130 m high and 80 m wide with an overhang of 20° and has a crack starting at half the cliff height with an opposite tilt angle of 10°. Only the debris pile is shown here. Graphical representation as in Fig. 4, but additionally with sinter bonds (thick red bars). The material is rendered partly transparent.





**Fig. 9.** Simulated tensile strength test. (a) A 10 cm-high and 5 cm-wide cylinder made up of a mixture of dust (gray spheres) and ice (blue spheres) particles is mounted in a clamp (a numerical wall with the shape of a truncated cone) with its flat top side, while a gradually increasing force is pulling on the cylinder's flat bottom side until the cylinder breaks apart (shown here). (b) Time evolution of tensile stress for selected materials made up of particles with diameters of 1–2 mm. The horizontal dashed line pointing to the maximum of a curve is the stress at the breaking point, i.e., the material's tensile strength  $\sigma_{\max}$  (values given in plot legend for each material). The oscillations in the early phase of the stress build-up result from longitudinal waves in the cylinder excited by the stepwise increase of the force pulling at the bottom. Their amplitudes decrease as the tension in the cylinder increases. Stresses measured during the preparation of the material samples are omitted for better representation.

cliff wall but about 15 m away from it. The run-out length of the debris measured from this point is (on average) 70 m, which corresponds to a mean angle of repose of  $22^\circ$ . This is in the range of  $20\text{--}30^\circ$  measured for slopes of granular flows on 67P (Vincent et al. 2016) and at the lower end of what is measured for granular materials on other bodies (Kokelaar et al. 2017), possibly due to 67P's low surface acceleration (Kleinhans et al. 2011). Most of the sinter bonds (98% out of 6800) survive the collapse of the cliff, since the more stable sintered top layer does not fully disintegrate but breaks into large fragments. The still intact sinter bonds are mostly located in the upper debris layer and are unevenly distributed with distance from the new cliff face, with some small regions being devoid of sinter bonds and an accumulation of sinter bonds at the foot of the debris pile. We interpret each parcel cluster connected by sinter bonds as a boulder in the debris. From visual inspection, the largest boulders on top of the debris pile have a diameter of about 10 m. Overall, the simulation outcome therefore demonstrates that the observed Aswan cliff post-collapse morphology is compatible with the material and the mechanical parameters we used in this simulation.

As for the boulder stability scenario, we found the coarse-graining factor to have only a minor effect on the morphologic behavior when interpreted within reasonable tolerances given by slight changes in the parcel configuration at fixed  $cg$ .

#### 4.3. Tensile strength test

Proceeding as described in Sect. 3.3, we investigated the tensile strengths of materials with constituent size distributions and friction coefficients favored by the previous scenarios. We performed this test for all three dust-ice mixtures, with and without sintering of ice, for particles with diameters of 1–2 mm. As discussed in Sect. 4.1, the tensile strengths for the other particle

sizes used in our simulations can be obtained by scaling with respect to the particle radius ( $\propto R^{-1}$ ). Figure 9 shows the recorded tensile stress diagrams, where the tensile strength is given by the maximum of the respective curve. Scaled with respect to our different used particle diameter ranges (from 10–20 mm to 0.2–0.4 mm), the resulting tensile strengths without sintering are in the range of 0.23–11 Pa (pure dust), 0.39–20 Pa (2:1 dust-ice volume ratio), and 0.47–23 Pa (1:1 dust-ice volume ratio), respectively, which shows the generally higher strength of the less porous, relatively ice-rich materials.

While we used “high friction” in these simulations, lower (higher) levels of friction can decrease (increase) the given numbers by several tens of percent. In contrast, in two additional simulations with a restitution coefficient of 0.1 and 0.8, respectively, instead of 0.3, the measured tensile strength differed by less than 1%, suggesting that the restitution coefficient has virtually no effect on tensile strength. This does not contradict the larger but still moderate influence of the restitution coefficient in the boulder drop tests, which are highly dynamic processes where energy dissipation plays a much more important role than in the quasi-static tensile strength test.

Additional tests with a timestep of 3% instead of 10% of the minimum of Rayleigh time and Hertz time resulted in less than 1% difference in the measured tensile strength of the material.

Sintering of ice has a comparatively small effect by increasing these values by less than 10%, which does not explain the partly surprisingly tough terrain observed for 67P's consolidated areas (Spohn et al. 2015). We believe this is because of the porous and homogeneous structure of our materials, where the ice particles have only a few contacting neighbors (low coordination number) with less than half of them being other ice grains. For such a configuration, the formation of long sinter chains extending across many particles through large parts of the material is highly improbable. However, a still higher ice content and

the associated stronger sintering effect can lead to much stronger materials. A series of numerical experiments for pure ice changing the sinter bond radius scaling factor  $\bar{\lambda}$  (0.01, 0.1, 0.5, 1.0) confirms that the macroscopic material's tensile strength scales with  $\bar{\lambda}^2$  as expected. However, in case of a low ice content, the lack of long sinter chains results only in a small dependence on  $\bar{\lambda}$ . We note that our sintered low-ice-content boulders become rather more brittle than stable for increased  $\bar{\lambda}$ , likely due to the reduced flexibility of the thicker sinter bonds while the overall dynamics is not yet governed by sinter bonds due to their relatively low number.

We also checked the applicability of the coarse-graining technique. The tensile strength of the cylinder was found to only weakly depend on the coarse-graining factor  $cg$  as long as the parcel number is generally not too small and not more than a few percent of the parcels are at the boundaries. Our results compare well with tensile strength estimates on the order of 10 Pa derived from Rosetta data (Groussin et al. 2015; Attree et al. 2018).

Parallel to the numerical simulations, tensile strength measurements have been performed in the laboratory (Haack et al. 2019, and in prep.). For this purpose, a different experimental setup in the form of the Brazilian disc test (Gundlach et al. 2018) was chosen, which is more suitable for handling weak and brittle materials under terrestrial conditions. Here, centimeter-sized disks of compacted test material are exposed to gradually increasing pressure against their curved side. The force at which a disk cracks can be used to calculate the material's tensile strength. The utilized cometary analog materials were mixtures of polydisperse spherical silicate (fly ash) and water ice particles, with roughly power-law-distributed sizes but smaller power-law indexes of about  $i_c = 1.5$  and smaller mean diameters of about  $4\ \mu\text{m}$  than used in our numerical simulations. The experimental setup, including the material samples, was cooled with liquid nitrogen under terrestrial conditions to prevent sintering of the ice particles.

The tensile strength of pure water ice samples with a filling factor of  $\phi = 0.74$  was determined to 1800 Pa, which is compatible with similar experiments performed by Gundlach et al. (2018). Moreover, Haack et al. (2019, and in prep.) found a tensile strength of only 140 Pa for pure silicate samples at  $\phi = 0.84$ . The strength of mixtures of both materials has proven to be close to the tensile strength of water ice and decreases to the lower value of fly ash when the volume fraction of fly ash exceeds 75%. Scaling the tensile strengths of our model materials to the particle sizes used in the laboratory experiments gives values of  $\sim 400\text{--}1000$  Pa. Although this neglects the influence of the different size distributions and filling factors, this is between the measured tensile strengths of pure fly ash and pure water ice, which demonstrates that our numerical results are compatible with laboratory measurements.

## 5. Conclusions and outlook

In this work, we applied the discrete element method (DEM) to perform numerical simulations of dynamical surface processes on comet 67P in order to investigate the mechanical properties of the surface material. We modeled our materials as different mixtures of polydisperse dust and water ice spheres and took into account the ambient surface acceleration, the Hertz contact model, translational and rolling friction, and cohesive forces from unsintered contacts, as well as sinter bonds between ice particles. To enable the modeling of large scenarios with realistically small constituent particles, we employed

the coarse-graining technique, where an effective medium of computational parcels is considered, each parcel of radius  $cgR$  representing groups of several physical particles of radius  $R$ . Here,  $cg$  is referred to as the coarse-graining factor.

The presence of boulders on the surface of 67P requires the cometary bulk material to have a certain strength to sustain the ambient surface acceleration and survive drops from small heights, but also the possibility to break into fragments. In general, objects made of larger spherical particles are less stable, and increasing the friction between the particles leads to a less elastic, more brittle, but somewhat stronger material. From simulating the drop of two-meter-sized boulders from small heights, a reasonable behavior between total disintegration and no damage upon impact was observed for constituent particles with diameters on the order of 1 mm for a surface energy density of  $\omega = 0.028\ \text{J m}^{-2}$ . Changing the latter by a certain factor, the particle sizes have to be scaled by the same factor to approximately maintain the post-impact morphology. These observations can be carried over when heterogeneities are allowed by introducing locally more stable regions (e.g., smaller or less rough particles, higher coordination number). The breaking of boulders into large fragments and the formation of realistically rough debris fields required high levels of friction, which suggests that the constituents of the cometary bulk material are probably not all spherical but at least partly highly angular or very rough. This translates to weaker cohesive forces from unsintered contacts (asperity effect, Sect. 2.3), which has to be compensated by a correspondingly smaller particle size to again arrive at the same post-impact morphology.

We also investigated collapses of cliffs and overhangs of typical dimensions observed on 67P. For the DEM modeling, the cliff material was carried over from the boulder drop scenarios with the most realistic outcomes, such that the pre-collapse cliffs, which additionally exhibit a sintered top layer, are statically only just self-sustained. In the absence of material heterogeneities, we find that reasonable seismic activity generally does not suffice to trigger the collapses without resorting to a fine-tuning of parameters. In order to force a collapse, we introduced artificial cracks in the cliff material. Then, assuming otherwise homogeneous pre-collapse material, our numerical results suggest that most debris fields associated with collapses of cliffs on 67P probably originate from not overly strong and steep overhangs. However, the 67P observations are also compatible with heterogeneous pre-collapse materials or the occurrence of pre-collapse micro-cracks. In the case of a dedicated simulation of the Aswan cliff collapse, which was imaged on 67P before and after the event, we find the observed morphology to be compatible with our utilized material and mechanical parameters.

For our model materials, the influence of ice sintering on the material strength quadratically decreases with decreasing ice content. Sintering had a significant effect in the case of our ice-rich material (1:1 dust-to-ice-volume ratio) as it noticeably increased the overall strength and brittleness and led to a more distinct clustering of the post-impact and post-collapse debris. At very low dust-to-ice ratios, sintering can provide an explanation for the partly surprisingly tough terrain observed on 67P (Spohn et al. 2015). In contrast, other measurements (Fulle et al. 2017) suggest a global ice content that is lower than that of our ice-rich material and more similar to that of our ice-poor material (2:1 dust-to-ice-volume ratio), where sintering had a very small effect. However, the ice particles do not need to be distributed homogeneously across the comet, and in fact they are not (Oklay et al. 2017), such that it is still possible to have areas



of weaker surface material mixed with areas of stronger surface material.

We also determined the tensile strengths of materials favored by the previous test scenarios. For this purpose, we pulled a cylinder made out of these materials to its breaking point. Not taking into account sintering, the calculated tensile strengths are in the range of 0.23–11 Pa (pure dust), 0.39–20 Pa (2:1 dust-ice volume ratio), and 0.47–23 Pa (1:1 dust-ice volume ratio), respectively, for our different particle diameter ranges (from 10–20 mm to 0.2–0.4 mm). A comparison of these measurements with the results from the boulder drops confirms a clear correlation between the tensile strength of the material and the stability of the boulders. In particular, we find that boulders made up of material with a tensile strength much larger than 10 Pa remain undamaged after impact, while boulders made up of material with a tensile strength much smaller than 1 Pa totally disintegrate. Sintering of ice increases these values by less than 10% for our considered dust–ice mixtures. Our results compare well with tensile strength estimates on the order of 10 Pa derived from Rosetta data (Groussin et al. 2015; Attree et al. 2018). They are also compatible with tensile strength measurements of cometary analogue materials Haack et al. (2019, and in prep.). This demonstrates that DEM modeling can be a powerful tool to investigate and constrain the macroscopic properties of cometary surface material. Once calibrated, numerical simulations can also be used to study problems that have been difficult to access experimentally such as the only partly explained mechanism of dust ejection from cometary surfaces (cometary activity paradox).

We find the coarse-graining technique to largely preserve the general trend in the tensile strength and the morphologic behavior. Here, the simulation outcomes have to be interpreted within tolerances given by slight changes in the geometric arrangement of the computational parcels at unchanged coarse-graining factor  $cg$ , which can by themselves, in a nonlinear way, lead to significant differences in the details of for example the fragmentation. Taking this into account, it proved to be successful to apply coarse-graining, as long as the parcel number is generally not too small and not more than a few percent of the parcels are at the boundaries. To improve the behavior in such cases, the simulation resolution has to be increased (i.e.,  $cg$  decreased). Since the required computer memory scales with  $cg^{-3}$  and the computation time with  $cg^{-4}$ , this approach has its limits. But it might be an option in future simulations to nonuniformly increase the resolution in the vicinity of existing boundaries and of expected new ones. Either way, we recommend to always, at least exemplarily, check the influence of coarse-graining on the simulation outcomes, in particular in cases where the fraction of parcels close to a boundary is not small.

In general, the details of the simulation outcomes (e.g., location and shape of cracks, exact number of fragments, trajectories of individual particles) can differ for slight changes in the numerical setup (e.g., initial microscopic geometrical arrangement of the particles, or order of summation given by choice of cutoff distance for the neighbor lists or by execution order when using parallel processing – the dependence on the summation order is a consequence of using finite precision floating point arithmetic which is not necessarily associative or distributive leading to noise in the numerical reproducibility). However, when again interpreted within tolerances as stated for the investigation of  $cg$ -changes, the boulder post-impact morphology was found to be only moderately sensitive when the coefficients of restitution of the parcels are changed from 0.3 to 0.1 or 0.8 or when increasing the Young’s modulus by a factor of ten. It was found to be weakly sensitive when the coefficient of restitution (Young’s modulus)

of the bottom surface impacted by the boulder is changed from 0.3 to 0.1 (from  $10^8$  Pa to  $10^7$  Pa), when the impact angle of the boulder is changed from  $30^\circ$  to  $0^\circ$ , when moderately increasing the particle size range around a center particle radius, or when using a finer particle size binning. Weak sensitivity also resulted when setting the ratio of shear and tensile strength of bond cement to 0.3 instead of 1.0, when decreasing the time step from 10% of the minimum of Rayleigh and Hertz time to 3%, or when decreasing the neighbor list cutoff distances.

The morphologically most interesting boulder and cliff cases where the material broke into large (meter-sized) fragments with some debris occurred only for a comparatively small range of constituent sizes. One possible reason for this selective behavior could be the relatively narrow particle size distribution that we had to use because of the limited available computational resources (ratio of two between the largest and the smallest particle diameters) and our modeling assumption of a homogeneous material. This might have generated materials where the contact forces between the particles are still relatively uniform. As a result, the material totally disintegrates upon impact if the constituents are somewhat larger than a critical size or remains almost undamaged if the constituents are somewhat smaller than this size. Although the present situation is already improved compared to our earliest simulations with even narrower and more degenerate size distributions, this necessitated some fine-tuning to obtain a specific morphologic behavior. A possible solution for a more realistic simulation outcome where the level of fragmentation depends less critically on the constituent size could be to introduce local variations in the material properties.

A major source of uncertainty of our model is the assumed structure of the material, in particular the geometrical arrangement of the particles and their coordination number. We use a homogeneous mixture of two types of particles – dust and ice – that does not feature local variations in the arrangement of the particles or the material strength. Also, we do not consider the presence of small interstitial particles partially filling the voids between the larger particles and their potential cohesive effects. In reality, the cometary bulk material is most certainly not completely homogeneous and might have a structure that varies, possibly on different length scales. Since there is a high degeneracy between particle sizes, size distributions, and geometrical configuration as well as dust and ice abundance and mixing modalities, it is not possible at the present stage to draw definite conclusions on the dust-ice ratio on 67P from our DEM simulations alone. It always has to be kept in mind that the way dust and ice interact on 67P is much more complicated than we are able to model within the limits of our simulation setups.

An actual breaking (in contrast to a viscous deformation) of the bulk material forming our boulders needed high (rolling) friction between the particles. As mentioned above, since one of the main causes for rolling resistance are aspherical particle shapes, this suggests that the constituents of the cometary material are not all spherical, but include very rough, possibly even angular, interlocked particles. This is compatible with coma particles measured by the GIADA and MIDAS instruments aboard Rosetta partly showing highly complex aggregates (Fulle et al. 2015; Mannel et al. 2016) that probably originated from the nucleus surface. To better approximate such an almost fractal topology, we might need to introduce a further intermediate modeling level in addition to the basic coarse-graining technique employed in our simulations. Basic unsintered cohesive and frictional spherical particles on a micron scale would then be used to form complex agglomerates on a mesoscopic level, the mechanical properties of which (effective mesoscopic cohesion, friction,

Young's modulus, etc.) have to be explored by numerical experiments with several different realizations of such agglomerate blocks. These agglomerates are then treated as DEM building blocks in macroscopic scenarios, with properties as derived in the mesoscale experiments. This approach resembles the coarse-graining technique, but now with a refined focus on the details of the underlying microscopic material structure.

As the next step (Kappel et al. 2018a,b), we plan to study other surface processes on comet 67P that formed for example wind-tail-like structures and moats that have been observed around many exposed boulders (Mottola et al. 2015), and fracture polygons that have been observed in many places where consolidated material is exposed on the nucleus surface (Auger et al. 2018). We also intend to include Monte-Carlo-based modeling of sublimation and recondensation of volatiles and Knudsen gas flow through the surface layer, which will provide us with a tool to investigate more complex scenarios like triggers and early phases of cometary outbursts as well as other processes related to volatile compounds on comet 67P and other small Solar System bodies.

**Acknowledgements.** This work is part of the research project "The Physics of Volatile-Related Morphologies on Asteroids and Comets". D.K., M.S., D.H., and K.O. would like to gratefully acknowledge the financial support and endorsement from the DLR Management Board Young Research Group Leader Program and the Executive Board Member for Space Research and Technology. We acknowledge the insightful comments and suggestions of an anonymous reviewer that greatly improved this work.

## References




- Ai, J., Chen, J.-F., Rotter, J. M., & Ooi, J. Y. 2011, *Powder Technol.*, 206, 269
- Attree, N., Groussin, O., Jorda, L., et al. 2018, *A&A*, 611, A33
- Auger, A.-T., Groussin, O., Jorda, L., et al. 2018, *Icarus*, 301, 173
- Barthel, E. 2008, *J. Phys. D: Appl. Phys.*, 41, 163001
- Basilevsky, A. T., Krasil'nikov, S. S., Shiryaev, A. A., et al. 2016, *Sol. Syst. Res.*, 50, 225
- Bertini, I., Gutiérrez, P. J., Lara, L. M., et al. 2015, *A&A*, 583, A19
- Bibring, J.-P., Langevin, Y., Carter, J., et al. 2015, *Science*, 349, aab0671
- Biele, J., Ulamec, S., Maibaum, M., et al. 2015, *Science*, 349, aaa9816
- Bierwisch, C., Kraft, T., Riedel, H., & Moseler, M. 2009, *J. Mech. Phys. Solids*, 57, 10
- Blackford, J. R. 2007, *J. Phys. D Appl. Phys.*, 40, R355
- Blum, J., Gundlach, B., Krause, M., et al. 2017, *MNRAS*, 469, S755
- Brilliantov, N. V., Spahn, F., Hertzsch, J.-M., & Pöschel, T. 1996, *Phys. Rev. E*, 53, 5382
- Brownlee, D. E., Horz, F., Newburn, R. L., et al. 2004, *Science*, 304, 1764
- Capaccioni, F., Coradini, A., Filacchione, G., et al. 2015, *Science*, 347, aaa0628
- Castellanos, A. 2005, *Adv. Phys.*, 54, 263
- Cheng, B., Yu, Y., & Baoyin, H. 2017, *Sci. Rep.*, 7, 10004
- Cheng, B., Yu, Y., & Baoyin, H. 2019, *MNRAS*, 485, 3088
- Colwell, J. E. 1993, *Lunar Planet. Sci. Conf.*, 24, 325
- Cundall, P. A., & Strack, O. D. L. 1979, *Géotechnique*, 29, 47
- DCS Computing GmbH 2016, LIGGGHTS User Manual
- Di Renzo, A., & Di Maio, F. P. 2004, *Chem. Eng. Sci.*, 59, 525
- Di Renzo, A., & Di Maio, F. P. 2005, *Chem. Eng. Sci.*, 60, 1303
- El-Maarry, M. R., Thomas, N., Giacomini, L., et al. 2015, *A&A*, 583, A26
- El-Maarry, M. R., Thomas, N., Gracia-Berná, A., et al. 2016, *A&A*, 593, A110
- El-Maarry, M. R., Thomas, N., Gracia-Berná, A., et al. 2017, *A&A*, 598, C2
- El-Maarry, M. R., Groussin, O., Keller, H. U., et al. 2019, *Space Sci. Rev.*, 215, 36
- Fornasier, S., Hasselmann, P. H., Barucci, M. A., et al. 2015, *A&A*, 583, A30
- Fuller, K. N. G., & Tabor, D. 1975, *Proc. R. Soc. London Ser. A*, 345, 327
- Fulle, M., Corte, V. D., Rotundi, A., et al. 2015, *ApJ*, 802, L12
- Fulle, M., Della Corte, V., Rotundi, A., et al. 2016, *MNRAS*, 462, S132
- Fulle, M., Della Corte, V., Rotundi, A., et al. 2017, *MNRAS*, 469, S45
- Gold, L. W. 1958, *Can. J. Phys.*, 36, 1265
- Groussin, O., Jorda, L., Auger, A. T., et al. 2015, *A&A*, 583, A32
- Gulkis, S., Allen, M., Allmen, P. v., et al. 2015, *Science*, 347, aaa0709
- Gundlach, B., Schmidt, K. P., Kreuzig, C., et al. 2018, *MNRAS*, 479, 1273
- Haack, D., Otto, K., Kührt, E., et al. 2019, EPSC-DPS Joint Meeting, 13, EPSC
- Haas, C. J. 1989, *Static Stress-strain Relationships*, ed. C. Ho5210 (New York: Hemisphere Publishing), 123
- Heim, L.-O., Blum, J., Preuss, M., & Butt, H.-J. 1999, *Phys. Rev. Lett.*, 83, 3328
- Hertz, H. 1882, *Journal für die reine und angewandte Mathematik*, 92, 156
- Hirabayashi, M., Sánchez, D. P., & Scheeres, D. J. 2015, *ApJ*, 808, 63
- Hobbs, P. 1974, *Ice Physics* (Oxford: Clarendon Press)
- Holsapple, K. A., & Housen, K. R. 2007, *Icarus*, 191, 586
- Hviid, S. F., Hüttig, C., Groussin, O., et al. 2016, *AAS/Div. Planet. Sci. Meeting Abs.*, 48, 211.05
- Johnson, K. L., Kendall, K., & Roberts, A. D. 1971, *Proc. Roy. Soc. London Ser. A*, 324, 301
- Jorda, L., Gaskell, R., Capanna, C., et al. 2016, *Icarus*, 277, 257
- Kappel, D., Otto, K., Oklay-Vincent, N., et al. 2018a, *Lunar Planet. Sci. Conf.*, 49, 2696
- Kappel, D., Otto, K., Oklay, N., et al. 2018b, *Euro. Planet. Sci. Conf.*, 12, EPSC2018
- Keller, H. U., Barbieri, C., Lamy, P., et al. 2007, *Space Sci. Rev.*, 128, 433
- Keller, H. U., Mottola, S., Davidsson, B., et al. 2015, *A&A*, 583, A34
- Keller, H. U., Mottola, S., Hviid, S. F., et al. 2017, *MNRAS*, 469, S357
- Kimura, H., Wada, K., Senshu, H., & Kobayashi, H. 2015, *ApJ*, 812, 67
- Kleinbans, M. G., Markies, H., de Vet, S. J., in't Veld, A. C., & Postema, F. N. 2011, *J. Geophys. Res. Planets*, 116, E11004
- Kloss, C., Goniva, C., Hager, A., Amberger, S., & Pirker, S. 2012, *Prog. Comput. Fluid Dyn.*, 12, 140
- Knapmeyer, M., Fischer, H. H., Knollenberg, J., et al. 2018, *Icarus*, 310, 165
- Kofman, W., Herique, A., Barbin, Y., et al. 2015, *Science*, 349, 2.639
- Kokelaar, B. P., Bahia, R. S., Joy, K. H., Viroulet, S., & Gray, J. M. N. T. 2017, *J. Geophys. Res. Planets*, 122, 1893
- Küppers, M., Keller, H. U., Kührt, E., et al. 2009, *Exp. Astron.*, 23, 809
- Leite, F. L., Bueno, C. C., Da Róz, A. L., Ziemath, E. C., & Oliveira, O. N. 2012, *Int. J. Mol. Sci.*, 13, 12773
- Maeno, N., & Ebinuma, T. 1983, *J. Phys. Chem.*, 87, 4103
- Mannel, T., Bentley, M. S., Schmied, R., et al. 2016, *MNRAS*, 462, S304
- Martin, C. L., & Bordia, R. K. 2008, *Phys. Rev. E*, 77, 031307
- Matonti, C., Attree, N., Groussin, O., et al. 2019, *Nat. Geosci.*, 12, 157
- Mellon, M. T. 1997, *J. Geophys. Res.*, 102, 25617
- Molaro, J. L., Choukroun, M., Phillips, C. B., et al. 2019, *J. Geophys. Res. Planets*, 124, 243
- Mottola, S., Arnold, G., Grothues, H.-G., et al. 2015, *Science*, 349, aab0232
- Muller, V., Derjaguin, B., & Toporov, Y. 1983, *Colloids Surf.*, 7, 251
- Oklay, N., Mottola, S., Vincent, J.-B., et al. 2017, *MNRAS*, 469, S582
- Pajola, M., Vincent, J.-B., Güttler, C., et al. 2015, *A&A*, 583, A37
- Pajola, M., Oklay, N., Forgia, F. L., et al. 2016, *A&A*, 592, A69
- Pajola, M., Höfner, S., Vincent, J. B., et al. 2017, *Nat. Astron.*, 1, 0092
- Potyondy, D., & Cundall, P. 2004, *Int. J. Rock Mech. Mining Sci.*, 41, 1329
- Preusker, F., Scholten, F., Matz, K. D., et al. 2017, *A&A*, 607, L1
- Radl, S., Radeke, C., Khinast, J., & Sundaresan, S. 2011, in 8th International Conference on CFD in Oil & Gas, Metallurgical and Process Industries
- Richardson, J. E., Melosh, H. J., Greenberg, R. J., & O'Brien, D. P. 2005, *Icarus*, 179, 325
- Richter, C. 2015, LIGGGHTS-WITH-BONDS, <https://github.com/richti83/LIGGGHTS-WITH-BONDS>
- Rotundi, A., Sierks, H., Corte, V. D., et al. 2015, *Science*, 347, aaa3905
- Scheeres, D. J., Hartzell, C. M., Sánchez, P., & Swift, M. 2010, *Icarus*, 210, 968
- Schultz, R. A. 1995, *Rock Mech. Rock Eng.*, 28, 1
- Schwartz, S. R., Michel, P., Jutzi, M., et al. 2018, *Nat. Astron.*, 2, 379
- Sierks, H., Barbieri, C., Lamy, P. L., et al. 2015, *Science*, 347, aaa1044
- Silbert, L. E., Ertas, D., Grest, G. S., et al. 2001, *Phys. Rev. E*, 64, 051302
- Spohn, T., Knollenberg, J., Ball, A. J., et al. 2015, *Science*, 349, aab0464
- Squyres, S. W., Nakamura-Messenger, K., Mitchell, D. F., et al. 2018, *Lunar Planet. Sci. Conf.*, 49, 1332
- Sunshine, J. M., Thomas, N., El-Maarry, M. R., & Farnham, T. L. 2016, *J. Geophys. Res. Planets*, 121, 2194
- Swope, W. C., Andersen, H. C., Berens, P. H., & Wilson, K. R. 1982, *J. Chem. Phys.*, 76, 637
- Tancredi, G., Maciel, A., Heredia, L., Richeri, P., & Nesmachnow, S. 2012, *MNRAS*, 420, 3368
- Teanby, N. A., & Wookey, J. 2011, *Phys. Earth Planet. Interiors*, 186, 70
- Thomas, N., Sierks, H., Barbieri, C., et al. 2015a, *Science*, 347, aaa0440
- Thomas, N., Davidsson, B., El-Maarry, M. R., et al. 2015b, *A&A*, 583, A17
- Vincent, J.-B., Bodewits, D., Besse, S., et al. 2015, *Nature*, 523, 63
- Vincent, J.-B., Oklay, N., Pajola, M., et al. 2016, *A&A*, 587, A14
- Vincent, J.-B., Birch, S., Hayes, A., et al. 2019, EPSC-DPS Joint Meeting, 13, EPSC

### 2.3.2 Sachse et al. (2022)

Sachse, M., Kappel, D., Tirsch, D., & Otto, K. A. (2022). Discrete Element Modeling of Aeolian-like Morphologies on Comet 67P/Churyumov-Gerasimenko. *Astronomy & Astrophysics*, 662(A2), 1–15. <https://doi.org/10.1051/0004-6361/202141296>.

This article takes up and expands on observations of aeolian-like features on comet 67P that I had previously described in two conference abstracts (Otto et al. 2017a; 2017b) after their initial detection (Mottola et al., 2015). Together with D. Tirsch, I provided information on the morphology of aeolian-like features on 67P. I globally mapped boulders with wind tail-like features and determined their morphometry, distribution and orientation. While D. Tirsch produced Figures 1, 2 and 5, I generated the data for Figures 3 and 4. M. Sasche prepared and conducted the simulations in consultation with and support by D. Kappel. All authors assisted with refining the manuscript. After the initial submission of the article, I took on the organisation of the manuscript as corresponding author.

# Discrete element modeling of aeolian-like morphologies on comet 67P/Churyumov-Gerasimenko

M. Sachse<sup>1</sup>, D. Kappel<sup>1,2</sup> , D. Tirsch<sup>1</sup> , and K. A. Otto<sup>1</sup> 

<sup>1</sup> Institute of Planetary Research, German Aerospace Center (DLR), Rutherfordstr. 2, 12489 Berlin, Germany  
e-mail: katharina.otto@dlr.de

<sup>2</sup> Institute of Physics and Astronomy, University of Potsdam, Potsdam, Germany

Received 12 May 2021 / Accepted 13 August 2021

## ABSTRACT

**Context.** Even after the Rosetta mission, some of the mechanical parameters of comet 67P/Churyumov-Gerasimenko's surface material are still not well constrained. They are needed to improve our understanding of cometary activity or for planning sample return procedures.

**Aims.** We discuss the physical process dominating the formation of aeolian-like surface features in the form of moats and wind tail-like bedforms around obstacles and investigate the mechanical and geometrical parameters involved.

**Methods.** By applying the discrete element method (DEM) in a low-gravity environment, we numerically simulated the dynamics of the surface layer particles and the particle stream involved in the formation of aeolian-like morphological features. The material is composed of polydisperse spherical particles that consist of a mixture of dust and water ice, with interparticle forces given by the Hertz contact model, cohesion, friction, and rolling friction. We determined a working set of parameters that enables simulations to be reasonably realistic and investigated morphological changes when modifying these parameters.

**Results.** The aeolian-like surface features are reasonably well reproduced using model materials with a tensile strength on the order of 0.1–1 Pa. Stronger materials and obstacles with round shapes impede the formation of a moat and a wind tail. The integrated dust flux required for the formation of moats and wind tails is on the order of  $100 \text{ kg m}^{-2}$ , which, based on the timescale of morphological changes inferred from Rosetta images, translates to a near-surface particle density on the order of  $10^{-6}$ – $10^{-4} \text{ kg m}^{-3}$ .

**Conclusions.** DEM modeling of the aeolian-like surface features reveals complex formation mechanisms that involve both deposition of ejected material and surface erosion. More numerical work and additional in situ measurements or sample return missions are needed to better investigate mechanical parameters of cometary surface material and to understand the mechanics of cometary activity.

**Key words.** comets: general – comets: individual: 67P/Churyumov-Gerasimenko – methods: numerical

## 1. Introduction

The visit of the Rosetta spacecraft at comet 67P/Churyumov-Gerasimenko (hereafter 67P) revealed a previously unknown diversity of geomorphologic surface features and landforms on a comet (Thomas et al. 2015c; El-Maarry et al. 2019). These features are influenced by the physical material properties and environment in which they form and they have been used to constrain physical parameters of the cometary regolith (Attree et al. 2018; Biele et al. 2015).

One of the most surprising morphologic observations on 67P is the presence of aeolian-like bedforms (e.g., Mottola et al. 2015; Thomas et al. 2015a,c) identified in high-resolution image data of the ROLIS descent imager (Mottola et al. 2007) onboard the Philae lander and the OSIRIS orbiter camera (Keller et al. 2007) onboard the Rosetta spacecraft. These bedforms involve ripple-like structures in the Hapi region (the “neck” of the comet) (Thomas et al. 2015c) as well as elongated deposits of granular material and semicircular depressions around several larger boulders (>5 m) resembling wind tails and moats as known from planets with atmospheres (Fig. 1). These features commonly form by the accumulation or erosion of granular media such as sand by wind. Examples of wind tails and moats have been observed on Earth and Mars (e.g., Greeley et al. 1999, 2002; Golombek et al. 2006) (Fig. 2) and are usually associated with

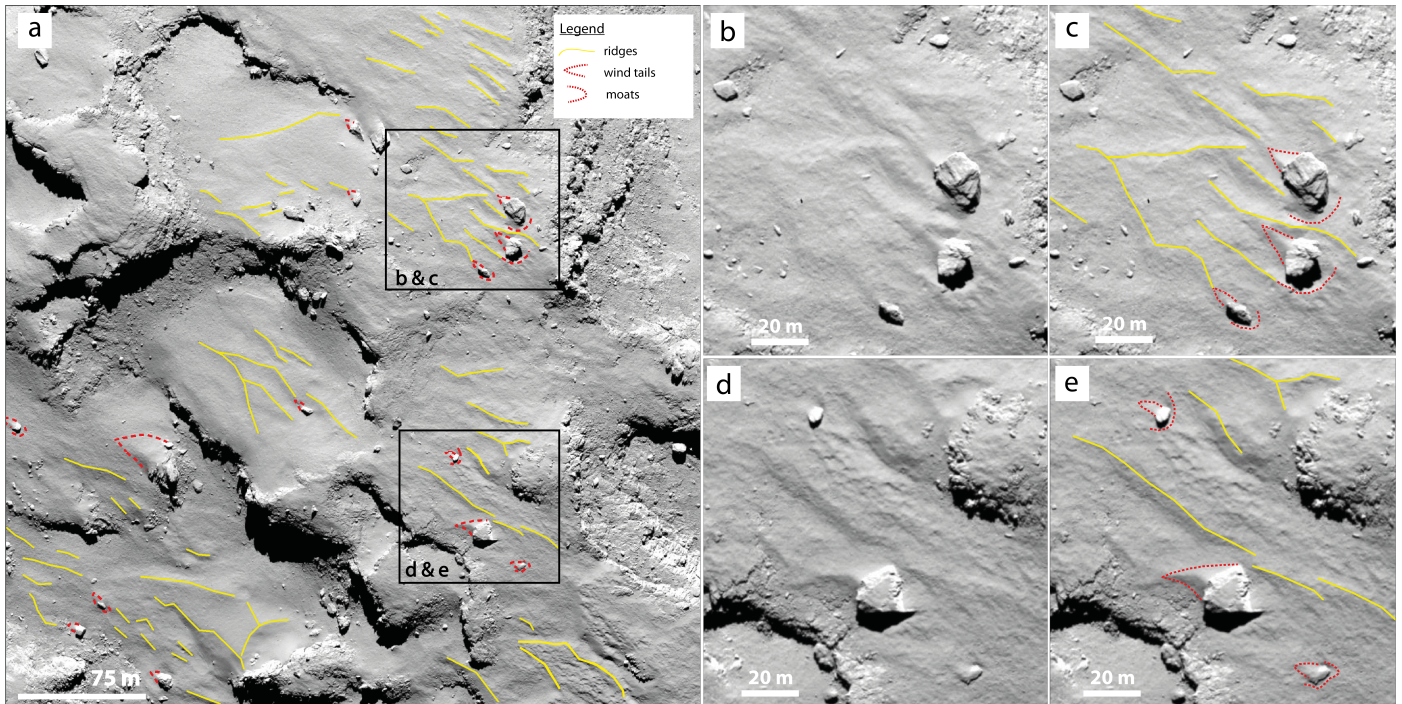
turbulences. However, turbulences do not occur on an almost atmosphereless comet, and the features are certainly of different origin. Nevertheless, the existence of these bedforms indicates that aeolian-like processes can transport particles across the surface of the nucleus and become manifest where they interact with obstacles such as boulders.

Previous studies have been aimed at finding an answer to the question of how to explain aeolian-like granular transport on a planetary body with an extremely rarefied exosphere and with an almost negligible gravitation, hence, without some of the fundamental physical mechanisms generally responsible for particle motion (Thomas et al. 2015b). Several studies have suggested that they form as a result of abrasion of a sand bed induced by air fall particles (Kramer & Noack 2015; Mottola et al. 2015; Thomas et al. 2015a).

In this paper, we concentrate on the identification of the physical processes dominating the formation of moats and wind tail-like bedforms around obstacles and investigate mechanical and geometrical parameters involved. Due to the similarity in morphology to the well-known bedforms on Mars and Earth, we use the term “wind tails” for the elongated bedforms associated with obstacles. However, we do not intend to imply that wind is involved in the formation of these features on the nucleus.

To complement the available measurements, improve our understanding of the dynamic processes involved in forming





**Fig. 1.** Mapping of aeolian-like morphologies on OSIRIS image data at the Agilkia touchdown 1 site, as an example for the 362 images analyzed. The orientation of the moats, wind tails, and smooth ridges indicate material transport from the same source direction, i.e., from the lower right to the upper left of this image (OSIRIS image NAC\_2014-11-12T15.43.51.584Z; image credit: MPS/UPD/LAM/IAA/SSO/INTA/UPM/DASP/IDA).

wind tails and moats, and constrain the physical parameter space of the materials involved, we applied numerical simulations. These can be used to constrain some of the micro- and macro-mechanical parameters, for example, by excluding certain parameter ranges or combinations incompatible with the development of the observed morphological features. The DEM is a widely accepted method for modeling granular and discontinuous materials. It is well suited to describe the separate, discrete particles presumably involved in the formation of the moat and wind tail structures. The present study continues previous work (Kappel et al. 2020), where we applied the DEM method to investigate the morphologies of boulders and cliffs observed on 67P.

Section 2 shows the distribution of moats and wind tails on comet 67P as well as more detailed measurements for two selected boulders. Section 3.1 gives an overview of our numerical DEM modeling of these features. The investigated simulation scenario is introduced in Sect. 3.2, and the simulation outcomes and changes when varying its setup are presented and discussed in Sect. 4. Finally, conclusions and an outlook are given in Sect. 5.

## 2. Bedform description and distribution

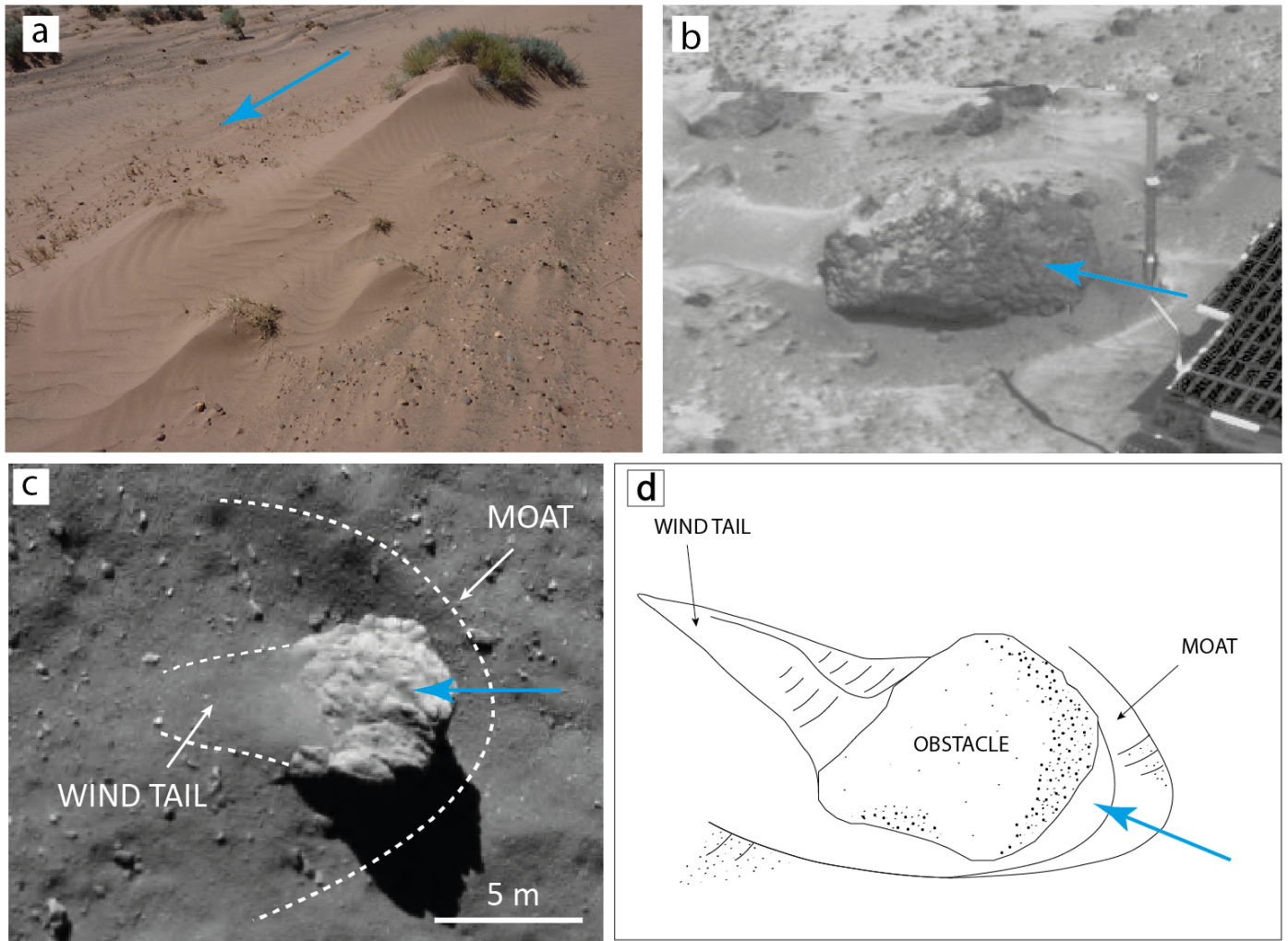
Using preperihelion OSIRIS images with resolutions of 50 cm/pixel or better, we identified boulders with aeolian-tail-like morphologies globally. Although we examined the entire illuminated surface of 67P, we focused on areas with air fall deposits given their association of aeolian-like features. In total, we examined 362 images taken between October 2014 and February 2015 of which 41 were used to take measurements of boulders and wind tails.

The majority of the wind tails on comet 67P is located on the small lobe of the nucleus in the Ma'at region (see

El-Maarry et al. (2015) for regional boundaries and nomenclature), whereas other areas are depleted in this respect (Fig. 3). All wind tails occur in regions covered with air fall deposits. The average boulder size (measured as the mean of length and width of a boulder along and perpendicular to the wind tail direction) is  $15.9 \text{ m} \pm 6.7 \text{ m}$  (one standard deviation) with a minimum of 4.6 m (possibly biased due to the spatial resolution limit) and a maximum of 35.5 m. The average length of the wind tails is around  $15.2 \text{ m} \pm 9.9 \text{ m}$  with a minimum of 4.9 m and a maximum of 73.6 m, reflecting the variable size of boulders on the nucleus. Most wind tails are shorter than 30 m, and the lower limit of measured wind tail length as well as boulder size depends largely on the image resolution. Boulder height and wind tail length are moderately correlated (Fig. 4) with a Pearson correlation coefficient of 0.52. A linear fit to the data has a slope of 0.94, which – assuming the wind tail is simply the geometrically shielded region behind the boulder – corresponds to an incident angle of the particle wind of about  $45^\circ$ .

We measured the heights of two wind tails at Philae's first touchdown site in the Agilkia region in a digital terrain model (L. Jorda, personal comm.), which was generated from OSIRIS images using the method described by Jorda et al. (2016). One of those wind tails is associated with the  $\sim 5$ -m-sized boulder located right at the first touchdown site, and the other one is at a  $\sim 13$ -m-sized boulder about 60 m northwest of the first boulder (Figs. 5a,b). The maximum wind tail elevations range between 0.5 m and about 3 m depending on the boulder and the location of the cross section relative to the wind tail (Figs. 5c–f). Typically, the height of a wind tail on 67P reaches one third of the boulder's height. It is noteworthy that the size of the wind tails in relation to their obstacles on 67P is much larger than those known from Earth and Mars (Golombek et al. 2006).

The moat at the 5-m-sized boulder spans up to 2 m at its widest extent and has a maximum depth of about 40 cm



**Fig. 2.** Wind tails and moats on different planetary bodies. (a) Wind tails associated with vegetation acting as obstacles at Grand Falls Dune Field, Arizona, USA (Photo: D. Tirsch). (b) Boulder “Barnacle Bill” at the Mars Path Finder landing site. This 43-by-22-cm-sized rock is associated with a distinctive moat to its right and a wind tail to its left (subset of MPF image 81008 with parts of the Sojourner rover at the lower right). (c) 5-m-sized boulder at Philae’s first touchdown site “Agilkia” on comet 67P. White dashed lines trace the shape of the moat and the wind tail associated with this boulder (subset of ROLIS image ROL\_FS3\_141112153316\_336\_02). (d) Sketch showing the typical shape of a moat and a wind tail associated with an obstacle. Blue arrows indicate the wind direction in panels a, b, and d as well as the transport direction of air fall particles in panel c.

(cf. Fig. 2c and longitudinal profile in Fig. 5d). It is difficult to estimate how many boulders on the comet’s surface exhibiting a wind tail are also associated with a moat, since identification of the latter strongly depends on image resolution. Our survey can only provide a conservative estimate on the order of 20%, representing 14 boulders with moats identified out of a total of 65 boulders with wind tails. However, due to the observation bias and due to the fact that many moats might be hard to discern because they are optically occluded by the boulders, it is plausible to assume that the actual number of moats is substantially higher.

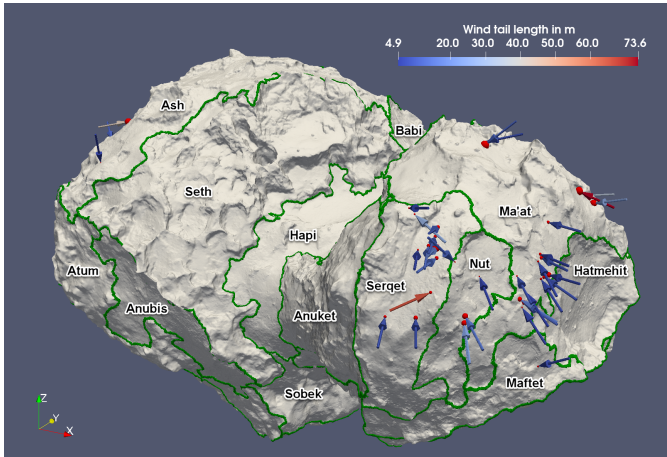
Tirsch et al. (2017b,a) noted a clear correlation of wind tail orientation in a given vicinity indicating a common source of the transport process. For instance, the preferred orientation of the wind tails in the Ma’at region is to the north (Fig. 3). Wind tails located in other parts of the comet mostly have a different orientation than to the north indicating different source regions of the air fall stream. The clustering of wind tails in the Ma’at region is consistent with the findings of Kramer & Noack (2015) based on global gas and dust dynamics simulations and Lai et al. (2016)

suggesting erosion of particles in Ma’at and Ash. In addition, the orientation of the wind tails agrees with the seasonal particle transport from south to north as suggested by Keller et al. (2017).

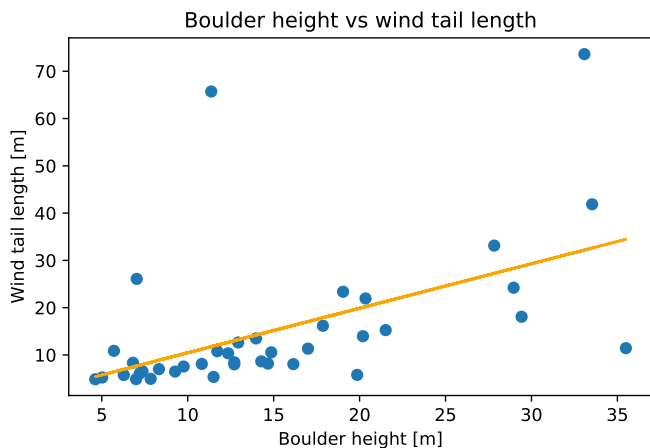
Variations in the covering of boulders with air fall particles indicate a dynamic formation process. However, the temporal evolution of these features could not be directly observed and probably takes place on scales below the image resolution.

Mottola et al. (2015) modeled the formation of wind tails using a simple, three-dimensional cellular automaton model that allowed air fall particles to erode a preexisting particle bed around a buried boulder. Although this model does not take into consideration particle deposition and redistribution, it successfully explains the morphologic formation of wind tails and moats as a purely erosive process. However, this model may be over-simplified and physical parameters related to the particle bed and boulder could not be derived. Additionally, Davidsson et al. (2020) suggested a net accumulation of air fall material in this region of up to 3.6 m based on a numerical model including orbit dynamics, thermophysics of the nucleus, and hydrodynamics of the gas flow. In the following, we complement our measurements





**Fig. 3.** Distribution of boulders (red spheres) with wind tails (arrows) on 67P projected onto a digital shape model by Preusker et al. (2017) with 67P’s morphologic regions outlined (El-Maarry et al. 2015). The arrows’ directions represent wind tail orientation including inclination and thus illustrate the presumed directions of the incoming particle streams, and their colors indicate the wind tail lengths. The boulder sizes are matched by the red sphere sizes. Most of these features are found in the Ma’at and Serqet regions, which are located at “the top of the head”, i.e., the northern part of the small lobe (Otto et al. 2017).



**Fig. 4.** Scatter plot of boulder height and wind tail length. The orange line is a linear fit with a slope of 0.94.

of wind tails and moats on 67P with new improved numerical simulations including both particle deposition and erosion.

### 3. Numerical simulations

#### 3.1. Discrete element modeling

The dynamics of the granular cometary surface material is modeled with the open source DEM simulation code LIGGGHTS (Kloss et al. 2012). Generally, we assume the particles to be represented by polydisperse spheres consisting of a mixture of dust and water ice, in contrast to Kappel et al. (2020), where the material consisted of a mixture of particles consisting either of dust or of ice. The spheres interact according to the Hertz contact model (Hertz 1882) and additionally are subject to cohesion from unsintered contacts, translational friction, rolling friction (Ai et al. 2011), and ambient surface acceleration. Furthermore, parallel bonds (Potyondy & Cundall 2004) between the spheres can be introduced that break when the interparticle stresses exceed

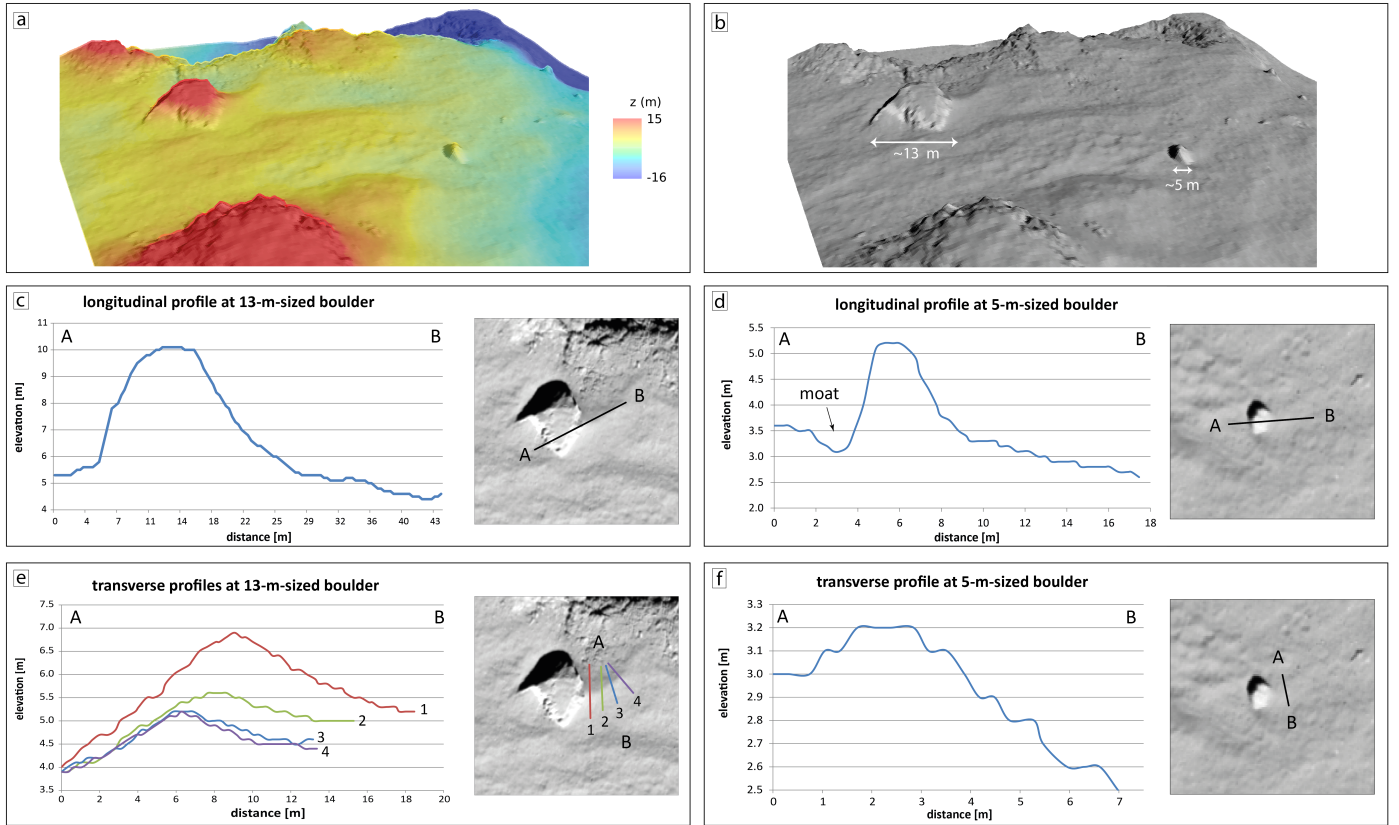
certain threshold values. This way, we can also model the hard consolidated terrain that was found at many places on the surface of 67P and may result from water ice sintering (Spohn et al. 2015). However, this aspect is not considered in the present work, which causes the ice to differ from the dust only by its solid mass density and limits the influence of the ice on the results: When the bulk material’s mass density is fixed to that of 67P, the ice’s lower solid mass density leads to a less porous, slightly stronger bulk material (calculations provided in Sect. 3.2). To enable the simulation of macroscopic scenarios with relatively small particles, we apply the coarse-graining technique (Bierwisch et al. 2009). A detailed description of each of these aspects has been provided with our first application of this model in Kappel et al. (2020). Since then no fundamental changes to the model have been applied, but in the present work we use a partly different set of model parameters, which are given and whose choice is motivated in Sect. 3.2.

#### 3.2. Simulation scenario

To model the scenario of wind tail and moat formation, we introduce a steady stream of particles colliding with a large obstacle in a particle bed. The incoming particles are set to move at a certain velocity on inclined, unidirectional trajectories. In the following, by the use of the words “in front of” (“behind”) we refer to the area facing (shadowed from) the particle stream as seen from the obstacle. To avoid boundary effects, the simulation geometry is set to be periodic in the horizontal dimensions.

The simulation is composed of two main parts – first the construction of a particle bed and the placement of an obstacle in the center of it, and then the insertion of a particle wind from above the obstacle. It starts by loosely filling a horizontal layer at the bottom of a cuboid simulation domain with non-contacting randomly positioned and sized (chosen from eight discrete sizes) spherical particles. Particles from a region in the center of the particle cloud are removed and replaced by an obstacle made up of wall elements or of a primitive sphere. The particle cloud is then compacted to the desired level by uniformly accelerating all particles to the same given downward velocity. As the particles fall down, they collide with each other or a wall at the bottom and dissipate their kinetic energy. By changing the given downward velocity and (temporarily) the interparticle contact parameters, we can control the bulk mass density and porosity of the emerging particle layer. After settling, the upper excess particles beyond the given layer thickness are removed and the simulation continued until relaxation. Then a stream of particles (“wind”) with a given mass rate and downward velocity (inclination  $45^\circ$ ) is continuously inserted in a horizontal layer above the obstacle. When impacting the obstacle or the particle bed, the wind particles can either get scattered or absorbed and cause the ejection of secondary particles, all together forming a particle cloud (“atmosphere”) above the particle bed. Since the deeper particles in the bed are also stirred, it sometimes becomes challenging to define which of the particles still belong to the bed and which to the atmosphere. The simulation is run until a steady atmosphere is established and no further morphological changes of the surface are observed (apart from changes of the overall level). An example of this scenario is shown in Fig. 6. The definition of the coordinate axes ( $x$ ,  $y$ ,  $z$ ) is as seen in this figure, where  $z$  increases with increasing altitude counting from the initial surface level right before the onset of the particle wind as level zero.

Due to the limited available computational resources, the simulations have to be restricted to a finite portion of the nucleus



**Fig. 5.** Morphometry of wind tails at the Agilkia landing site. (*a* and *b*): perspective views showing the two boulders based on OSIRIS images and DTM data (Jorda et al. 2016). Colors in *a* encode elevations from  $-16$  m (blue) to  $+15$  m (red). Labels in *b* indicate boulder sizes. The lateral and vertical DTM resolutions are about 35 and 10 cm per pixel, respectively. (*c*–*f*): longitudinal and transverse cross sections of the wind tails (and the moat) associated with the two boulders at Agilkia (Tirsch et al. 2017a). The size of the wind tail in profile (*f*) is at the limit of the DTM resolution which is the reason for the step-like shape of the profile.

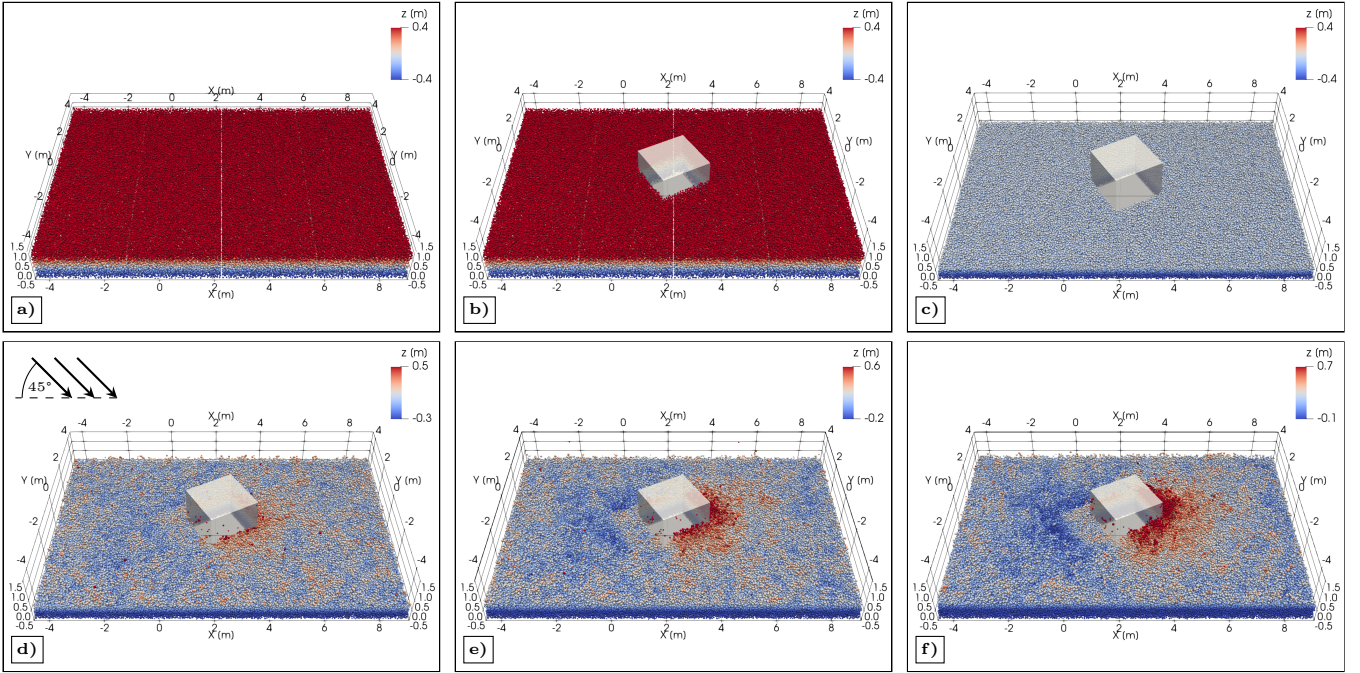
surface. Our particle bed measures  $13.5 \text{ m} \times 9 \text{ m}$  in the horizontal dimensions to significantly exceed our obstacle size (order of 3 m) and give room for the dynamics that dominate in the direction of particle insertion. In contrast, the vertical direction is only bounded by a wall at the bottom of the particle bed and is always expanded upwards to the particle with the currently highest altitude. The obstacle in the center of the particle bed is either a half-sphere, an upright cylinder, or a cube, whereas the cube can be rotated around its vertical axis to change its alignment with the particle wind. The rotation angle is set to  $30^\circ$ , which allows us to investigate the effect of two different front face alignments in a single simulation. The edge length of the cube and the diameter and height of the cylinder are 2.1 m, while the sphere is larger having a diameter of 2.7 m. Since the obstacles' lower parts are buried in the particle bed, the initial height of the cube and cylinder and that of the sphere above the surrounding particle bed level is only 1.5 m and 1 m, respectively, and slowly decreases as the surface level rises due to the insertion of additional particles.

Our particles are polydisperse spheres that each consist of a mixture of dust and water ice. They are assumed to resemble fluffy aggregates (motivated by the appearance of the particle beds in OSIRIS images and MIDAS measurements of coma particles, Mannel et al. 2019, that may present a source of our studied particle beds) that, in addition to the porosity of the particle bed  $1 - \phi_1$ , also have an internal porosity  $1 - \phi_2$ . For simplicity, we assume that both filling factors are the same, that is  $\phi = \phi_1 = \phi_2$ . Then the mass density of the bulk material is

given by  $\phi^2 \rho$ , where  $\rho = (1 - x)\rho_{\text{dust}} + x\rho_{\text{ice}}$  is the mixing density of the solid material for an ice volume fraction  $x$  and solid mass densities  $\rho_{\text{dust}} = 2000 \text{ kg m}^{-3}$  and  $\rho_{\text{ice}} = 920 \text{ kg m}^{-3}$  for the dust and the water ice particles, respectively. For a mixture with a dust-to-ice solid volume ratio of 2:1 (Pätzold et al. 2016), this mixing density is  $1640 \text{ kg m}^{-3}$ . With this, the filling factor results in 57% (corresponding to a bulk density of the aggregates of  $940 \text{ kg m}^{-3}$ ) in order to achieve an overall bulk density that is similar to the global mean value of  $538 \text{ kg m}^{-3}$  of comet 67P (Preusker et al. 2017).

To avoid a degeneration of the size-dependent contact forces, we use a discrete particle size distribution with eight different equally spaced radii ( $R = 3\text{--}6 \text{ cm}$ ). The cumulative distribution is set to follow a power-law with index  $i_c$  such that the number of particles with radius larger than  $R$  is proportional to  $R^{-i_c}$ . Mottola et al. (2015) reported ROLIS measurements for the Agilkia region on 67P, the initial touchdown site of Rosetta's Philae lander, exhibiting values of  $i_c$  in the range from 2.2 to 3.5. In our simulations, we use  $i_c = 2.5$ , and the ratio between the largest and the smallest particle radius is 2, meaning that eight of the smallest particles have the same mass as one of the largest ones. The mechanical parameters of the particles are largely adopted from our previous work regarding the stability of boulders and cliffs on 67P (Kappel et al. 2020), with some necessary changes to account for the particles resembling fluffy aggregates in this work. As default we set Poisson's ratio of both the particles and the obstacle to  $\nu = 0.3$ . The three friction coefficients (sliding and rolling friction coefficients  $\mu$  and  $\mu_r$ , rolling





**Fig. 6.** Construction of an obstacle in the center of a cometary particle bed made up of 140 000 polydisperse spheres consisting of a porous dust-ice mixture with a volume ratio of 2:1, and exposure to a particle wind. *Top row:* construction of the particle bed. (a) Loose filling of a horizontal layer at the bottom of the simulation domain with non-contacting randomly positioned and sized (chosen from eight discrete sizes) spherical particles. (b) Removal of particles in the center region and insertion of an obstacle built of wall elements. (c) Compaction of the particle layer to the bulk mass density and porosity of comet 67P and removal of particles above the given layer thickness. *Bottom row:* (d–f) several stages after the introduction of the particle wind. Particles from the granular atmosphere are removed for better representation. The color bar is adapted to the changing overall level of the particle bed.

viscous damping ratio  $\eta_r$ ) are all set to 1.0, which has led to realistic morphologies in our boulder and cliff simulations (Kappel et al. 2020). Young’s modulus and the coefficient of restitution are set to lower values than in the cited paper, that is  $Y = 10^5$  Pa and  $e_r = 0.2$  instead of  $Y = 10^8$  Pa and  $e_r = 0.3$ , respectively, in both cases reflecting the more deformable and dissipative nature of our fluffy particles and that our particles collide with higher speeds on the order of  $1 \text{ m s}^{-1}$  instead of  $0.1 \text{ m s}^{-1}$ , compare Brilliantov et al. (1996). For the calculation of the cohesion, we use the Derjaguin-Muller-Toporov model (DMT) (Muller et al. 1983), where the cohesive force is given by  $F_c = -2\pi R^* \omega$ , with the effective radius  $R^* = (R_1^{-1} + R_2^{-1})^{-1}$  of two contacting particles with radii  $R_1$  and  $R_2$  and the surface energy density  $\omega$ . We take, in our notation,  $\omega = 0.028 \text{ J m}^{-2}$  determined by pull-off force measurements of micron-sized silica spheres by Heim et al. (1999). Deviations from this reference set of parameters, for example, when discussing the influence of these parameters, are mentioned separately.

The incoming particles are likely to have a velocity  $v_{\text{ins}}$  on the order but somewhat slower than the orbital velocity, because much faster particles are not bound by 67P’s gravity and therefore less likely contribute to our steady model particle stream, and much slower ones have a too short trajectory length to be compatible with an emission in a well separated source region, such as the southern hemisphere in the frame of the seasonal global mass transfer discussed by Keller et al. (2017). We do not regard slow particles mobilized by impacting other particles as a driver of the wind tail and moat formation but already as a secondary effect that we aim to self-consistently reproduce with our model. For a rough estimate of  $v_{\text{ins}}$ , we neglect the complex dust dynamics near the comet and instead assume the particles to be solely governed by the gravity of a spherical body with the

same mass ( $9.982 \times 10^{12} \text{ kg}$ ) and bulk density ( $538 \text{ kg m}^{-3}$ , both Preusker et al. 2017) as 67P. Such a body has an equivalent radius of  $R = 1640 \text{ m}$  and a surface acceleration of  $g = 2.4 \times 10^{-4} \text{ m s}^{-2}$  (neglecting the centrifugal force due to the rotation of the comet), which gives a speed of  $v_r = \sqrt{g \cdot R} = 0.65 \text{ m s}^{-1}$  for a circular orbit close to the surface. Therefore the speed of the wind particles is set to a somewhat lower value of  $v_{\text{ins}} = 0.5 \text{ m s}^{-1}$ , where the exact choice is not so important for the simulation. In our simulations, we use a typical surface acceleration of  $1.8 \times 10^{-4} \text{ m s}^{-2}$  calculated as the median over all facets of the 67P shape model (Preusker et al. 2017) taking into account the centrifugal force. Regarding the flux density of the incoming particles, we need to set a model value that, on the one hand, exceeds a certain lower limit in order to see erosional and depositional effects at all within a reasonable simulation time, and, on the other hand, should not be too large to avoid excessive shielding of the incoming particles by the developing atmosphere. We use a value of  $f_{\text{ins}} = 2.5 \times 10^{-3} \text{ kg m}^{-2} \text{ s}^{-1}$  (measured perpendicular to the surface normal), which was found to cause atmospheric collisions for less than 5% of the incoming particles. The actual value on 67P will be estimated later and is much smaller than that, but as long as the stated conditions are met, the effect on the morphologic development should be sufficiently linear to scale the elapsed simulation time with regard to the incoming flux density.

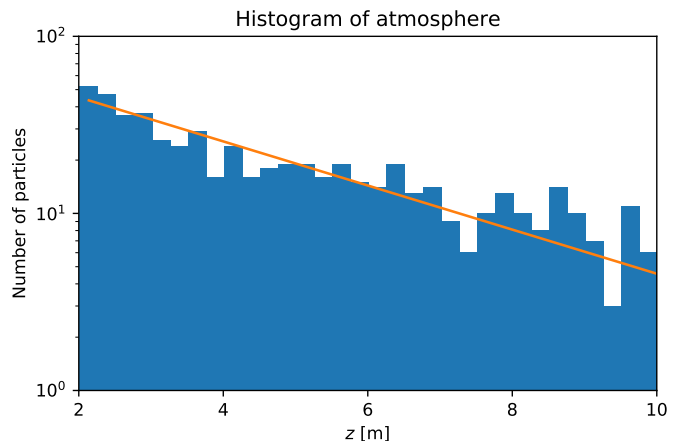
## 4. Results and discussion

In this section, we report the outcomes of our simulations for the wind tail scenario and the changes when modifying the setup or varying the parameters. We obtain a slowly rising particle equilibrium surface resulting from the local balance between erosion

by impacting fast particles and deposition of mobilized slow particles. This re-distribution of surface material is the key difference to the simpler model of Mottola et al. (2015), which only includes erosion from the initial impact but not the deposition of created ejecta. In our model the obstacle partly shields the area behind it from erosion, which results in the formation of a “wind tail”, where deposition predominates erosion. In front of the obstacle, additional erosion by incoming particles reflected at the obstacle can yield a moat. This depends on the shape of the obstacle, the flat front face of a cube being more effective in eroding a localized area than the rounded shapes of cylinders or spheres that distribute the reflected particles into many directions. Particle sizes, interparticle forces as well as velocity and inclination of the incoming particles affect the morphology of these surface features, which enables us to constrain some of these parameters by comparing simulation results to observations.

**Avoiding boundary effects.** First we start without periodicity in the horizontal dimensions. The simulation domain is arranged so that the obstacle is roughly in the center. The incoming particle stream is inserted starting from just above the highest point of the obstacle (to minimize interferences with the developing atmosphere), and such that it covers the entire particle bed (also after parts of it have been eroded). The insertion height has to account for the inclination of the incoming particle stream, that is a sufficient horizontal extent of the source region or a corresponding lateral shift with respect to the particle bed counteracting the offset between the positions of the particle insertion and the particle interaction with the surface. We choose an orientation where the stream is coming from the left (with respect to the representation of the simulations in the figures). However, we found this setup to lead to boundary effects: the erosion of the particle bed is most pronounced at its leftmost part. Furthermore, particles approaching the other three horizontal sides are affected as well when either they can leave the domain (and are deleted) or when a (high or low) wall keeps them from leaving. One option to avoid such boundary effects in a given region around the obstacle would be to use a simulation domain with boundaries horizontally farther away from the obstacle, but this is numerically inefficient, and after a certain elapsed time, the boundary effects will have reached this region even then. We choose another option where particles leaving the domain on one side are re-introduced in the domain from exactly the opposite side with the same velocity vector. In other words, we use a periodic geometry in the horizontal dimensions. In this case, the particle stream is injected from a region that horizontally extends exactly over the particle bed, and there is no need to shift this source region to the left because of the inclination as described above. Consequently, the simulation setup is equivalent to a domain with infinite horizontal extent and infinitely many periodically placed obstacles, with a horizontally infinitely extended source region of the particle stream. This way, no boundary effects can develop, but we have to ensure that the vertical boundaries of the basic domain are reasonably far away from the basic obstacle such that the distances between obstacles in the periodic geometry suffice to keep interferences between them low. This setup has the side effect that the number of particles in the basic domain continually increases, raising the level of the particle bed and slowing down the simulation with time. The flux density of the incoming particles is constant throughout the simulation.

**Formation of dust atmosphere.** An interesting effect we could observe is the formation of an atmosphere-like particle



**Fig. 7.** Histogram of the atmosphere above the particle bed populated by about 500 particles. The orange line is a fit with an exponential function,  $p(z) \sim \exp(-z/h)$ , where the scale height  $h$  is about 3 m.

assembly above the surface. We use the term “atmosphere” for it, because of the obvious analogy to the usual gas molecule atmosphere. This granular atmosphere is caused by particles originating from the surface that have been mobilized by the impinging particle stream. Here we exclude the incoming particle stream itself (the “wind”) that has a different dynamical character as well as the static or nearly static surface particles.

At any given time only a few wind particles are on their incoming ballistic trajectories before impacting the surface or colliding with atmospheric particles. Once they hit the surface, they typically cause one or more surface particles to be ejected, mostly at slower speed than that of the wind stream, but this depends on the collision geometry, relative particle sizes, and interparticle forces. The ejected particles and the deflected injected ones become new members of the atmosphere and move on ballistic curves until they collide with other particles, either on the surface, thereby possibly mobilizing further surface particles, or in the atmosphere. The slowest particles settle and are finally deposited on the surface, thereby leaving the atmosphere and raising the surface level. This way, energy and momentum of the wind are not only dissipated into the surface layer but are also distributed into the atmosphere, into translational and rotational degrees of freedom. Until a stationary equilibrium is achieved, the density of the atmosphere increases with time.

The atmosphere exhibits a slight drift in the direction of the wind, but at sub-injection speed ( $\sim 10\text{--}20\%$  of  $v_{\text{ins}}$ ), as can be seen from the average velocity vector of the atmospheric particles. Also, the density of the atmosphere decreases with increasing altitude, which can be seen from a corresponding particle number histogram (Fig. 7). Typically, the yield for the given impact conditions is about 1, which means that each incoming injected particle mobilizes about 1 surface particle. Most ejected particles reach a maximum height below 10 m, but some outliers can be found at altitudes of over 100 m. Depending on the model parameters, the atmospheric scale height is on the order of 1–10 m, which means that this atmosphere may be contributing to the near-nucleus dust coma. The average lifetime of the atmospheric particles is several minutes. This is much shorter than the time scale of the morphologic changes of the bedforms, which can be estimated from images of the OSIRIS camera aboard Rosetta to occur within the order of days to months (El-Maarry et al. 2017). As the real world particle flux is probably below our lower simulation limit, the real world “particle

**Table 1.** Overview of the performed simulations and their results with regard to the extend of moat and wind tail.

Simulation	Varied parameter	Moat	Wind tail
Reference case	–	Yes	Yes
Higher Young’s modulus	$Y = 10^6$ Pa	Slightly wider	Unchanged
Low friction	$\mu = 0.1, \mu_r = 0.1, \eta_r = 0.1$	Wider	Smaller
High friction	$\mu = 2.0, \mu_r = 2.0, \eta_r = 2.0$	Wider	Smaller
Higher tensile strength	$R = 3 \dots 6$ mm	Smaller	Smaller
Larger wind particles	$R_{\text{wind}} = 6 \dots 12$ cm	Irregular	Irregular
Spherical obstacle	–	Much smaller	Much smaller
Erosion case	–	Smaller	Much Smaller

**Notes.** Parameter variations are given with respect to the reference case: rotated cuboid boulder, particles with radii  $R = 3 \dots 6$  cm, Young’s modulus  $Y = 10^5$  Pa, restitution coefficient  $e_r = 0.2$ , triplet of friction coefficients  $\mu/\mu_r/\eta_r$  of 1.0/1.0/1.0, cohesive energy density  $\omega = 0.028$  J m<sup>-2</sup>, insertion speed of particle wind  $v_{\text{ins}} = 0.5$  m s<sup>-1</sup>.

atmosphere” above a dusty area is less dense with accordingly fewer collisions in the atmosphere. An identification of such a particle atmosphere with Rosetta instruments is therefore unlikely.

Impact-generated dust atmospheres are a well known and studied (Krivov et al. 2003; Sremčević et al. 2003; Sachse et al. 2015) phenomenon that have been observed to surround the Galilean moons Europa (Krüger et al. 2003), Ganymede (Krüger et al. 1999), and Callisto (Krüger et al. 2003) as well as Earth’s Moon (Horányi et al. 2015). The difference between the dust atmosphere reported here and these cases is the impactor size and speed. For the large moons, the impactors are smaller ( $\sim 1\text{--}10$   $\mu\text{m}$ ) but faster ( $\sim 10$  km s<sup>-1</sup>) interplanetary dust particles that yield a lot more ejecta upon impact.

*Formation of moat and wind tail.* In our simulations we were able to reproduce the formation of moats and wind tails for a wide range of model parameters as summarized in Table 1. The shapes and dimensions of these features, however, depend on the shape of the obstacle and the properties of the particles, which will be discussed in more detail below.

In front of the obstacle, we observe the formation of a moat. As viewed from above, the moat’s shape follows the contour of the obstacle, and its width (in  $x$ -direction) is typically larger than its depth, both being on the order of 0.1 m. Behind the boulder, we observe the formation of a wind tail-shaped elevation. The highest point of this elevation is located directly adjacent to the boulder and decreases with distance from it. The wind tail can reach a height that is nearly identical to the height of the obstacle. Additionally, we sometimes also observe a smaller deposition in front of the boulder.

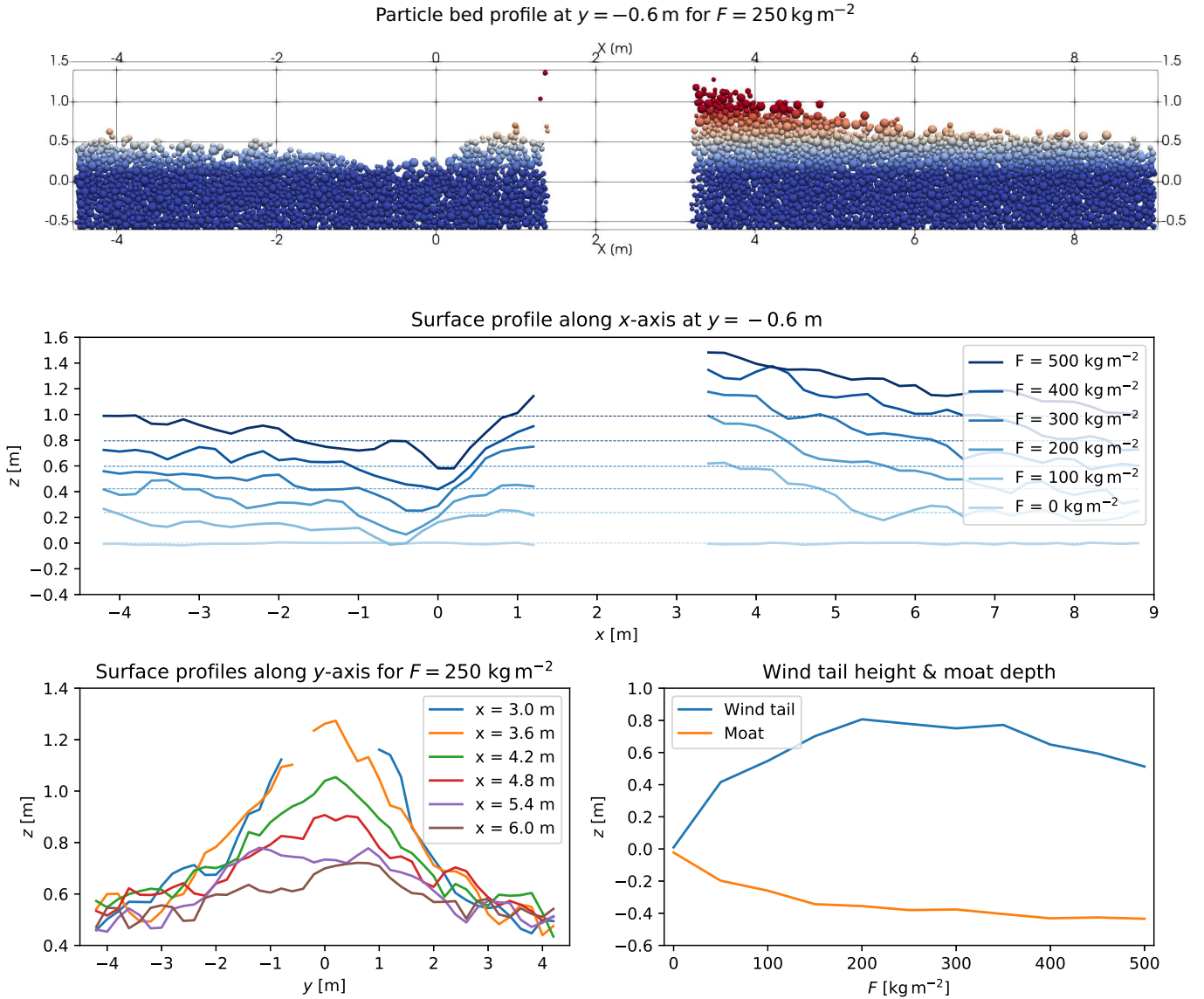
For our reference case with the parameter set given in Sect. 3.2, the evolution of the surface is shown in Fig. 8 after removal of particles from the granular atmosphere, that is when their velocities exceed a certain threshold (0.01 m s<sup>-1</sup>). Surface profiles along the  $x$ - (Fig. 8, middle panel) and  $y$ -axis (bottom left panel) have been obtained from superimposing the granular surface with a grid and providing a statistically robust measure to determine the surface level at the grid’s sampling points: We divided the surface into overlapping quadratic patches at intervals of 0.2 m in  $x$ - and  $y$ -direction with sizes of  $0.4 \text{ m} \times 0.4 \text{ m}$ . For each patch, we removed free particles not in direct contact with those lying underneath, and defined the surface level as the scaled 0.98-quantile ( $z_\alpha = \frac{Q_\alpha - z_{\text{min}}}{\alpha} + z_{\text{min}}$  with  $\alpha = 0.98$  and  $Q_\alpha$  the  $\alpha$ -quantile) of the  $z$ -coordinates of the remaining particles. This procedure assumes a nearly constant particle number density with  $z$  in the particle bed and was found to provide a

similar surface level as one would obtain by visually estimating this elevation from cuts of 3D representations of the particle bed (Fig. 8, top panel). To obtain the time evolution of the surface, we performed this analysis for several stages after starting the introduction of the particle wind. Here, the (unscaled) time coordinate was converted into an integrated areal dust flux density  $F$  (mass per square meter) describing the total dust mass per square meter that has been inserted into the simulation domain. Neglecting the comparatively few particles in the atmosphere, this corresponds to the spatially averaged mass per square meter deposited on the surface up to that point in time. For each of the considered stages, we determined the minimum elevation of all profiles in front of the obstacle and the maximum elevation behind the obstacle and subtracted a reference surface level (determined as the scaled 0.98-quantile of the outer part of the simulation domain that is less affected by the obstacle) to obtain the relative height of the wind tail and the relative depth of the moat (bottom right panel). We note that in the simulations there is also a small increase (by about 20%) in the bulk density of the upper surface layer (few particle radii) after the introduction of the particle wind, which results from a compaction of the near-surface material by the impacting particles and the resulting perturbation waves. This effect is most likely enhanced in the simulation due to the large size of our particles.

The wind tail is formed by the indirect flux of ejected particles moving surface material into the shielded region behind the boulder rather than due to the erosion of the surrounding area. This is illustrated in Fig. 8, middle panel, where it can be seen that the surface level behind the boulder continually rises everywhere with time. The smaller deposition in front of the boulder possibly results from slow ejected particles getting stopped at and falling down from the boulder’s front face or particles getting “trapped” in the edge when impacting close to the foot of the boulder.

*Minimum flux for moat formation.* Wind tail and moat develop quickly directly after the onset of the particle wind, and both reach about 50% of their maximum height or depth with respect to the corresponding reference surface level after the insertion of a total of about  $50 \text{ kg m}^{-2}$  of dust. From there onward, their growth continues up to an inserted total dust mass of about  $250 \text{ kg m}^{-2}$ . At this point the top of the wind tail has almost reached the upper edge of the boulder, and further growth of the wind tail is prevented by the ongoing rise of the reference surface level. Across all simulations, the lower limit to the integrated areal dust flux density required for the formation of a moat is on the order of  $10 \text{ kg m}^{-2}$ .





**Fig. 8.** Surface profiles of the reference case (Figs. 9a and 10a). *Top panel:* cut along the  $x$ -axis at  $y = -0.6$  m (because of the asymmetry from rotating the cubic obstacle) of a 3D representation of the particle bed after the insertion of  $F = 250$  kg m<sup>-2</sup> of dust. *Middle panel:* evolution of the surface profile along the  $x$ -axis at  $y = -0.6$  m for the reference case and up to a total inserted areal dust mass density of  $F = 500$  kg m<sup>-2</sup>. The dashed lines are the reference surface levels determined from the less affected outer part of the simulation domain. The obstacle is in the center of the profiles (missing data). *Bottom left panel:* surface profiles of the wind tail along the  $y$ -axis at various distances from the boulder for the case  $F = 250$  kg m<sup>-2</sup>. *Bottom right panel:* time evolution of the relative (i.e., with the reference level at this time step subtracted) height of the wind tail (blue solid line) and of the relative depth of the moat (orange solid line). Compare middle and bottom left panels to Fig. 5.

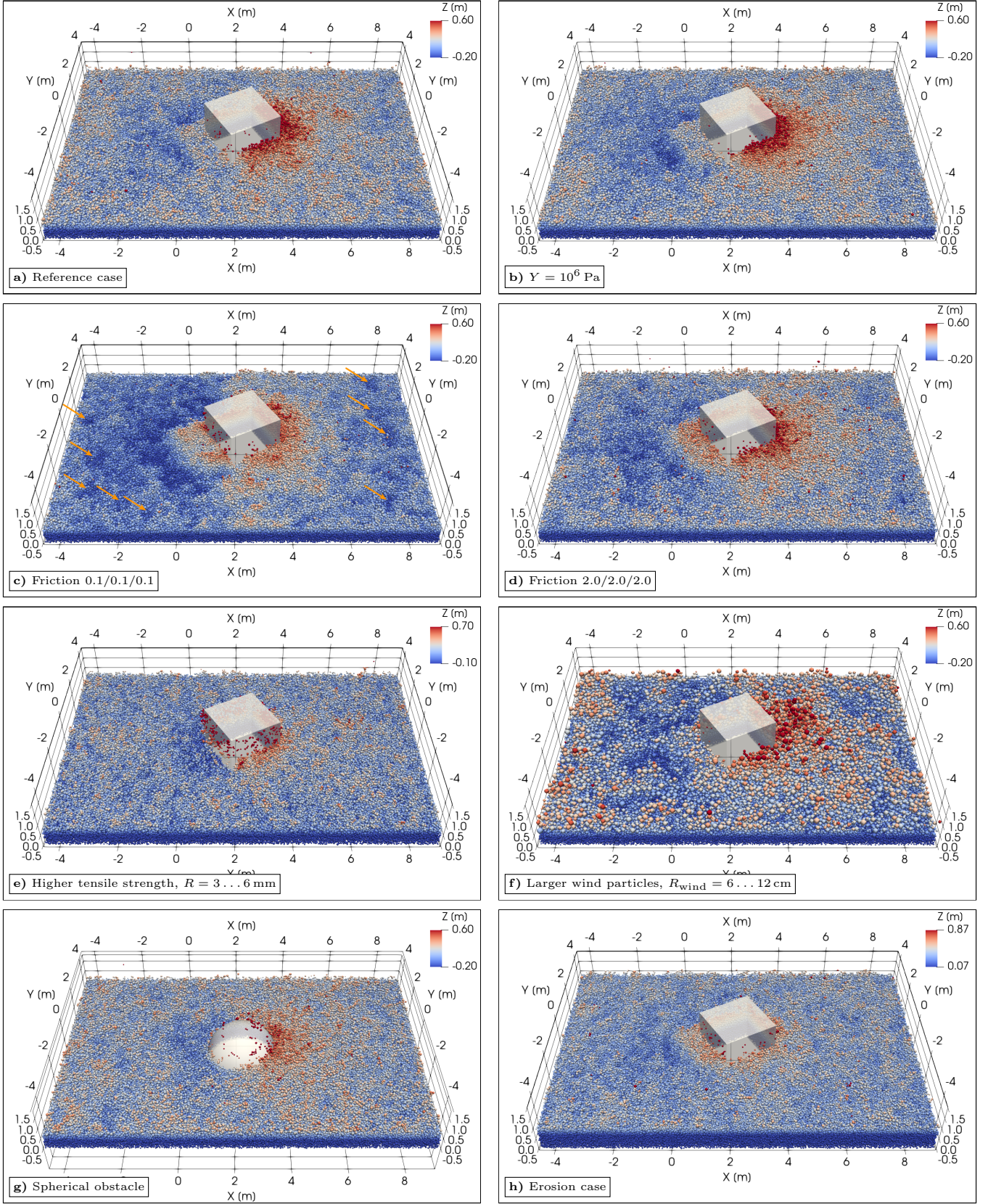
Assuming morphologic changes of dust beds on the cometary surface typically to occur within the order of days to months, an inserted dust mass of  $250$  kg m<sup>-2</sup> translates to a real world flux density on the order of  $10^{-6}$ – $10^{-5}$  kg m<sup>-2</sup> s<sup>-1</sup>. For a typical wind speed on the order of  $0.1$ – $1$  m s<sup>-1</sup>, the density of the wind near the surface of the nucleus can be estimated to be on the order of  $10^{-6}$ – $10^{-4}$  kg m<sup>-3</sup>. Comparing this to the particle insertion flux density of  $f_{\text{ins}} = 2.5 \times 10^{-3}$  kg m<sup>-2</sup> s<sup>-1</sup> used in our simulations, the calculations have therefore been accelerated by a factor of  $10$ – $100$  with respect to the real world elapsed time, which has proven to be necessary to perform the simulations within reasonable CPU time.

The total amount of fall back material onto the comet surface for the two years duration of the Rosetta mission has been estimated to range between  $1.9$ – $4.5 \times 10^{10}$  kg (Pätzold et al.

2019). With a comet surface area of  $46.9$  km<sup>2</sup> (Jorda et al. 2016) this results in a global average of  $6.4$ – $15.2 \times 10^{-6}$  kg m<sup>-2</sup> s<sup>-1</sup> comparable to the flux density estimated from our simulation.

In the following, we report and discuss the influence of various model parameters on the formation of aeolian-like features including the shape of the obstacle and the mechanical and physical properties of our particles. Figures 9 and 10 show the simulation outcome after the insertion of a particle wind with an integrated flux density of  $100$  and  $250$  kg m<sup>-2</sup>, respectively. During that time the number of particles in the simulation domain has increased from initially  $140\,000$  to about  $190\,000$  and  $260\,000$ , raising the equilibrium surface level from  $z = 0$  to about  $0.2$  m and  $0.5$  m, respectively. The top left panel shows our reference case, the other panels show cases where one of the model parameters has been changed with respect to the reference





**Fig. 9.** Simulated moats and wind tails around a boulder on the surface of comet 67P, for various sets of model parameters. Each panel shows the situation after the insertion of a particle wind with an integrated areal flux density of  $100 \text{ kg m}^{-2}$ . (a) Reference case: rotated cuboid boulder, particles with radii  $R = 3 \dots 6$  cm, Young's modulus  $Y = 10^5$  Pa, restitution coefficient  $e_r = 0.2$ , triplet of friction coefficients  $\mu/\mu_r/\eta_r$  of 1.0/1.0/1.0, cohesive energy density  $\omega = 0.028 \text{ J m}^{-2}$ , insertion speed of particle wind  $v_{\text{ins}} = 0.5 \text{ m s}^{-1}$ . (b–h) Cases, where one of the model parameters (given in the label of the subfigure) has been changed with respect to the reference case. Graphical representation as in Fig. 6. Orange arrows indicate additional local depressions in the low friction case.



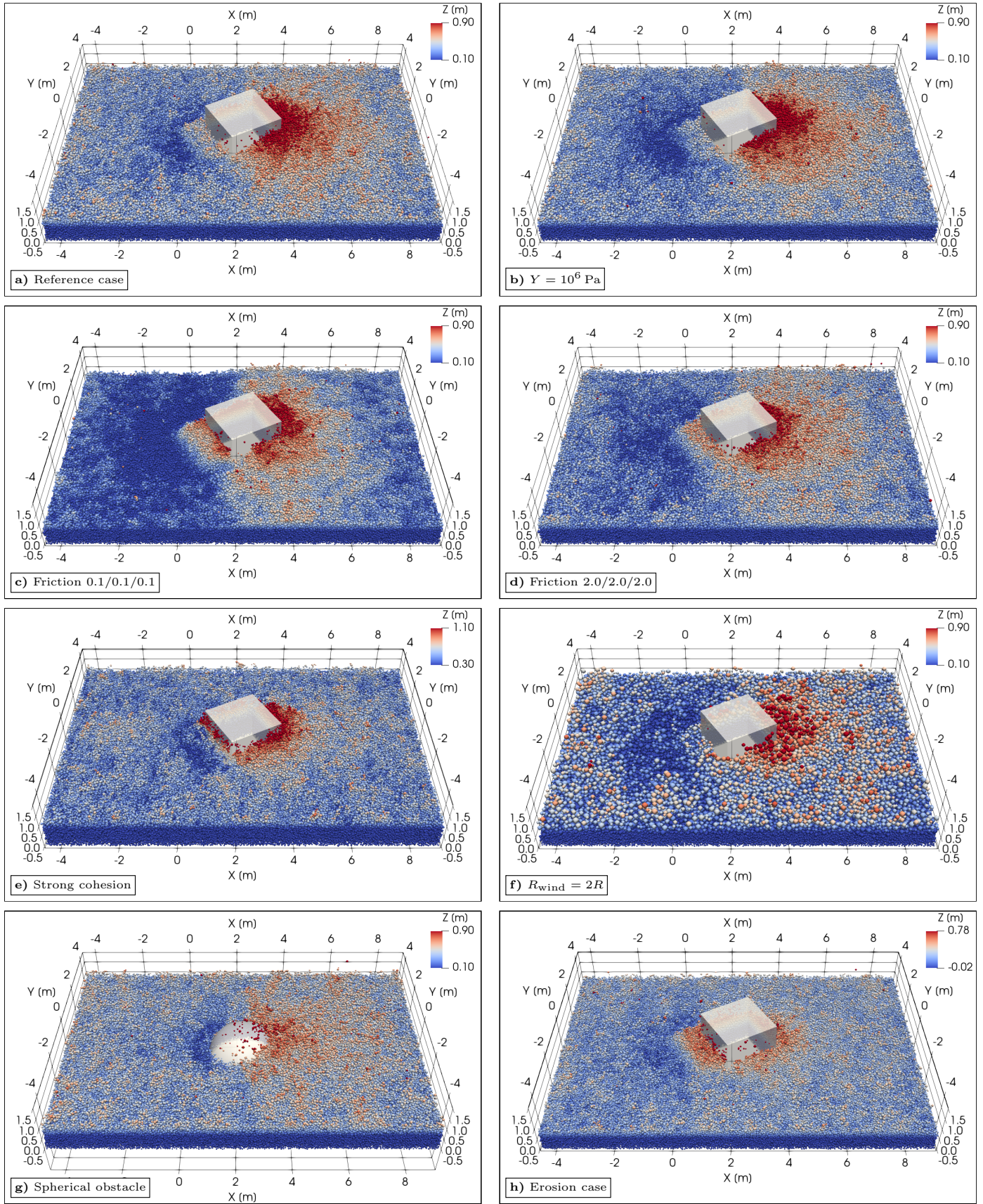


Fig. 10. Same as Fig. 9, but after the insertion of a particle wind with an integrated areal flux density of  $250 \text{ kg m}^{-2}$ .



case. Each of these simulations was carried out using parallel processing on a modern Intel Broadwell-type Xeon workstation taking 5000–10000 CPU-core hours of processing time per case.

**Young's modulus.** An increase of Young's modulus by one order of magnitude with respect to our reference case ( $Y = 10^5$  Pa) leads to an overall very similar morphology of the moat and the wind tail (Figs. 9b and 10b), with the largest difference being a wider and slightly deeper moat. This shows that although we can only assume our fluffy aggregates to likely have a relatively low Young's modulus and do not know the exact value of this parameter, our choice has only a limited impact on our results.

**Friction.** The effect of particle friction was investigated using three test cases with distinct levels of friction: the reference case with medium friction (triplet of friction coefficients – sliding friction  $\mu$ /rolling friction  $\mu_r$ /viscous damping  $\eta_r$  – of 1.0/1.0/1.0, Figs. 9a and 10a), one case with lower (coefficients 0.1/0.1/0.1, Figs. 9c and 10c) and another one with higher friction (coefficients 2.0/2.0/2.0, Figs. 9d and 10d), respectively. The reference case shows a clearly defined, relatively narrow (in  $x$ -direction) moat and a large wind tail.

For low friction, the moat is deeper and wider, and it does not have a clearly defined outer edge. The surface is more irregular than in the other cases and there are additional local depressions besides the moat. In total, a noticeably larger amount of surface material has been mobilized, which is due to the low-friction particles being easier to mobilize and harder to stop as they dissipate less kinetic energy when in contact with other grains. For high friction, the moat has a similar depth but larger width compared to the reference case.

In both the low- and high-friction case, the wind tail is somewhat smaller than in the reference case, because low-friction particles are also harder to demobilize and typically form lower wider piles of material and possibly because high-friction particles carry away other particles from the pile. The mobilization of a larger amount of surface material in the low- and high-friction cases is also reflected in the density of the atmosphere, which is about 2–3 times more densely populated compared to the reference case. In this way, the reference case constitutes or is close to a local extremum, leading to the highest wind tails and least dense atmospheres.

**Cohesion.** In general, stronger cohesion more likely keeps surface particles from being ejected by impinging particles. For a quantitative analysis of the effect of cohesion, we consider the tensile strength of the bulk material, which depends on the particle sizes and configuration as well as the cohesive energy density  $\omega$ , see discussion in Kappel et al. (2020). Assemblies of larger spherical particles are less stable, because the tensile strength of the material scales inversely with particle size ( $\propto R^{-1}$ ). The number of contacts between two particle layers scales with  $R^{-2}$ , while in the DMT model the cohesive force of a single contact scales with  $R$ . This means that increasing the cohesive energy density  $\omega$  or decreasing the particle size  $R$  by one order of magnitude increases the tensile strength of the bulk material by a factor of ten.

The tensile strength of the bulk material can also be estimated by a numerical tensile strength test (Kappel et al. 2020). For the reference particle sizes used in our simulations (radii of 3–6 cm) and the reference surface energy density of  $\omega = 0.028 \text{ J m}^{-2}$ , the tensile strength is on the order of 0.1 Pa. An

increase of the tensile strength by one order of magnitude (Figs. 9e and 10e), that is by decreasing the particle size by a factor of ten and applying coarse-graining by the same factor, significantly reduced the extend of the moat and the wind tail. In comparison to the tensile strength required for the stability of overhanging cliffs on 67P on the order of 1–10 Pa (Attree et al. 2018; Groussin et al. 2015), the tensile strength of our material is roughly one order of magnitude smaller, which is plausible considering our material consists of air fall particles, while cliffs are composed of more consolidated material.

**Wind particle size.** Keeping the particle sizes in the initial particle bed unchanged, the surface erosion increases with increasing incoming particle sizes. When the impinging particles are significantly larger than the particles in the bed, small crater-like features or distinct streaks can be formed in addition to the general erosion, and the surface can become uneven (Figs. 9f and 10f). On the other hand, incoming particles significantly smaller than particles in the bed will cause no erosion at all, because they are not able to eject any surface particles and are just scattered by the surface or even caught by it, depending on cohesion and friction. After settling they raise the average surface level.

67P surface observations of a moat in front of an obstacle and a wind tail behind it in the absence of craters or an uneven morphology indicate that the sizes of the incoming particles are in the same order as those of the surface particles. This suggests that the particles in the bed may originate from the same incoming particle stream in the first place. A change in the sizes of the incoming particles could be related to a change in the emission mode or place.

**Shape of obstacle.** From the slope and extent of the wind tail-like feature one can purely geometrically infer the local inclination of the incoming particle stream assuming the stream direction and wind tail slope are the same (as has been done in the Mottola et al. 2015 model). The length of the wind tail allows an estimate of the inclination by simple triangulation when knowing the height of the obstacle with respect to the local reference level. However, the slope is also sensitive to interparticle forces like cohesion and rolling friction, as it is related to the (static) angle-of-repose of the material.

While a wind tail was visible in all our simulations, the existence of a moat depends on the shape of the obstacle. An obstacle with the shape of a half-sphere (like a dome) distributes the incoming particles into many directions, which makes it more difficult for a moat to be formed (Figs. 9g and 10g). To a lesser extent the same applies to an upright cylinder. Choosing a cube with one side (called the “front face”) facing the incoming particle stream, the particles impinging on this face are simply reflected into the particle bed and not laterally distributed. This additional erosion in front of the boulder can lead to a more effective moat formation. Also, when the cube is rotated around its vertical axis, moats can be formed not (only) in front of the boulder but also along the boulder walls. Therefore we suggest that aeolian-like features also represent form and orientation of the front face of the obstacle.

**Velocity of incoming particle stream.** If the incoming particles have just 20% of the orbital velocity ( $0.1 \text{ m s}^{-1}$ ), the surface erosion is minimal and the particles are rather just deposited near their first point of contact with the surface. At the front face of the obstacle they are reflected leading to additional deposition in front of the obstacle. Furthermore, they cannot reach the region behind it, leading to less deposition there. Consequently,

an inverted moat-wind tail morphology can develop, with the moat behind the obstacle and the wind tail-like feature in front. However, the depositional feature is broader than the obstacle in contrast to the not-inverted case. The observed features on the 67P surface indicate the not-inverted case to be the usual one on the nucleus, corroborating the argument about the orbital velocity of the incoming particle stream.

Changing the individual insertion velocities by small random terms (direction and velocity) does not change our results. A change of inclination of the particle stream causes the wind tail to adapt to the according geometry.

**Erosion case.** In the simulation cases discussed so far, the steady insertion of particles led to a slowly but continually rising reference surface, which would eventually completely bury the boulder and obliterate the surface features associated with it. We recall that this is not an unphysical but an actually observed effect that results from the transfer of material from one side of the nucleus to another, here modeled by the particle wind and the assumption that our simulation domain is part of an infinitely extended plane composed of many such domains modeled by the use of periodic boundary conditions. The “opposite” case is the assumption that our simulation domain is in some way, for example, by long distances, being on a plateau, or shielded by cliffs, isolated from a larger particle bed. We performed such a simulation and modeled the absence of the ejecta flux from neighboring cells by keeping the periodic geometry but removing all ejecta whose ejection range exceeded half the basic simulation dimension in  $x$ - or  $y$ -direction. This way we still avoid the strong boundary effects in absence of periodic boundary conditions and are able to simulate a net erosion of the particle bed, a situation that has been actually observed on the nucleus surface (Hu et al. 2017).

In the erosion case (Figs. 9h and 10h), the perpetual removal of far-reaching ejecta leads to a very slowly decreasing reference surface level, which would eventually excavate the initially buried base of the boulder. Despite the different evolution of the surface level, it is still possible to form a moat. The wind tail, however, is less developed, and its formation process is different from that of the deposition case. In the erosion case, the wind tail mostly results from the erosion of the area not shielded by the boulder as the indirect flux of slow ejecta is smaller. The extent of the wind tail is noticeably smaller (about half in every dimension) and, in particular, it is lower than the deposition in front of the obstacle, creating the impression of an inverted moat-wind tail morphology. The timescale for the formation of the wind tail is about the same in the erosion case (Fig. 11), but this depends on the ejecta speed distribution, which determines the fraction of particles launched beyond the domain boundaries that are lost. As a result, the observed extended wind tails on the 67P surface are less compatible with the erosion case and indicate the depositional case to be the usual one on the nucleus.

## 5. Conclusions and outlook

In this work, we have applied the DEM to perform numerical simulations of dynamical surface processes on comet 67P in order to investigate local transport processes and mechanical properties of the surface material. We modeled air fall particles as polydisperse spheres consisting of a mixture of dust and water ice and took into account the ambient surface acceleration, the Hertz contact model, translational and rolling friction, and cohesion. To enable the modeling of large scenarios with

realistically small constituent particles, we employed the coarse-graining technique. Recently, we applied the DEM method to investigate morphologies of boulders and cliffs on 67P (Kappel et al. 2020). Now we applied our model to study the formation of moat- and wind tail-like features around exposed boulders in a particle bed as observed for instance by Mottola et al. (2015).

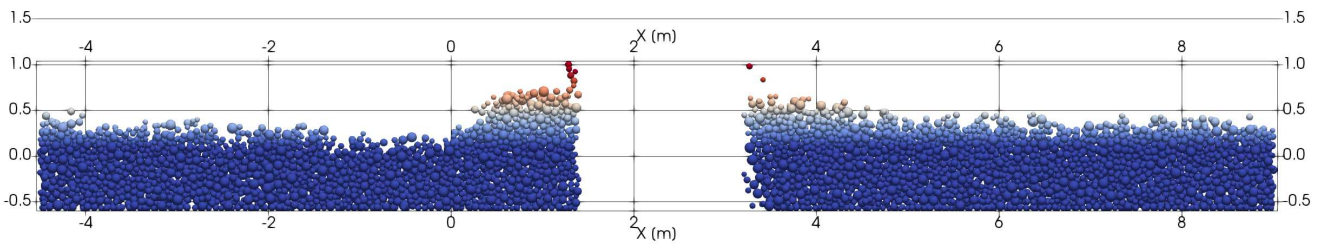
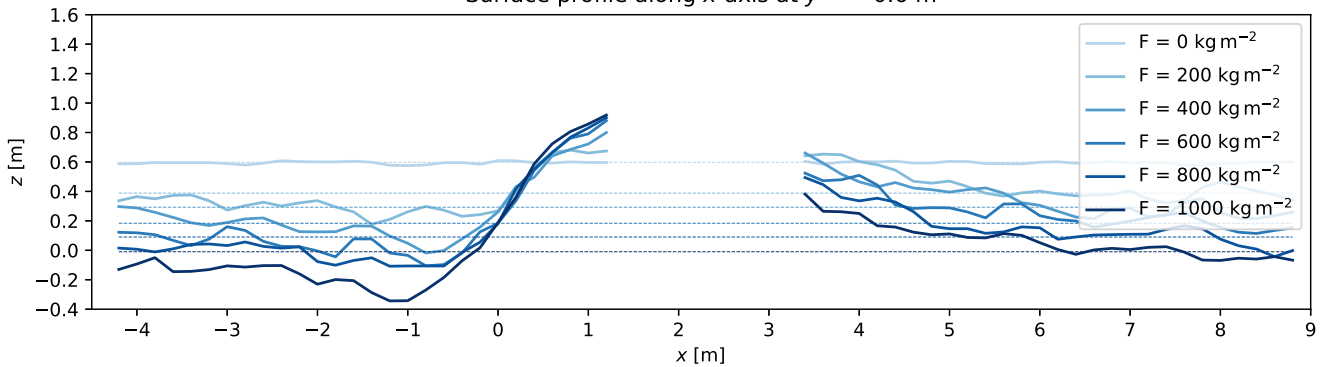
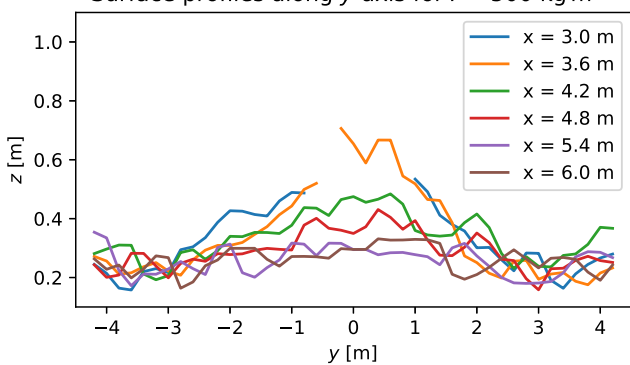
With our DEM model, we constructed a rectangular cometary particle bed with a boulder in its center and an oblique particle wind coming from above the obstacle. We investigated two limiting cases – a deposition case, where we assumed that our simulation domain is part of an infinitely extended plane composed of many such domains and modeled the indirect flux from the neighboring domain using periodic boundary conditions; and an erosion case, where we instead assumed that our simulation domain constitutes a somewhat isolated part on the nucleus and removed all ejecta whose ejection range exceeded half the basic horizontal domain dimensions. The differences to the simpler cell-based model of Mottola et al. (2015), which only considers erosion, are the re-distribution of mobilized surface particles and physical or geometric effects like friction, cohesion, rotation, compression waves, and porosity.

In the deposition case, where no particles are lost, it can be seen that, despite a slowly but continually rising surface level, the formation of the wind tail occurs entirely due to the indirect flux of ejected particles moving surface material into the region behind the boulder shielded from the particle stream rather than due to the erosion of the surrounding area suggested by Mottola et al. (2015). Here, the moat and wind tail reached their maximum depth or height after being exposed to an integrated areal dust flux density of about  $250 \text{ kg m}^{-2}$ . Based on the timescale of morphological changes on the surface of comet 67P inferred from Rosetta images, the density of the wind near the surface was estimated to be on the order of  $10^{-6}$ – $10^{-4} \text{ kg m}^{-3}$ .

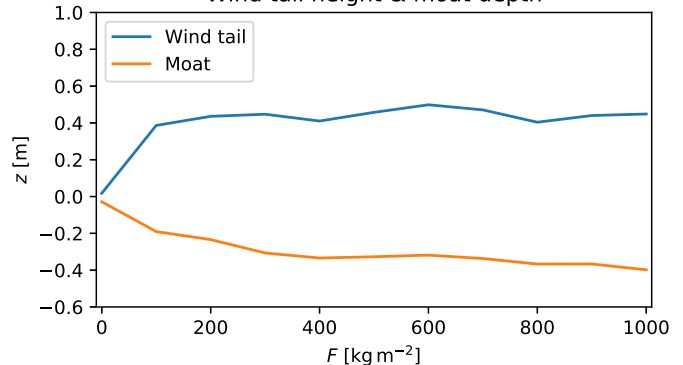
In the erosion case, we also observed the formation of a wind tail and a moat. However, the process generating the wind tail is different: it mostly forms as a result of shielding of the pre-existing particle bed from the particle stream as the flux of ejecta accumulating in the region behind the boulder is smaller. The moat develops as a result of increased erosion as observed in the deposition case. This scenario is comparable to the model by Mottola et al. (2015).

In our simulations, we were able to reproduce the formation of a moat and wind tail for a wide range of model parameters. However, a clearly defined, relatively narrow moat and an extended wind tail as typically observed on 67P was obtained only for a medium level of particle friction in the depositional case. Both lower and higher friction levels resulted in moats with less defined edges. The erosional case led to much smaller wind tails creating the impression of an inverted moat-wind tail morphology that is less compatible with observations. Reasonable changes to Young’s modulus within the range of  $10^5 \text{ Pa}$  to  $10^6 \text{ Pa}$  impacted the morphology of the moat or the wind tail only to a small degree. However, the extend of the moat and the wind tail was significantly reduced when the tensile strength of the material, given by the material’s constituent sizes, internal structures and/or cohesive energy density, was increased from  $0.1 \text{ Pa}$  to  $1 \text{ Pa}$ . A cube was the most effective shape for the formation of a moat, while obstacles with rounder shapes, a cylinder and, in particular, a half-sphere (like a dome), distributed the incoming particles into many directions, which made it more difficult for a moat to form. Therefore, for future analyses of the particle stream and bed conditions based on wind tail and moat morphology, we suggest, in cases where discernible from the imaging data, to also include form and orientation of the front face of the



Particle bed profile at  $y = -0.6$  m for  $F = 250$  kg m $^{-2}$ Surface profile along x-axis at  $y = -0.6$  mSurface profiles along y-axis for  $F = 500$  kg m $^{-2}$ 

Wind tail height &amp; moat depth



**Fig. 11.** Surface profiles of the erosion case (Figs. 9h and 10h). Representation as in Fig. 8, but up to a total inserted areal dust mass density of  $F = 1000$  kg m $^{-2}$ .

obstacle, in addition to obstacle height and moat and wind tail geometry. Particles responsible for the formation of these features likely originate from distant locations on the nucleus as impactors significantly slower than the orbital velocity failed to reproduce the observed morphologies.

Our simulations have shown that morphologic investigations of wind tails and moats can be used to constrain physical parameters of cometary material and air fall processes. This method can be adapted to future morphologic investigations of features on comets as well as in the laboratory and is the base for more advanced simulations.

As the next step (Kappel et al. 2018b,a), we plan to study further surface processes on comet 67P, for instance the formation of fracture polygons (possibly induced by thermal stress) that have been observed in many places where consolidated material is exposed on the nucleus surface (Auger et al. 2018). We also intend to include Monte-Carlo-based modeling of sublimation and recondensation of volatiles and Knudsen gas flow through the surface layer, which will provide us with a tool to investigate more complex scenarios such as triggers and early phases

of cometary outbursts as well as other volatile-related processes, on comet 67P and other small Solar System bodies.

*Acknowledgements.* We very much thank Laurent Jorda for providing the DTM of the Agilkia landing site. This work is part of the research project “The Physics of Volatile-Related Morphologies on Asteroids and Comets”. M.S., D.K., and K.O. would like to gratefully acknowledge the financial support and endorsement from the DLR Management Board Young Research Group Leader Program and the Executive Board Member for Space Research and Technology.

## References

- Ai, J., Chen, J.-F., Rotter, J. M., & Ooi, J. Y. 2011, *Powder Technol.*, 206, 269
- Attree, N., Groussin, O., Jorda, L., et al. 2018, *A&A*, 611, A33
- Auger, A.-T., Groussin, O., Jorda, L., et al. 2018, *Icarus*, 301, 173
- Biele, J., Ulamec, S., Maibaum, M., et al. 2015, *Science*, 349, aaa9816
- Bierwisch, C., Kraft, T., Riedel, H., & Moseler, M. 2009, *J. Mech. Phys. Solids*, 57, 10
- Brilliantov, N. V., Spahn, F., Hertzsch, J.-M., & Pöschel, T. 1996, *Phys. Rev. E*, 53, 5382
- Davidsson, B. J. R., Birch, S., Blake, G. A., et al. 2020, *Icarus*, 354, 114004
- El-Maarry, M. R., Groussin, O., Keller, H. U., et al. 2019, *Space Sci. Rev.*, 215, 36

- El-Maarry, M. R., Thomas, N., Giacomini, L., et al. 2015, *A&A*, **583**, A26
- El-Maarry, M. R., Groussin, O., Thomas, N., et al. 2017, *Science*, **355**, 1392
- Golombek, M. P., Crumpler, L. S., Grant, J. A., et al. 2006, *J. Geophys. Res. Planets*, **111**, E02S07
- Greeley, R., Kraft, M., Sullivan, R., et al. 1999, *J. Geophys. Res.*, **104**, 8573
- Greeley, R., Bridges, N. T., Kuzmin, R. O., & Laity, J. E. 2002, *J. Geophys. Res. Planets*, **107**, 5005
- Groussin, O., Jorda, L., Auger, A. T., et al. 2015, *A&A*, **583**, A32
- Heim, L.-O., Blum, J., Preuss, M., & Butt, H.-J. 1999, *Phys. Rev. Lett.*, **83**, 3328
- Hertz, H. 1882, *J. reine angewandte Mathematik*, **92**, 156
- Horányi, M., Szalay, J. R., Kempf, S., et al. 2015, *Nature*, **522**, 324
- Hu, X., Shi, X., Sierks, H., et al. 2017, *A&A*, **604**, A114
- Jorda, L., Gaskell, R., Capanna, C., et al. 2016, *Icarus*, **277**, 257
- Kappel, D., Otto, K., Oklay, N., et al. 2018a, *Eur. Planet. Sci. Cong.*, **12**, EPSC2018
- Kappel, D., Otto, K., Oklay-Vincent, N., et al. 2018b, in *Lunar and Planetary Inst. Technical Report*, **49**, *Lunar and Planetary Science Conference*, 2696
- Kappel, D., Sachse, M., Haack, D., & Otto, K. 2020, *A&A*, **641**, A19
- Keller, H. U., Barbieri, C., Lamy, P., et al. 2007, *Space Sci. Rev.*, **128**, 433
- Keller, H. U., Mottola, S., Hviid, S. F., et al. 2017, *MNRAS*, **469**, S357
- Kloss, C., Goniva, C., Hager, A., Amberger, S., & Pirker, S. 2012, *Prog. Comput. Fluid Dyn.*, **12**, 140
- Kramer, T., & Noack, M. 2015, *ApJ*, **813**, L33
- Krivov, A. V., Sremčević, M., Spahn, F., Dikarev, V. V., & Kholshchevnikov, K. V. 2003, *Planet. Space Sci.*, **51**, 251
- Krüger, H., Krivov, A. V., Hamilton, D. P., & Grün, E. 1999, *Nature*, **399**, 558
- Krüger, H., Krivov, A. V., Sremčević, M., & Grün, E. 2003, *Icarus*, **164**, 170
- Lai, I.-L., Ip, W.-H., Su, C.-C., et al. 2016, *MNRAS*, **462**, S533
- Mannel, T., Bentley, M. S., Boakes, P. D., et al. 2019, *A&A*, **630**, A26
- Mottola, S., Arnold, G., Grothues, H.-G., et al. 2007, *Space Sci. Rev.*, **128**, 241
- Mottola, S., Arnold, G., Grothues, H. G., et al. 2015, *Science*, **349**, 2.232
- Muller, V., Derjaguin, B., & Toporov, Y. 1983, *Colloids Surf.*, **7**, 251
- Otto, K. A., Tirsch, D., Mottola, S., et al. 2017, in *Asteroids, Comets, Meteors* (UK: Wayland)
- Pätzold, M., Andert, T., Hahn, M., et al. 2016, *Nature*, **530**, 63
- Pätzold, M., Andert, T. P., Hahn, M., et al. 2019, *MNRAS*, **483**, 2337
- Potyondy, D., & Cundall, P. 2004, *Int. J. Rock Mech. Mining Sci.*, **41**, 1329
- Preusker, F., Scholten, F., Matz, K. D., et al. 2017, *A&A*, **607**, L1
- Sachse, M., Schmidt, J., Kempf, S., & Spahn, F. 2015, *J. Geophys. Res. Planets*, **120**, 1847
- Spohn, T., Knollenberg, J., Ball, A. J., et al. 2015, *Science*, **349**, aab0464
- Sremčević, M., Krivov, A. V., & Spahn, F. 2003, *Planet. Space Sci.*, **51**, 455
- Thomas, N., Davidsson, B., El-Maarry, M. R., et al. 2015a, *A&A*, **583**, A17
- Thomas, N., Davidsson, B., El-Maarry, M. R., et al. 2015b, *Lunar Planet. Sci. Conf.*, 1712
- Thomas, N., Sierks, H., Barbieri, C., et al. 2015c, *Science*, **347**, aaa0440
- Tirsch, D., Otto, K. A., Mottola, S., et al. 2017a, *Eur. Planet. Sci. Cong.*, 11
- Tirsch, D., Otto, K. A., Mottola, S., et al. 2017b, in *5th International Planetary Dunes Workshop*, 1961, 3011



### 3 Summary and Conclusion

This cumulative habilitation thesis presents eleven peer-reviewed publications concerning the physics of volatile related morphologies on asteroids and comets. The research applies three major techniques: remote sensing and in situ data analysis of space missions to a variety of small bodies, laboratory experiments of sublimating analogue materials and DEM modelling of dynamic processes in volatile-rich regoliths. A twelfth publication furthering the initiated research is presented in the Outlook (Chapter 4).

The research provides a comprehensive view on the processes acting on volatile-rich regolith through a combination of multiple analysis techniques and data sets. Chapter 2 introduces five articles focussing on the morphologic analysis of images from small bodies. In particular, remote sensing data of Ceres and Vesta and in situ data of Ryugu and 67P were used to constrain the processes and morphologies caused by volatiles in the imaged regoliths (Section 2.1). Three articles present the preparation and implementation of sublimation experiments of comet analogue materials in the laboratory. The experiments focused on the physical parameters of the analogue materials and the evolution of morphologic features under sublimation conditions (Section 2.2). Finally, two articles introduce and apply a DEM code adjusted to reproduce dynamic volatile-driven processes on comet 67P. These simulations allowed to constrain the physical properties of the regolith (Section 2.3).

The research did not only combine these three methods, but it also applied an interplanetary body comparison including small asteroids and comets such as Ryugu and 67P and larger objects such as Vesta and Ceres. Other small bodies, such as Eros, Itokawa and the Moon, have also been considered to support this comparison. The different physical environments on these bodies enabled a comprehensive interpretation of volatile-related morphologies. Additionally, multi-scale analyses of volatile-related morphologic features enhanced our understanding of the scale-dependent processes generating and shaping small body regoliths, from sub-millimeter surface roughness to kilometre-sized impact cratering.

The major scientific advance of this thesis is its revelation that volatiles are present on all investigated small planetary bodies. In some cases, volatiles are only local occur-



### 3 Summary and Conclusion

rences, but they exist even on otherwise dry asteroids, such as Vesta, and interact with the regolith and its morphology. This work shows that volatile-related morphologies are a reliable method to constrain the presence of volatiles, even when other space mission instruments, e.g. spectrometers, gamma ray and neutron detectors that only access the top layer of the regolith, are unable to detect them. Moreover, this work establishes the link between specific morphologies (crater fractures, mass-wasting features, pond-like features, PIDs, roughness and texture) and the volatile content in the regolith while considering the bodies' environmental conditions.

In detail, the articles presented in this thesis provide the following results to the key scientific questions raised in Chapter 1:

#### **What is the relationship between surface morphologies and the presence of volatiles on small bodies?**

With the exception of Otto et al. (2021a), which focuses on carbonaceous chondrites as regolith analogues for Ryugu, all articles presented in Section 2.1 address this question by focusing on individual features that are related to volatiles. While Otto et al. (2019) concentrates on volatiles in the subsurface, the remaining articles address the effect of volatiles mixed in the regolith that forms the morphologic feature (e.g. volatiles in mass-wasting material (Parekh et al., 2021a), impact ejecta (Michalik et al., 2021; Parekh et al., 2021b) and intrinsic volatile content (Otto et al., 2021a)).

Volatile sublimation in comets increases the surface roughness on small scales compared to aqueously altered asteroids by about 6% (Otto et al., 2021a). It can also cause the formation of pond-like features through regolith fluidisation (Parekh et al., 2021b) and volatile loss is responsible for the creation of pitted impact deposits (Michalik et al., 2021). However, Parekh et al. (2021a) also show that volatile lubrication alone cannot explain the reduced effective coefficient of friction in landslides on Vesta and Ceres, but may be responsible for an increased run-out length. Additionally, Otto et al. (2019) reveal that volatiles in the subsurface can influence geologic processes such as crater relaxation generating concentric fracturing.

Finally, Sachse et al. (2022) show that volatile-driven redistribution of regolith particles on comet 67P can lead to the formation of aeolian-like features, such as wind tails and moats.

#### **Can we constrain the volatile content and abundance from surface morphologies observed in small body environments?**

The volatile content in the regolith is addressed using all three techniques described above. Otto et al. (2019) and Michalik et al. (2021)

use remote sensing images from the Dawn Mission and estimate the local volatile distribution and content from morphologies observed on Ceres and Vesta, respectively. Although Otto et al. (2019) do not directly constrain the volatile content in Ceres' regolith, they are able to derive the depth ( $\sim 1$  km) and thickness ( $\sim 2$  km) of a volatile-rich layer in the subsurface. Michalik et al. (2021) estimates the volatile content from the PIDs associated with the crater Marcia on Vesta and finds that only small amounts of volatiles of about 1 wt% are necessary to form such features.

In the laboratory Haack et al. (2020) and Haack et al. (2021a) were able to constrain the volatile content in cometary regolith by studying the effect of varying volatile content on the tensile strength and morphologic evolution under sublimation conditions. Haack et al. (2020) finds that only small amounts of ice ( $>20\%$ ) are sufficient to increase the tensile strength of cometary regolith analogue materials above values measured on 67P (Groussin et al., 2015; Attree et al., 2018).

Haack et al. (2021a) show that the volatile content plays a role in the morphology that is created through sublimation on comets. Using a two component mixture of ice and fly ash, they illustrate that 66 vol% ice in the regolith generates exotic surface features that have not been observed on real comets. 33-50 vol% ice in a dust-ice mixture generates morphologic features comparable to features observed on comet 67P. Lower ice contents result in episodic rather than continuous sublimation processes. As continuous sublimation as well as local outbursts have been observed on comet 67P (Lara et al., 2015; Sierks et al., 2015), this research suggests that the volatile content is below 50 vol% and may be locally as low as 20 vol%.

Kappel et al. (2020) also investigate the effect of different ice-dust mixing ratios on morphologic features on 67P using DEM modelling. However, given the large parameter space including the particle sizes, size distributions and geometrical configuration, they are unable to conclude on a dust-ice ratio from the simulations alone.

**How are asteroidal and cometary outgassing features related?** Otto et al. (2021a) address this question by evaluating the surface roughness on sub-millimetre and metre scales on asteroid Ryugu and comet 67P. They find that, in terms of the root-mean-square slope (RMS-slope), small scale roughness parameter and Hapke mean slope angle, comet 67P is  $\sim 6\%$  rougher than Ryugu and attribute the higher roughness to active volatile sublimation. Micrometeoroid bombardment, thermal fatigue and solar weathering appear to be the main causes for the surface evolution on Ryugu resulting in a less rough appearance.

The tensile strength of regolith, which for example allows overhangs and cliffs to exist,

### 3 Summary and Conclusion

is investigated by Haack et al. (2020) using regolith analogue materials in the laboratory. They find that dry spherical regolith dust possesses a lower tensile strength than the same dust mixed with ice particles. However, if the dust particles are angular, which can be assumed for impact gardened asteroid regoliths, the volatile content only plays a minor role. Thus the tensile strength of asteroidal regolith is probably higher compared to cometary regolith with less angular dust particles. This is confirmed by independent measurements of the tensile strength on 67P ( $\sim 10$  Pa (Biele et al., 2022)) and Ryugu ( $\sim 280$  kPa (Grott et al., 2019)).

**What is the role of volatiles in the evolution of small body surfaces and their interiors?** The features described in this habilitation theses all contribute to the surface evolution of small bodies. On asteroids, volatiles influence the surface evolution mainly by generating localized volatile-related features. These can be large, up to kilometre-sized geologic features, such as fractures around craters (Otto et al., 2019), PIDs (Michalik et al., 2021), mass-wasting (Parekh et al., 2021a) and pond-like features (Parekh et al., 2021b), or small, intrinsic regolith features, such as surface roughness (Otto et al., 2021a) and texture (Otto et al., 2021b). Comets on the other hand show global signs of evolution through volatiles in local volatile-triggered outbursts and a continuous sublimation (Vincent et al., 2019).

PIDs and pond-like features are generated through local volatile outgassing on Vesta (Michalik et al., 2021; Parekh et al., 2021b). The outgassing process not only creates kilometre scale geologic PIDs and smooths crater infills through regolith fluidisation, but it also initiates regolith mixing that locally contributes to the surface evolution. This mixing process becomes visible as colour variations associated with PIDs (Michalik et al., 2021) and is also suggested to have taken place during the formation of pond-like features (Parekh et al., 2021b). Mass-wasting features contribute to the evolution of the surface of small bodies, but they are gravity driven and occur with or without volatile contribution. Volatiles in the regolith can, however, change the morphology of mass-wasting deposits compared to mass-wasting features in dry regolith (e.g. the run-out length and/or deposit thickness) (Parekh et al., 2021a).

Concentric fracturing around some relaxing craters on Ceres phyllosilicate-rich crust are indicative of volatiles in the interior. The low-viscosity of a subsurface volatile-rich layer gives rise to these fractures reflecting the ongoing evolution of Ceres' interior and geologic activity (Otto et al., 2019).

The regolith of comets is richer in volatiles compared to the regolith of asteroids and thus mass wasting can be triggered by weakening the material through the sublimation

of volatiles (Kappel et al., 2020). Here, volatiles are directly involved in the large-scale (tens of metre-sized) surface evolution. Another surface evolution process on comets is the volatile-driven redistribution of regolith particles that generates aeolian-like surface features (Sachse et al., 2022).

In the laboratory, Haack et al. (2021a) and Haack et al. (2021b) show how the process of volatile sublimation and the volatile content in the regolith influence the surface evolution of cometary analogue materials. They find that local and continuous evolution is dependent on the volatile content with low volatile contents (<20-33%) causing episodic changes in the surface morphology while higher ice contents (>33%) support a continuous morphologic evolution.

Finally, Otto et al. (2021b) use the size, colour and brightness of inclusions and the matrix abundance of the regolith imaged on Ryugu to link Ryugu's regolith to carbonaceous chondrites (here: CM2, CO3, CV3, and CK4 groups) which underwent different evolutionary paths in their parent body asteroids. Although they find that Ryugu's inclusions and matrix properties fit well in the parameter space spanned by the investigated carbonaceous chondrites, a definite match cannot be made. The possibility that Ryugu's regolith is not represented in the terrestrial meteorite collection has also been suggested from estimates of the regolith strength suggesting that Ryugu's regolith would be too weak to survive the entry through Earth's atmosphere (Grott et al., 2019).

In conclusion, this habilitation thesis shows that the combination of physical and geological analyses techniques works well to approach complex questions in planetary science. Three major methods including the geologic analysis of space mission remote sensing and in situ image data, laboratory experiments of sublimating small body analogue materials and numerical DEM modelling of dynamic regolith processes were combined to assess the the physics of volatile-related morphologies on asteroids and comets. The research reveals that these morphologies are not only suitable to constrain regolith volatile contents and their distribution, but also represent small body evolutionary processes on multiple spatial scales. Thus, volatiles initiate complex processes contributing to the divers geology of small planetary bodies.





## 4 Outlook

In the future, the list of features investigated in this thesis may be extended by space missions to other asteroids, comets and airless bodies such as the icy satellites of the outer planets and Kuiper belt objects as well as by returned samples and data sets from other space mission instruments. A first step towards evaluating multi-instrumental and multi-scale data sets including the returned samples from Ryugu is presented in Section 4.1.

A number of upcoming small body space missions arriving at their target bodies in the coming years (e.g. JAXA's MMX mission to Mars moon Phobos, JAXA's *Destiny+* mission to active asteroid Phaethon, ESA's Hera mission to the binary asteroid system of Didymos and Dimorphos, NASA's Psyche mission to metal-rich asteroid Psyche and NASA's Lucy mission to Jupiter's Trojans) will visit exciting new targets whose surface morphologies will enhance and complement the research initiated with this thesis. For example, it will be fruitful to explore which of the features described in this thesis can also be identified on other small bodies and how the environmental conditions (e.g. temperature, surface gravity, composition, rotational speed) may influence their appearance. Also, additional volatile-related morphologic features, such as polygonal impact craters or intersecting fractures, may complement the initiated research.

Finally, it will be beneficial to extend the research to the icy satellites of the outer planets and other volatile-rich objects such as dwarf-planet Pluto and trans-Neptunian Arrokoth. Although their surface environment (in particular their temperature, surface gravity and composition) as well as their geologic evolution may be different from the objects investigated in this thesis, these objects will provide an additional perspective on the effect of volatiles in planetary regoliths. For example, comparing common geologic features, such as landslides and impact craters, in the volatile-rich regoliths of the dwarf-planets Ceres and Pluto may be used to establish the link between the environmental conditions and the way the volatiles affect the morphology of these bodies.

## 4.1 Multi-scale and Multi-instrument Analyses

This thesis focuses on small body surface morphologies generated through volatiles observed with remote sensing and in situ cameras, but other space missions instruments also provide measurements that can be linked to volatile content and/or specific morphologies. For example, the Visible and Infrared Mapping Spectrometer (VIR) on the Dawn mission identified hydrated sodium chloride deposits on Ceres suggesting the presence of ascending salty liquids on Ceres (De Sanctis et al., 2020) and the Thermal Infrared Imager (TIR) on the Hayabusa2 spacecraft determined the porosity of boulders and found some anomalously porous ones (Sakatani et al., 2021). Such instruments provide independent information on the regolith volatile content from another physical perspective.

Additionally, the returned samples from Ryugu by Hayabusa2 and from current and future sample return missions to small bodies (e.g. NASA’s OSIRIS-REx mission, JAXA’s MMX mission) have been enabling and will enable a detailed look at the volatiles present in planetary regoliths on scales below the ones observable by space mission instruments. The samples allow accessing the intrinsic properties of regoliths and provide insight into the contribution of volatiles to the mechanical and physical properties that shape the regolith’s morphologic appearance over multiple spatial scales.

The following article presents a first step towards a multi-scale and multi-instrument analysis of the volatile-rich regolith of asteroid Ryugu. The Hayabusa2 mission, its lander MASCOT and the returned samples provide a broad data set of partially matching instruments covering a wide spatial range from sub-millimetres to kilometers. Otto et al. (2023) compare the data sets from the Hayabusa2 orbiter, the MASCOT lander and the returned samples focussing on the common measurements that were retrieved at all scales: colour images and radiometer and magnetometer measurements. They find that although MASCOT operates at a scale at which some physical properties, such as the thermal inertia and reflectance, undergo scale dependent changes, its measurements including the rock morphology, colour in the visible wavelengths, possible meteorite analogue, density, and porosity are in good agreement with those of the orbiter and the returned samples. Some of the in situ observations by MASCOT, such as the presence of inclusions in rocks and the absence of fine particles at MASCOT’s landing site, were uniquely identified by MASCOT. The article concludes that multi-scale and multi-instrument investigations are crucial to comprehensively capture small body regolith properties and the processes that act on them.

The article can be cited using:

#### 4.1 Multi-scale and Multi-instrument Analyses

- Otto, K. A., Ho, T.-M., Ulamec, S., Bibring, J.-P., Biele, J., Grott, M., Hamm, M., Hercik, D., Jaumann, R., . . . Yabuta, H. (2023). MASCOT's in Situ Analysis of Asteroid Ryugu in the Context of Regolith Samples and Remote Sensing Data Returned by Hayabusa2. *Earth, Planets and Space*, 75(51), 1–16. <https://doi.org/10.1186/s40623-023-01805-8>.



#### 4.1.1 Otto et al. (2023)

Otto, K. A., Ho, T.-M., Ulamec, S., Bibring, J.-P., Biele, J., Grott, M., Hamm, M., Hercik, D., Jaumann, R., . . . Yabuta, H. (2023). MASCOT's in Situ Analysis of Asteroid Ryugu in the Context of Regolith Samples and Remote Sensing Data Returned by Hayabusa2. *Earth, Planets and Space*, 75(51), 1–16.  
<https://doi.org/10.1186/s40623-023-01805-8>.


As first author I wrote significant parts of the article and organized the contributions of the co-authors. T.-M. Ho and S. Ulamec wrote the introduction and the comparison of the MASCOT and orbiter instruments, respectively. J. Biele and J. Knollenberg provided input to the strength estimates of regolith on various spatial scales and M. Grott and M. Hamm wrote the summary and comparison of the radiometer measurements. M. Grott also plotted Figure 6. D. Hercik and M. Sato contributed the summary and comparison of the magnetometer measurements. I wrote the summary and comparison of the camera findings and created Figures 1-5. I also populated Table 1 and wrote the discussion and conclusions. J.-P. Bibring, T.-M. Ho, R. Jaumann, S. E. Schröder and S. Ulamec proofread the article before submission. All authors provided instrument and/or operational support and contributed to discussions on the results as well as refining the manuscript.

FULL PAPER

Open Access



# MASCOT's in situ analysis of asteroid Ryugu in the context of regolith samples and remote sensing data returned by Hayabusa2

Katharina Otto<sup>1,2\*</sup> , Tra-Mi Ho<sup>3</sup>, Stephan Ulamec<sup>4</sup>, Jean-Pierre Bibring<sup>5</sup>, Jens Biele<sup>4</sup>, Matthias Grott<sup>1</sup>, Maximilian Hamm<sup>1,6</sup>, David Hercik<sup>7</sup>, Ralf Jaumann<sup>6</sup>, Masahiko Sato<sup>8</sup>, Stefan E. Schröder<sup>9</sup>, Satoshi Tanaka<sup>10</sup>, Ulrich Auster<sup>11</sup>, Kohei Kitazato<sup>12</sup>, Jörg Knollenberg<sup>1</sup>, Aurelie Moussi<sup>13</sup>, Tomoki Nakamura<sup>14</sup>, Tatsuaki Okada<sup>10</sup>, Cedric Pilorget<sup>5</sup>, Nicole Schmitz<sup>1</sup>, Seiji Sugita<sup>8</sup>, Koji Wada<sup>15</sup> and Hikaru Yabuta<sup>2</sup>

## Abstract

The Hayabusa2 mission provided a unique data set of asteroid Ryugu that covers a wide range of spatial scale from the orbiter remote sensing instruments to the returned samples. The MASCOT lander that was delivered onto the surface of Ryugu aimed to provide context for these data sets by producing in situ data collected by a camera (MasCam), a radiometer (MARA), a magnetometer (MasMag) and a spectrometer (MicrOmega). In this work, we evaluate the success of MASCOT as an integrated lander to bridge the gap between orbiter and returned sample analysis. We find that MASCOT's measurements and derivatives thereof, including the rock morphology, colour in the visible wavelengths, possible meteorite analogue, density, and porosity of the rock at the landing site are in good agreement with those of the orbiter and the returned samples. However, it also provides information on the spatial scale (sub-millimetres to centimetres) at which some physical properties such as the thermal inertia and reflectance undergo scale-dependent changes. Some of the in situ observations such as the presence of clast/inclusions in rocks and the absence of fine particles at the landing site was uniquely identified by MASCOT. Thus, we conclude that the delivery of an in situ instrument like MASCOT provides a valuable data set that complements and provides context for remote sensing and returned sample analyses.

**Keywords** Asteroid Ryugu, In situ analyses, Asteroid sample return, Multi-scale analysis, Asteroid regolith properties, Asteroid regolith, MASCOT, Hayabusa2

\*Correspondence:

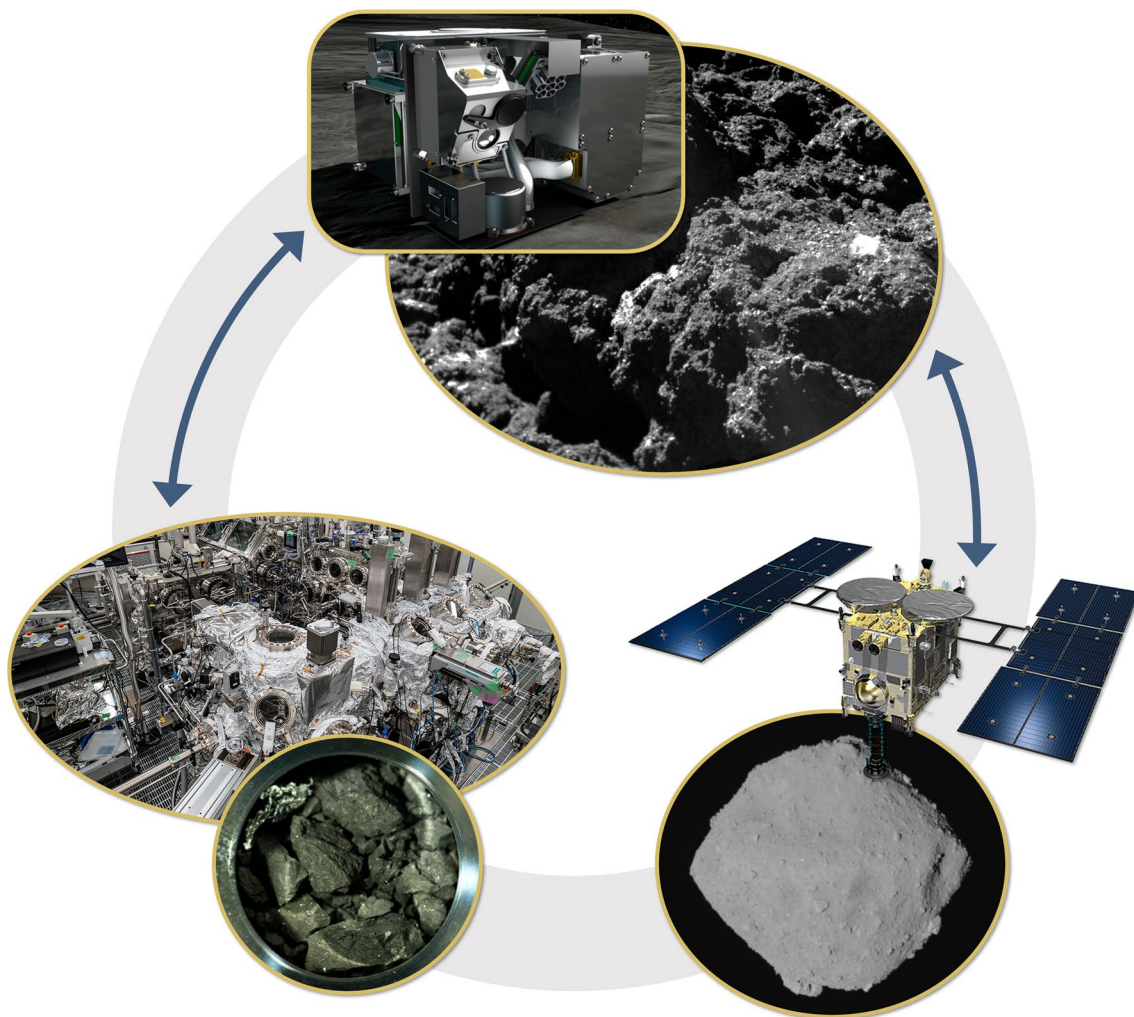
Katharina Otto  
katharina.otto@dlr.de

Full list of author information is available at the end of the article



© The Author(s) 2023. **Open Access** This article is licensed under a Creative Commons Attribution 4.0 International License, which permits use, sharing, adaptation, distribution and reproduction in any medium or format, as long as you give appropriate credit to the original author(s) and the source, provide a link to the Creative Commons licence, and indicate if changes were made. The images or other third party material in this article are included in the article's Creative Commons licence, unless indicated otherwise in a credit line to the material. If material is not included in the article's Creative Commons licence and your intended use is not permitted by statutory regulation or exceeds the permitted use, you will need to obtain permission directly from the copyright holder. To view a copy of this licence, visit <http://creativecommons.org/licenses/by/4.0/>.

**Graphical Abstract**



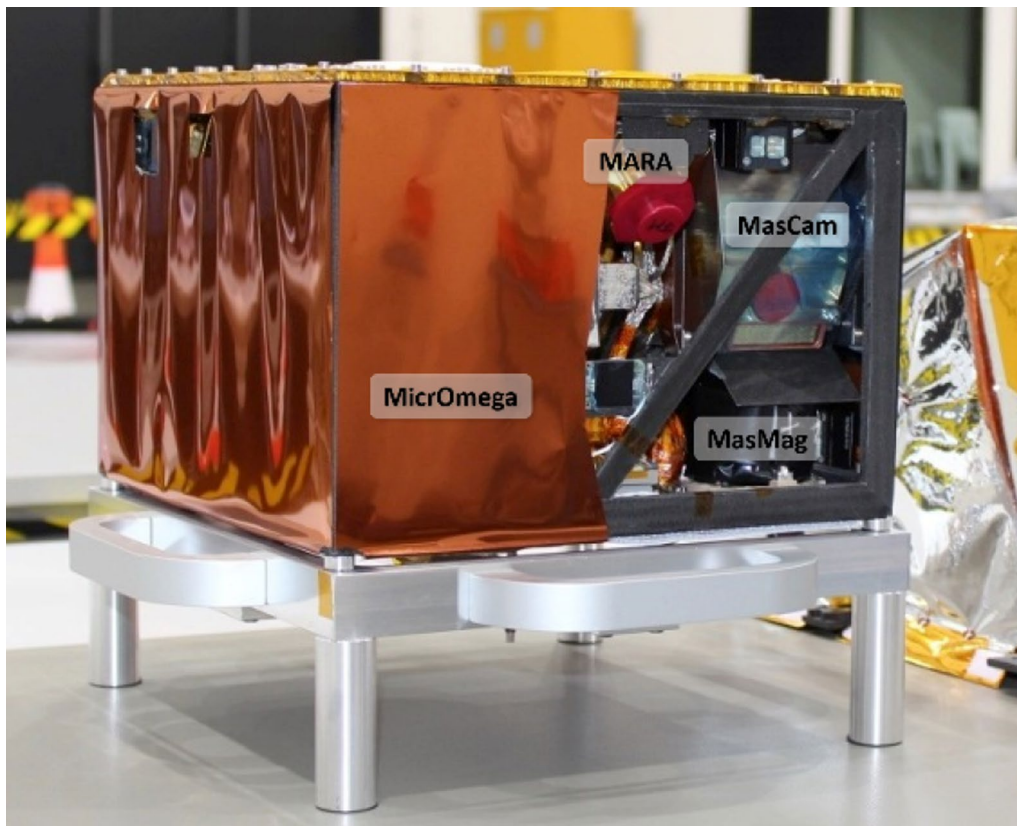
**Introduction**

Hayabusa2 is a mission by the Japan Aerospace Exploration Agency (JAXA) that was launched in December 2014 to the near-Earth asteroid (162,173) Ryugu. After arrival at the asteroid in June 2018 and an observation phase that not only included remote observations but also the delivery of the MINERVA II and MASCOT landers (Lange et al. 2020), as well as an impact experiment (Arakawa et al. 2020), samples were returned to Earth in December 2020. These samples can now be put into context with the observations at and on the asteroid.

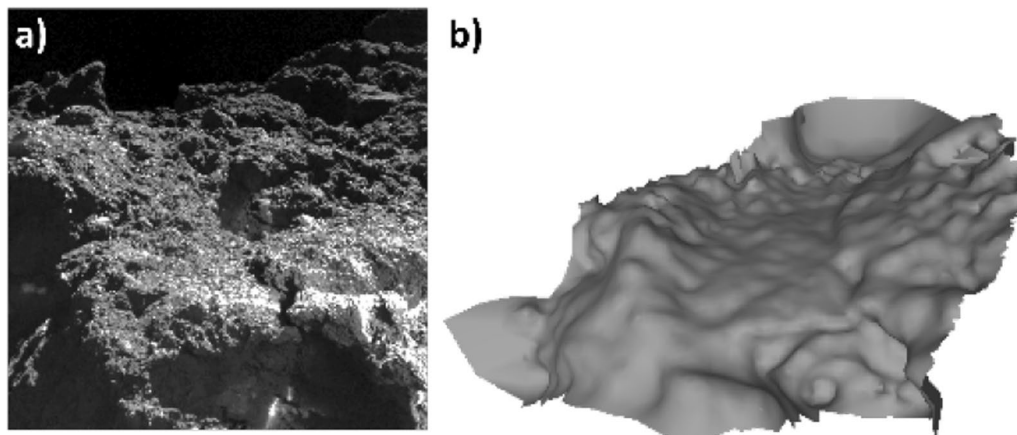
The small, agile Mobile Asteroid Surface Scout, MASCOT (Fig. 1), was delivered by the Hayabusa2 main spacecraft to the surface of Ryugu on October 3rd, 2018 to perform in-situ measurements on the surface of the

asteroid (Jaumann et al. 2019; Ho et al. 2021). There, it landed in front of a rough-looking rock of approximately 15 cm in size free of fine-grained deposits (Fig. 2). Instead, bright spots, potentially inclusions, were visible on the rock surface (Fig. 3) (Jaumann et al. 2019).

While the main objectives of the Hayabusa2 mission were to understand the origin and evolution of materials in the early solar nebula and in a C-type asteroid, Ryugu (Watanabe et al. 2017), MASCOT was to focus on in situ science, including the measurement of physical properties of the surface material and high-resolution imaging of undisturbed surface material (Ho et al. 2017). The combination of remote sensing from the main spacecraft, in situ surface measurements by landers, and returned sample analysis allow the Hayabusa2 mission to conduct



**Fig. 1** Photo of the MASCOT lander with its scientific instruments labeled. Note that MIRA and MasCam have overlapping field of views



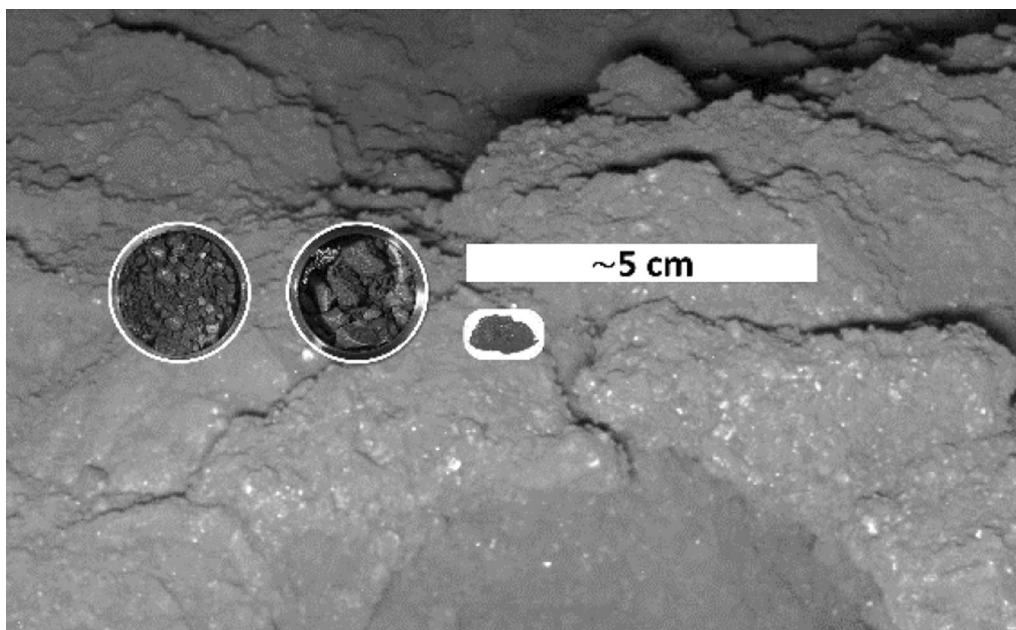
**Fig. 2** **a** MASCOT's landing site imaged by MasCam at day time and **b** shape model of the scene. The scene is approximately 25 cm across. The illuminated flat plateau (~ 15 cm across) is referred to as the MASCOT rock. The overexposed streaks in the foreground in **a** are reflections of MASCOT's housing

global-, local-, and micro-scale observations. Thus, MASCOT bridges the gap between the samples returned and the orbiter observations (Ho et al. 2017, 2021).

MASCOT has a payload of four scientific instruments: a camera, MasCam, which resolved structures near the

landing site with a spatial pixel resolution of up to 200  $\mu\text{m}$  (Jaumann et al. 2017), a radiometer, MIRA, to measure thermal emission of the surface during a day–night cycle and thus determine the thermal conductivity of surface material (Grott et al. 2017), a hyperspectral near-infrared





**Fig. 3** Rock illuminated by MasCam's red LED at night in relation to the returned sample. Sub-millimetre-sized bright spots are clearly visible in the front. The two circles illustrate the  $\sim 1.7$  cm across opening of the sample holders with the returned samples. The largest returned fragment (C9000) with 1 cm in size is also shown for reference. Due to the distortion in the MasCam image, the dimensions of the samples and the MASCOT scene are only approximately to scale at the indicated location. Please note that the samples were not collected at this site and are shown here for reference only. The images of the samples were retrieved from (Astromaterials Science Research Group (ASRG) 2022)

(NIR) microscope, MicrOmega, designed to determine the surface mineralogical and molecular composition at the grain scale (Bibring et al. 2017), and a magnetometer, MasMag, to search for any sign of possible remnant magnetization (Herčík et al. 2017) (Fig. 1). With the exception of the magnetometer MasMag, MASCOT's instruments have corresponding orbiter instruments: A telescopic camera (ONC (Kameda et al. 2017)), a thermal mapper (TIR (Okada et al. 2017)) and a spectrometer (NIRS3 (Iwata et al. 2017)). An overview of the MASCOT lander design is given by Ho et al. (2017), while the actual mission activities including the on-asteroid operations is summarised by (Ho et al. 2021).

Unfortunately, MASCOT landed on a depression with the consequence that the surface to be characterized was too far away to be illuminated and imaged by MirOmega (Bibring et al. 2022). Nevertheless, an instrument identical to MicrOmega has been applied in the curatorial work of the returned Ryugu samples and revealed sub-millimetre chemical heterogeneities including carbonates and NH-rich compounds (Pilorget et al. 2022).

On December 6<sup>th</sup>, Hayabusa2 returned samples from Ryugu to Earth. The samples were collected from two sites on Ryugu and stored in separate sample containers. Chamber A contained  $(3.237 \pm 0.002)$  g surface material from Ryugu's equatorial ridge and Chamber C contained  $(2.025 \pm 0.003)$  g of surface and potentially subsurface

material collected near an artificial crater created by Hayabusa2's SCI impact experiment (Arakawa et al. 2020; Yada et al. 2022). The samples are composed of predominantly millimetre-sized particles embedded in fine sub-millimetre dust, with the largest fragment being  $\sim 8$  mm across (Yada et al. 2022). Preliminary investigations indicate that the collected samples are representative of Ryugu's surface based on their colour, shape and structure (Pilorget et al. 2022; Tachibana et al. 2022).

In this paper, we discuss the extent to which conclusions from the measurements performed in situ at the surface of Ryugu have been confirmed by ongoing sample analysis, as well as how in situ data on undisturbed material on the asteroid surface can enhance the interpretation of the returned samples.

### In situ observations

#### Observations with MasCam

MASCOT's MasCam is a scientific camera equipped with a Scheimpflug optic that allows it to image the entire scene along the camera's depth of field (150 mm to infinity) in focus. In addition, MasCam had the ability to illuminate Ryugu's surface with an array of light-emitting diodes (LEDs), equipped with  $4 \times 36$  monochromatic LEDs working in four spectral bands (Jaumann et al. 2017). MasCam took images both during descent and on the surface with scales down to 0.1 mm/pixel (Jaumann

et al. 2019). These observations revealed a number of important properties of Ryugu, most of which were unexpected before landing. As already identified in Hayabusa2 ONC images, two types of boulders are clearly distinguished in lower resolution MasCam descent images: brighter ones with smooth surfaces, non-dendritic fractures and modified by a process that has resulted in both sharp edges and rounded structures, and darker ones with cauliflower-like surfaces and characteristics suggestive of thermal-fatigue. Boulder sizes range from a few millimetres to a few tens of metres and the sorting of grains, pebbles and boulders is poor. The relatively large sizes of boulders and their different morphologies reflected by the two boulder types described above suggest that they may be fragments from Ryugu's parent body/bodies that reaccumulated to form Ryugu itself and reflect heterogeneities in Ryugu's parent body/bodies (Jaumann et al. 2019).

At the location of  $22.32^{\circ}\text{S} \pm 0.05^{\circ}/317.16^{\circ}\text{E} \pm 0.05^{\circ}$ , MASCOT came to rest on Ryugu's surface and the fine structure of boulders imaged there at the highest resolution exhibit a matrix with sub-millimetre size inclusions and morphologies similar to carbonaceous chondrites.

In the context of the Ryugu rock, the word "inclusion" has been used to describe bright spots surrounded by a darker matrix (Fig. 3) (Schröder et al. 2021; Otto et al. 2021). Given the limitation in actually identifying the composition and structure of these spots, the term "clast" as used in sedimentary geology may also be adequate. To maintain consistency with previous publications, we will call the bright spots surrounded by a darker matrix "inclusions" in this article.

No accumulation of fine dust is identified in the MasCam images. Close-up observations show the presence of inclusions (Jaumann et al. 2019; Schröder et al. 2021; Otto et al. 2021). Small inclusions have the characteristic size (sub-millimetre) of chondrules, whereas the larger ones may be refractory, calcium–aluminium-rich inclusions (CAI). This suggests that Ryugu's material has experienced heating but is not fully hydrated, which is consistent with the absence of the  $0.7\ \mu\text{m}$  absorption feature in ground-based reflectance spectra, confirmed by ONC (Tatsumi et al. 2021). The visible colours of the inclusions provide compositional clues, but their interpretation is limited by the lack of reflectance data in the IR wavelength range, where most bands that are diagnostic for the mineralogy are located. However, the spectral characteristics of the inclusions are similar to those in carbonaceous chondrites (Schröder et al. 2021; Otto et al. 2021). A systematic comparison of the inclusions' size distribution, relative spectral slope and brightness relative to the matrix, and the matrix volume abundance imaged within the rock on Ryugu and a set

of carbonaceous chondrites including CM2, CO3, CV3 and CK3 revealed that Ryugu's rock fits well within the parameter space of these meteorites. However, Ryugu's material tends to have slightly larger inclusions and a higher matrix volume abundance (Schröder et al. 2021; Otto et al. 2021). MasCam also allowed the derivation of the surface roughness on small spatial scales (sub-millimetre) by applying a shadow tracing method to the images taken at night when the scene was illuminated with MasCam's LEDs. The result showed that Ryugu's rock surface has a fractal dimension of  $1.16 \pm 0.04$  and a root mean square (RMS) slope of  $36.6^{\circ} \pm 1.4^{\circ}$ . It thus appears less rough ( $\sim 6\%$ ) compared to material imaged on comet 67P/Churyumov-Gerasimenko (Otto et al. 2020). The difference in roughness may be explained by the different processes altering the surfaces of asteroids and comets. While sublimation of volatiles seems to be the main process to generate roughness on comets, micrometeoroid bombardment, thermal fracturing and solar weathering may play a significant role in shaping asteroid surfaces (Otto et al. 2020).

#### Observations with MARA

The MASCOT radiometer MARA is an instrument that measured radiative flux emitted from the surface of Ryugu in the thermal infrared wavelength range in six dedicated channels (Grott et al. 2017). MARA operated during the entire MASCOT mission starting at MASCOT's separation from the Hayabusa2 spacecraft and gathered data throughout the 17 h of operation (Ho et al. 2021). After landing, MARA measured emitted flux of a rock at the MASCOT landing site over the period of a full asteroid rotation (7:38 h). Two of MARA's infrared channels were dedicated to measuring low night time temperatures, and a bandpass filter between 8 and  $12\ \mu\text{m}$  as well as a  $>3\ \mu\text{m}$  long pass filter were employed for this purpose. Four additional bandpass channels in the 5.5–7, 8–9.5, 9.5–11.5, and 13.5–15.5  $\mu\text{m}$  wavelength range were dedicated to recording emissivity as a function of wavelength and to constrain surface composition. MARA's field of view covers about 10–15  $\text{cm}^2$  and is within MasCam's view (Grott et al. 2017; Hamm et al. 2018).

At the landing site, asteroid surface temperatures were found to vary between 210 and 300 K based on measurements in the 8–12  $\mu\text{m}$  wavelength range (Grott et al. 2019). Using a thermophysical model of the asteroid and taking surface roughness into account, the thermal inertia of the rock was found to be  $282_{-25}^{+93}\ \text{J m}^{-2}\ \text{K}^{-1}\ \text{s}^{-1/2}$  (Hamm et al. 2018; Grott et al. 2019), a value similar to the  $(225 \pm 45)\ \text{J m}^{-2}\ \text{K}^{-1}\ \text{s}^{-1/2}$  later found to be globally representative for Ryugu's boulders and surrounding material based on Hayabusa2 TIR data (Okada et al.

2020; Shimaki et al. 2020). As there was no indication for a masking layer of surface dust (Biele et al. 2019), the low thermal inertia derived from MARA data was interpreted to be caused by a high intrinsic (micro-)porosity of the rock. Thus, porosities between 0.28 and 0.55 were derived based on an extrapolation of laboratory data for the thermal conductivity of meteorites as a function of porosity (Grott et al. 2019). A re-analysis of the MARA data set using data assimilation techniques narrowed down the range of uncertainties to thermal inertias around  $(295 \pm 18) \text{ J m}^{-2} \text{ K}^{-1} \text{ s}^{-1/2}$  and porosities between 0.30 and 0.52 (Hamm et al. 2020). With the availability of a detailed shape model of the MASCOT rock (Scholten et al. 2019) (Fig. 2b) to refine thermal re-radiation and illumination conditions, and taking into account the effect of sunlight reflection casted by MASCOT into the MARA field of view (Fig. 2a), the data were re-analysed (Hamm et al. 2022). The thermal inertia was found to be lower with  $256 \pm 34) \text{ J m}^{-2} \text{ K}^{-1} \text{ s}^{-1/2}$  and porosity between 0.46 and 0.56 depending on the empirical model used to relate porosity and thermal conductivity (Krause et al. 2011; Flynn et al. 2018). Based on estimates of Ryugu's packing state and the constraint posed by Ryugu's bulk density, porosities around  $0.50 \pm 0.02$  were later favoured using semi-empirical mixing models (Grott et al. 2020). Such porosities imply grain densities of  $(2848 \pm 152) \text{ kg m}^{-3}$ , values similar to those found in CM meteorites as well as CI Tagish Lake (Grott et al. 2020).

The infrared emissivity in the MARA bandpass channels was estimated by combing the thermal model of a rock with a data assimilation scheme (Hamm et al. 2022). The emissivity estimates were compared to spectra of thin sections of powder samples of meteorites. These data show that the spectral variation of the rock's emissivity shares similarities with the bulk samples of the most aqueously altered meteorites (CI, CM, and CR carbonaceous chondrites), indicating Ryugu experienced strong aqueous alteration prior to any dehydration.

### Observations with MasMag

The MASCOT magnetometer MasMag is a triaxial flux-gate magnetometer which acquired data from the beginning of the lander descent, through the several bounces, touchdown and at the final resting position (Hercik et al. 2020). The descent profile of the observed magnetic field, after calibration and de-spinning, does not show any detectable change in the magnetic field above the background level. The observed magnetic field vector fluctuates within a  $\pm 1 \text{ nT}$  range and no systematic change was visible when approaching the surface down to  $\sim 10 \text{ cm}$  (distance of the sensor to the surface at resting position). Such behaviour directly excludes any global magnetic field and larger magnetization down to metre-scales.

However, based on the accuracy of the measurement, we can assess the upper limit of the magnetization under certain assumptions. The specific magnetic moment (level of magnetization) is the effective magnetic moment ( $\text{Am}^2$ ) per kg of the material. Measuring this parameter assumes, a priori, a homogeneous magnetization through the sample. If the material was built from smaller magnetized particles, e.g., in a process of accretion and coagulation, the mutual orientation of the domains would be random and the contributions from magnetized individual domains would cancel each other. The total magnetic moment of the bulk is then negligible, while the domains themselves can retain high levels of magnetization. Therefore, we speak about the magnetization scale as the representative scale at which the material is homogeneously (unidirectionally) magnetized. Microscopic observation of the returned samples revealed that the Ryugu particles were composed of lithologically different domains of several 100 s of micrometre in size (Nakamura et al. 2022). Assuming a magnetization scale of centimetre sized domains within a material with a density of  $1200 \text{ kg/m}^3$  leads to an upper limit of the specific magnetic moment on the order of  $10^{-2} \text{ Am}^2/\text{kg}$ . The investigations of chondrite meteorites show the natural remnant magnetization from  $10^{-4}$  to  $10^{-2} \text{ Am}^2/\text{kg}$  (Terho et al. 1996; Gattacceca and Rochette 2004). This agrees with MasMag's measurement and is to be further refined by magnetization analysis of the returned samples (see section below).

However, it shall be noted that there is a discrepancy between the meteorite measurements, which in general show bulk magnetization (even on  $>10 \text{ cm}$  scales) and the measurements on solar system bodies. So far, only three magnetic measurements were performed on the surface of small bodies: Ryugu, S-type asteroid Eros (Acuña et al. 2002) and comet 67P/Churyumov-Gerasimenko (Auster et al. 2015). All three measurements show no magnetic signal that can be directly related to the body or the regolith. At least in case of Ryugu and comet 67P/Churyumov-Gerasimenko, the discrepancy could be that the pristine material has rather low coherence (tensile strength), which might prevent the material to reach the Earth's surface. The fact that Ryugu's samples contain no chondrules and that the material has a very low grain density of  $1380 \text{ kg/m}^{-3}$  and tensile strengths, leads to the conclusion that Ryugu is not lithified enough to survive atmospheric entry (Herbst and Greenwood 2022). Consequently, we may not have a representative meteorite sample on Earth, although initial sample analysis revealed that Ryugu's mineralogy is similar to CI chondrites (Tsuchiyama et al. 2022). Therefore, it is not excluded that future observations will reveal small bodies



with significant magnetic signatures, as it is expected for metal-rich asteroid types.

#### **MASCOT results in context of orbiter instruments**

The Hayabusa2 orbiter was also equipped with a telescopic camera (ONC), a Spectrometer (NIRS3) and a radiometer (TIR) that allow a cross interpretation of MASCOT data and orbiter data spanning multiple spatial scales (Ho et al. 2021).

Within the landing site of MASCOT, MasCam confirmed two of the four types of rock morphologies identified in the ONC images of Hayabusa2 (Sugita et al. 2019): the dark and rough type 1 boulders and the bright and smooth type 2 boulders (Jaumann et al. 2019). In addition, MasCam provided close-up fine-scale texture identification. Sugita et al. (2019) derived from their data that the rugged surfaces and edges of the type 1 boulders showed uneven layered structures that could be related to the inclusion of coarse-grained clasts. This assumption is supported by the high-resolution of the MasCam images, in which the mm-size structure of type 1 boulder results in a granular friable surface texture (Jaumann et al. 2019). The images of MasCam at the MASCOT landing site revealed a rock with a cauliflower-like surface texture consisting of undulations of  $\sim 1$  cm scale and 2–3 mm scale. This topographic surface roughness at the sub-millimetre scale could be quantified by surface roughness parameters (Otto et al. 2020). Compared with roughness values derived from thermal modelling of Ryugu's surface, the small-scale analysis of Ryugu's rock revealed a lower RMS slope of  $36.6^\circ \pm 1.4^\circ$  compared to  $47^\circ \pm 5^\circ$  (Shimaki et al. 2020; Otto et al. 2020). Applying the image analysis technique to a global image of Ryugu and deriving the RMS slope from MARA day time measurements through fitting the thermal model to the measured data also reveal lower RMS values ( $32.9^\circ \pm 2.2^\circ$  and  $28.6^\circ$ , respectively) (Otto et al. 2020). The discrepancy between these values can be explained by the different methods to derive the RMS slope and reflects the dependence of the roughness parameters on the spatial scale on which they are derived.

MARA results serve as an important anchoring point for the interpretation of global thermal imaging data, which was provided by Hayabusa2's TIR instrument. TIR data indicate boulders, such as observed by MasCam during MASCOT's descent, cover a large part of Ryugu's surface and only a minority of boulders were found to have thermal inertias exceeding  $600 \text{ J m}^{-2} \text{ K}^{-1} \text{ s}^{-1/2}$ , which is similar to that of typical dense carbonaceous chondrites (Okada et al. 2020). A thermal inertia of  $(225 \pm 45) \text{ J m}^{-2} \text{ K}^{-1} \text{ s}^{-1/2}$  was found to be globally representative for Ryugu (Okada et al. 2020; Shimaki et al. 2020). Therefore, the majority of boulders as well as the

surrounding large ( $> 10$  cm) rock fragments are interpreted to be highly porous (Okada et al. 2020), consistent with estimates of inter-boulder porosity of about 16% (Grott et al. 2020) and a bulk porosity of approximately 50–60% (Watanabe et al. 2019).

MASCOT was able to complement the Hayabusa2 orbiter data with necessary constraints by providing local high-resolution data. For example, the presence of a dust-free surface, small scale surface texture, the thermal inertia of an individual rock sample or the lack of magnetization were delivered by MASCOT (Ho et al. 2021). In particular, the lack of a dust layer observed by MASCOT, significantly helped to interpret TIR orbiter data. Dust covering a rock influences the surface temperature and alters the apparent thermal inertia of the underlying material (Biele et al. 2019). This, could have led to the misinterpretation of TIR data. In addition, Shimaki et al. (2020) found that the area around MASCOT's landing site ( $\sim 9 \times 9 \text{ m}^2$ ) has a 30% lower thermal inertia compared to MARA's measurements ( $(200 \pm 7) \text{ J m}^{-2} \text{ K}^{-1} \text{ s}^{-1/2}$  and  $(282 \pm 9535) \text{ J m}^{-2} \text{ K}^{-1} \text{ s}^{-1/2}$ , respectively) indicating a scale dependence of the thermal inertia that could not have been detected without MASCOT. The application of this multi-scale analysis technique is promising for future planetary explorations.

A detailed comparison between orbiter and lander measurements and results can also be found in Ho et al. (2021). Table 1 summarizes the results of the sample analysis, MASCOT and the relevant orbiter instruments.

#### **Sample analysis results in context of MASCOT observations**

On December 6th, 2020, Hayabusa2 returned samples of the surface of Ryugu in two sample containers totalling 5.4 g of Ryugu material (Yada et al. 2022). The intense suite of analysis that these samples will have been undergoing also includes the determination of morphologic and physical properties (Tachibana 2019; Tanaka et al. 2022) which were previously derived from MASCOT data. This gives MASCOT the unique opportunity to link orbiter data and returned samples and relate these properties on different spatial scales. Table 1 summarizes the findings of MASCOT that have overlap with the Hayabusa2 orbiter instruments and the analysis of the returned samples. Figure 3 illustrates the spatial relation between the returned samples and the scene around MASCOT imaged by

#### **Comparison with MasCam**

The majority of particles returned from Ryugu are in the sub-millimetre size range, but there are also particles up to  $\sim 8$  mm in size. Initial visual classification of fragments larger than 1 mm included two types of particles: 1) Rugged, predominantly round, and 2) smooth,



**Table 1** Summary of the findings of the Hayabusa2 orbiter, MASCO<sub>T</sub>, and the returned samples

Feature	Orbiter Observation	MASCO <sub>T</sub> Observation	Returned Sample Observation
Particle size frequency distribution	Power index -2.65 for boulder > 5 m (Michikami et al. 2019) <sup>b</sup>	No particles observed <sup>b</sup>	Power index -3.88 for particles > 1 mm (Yada et al. 2022) <sup>b</sup>
Inclusions	Inclusions below detection limit	Bright inclusions of (0.63 ± 0.91) mm in size (Schroder et al. 2021) <sup>b</sup>	No inclusions (chondrules/CA) observed but sub-millimetre sized grains of specific colour found (Plogget et al. 2022) <sup>b</sup>
Surface structure/pebbles/boulders	Four types of boulders (dark and rugged, bright and smooth, bright and mottled, and Otohime Saxum) (Sugita et al. 2019), elongated impact fragments (Michikami et al. 2019) for metre sized boulders <sup>a</sup>	Two types of boulders (smooth, rough), locally rough surface texture (fractal dimension 1.18 (Otto et al. 2020)) <sup>a</sup>	Rugged and smooth as well as angular and round particles (Yada et al. 2022) elongated and sub-equant blocks with concave portions (Tsuchiyama et al. 2022; Tachibana et al. 2022b) in predominantly millimetre scale, flat saponite-rich surface layers (Nakamura et al. 2022) <sup>a</sup>
Colour in visible wavelength range	Consistent with C-complex asteroids (Sugita et al. 2019; Tatsumi et al. 2020) <sup>a</sup>	Neutral spectrum with individual inclusions with red or blue spectral slopes (Schroder et al. 2021) <sup>a</sup>	Overall slightly reddish slope, but with individual particles also being blue, consistent with C/Cb-type asteroids (Yumoto et al. 2022) <sup>a</sup>
Reflectance/albedo	Geometric albedo of 0.045 ± 0.002 (Sugita et al. 2019)/0.040 ± 0.005 at 0.55 µm (Tatsumi et al. 2020), Bond albedo of 0.014 ± 0.001 (Tatsumi et al. 2020) <sup>a</sup>	I/F of 0.034 ± 0.003 at 0.53 µm and phase angle 4.5° ± 0.1°, consistent with geometric albedo of 0.045 (Schroder et al. 2021) <sup>a</sup>	I/F at 0.55 µm and 30° phase angle is 30–70% higher than remote sensing observations, but darker than CI meteorites (Yumoto et al. 2022; Yada et al. 2022) <sup>b</sup>
Meteorite analogue	Thermally metamorphosed CI and/or shocked CM carbonaceous chondrites (Kitazato et al. 2019; Sugita et al. 2019) <sup>a</sup>	CI or CM carbonaceous chondrites based on inclusions characterization (Jaumann et al. 2019; Schroder et al. 2021; Otto et al. 2021), similar to CI based on thermal modelling (Hamm et al. 2022) <sup>a</sup>	CI chondrites but with lower albedo, higher porosity and more fragile characteristics as well as a lag of sulfates, ferrihydrites and interlayer water (Tanaka et al. 2022; Yada et al. 2022; Yokoyama et al. 2022; Ito et al. 2022) <sup>a</sup>
Thermal inertia	(225 ± 45) J m <sup>-2</sup> K <sup>-1</sup> s <sup>-1/2</sup> (Okada et al. 2020; Shimaki et al. 2020) <sup>a</sup>	(256 ± 34) J m <sup>-2</sup> K <sup>-1</sup> s <sup>-1/2</sup> at 230 K (Hamm et al. 2022) <sup>a</sup>	892 J m <sup>-2</sup> K <sup>-1</sup> s <sup>-1/2</sup> at a temperature of 298 K (Tanaka et al. 2022) <sup>b</sup>
Tensile strength	~229 kPa following the approach from Grott et al. (2019) (L ≈ 10 cm) ; Okada et al. (2020); Shimaki et al. (2020) <sup>a</sup>	200–280 kPa at a scale of ~ 10 cm assuming a Young's modulus representative of carbonaceous chondrites (Grott et al. 2019) <sup>a</sup>	4900 kPa (Tanaka et al. 2022) at a scale of 3 × 3 mm <sup>b</sup>
Density <sup>1</sup>	Asteroid bulk density including microporosity of (1190 ± 20) kg/m <sup>3</sup> (Watanabe et al. 2019) <sup>a</sup>	Grain density of (2848 ± 152) kg/m <sup>3</sup> , bulk density of (1424 ± 135) kg/m <sup>3</sup> (Grott et al. 2020) and (1380 ± 70) kg/m <sup>3</sup> (Herbst et al. 2021) based on semi-empirical mixing models <sup>a</sup>	Sample bulk density of (1282 ± 231) kg/m <sup>3</sup> (Yada et al. 2022) and (1790 ± 80) kg/m <sup>3</sup> considering the full 3D structure (Nakamura et al. 2022) <sup>a</sup>
Porosity	Globally 0.3–0.5 (Okada et al. 2020), boulders with > 0.7 found on the floor of fresh craters (Sakaitani et al. 2021) <sup>a</sup>	0.5 ± 0.02 (Grott et al. 2020) based on semi-empirical mixing models. 0.46 (Hamm et al. 2022) based on the model by Krause et al. (2011) <sup>a</sup>	Higher than CI chondrites, 0.46 based on typical CI grain densities (Yada et al. 2022; Nakamura et al. 2022) <sup>a</sup>
Homogeneous magnetization scale	n.a. <sup>c</sup>	Less than centimetre scale (Hercik et al. 2020) <sup>a</sup>	Roughly several 100s of micrometres (Saito et al. 2022; Nakamura et al. 2022) <sup>a</sup>
Specific magnetic moment	n.a. <sup>c</sup>	10 <sup>-5</sup> Am <sup>2</sup> /kg for decimetre sized particles (Hercik et al. 2020) <sup>a</sup>	10 <sup>-2</sup> Am <sup>2</sup> /kg for 0.1–1 mm sized particles (Saito et al. 2022) <sup>a</sup>

<sup>1</sup> Bulk density = mass/volume, including cracks and pores; grain density = mass/volume, excluding cracks and pores (intrinsic material density)

<sup>a</sup> Fields with bold text: indicate an agreement of measurements

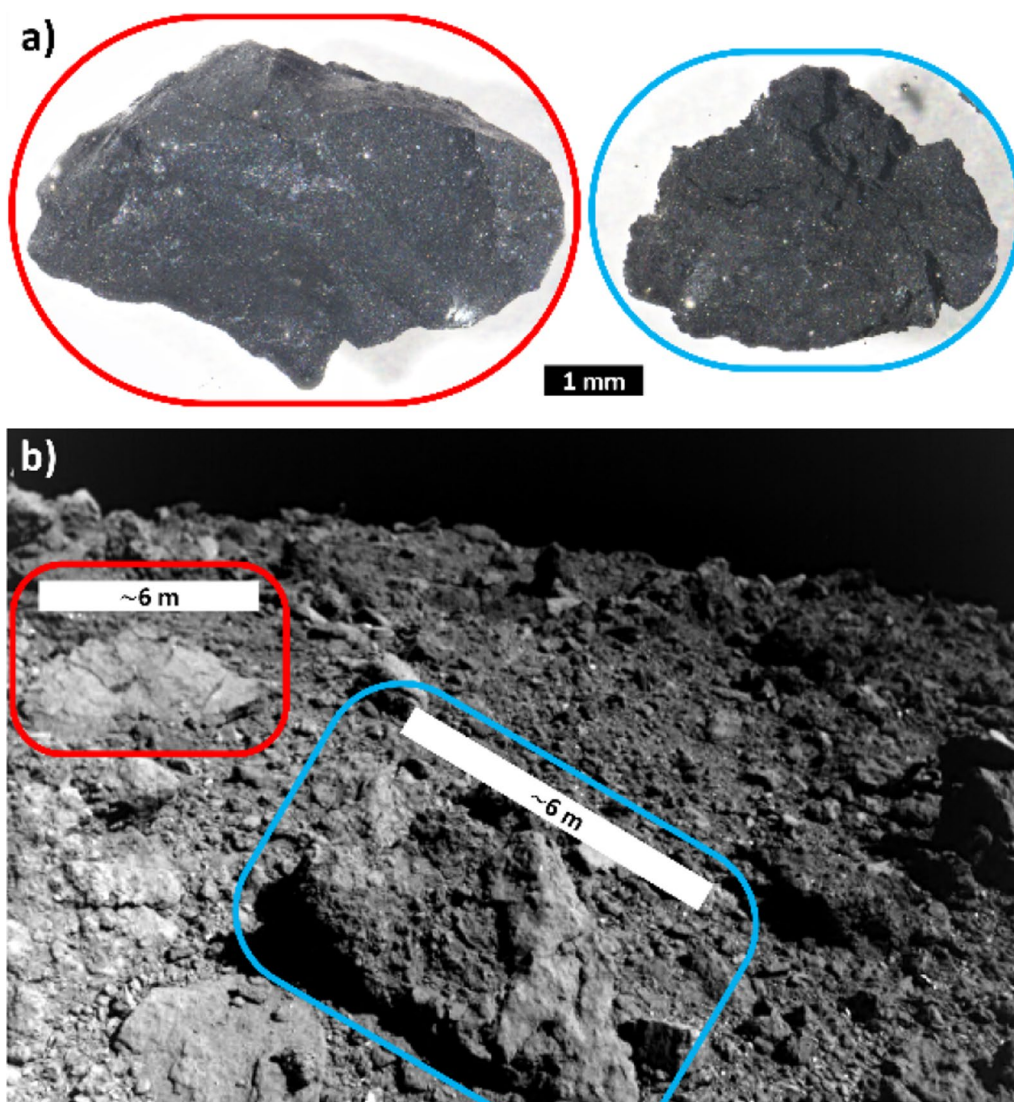
<sup>b</sup> Fields with text in italics: indicate a disagreement

<sup>c</sup> If a comparison is not feasible, the text is not highlighted

angular particles (Yada et al. 2022) (Fig. 4a). During its descent, MasCam (as well as ONC) also identified such distinct types of boulders: a rough and dark and a smooth and comparatively brighter type. Thus, the morphologic heterogeneity appears to be present over a large spatial scale covering three orders of magnitude from millimetre scales of the returned samples to metre scales of the boulders on Ryugu. These different morphologic types and their distribution may hint at the presence of regolith with different degrees of material alteration (Jau-mann et al. 2019; Morota et al. 2020; Sakatani et al. 2021) and their mixing through impact gardening or regolith migration. The fact that the morphologic differences can

be traced down to the millimetre scale implies that the rough and smooth boulders' materials are physically different rather than being the product of, for example, varying exposure times to space weathering.

While the orbiter identified a boulder size frequency distribution with power index of  $-2.65$  for boulders  $> 5$  m (Michikami et al. 2019), the returned samples have a size frequency distribution with a power index of  $-3.88$  for particles  $> 1$  mm (Yada et al. 2022). The discrepancy may be caused by the different scales on which the measurements have been taken as well as the sampling, curation and/or delivering process (Yada et al. 2022). However, MasCam did not identify any pebbles (defined as the size



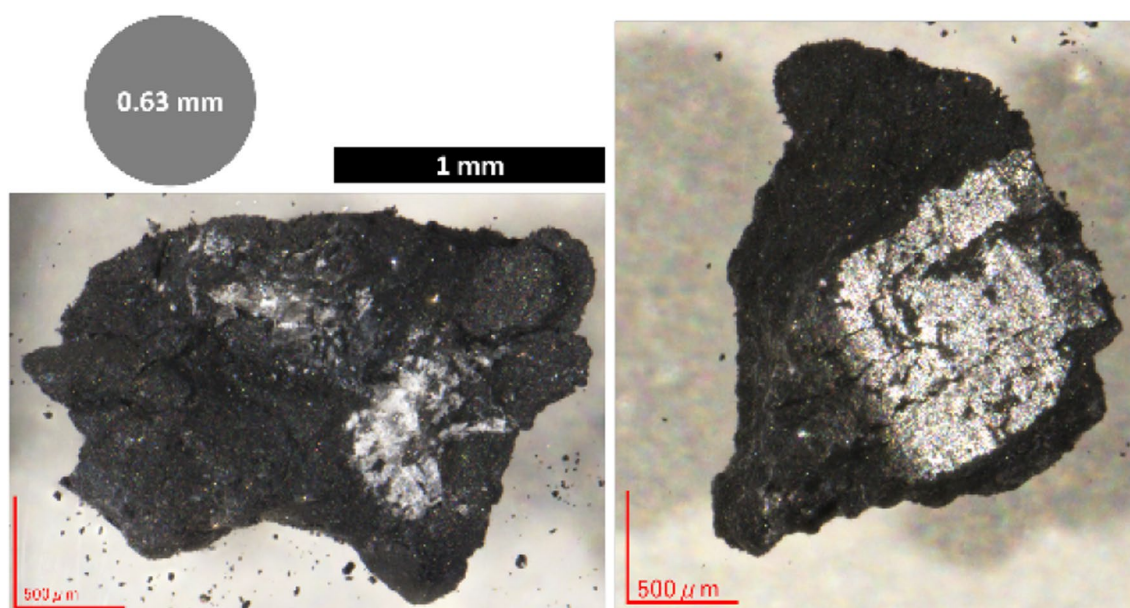
**Fig. 4** **a** Two fragments of returned samples showing smooth (red) and rough (blue) surface textures and **b** smooth (red) and rough (blue) boulders imaged by MasCam during its descent. The scale bars are only approximately applicable at the indicated location. Note the different scale in a) and b). The shown fragments in a) are labeled C0005 (left) and C0008 (right) and were retrieved from the Hayabusa2, Ryugu Sample Curatorial Data Set (Astromaterials Science Research Group (ASRG) 2022)

range from 4 to 64 mm) or dust at its landing site. Instead MasCam imaged a dust-free, dark and rough rock (Fig. 2) nearby its landing site. Within this rock MasCam identified a number of bright millimetre-sized spots that were interpreted to be inclusions (e.g., CAI) as similar features are observed in some carbonaceous chondrites (Jaumann et al. 2019; Schröder et al. 2021; Otto et al. 2021). With a spatial resolution down to 0.1 mm/pixel, these features have sizes ranging between 0.2 mm and 5.4 mm in diameter (Schröder et al. 2021; Otto et al. 2021) and comprise about 7.6% of the rock imaged with the rest being darker matrix (Schröder et al. 2021). Their average size appears to be slightly larger than that of similar features common to carbonaceous chondrites (Otto et al. 2021). However, such inclusions could not be identified in the returned samples, in fact there are no intact CAI or chondrules in the returned samples even on the sub-millimetre scale (Yada et al. 2022; Nakamura et al. 2022), which reflects a high degree of aqueous alteration. However, Pilorget et al. (2022) report on the presence of bright isolated grains and structures on scales  $< 50 \mu\text{m}$  that are comparable to MasCam's observations of bright spots. Most of these, however, fade to average brightness when changing the observation geometry, which was not possible to do with MasCam. Yumoto et al. (2022) explained the bright spots in the samples and the ones seen by MasCam as specular reflections and Nakamura et al. (2022) identified flat surfaces covered with a  $2 \mu\text{m}$  thick saponite-rich layer that may cause such reflections. However, the large number as

well as the variation in colour of the bright spots seen by MasCam make this unlikely to be the sole explanation for the bright spots. It is more realistic that MasCam imaged inclusions (Schröder et al. 2022). The presence of inclusions in the rock imaged by MasCam and the lack of such features in the returned samples may hint that there are different types of material present on Ryugu, possibly originating from the two impacting parent bodies.

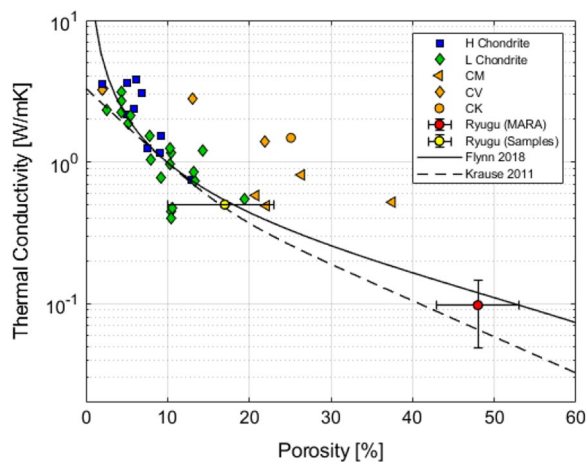
The Ryugu Sample Database (Astromaterials Science Research Group (ASRG) 2022) shows microscope images and photos of 704 individual returned particles between 0.6 mm and 10.3 mm in size. Although this collection may not be complete, some grains show distinct specular reflections and brighter patches in the sub-millimetre size range (e.g., A0038, A0136, A306, C0041). However, unlike inclusions, the brighter patches exhibit indistinct boundaries (Fig. 5). It is possible that MasCam imaged a rock with brighter patches similar to those seen in the returned samples, but did not resolve the boundary making a distinction between inclusions and areas with indistinct boundaries difficult.

Pilorget et al. (2022) show individual carbonate and NH-rich grains in the returned sample material. Although, the grains are not illustrated in the visible wavelengths at which MasCam operated, compositional heterogeneities appear to exist at the sub-millimetre scale. It is possible that such grains are fragments of larger grains that may have been shattered during the sampling process or the landing of the return capsule and



**Fig. 5** Two examples of grains with brighter patches (left: C0041, right: A0038). The gray circle in the top left illustrates the average size of the inclusions identified by MasCam. The images are retrieved from the Hayabusa2, Ryugu Sample Curatorial Data Set (Astromaterials Science Research Group (ASRG) 2022)





**Fig. 6** Thermal conductivity as a function of porosity for different meteorite samples. For reference, the models proposed by Flynn et al. (2018) and Krause et al. (2011) are also shown. Thermal conductivity of the MASCOT rock was estimated based on the analysis of Hamm et al. (2022). Thermal inertia and thermal conductivity relate to each other following Eq. 1. The porosity and thermal conductivity for the Ryugu samples (Nakamura et al. 2022) is indicated

that these grains could have been identified as inclusions by MasCam.

Schröder et al. (2021) also investigated the colour and reflectivity of the inclusions imaged by MasCam in the visible wavelengths and found blue as well as red inclusions. These inclusions are up to two times brighter than the surrounding matrix, independent of their size or colour. A possible explanation for their colour may be the presence of phyllosilicates, Fe-rich oxides, or spinel which may give rise to a red slope and an enrichment in olivine may cause a blue appearance (Schröder et al. 2021). The spots imaged by MasCam have a mean diameter of  $0.63 \pm 0.91$  mm, which is comparatively large in the context of other carbonaceous chondrites (Schröder et al. 2021; Otto et al. 2021). Yumoto et al. (2022) imaged the returned samples as a whole as well as 69 individual particles with sizes ranging between 1 and 7 mm at visible wavelengths corresponding to the ONC filters with a spatial resolution down to  $\sim 20$   $\mu\text{m}/\text{pixel}$ . They report on predominantly red sub-millimetre sized spots in the returned samples, which are up to ten times brighter than the average and ubiquitous on the returned samples. They argue that these spots, and similarly the red spots identified by MasCam, may be specular reflections, while the blue spots may be carbonate-rich inclusions. Other materials that could give rise to the spot-like bright appearance, such as sulphides, have also been detected within the returned samples (Nakamura et al. 2022).

Yumoto et al. (2022) and Schröder et al. (2021) also investigated the reflectivity in the visible wavelength of

the returned samples and the rock in front of MasCam, respectively. While Yumoto et al. (2022) found that the reflectance of some individual returned fragments is about 30–70% higher than that of global Ryugu as measured by ONC, Schröder et al. (2021) found a reflectance of the rock in front of MasCam in agreement with ONC observations. ONC measured the geometric albedo (phase angle of zero) at which no shadows are visible and MasCam imaged the rock at a low phase angle with almost no shadows, making the comparison straightforward (Schröder et al. 2021).

In general, the reflectance measured by ONC and the powdered returned samples agrees well. The fact that the average Ryugu observed by ONC is slightly brighter than the powdered samples (ratio of 0.9) may be attributed to the particle size of the samples (Nakamura et al. 2022). The dust covered surface on Ryugu before sample collection was brighter than the surface after the dust had been removed by the spacecraft thrusters during the sampling process (Morota et al. 2020). Given that the dust-free rock imaged by MasCam is not significantly darker than average Ryugu, this may imply that dust free surfaces similar to those observed by MasCam are common on Ryugu.

Based on the low reflectivity, the flat spectral slope in the visible wavelengths and the inclusions identified in the rock imaged by MasCam, the rock appears to be similar to carbonaceous chondrites (Jaumann et al. 2019; Schröder et al. 2021; Otto et al. 2021). However, the analyses did not allow to constrain a specific type of carbonaceous chondrite confidently. Suggestions range from CI similar to the Tagish Lake meteorite (Jaumann et al. 2019) to CR or CV based on the relatively large size of the inclusions (Schröder et al. 2021) and also include the possibility that there is no Ryugu equivalent in our terrestrial meteorite collection (Grott et al. 2019; Schröder et al. 2021; Otto et al. 2021). ONC global data hints at thermally metamorphosed carbonaceous chondrites as an appropriate meteorite analogue given the dark nature of Ryugu’s regolith (Sugita et al. 2019). Preliminary investigations of the returned samples suggest that based on their physical properties and bulk chemical composition, CI type carbonaceous chondrites appear to be having most similarities to Ryugu’s samples (Tanaka et al. 2022; Yokoyama et al. 2022), but Ryugu has higher porosity, lower albedo and is more fragile in nature (Yada et al. 2022) and also is compositionally also nearly free of sulfates, ferrihydrites and interlayer water (Yokoyama et al. 2022). This evaluation is shared by the investigation of MARA of the Ryugu rock which is discussed in the following section.



### Comparison with MARA

The thermal inertia of the rock at the MASCOT landing site of  $256 (\pm 43) \text{ J m}^{-2} \text{ K}^{-1} \text{ s}^{-1/2}$  derived from MARA measurements (Hamm et al. 2018, 2022; Grott et al. 2019) is significantly lower than the value determined for the samples, which is  $890 \pm 45 \text{ J m}^{-2} \text{ K}^{-1} \text{ s}^{-1/2}$  (at 298 K) (Nakamura et al. 2022). However, this discrepancy may be caused by the different scales on which the measurements have been taken (Nakamura et al. 2022). Furthermore, it is conceivable that the sampling process introduced a bias towards more consolidated material, while friable particles may have been shed off or destroyed in the process. In situ measurements by MASCOT may have probed material which could have been mechanically weakened by thermal fatigue. The induced cracks would result in a thermal inertia that was lower than that of the more consolidated returned samples.

Preliminary analysis of samples returned to Earth show that the average bulk density of Ryugu sample particles is  $(1282 \pm 231) \text{ kg m}^{-3}$  (Yada et al. 2022), but later analysis taking the 3D shape of the particles into account arrive at higher densities between 1700 and 1900  $\text{kg m}^{-3}$  (Nakamura et al. 2022). Assuming sample grain densities representative for CI and CM carbonaceous chondrites, the microporosity of Ryugu samples can be estimated to be close to 0.10 to 0.23 (Nakamura et al. 2022). This is much smaller than the value derived from in situ measurements (Grott et al. 2019) and the value favoured by Grott et al. (2020), which indicated high microporosities. This may be due to a selection bias for the samples, which need to exhibit some internal strength to survive the energetic sampling process.

To put MARA measurements into context, a summary of meteorite thermal conductivity as a function of porosity is shown in Fig. 6 together with estimates of thermal conductivity for the MASCOT rock and returned samples. The thermal conductivity  $k$  of the rock is derived from the measured thermal inertia  $\Gamma$  using

$$k = \frac{\Gamma^2}{\rho c_p} \quad (1)$$

where  $\rho$  is the bulk density and the heat capacity of the material calculated using Ryugu's average night time temperature of 230 K. The thermal conductivity has then been estimated assuming a heat capacity of  $635 \text{ J kg}^{-1} \text{ K}^{-1}$  (Hemingway et al. 1973). The density  $\rho$  is determined from  $\rho = (1 - \phi)\rho_s$ , where  $\phi$  is porosity and  $\rho_s$  the grain density, for which we assume values between 2120 and 2210  $\text{kg m}^{-3}$ , representative for CI and CM chondrites, respectively (Nakamura et al. 2022). Using the models by Flynn et al., (2018) and Krause et al. (2011), we then derive porosities between 0.43 and,

resulting in thermal conductivities between  $0.049 \text{ W m}^{-1} \text{ K}^{-1}$  and  $0.146 \text{ W m}^{-1} \text{ K}^{-1}$ . Spectral analysis of the returned samples shows an extremely dark optical to near-infrared reflectance and a spectral profile with weak absorptions at 2.7 and 3.4  $\mu\text{m}$  (Pilorget et al. 2022; Yada et al. 2022). This implies the presence of hydrous minerals and organic matter and/or carbonate consistent with the spectral trend found by Hamm et al. (2022). Taken together and considering the absence of submillimetre CAIs and chondrules and the samples' bulk chemical composition (Yokoyama et al. 2022), these findings indicate that Ryugu is most similar to CI chondrites but has lower albedo and higher porosity. Considering that the thermal inertia and tensile strength of a material are both influenced by grain contacts, the thermal conductivity can be used to estimate the tensile strength  $\sigma_t$  (Grott et al. 2019) following the formula:

$$\sigma_t = \frac{\pi}{4000} \frac{k}{k_s} E \quad (2)$$

where  $k$  and  $k_s$  are the thermal conductivity of the bulk material and grain, respectively, and  $E$  is the Young's modulus. This results in an approximate tensile strength of 200–280 kPa for Ryugu's rock investigated by MARA (Grott et al. 2019) and  $\sim 229$  kPa following the same approach applied to TIR data (Grott et al. 2019; Okada et al. 2020; Shimaki et al. 2020). To derive the tensile strength of the returned samples, Kurosawa et al. (2022) (also see (Nakamura et al. 2022)) conducted a three-point flexural bending test. They placed two  $3 \times 3 \text{ mm}^2$  cut pieces of 0.788 mm and 0.950 mm thickness onto two bars of a testing machine and broke the samples by slowly pushing a piston down onto the sample while monitoring the load. They found a peak tensile strength between 3 and 8 MPa much higher than that of estimates using the thermal conductivity and MARA and TIR data. This discrepancy can be explained by the different size scales on which the tensile strength was derived. The tensile strength of brittle materials scales with  $1/\sqrt{L}$  (Bažant 1999), where  $L$  is the characteristic length of the investigated sample. The size of the sample on which the tensile strength test has been conducted is about two orders of magnitude smaller than the characteristic length (a few thermal skin depths,  $\sim$  decimetre) of the rocks on Ryugu. Thus, considering the above-mentioned scaling relation, these values agree with each other (Biele et al. 2022).

### Comparison with MasMag

Magnetic mineral characterization based on microscopic measurements of Ryugu samples show magnetite particles of various shapes (framboid, spherulite particles or dodecahedrons) and sizes (0.2–10  $\mu\text{m}$ ) (Dobrić et al.

2022; Yamaguchi et al. 2022) comprising 4–7% of the total grain volume (Yamaguchi et al. 2022). The measured mass specific susceptibility ( $8.39 \times 10^{-5} \text{ m}^3/\text{kg}$ ), the saturation remanence/saturation magnetization ratio (0.09), and the coercivity of remanence/coercivity ratio (5) (Sato et al. 2022; Tanaka et al. 2022; Nakamura et al. 2022) corresponds to values similar to those observed in carbonaceous chondrites (e.g., Thorpe et al. 2002; Rochette et al. 2003; Sridhar et al. 2021). The particles were also characterized magnetically in terms of low-temperature remanence cycles, isothermal remanence gradient curve, and first-order reversal curve measurements, indicating that the fine-grained framboidal magnetite, coarse-grained magnetite, and pyrrhotite are dominant ferromagnetic minerals in Ryugu particles (Sato et al. 2022). The natural remanence measurements of two Ryugu particles of 0.1–1 mm scale show stable vector components with a total specific moment of  $\sim 10^{-2} \text{ Am}^2/\text{kg}$ , and the stable components are likely carried by the framboidal magnetite (Sato et al. 2022; Nakamura et al. 2022). The value corresponds well to the specific magnetic moment of chondrites. The lithological structure of the returned samples indicates that the magnetization scale is likely within the scale of the brecciated domain size of a few 100s of micrometres as these are randomly distributed in the matrix. This is consistent with the observations that the remanence intensity of 0.1–1 mm sized materials ( $\sim 10^{-2} \text{ Am}^2/\text{kg}$  (Sato et al. 2022)) is orders of magnitude larger than those of decimetre sized materials ( $\sim 10^{-5} \text{ Am}^2/\text{kg}$  (Hercik et al. 2020)).

## Discussion

A primary scientific objective of MASCOT was to provide a link between orbiter observations of the asteroid Ryugu and the samples returned from it by conducting in situ asteroid science. Table 1 lists the measurements conducted by MASCOT and their corresponding findings from the returned samples and the orbiter instruments where available. Most of the listed properties could be derived from MasCam and MARA. Properties that agree at all scales, from the returned sample, in situ and orbiter investigations include characteristics derived from images, such as the surface texture of particles/boulders, the colour in the visible wavelength, and the potential meteorite analogue (suggested to be a CI carbonaceous chondrite), as well as characteristics derived from thermal measurements, such as density, porosity and closest meteorite analogue.

In general, MASCOT's observations appear to have a greater overlap with orbiter observations, including the reflectance in the visible wavelengths, thermal inertia and derived tensile strength, compared to returned

samples measured at smaller scales. This seems to imply that at a spatial scale below MASCOT's resolution (sub-millimetre to centimetre), these properties increase in magnitude. With returned particles being several millimetres in size at most, the scale at which the reflectance and thermal inertia (and the derived scale-dependent tensile strength) change appears to be in the millimetre range. Indeed, this range also describes the scale, and below, at which roughness begins to dominate the photometric behaviour of a regolith (Labarre et al. 2017). The scale also represents the diurnal skin depth of Ryugu regolith ( $\sim 3\text{--}10 \text{ mm}$  (Hamm et al. 2022)), the characteristic length scale for thermal measurements. Thus, it is not surprising that measurements from MASCOT and the returned samples differ and the spatial scale at which this difference occurs is in agreement with MASCOT's observations.

There is a divergence of the particle size frequency distributions observed on different scales. While MasCam did not see any grains or fine particles, the power index of boulders  $> 5 \text{ m}$  is much smaller than the one of the returned sample fragments, possibly caused by further fragmentation of the samples during and after the sampling process (Yada et al. 2022). This can also explain why there are no particles visible in the MasCam images equivalently sized to the returned sample fragments. Another possible explanation for the absence of fine particles at the MASCOT landing site is that fine grains may be present inside pores (Morota et al. 2020) and are thus not visible in images from MasCam.

MasCam identified inclusions (Jaumann et al. 2019), while the returned samples are depleted in inclusions (Yada et al. 2022), but no equivalent observation could be made by the orbiter because of its lower spatial resolution. Due to the presence of different rock types on Ryugu that have been identified by ONC and MasCam data (Sugita et al. 2019; Jaumann et al. 2019), it cannot be excluded that the rock imaged by MasCam is of a different type than the returned samples. In addition, some of the identified inclusions could also be specular reflections (Yumoto et al. 2022; Schröder et al. 2022).

In all cases in which the orbiter and returned sample observations agree, MASCOT confirmed these observations and thus links meter and sub-millimetre scale observations. However, there are also some observations that are unique to MASCOT, such as the detection of inclusions/clasts in the rock at MASCOT's landing site and absence of fine particles on the asteroid surface (Jaumann et al. 2019). Although it can be assumed that the returned samples are generally a good representative of Ryugu's regolith in terms of their morphology and composition (Yada et al. 2022; Tachibana et al. 2022), MASCOT shows that heterogeneities within the rock and on

the asteroid surface exist on millimetre scales. Although some of MASCOT's unique observations could also be retrieved from more returned sample material, this is not a highly ranked requirement for future missions given that Earth-based analytical methods can be performed on much smaller samples (Sawada et al. 2017). Thus, MASCOT has proven to be a valuable addition to the Hayabusa2 mission providing additional scientific output, confirming observations, and bridging the gap in spatial resolution between the orbiter and the returned samples. MASCOT provides critical in situ context for the returned samples and confirms the value of including surface science packages on future sample return missions (Ulamec et al. 2014; Lange et al. 2018).

## Conclusion

We have revisited the findings of the MASCOT lander onboard Hayabusa2 that was delivered to the surface of asteroid Ryugu and related its scientific findings to those of the returned samples and the orbiter instruments. MASCOT's in situ observations on centimetre to millimetre spatial scales has proven to be a valuable link between orbiter observations and laboratory investigations of the returned samples. MASCOT allowed a close view of undisturbed surface material of a C-type asteroid, a first measurement of its kind. While confirming some observations, such as the surface texture of particles/boulders, the colour in the visible wavelength, the density, the porosity and the type of potential meteorite analogue, MASCOT has also provided knowledge about inclusions in rocks and the presence of dust-free surfaces at scales that could not be retrieved from the returned samples and the Hayabusa2 orbiter. We conclude that the delivery of a lander on a planetary body provides valuable information that supports remote sensing as well as returned sample analyses.

## Abbreviations

CAI	Calcium–aluminium-rich inclusions
LED	Light emitting diode
MARA	MASCOT Radiometer
MasCam	MASCOT Camera
MASCOT	Mobile Asteroid Surface Scout
MasMag	MASCOT Magnetometer
MicrOmega	MASCOT Hyperspectral Microscope
ONC	Optical Navigation Camera
TIR	Thermal Infrared Imager
NIRS3	Near Infrared Spectrometer
SCI	Small Carry-on Impactor
RMS	Root Mean Square

## Acknowledgements

We gratefully acknowledge the dedication and commitment of the Hayabusa2 and MASCOT teams that made this work possible. We thank two anonymous reviewers for their helpful comments.

## Author contributions

K.A.O. coordinated co-author contributions, led interpretations and compiled the article. M.G., D.H., M.H., T.-M.H., R.J., M.S. and S.U. contributed to the writing. J.B., J.K., T.N., S.E.S., S.T. and H.Y. contributed to the interpretation and provided information on specific topics. All authors discussed the results and commented on the manuscript. All authors read and approved the final manuscript.

## Funding

Open Access funding enabled and organized by Projekt DEAL. The team acknowledges funding by DLR and CNES.

## Availability of data and materials

This manuscript is based on previously published data. Please refer to the quoted references for details.

## Declarations

### Ethics approval and consent to participate

Not applicable.

### Consent for publication

Not applicable.

### Competing interests

The authors declare that they have no known competing financial interests or personal relationships that could have appeared to influence the work reported in this paper.

## Author details

<sup>1</sup>German Aerospace Center (DLR), Institute of Planetary Research, Berlin, Germany. <sup>2</sup>Hiroshima University, Department of Earth and Planetary Systems Science, Higashi-Hiroshima, Japan. <sup>3</sup>German Aerospace Center (DLR), Institute of Space Systems, Bremen, Germany. <sup>4</sup>German Aerospace Center (DLR), Space Operations and Astronaut Training, Cologne, Germany. <sup>5</sup>Institute d'Astrophysique Spatiale, Orsay, France. <sup>6</sup>Free University Berlin, Institute of Geological Sciences, Berlin, Germany. <sup>7</sup>Institute of Atmospheric Physics (CAS), Prague, Czech Republic. <sup>8</sup>University of Tokyo, Department of Earth and Planetary Science, Tokyo, Japan. <sup>9</sup>Luleå University of Technology, Department of Computer Science, Electrical and Space Engineering, Kiruna, Sweden. <sup>10</sup>Japan Aerospace Exploration Agency (JAXA), Institute of Space and Astronautical Science (ISAS), Sagami-hara, Japan. <sup>11</sup>Technical University Braunschweig, Institute of Geophysics and Extraterrestrial Physics, Brunswick, Germany. <sup>12</sup>University of Aizu, Center for Advanced Information Science and Technology (CAIST), Fukushima, Japan. <sup>13</sup>Centre National d'Etudes Spatiales (CNES), Toulouse, France. <sup>14</sup>Tohoku University, Department of Earth Sciences, Sendai, Japan. <sup>15</sup>Planetary Exploration Research Center, Chiba Institute of Technology, Chiba, Japan.

Received: 26 August 2022 Accepted: 27 February 2023

Published online: 06 April 2023

## References

- Acuña MH, Anderson BJ, Russell CT et al (2002) NEAR Magnetic Field Observations at 433 Eros: first Measurements from the Surface of an Asteroid. *Icarus* 155:220–228. <https://doi.org/10.1006/icar.2001.6772>
- Arakawa M, Saiki T, Wada K et al (2020) An artificial impact on the asteroid (162173) Ryugu formed a crater in the gravity-dominated regime. *Science* 368:67–71. <https://doi.org/10.1126/science.aaz1701>
- Astromaterials Science Research Group (ASRG) (2022) Institute of Space and Astronautical Science (ISAS), Japan Aerospace Exploration Agency (JAXA), CNES TIDS (IAS): Hayabusa2, Ryugu Sample Curatorial Dataset. <https://doi.org/10.17597/ISAS.DARTS/CUR-Ryugu-description>
- Auster H-U, Apathy I, Berghofer G et al (2015) The nonmagnetic nucleus of comet 67P/Churyumov-Gerasimenko. *Science* 349:5102. <https://doi.org/10.1126/science.aaa5102>

- Bažant ZP (1999) Size effect on structural strength: a review. *Arch Appl Mech* 69:703–725. <https://doi.org/10.1007/s004190050252>
- Bibring J-P, Hamm V, Langevin Y et al (2017) The MicrOmega Investigation Onboard Hayabusa2. *Space Sci Rev* 208:401–412. <https://doi.org/10.1007/s11214-017-0335-y>
- Bibring J-P, Pilorget C, Riu L et al (2022) MicrOmega/MASCOT first results. *Planet Space Sci* 210:105393. <https://doi.org/10.1016/j.pss.2021.105393>
- Biele J, Kührt E, Senshu H et al (2019) Effects of dust layers on thermal emission from airless bodies. *Prog Earth Planet Sci* 6:48. <https://doi.org/10.1186/s40645-019-0291-0>
- Biele J, Vincent J-B, Knollenberg J (2022) Mechanical properties of cometary surfaces. *Universe* 8:487. <https://doi.org/10.3390/universe8090487>
- Dobrică E, Ishii HA, Bradley JP et al (2022) Nanoscale Investigation of Various Magnetite Morphologies in the Samples Returned from C-Type Asteroid Ryugu: Insights into the Aqueous Alteration Processes. In: 53rd Lunar and Planetary Science Conference. LPI Contribution No. 2678, The Woodlands, Texas, USA, 7–11 March 2022, #2188
- Flynn GJ, Consolmagno GJ, Brown P, Macke RJ (2018) Physical properties of the stone meteorites: Implications for the properties of their parent bodies. *Geochemistry* 78:269–298. <https://doi.org/10.1016/j.chemer.2017.04.002>
- Gattacceca J, Rochette P (2004) Toward a robust normalized magnetic paleointensity method applied to meteorites. *Earth Planet Sci Lett* 227:377–393. <https://doi.org/10.1016/j.epsl.2004.09.013>
- Grott M, Knollenberg J, Borgs B et al (2017) The MASCOT radiometer MARA for the Hayabusa 2 mission. *Space Sci Rev* 208:413–431. <https://doi.org/10.1007/s11214-016-0272-1>
- Grott M, Knollenberg J, Hamm M et al (2019) Low thermal conductivity boulder with high porosity identified on C-type asteroid (162173) Ryugu. *Nat Astron* 3:971–976. <https://doi.org/10.1038/s41550-019-0832-x>
- Grott M, Biele J, Michel P et al (2020) Macroporosity and grain density of rubble pile asteroid (162173) Ryugu. *J Geophys Res: Planets* 125:6519. <https://doi.org/10.1029/2020JE006519>
- Hamm M, Grott M, Kührt E et al (2018) A method to derive surface thermophysical properties of asteroid (162173) Ryugu (1999JU3) from in-situ surface brightness temperature measurements. *Planet Space Sci* 159:1–10. <https://doi.org/10.1016/j.pss.2018.03.017>
- Hamm M, Pelivan I, Grott M, de Wiljes J (2020) Thermophysical modelling and parameter estimation of small Solar system bodies via data assimilation. *Mon Not R Astron Soc* 496:2776–2785. <https://doi.org/10.1093/mnras/staa1755>
- Hamm M, Grott M, Senshu H et al (2022) Mid-infrared emissivity of partially dehydrated asteroid (162173) Ryugu shows strong signs of aqueous alteration. *Nat Commun* 13:364. <https://doi.org/10.1038/s41467-022-28051-y>
- Hemingway BS, Robie RA, Wilson WH (1973) Specific heats of lunar soils, basalt, and breccias from the Apollo 14, 15, and 16 landing sites, between 90 and 350°K. *Lunar and Planetary Science Conference Proceedings*. 4:2481
- Herbst W, Greenwood JP, Yap TE (2021) The Macroporosity of Rubble Pile Asteroid Ryugu and Implications for the Origin of Chondrules. *Planet Sci J* 2:110. <https://doi.org/10.3847/PSJ/abf7c0>
- Herbst W, Greenwood JP (2022) Why are chondrules rare or absent in the Ryugu samples? In: 53rd Lunar and Planetary Science Conference. LPI Contribution No. 2678, The Woodlands, Texas, USA, 7–11 March 2022, #1589
- Herčík D, Auster H-U, Blum J et al (2017) The MASCOT Magnetometer. *Space Sci Rev* 208:433–449. <https://doi.org/10.1007/s11214-016-0236-5>
- Hercik D, Auster H-U, Constantinescu D et al (2020) Magnetic properties of asteroid (162173) Ryugu. *J Geophys Res: Planets* 125:6035. <https://doi.org/10.1029/2019JE006035>
- Ho T-M, Baturkin V, Grimm C et al (2017) MASCOT—the mobile asteroid surface scout onboard the Hayabusa2 mission. *Space Sci Rev* 208:339–374. <https://doi.org/10.1007/s11214-016-0251-6>
- Ho T-M, Jaumann R, Bibring J-P et al (2021) The MASCOT lander aboard Hayabusa2: the in-situ exploration of NEA (162173) Ryugu. *Planet Space Sci*. <https://doi.org/10.1016/j.pss.2021.105200>
- Ito M, Tomioka N, Uesugi M et al (2022) A pristine record of outer Solar System materials from asteroid Ryugu's returned sample. *Nat Astron* 6:1163–1171. <https://doi.org/10.1038/s41550-022-01745-5>
- Iwata T, Kitazato K, Abe M et al (2017) NIRS3: the near infrared spectrometer on Hayabusa2. *Space Sci Rev* 208:317–337. <https://doi.org/10.1007/s11214-017-0341-0>
- Jaumann R, Schmitz N, Koncz A et al (2017) The camera of the MASCOT asteroid lander on board Hayabusa 2. *Space Sci Rev* 208:375–400. <https://doi.org/10.1007/s11214-016-0263-2>
- Jaumann R, Schmitz N, Ho T-M et al (2019) Images from the surface of asteroid Ryugu show rocks similar to carbonaceous chondrite meteorites. *Science* 365:817–820. <https://doi.org/10.1126/science.aaw8627>
- Kameda S, Suzuki H, Takamatsu T et al (2017) Preflight calibration test results for optical navigation camera telescope (ONC-T) onboard the Hayabusa2 spacecraft. *Space Sci Rev* 208:17–31. <https://doi.org/10.1007/s11214-015-0227-y>
- Kitazato K, Milliken RE, Iwata T et al (2019) The surface composition of asteroid 162173 Ryugu from Hayabusa2 near-infrared spectroscopy. *Science* 364:272–275. <https://doi.org/10.1126/science.aav7432>
- Krause M, Blum J, Skorov YuV, Trieloff M (2011) Thermal conductivity measurements of porous dust aggregates: I. technique, model and first results. *Icarus* 214:286–296. <https://doi.org/10.1016/j.icarus.2011.04.024>
- Kurosawa K, Tanaka S, Ino Y, et al (2022) Tensile (Flexural) Strength of Ryugu Grain C0002. In: 53rd Lunar and Planetary Science Conference. LPI Contribution No. 2678, The Woodlands, Texas, USA, 7–11 March 2022, #1378
- Labarre S, Ferrari C, Jacquemoud S (2017) Surface roughness retrieval by inversion of the Hapke model: a multiscale approach. *Icarus* 290:63–80. <https://doi.org/10.1016/j.icarus.2017.02.030>
- Lange C, Ho T-M, Grimm CD et al (2018) Exploring small bodies: nano- and microlander options derived from the mobile asteroid surface scout. *Adv Space Res* 62:2055–2083. <https://doi.org/10.1016/j.asr.2018.05.013>
- Lange C, Yoshimitsu T, Ulamec S et al (2020) Micro- and nanolander on the surface of Ryugu – Commonalities, differences and lessons learned for future microgravity exploration. *Planet Space Sci* 194:105094. <https://doi.org/10.1016/j.pss.2020.105094>
- Michikami T, Honda C, Miyamoto H et al (2019) Boulder size and shape distributions on asteroid Ryugu. *Icarus* 331:179–191. <https://doi.org/10.1016/j.icarus.2019.05.019>
- Morota T, Sugita S, Cho Y et al (2020) Sample collection from asteroid (162173) Ryugu by Hayabusa 2: Implications for surface evolution. *Science* 368:654–659. <https://doi.org/10.1126/science.aaz6306>
- Nakamura T, Matsumoto M, Amano K et al (2022) Formation and evolution of carbonaceous asteroid Ryugu: direct evidence from returned samples. *Science*. <https://doi.org/10.1126/science.abn8671>
- Okada T, Fukuhara T, Tanaka S et al (2017) Thermal infrared imaging experiments of C-type asteroid 162173 Ryugu on Hayabusa2. *Space Sci Rev* 208:255–286. <https://doi.org/10.1007/s11214-016-0286-8>
- Okada T, Fukuhara T, Tanaka S et al (2020) Highly porous nature of a primitive asteroid revealed by thermal imaging. *Nature*. <https://doi.org/10.1038/s41586-020-2102-6>
- Otto KA, Matz K-D, Schröder SE et al (2020) Surface roughness of asteroid (162173) Ryugu and comet 67P/Churyumov–Gerasimenko inferred from in situ observations. *Mon Not R Astron Soc* 500:3178–3193. <https://doi.org/10.1093/mnras/staa3314>
- Otto KA, Schröder SE, Scharf HD et al (2021) Spectral and petrographic properties of inclusions in carbonaceous chondrites and comparison with in situ images from asteroid Ryugu. *Planet Sci J* 2:188. <https://doi.org/10.3847/PSJ/ac034b>
- Pilorget C, Okada T, Hamm V et al (2022) First compositional analysis of Ryugu samples by the MicrOmega hyperspectral microscope. *Nat Astron* 6:221–225. <https://doi.org/10.1038/s41550-021-01549-z>
- Rochette P, Sagnotti L, Bourot-Denise M et al (2003) Magnetic classification of stony meteorites: 1 Ordinary Chondrites. *Meteorit Planet Sci* 38:251–268. <https://doi.org/10.1111/j.1945-5100.2003.tb00263.x>
- Sakatani N, Tanaka S, Okada T et al (2021) Anomalously porous boulders on (162173) Ryugu as primordial materials from its parent body. *Nat Astron* 5:766–774. <https://doi.org/10.1038/s41550-021-01371-7>
- Sato M, Kimura Y, Tanaka S et al (2022) Rock Magnetic Characterization of Returned Samples From Asteroid (162173) Ryugu: Implications for Paleomagnetic Interpretation and Paleointensity Estimation. *J Geophys Res: Planets* 127:e2022JE7405. <https://doi.org/10.1029/2022JE007405>
- Sawada H, Okazaki R, Tachibana S et al (2017) Hayabusa2 Sampler: collection of asteroidal surface material. *Space Sci Rev* 208:81–106. <https://doi.org/10.1007/s11214-017-0338-8>
- Scholten F, Preusker F, Elgner S et al (2019) The Hayabusa2 lander MASCOT on the surface of Asteroid (162173) Ryugu - Stereo-photogrammetric



- analysis of MASCam image data. *A&A* 632:1–6. <https://doi.org/10.1051/0004-6361/201936760>
- Schröder S, Otto K, Scharf H et al (2021) Spectrophotometric analysis of the Ryugu rock seen by MASCOT: searching for a carbonaceous chondrite analog. *Planet Sci J* 2:58. <https://doi.org/10.3847/PSJ/abbb97>
- Schröder S, Sakatani N, Honda R et al (2022) Characterization of the MASCOT landing area by Hayabusa2. *A&A* 666:A164. <https://doi.org/10.1051/0004-6361/202244059>
- Shimaki Y, Senshu H, Sakatani N et al (2020) Thermophysical properties of the surface of asteroid 162173 Ryugu: infrared observations and thermal inertia mapping. *Icarus* 348:113835. <https://doi.org/10.1016/j.icarus.2020.113835>
- Sridhar S, Bryson JFJ, King AJ, Harrison RJ (2021) Constraints on the ice composition of carbonaceous chondrites from their magnetic mineralogy. *Earth Planet Sci Lett* 576:117243. <https://doi.org/10.1016/j.epsl.2021.117243>
- Sugita S, Honda R, Morota T et al (2019) The geomorphology, color, and thermal properties of Ryugu: Implications for parent-body processes. *Science* 364:1–11. <https://doi.org/10.1126/science.aaw0422>
- Tachibana S (2019) Hayabusa2: sample acquisition at a near-earth C-type Asteroid Ryugu and analysis plan of returned samples. *Microsc Microanal* 25:2442–2443. <https://doi.org/10.1017/S1431927619012947>
- Tachibana S, Sawada H, Okazaki R et al (2022) Pebbles and sand on asteroid (162173) Ryugu: in situ observation and particles returned to Earth. *Science* 375:1011–1016. <https://doi.org/10.1126/science.abj8624>
- Tanaka S, Nagano H, Yagi T, et al (2022) Physical properties of the returned sample of Ryugu by Hayabusa2 mission. In: 53rd Lunar and Planetary Science Conference. LPI Contribution No. 2678, The Woodlands, Texas, USA, 7–11 March 2022, #1373
- Tatsumi E, Domingue D, Yokota Y et al (2020) Global photometric properties of (162173) Ryugu. *Astron Astrophys* 639:1–19. <https://doi.org/10.1051/0004-6361/201937096>
- Tatsumi E, Sakatani N, Riu L et al (2021) Spectrally blue hydrated parent body of asteroid (162173) Ryugu. *Nat Commun* 12:5837. <https://doi.org/10.1038/s41467-021-26071-8>
- Terho M, Pesonen LJ, Kukkonen IT (1996) Magnetic properties of asteroids from meteorite data — Implications for magnetic anomaly detections. *Earth Moon Planet* 72:225–231. <https://doi.org/10.1007/BF00117522>
- Thorpe AN, Senftle FE, Grant JR (2002) Magnetic study of magnetite in the Tagish Lake meteorite. *Meteorit Planet Sci* 37:763–771. <https://doi.org/10.1111/j.1945-5100.2002.tb00853.x>
- Tsuchiyama A, Matsumoto M, Matsuno J, et al (2022) Mineralogical, Petrological, and Physical Properties of Ryugu Samples Using X-Ray Nanotomography. In: 53rd Lunar and Planetary Science Conference. LPI Contribution No. 2678, The Woodlands, Texas, USA, 7–11 March 2022, #1858
- Ulamec S, Biele J, Bousquet P-W et al (2014) Landing on small bodies: from the Rosetta Lander to MASCOT and beyond. *Acta Astronaut* 93:460–466. <https://doi.org/10.1016/j.actaastro.2013.02.007>
- Watanabe S, Tsuda Y, Yoshikawa M et al (2017) Hayabusa2 mission overview. *Space Sci Rev* 208:3–16. <https://doi.org/10.1007/s11214-017-0377-1>
- Watanabe S, Hirabayashi M, Hirata N et al (2019) Hayabusa2 arrives at the carbonaceous asteroid 162173 Ryugu - A spinning top-shaped rubble pile. *Science* 364:268–272. <https://doi.org/10.1126/science.aav8032>
- Yada T, Abe M, Okada T et al (2022) Preliminary analysis of the Hayabusa2 samples returned from C-type asteroid Ryugu. *Nat Astron* 6:214–220. <https://doi.org/10.1038/s41550-021-01550-6>
- Yamaguchi A, Kimura M, Ito M, et al (2022) Petrology of Asteroid Ryugu particles Allocated to the Phase2 Curation Kochi Team. In: 53rd Lunar and Planetary Science Conference. LPI Contribution No. 2678, The Woodlands, Texas, USA, 7–11 March 2022, #1822
- Yokoyama T, Nagashima K, Nakai I, et al (2022) Samples returned from the asteroid Ryugu are similar to Ivuna-type carbonaceous meteorites. *Science* 375:7850. <https://doi.org/10.1126/science.abn7850>
- Yumoto K, Cho Y, Yabe Y, et al (2022) Visible Multi-Band Spectra and Specular Reflectivity of Ryugu Returned Samples. In: 53rd Lunar and Planetary Science Conference. LPI Contribution No. 2678, The Woodlands, Texas, USA, 7–11 March 2022, #1326

## Publisher's Note

Springer Nature remains neutral with regard to jurisdictional claims in published maps and institutional affiliations.

Submit your manuscript to a SpringerOpen® journal and benefit from:

- Convenient online submission
- Rigorous peer review
- Open access: articles freely available online
- High visibility within the field
- Retaining the copyright to your article

Submit your next manuscript at ► [springeropen.com](https://www.springeropen.com)

## 5 References

- Arakawa, M., Saiki, T., Wada, K., Ogawa, K., Kadono, T., Shirai, K., Sawada, H., Ishibashi, K., Honda, R., . . . Miura, A. (2020). An Artificial Impact on the Asteroid (162173) Ryugu Formed a Crater in the Gravity-dominated Regime. *Science*, *368*(6486), 67–71. <https://doi.org/10.1126/science.aaz1701>
- Attree, N., Groussin, O., Jorda, L., Nébouy, D., Thomas, N., Brouet, Y., Kührt, E., Preusker, F., Scholten, F., . . . Shi, X. (2018). Tensile Strength of 67P/Churyumov-Gerasimenko Nucleus Material from Overhangs. *Astronomy & Astrophysics*, *611*(A33), 1–12. <https://doi.org/10.1051/0004-6361/201732155>
- Belton, M. J. S., Veverka, J., Thomas, P., Helfenstein, P., Simonelli, D., Chapman, C., Davies, M. E., Greeley, R., Greenberg, R., . . . Pilcher, C. (1992). Galileo Encounter with 951 Gaspra: First Pictures of an Asteroid. *Science*, *257*(5077), 1647–1652. <https://doi.org/10.1126/science.257.5077.1647>
- Biele, J., Vincent, J.-B., & Knollenberg, J. (2022). Mechanical Properties of Cometary Surfaces. *Universe*, *8*(99), 487. <https://doi.org/10.3390/universe8090487>
- Bierwisch, C., Kraft, T., Riedel, H., & Moseler, M. (2009). Three-dimensional Discrete Element Models for the Granular Statics and Dynamics of Powders in Cavity Filling. *Journal of the Mechanics and Physics of Solids*, *57*(1), 10–31. <https://doi.org/10.1016/j.jmps.2008.10.006>
- Bischoff, D., Gundlach, B., Neuhaus, M., & Blum, J. (2019). Experiments on Cometary Activity: Ejection of Dust Aggregates from a Sublimating Water-ice Surface. *Monthly Notices of the Royal Astronomical Society*, *483*(1), 1202–1210. <https://doi.org/10.1093/mnras/sty3182>
- Bockelée-Morvan, D., Crovisier, J., Mumma, M. J., & Weaver, H. A. (2004). The Composition of Cometary Volatiles. In M. Festou, H. U. Keller, & H. A. Weaver (Eds.), *Comets II* (pp. 391–423). The University of Arizona Press.
- Boehnhardt, H., Bibring, J.-P., Apathy, I., Auster, H. U., Ercoli Finzi, A., Goesmann, F., Klingelhöfer, G., Knapmeyer, M., Kofman, W., . . . Wright, I. (2017). The Philae Lander Mission and Science Overview. *Philosophical Transactions of the*

## 5 References

- Royal Society A: Mathematical, Physical and Engineering Sciences*, 375(2097), 20160248. <https://doi.org/10.1098/rsta.2016.0248>
- Bus, S. J., & Binzel, R. P. (2002). Phase II of the Small Main-Belt Asteroid Spectroscopic Survey: A Feature-Based Taxonomy. *Icarus*, 158(1), 146–177. <https://doi.org/10.1006/icar.2002.6856>
- Castillo-Rogez, J. C., Neveu, M., Scully, J. E., House, C. H., Quick, L. C., Bouquet, A., Miller, K., Bland, M., De Sanctis, M. C., . . . Young, E. (2020). Ceres: Astrobiological Target and Possible Ocean World. *Astrobiology*, 20(2), 269–291. <https://doi.org/10.1089/ast.2018.1999>
- Clark, B. E., Hapke, B., Pieters, C., & Britt, D. (2002). Asteroid Space Weathering and Regolith Evolution. *Asteroids III*, 1, 585–599.
- De Sanctis, M. C., Ammannito, E., Raponi, A., Frigeri, A., Ferrari, M., Carrozzo, F. G., Ciarniello, M., Formisano, M., Rousseau, B., . . . Russell, C. T. (2020). Fresh Emplacement of Hydrated Sodium Chloride on Ceres from Ascending Salty Fluids. *Nature Astronomy*, 4(8), 786–793. <https://doi.org/10.1038/s41550-020-1138-8>
- DellaGiustina, D., Golish, D. R., Guzewich, S., Moreau, M., Nolan, M. C., Polit, A. T., & Simon, A. A. (2022). OSIRIS-APEX: A Proposed OSIRIS-REx Extended Mission to Apophis. *Apophis T-7 Years: Knowledge Opportunities for the Science of Planetary Defense, virtually, 11.-12. May 2022, LPI Contrib. No. 2681, #2011*.
- DeMeo, F. E., Binzel, R. P., Slivan, S. M., & Bus, S. J. (2009). An Extension of the Bus Asteroid Taxonomy into the Near-infrared. *Icarus*, 202(1), 160–180. <https://doi.org/10.1016/j.icarus.2009.02.005>
- DeMeo, F. E., Alexander, C. M. O., Walsh, K. J., Chapman, C. R., & Binzel, R. P. (2015). The Compositional Structure of the Asteroid Belt. In P. Michel, F. E. DeMeo, & W. F. Bottke (Eds.), *Asteroids IV*. University of Arizona Press. [https://doi.org/10.2458/azu\\_uapress\\_9780816532131-ch002](https://doi.org/10.2458/azu_uapress_9780816532131-ch002)
- DeMeo, F. E., Burt, B. J., Marsset, M., Polishook, D., Burbine, T. H., Carry, B., Binzel, R. P., Vernazza, P., Reddy, V., . . . Bus, S. J. (2022). Connecting Asteroids and Meteorites with Visible and Near-infrared Spectroscopy. *Icarus*, 380, 114971. <https://doi.org/10.1016/j.icarus.2022.114971>
- Denevi, B. W., Blewett, D. T., Buczkowski, D. L., Capaccioni, F., Capria, M. T., De Sanctis, M. C., Garry, W. B., Gaskell, R. W., Le Corre, L., . . . Wyrick, D. (2012). Pitted Terrain on Vesta and Implications for the Presence of Volatiles. *Science*, 338(6104), 246–249. <https://doi.org/10.1126/science.1225374>
- Emery, J. P., Marzari, F., Morbidelli, A., French, L. M., & Grav, T. (2015). The Complex History of Trojan Asteroids. In P. Michel, F. E. DeMeo, & W. F. Bottke (Eds.),

- Asteroids IV*. University of Arizona Press. [https://doi.org/10.2458/azu\\_uapress\\_9780816532131-ch011](https://doi.org/10.2458/azu_uapress_9780816532131-ch011)
- Ernst, C. M., Barnouin, O. S., Daly, R. T., & the Small Body Mapping Tool Team. (2018). The Small Body Mapping Tool (SBMT) for Accessing, Visualizing, and Analyzing Spacecraft Data in Three Dimensions. *49th Lunar and Planetary Science Conference, The Woodlands, TX, USA, 19.-23. Mar. 2018, LPI Contrib. No. 2083*, #1043.
- Feierberg, M. A., Lebofsky, L. A., & Larson, H. P. (1981). Spectroscopic Evidence for Aqueous Alteration Products on the Surfaces of Low-albedo Asteroids. *Geochimica et Cosmochimica Acta*, *45*(6), 971–981. [https://doi.org/10.1016/0016-7037\(81\)90121-6](https://doi.org/10.1016/0016-7037(81)90121-6)
- Ferrari, F., & Tanga, P. (2020). The Role of Fragment Shapes in the Simulations of Asteroids as Gravitational Aggregates. *Icarus*, *350*, 113871. <https://doi.org/10.1016/j.icarus.2020.113871>
- Fornasier, S., Hasselmann, P. H., Barucci, M. A., Feller, C., Besse, S., Leyrat, C., Lara, L., Gutierrez, P. J., Ockay, N., ... Vincent, J.-B. (2015). Spectrophotometric Properties of the Nucleus of Comet 67P/Churyumov-Gerasimenko from the OSIRIS Instrument onboard the ROSETTA Spacecraft. *Astronomy & Astrophysics*, *583*, A30. <https://doi.org/10.1051/0004-6361/201525901>
- Fujiwara, A., Kawaguchi, J., Yeomans, D. K., Abe, M., Mukai, T., Okada, T., Saito, J., Yano, H., Yoshikawa, M., ... Uesugi, K. (2006). The Rubble-Pile Asteroid Itokawa as Observed by Hayabusa. *Science*, *312*(5778), 1330–1334. <https://doi.org/10.1126/science.1125841>
- Gaskell, R. W., Barnouin-Jha, O. S., Scheeres, D. J., Konopliv, A. S., Mukai, T., Abe, S., Saito, J., Ishiguro, M., Kubota, T., ... Demura, H. (2008). Characterizing and Navigating Small Bodies with Imaging Data. *Meteoritics & Planetary Science Archives*, *43*(6), 1049–1061.
- Greshake, A., & Fritz, J. (2018). Meteorites. In A. P. Rossi & S. van Gasselt (Eds.), *Planetary Geology* (pp. 103–121). Springer International Publishing. [https://doi.org/10.1007/978-3-319-65179-8\\_6](https://doi.org/10.1007/978-3-319-65179-8_6)
- Grott, M., Knollenberg, J., Hamm, M., Ogawa, K., Jaumann, R., Otto, K. A., Delbo, M., Michel, P., Biele, J., ... Moussi-Soffys, A. (2019). Low Thermal Conductivity Boulder with High Porosity Identified on C-type Asteroid (162173) Ryugu. *Nature Astronomy*, *3*(11), 971–976. <https://doi.org/10.1038/s41550-019-0832-x>
- Groussin, O., Jorda, L., Auger, A.-T., Kürt, E., Gaskell, R., Capanna, C., Scholten, F., Preusker, F., Lamy, P., ... Vincent, J.-B. (2015). Gravitational Slopes, Geo-



## 5 References

- morphology, and Material Strengths of the Nucleus of Comet 67P/Churyumov-Gerasimenko from OSIRIS Observations. *Astronomy & Astrophysics*, 583(A32), 1–12. <https://doi.org/10.1051/0004-6361/201526379>
- Grün, E., Bar-Nun, A., Benkhoff, J., Bischoff, A., Düren, H., Hellmann, H., Hesselbarth, P., Hsiung, P., Keller, H. U., ... Thiel, K. (1991). Laboratory Simulation of Cometary Processes: Results From First Kosi Experiments. In R. L. Newburn, M. Neugebauer, & J. Rahe (Eds.), *Comets in the Post-Halley Era* (pp. 277–297). Springer Netherlands. [https://doi.org/10.1007/978-94-011-3378-4\\_12](https://doi.org/10.1007/978-94-011-3378-4_12)
- Gwinner, K., Scholten, F., Spiegel, M., Schmidt, R., Giese, B., Oberst, J., Heipke, C., Jaumann, R., & Neukum, G. (2009). Derivation and Validation of High-resolution Digital Terrain Models from Mars Express HRSC Data. *Photogramm. Eng. Remote Sens*, 75(9), 1127–1142.
- Haack, D., Otto, K. A., Gundlach, B., Kreuzig, C., Bischoff, D., Kührt, E., & Blum, J. (2020). Tensile Strength of Dust-ice Mixtures and their Relevance as Cometary Analog Material. *Astronomy & Astrophysics*, 642, A218. <https://doi.org/10.1051/0004-6361/202037763>
- Haack, D., Lethuillier, A., Kreuzig, C., Feller, C., Gundlach, B., Pommerol, A., Blum, J., & Otto, K. A. (2021a). Sublimation of Ice-dust Mixtures in Cooled Vacuum Environments to Reproduce Cometary Morphologies. *Astronomy & Astrophysics*, 649, A35. <https://doi.org/10.1051/0004-6361/202140435>
- Haack, D., Kreuzig, C., Gundlach, B., Blum, J., & Otto, K. A. (2021b). Sublimation of Organic-rich Comet Analog Materials and their Relevance in Fracture Formation. *Astronomy & Astrophysics*, 653, A153. <https://doi.org/10.1051/0004-6361/202142069>
- Hapke, B. (2001). Space weathering from Mercury to the Asteroid Belt. *Journal of Geophysical Research: Planets*, 106(E5), 10039–10073. <https://doi.org/10.1029/2000JE001338>
- Hirabayashi, M., Sánchez, D. P., & Scheeres, D. J. (2015). Internal Structure of Asteroids Having Surface Shedding Due to Rotational Instability. *The Astrophysical Journal*, 808(1), 63. <https://doi.org/10.1088/0004-637X/808/1/63>
- Ho, T.-M., Jaumann, R., Bibring, J.-P., Grott, M., Glaßmeier, K.-H., Moussi, A., Krause, C., Auster, U., Baturkin, V., ... Ziach, C. (2021). The MASCOT Lander Aboard Hayabusa2: The in-situ Exploration of NEA (162173) Ryugu. *Planetary and Space Science*, 200. <https://doi.org/10.1016/j.pss.2021.105200>
- Jaumann, R., Schmitz, N., Koncz, A., Michaelis, H., Schroeder, S. E., Mottola, S., Trauthan, F., Hoffmann, H., Roatsch, T., ... Yabuta, H. (2017). The Camera

- of the MASCOT Asteroid Lander on Board Hayabusa2. *Space Science Reviews*, 208(1–4), 375–400. <https://doi.org/10.1007/s11214-016-0263-2>
- Jaumann, R., Schmitz, N., Ho, T.-M., Schröder, S. E., Otto, K. A., Stephan, K., Elgner, S., Krohn, K., Preusker, F., ... Kouyama, T. (2019). Images from the surface of asteroid Ryugu show rocks similar to carbonaceous chondrite meteorites. *Science*, 365(6455), 817–820. <https://doi.org/10.1126/science.aaw8627>
- Kappel, D., Sachse, M., Haack, D., & Otto, K. A. (2020). Discrete Element Modeling of Boulder and Cliff Morphologies on Comet 67P/Churyumov-Gerasimenko. *Astronomy & Astrophysics*, 641(A19), 1–22. <https://doi.org/10.1051/0004-6361/201937152>
- Kaufmann, E., & Hagermann, A. (2018). Constraining the Parameter Space of Comet Simulation Experiments. *Icarus*, 311, 105–112. <https://doi.org/10.1016/j.icarus.2018.03.025>
- Keller, H. U., Kramm, R., & Thomas, N. (1988). Surface Features on the Nucleus of Comet Halley. *Nature*, 331(6153), 227–231. <https://doi.org/10.1038/331227a0>
- Keller, H. U., Mottola, S., Hviid, S. F., Agarwal, J., Kührt, E., Skorov, Y., Otto, K. A., Vincent, J.-B., Oklay, N., ... Thomas, N. (2017). Seasonal Mass Transfer on the Nucleus of Comet 67P/Churyumov-Gerasimenko. *Monthly Notices of the Royal Astronomical Society*, 469(Suppl\_2), S357–S371. <https://doi.org/10.1093/mnras/stx1726>
- Kleinhans, M. G., Markies, H., Vet, S. J. d., Veld, A. C. i. ', & Postema, F. N. (2011). Static and Dynamic Angles of Repose in Loose Granular Materials under Reduced Gravity. *Journal of Geophysical Research*, 116(E11), E11004. <https://doi.org/10.1029/2011JE003865>
- Kohnert, F., Otto, K. A., Jaumann, R., Krohn, K., Kersten, E., Preusker, F., Roatsch, T., Raymond, C. A., & Russell, C. T. (2016). Mobility of Landslides on Asteroid Vesta. *79th Annual Meeting of the Meteoritical Society; Berlin, Germany, 7.-12. Aug. 2016*, 79, 6465. <http://www.metsoc-berlin.de/>
- Kreuzig, C., Kargl, G., Pommerol, A., Knollenberg, J., Lethuillier, A., Molinski, N. S., Gilke, T., Bischoff, D., Feller, C., ... Blum, J. (2021). The CoPhyLab Comet-simulation Chamber. *Review of Scientific Instruments*, 92(11), 115102. <https://doi.org/10.1063/5.0057030>
- Küppers, M., O'Rourke, L., Bockelée-Morvan, D., Zakharov, V., Lee, S., von Allmen, P., Carry, B., Teyssier, D., Marston, A., ... Moreno, R. (2014). Localized Sources of Water Vapour on the Dwarf Planet (1) Ceres. *Nature*, 505(7484), 525–527. <https://doi.org/10.1038/nature12918>

## 5 References

- Kuramoto, K., Kawakatsu, Y., Fujimoto, M., Araya, A., Barucci, M. A., Genda, H., Hirata, N., Ikeda, H., Imamura, T., . . . Yokota, S. (2022). Martian Moons Exploration MMX: Sample Return Mission to Phobos Elucidating Formation Processes of Habitable Planets. *Earth, Planets and Space*, *74*(1), 12. <https://doi.org/10.1186/s40623-021-01545-7>
- Lamy, P. L., Toth, I., Davidsson, B. J. R., Groussin, O., Gutiérrez, P., Jorda, L., Kaasalainen, M., & Lowry, S. C. (2007). A Portrait of the Nucleus of Comet 67P/Churyumov-Gerasimenko. *Space Science Reviews*, *128*(1), 23–66. <https://doi.org/10.1007/s11214-007-9146-x>
- Lange, C., Yoshimitsu, T., Ulamec, S., Düvel, C., & Ho, T.-M. (2020). Micro- and Nanolander on the Surface of Ryugu - Commonalities, Differences and Lessons Learned for Future Microgravity Exploration. *Planetary and Space Science*, *194*, 105094. <https://doi.org/10.1016/j.pss.2020.105094>
- Lara, L. M., Lowry, S., Vincent, J.-B., Gutiérrez, P. J., Rožek, A., Forgia, F. L., Oklay, N., Sierks, H., Barbieri, C., . . . Tubiana, C. (2015). Large-scale Dust Jets in the Coma of 67P/Churyumov-Gerasimenko as Seen by the OSIRIS Instrument onboard Rosetta. *Astronomy & Astrophysics*, *583*(A9), 1–11. <https://doi.org/10.1051/0004-6361/201526103>
- Lauretta, D. S., Hergenrother, C. W., Chesley, S. R., Leonard, J. M., Pelgrift, J. Y., Adam, C. D., Asad, M. A., Antreasian, P. G., Ballouz, R.-L., . . . Wolner, C. W. V. (2019b). Episodes of Particle Ejection from the Surface of the Active Asteroid (101955) Bennu. *Science*, *366*(6470). <https://doi.org/10.1126/science.aay3544>
- Lauretta, D. S., DellaGiustina, D. N., Bennett, C. A., Golish, D. R., Becker, K. J., Balram-Knutson, S. S., Barnouin, O. S., Becker, T. L., Bottke, W. F., . . . Wolner, C. W. V. (2019a). The Unexpected Surface of Asteroid (101955) Bennu. *Nature*, *568*(7750), 55. <https://doi.org/10.1038/s41586-019-1033-6>
- Levison, H. F. (1996). Comet Taxonomy. In T. W. Rettig & J. M. Hahn (Eds.), *Completing the Inventory of the Solar System, Astronomical Society of the Pacific Conference Proceedings* (pp. 173–191).
- Maurel, C., Michel, P., Biele, J., Ballouz, R.-L., & Thuillet, F. (2018). Numerical Simulations of the Contact between the Lander MASCOT and a Regolith-covered Surface. *Advances in Space Research*, *62*(8), 2099–2124. <https://doi.org/10.1016/j.asr.2017.05.029>
- Michalik, T., Matz, K.-D., Schröder, S., Jaumann, R., Stephan, K., Krohn, K., Preusker, F., Raymond, C., Russell, C., & Otto, K. A. (2021). The Unique Spectral and Geomorphological Characteristics of Pitted Impact Deposits Associated with Mar-

- cia Crater on Vesta. *Icarus*, 369, 114633. <https://doi.org/10.1016/j.icarus.2021.114633>
- Michel, P., Küppers, M., Bagatin, A. C., Carry, B., Charnoz, S., Leon, J. d., Fitzsimmons, A., Gordo, P., Green, S. F., ... Carnelli, I. (2022). The ESA Hera Mission: Detailed Characterization of the DART Impact Outcome and of the Binary Asteroid (65803) Didymos. *The Planetary Science Journal*, 3(7), 160. <https://doi.org/10.3847/PSJ/ac6f52>
- Mimasu, Y., Kikuchi, S., Takei, Y., Saiki, T., Watanabe, S.-i., Tanaka, S., Hirabayashi, M., Sakatani, N., Kouyama, T., ... Tsuda, Y. (2022). Extended Mission of Hayabusa2. In M. Hirabayashi & Y. Tsuda (Eds.), *Hayabusa2 Asteroid Sample Return Mission* (pp. 557–571). Elsevier. <https://doi.org/10.1016/B978-0-323-99731-7.00027-1>
- Mottola, S., Arnold, G., Grothues, H.-G., Jaumann, R., Michaelis, H., Neukum, G., Bibring, J.-P., Schröder, S. E., Hamm, M., ... Dolives, B. (2015). The Structure of the Regolith on 67P/Churyumov-Gerasimenko from ROLIS Descent Imaging. *Science*, 349(6247), aab0232. <https://doi.org/10.1126/science.aab0232>
- Mottola, S., Arnold, G., Grothues, H.-G., Jaumann, R., Michaelis, H., Neukum, G., & Bibring, J.-P. (2007). The Rolis Experiment on the Rosetta Lander. *Space Science Reviews*, 128(1), 241–255. <https://doi.org/10.1007/s11214-006-9004-2>
- Murdoch, N., Drilleau, M., Sunday, C., Thuillet, F., Wilhelm, A., Nguyen, G., & Gourinat, Y. (2021). Low-velocity Impacts into Granular Material: Application to Small-body Landing. *Monthly Notices of the Royal Astronomical Society*, 503(3), 3460–3471. <https://doi.org/10.1093/mnras/stab624>
- Nakashima, H., Shioji, Y., Kobayashi, T., Aoki, S., Shimizu, H., Miyasaka, J., & Ohdoi, K. (2011). Determining the Angle of Repose of Sand under Low-gravity Conditions Using Discrete Element Method. *Journal of Terramechanics*, 48(1), 17–26. <https://doi.org/10.1016/j.jterra.2010.09.002>
- Otto, K. A., Ho, T.-M., Ulamec, S., Bibring, J.-P., Biele, J., Grott, M., Hamm, M., Hercik, D., Jaumann, R., ... Yabuta, H. (2023). MASCOT's in Situ Analysis of Asteroid Ryugu in the Context of Regolith Samples and Remote Sensing Data Returned by Hayabusa2. *Earth, Planets and Space*, 75(51), 1–16. <https://doi.org/10.1186/s40623-023-01805-8>
- Otto, K. A., Jaumann, R., Krohn, K., Matz, K.-D., Preusker, F., Roatsch, T., Schenk, P., Scholten, F., Stephan, K., ... Russell, C. T. (2013). Mass-wasting Features and Processes in Vesta's South Polar Basin Rheasilvia. *Journal of Geophysical Research: Planets*, 118(11), 1–16. <https://doi.org/10.1002/2013JE004333>



## 5 References

- Otto, K. A., Tirsch, D., Mottola, S., Hviid, S., Jaumann, R., Keller, H. U., Knollenberg, J., Kührt, E., Michaelis, H., . . . Sierks, H. (2017a). Distribution and Orientation of Aeolian-like Wind-tails on Comet 67P/Churyumov-Gerasimenko. *Asteroids, Comets, Meteors; Montevideo, Uruguay, 10.-14. Apr. 2017*.
- Otto, K. A., Tirsch, D., Mottola, S., Matz, K.-D., Hviid, S., Jaumann, R., Keller, H. U., Kührt, E., Schröder, S., . . . the OSIRIS Team. (2017b). The Evolution of Aeolian-Like Morphologies on Comet 67P Churyumov-Gerasimenko. *11th European Planetary Science Congress; Riga, Lettland, 17.-22. Sep. 2017, #233233*.
- Otto, K. A., Marchi, S., Trowbridge, A., Melosh, H. J., & Sizemore, H. G. (2019). Ceres Crater Degradation Inferred from Concentric Fracturing. *Journal of Geophysical Research: Planets*, *124*(0), 1–16. <https://doi.org/10.1029/2018JE005660>
- Otto, K. A., Matz, K.-D., Schröder, S. E., Parekh, R., Krohn, K., Honda, R., Kameda, S., Jaumann, R., Schmitz, N., . . . Yoshioka, K. (2021a). Surface Roughness of Asteroid (162173) Ryugu and Comet 67P/Churyumov-Gerasimenko Inferred from in Situ Observations. *Monthly Notices of the Royal Astronomical Society*, *500*(3), 3178–3193. <https://doi.org/10.1093/mnras/staa3314>
- Otto, K. A., Schröder, S. E., Scharf, H. D., Greshake, A., Schmitz, N., Trauthan, F., Pieth, S., Stephan, K., Ho, T.-M., . . . Yabuta, H. (2021b). Spectral and Petrographic Properties of Inclusions in Carbonaceous Chondrites and Comparison with In Situ Images from Asteroid Ryugu. *The Planetary Science Journal*, *2*(5), 188. <https://doi.org/10.3847/PSJ/ac034b>
- Ozaki, N., Yamamoto, T., Gonzalez-Franquesa, F., Gutierrez-Ramon, R., Pushparaj, N., Chikazawa, T., Tos, D. A. D., Çelik, O., Marmo, N., . . . Takashima, T. (2022). Mission Design of DESTINY+: Toward Active Asteroid (3200) Phaethon and Multiple Small Bodies. *Acta Astronautica*, *196*, 42–56. <https://doi.org/10.1016/j.actaastro.2022.03.029>
- Parekh, R., Otto, K. A., Jaumann, R., Matz, K. D., Roatsch, T., Kersten, E., Elgner, S., & Raymond, C. A. (2021a). Influence of Volatiles on Mass Wasting Processes on Vesta and Ceres. *Journal of Geophysical Research: Planets*, *126*(3), e2020JE006573. <https://doi.org/https://doi.org/10.1029/2020JE006573>
- Parekh, R., Otto, K. A., Matz, K. D., Jaumann, R., Krohn, K., Roatsch, T., Kersten, E., Elgner, S., Russell, C. T., & Raymond, C. A. (2021b). Formation of Ejecta and Dust Pond Deposits on Asteroid Vesta. *Journal of Geophysical Research: Planets*, *126*(11), e2021JE006873. <https://doi.org/10.1029/2021JE006873>
- Perna, D., Dotto, E., Ieva, S., Barucci, M. A., Bernardi, F., Fornasier, S., Luise, F. D., Perozzi, E., Rossi, A., . . . Deshapriya, J. D. P. (2015). Grasping the Nature of

- Potentially Hazardous Asteroids. *The Astronomical Journal*, 151(1), 11. <https://doi.org/10.3847/0004-6256/151/1/11>
- Pieters, C. M., & Noble, S. K. (2016). Space Weathering on Airless Bodies. *Journal of Geophysical Research: Planets*, 121(10), 1865–1884. <https://doi.org/10.1002/2016JE005128>
- Pommerol, A., Jost, B., Poch, O., El-Maarry, M. R., Vuitel, B., & Thomas, N. (2015). The SCITEAS Experiment: Optical Characterizations of Sublimating Icy Planetary Analogues. *Planetary and Space Science*, 109–110, 106–122. <https://doi.org/10.1016/j.pss.2015.02.004>
- Preusker, F., Scholten, F., Matz, K.-D., Roatsch, T., Willner, K., Hviid, S. F., Knollenberg, J., Jorda, L., Gutiérrez, P. J., ... Vincent, J.-B. (2015). Shape Model, Reference System Definition, and Cartographic Mapping Standards for Comet 67P/Churyumov-Gerasimenko - Stereo-photogrammetric Analysis of Rosetta/OSIRIS Image Data. *Astronomy & Astrophysics*, 583(A33), 1–19. <https://doi.org/10.1051/0004-6361/201526349>
- Preusker, F., Scholten, F., Matz, K.-D., Roatsch, T., Hviid, S. F., Mottola, S., Knollenberg, J., Kührt, E., Pajola, M., ... Tubiana, C. (2017). The Global Meter-level Shape Model of Comet 67P/Churyumov-Gerasimenko. *Astronomy & Astrophysics*, 607(L1), 1–5. <https://doi.org/10.1051/0004-6361/201731798>
- Preusker, F., Scholten, F., Elgner, S., Matz, K.-D., Kameda, S., Roatsch, T., Jaumann, R., Sugita, S., Honda, R., ... Kouyama, T. (2019). The MASCOT Landing Area on Asteroid (162173) Ryugu: Stereo-photogrammetric Analysis Using Images of the ONC Onboard the Hayabusa2 Spacecraft. *Astronomy & Astrophysics*, 632(L4), 1–6. <https://doi.org/10.1051/0004-6361/201936759>
- Rayman, M. D. (2020). Lessons from the Dawn mission to Ceres and Vesta. *Acta Astronautica*, 176, 233–237. <https://doi.org/10.1016/j.actaastro.2020.06.023>
- Raymond, C. A., Jaumann, R., Nathues, A., Sierks, H., Roatsch, T., Preusker, F., Scholten, F., Gaskell, R. W., Jorda, L., ... Mottola, S. (2011). The Dawn Topography Investigation. *Space Science Reviews*, 163(1–4), 487–510. <https://doi.org/10.1007/s11214-011-9863-z>
- Reddy, V., Nathues, A., Le Corre, L., Sierks, H., Li, J.-Y., Gaskell, R., McCoy, T., Beck, A. W., Schroder, S. E., ... Russell, C. (2012). Color and Albedo Heterogeneity of Vesta from Dawn. *Science*, 336(6082), 700–704. <https://doi.org/10.1126/science.1219088>
- Rivkin, A. S., & Emery, J. P. (2010). Detection of Ice and Organics on an Asteroidal Surface. *Nature*, 464(7293), 1322–1323. <https://doi.org/10.1038/nature09028>

## 5 References

- Roatsch, T., Kersten, E., Matz, K.-D., Preusker, F., Scholten, F., Jaumann, R., Raymond, C. A., & Russell, C. T. (2012). High Resolution Vesta High Altitude Mapping Orbit (HAMO) Atlas Derived from Dawn Framing Camera Images. *Planetary and Space Science*, *73*(1), 283–286. <https://doi.org/10.1016/j.pss.2012.08.021>
- Roatsch, T., Kersten, E., Matz, K.-D., Preusker, F., Scholten, F., Elgner, S., Jaumann, R., Raymond, C. A., & Russell, C. T. (2013). High-resolution Vesta Low Altitude Mapping Orbit Atlas Derived from Dawn Framing Camera Images. *Planetary and Space Science*, *85*, 293–298. <https://doi.org/10.1016/j.pss.2013.06.024>
- Ruesch, O., Platz, T., Schenk, P., McFadden, L. A., Castillo-Rogez, J. C., Quick, L. C., Byrne, S., Preusker, F., O'Brien, D. P., ... Russell, C. T. (2016). Cryovolcanism on Ceres. *Science*, *353*(6303), aaf4286. <https://doi.org/10.1126/science.aaf4286>
- Russell, C., Coradini, A., Christensen, U., De Sanctis, M. C., Feldman, W. C., Jaumann, R., Keller, H. U., Konopliv, A. S., McCord, T. B., ... Zuber, M. T. (2004). Dawn: A journey in space and time. *Planetary and Space Science*, *52*(5-6), 465–489. <https://doi.org/10.1016/j.pss.2003.06.013>
- Sachse, M., Kappel, D., Tirsch, D., & Otto, K. A. (2022). Discrete Element Modeling of Aeolian-like Morphologies on Comet 67P/Churyumov-Gerasimenko. *Astronomy & Astrophysics*, *662*(A2), 1–15. <https://doi.org/10.1051/0004-6361/202141296>
- Sakatani, N., Tanaka, S., Okada, T., Fukuhara, T., Riu, L., Sugita, S., Honda, R., Morota, T., Kameda, S., ... Tsuda, Y. (2021). Anomalously Porous Boulders on (162173) Ryugu as Primordial Materials from its Parent Body. *Nature Astronomy*, *5*(88), 766–774. <https://doi.org/10.1038/s41550-021-01371-7>
- Schmidt, B. E., Hughson, K. H. G., Chilton, H. T., Scully, J. E. C., Platz, T., Nathues, A., Sizemore, H., Bland, M. T., Byrne, S., ... Raymond, C. A. (2017). Geomorphological Evidence for Ground Ice on Dwarf Planet Ceres. *Nature Geoscience*, *10*(5), 338–343. <https://doi.org/10.1038/ngeo2936>
- Scholten, F., Preusker, F., Elgner, S., Matz, K.-D., Jaumann, R., Hamm, M., Schröder, S. E., Koncz, A., Schmitz, N., ... Sugita, S. (2019). The Hayabusa2 Lander MASCOT on the Surface of Asteroid (162173) Ryugu - Stereo-photogrammetric Analysis of MASCam Image Data. *Astronomy & Astrophysics*, *632*(L5), 1–6. <https://doi.org/10.1051/0004-6361/201936760>
- Schröder, S. E., Mottola, S., Keller, H. U., Raymond, C. A., & Russell, C. T. (2013a). Resolved Photometry of Vesta Reveals Physical Properties of Crater Regolith. *Planetary and Space Science*, *85*, 198–213. <https://doi.org/10.1016/j.pss.2013.06.009>

- Schröder, S. E., Maue, T., Gutiérrez Marqués, P., Mottola, S., Aye, K. M., Sierks, H., Keller, H. U., & Nathues, A. (2013b). In-flight Calibration of the Dawn Framing Camera. *Icarus*, *226*(2), 1304–1317. <https://doi.org/10.1016/j.icarus.2013.07.036>
- Schröder, S. E., Mottola, S., Arnold, G., Grothues, H.-G., Jaumann, R., Keller, H. U., Michaelis, H., Bibring, J.-P., Pelivan, I., . . . Dolives, B. (2017a). Close-up Images of the Final Philae Landing Site on Comet 67P/Churyumov-Gerasimenko Acquired by the ROLIS Camera. *Icarus*, *285*, 263–274. <https://doi.org/10.1016/j.icarus.2016.12.009>
- Schröder, S. E., Mottola, S., Carsenty, U., Ciarniello, M., Jaumann, R., Li, J.-Y., Longobardo, A., Palmer, E., Pieters, C., . . . Russell, C. (2017b). Resolved Spectrophotometric Properties of the Ceres Surface from Dawn Framing Camera Images. *Icarus*, *288*, 201–225. <https://doi.org/10.1016/j.icarus.2017.01.026>
- Schröder, S. E., Otto, K. A., Scharf, H., Matz, K.-D., Schmitz, N., Scholten, F., Mottola, S., Trauthan, F., Koncz, A., . . . Sugita, S. (2021). Spectrophotometric Analysis of the Ryugu Rock Seen by MASCOT: Searching for a Carbonaceous Chondrite Analog. *The Planetary Science Journal*, *2*(2), 58. <https://doi.org/10.3847/PSJ/abbb97>
- Scully, J. E. C., Russell, C. T., Yin, A., Jaumann, R., Carey, E., Castillo-Rogez, J., McSween, H. Y., Raymond, C. A., Reddy, V., & Le Corre, L. (2015). Geomorphological Evidence for Transient Water Flow on Vesta. *Earth and Planetary Science Letters*, *411*, 151–163. <https://doi.org/10.1016/j.epsl.2014.12.004>
- Scully, J. E. C., Bowling, T., Bu, C., Buczkowski, D. L., Longobardo, A., Nathues, A., Neesemann, A., Palomba, E., Quick, L. C., . . . Jaumann, R. (2019). Synthesis of the Special Issue: The Formation and Evolution of Ceres' Occator Crater. *Icarus*, *320*, 213–225. <https://doi.org/10.1016/j.icarus.2018.08.029>
- Sierks, H., Barbieri, C., Lamy, P. L., Rodrigo, R., Koschny, D., Rickman, H., Keller, H. U., Agarwal, J., A'Hearn, M. F., . . . Pätzold, M. (2015). On the Nucleus Structure and Activity of Comet 67P/Churyumov-Gerasimenko. *Science*, *347*(6220), aaa1044. <https://doi.org/10.1126/science.aaa1044>
- Sizemore, H. G., Schmidt, B. E., Buczkowski, D. A., Sori, M. M., Castillo-Rogez, J. C., Berman, D. C., Ahrens, C., Chilton, H. T., Hughson, K. H. G., . . . Raymond, C. A. (2019). A Global Inventory of Ice-Related Morphological Features on Dwarf Planet Ceres: Implications for the Evolution and Current State of the Cryosphere. *Journal of Geophysical Research: Planets*, *124*(7), 1650–1689. <https://doi.org/10.1029/2018JE005699>



## 5 References

- Stooke, P. J. (1998). Mapping Worlds with Irregular Shapes. *42*, 61–78. <https://doi.org/10.1111/j.1541-0064.1998.tb01553.x>
- Sugita, S., Honda, R., Morota, T., Kameda, S., Sawada, H., Tatsumi, E., Yamada, M., Honda, C., Yokota, Y., ... Tsuda, Y. (2019). The Geomorphology, Color, and Thermal Properties of Ryugu: Implications for Parent-body Processes. *Science*, *364*(6437), 1–11. <https://doi.org/10.1126/science.aaw0422>
- Sunday, C., Murdoch, N., Wilhelm, A., Drilleau, M., Zhang, Y., Tardivel, S., & Michel, P. (2022). The Influence of Gravity on Granular Impacts - II. A Gravity-scaled Collision Model for Slow Interactions. *Astronomy & Astrophysics*, *658*, A118. <https://doi.org/10.1051/0004-6361/202142098>
- Sunday, C., Zhang, Y., Thuillet, F., Tardivel, S., Michel, P., & Murdoch, N. (2021). The Influence of Gravity on Granular Impacts - I. A DEM Code Performance Comparison. *Astronomy & Astrophysics*, *656*, A97. <https://doi.org/10.1051/0004-6361/202141412>
- Tancredi, G., Maciel, A., Heredia, L., Richeri, P., & Nesmachnow, S. (2012). Granular Physics in Low-gravity Environments Using Discrete Element Method. *Monthly Notices of the Royal Astronomical Society*, *420*(4), 3368–3380. <https://doi.org/10.1111/j.1365-2966.2011.20259.x>
- Tatsumi, E., Kouyama, T., Suzuki, H., Yamada, M., Sakatani, N., Kameda, S., Yokota, Y., Honda, R., Morota, T., ... Sugita, S. (2019). Updated Inflight Calibration of Hayabusa2's Optical Navigation Camera (ONC) for Scientific Observations during the Cruise Phase. *Icarus*, *325*, 153–195. <https://doi.org/10.1016/j.icarus.2019.01.015>
- Taylor, M. G. G. T., Altobelli, N., Buratti, B. J., & Choukroun, M. (2017). The Rosetta Mission Orbiter Science Overview: The Comet Phase. *Philosophical Transactions of the Royal Society A: Mathematical, Physical and Engineering Sciences*, *375*(2097), 20160262. <https://doi.org/10.1098/rsta.2016.0262>
- Tholen, D. J. (1989). Asteroid Taxonomic Classifications. *Asteroids II, Proceedings of the Conference; Tucson, AZ, USA, 08.-11. Mar. 1988*, 1139–1150. <http://adsabs.harvard.edu/abs/1989aste.conf.1139T>
- Thomas, N., Sierks, H., Barbieri, C., Lamy, P. L., Rodrigo, R., Rickman, H., Koschny, D., Keller, H. U., Agarwal, J., ... Wenzel, K.-P. (2015). The Morphological Diversity of Comet 67P/Churyumov-Gerasimenko. *Science*, *347*(6220), aaa0440-1–6. <https://doi.org/10.1126/science.aaa0440>
- Thuillet, F., Michel, P., Tachibana, S., Ballouz, R.-L., & Schwartz, S. R. (2020). Numerical Modelling of Medium-speed Impacts on a Granular Surface in a Low-gravity

- Environment Application to Hayabusa2 Sampling Mechanism. *Monthly Notices of the Royal Astronomical Society*, 491(1), 153–177. <https://doi.org/10.1093/mnras/stz3010>
- Thuillet, F., Zhang, Y., Michel, P., Biele, J., Kameda, S., Sugita, S., Tatsumi, E., Schwartz, S. R., & Ballouz, R.-L. (2021). Numerical Modeling of Lander Interaction with a Low-gravity Asteroid Regolith Surface - II. Interpreting the Successful Landing of Hayabusa2 MASCOT. *Astronomy & Astrophysics*, 648, A56. <https://doi.org/10.1051/0004-6361/201936128>
- Tubiana, C., Güttler, C., Kovacs, G., Bertini, I., Bodewits, D., Fornasier, S., Lara, L., Forgia, F. L., Magrin, S., . . . Vincent, J.-B. (2015). Scientific Assessment of the Quality of OSIRIS Images. *Astronomy & Astrophysics*, 583, A46. <https://doi.org/10.1051/0004-6361/201525985>
- van Gasselt, S., & Nass, A. (2011). Planetary Mapping - The Datamodel's Perspective and GIS Framework. *Planetary and Space Science*, 59(11), 1231–1242. <https://doi.org/10.1016/j.pss.2010.09.012>
- Veverka, J., Robinson, M., Thomas, P., Murchie, S., Bell III, J. F., Izenberg, N., Chapman, C., Harch, A., Bell, M., . . . Yeomans, D. K. (2000). NEAR at Eros: Imaging and Spectral Results. *Science*, 289(5487), 2088–2097. <https://doi.org/10.1126/science.289.5487.2088>
- Vincent, J.-B., Farnham, T., Kührt, E., Skorov, Y., Marschall, R., Oklay, N., El-Maarry, M. R., & Keller, H. U. (2019). Local Manifestations of Cometary Activity. *Space Science Reviews*, 215(4), 30. <https://doi.org/10.1007/s11214-019-0596-8>
- Wada, K., Senshu, H., & Matsui, T. (2006). Numerical Simulation of Impact Cratering on Granular Material. *Icarus*, 180(2), 528–545. <https://doi.org/10.1016/j.icarus.2005.10.002>
- Watanabe, S., Hirabayashi, M., Hirata, N., Hirata, N., Noguchi, R., Shimaki, Y., Ikeda, H., Tatsumi, E., Yoshikawa, M., . . . Tsuda, Y. (2019). Hayabusa2 Arrives at the Carbonaceous Asteroid 162173 Ryugu - A spinning top-shaped rubble pile. *Science*, 364(6437), 268–272. <https://doi.org/10.1126/science.aav8032>
- Yada, T., Abe, M., Okada, T., Nakato, A., Yogata, K., Miyazaki, A., Hatakeda, K., Kumagai, K., Nishimura, M., . . . Tsuda, Y. (2022). Preliminary Analysis of the Hayabusa2 Samples Returned from C-type Asteroid Ryugu. *Nature Astronomy*, 6(22), 214–220. <https://doi.org/10.1038/s41550-021-01550-6>



## 6 Acknowledgments

My deepest gratitude goes to the members of my junior research group at DLR without whom this thesis would not have been written: Tanja, David H., Rutu, David K. and Manuel. Thank you for the stimulating working atmosphere. You made this group a huge success and it was always fun working with you. I look back very fondly on the time we worked together.

I would also like to express my deepest gratitude to Prof. Ralf Jaumann, who encouraged me to write this thesis. I deeply appreciate all the support you gave me throughout my career. I feel very lucky to have had such a great mentor. Thanks also to Prof. Frank Postberg at Freie Universität Berlin for initiating the habilitation process and taking me under his wing.

I would like to thank my colleagues at DLR, who supported me and the group in many ways. Working with you was, and is, a great pleasure.

Last but not least, many thanks to my family, Jon and Tristan, for a loving and supportive home.